Plasmonic Optical Metasurfaces for Passive and Active Wavefront Shaping

Deng, Yadong

Go to publication entry in University of Southern Denmark's Research Portal

![SDU logo](University of Southern Denmark logo)

University of Southern Denmark

PhD Thesis

Plasmonic Optical Metasurfaces for Passive and Active Wavefront Shaping

Author:

Yadong Deng

Supervisors:

Associate Professor: Fei Ding

Professor: Sergey I. Bozhevolnyi

A thesis submitted in partial fulfillment of the requirements

for the degree of Doctor of Philosophy (PhD)

at the

Centre for Nano Optics

Mads Clausen Institute

University of Southern Denmark

August 2024, Odense, Denmark

Plasmonic Optical Metasurfaces for Passive and Active Wavefront Shaping

Abstract (English)

Metasurfaces, ultrathin surfaces engineered at the nanoscale with artificial nanostructures, have fundamentally revolutionized optical wavefront manipulation by providing superior and precise control over light properties, such as polarization, amplitude, and phase. This innovation has facilitated the development of miniaturized and highly performant photonic systems, driving significant advancements in energy, sensing, imaging, and computing through novel light-matter interactions, thereby showing promise in supplanting traditional bulky optics used for wavefront control. The advanced and refined micro- and nano-fabrication techniques render metasurfaces exceptionally well-suited for integration with a wide range of nanotechnology platforms, unlocking substantial potential for the creation of state-of-the-art optical devices. Building on the foundation of these passive metasurfaces characterized by well-defined optical responses set during fabrication, the integration of active control mechanisms promises to further revolutionize these structures, transforming them into versatile components for reconfigurable and adaptive optical networks and systems, and substantially enhancing their functionality and application potential. Furthermore, the pursuit of extremely fast responses among these dynamic control mechanisms enables real-time and flexible control of light, potentially improving the performance and adaptability of optical systems in applications such as high-speed communications, adaptive optics, and rapid sensing technologies.

In this thesis, I first review recent advancements in metasurface-based wavefront shaping, focusing on both passive and active methodologies and their applications in optical waveplates, beam steering, metalenses, as well as dynamic chirality and polarization control, providing an overview of the cutting-edge developments in this swiftly advancing field. Following this, I present the key theoretical concepts and analytical methods employed in this thesis, including the fundamental principles of polarization states and their mathematical representations, three common phase control techniques, the numerical simulation method, the detailed sample fabrication process, as well as the characterization setup. Then I present an account of passive wavefront shaping using gap-surface plasmon metasurfaces, detailing our research works on optical waveplates, beam steering, and metalenses. Lastly, transitioning from passive to active metasurfaces, I highlight our pioneering dynamic platform developed through the integration of metasurfaces with piezoelectric thin-film PZT microelectromechanical systems. Two research projects based on this platform are introduced in detail: dynamic linear polarizers and applications, as well as non-Hermitian metasurfaces for tunable topological phase transitions. In summary, this thesis centers on wavefront shaping through both passive and active approaches to develop ultra-thin and compact optical metasurface devices, laying a solid foundation for a diverse array of industrial applications.

Resumé (Dansk)

Metaflader, ultratynde overflader konstrueret i nanoskalamed kunstige nanostrukturer, har fundamentalt revolutioneret manipulationen af optiske bølgefronter ved at give overlegen og præcis kontrol over lys egenskaber som polarisering, amplitude og fase. Denne innovation har muliggjort udviklingen af miniaturiserede og højtydende fotoniske systemer, hvilket har drevet betydelige fremskridt inden for energi, sensing, billeddannelse og computing gennem nye lys-materie-interaktioner og dermed vist potentiale til at erstatte traditionelle voluminøse optiske komponenter, der anvendes til bølgefrontkontrol. De avancerede og raffinerede mikro- og nanofabrikations teknikker gør metaflader særdeles velegnede til integration med en bred vifte af nanoteknologiplatforme, hvilket åbner betydelige muligheder for skabelsen af avancerede optiske enheder. Bygger videre på grundlaget af disse passive metaflader, kendetegnet ved veldefinerede optiske egenskaber fastlagt under fabrikationen, lover integrationen af aktive kontrolmekanismer at revolutionere disse strukturer yderligere, hvilket vil omdanne dem til alsidige komponenter for rekonfigurerbare og adaptive optiske netværk og systemer samt markant forbedre deres funktionalitet og anvendelses potentiale. Desuden muliggør jagten på ekstremt hurtige reaktioner blandt disse dynamiske kontrolmekanismer realtids- og fleksibel kontrol af lys, hvilket potentielt kan forbedre ydeevnen og tilpasningsevnen af optiske systemer i applikationer som højhastighedskommunikation, adaptive optikker og hurtige sensingteknologier.

I denne afhandling gennemgår jeg først de seneste fremskridt inden for metasurface-baseret bølgefrontformning, med fokus på både passive og aktive metoder og deres anvendelser i optiske bølgeplader, stråleafbøjning, metalinser samt dynamisk chiralitet og polarisationskontrol, og giver et overblik over de nyeste udviklinger inden for dette hastigt fremskridende felt. Derefter præsenterer jeg de centrale teoretiske begreber og analytiske metoder, der anvendes i denne afhandling, herunder de grundlæggende principper for polarisations tilstande og deres matematiske repræsentationer, tre almindelige fasekontrolteknikker, den numeriske simuleringsmetode, den detaljerede prøvefabrikations proces samt opsætningen til karakterisering. Dernæst præsenterer jeg en redegørelse for passiv bølgefrontformning ved brug af gap-overflade plasmon metasurfaces og beskriver vores forskningsarbejde inden for optiske bølgeplader, stråleafbøjning og metalinser. Endelig, ved at overgå fra passive til aktive metasurfaces, fremhæver jeg vores banebrydende dynamiske platform udviklet gennem integration af metasurfaces med piezoelektriske tyndfilm PZT mikromekaniske systemer. To forskningsprojekter baseret på denne platform introduceres i detaljer: dynamiske lineære polarisatorer og deres anvendelser, samt ikke-Hermitiske metasurfaces til justerbare topologiske faseovergange. Sammenfattende fokuserer denne afhandling på bølgefrontformning gennem både passive og aktive tilgange for at udvikle ultratynde og kompakte optiske metasurface-enheder og lægger dermed et solidt fundament for en bred vifte af industrielle anvendelser.

Acknowledgements

Odense, Denmark

08/2024

Yadong Deng

Yadong Deng

List of publications

†These authors contributed equally to this work.

Journal publications included in this thesis:

1. **Spin-controlled gap-surface plasmon metalenses for focused scalar and vector beam generation**
   Y. Deng, C. Meng, S. I. Sande, S. I. Bozhevolnyi, and F. Ding
   To be submitted (2024)

2. **MEMS-Integrated metasurfaces for dynamic linear polarizers**
   Y. Deng, C. Meng, P. C. V. Thrane, S. I. Sande, S. I. Bozhevolnyi, and F. Ding
   Optica, 11(3), 326-332 (2024); DOI: 10.1364/OPTICA.515524

3. **Electrically tunable topological phase transition in non-Hermitian optical MEMS metasurfaces**
   F. Ding†, Y. Deng†, C. Meng†, P. C. V. Thrane, and S. I. Bozhevolnyi
   Science Advances, 10(5), eadl4661 (2024); DOI: 10.1126/sciadv.adl4661

4. **Recent progress in metasurface-enabled optical waveplates**
   Y. Deng†, Z. Cai†, Y. Ding, S. I. Bozhevolnyi, and F. Ding
   Nanophotonics, 11(10), 2219-2244 (2022); DOI: 10.1515/nanoph-2022-0030

5. **Functional metasurface quarter-wave plates for simultaneous polarization conversion and beam steering**
   Y. Deng, C. Wu, C. Meng, S. I. Bozhevolnyi, and F. Ding
   ACS Nano, 15(11), 18532-18540 (2021); DOI: 10.1021/acsnano.1c08597

6. **Dual-Functional optical waveplates based on gap-surface plasmon metasurfaces**
   Z. Cai†, Y. Deng†, C. Wu, C. Meng, Y. Ding, S. I. Bozhevolnyi, and F. Ding
   Advanced Optical Materials, 9(11), 2002253 (2021); DOI: 10.1002/adom.202002253

Other journal publications:

7. **Rotation-Induced plasmonic chiral quasi-bound states in the continuum**
   C. Qin, Y. Deng, T. Lyu, C. Meng, S. I. Sande, S. I. Bozhevolnyi, J. Shi, and F. Ding
   Under review (2024)

8. **Spin-Controlled generation of a complete polarization set with randomly-interleaved plasmonic metasurfaces**
   S. I. Sande, Y. Deng, S. I. Bozhevolnyi, and F. Ding
   Opto-Electronic Advances, 7(8), 240076 (2024); DOI: 10.29026/oea.2024.240076

9. **Optical reflective metasurfaces based on mirror-coupled slot antennas**

S. Ebel[†], <u>Y. Deng</u>[†], M. Hentschel, C. Meng, S. I. Sande, H. Giessen, F. Ding, and S. I. Bozhevolnyi

Advanced Photonics Nexus, 2(1), 016005 (2023); DOI: 10.1117/1.APN.2.1.016005

10. Quantum hybrid plasmonic nanocircuits for versatile polarized photon generation
C. Wu, S. Kumar, D. Komisar, C. Meng, <u>Y. Deng</u>, Z. Wang, S. I. Bozhevolnyi, and F. Ding
Advanced Optical Materials, 10(6), 2101596 (2021); DOI: 10.1002/adom.202101596

Conference papers and presentations:

11. Electrically tunable MEMS optical metasurfaces
<u>Y. Deng</u>, C. Meng, P. C. V. Thrane, S. I. Sande, S. I. Bozhevolnyi, and F. Ding
SPIE Photonics Europe 2024, Strasbourg, France
Poster

12. Electrically tunable MEMS optical metasurfaces
<u>Y. Deng</u>, C. Meng, P. C. V. Thrane, S. I. Sande, S. I. Bozhevolnyi, and F. Ding
National Optics Congress 2024, Odense, Denmark
Oral presentation & Poster

13. Piezoelectric MEMS-Empowered dynamic chiral metasurfaces
<u>Y. Deng</u>, C. Meng, P. C. V. Thrane, S. I. Bozhevolnyi, and F. Ding
NIBS 2023 conference, Sønderborg, Denmark
Oral presentation

14. Functional metasurface quarter-wave plates for simultaneous polarization conversion and beam steering
<u>Y. Deng</u>, C. Wu, C. Meng, S. I. Bozhevolnyi, and F. Ding
SPIE Photonics Europe 2022, Strasbourg, France
Oral presentation

List of acronyms

Abbreviations/Symbol	Definition/Explanation
OMS	optical metasurface
2D	two-dimensional
EM	electromagnetic
HWPs	half-wave plates
QWPs	quarter-wave plates
LP	linearly polarized
AoLP	angle of linear polarization
Ag	silver
CP	circularly polarized
GSP	gap-surface plasmon
MIM	metal-insulator-metal
Au	gold
SiO_2	silicon dioxide
PCRs	polarization conversion ratios
Si	silicon
SEM	scanning electron microscope
LiDAR	light detection and ranging
AR	augmented reality
VR	virtual reality
DoCP	degree of circular polarization
NA	numerical aperture
LCs	liquid crystals
Al	aluminium
CD	circular dichroism
LCP	left-handed circularly polarized
RCP	right-handed circularly polarized
MEMS	micro-electro-mechanical system
DWP	dynamic waveplate
E	electric
H	magnetic
DoP	degree of polarization
DoCP	degree of circular polarization
ψ	azimuth angle
χ	ellipticity
FEM	finite element method
FDTD	finite difference time domain
PB	Pancharatnam-Berry
SPP	surface plasmon polariton
FP	Fabry-Perot
SiNx	silicon nitride
NFC	near-field coupling
IMI	insulator-metal-insulator
PML	perfectly matched layer
EBL	electron beam lithography

VVB	vector vortex beam
OAM	orbital angular momentum
RP	radially polarized
AP	azimuthally polarized
PZT	lead zirconate titanate
DLP	dynamic linear polarizer
Pb	lead
Zr	zirconium
Ti	titanium
O	oxygen
ER	extinction ratio
SOI	silicon-on-insulator
DRIE	deep reactive ion etching
EPs	exceptional points
DPs	diabolic points
TMM	transfer matrix method
FIB	focused ion beam

Contents

1   Introduction

The optical metasurface (OMS) is a two-dimensional (2D) artificial and advanced nanostructure composed of ultrathin arrays of precisely engineered meta-atoms, enabling the versatile manipulation of electromagnetic (EM) waves in ways unattainable with natural materials. By meticulously designing the shapes, dimensions, orientations, and locations of structural elements, metasurfaces achieve unparalleled abilities to manipulate EM waves through surface-confined configurations, allowing for sub-wavelength spatial resolutions and making them a rapidly emerging and promising platform in the realm of photonics [1-11]. To date, numerous wavefront shaping works based on metasurfaces, such as optical waveplates [12-15], beam steering [16-19], metalenses [20-26], optical holograms [27-31], and polarimeters [32], have been extensively demonstrated. Despite these advancements, functionalized metasurface devices remain predominantly static, with their optical responses fixed after fabrication. This inherent static nature imposes significant limitations, particularly the absence of real-time adjustability, which impedes the progression of innovative metasurface solutions towards the realization of cutting-edge, seamlessly integrated adaptive photonic systems. A widely adopted strategy entails incorporating active media directly into the metasurface structure, thereby facilitating active control of its optical response through external stimuli [33-46]. While these methods are feasible, they generally necessitate highly precise nanofabrication and assembly techniques, and are often constrained by limited tuning capabilities. Therefore, in addition to further advancing the applications of passive metasurfaces, a primary objective of this PhD thesis is to develop a dynamically reconfigurable platform featuring straightforward fabrication and assembly processes, extremely fast responses, stable switching processes, ample tuning ranges, and high modulation efficiencies.

In this chapter, I first provide a concise review of recent developments in metasurface-based passive wavefront shaping, with a primary focus on optical waveplates [15], beam steering [16-18], and metalenses [20-22]. Then I examine prevalent active control methods, highlighting examples such as dynamic amplitude control [47], chirality switching [48-49], and tunable polarization conversion [50-51]. Examples presented in this chapter are partially derived from one review article we published in 2022 (**Appendix A** [52]), which constitutes a significant part of my PhD work described here, and have been supplemented with updated contents to reflect the latest advancements. Finally, the structure of this PhD thesis is outlined.

1.1   Recent progress in metasurface-based passive wavefront shaping

This section is based on my previous publication **Appendix A** [52], and incorporates pieces of text from that work.

1.1.1   Passive metasurface waveplates

Traditional commercial waveplates, including half-wave plates (HWPs) and quarter-wave plates (QWPs), are usually constructed from birefringent materials such as plastics and crystals, which cause and accumulate the phase delay between two orthogonal fast and slow axes as light travels distances significantly longer than its wavelength [53]. Although advanced fabrication and coating techniques endow these waveplates with high polarization conversion efficiency, stable phase retardation under varying temperatures, and excellent transmittance, their intrinsic bulkiness significantly hampers their potential for miniaturization and integration into nanoscale photonic systems. In contrast, by engineering nanostructures with distinctive and polarization-sensitive optical properties, metasurfaces can achieve pronounced optical anisotropy across any desired operating band, enabling

the development of ultrathin, planner, and miniaturized meta-waveplates with exceptional and novel functionalities that surpass those traditional counterparts. In this thesis, we use Jones matrix composed of complex transmission or reflection coefficients to characterize the optical behaviour of an anisotropic nanoparticle under a pair of orthogonal linearly polarized (LP) excitations (e.g., E_x and E_y) [52]:

$$J_{LP} = \begin{pmatrix} |J_{xx}|e^{i\varphi_{xx}} & 0 \\ 0 & |J_{yy}|e^{i\varphi_{yy}} \end{pmatrix} \qquad 1.1$$

where $|J_{xx}|$ and $|J_{yy}|$ indicate amplitudes, φ_{xx} and φ_{yy} indicate their corresponding phase delays, and $\Delta\varphi = \varphi_{xx} - \varphi_{yy}$ ($\varphi_{yy} - \varphi_{xx}$) is described as the relative phase difference. For example, when amplitudes $|J_{xx}|$ and $|J_{yy}|$ are approximately equal and $\Delta\varphi$ is equal to π or $\pm\pi/2$, related meta-HWPs or meta-QWPs can be achieved in the designed wavelength range [12-15, 52, 54-62]. Dating back to 2011, based on this strategy, Prof. Bozhevolnyi's research group demonstrated both theoretically and experimentally a reflected brick-shaped retarder that supports orthogonal electrical dipoles to function as a single-layer meta-QWP scatterer at the center wavelength of 770 nm [12]. In particular, when they optimized the length and width of the gold nano-brick to respective 140 nm and 90 nm, a meta-QWP scatterer with phase difference of $\pi/2$ can be achieved over a limited operating bandwidth between 748 nm and 796 nm under LP excitation with an angle of linear polarization (AoLP) of 45°. This work successfully validated the feasibility of the meta-waveplate design theory and provided a reference for future design efforts. However, challenges such as low polarization conversion ratios (PCRs) of these single-layered waveplates [12-13, 55-56, 60, 62] caused by unwanted channels (transmission in this case), and an obviously narrow effective working bandwidth still need to be addressed [52]. At the same year, Zhao et al. proposed a meta-QWP whose constituent unit consists of two perpendicular rectangular nano-slits in an ultrathin silver (Ag) layer, working in the transmission channel [13]. Nevertheless, their efforts only succeeded in broadening the operating bandwidth of the meta-QWP from 616 nm to 746 nm under circularly polarized (CP) excitations. Despite this improvement, the complementary device is still experiencing a low PCR caused by the unwanted reflection loss.

This paragraph is based on my previous publication **Appendix A** [52], and incorporates pieces of text from that work. To further broaden the working bandwidth and increase the PCR, gap-surface plasmon (GSP) metasurfaces consisting of an array of metallic meta-atoms, a subwavelength dielectric spacer, and a thick metallic substrate, forming a typically metal–insulator–metal (MIM) resonator [63], have been employed to realize compact and ultrathin meta-waveplates [14-15, 52, 54, 57-59]. For GSP metasurfaces, the bottom thick metallic layer serves as a perfect reflector that completely blocks transmission channels, effectively preventing losses. Meanwhile, the designed meta-atom possesses equally high reflection amplitudes and a proper phase difference (e.g., $\pm\pi/2$ or π) under linear excitations [52, 65-66]. For example, in 2014, Jiang et al. experimentally demonstrated a meta-HWP and a meta-QWP by employing such an MIM structure for high reflection efficiency, angle-independent polarization conversion and extremely broad bandwidth that spans over more than an octave [15]. The ultrathin reflective broadband waveplates were designed by optimizing the anisotropic responses of a nanorod resonator array with strong coupling to tailor the interference of light between the top array and the ground plane at a subwavelength scale [52]. The meta-waveplate comprising top gold (Au) meta-atoms, an intermediate silicon dioxide (SiO_2) spacer, and a bottom thick Au reflector [52], can reflect the incident *s*-polarized light to orthogonal *p*-polarized light which acts as a meta-HWP shown in Figure 1.1(a-c), or reflect the incident CP light to LP light which acts as a meta-QWP shown in Figure 1.1(d-f). For the fabricated meta-HWP and meta-QWP devices, both measured PCRs are higher than 91% and both reflection magnitudes are greater than 92% across the

anticipated broadband wavelength range for an incident angle up to 40°. Although the conversion efficiencies of MIM meta-waveplates could be increased to some degree, Ohmic losses in the metal do exist, especially at the short wavelength region [52]. Therefore, a hybrid MIM metasurface composed of single-crystalline silicon (Si) bricks and an Ag back-reflector separated by a dielectric spacer has been implemented as an efficient HWP in the telecom range [52, 64].
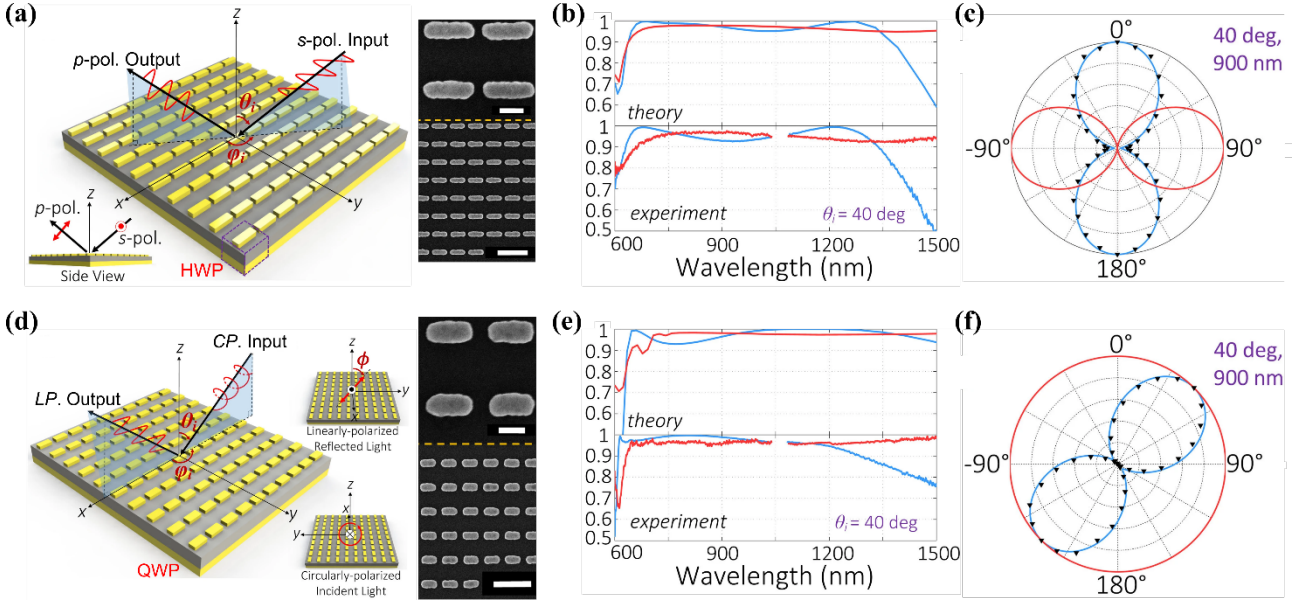
Figure 1.1 The broadband and wide-angle MIM (a-c) meta-HWP and (d-f) meta-QWP. (a) and (d) Left panel: schematic of a meta-HWP that transforms an incident *s*-polarized light into an orthogonal *p*-polarized light (a), and a meta-QWP that transforms an incident CP light into a LP light (d) [52]. Right panel: Scanning electron microscope (SEM) image of part of the fabricated meta-HWP (a) and meta-QWP (d) sample, the scale bars for the top and bottom of each SEM image are respective 100 nm and 400 nm. (b) and (e) Theoretical and experimental PCRs and reflection magnitudes as a function of different wavelengths under one incident CP wave with $\theta_i = 40°$ [52], (b) is for the meta-HWP and (e) is for the meta-QWP. (c) and (f) Theoretical and experimental polarization states at the wavelength of 900 nm under one incident CP wave with $\theta_i = 40°$ [52], (c) is for the meta-HWP and (f) is for the meta-QWP. The theoretical predictions for incident and reflected light are depicted by red and blue lines, respectively, while the experimental data for reflected light is indicated by black inverted triangles. Reprinted from Ref. [15]

This paragraph is based on my previous publication **Appendix A** [52], and incorporates pieces of text from that work. In addition, given that MIM metasurfaces are limited to operating in the reflection mode, their practical applications are restricted, particularly for communication systems. As such, all-dielectric anisotropic meta-atoms that consist of high-refractive-index and low-loss materials could also be employed to realize ultrathin optical waveplates [20, 52, 61, 67-69]. In such all-dielectric metasurfaces, electric and magnetic Mie resonances exploited by corresponding electric and magnetic hotspots with nanoscale volumes could be enhanced with similar strengths at a single frequency or a frequency range, thereby enabling complete and independent manipulations of amplitudes and phases for the transmitted fields [52]. Furthermore, under the Kerker condition [70], the reflection fields can be effectively forbidden, thus leading to a substantial improvement in transmission efficiencies. In 2016, Kruk and colleagues experimentally demonstrated a groundbreaking transparent all-dielectric meta-waveplate formed by densely arranged Si nanopillars, achieving broadband performance and high PCRs in transmission fields [61]. According to the generalized Huygens principle, the scattering profiles of Si meta-atoms arise from the overlapping spectra of multipole modes of electric and magnetic fields, inducing destructive interference in the reflection fields and effectively suppressing

reflections across a broad wavelength range [52]. Notably, the fabricated meta-HWP sample demonstrated a transmission efficiency of nearly 90% with a PCR close to 99% between 1476 nm and 1607 nm. In particular, the equivalent birefringence Δn for a π phase difference was calculated to be as high as 0.9 at the wavelength of 1550 nm, almost one magnitude larger than those of natural birefringent materials [52].

1.1.2 Passive metasurfaces for beam steering and metalenses

Beyond the development of ultrathin and compact optical waveplates, metasurfaces have garnered significant attention for their exceptional capabilities in beam steering and the development of metalenses. This section offers a succinct overview of these two pivotal applications, serving as a foundation for a diverse array of fields, including communication technology, LiDAR (Light Detection and Ranging), radar systems, optical imaging, and augmented reality (AR) and virtual reality (VR). This discussion sets the stage for the research presented in *Section 3* of this thesis.

This paragraph is based on my previous publication **Appendix A** [52], and incorporates pieces of text from that work. Beam steering refers to the capability to manage the direction of a signal or beam without requiring physical movement of the emitting device [71-72]. For example, Yu and colleagues showcased a meta-QWP with a supercell design that interweaves two subunits, each containing eight *V*-shaped Au meta-atoms with different phases due to varying dimensions and orientations [16], enabling simultaneous LP-to-CP conversion and beam steering with background-free performance in an ultra-broadband mid-infrared wavelength range [52], as shown the left panel in Figure 1.2(a). Specifically, the generated extraordinary CP beam, directed away from the ordinary wave, originates from the interference of two transmitted beams that propagate in the same direction and have identical scattering amplitudes, but possess orthogonal polarization states and a phase difference of $\pi/2$ when LP light is incident (middle panel of Figure 1.2(a)) [52]. Impressively, the calculated degree of circular polarization (DoCP) of the steered beam is larger than 0.95 from 6 to 10 μm (right panel of Figure 1.2(a)) [52]. However, the efficiency of this meta-QWP is low because a significant amount of energy is wasted in ordinary reflection and refraction channels. As we mentioned earlier, using MIM or all-dielectric structures can effectively improve efficiency. For example, in 2015, Ding and co-workers experimentally demonstrated a compact background-free GSP meta-HWP that integrates the functionalities of linear-to-linear polarization conversion and beam-steering in the near-infrared region [17], as shown the left and middle panel of Figure 1.2(b) [52]. Due to the complete suppression of reflection in the co-polarized channel, the reflectance in the cross-polarized channel becomes dominant in the designed direction, nearly matching the total reflectance (right panel of Figure 1.2(b)), which can effectively prove the required multi-functionality with an integrated PCR exceeding 95%. Apart from the beam steering in a single transmission or reflection direction with the designed polarization conversion, Pors et al. experimentally demonstrated an MIM meta-grating that simultaneously achieves 6-channel beam steering, accompanied by six typical polarization outputs used to calculate Stokes parameters to identify the polarization state of an incident light with arbitrary polarization state at 800 nm working wavelength [18] (left and middle panel of Figure 1.2(c)). The meta-grating consists of three interleaved metasurfaces, each independently splitting the beam according to one of the three polarization bases, and featuring its own unique periodicity. After averaging over three successive measurements, the diffraction contrast closely matches the normalized input Stokes parameters, successfully reconstructing the Poincaré sphere. As shown in the right panel of Figure 1.2(c), the deviation between the measured diffraction contrast and the Stokes parameters, calculated using the two-norm, is around 0.1, indicating excellent accuracy.
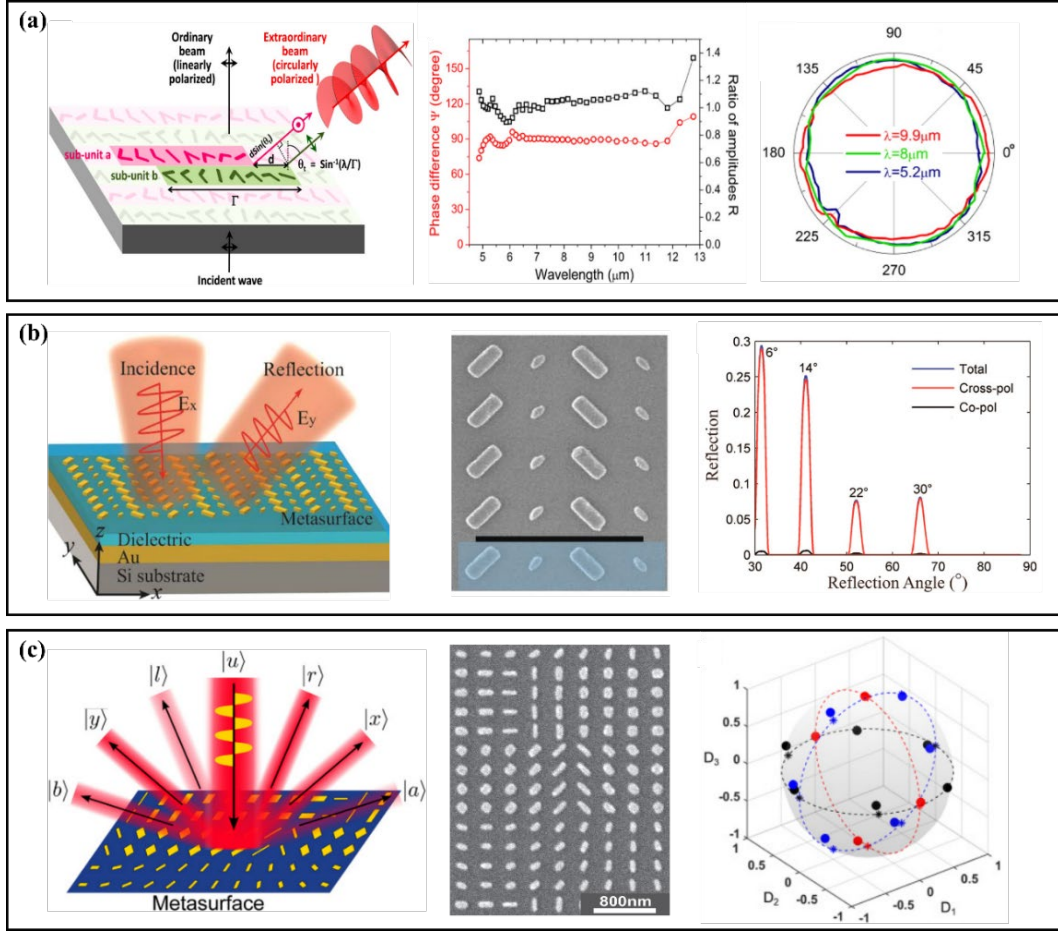
Figure 1.2 Metasurface-based passive beam steering. (a) Left panel: schematic of the background-free meta-QWP composed of two Au *V*-shaped antenna subunits. Middle panel: simulated phase difference and ratio of amplitudes between the two scattered waves from the subunits as a function of the wavelength. Right panel: measured SoPs of the extraordinary beam at wavelengths of 5.2, 8, and 9.9 μm [52]. Reprinted from Ref. [16]. (b) Left panel: schematic of the background-free plasmonic meta-HWP that enables polarization conversion and anomalous reflection in the cross-polarized channel. Middle panel: SEM image of the fabricated structure. Right panel: measured normalized reflection of the fabricated sample as a function of incident angle under *x*-polarized excitation at λ = 1000 nm [52]. Reprinted from Ref. [17]. (c) Left panel: schematic of the designed MIM meta-grating. Middle panel: SEM image of the fabricated sample. Right panel: measurement of diffraction contrasts corresponding to polarization states, specifically aligned with the principal axes of the Poincaré sphere. Reprinted from Ref. [18].

This paragraph is based on my previous publication **Appendix A** [52], and incorporates pieces of text from that work. Metalenses, a specialized type of metasurface, have attracted considerable research interest due to their capability to replicate conventional optical components and systems while offering innovative functionalities such as efficiently focusing light into subwavelength spots, providing multifunctionality, featuring a lightweight and flat design, and enabling economical production [73-76]. For instance, Capasso's research team presented a high-aspect-ratio metalens made from TiO$_2$ nano-HWPs with varying rotation angles situated on a glass [21] (left and middle panel of Figure 1.3(a)). The metalens featuring a numerical aperture (NA) of 0.8 is capable of providing the diffraction-limited focusing at wavelengths of 405, 532, and 660 nm with respective efficiencies of 86, 73, and 66% [52]. In addition, the fabricated metalens sample can reach magnifications of up to 170× [52], delivering image quality on par with the most advanced commercial objectives available (right panel of Figure 1.3(a)). Similarly operating within the

transmission channel, Arbabi and colleagues experimentally showcased an all-dielectric metalens constructed from Si ellipse-shaped nano-HWPs, which can not only focus beams but also generate vector beams under LP excitations, such as transforming an *x*-polarized (or *y*-polarized) Gaussian beam into a focused radially (or azimuthally) polarized Bessel-Gauss beam [52], thereby integrating the multifunctionalities of a *q*-plate and a lens [20], as shown in Figure 1.3(b). Impressively, the measured conversion efficiencies for both *x*- and *y*-polarized waves are higher than 85%, due to the satisfied Kerker condition through spectrally overlapping the electric and magnetic resonances with identical strengths [52]. Furthermore, to be suitable for commercial applications, metalenses must address the significant challenge of severe chromatic aberration, which results from phase dispersion occurring as light propagates through the device. As shown in Figure 1.3(c), Tsai's research team significantly developed an innovative design for broadband achromatic metalenses that utilize integrated resonant unit elements with linear and smooth phase dispersion, in conjunction with geometric phase, to effectively mitigate chromatic aberration [22]. This approach enables the metalens to maintain a consistent focal plane for light over a broad wavelength range, achieving approximately 12% efficiency for CP light in a reflection setup, spanning from 1200 to 1680 nm. The innovative use of metallic nano-rods within a MIM structure allows for precise phase control, overcoming traditional challenges of phase dispersion and chromatic aberration in metasurfaces. In addition to metalenses, this versatile method is applicable for developing an extensive variety of flat achromatic components, opening up new possibilities for full-colour imaging and the miniaturization of optical devices.

Figure 1.3 Metasurface-based passive metalenses. (a) Left panel: schematic of the reflective metasurface hologram under a CP incident light. Middle panel: SEM image of part of the fabricated sample. Right panel:

measured holographic image and zero-order efficiencies as a function of the wavelength [52]. Reprinted from Ref. [21]. (b) Left panel: schematic, SEM, and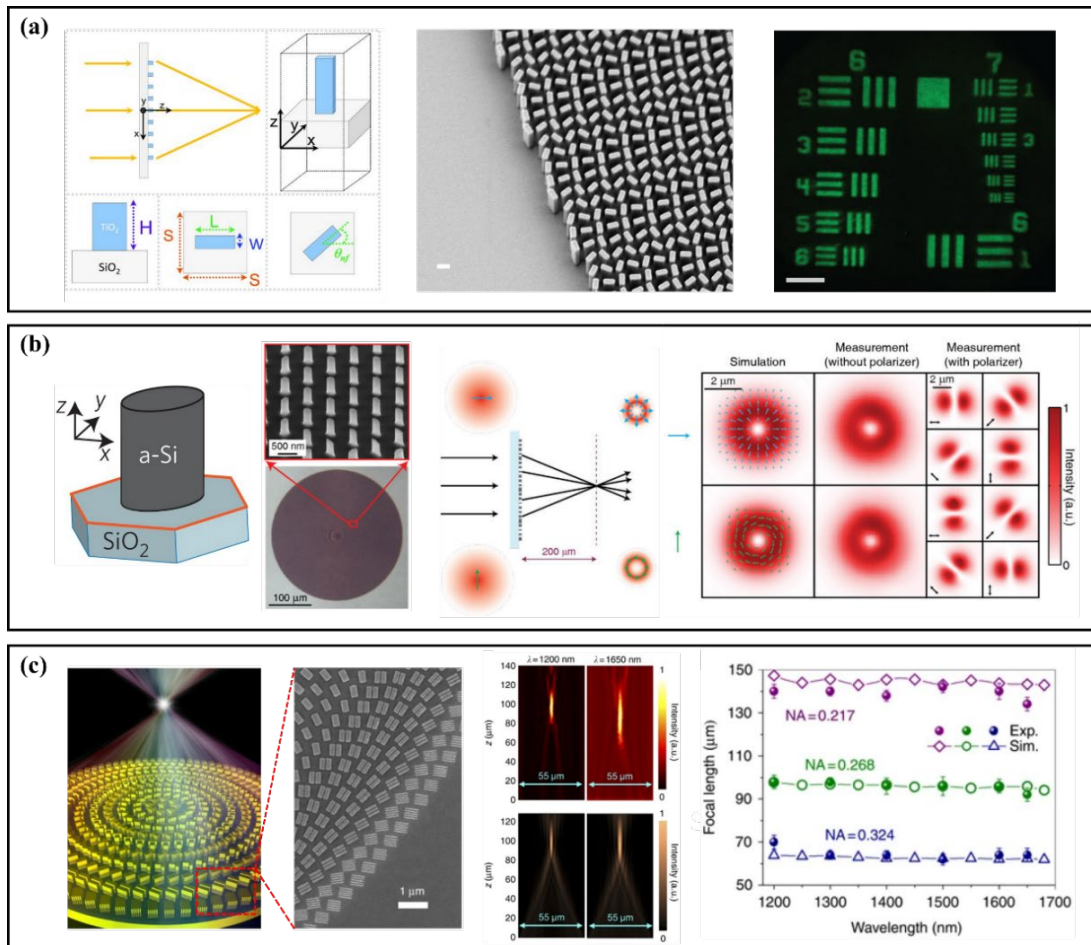 optical microscope images of the elliptical Si posts on top of a SiO2 substrate. Right panel: illustration and demonstration of focused radially (azimuthally) polarized Bessel–Gauss beam generation under the excitation of an *x*-polarized (*y*-polarized) Gaussian beam [52]. Reprinted from Ref. [20]. (c) Left panel: schematic of the designed achromatic metalens, and SEM image of part of the sample. Middle panel: measured (top row) and simulated (bottom row) intensity distribution patterns of the designed metalens along the axes at 1200 nm and 1650 nm wavelengths. Right panel: the focal lengths of the achromatic metalens, both measured and simulated, for different NA values. Reprinted from Ref. [22].

1.2   Active metasurfaces for wavefront shaping

Despite notable progress, the metasurfaces discussed above for versatile applications remain passive and lack real-time tunability, rendering them unsuitable for modern photonic systems that require adaptability. To address the limitation of the static optical response due to fixed nanostructures at the time of synthesis or fabrication, various active control methods were developed like applying external optical or electric stimuli, employing phase-change materials, using external chemical reagents or gases, integrating with liquid crystals (LCs) and utilizing mechano-tunability. This section is also based on my previous publication **Appendix A** [52], and incorporates pieces of text from that work.

For example, Tittl et al. developed the first tunable perfect absorber by leveraging the temperature-induced phase transition of the phase-change material $Ge_3Sb_2Te_6$ (GST-326) from amorphous to crystalline states in the mid-infrared range [47] (Figure 1.4(a)). The core components of this device are absorptive units, made up of aluminum (Al) brick-shaped nanoantennas placed on a GST-326 spacer layer, which is then situated on an Al mirror. The engineered nanoantennas with various geometries achieved nearly perfect absorption (>90%) in both amorphous and crystalline states, leading to a resonance shift of more than 500 nm and a significant contrast in reflectance, which enables the efficient temperature-dependent amplitude control. In 2016, Liu's research group experimentally demonstrated a novel hybrid plasmonic metasurface [49], consisting of metamolecules made up of four Mg meta-atoms surrounded by four Au satellite meta-atoms, achieving hydrogen-regulated chirality switching in the visible spectral range (Figure 1.4(b)). The optical chirality of plasmonic metamolecules could be toggled dynamically by loading and unloading hydrogen, without necessitating a structural reconfiguration, as observed through real-time circular dichroism (CD) spectroscopy. However, the lengthy chemical reaction times, about 100 minutes for hydrogenation and approximately 27 hours for dehydrogenation, and the slight alterations in chiroptical response after recovery, pose significant obstacles to achieving fast-switching and stable optoelectronic devices. In addition to on-off chiroptical response switching, Zhang's research group demonstrated handedness switching using a unique series of tailored terahertz composite materials featuring deep subwavelength elements, activated by an external ultrafast laser [48] (Figure 1.4(c)). Under optical excitation, the metamolecule monolayer achieves a flip in ellipticity and a polarization angle rotation of over 10°, demonstrating a significantly stronger electromagnetic effect compared to naturally occurring molecules. Although the switching process similarly does not involve structural reconfiguration, it introduces a certain level of complexity in the manufacturing process.

This paragraph is based on my previous publication **Appendix A** [52], and incorporates pieces of text from that work. In contrast to optically-triggered dynamic meta-waveplates that necessitate ultrafast lasers, electrically tunable meta-waveplates can be stimulated by integrated electronics and thus are naturally appealing for miniaturized reconfigurable photonic networks and systems [52]. Yu et al. has experimentally demonstrated an electrically-driven metasurface integrated with LCs for polarization conversion at visible frequencies [50, 52], as shown in Figure 1.4(d). The metasurface supercell consists of two rows of Au nanorods with opposite rotation angles to produce reflected left-handed

circularly polarized (LCP) and right-handed circularly polarized (RCP) beams in the same direction upon an LP excitation at normal incidence [52]. By covering these two rows with PMMA and LC layers, the reflected RCP and LCP beams gain different and tunable propagation phases and finally superpose as an LP beam with the rotation angle controlled by the applied voltage [52]. When the applied voltage is increased from 4 to 20 V, the polarization angle can be dynamically tuned from 90° to 0° with a measured switching speed of 100 ms [52]. Recently, Prof. Bozhevolnyi's group developed a piezoelectric micro-electro-mechanical system (MEMS)-OMS platform for dynamic beam steering, beam focusing, and waveplates in the optical range by integrating a thin-film MEMS mirror with a judiciously designed plasmonic OMS and precisely adjusting the air gap between them using varying driving voltages [51, 77-78]. For example, Figure 1.4(e) illustrates the schematic of an electrically controlled MEMS-OMS-based dynamic waveplate (DWP), which can achieve full-range birefringence control in the reflected field [51]. The DWP component comprising a glass substrate with an array of Au nano-bricks and an actuated MEMS mirror, features continuously adjustable anisotropy with varying actuation voltages, allowing complete traversal of the Poincaré sphere such as the polarization conversion from LP to CP, orthogonal LP and opposite CPs with extremely fast response time (< 0.4 ms) in a broadband wavelength range. Furthermore, by varying the DWP orientations under LP excitation, the polarization state of the reflected light can be continuously modulated through adjustments in the actuation voltage, allowing for the generation of diverse polarization trajectories that trace paths around the Poincaré sphere. Two active wavefront shaping works presented in this thesis utilize this electrically tunable MEMS-OMS platform (*Section 4*).
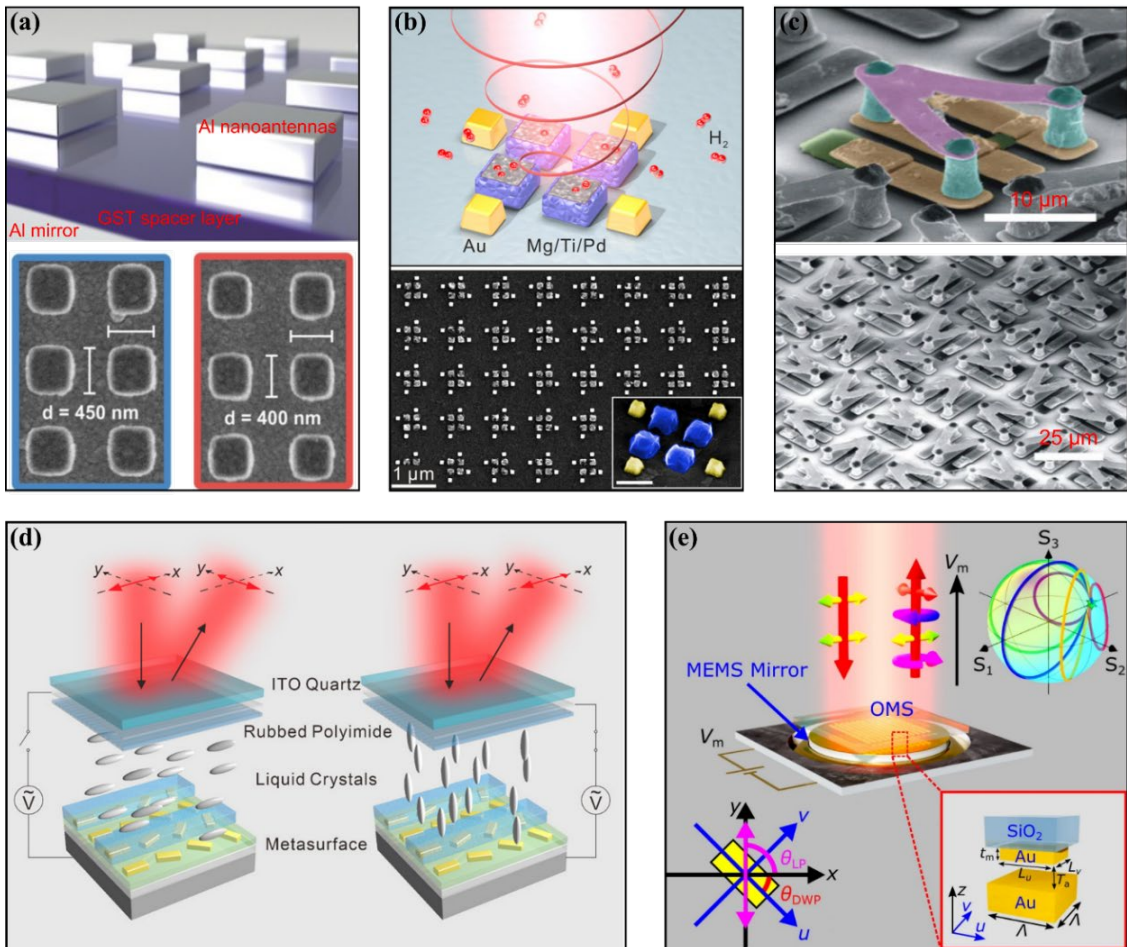
Figure 1.4 Metasurface-based active wavefront shaping. (a) Schematic of the switchable perfect absorber, featuring Al nano-brick arrays placed on a GST-326 spacer with an Al mirror beneath, along with SEM images of the samples showcasing various antenna dimensions. Reprinted from Ref. [47]. (b) Schematic of the hybrid plasmonic metamolecule made up of four Mg meta-atoms surrounded by four Au satellite meta-atoms on a glass substrate, and SEM image of the hybrid plasmonic structures. Reprinted from Ref. [49]. (c) SEM images of the fabricated chiral switching sample with different magnifications. Reprinted from Ref. [48]. (d) Working principle of the electrically tunable metasurface for active polarization conversion by combining both geometric from Au antennas and tunable propagation phase supplied by an LC layer [52]. Reprinted from Ref. [50]. (e) Illustration of the DWP device, showing an OMS mounted on a glass substrate with an adjustable MEMS mirror. The air gap between the MEMS mirror and OMS is modulated by changing the applied voltage (V_m), providing fine-tuned control over the birefringence of the reflected light. Reprinted from Ref. [51].

1.3   Outline

In *Chapter 1*, recent advancements in metasurface-based passive and active wavefront shaping are presented, corresponding to **Appendix A** [52]. *Chapter 2* delves into the key theoretical concepts and primary analytical methods employed in this thesis. *Chapter 3* provides an account of passive wavefront shaping using GSP metasurfaces, detailing our research on optical waveplates, beam steering, and metalenses, corresponding to **Appendices B-D** [79-81]. *Chapter 4* explores active wavefront shaping based on our developed MEMS-OMS platform, including two research projects: dynamic linear polarizers and applications, as well as non-Hermitian metasurfaces for tunable topological phase transitions, as detailed in **Appendices E-F** [82-83]. Figure 1.5 presents an overview of the research works in this thesis. Finally, *Chapter 5* presents a comprehensive summary and offers a forward-looking perspective.
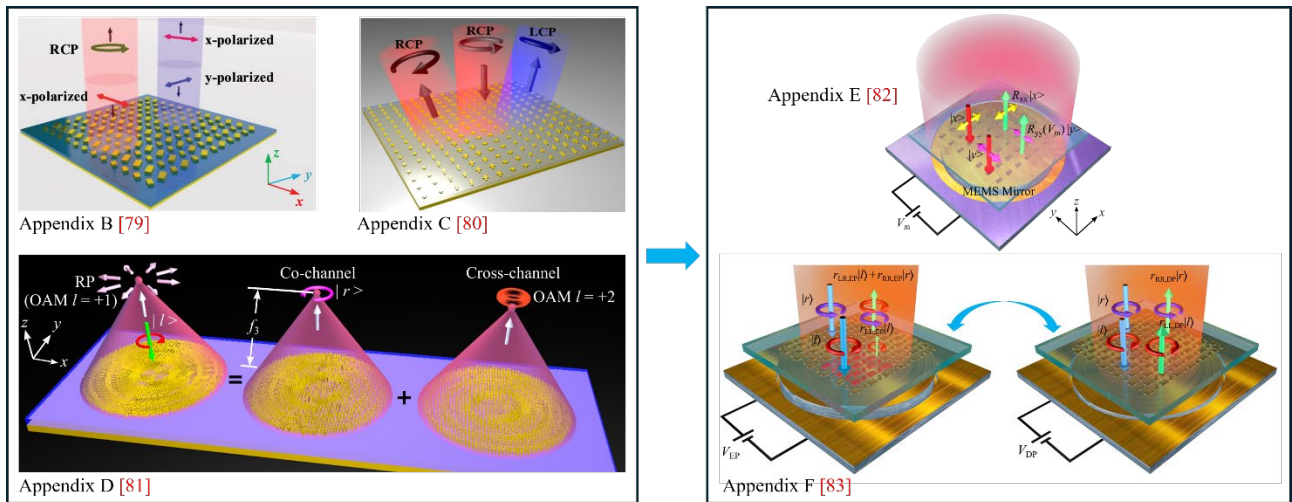
Figure 1.5 An overview of the research works in this thesis focuses on plasmonic optical metasurfaces for both passive and active wavefront shaping.

2 Theory and analytical methods for wavefront shaping

This chapter outlines the key theoretical concepts and primary analytical approaches utilized throughout this thesis. The manipulation and analysis of the polarization state of waves, a fundamental characteristic of EM radiation, are central to our research. I begin by outlining the basic principles of polarization states and their common mathematical expressions, which lay the groundwork for our subsequent studies on wavefront shaping. Next, I provide a concise review of three common phase control methods, which serve as the core concepts for metasurface design. Following this, I thoroughly discuss the numerical simulation model and method employed in this thesis, illustrated with a classic example. Finally, I present the detailed sample fabrication process, along with the characterization setup and measurement methods.

2.1 Polarization state and its analytical methods

2.1.1 Polarization state overview

As EM waves travel through free space, the electric (E) and magnetic (H) field vectors oscillate at right angles to each other and to the direction in which the wave propagates [84]. In directions orthogonal to the wave propagation, the electric field vector of EM waves can exhibit various oscillation states, known as polarization states. For polarized light, which is a type of plane EM wave, the electric field vector oscillates exclusively in a specific direction. Suppose a monochromatic polarized plane wave traveling in z-direction, with the E and H field vectors lying in the *xoy*-plane (Figure 2.1).
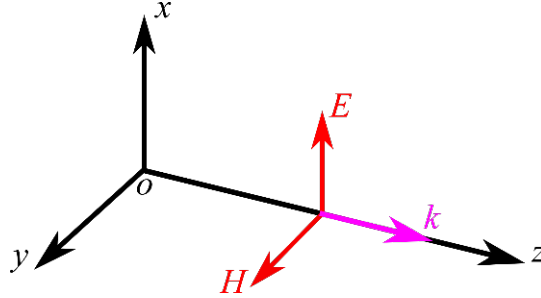
Figure 2.1 Schematic of a plane EM wave propagating along the *z*-axis.

Then its electric field vector $\hat{E}(z,t)$ in terms of time t could be decomposed into two components, $E_x(z,t)$ and $E_y(z,t)$, and can be expressed as:

$$\hat{E}(z,t) = \hat{x}E_x(z,t) + \hat{y}E_y(z,t) \qquad 2.1$$

$$E_x(z,t) = A_x\cos{(wt - kz + \varphi_x)} \qquad 2.2$$

$$E_y(z,t) = A_y\cos{(wt - kz + \varphi_y)} \qquad 2.3$$

where A_x and A_y denote the amplitudes of the electric field vector along the respective x and y axes; φ_x and φ_y are the corresponding phases; w is the angular frequency, and k represents the wave number. For any given point z_0 in the electric field, to determine the trajectory of the tail of the electric field vector over time, term "$wt - kz$" in equations 2.2 and 2.3 can be eliminated:

$$\left(\frac{E_x(z_0,t)}{A_x}\right)^2 - 2\frac{E_x(z_0,t)}{A_x}\frac{E_y(z_0,t)}{A_y}\cos(\Delta\varphi) + \left(\frac{E_y(z_0,t)}{A_y}\right)^2 = \sin^2(\Delta\varphi) \qquad 2.4$$

$$\Delta\varphi = \varphi_y - \varphi_x \qquad\qquad 2.5$$

The resulting equation 2.4 is a curve with time t as the variable, providing an intuitive description of the trajectory of the tail of the electric field vector within the plane orthogonal to the propagation direction at the field point z_0. $\Delta\varphi$ in equation 2.5 indicates the relative phase difference between the x and y components.

If $\Delta\varphi = 0°$ or $\pm180°$, equation 2.4 can be simplified to:

$$\frac{E_y(z_0,t)}{E_x(z_0,t)} = \pm\frac{A_y}{A_x} \qquad\qquad 2.6$$

it is evident that equation 2.6 represents the linear motion trajectories with $E_x(z_0, t)$ and $E_y(z_0, t)$ as the abscissa and ordinate, respectively. In this scenario, the electric field vector's tail oscillates back and forth along a line passing through the origin as time t progresses. This polarization state is referred to as LP. In equation 2.6, the symbols "+" and "−" indicate oscillations between the first and third quadrants, and the second and fourth quadrants, respectively. Moreover, DoLP is determined by the inclination between the trajectory line and the positive x-axis, which can be calculated as:

$$\text{DoLP} = tan^{-1}(\pm\frac{A_y}{A_x}) \qquad\qquad 2.7$$

If $\Delta\varphi = \pm90°$, equation 2.4 can be simplified to:

$$\left(\frac{E_x(z_0,t)}{A_x}\right)^2 + \left(\frac{E_y(z_0,t)}{A_y}\right)^2 = 1 \qquad\qquad 2.8$$

when $A_x = A_y = A_m$, we have:

$$E_x(z,t)^2 + E_y(z,t)^2 = A_m{}^2 \qquad\qquad 2.9$$

Equation 2.9 illustrates that the electric field vector's tail follows a circular motion over time t, with the circle's radius representing the amplitude in the x or y direction, corresponding to a polarization state known as CP. When $\Delta\varphi = 90°$, the electric field vector's tail rotates in a clockwise direction when observed along the wave vector, which signifies an LCP state. Conversely, when $\Delta\varphi = -90°$, the vector rotates counterclockwise, defining the polarization state as RCP.

However, for the general case, where $\Delta\varphi$ is not equal to $0°$, $\pm90°$, or $\pm180°$, and $A_x \neq A_y$, equation 2.4 can be considered as a general ellipse equation and cannot be simplified. As time t progresses, the tail of the electric field vector traces the path of the corresponding ellipse. This condition is known as elliptical polarization. When $0° < \Delta\varphi < 180°$, the associated polarization state could be further characterized as left-handed elliptical polarization; while when $-180° < \Delta\varphi < 0°$, the associated polarization state could be further characterized as right-handed elliptical polarization. As illustrated in Figure 2.2, the polarization state of the EM wave can be characterized by the ellipse's major axis a, minor axis b, and the inclination angle α, which is the angle between the major axis and the positive x-axis. When $a = b$, the EM wave is in a state of CP. When $a = 0$ or $b = 0$, the EM wave is in a state of LP. Based on this, the ratio b/a is known as the ellipticity. An ellipticity of 1 corresponds to the ideal CP.
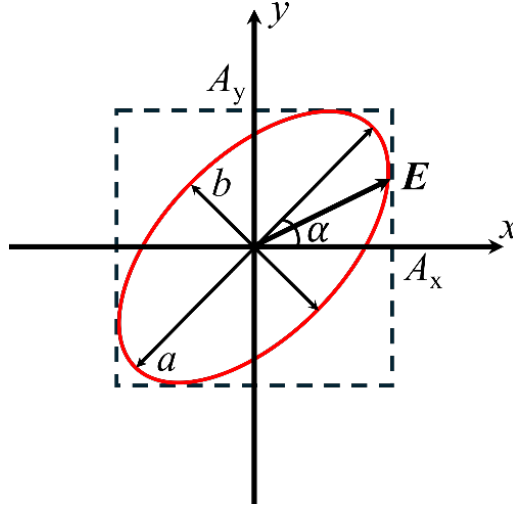
Figure 2.2 Schematic of elliptical polarization.

To achieve a more detailed and intuitive understanding of the polarization state, additional methods can be used alongside the electric field vector description, such as Jones vectors, Stokes parameters and Poincaré spheres.

2.1.2 Jones vectors

Jones vectors, introduced by physicist R. Clark Jones in 1941, represent the electric field vector components of an EM wave along two orthogonal directions (such as the x and y axes) in vector form:

$$E = \begin{pmatrix} E_x \\ E_y \end{pmatrix} = \begin{pmatrix} A_x e^{-i(wt-kz-\varphi_x)} \\ A_y e^{-i(wt-kz-\varphi_y)} \end{pmatrix} = e^{-i(wt-kz-\varphi_x)} \begin{pmatrix} A_x \\ A_y e^{i\Delta\varphi} \end{pmatrix} \qquad 2.10$$

When considering time averaging, the exact phase of the electric field could be disregarded, leaving only the relative phase to be considered. Thus, the phase term $e^{-i(wt-kz-\varphi_x)}$ can be omitted. By normalizing the amplitudes, the simplified Jones vector expression of the electric field is obtained as follows:

$$E = \sqrt{A_x^2 + A_y^2} \begin{pmatrix} \dfrac{A_x}{\sqrt{A_x^2+A_y^2}} \\ \dfrac{A_y}{\sqrt{A_x^2+A_y^2}} e^{i\Delta\varphi} \end{pmatrix} \qquad 2.11$$

Jones vectors provide a clear depiction of the amplitude and phase relationships between the components of an EM wave in orthogonal directions at a specific time and place. Table 2.1 provides some typical polarization states represented by Jones vectors.

Table 2.1 Jones vectors of some typical polarization states.

Polarization state	Jones vector
0° LP	$(1 \quad 0)^T$
90° LP	$(0 \quad 1)^T$
45° LP	$\dfrac{\sqrt{2}}{2}(1 \quad 1)^T$

−45° LP	$\frac{\sqrt{2}}{2}(1 \quad -1)^T$
LCP	$\frac{\sqrt{2}}{2}(1 \quad i)^T$
RCP	$\frac{\sqrt{2}}{2}(1 \quad -i)^T$

2.1.3 Stokes parameters

Although Jones vectors offer a comprehensive description of fully polarized light, they are not capable of representing partially polarized light or unpolarized light. Physicist Sir George Gabriel Stokes, in 1852, found that the polarization state of EM waves could be intuitively described using four observable and intensity-related parameters: S_0, S_1, S_2 and S_3. These parameters, known as Stokes parameters, can completely describe both the polarization degree and the total intensity of any light, and are typically represented using the Stokes parameter vector:

$$S = \begin{pmatrix} S_0 \\ S_1 \\ S_2 \\ S_3 \end{pmatrix} = \begin{pmatrix} I_H + I_V \\ I_H - I_V \\ I_D - I_A \\ I_R - I_L \end{pmatrix} = \begin{pmatrix} A_x{}^2 + A_y{}^2 \\ A_x{}^2 - A_y{}^2 \\ 2A_xA_y\cos\Delta\varphi \\ 2A_xA_y\sin\Delta\varphi \end{pmatrix} \qquad 2.12$$

In this context, S_0 represents the total light intensity. S_1 indicates the intensity difference between the two orthogonal polarization components aligned with x and y axes, which relate to the horizontal ($|H>$) and vertical ($|V>$) LP characteristics. S_2 denotes the difference in intensity between the orthogonal polarization components along the 45° and −45° directions, corresponding to diagonal ($|D>$) and anti-diagonal ($|A>$) LP characteristics. While S_3 represents the difference in intensity between the two orthogonal polarization components after decomposing light into right-handed ($|R>$) and left-handed ($|L>$) CP components, corresponding to the CP characteristics. Since polarization states are independent of intensity, all parameters are normalized by S_0. These normalized values, ranging from −1 to +1, can describe all possible polarization states. Table 2.2 presents the normalized Stokes parameters for some typical polarization states.

Table 2.2 Normalized Stokes parameters of some typical polarization states.

Polarization state	Stokes parameter
0° LP ($|H>$)	$(1 \quad 1 \quad 0 \quad 0)^T$
90° LP ($|V>$)	$(1 \quad -1 \quad 0 \quad 0)^T$
45° LP ($|D>$)	$(1 \quad 0 \quad 1 \quad 0)^T$
−45° LP ($|A>$)	$(1 \quad 0 \quad -1 \quad 0)^T$
LCP ($|L>$)	$(1 \quad 0 \quad 0 \quad -1)^T$
RCP ($|R>$)	$(1 \quad 0 \quad 0 \quad 1)^T$

Additionally, Stokes parameters can also be used to express the degree of polarization (DoP), DoLP, and the degree of circular polarization (DoCP) of light based on their definitions:

$$\text{DoP} = \frac{\sqrt{S_1{}^2 + S_2{}^2 + S_3{}^2}}{S_0} \qquad 2.13$$

$$DoLP = \frac{\sqrt{S_1{}^2 + S_2{}^2}}{S_0} \qquad\qquad 2.14$$

$$DoCP = \frac{S_3}{S_0} \qquad\qquad 2.15$$

where DoP and DoLP range from 0 to 1 and DoCP ranges from −1 to 1. DoP = 0 signifies light that is completely unpolarized, DoP = 1 represents light that is fully polarized, and a DoP value ranging from 0 to 1 signifies that the light is partially polarized.

To visualize the polarization state of EM waves, in 1892, physicist Henri Poincaré proposed the concept of Poincaré sphere, a geometric representation based on Stokes parameters. Similar to how longitude and latitude pinpoint locations on Earth, the Poincaré sphere uses two angles and the distance from the origin to represent points on and within its surface, as shown in Figure 2.3. The Poincaré sphere forms a spherical structure with a radius normalized to 1, centered at the origin, by using the Stokes parameters S_1, S_2, and S_3 as the axes in a Cartesian coordinate system, with the parameter S_0 providing the normalization. The Stokes parameters can be expressed in terms of the azimuth angle (ψ) and ellipticity (χ) as follows:

$$S_1 = \cos(2\chi)\cos(2\psi) \qquad\qquad 2.16$$

$$S_2 = \cos(2\chi)\sin(2\psi) \qquad\qquad 2.17$$

$$S_3 = \sin(2\psi) \qquad\qquad 2.18$$

In this context, 2ψ starts from the positive direction of the S_1 axis on the equatorial plane of the Poincaré sphere, with values ranging from −180° to 180°. 2χ ranges from −90° to 90° based on the equatorial reference of the Poincaré sphere. Each point on the Poincaré sphere surface, with a distance of 1 from the origin, represents a polarization state. Points along the equator correspond to LPs with various orientations. The North and South poles denote RCP and LCP, respectively. All other points on the sphere's surface represent elliptical polarization states. Additionally, any straight line passing through the origin and intersecting the sphere's surface at two points represents a pair of orthogonal polarization states. As the proportion of unpolarized light increases, the corresponding points on the Poincaré sphere move closer to the origin. When a point reaches the origin, the light is completely unpolarized. The normalized Stokes parameters listed in Table 2.2 can be intuitively visualized as polarization states on the Poincaré sphere (Figure 2.3).
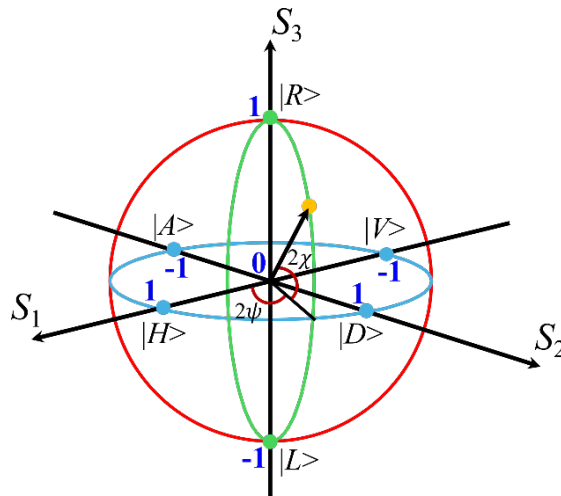
Figure 2.3 Schematic of a Poincaré sphere with a radius normalized to 1.

2.2   Phase control: principles and methods

In this chapter, three common methods for phase modulation in metasurfaces are discussed: resonance phase, geometric phase (Pancharatnam-Berry phase, PB phase) and a combination of both [85-87], with relevant case studies included to illustrate each method. Some cases are also selected from my previous publication **Appendix A** [52], and incorporates pieces of text from that work.

2.2.1   Resonance phase

This paragraph is based on my previous publication **Appendix A** [52], and incorporates pieces of text from that work. The resonance phase, which can be precisely controlled by adjusting the shape and size of the nanostructures to achieve specific functionalities in orthogonal LP bases for cross-polarized optical fields, utilizes the birefringent properties of the nanostructures and can be represented using the Jones matrix in LP bases:

$$M_{\text{LP}} = \begin{pmatrix} M_{\text{xx}} & M_{\text{xy}} \\ M_{\text{yx}} & M_{\text{yy}} \end{pmatrix} \qquad 2.19$$

where M_{xx} (M_{yy}) and M_{xy} (M_{yx}) represent the co-polarized and cross-polarized complex transmitted (reflected) coefficients, respectively. For example, Yu and colleagues demonstrated a classic gold V-shaped nanorod capable of supporting both symmetric and antisymmetric electric dipole resonances when excited by incident field components along a pair of orthogonal $\hat{s}$ and $\hat{a}$ axes, respectively (left panel of Figure 2.4(a)) [88]. By simultaneously optimizing both the opening angle Δ and the length h of the V-shaped nanorods, a series of four nanorods were meticulously crafted with a phase interval of π/4, as shown the four small write circles (middle panel of Figure 2.4(a)). To achieve the full 2π phase coverage, another four nanorods were created by duplicating the original four and rotating them 90°, introducing an additional π phase shift in the xy-plane. As a preliminary validation, they demonstrated a phase gradient metasurface featuring a super-cell built from these eight nanorods, which produces a phase variation that changes continuously in eight distinct increments along the x-axis (right panel of Figure 2.4(a)), enabling arbitrary angles of reflection and refraction for incident LP beams in the mid-infrared range. Additionally, Yang et al. experimentally realized a metasurface using Si-PMMA-Ag hybrid nano-HWPs, which deliver a spiral phase profile that varies azimuthally from 0 to 2π, generating optical vortex beams with orthogonal LP conversion, as shown in Figure 2.4(b) [64]. Similarly, by varying geometry dimensions of the topmost Si structures, four different meta-HWPs with relatively high cross-polarized reflectance and phase modulation are selected to provide a phase coverage of π for the cross-polarized reflected light with an incremental step of π/4 [52]. The additional π-phase range could be attained by simply rotating these antennas with an angle of 90°, thereby resulting in the full 2π coverage with near-unity efficiencies in cross-polarization [52]. The efficiency of the simulated vortex beam is around 94.5% across wavelengths ranging from 1500 to 1600 nm.
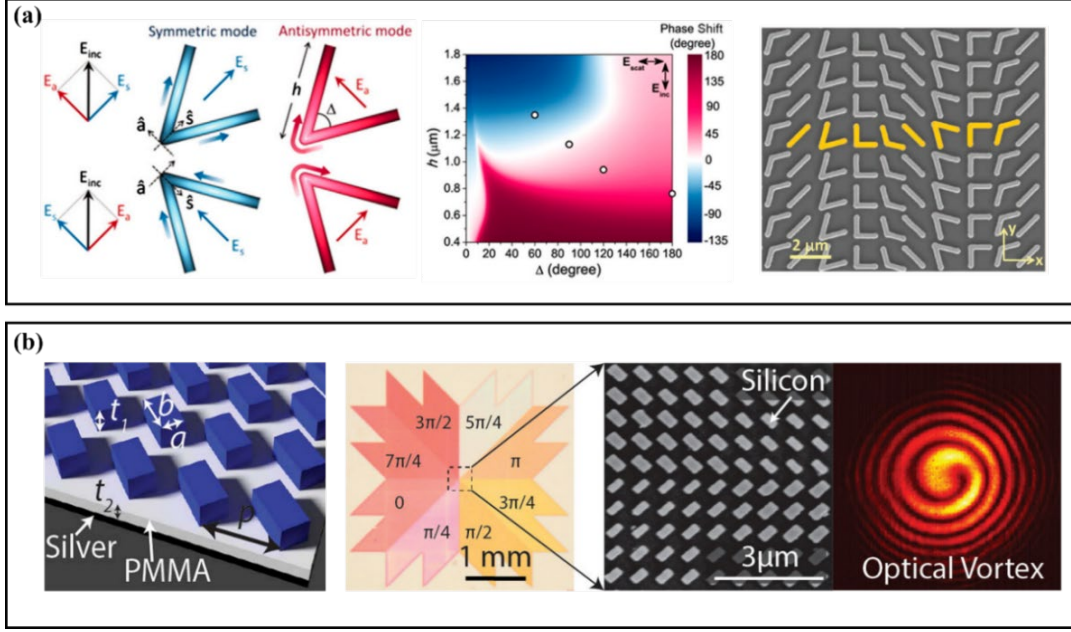
Figure 2.4 Metasurface wavefront shaping solely on resonance phase. (a) Left panel: illustration of the *V*-shaped nanorod, highlighting its ability to support both symmetric (blue) and antisymmetric (red) modes, activated by the cross-polarized components of the incoming light. Middle panel: simulated phase shift of the cross-polarized scattered light for *V*-shaped nanorods as a function of the opening angle Δ and the length *h* at 8 μm working wavelength. Right panel: SEM image of the sample. Reprinted from Ref. [88]. (b) Left panel: schematic of a reflective meta-HWP array consisting of Si bricks, a PMMA spacer, and an Ag reflector. Right panel: design and experimental demonstration of optical vortex beam generation in cross-polarization [52]. Reprinted from Ref. [64].

2.2.2 Geometric phase (PB phase)

This paragraph is based on my previous publication **Appendix A** [52], and incorporates pieces of text from that work. In the aforementioned cases, the resonance phase closely associated with the geometric dimensions of nanostructures typically involves the occurrence of an abrupt phase discontinuity in the LP basis. While for CP lights, another distinct method known as the geometric phase or PB phase, allows complete phase manipulation in the cross-polarized output field through the use of anisotropic meta-atoms. These meta-atoms share the same geometric design, yet they display rotation angles that vary across different spatial locations. The principle of geometric phase can be vividly illustrated through Jones matrix. Typically, the following Jones matrix generally describes an anisotropic meta-atom rotated by an angle θ relative to the *x*-axis:

$$M_\theta = R(\theta)^{-1} \begin{pmatrix} M_{\mathrm{xx}} & 0 \\ 0 & M_{\mathrm{yy}} \end{pmatrix} R(\theta) \qquad\qquad 2.20$$

$$R(\theta) = \begin{pmatrix} \cos\theta & \sin\theta \\ -\sin\theta & \cos\theta \end{pmatrix} \qquad\qquad 2.21$$

where $R(\theta)$ stands for the rotation matrix. Considering the incident LCP and RCP light, denoted as $E_i^\pm = \frac{\sqrt{2}}{2}\begin{pmatrix} 1 \\ \pm i \end{pmatrix}$, respectively, the Jones matrix of the output fields can be expressed as:

$$M_{\mathrm{out}} = \frac{1}{2\sqrt{2}}(M_{\mathrm{xx}} + M_{\mathrm{yy}})\begin{pmatrix} 1 \\ \pm i \end{pmatrix} + \frac{1}{2\sqrt{2}}(M_{\mathrm{xx}} - M_{\mathrm{yy}}) \cdot e^{\pm i2\theta}\begin{pmatrix} 1 \\ \mp i \end{pmatrix} \qquad 2.22$$

In the right of equation 2.22, the initial term pertains to the output light that maintains the polarization state of the incoming CP light, aligning with the co-polarized CP channel. Conversely, the subsequent term refers to output light with a reversed polarization state, corresponding to the cross-polarized CP channel. When $M_{xx} \neq M_{yy}$, the cross-polarized CP channel will carry an extra PB phase of $\pm 2\theta$, whose sign is contingent upon the incident polarization state. As a result, rotating the meta-atom from $0°$ to $180°$ counterclockwise relative to the x-axis allows for the achievement of a complete 2π phase shift in the cross-polarized CP channel. When $M_{xx} = -M_{yy}$, the meta-atom functions as a standard nano-HWP, resulting in the complete conversion of the output field into the cross-polarized CP channel and the elimination of the co-polarized CP channel. Hence, by varying the rotation angles of meta-atoms at different spatial points within the array, diverse geometric phases can be introduced, offering enhanced flexibility in phase modulation for reflected or transmitted EM waves across a broadband spectrum. In 2015, Zheng and colleagues experimentally verified geometric metasurface holograms with up to 80% diffraction efficiency by employing spatially oriented nano-HWPs at $\lambda = $ 825 nm, as shown in Figure 2.5(a) [27]. This designed metasurface achieves 16 phase levels by precisely adjusting the spatial orientations of the nano-HWPs, ensuring high quality in manufacturing (middle panel of Figure 2.5(a)). Remarkably, the working bandwidth is quite wide, ranging from 630 to 1050 nm with a high measured efficiency greater than 50% (right panel of Figure 2.5(a)) [52]. Additionally, Brongersma's research group experimentally proposed a dielectric metalens employing geometric phase to achieve the efficient visible light focusing [89]. As shown in the left panel of Figure 2.5(b), the subwavelength-spaced Si nano-stripes act as nano-HWPs at the wavelength centered at 550 nm [52]. By discretizing the geometric phase in eight steps, a hyperboloidal phase profile could be approximated to mimic a conventional focusing lens (middle panel of Figure 2.5(b)) [52]. The fabricated metalens can concentrate the RCP incident light into an LCP focal spot with the focal length and the NA of 100 μm and 0.43 at $\lambda = $ 550 nm, respectively (right panel of Figure 2.5(b)) [52].
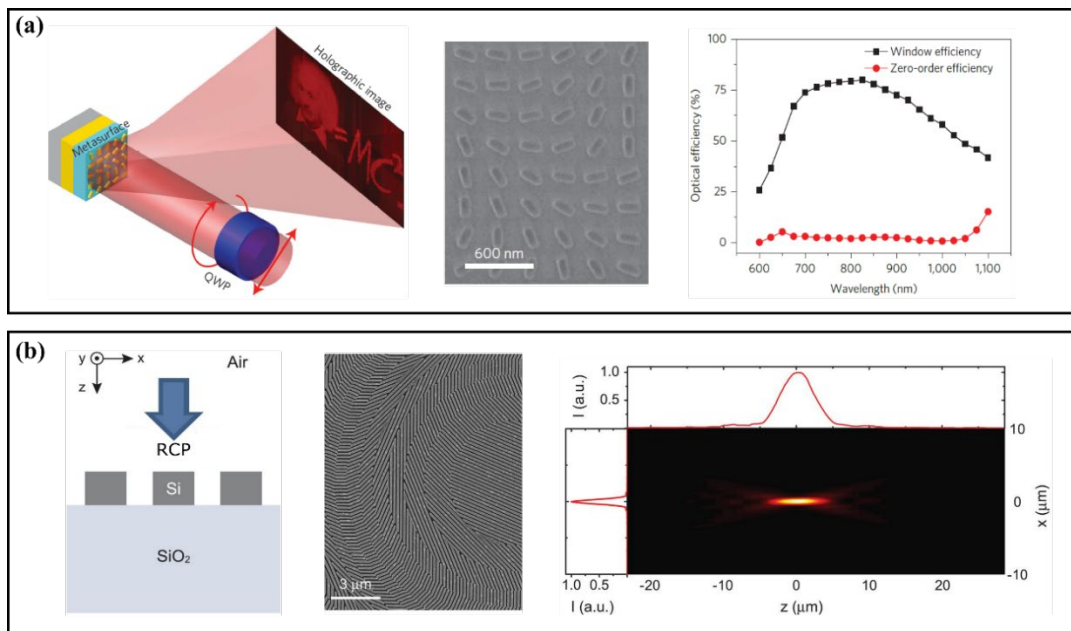
Figure 2.5 Metasurface wavefront shaping solely on geometric phase. (a) Left panel: schematic of the reflective metasurface hologram under a CP incident light. Middle panel: SEM image of part of the fabricated sample. Right panel: measured holographic image and zero-order efficiencies as a function of the wavelength [52]. Reprinted from Ref. [27]. (b) Left panel: schematic view of the designed Si meta-HWP. Middle panel: SEM image of part of the fabricated metalens. Right panel: measured intensity distributions of the focusing

light passing through the fabricated meta-lens along the vertical and horizontal axes in the *xz*-plane [52]. Reprinted from Ref. [89].

2.2.3 Resonance and geometric phases

This paragraph is based on my previous publication **Appendix A** [52], and incorporates pieces of text from that work. Although geometric metasurfaces can achieve extensive wavefront shaping in the cross-polarized channel under CP excitations, the co-polarized channel remains unmodulated. In designing a multifunctional metasurface, it is essential to utilize all available channels and enhance output efficiency by integrating both resonance and geometric phases. In 2020, Ding's group has experimentally demonstrated an efficient spin-decoupled multifunctional GSP meta-device [19] that enables unidirectional surface plasmon polariton (SPP) excitation and anomalous beam steering simultaneously under orthogonal CP incident beams in the near-infrared range (the left panel of Figure 2.6(a)) [52]. By simultaneously engineering both resonance and geometric phases, two optimized nano-HWPs with varying shapes and dimensions were rotated at different angles to create two distinct spin-sensitive linear phase gradients along the *x*-direction [52]. For RCP light, the phase gradient is designed to match the wavevector of SPPs supported by the substrate at normal incidence [52]. For LCP light, the phase gradient is designed smaller than the wavevector of free-space propagating light, which results in an anomalous deflection angle of the reflected light (middle and right panels of Figure 2.6(a)) [52]. The fabricated multifunctional meta-device shows efficient unidirectional SPP excitation with a coupling efficiency above 22% in the wavelength range from 850 to 950 nm under the RCP incident light. Once the input is switched to LCP light, the anomalous beam steering with an averaged efficiency of 48% is achieved at the same spectrum [52]. However, despite successfully achieving spin-decoupling by combining both resonance and geometric phases, the nano-HWPs block the co-polarized channel, restricting wavefront shaping exclusively to the cross-polarized channel. In 2021, Chen et al. experimentally proposed an independent all-dielectric spin-sensitive metasurface consisting of silicon nitride (SiN_x) nano-QWPs to generate different hologram images for co- and cross-polarized channels under the RCP excitation (Figure 2.6(b)) [90]. Specifically, the transmitted co-polarized RCP light could be manipulated with the resonance phase to generate a far-field hologram image with "NJU", while the cross-polarized LCP light could be engineered with both resonance and geometric phases to produce a hologram building image of Nanjing University (right panel of Figure 2.6(b)) [52].
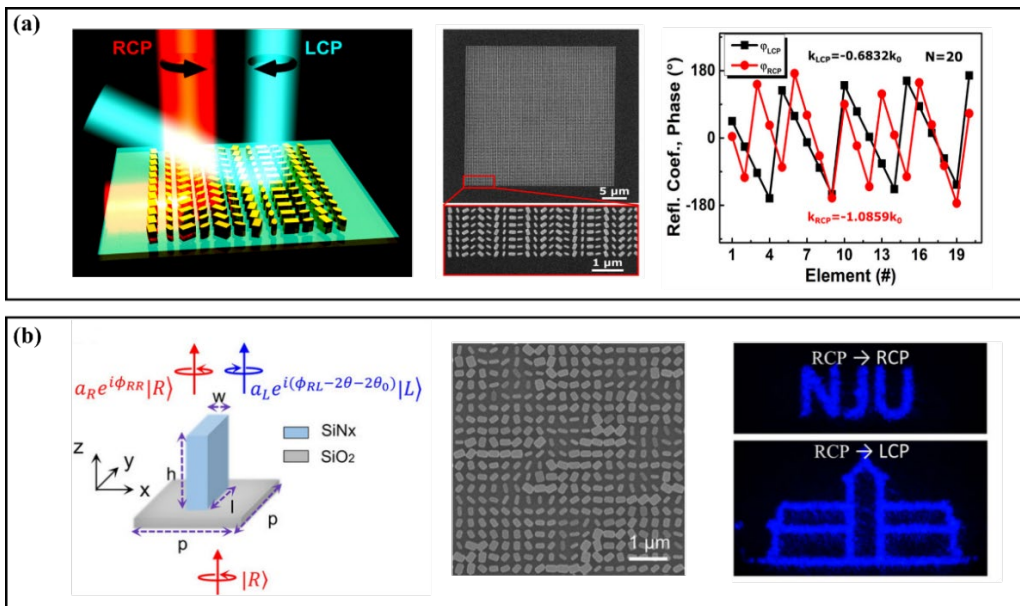
Figure 2.6 Metasurface wavefront shaping combining both resonance and geometric phases. (a) Left panel: schematic of the spin-decoupled GSP metasurface composed of nano-HWPs with different dimensions and orientations for unidirectional SPP excitation and beam-steering under RCP and LCP incidence, respectively. Middle panel: SEM images of the fabricated structure. Right panel: phase profiles of the reflected fields under RCP and LCP incident light at λ = 850 nm [52]. Reprinted from Ref. [19]. (b) Left panel: schematic of the SiNx nanopillar that acts as a meta-QWP. Middle panel: SEM image of the fabricated structure. Right panel: measured hologram images in the RCP and LCP channels under the RCP excitation [52]. Reprinted from Ref. [90].

2.3   Numerical simulation methods

Subwavelength-scale meta-atoms, which form metasurfaces, are typically composed of two or more complex materials. The differing EM properties of these materials add complexity, making it particularly challenging to solve the associated Maxwell's equations. In practical applications, designing subwavelength-scale meta-atoms is essential to ensure that the resulting metasurface achieves specific EM control functions. Consequently, accurately analysing the EM field distribution of these complex structures under specific excitations becomes crucial.

This paragraph is based on my previous publication **Appendix C** [80], and incorporates pieces of text from that work. In this thesis, we employed commercially available software Comsol Multiphysics (version 5.6) to conduct the 3D full-wave simulation [80]. Here, we use a classic MIM-based brick-shaped meta-atom as an example (Figure 2.7(a)), which illustrates a typical resonator element consisting of a top Au nano-brick, a bottom thick Au reflector, and an intermediate SiO$_2$ spacer separating them. In this reflective unit cell model, the bottom Au reflector generally has a thickness d set to 100 nm, allowing it to act as a perfect mirror. In the simulation, as shown the model screenshot from Comsol Multiphysics in Figure 2.7(b), an air domain is added above the meta-atom and truncated with a perfectly matched layer (PML) to minimize any reflection [80]. The relative permittivity of Au is described by the Drude model fitted with the experimental data [91], and SiO$_2$ is taken as a lossless material with a constant refractive index of 1.45 [80]. The respective thickness t_m and t_s of the top Au nano-brick and the SiO$_2$ spacer, as well as the period Λ of the unit cell are preset based on the operating wavelength and desired functionality. An x- or y-polarized plane wave is normally impinging on the MIM unit cell from the port, with periodic boundary conditions employed in both x- and y-directions [80]. For example, the length l and width w of the top Au nano-brick are parametrically swept to obtain the complex reflection amplitude and phase maps at the target wavelength, which correspond to the resonance phase mentioned earlier.
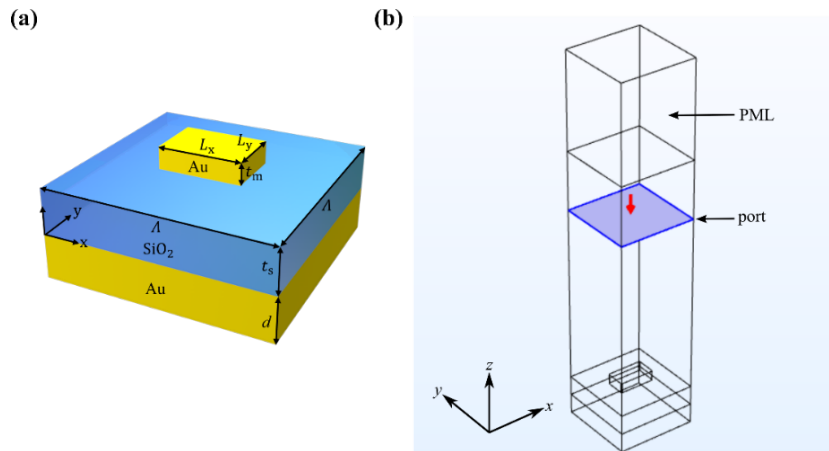
Figure 2.7 (a) Schematic of the anisotropic MIM brick-shaped meta-atom. (b) Screenshot of the unit cell model from the software Comsol Multiphysics (version 5.6).

2.4   Sample fabrication

This paragraph is based on my previous publication **Appendix C** [80], and incorporates pieces of text from that work. All metasurface samples in this thesis were fabricated utilizing standard thin-film deposition, electron beam lithography (EBL), and lift-off techniques [80]. Here, we take the fabrication of MIM GSP metasurfaces (**Appendix B-D**) as an example. Initially, a sequence of deposition processes was performed on a silicon substrate employing thermal evaporation. This included the successive deposition of a 3 nm Ti layer, a 100 nm Au layer, and a 2 nm Ti layer [80] (Figure 2.8(a)). Then, a SiO$_2$ spacer layer of a specific thickness was deposited using RF sputtering [80]. The thickness of the SiO$_2$ spacer layer, such as 70 nm or 100 nm, depends on the duration of the RF-sputtering. Next, a 100 nm PMMA (2% in anisole, Micro Chem) layer was spin-coated on the SiO$_2$ layer, baked at 180°C for 2 min, and exposed at an acceleration voltage of 30 keV to define the patterns [80] (Figure 2.8(b-c)). After exposure, the wafer was developed in the solution of methyl isobutyl ketone (MIBK) and isopropyl alcohol (IPA) of MIBK: IPA = 1:3 for 35 s followed by 60 s in an IPA bath [80] (Figure 2.8(d)). After development, a 1 nm Ti adhesion layer and a 40 nm (depending on the design) Au layer were deposited subsequently using thermal evaporation [80] (Figure 2.8(e)). Finally, top Au antennas were formed after a lift-off process [80] (Figure 2.8(f)). The other two works (**Appendix E-F**) in this thesis, which involve fabricating metasurfaces on glass substrates, follow the same processes and methods.
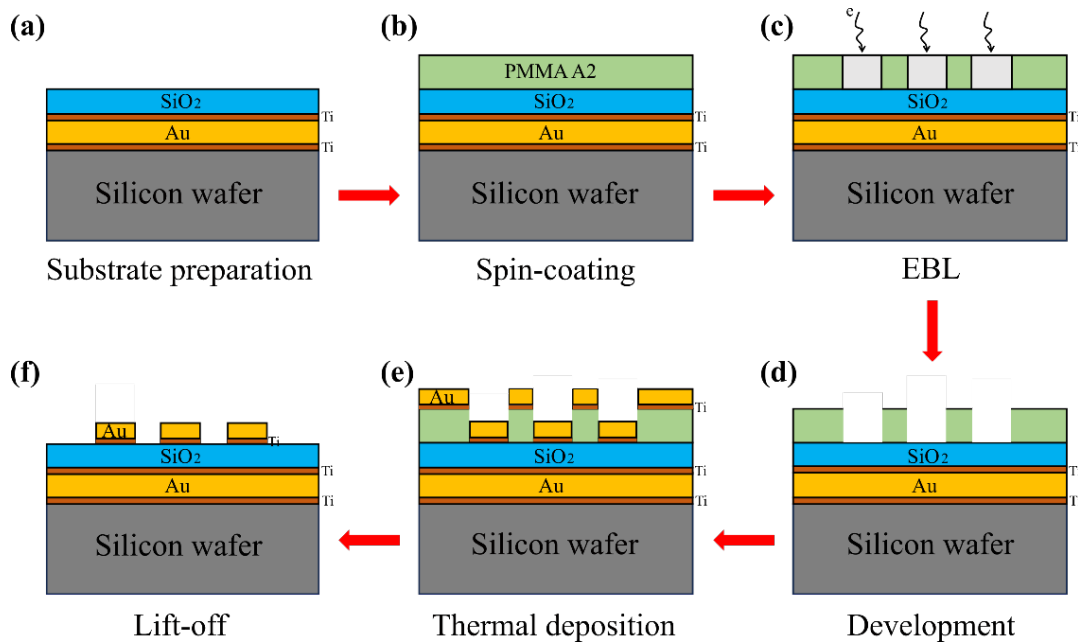
Figure 2.8 The flowchart of sample fabrication.

2.5   Optical characterizations

Given that all sample characterizations in *Sections 3* and *4* were based on the same custom-built setup, with only minor adjustments of optical components to meet specific needs, I will therefore provide a comprehensive overview of our measurement setup, schematic in Figure 2.9 and photograph in Figure 2.10, in this section, which is summarized based on my previous publications **Appendix B-C** [79-80] and **Appendix E-F** [82-83] and incorporates pieces of text from that works.

<u>Setup for light source incidence.</u> A collimated fiber-coupled laser firstly passes through a half-wave plate (HWP1, AHWP10M-980, Thorlabs) and an attenuator (NE01B, Thorlabs) to achieve the

appropriate light intensity [80], combining with the set of exposure time. Depending on the different requirements of sample measurements, either of the two light sources, cw Ti:sapphire laser (Spectra-Physics 3900 S, wavelength from 700 to 1000 nm) or supercontinuum laser (SuperK Extreme, NKT Photonics) can be freely selected to input into the setup. Then the light reflected by a sliver mirror (PF10-03-P01, Thorlabs) passes through a linear polarizer (LP1, LPNIR050-MP2, Thorlabs) and a half-wave plate (HWP2, AHWP10M-980, Thorlabs) mounted on a motorized precision rotation stage (MPRS, PRM1Z8, Thorlabs), two beam splitters (BS1 and BS2, CCM1-BS014/M, Thorlabs) successively, and then slightly focused onto the sample by a long working distance objective (Obj. M Plan Apo 20×/0.42NA, Mitutoyo) [83]. The combination of LP1 and HWP2 is to generate the required incident polarization states (e.g., x-/y- polarized state) in a controlled manner. Once HWP2 is replaced with a quarter-wave plate (QWP1, AQWP10M-980, Thorlabs), the incident polarization state can be flexibly switched between circular polarizations (e.g., LCP and RCP). The combination of BS1 and BS2 can not only change the propagation direction of the incident light, but also compensate for the polarization-dependent phase shifts caused by one single BS [83].

Setup for imaging and signal light collection. The reflected light is collected by the same objective and passes through BS2 and a tube lens (f = 200 mm; TTL200-S8, Thorlabs), generating the first real image plane where an iris (SM1D12SZ, Thorlabs) is positioned for filtering out the background outside the sample area [83]. The filtered first real image is transformed by a relay lens (RL, AC254-200-B-ML, f = 200 mm, Thorlabs) to create a Fourier image, which is captured by a complementary metal oxide semiconductor camera (DCC1545M, Thorlabs) when a flip mirror (PF10-03-P01, Thorlabs) is flipped up [83]. To switch between real and Fourier images, a flip lens (FL, AC254-100-B-ML, f = 100 mm, Thorlabs) is placed between the relay lens and the flip mirror [83]. If we only add a linear polarizer (LP2, LPNIR050-MP2, Thorlabs) between FL and RL, the polarization state of the output signal light can be easily detected by rotating LP2 360°. This configuration also allows us to collect a specific linear component of the signal light that we are interested in. Furthermore, by adding another quarter-wave plate (QWP2, AQWP10M-980, Thorlabs), we can construct co- and cross-polarized channels and flexibly switch them under CP incident lights using the combination of LP2 and QWP2. Therefore, by flexibly using LP2, QWP2 and their combination, we can gather spectral information and calculate full Stokes parameters for CP incident lights (Materials and methods, Optical characterization of **Appendix F**). In addition, a spectrometer (QE Pro, Ocean Optics) can be employed to collect the polarization-resolved reflection spectra when FM is flipped down.
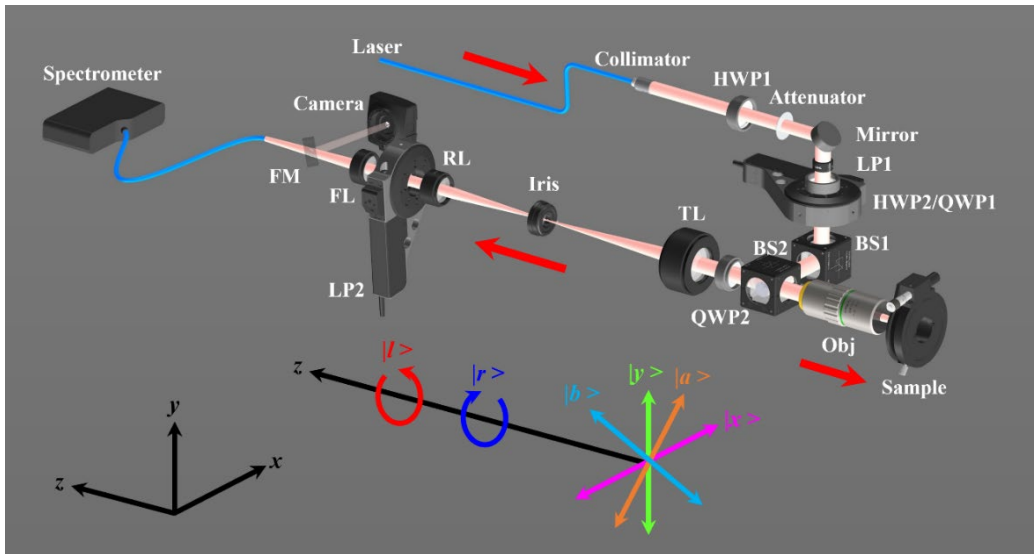

Figure 2.9 Schematic of the home-built experimental setup for characterizing the fabricated samples.
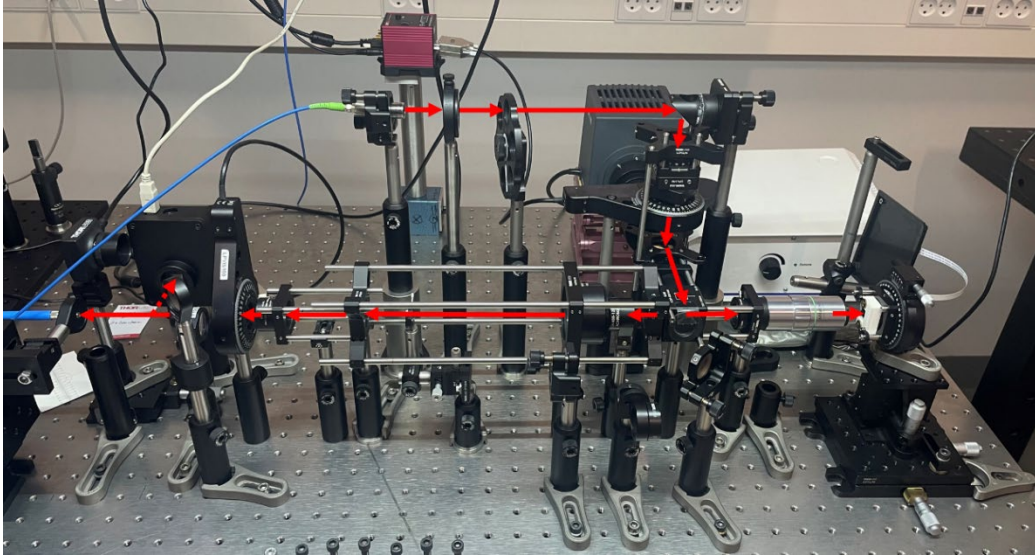
Figure 2.10 Photograph of the home-built experimental setup.

3   GSP metasurfaces for passive wavefront shaping

In this chapter, an overview to the physical model and configuration of GSP resonators is firstly provided, with special emphasis placed on a comparative analysis with Fabry-Perot (FP) resonators. Subsequently, we theoretically designed and experimentally validated a GSP metasurface waveplate for dual-functional polarization conversion under a pair of orthogonal LP excitations at the wavelength of 850 nm. The related journal article that we have published is referenced in **Appendix B** [79]. Finally, leveraging our developed cross-shaped GSP nano-QWP library in the near-infrared range, we expanded spin-decoupled applications of GSP multifunctional metasurfaces to encompass advanced beam steering (the related journal article that we have published is referenced in **Appendix C** [80]) and metalens (**Appendix D** [81], to be submitted) technologies. Moreover, this novel nano-QWP platform can be further utilized to explore applications such as multi-channel holographic imaging.

3.1   GSP resonators

To begin, we shall delve into the exploration of SPPs. Under EM excitation, the free electrons on the metal surface undergo collective oscillations that couple with the incident EM waves, forming a tightly confined near-field wave which travels along the interface between metal and dielectric. Once the incident EM wave frequency matches the free electrons' oscillation frequency, resonance occurs, concentrating the energy of the near-field EM waves within a subwavelength scale, which significantly enhances the intensity of the EM field. This coupled EM mode, arising from the interaction between free electrons and photons at the metal-dielectric interface, is referred to as a SPP [92]. As an evanescent wave, SPPs propagate laterally along the metal-dielectric interface, where their field intensity diminishing exponentially in the direction perpendicular to the interface. Owing to their exceptional ability to confine energy at the subwavelength scale and enhance EM fields, SPPs have a broad range of applications across various fields, including information technology and communication [93], quantum optics [94], sustainable energy [95], and biochemical sensing [96]. Nevertheless, when moving to the longer wavelength range within the visible band, SPPs approach the light line, which makes it challenging to achieve significantly enhanced local fields. An effective method to achieve strong field enhancement at the metal-dielectric interface under varying incident light wavelengths entails positioning two metal-dielectric interfaces in close proximity, thereby introducing near-field coupling (NFC) between SPPs of each interface. Within multilayer structures, MIM configurations involving GSPs exhibit superior performance in terms of strong mode confinement and high-quality factors compared to insulator-metal-insulator (IMI) resonators. Consequently, MIM structures find extensive applications in the realm of metasurfaces. In this section, we primarily focus on introducing three classic GSP resonators with MIM configurations [63].

By truncating an infinitely long MIM configuration, we obtain the first type of GSP resonator, composed of two Au strips separated by an intermediate SiO$_2$ layer, as depicted in Figure 3.1(a). The truncated terminations on both sides of this MIM structure act as mirrors, facilitating multiple reflections of the GSP modes traveling along the metal-dielectric interface and resulting in the formation of lateral standing-wave GSP modes. Since the MIM configuration closely resembles a FP cavity, the generated GSP modes can be effectively described using the simple FP formula:

$$w \frac{2\pi}{\lambda_0} n_{\text{GSP}} = m\pi - \phi \qquad\qquad 3.1$$

where w denotes the width of the Au strip, λ_0 is the wavelength of incident light in free space, n_{GSP} represents the real part of the equivalent refractive index of GSP, m is the integer order of the GSP

mode, and ϕ represents an additional phase shift acquired when GSPs are reflected between the two metal-dielectric interfaces of the MIM structure. By appropriately adjusting the structural parameters of the GSP resonator, such as the width of the top metal strip and the thickness of the SiO$_2$ layer, the targeted GSP resonance can be achieved at the design wavelength. This resonance predominantly exhibits scattering characteristics, making it highly suitable for the design and implementation of reflective metasurfaces. Notably, when the thickness of the SiO$_2$ layer is small, the NFC between the coupled EM modes at the two metal-dielectric interfaces becomes stronger, causing the GSP resonator to primarily exhibit absorption characteristics. With an increase in SiO$_2$ layer thickness, the NFC weakens, diminishing the support for GSP resonance and gradually transitioning the system from a horizontal GSP resonance to a vertical FP resonance.
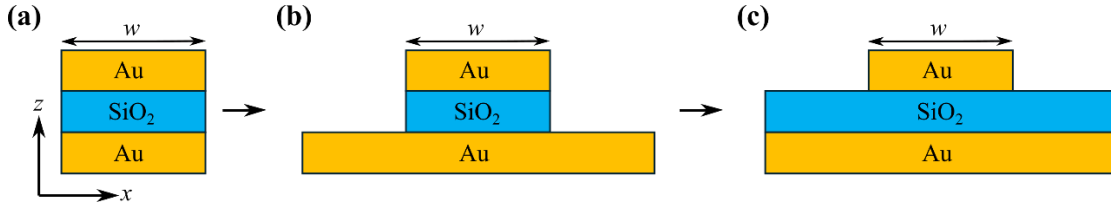
Figure 3.1 Schematics of three typical Au-SiO$_2$-Au GSP resonators. (a) Highly-symmetric configuration. (b) Configuration with continuous bottom Au layer. (c) Configuration with continuous SiO$_2$ spacer and bottom Au layer.

In addition to the highly symmetrical MIM configuration mentioned above, replacing the Au strip beneath the SiO$_2$ layer with an infinitely extending Au thin layer also allows the realization of a GSP resonator exhibiting similar scattering resonances (Figure 3.1(b)). The presence of the bottom Au thin layer slightly increases the effective width of the GSP resonator, causing the resonance wavelength of the 1st-order GSP mode to shift towards a longer wavelength region when other structural parameters remain the same. Furthermore, the bottom Au thin layer enhances the scattering intensity of the GSP resonator. The third type of GSP resonator replaces both the bottom Au strip and the SiO$_2$ layer of the conventional MIM structure with infinitely extending thin layers (Figure 3.1(c)). This structure, known as the continuous layer GSP resonator, exhibits scattering resonances similar to those of standard GSP resonators. Compared to the two previously mentioned GSP resonators, the continuous SiO$_2$ layer in this GSP resonator eliminates the refractive index difference between the SiO$_2$ layer and air along the horizontal axis, resulting in a stronger GSP mode. Consequently, with other structural parameters remaining the same, its GSP mode shifts further towards the longer wavelength region. Beyond the beneficial features of traditional GSP resonators, the continuous layer GSP resonator also provides the advantage of easier fabrication. Achieving this involves depositing Au directly into the resist pattern through a one-time lithography process, significantly simplifying the subsequent lift-off procedure. Therefore, most GSP metasurfaces are designed and fabricated using this third type of GSP resonator, with the top metal structure layer typically consisting of periodically arranged meta-atoms.

Here, utilizing the third type of GSP resonator, we present a comparative analysis of both GSP and FP resonance modes. We take the typical MIM resonator shown in Figure 2.7 as a model example. The structure parameter space $\Omega = [t_m, \Lambda, d] = [50 \text{ nm}, 400 \text{ nm}, 100 \text{ nm}]$ were pre-fixed. Figure 3.2 presents the amplitude and phase maps of the complex reflection coefficients in relation to varying nano-brick lengths L_x and L_y at 850 nm design wavelength for two different thicknesses t_s of the SiO$_2$ spacer, along with the corresponding electric field distributions for special dimensions. When $t_s = 50$ nm, a strong GSP resonance occurs around $L_x = 150$ nm, driven by NFC between the top nano-brick and the substrate, as shown the electric field distribution in Figure 3.2(a). Once we increase t_s to 350 nm, the NFC between the top nano-brick and the substrate disappears, replaced by a less sharp

resonance caused by a hybrid plasmonic FP resonance around $L_x = 170$ nm, as shown the electric field distribution in Figure 3.2(b). By comparing phase contours of both GSP and FP modes in Figure 3.2(a-b), we observe that the GSP mode offers a slightly broader range of available reflection phases; however, the FP mode demonstrates a relatively greater reflection amplitude [78]. Therefore, selecting the appropriate mode to manipulate the optical field is essential for us, depending on whether the control method is passive [79-81] or active [82-83], as well as on details and challenges of the sample fabrication process.
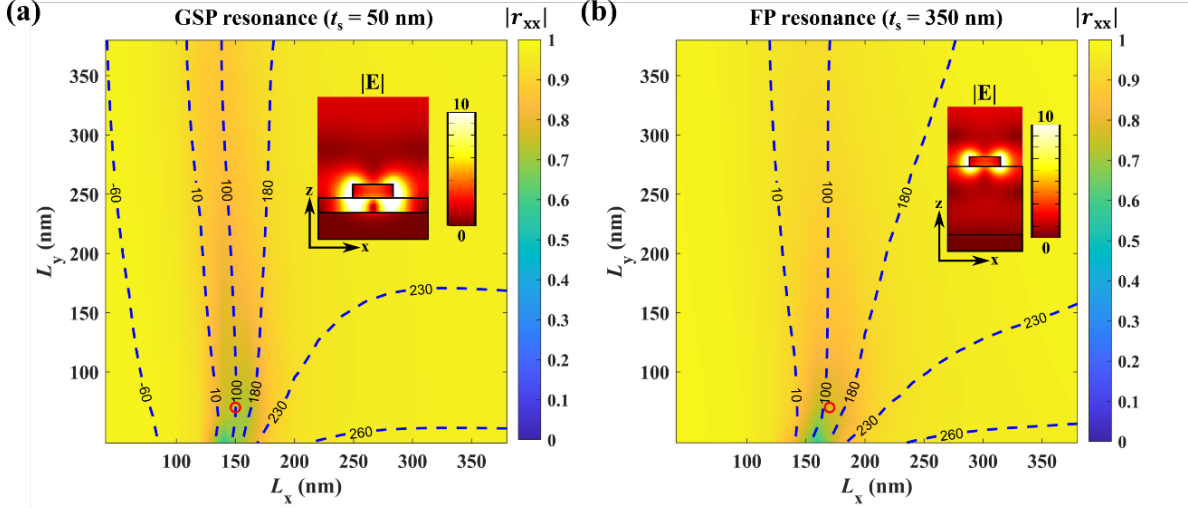
Figure 3.2 (a-b) Calculated reflection coefficient maps in relation to the varying lengths L_x and L_y of the top nano-brick at the wavelength of 850 nm for (a) $t_s = 50$ nm and (b) $t_s = 350$ nm. The colour maps display the reflection amplitudes for x-polarized light incident at normal incidence, with the blue dashed contour lines highlighting the corresponding phases of reflection. The insets in the upper right display the electric field distributions in the xz-plane at the center of the nano-brick for normal x-polarized incident light. Red circles: (a) $L_x = 150$ nm and $L_y = 70$ nm; (b) $L_x = 170$ nm and $L_y = 70$ nm.

3.2 GSP waveplates for dual-functional polarization conversions

This section is based on our previous publication (**Appendix B** [79]) and includes portions of text incorporated from that work. To advance the development of planar polarization optical devices with multifunctional capabilities, we designed and experimentally demonstrated a reflective dual-functional optical waveplate [79], as shown in Figure 3.3(a). This compact and ultra-thin optical waveplate is constructed using a periodically distributed GSP meta-molecule, comprising two Au nano-bricks with varying geometric dimensions and spatial rotation angles, positioned atop a continuous SiO_2 spacer layer, which rests on a thick bottom Au reflector (Figure 3.3(b)). The novel optical waveplate integrates the functionalities of both QWPs and HWPs, enabling simultaneous LP-to-CP and LP-to-LP polarization conversion at the same working wavelength of 850 nm.
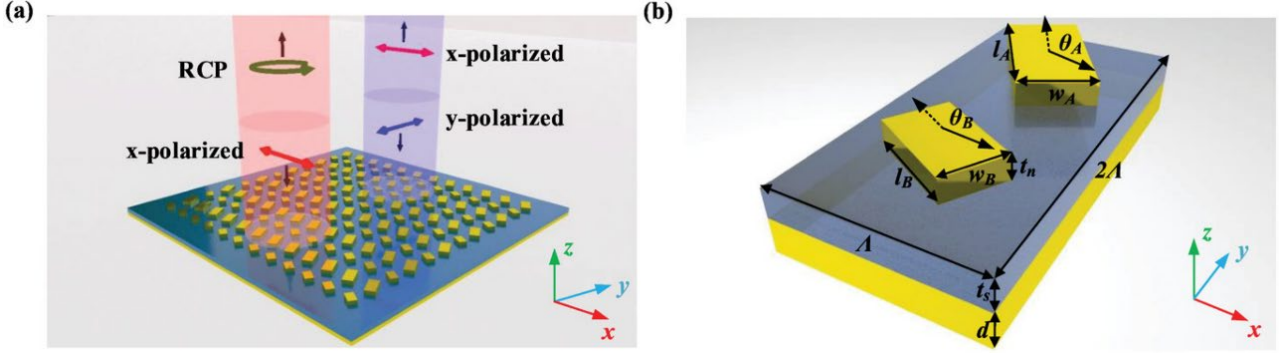
Figure 3.3 (a) Illustration of the working principle of the dual-functional optical waveplate. (b) Schematic of the meta-molecule unit cell [79]. Reprinted from Ref. [79].

3.2.1 Design and theoretical analysis

This section is based on my previous publication **Appendix B** [79], and incorporates pieces of text from that work. We initiate our discussion by considering the implementation of the dual-functional optical waveplate [79] employing a single meta-atom, analysed through derivations of the Jones matrix:

$$\begin{cases} \begin{pmatrix} R_{xx} & R_{xy} \\ R_{yx} & R_{yy} \end{pmatrix} \begin{pmatrix} 1 \\ 0 \end{pmatrix} = \begin{pmatrix} R_{xx} \\ R_{yx} \end{pmatrix} = \frac{\sqrt{2}}{2} \begin{pmatrix} 1 \\ i \end{pmatrix} \\ \begin{pmatrix} R_{xx} & R_{xy} \\ R_{yx} & R_{yy} \end{pmatrix} \begin{pmatrix} 0 \\ 1 \end{pmatrix} = \begin{pmatrix} R_{xy} \\ R_{yy} \end{pmatrix} = \begin{pmatrix} 1 \\ 0 \end{pmatrix} \end{cases} \tag{3.2}$$

where $\begin{pmatrix} R_{xx} & R_{xy} \\ R_{yx} & R_{yy} \end{pmatrix}$ represents the Jones matrix of the meta-atom, $\begin{pmatrix} 1 \\ 0 \end{pmatrix}$ and $\begin{pmatrix} 0 \\ 1 \end{pmatrix}$ denote the respective Jones vector for the incident *x*- and *y*-polarized light, with the resulting output Jones vectors being $\frac{\sqrt{2}}{2} \begin{pmatrix} 1 \\ i \end{pmatrix}$ for LCP and $\begin{pmatrix} 1 \\ 0 \end{pmatrix}$ for *x*-polarized light, respectively. Therefore, to attain the intended dual polarization conversion functionality, the four complex reflection coefficients in the Jones matrix must simultaneously meet the following conditions:

$$\begin{cases} R_{yx} = iR_{xx} \neq 0 \\ R_{xy} \neq 0 \\ R_{yy} = 0 \end{cases} \tag{3.3}$$

The reflection Jones matrix $R(\theta)$ of the meta-atom, rotated by an angle θ relative to the positive *x*-axis, and considering its anisotropic properties, is given by:

$$R(\theta) = \begin{pmatrix} \cos(\theta) & -\sin(\theta) \\ \sin(\theta) & \cos(\theta) \end{pmatrix} \begin{pmatrix} r_{xx}e^{i\varphi_{xx}} & 0 \\ 0 & r_{yy}e^{i\varphi_{yy}} \end{pmatrix} \begin{pmatrix} \cos(\theta) & \sin(\theta) \\ -\sin(\theta) & \cos(\theta) \end{pmatrix} \tag{3.4}$$

By calculating the above equation with the assumption that $|r_{xx}| = |r_{yy}| = |r|$, we could obtain:

$$R(\theta) = |r| \begin{pmatrix} e^{i\varphi_{xx}}\cos^2(\theta) + e^{i\varphi_{yy}}\sin^2(\theta) & (e^{i\varphi_{xx}} - e^{i\varphi_{yy}})\sin(\theta)\cos(\theta) \\ (e^{i\varphi_{xx}} - e^{i\varphi_{yy}})\sin(\theta)\cos(\theta) & e^{i\varphi_{xx}}\sin^2(\theta) + e^{i\varphi_{yy}}\cos^2(\theta) \end{pmatrix} \tag{3.5}$$

the complex reflection coefficients need to satisfy the conditions in equations 3.3, then we have:

$$\begin{cases} |r|(e^{i\varphi_{xx}} - e^{i\varphi_{yy}})\sin(\theta)\cos(\theta) = i|r|(e^{i\varphi_{xx}}\cos^2(\theta) + e^{i\varphi_{yy}}\sin^2(\theta)) \neq 0 \\ |r|e^{i\varphi_{yy}}\left(e^{i(\varphi_{xx}-\varphi_{yy})}\sin^2(\theta) + \cos^2(\theta)\right) = 0 \end{cases} \qquad 3.6$$

Since $|r|$ and $e^{i\varphi_{yy}}$ are both non-zero, the following equation must hold for the equality to be valid:

$$e^{i(\varphi_{xx}-\varphi_{yy})}\sin^2(\theta) + \cos^2(\theta) = 0 \qquad 3.7$$

By performing a simple calculation, it is evident that the above equation can only be satisfied when:

$$\begin{cases} \varphi_{xx} - \varphi_{yy} = \pm 180° \\ \theta = \pm 45°/\pm 135° \end{cases} \qquad 3.8$$

When we substitute $\theta = 45°/-135°$ and $\varphi_{xx} - \varphi_{yy} = \pm 180°$ into the first row of equation 3.6, we have:

$$-e^{i\varphi_{xx}} - e^{i\varphi_{yy}} = i(-e^{i\varphi_{xx}} + e^{i\varphi_{yy}}) \neq 0 \qquad 3.9$$

Obviously, for any φ_{yy}, equation 3.9 cannot be satisfied. Under this condition, the meta-atom functions as an HWP. When we substitute $\theta = -45°/+135°$ and $\varphi_{xx} - \varphi_{yy} = \pm 180°$ into the first row of equation 3.6, we have:

$$e^{i\varphi_{xx}} + e^{i\varphi_{yy}} = i(-e^{i\varphi_{xx}} + e^{i\varphi_{yy}}) \neq 0 \qquad 3.10$$

Similarly, for any φ_{yy}, it is also impossible for equation 3.10 to be satisfied. Under these conditions, the meta-atom still exhibits the functionality of an HWP. From above discussions, it is evident that a single meta-atom does not have sufficient design freedom to realize the required dual polarization conversion capability. In pursuit of achieving the dual polarization conversion functionality, this research focused on merging two meta-atoms, each with unique geometric parameters and rotation angles into a unified meta-molecule, enabling the realization of the desired dual polarization conversion functionality. In this work, thicknesses of the top Au meta-atoms and the SiO$_2$ spacer layer were preset to $t_n = 50$ nm and $t_s = 70$ nm, respectively, while the bottom Au layer had a thickness of $d=100$ nm, sufficient to prevent any light transmission. The GSP meta-molecules considered in this work are periodically distributed in both the x- and y-directions with periodicities of $\Lambda = 350$ nm and $2\Lambda = 700$ nm, respectively [79]. $\Omega = [l_A, w_A, \theta_A, l_B, w_B, \theta_B]$ is the system parameter space that needs to be designed and optimized shown in Figure 3.3(b).

Given the discussion and the assumption that $|r_{xx}| = |r_{yy}| = |r|$, the Jones matrices for meta-atom A and meta-atom B, with respective rotation angles θ_A and θ_B relative to the positive x-axis, can be formulated as:

$$R_A(\theta) = |r_A|\begin{pmatrix} e^{i\varphi_{Axx}}\cos^2(\theta_A) + e^{i\varphi_{Ayy}}\sin^2(\theta_A) & (e^{i\varphi_{Axx}} - e^{i\varphi_{Ayy}})\sin(\theta_A)\cos(\theta_A) \\ (e^{i\varphi_{Axx}} - e^{i\varphi_{Ayy}})\sin(\theta_A)\cos(\theta_A) & e^{i\varphi_{Axx}}\sin^2(\theta_A) + e^{i\varphi_{Ayy}}\cos^2(\theta_A) \end{pmatrix} \quad 3.11$$

$$R_B(\theta) = |r_B|\begin{pmatrix} e^{i\varphi_{Bxx}}\cos^2(\theta_A) + e^{i\varphi_{Byy}}\sin^2(\theta_B) & (e^{i\varphi_{Bxx}} - e^{i\varphi_{Byy}})\sin(\theta_B)\cos(\theta_B) \\ (e^{i\varphi_{Bxx}} - e^{i\varphi_{Byy}})\sin(\theta_B)\cos(\theta_B) & e^{i\varphi_{Bxx}}\sin^2(\theta_B) + e^{i\varphi_{Byy}}\cos^2(\theta_B) \end{pmatrix} \quad 3.12$$

Here, r_A and r_B represent the co-polarized complex reflection coefficients of meta-atom A and B, respectively, for the incident x- and y-polarized lights [79]. The terms φ_{Axx} and φ_{Ayy}, as well as the terms φ_{Bxx} and φ_{Byy}, denote the phase delays introduced to the reflected light by meta-atom A and B, respectively [79]. For two different meta-atom A and B, if we disregard the differences in their complex reflection coefficients under x- or y-polarized light, assuming $|r_A| = |r_B| = |r|$ and also

neglect the NFC between meta-atom A and B, the Jones matrix of the meta-molecule can be approximated as the direct summation of the Jones matrix of meta-atom A and B:

$$R_{A+B} = \frac{1}{2}(R_A(\theta) + R_B(\theta)) \tag{3.13}$$

$$R_A(\theta) = |r| \begin{pmatrix} e^{i\varphi_{Axx}}\cos^2(\theta_A) + e^{i\varphi_{Ayy}}\sin^2(\theta_A) & (e^{i\varphi_{Axx}} - e^{i\varphi_{Ayy}})\sin(\theta_A)\cos(\theta_A) \\ (e^{i\varphi_{Axx}} - e^{i\varphi_{Ayy}})\sin(\theta_A)\cos(\theta_A) & e^{i\varphi_{Axx}}\sin^2(\theta_A) + e^{i\varphi_{Ayy}}\cos^2(\theta_A) \end{pmatrix} \tag{3.14}$$

$$R_B(\theta) = |r| \begin{pmatrix} e^{i\varphi_{Bxx}}\cos^2(\theta_B) + e^{i\varphi_{Byy}}\sin^2(\theta_B) & (e^{i\varphi_{Bxx}} - e^{i\varphi_{Byy}})\sin(\theta_B)\cos(\theta_B) \\ (e^{i\varphi_{Bxx}} - e^{i\varphi_{Byy}})\sin(\theta_B)\cos(\theta_B) & e^{i\varphi_{Bxx}}\sin^2(\theta_B) + e^{i\varphi_{Byy}}\cos^2(\theta_B) \end{pmatrix} \tag{3.15}$$

To achieve the desired dual polarization conversion functionality, utilizing the Jones matrix obtained from the meta-molecule, we substitute its complex reflection coefficients into equations 3.3 and extract the corresponding real and imaginary parts. This yields the following conditional relationships:

$$\sin(\theta_A)\cos(\theta_A)\left(\cos(\varphi_{Axx}) - \cos(\varphi_{Ayy})\right) + \sin(\theta_B)\cos(\theta_B)\left(\cos(\varphi_{Bxx}) - \cos(\varphi_{Byy})\right)$$
$$= -\cos^2(\theta_A)\sin(\varphi_{Axx})$$
$$- \sin^2(\theta_A)\sin(\varphi_{Ayy}) - \cos^2(\theta_B)\sin(\varphi_{Bxx}) - \sin^2(\theta_B)\sin(\varphi_{Byy}) \neq 0$$

$$\tag{3.16}$$

$$\sin(\theta_A)\cos(\theta_A)\left(\sin(\varphi_{Axx}) - \sin(\varphi_{Ayy})\right) + \sin(\theta_B)\cos(\theta_B)\left(\sin(\varphi_{Bxx}) - \sin(\varphi_{Byy})\right)$$
$$= \cos^2(\theta_A)\cos(\varphi_{Axx})$$
$$+ \sin^2(\theta_A)\cos(\varphi_{Ayy}) + \cos^2(\theta_B)\cos(\varphi_{Bxx}) + \sin^2(\theta_B)\cos(\varphi_{Byy}) \neq 0$$

$$\tag{3.17}$$

$$\sin^2(\theta_A)\cos(\varphi_{Axx}) + \cos^2(\theta_A)\cos(\varphi_{Ayy}) + \sin^2(\theta_B)\cos(\varphi_{Bxx}) + \cos^2(\theta_B)\cos(\varphi_{Byy}) = 0 \tag{3.18}$$

$$\sin^2(\theta_A)\sin(\varphi_{Axx}) + \cos^2(\theta_A)\sin(\varphi_{Ayy}) + \sin^2(\theta_B)\sin(\varphi_{Bxx}) + \cos^2(\theta_B)\sin(\varphi_{Byy}) = 0 \tag{3.19}$$

Equations 3.16 to 3.19 present four mathematical relationships that collectively involve six different variables $[\theta_A, \theta_B, \varphi_{Axx}, \varphi_{Ayy}, \varphi_{Bxx}, \varphi_{Byy}]$. In theory, there are an infinite number of solutions that can satisfy these four equations. We employ a combination of mathematical approximation solution and physical model validation to determine the values of these six parameters. First, we choose to fix the values of either two rotation angles $[\theta_A, \theta_B]$ or four phases $[\varphi_{Axx}, \varphi_{Ayy}, \varphi_{Bxx}, \varphi_{Byy}]$ to decrease the number of unknown variables and simplify the problem [79]. Next, we use commercial software MATLAB to find approximate solutions for the remaining parameters, aiming for a combination that maximally satisfies equations 3.16 to 3.19. The obtained parameter combination $[\theta_A, \theta_B, \varphi_{Axx}, \varphi_{Ayy}, \varphi_{Bxx}, \varphi_{Byy}]$ is then input into the COMSOL model to simulate the periodic array of the meta-molecular and determine if it meets the physical objective of dual polarization conversions. If the parameter combination is successful, we output the parameter set. If not, we return to recalculate the approximate solutions or perform a more detailed scan and optimization of the existing parameter combination.

3.2.2 Numerical simulation and parameter optimization

This paragraph is based on my previous publication **Appendix B** [79], and incorporates pieces of text from that work. Prior to implementing the parameter determination process outlined above, we conducted the 3D full-wave simulation employing the same simulation method shown in *Section 2.3*, parametrically sweeping the length l and width w of a single GSP rectangular Au meta-atom [79], to obtain the complex reflection amplitude and phase maps at $\lambda = 850$ nm. Figure 3.4 illustrates the simulated complex reflection amplitude and phase maps, varying with the length l and width w of an Au antenna [79], which form the foundation for subsequent meta-atom selection.
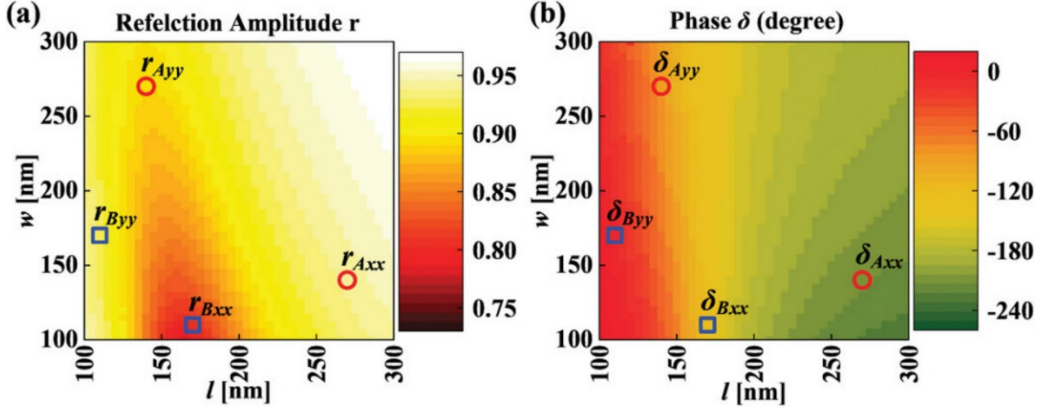
Figure 3.4 Simulated reflection (a) amplitude and (b) phase distributions of a single GSP meta-atom as functions of the meta-atom dimensions (i.e., l and w) for x-polarized incident light at the design wavelength λ = 850 nm [79]. Reprinted from Ref. [79].

In this section, we demonstrated the parameter combination design through the example of fixing two rotation angles, specifically $[\theta_A, \theta_B] = [120°, 150°]$. Then we used MATLAB to calculate the approximate numerical solutions for the phase delays of complex reflection coefficients of meta-atom A and B that satisfy the conditions given by equations 3.16 to 3.19: $[\varphi_{Axx}, \varphi_{Ayy}, \varphi_{Bxx}, \varphi_{Byy}] = [-212°, -79°, -128°, 6°]$. The obtained approximate numerical solutions were then substituted into equations 3.13 to 3.15. The resulting Jones matrix for the GSP meta-molecule is as follows:

$$R_{A+B} = \frac{|r|}{2}\begin{pmatrix} -0.282 - 1.168i & 1.1471 - 0.268i \\ 1.1471 - 0.268i & 0.0036 + 0.0334i \end{pmatrix} \qquad 3.20$$

and the corresponding complex reflection coefficients satisfy the conditions given by equations 3.16 - 3.19. Additionally, it is crucial to note that the approximate numerical solutions $[\varphi_{Axx}, \varphi_{Ayy}, \varphi_{Bxx}, \varphi_{Byy}]$ derived under the fixed conditions of $[\theta_A, \theta_B] = [120°, 150°]$ represent the relative relationship between the complex reflection coefficient phase delays of the two GSP meta-atoms. This implies that if the complex reflection coefficient phase delays of the two GSP meta-atoms adhere to the relative relationships specified by the approximate numerical solutions, then the conditions stipulated by equations 3.16 to 3.19 will be satisfied. In conjunction with the simulation results presented in Figure 3.4, when the lengths and widths of the two GSP meta-atoms are $[l_A, w_A, l_B, w_B] = [270$ nm, 140 nm, 170 nm, 110 nm], the corresponding complex reflection coefficient phase delays are $[-211.7°, -83.3°, -128.3°, -4.6°]$, as marked in Figure 3.4(b), which is quite close to the approximate numerical solutions obtained. Moreover, the complex reflection coefficient amplitudes of the two GSP meta-atoms under the excitation of x-polarized (y-polarized) light are 0.941 (0.892) and 0.923 (0.833), respectively, as marked in Figure 3.4(a), ensuring a high reflection efficiency.

Next, COMSOL Multiphysics was used again to perform simulation analysis on the designed GSP meta-molecule. This is done to study the polarization conversion functionalities achieved under the excitations of x- and y-polarized light. The simulation results are shown in Figure 3.5(a-c), displaying the reflection amplitudes $|r_{ji}|$, phase differences $\Delta\varphi_i(\lambda)$, and ellipticity $EP_i(\lambda)$ to characterize the polarization properties of the reflected waves, which are defined as:

$$\Delta\varphi_i(\lambda) = \varphi_{yi}(\lambda) - \varphi_{xi}(\lambda) \qquad\qquad 3.21$$

$$EP_i(\lambda) = \frac{2r_{xi}r_{yi}\sin(\Delta\varphi_i)}{r_{xi}^2 + r_{yi}^2} \qquad\qquad 3.22$$

where λ is the wavelength, and the subscript i stands for the direction of the incident LP state [79]. At $\lambda = 850$ nm, as illustrated in Figure 3.5(a), the amplitude of r_{xx}, r_{yx}, r_{xy} and r_{yy} is 0.709, 0.381, 0.381, and 0.373, respectively. Specifically, the x-polarized incident wave is not converted into the x- and y-polarized components with similar amplitudes, and the co-polarized reflection is not sufficiently suppressed under the y-polarized excitation [79]. The phase differences $\Delta\varphi_i(\lambda)$ between the two orthogonal LP components of the reflected light are $\Delta\varphi_x = 121°$ and $\Delta\varphi_y = -162°$ for the incident x- and y-polarized lights, respectively, as illustrated in Figure 3.5(b), which cannot satisfy the conditional relationship given by equation 3.3. Consequently, the calculated ellipticities are 0.71 and -0.31 for the x- and y-polarized excitations, respectively, deviating much from the theoretical values of 1 and 0 [79]. Therefore, based on the structural parameters of the current GSP meta-molecule, the resulting GSP optical waveplate does not achieve the expected dual polarization conversion functionality at our desired design wavelength [79]. The fact that the two selected meta-atoms do not add up to make a suitable meta-molecule should be ascribed to the intrinsic NFC between different meta-atoms neglected in our simplified design procedure [79]. Accounting for the NFC would require discarding simple calculation of the meta-molecule reflection, such as equation 3.4, a change that complicates enormously the design procedure [79].

However, it is observed that $|r_{yy}|$ significantly decreases to 0.059, while $|r_{xx}|$, $|r_{yx}|$, and $|r_{xy}|$ become nearly equal at a shorter wavelength of $\lambda = 844$ nm, which suggests that a suitable wavelength is found very close to the design one, the appropriate metamolecule parameters at the design wavelength should be located close to those obtained with the simple approach [79]. Therefore, based on the current simulation results, the key structural parameters $[\theta_A, \theta_B, l_A, w_A, l_B, w_B]$ of the designed two different GSP meta-atoms could be finely adjusted and optimized to achieve the desired dual polarization conversion functionality at $\lambda = 850$ nm. The optimized structural parameters were slightly modified to $[\theta_A, \theta_B, l_A, w_A, l_B, w_B] = [121°, 152°, 271$ nm, 135 nm, 175 nm, 110 nm$]$, and the corresponding simulation results based on the optimized structural parameters indicated a marked enhancement in performance [79] (Figure 3.5(d-f)). For example, at $\lambda = 850$ nm, as presented in Figure 3.5(d), the amplitude of r_{xx}, r_{yx}, r_{xy} and r_{yy} is 0.63, 0.53, 0.53, and 0.09, respectively, manifesting that the optimized structure is able to convert the x-polarized incidence into x- and y-polarized components with equal intensities, and the y-polarized incident beam is converted into the x-polarized component [79]. Moreover, the phase differences $\Delta\varphi_i(850)$ are $\Delta\varphi_x(850) = 85°$ and $\Delta\varphi_y(850) = 172°$, and the ellipticities are $EP_x(850) = 0.98$ and $EP_y(850) = 0.05$, respectively, manifesting the generation of the RCP and x-polarized reflected beams under the x- and y-excitations (Figure 3.5(e-f)) [79].
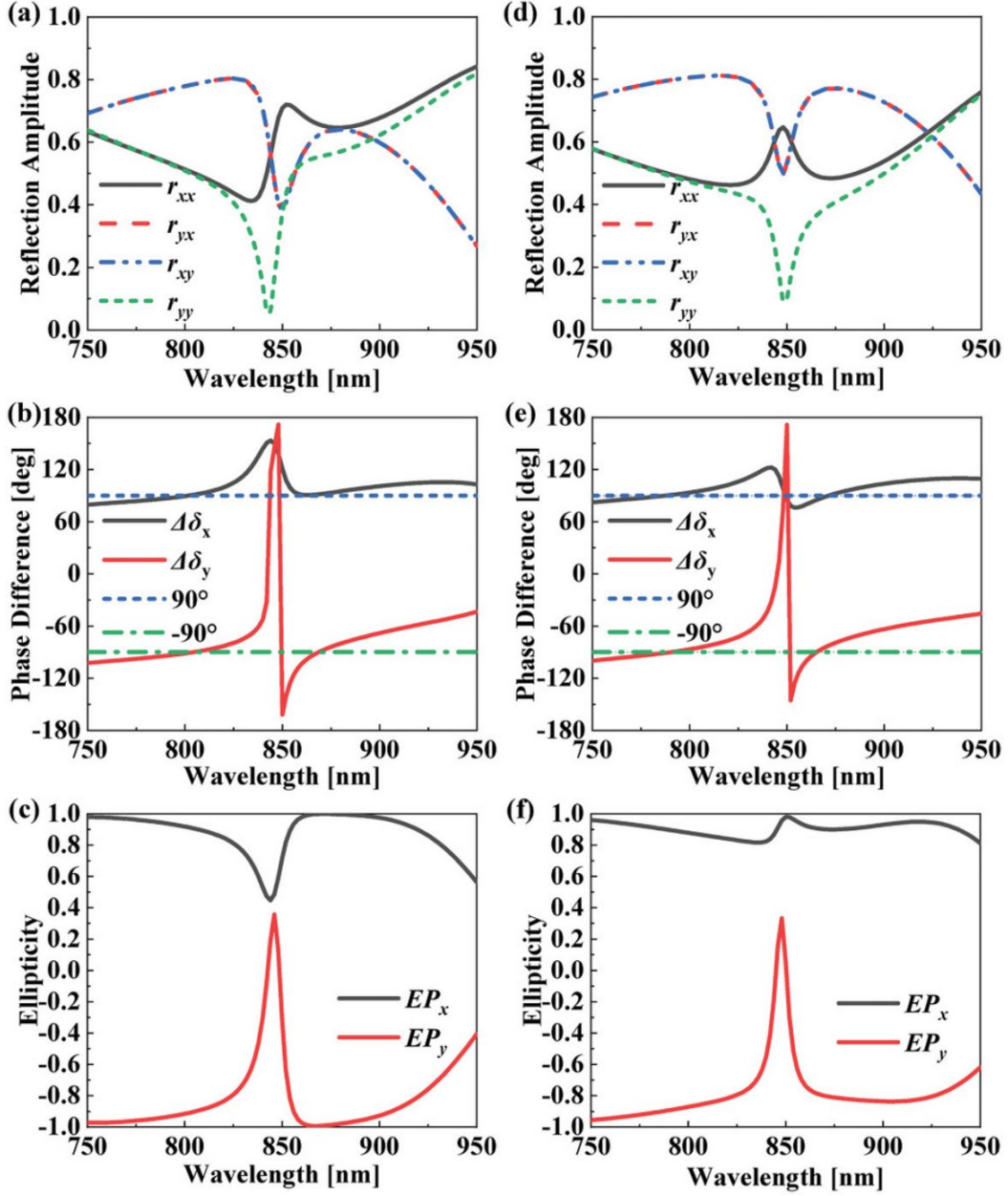
Figure 3.5 Simulated (a and d) reflection amplitudes, (b and e) phase differences, and (c and f) ellipticities for the (a-c) as-designed and (d–f) optimized GSP dual-functional waveplate [79]. Reprinted from Ref. [79].

3.2.3   Experimental results

Following the sample fabrication processes and procedures outlined in *Section 2.4*, we prepared the dual-function metasurface waveplate sample. The SEM images of the sample with different magnifications are shown in Figure 3.6 [79].
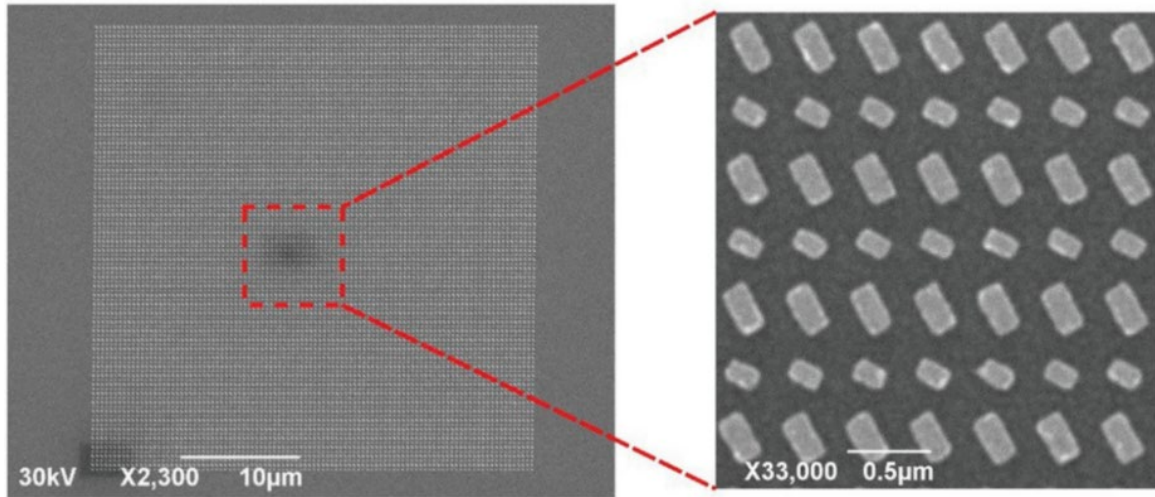
Figure 3.6 Top-view SEM images of the fabricated sample with different magnifications [79]. Reprinted from Ref. [79].

This paragraph is based on my previous publication **Appendix B** [79], and incorporates pieces of text from that work. After fabrication, we utilized our custom-built setup (*Section 2.5*) to make sample characterization. In the measurement, the cw Ti:sapphire laser and CMOS camera were chosen to characterize the dual-functional metasurface waveplate sample. Figure 3.7(a-b) display the polarization measurements of the fabricated sample for the *x*- and *y*-polarized incidences, respectively, where the reflected light was projected along the polarization axis of LP2 whose orientation is varied from 0° to 360° in a step of 10° with respect to the *x*-axis [79]. From the polar plots, it can be clearly seen that the *x*-polarized incident beam is converted into an RCP reflected beam with the ellipticity approaching 0.98 while the *y*-polarized incident beam is rotated to a linearly polarized beam with the ellipticity of 0, corresponding to the DoLP of 1 [79]. In addition, the measured efficiencies of the fabricated device reach $\approx 73\%$ and 30% under *x*- and *y*-polarized linear excitations at the design wavelength of 850 nm, which is defined as the ratio of the power carried by the reflected wave to the power reflected from a bare substrate composed of SiO_2 and Au films [79]. Compared to the simulated polar plots in Figure 3.7 (c-d), the measured results show excellent agreement in terms of the shapes and efficiencies [79]. Impressively, the measured efficiencies are very close to the calculated efficiencies in simulation, which are around 68% and 29% for the orthogonal linear polarizations [79]. Here it should be mentioned that due to the non-ideal amplitude and phase values, the dual-functional waveplate intrinsically (slightly) deviates in performance from a perfect QWP and an HWP under two LP excitations [79]. For example, under the *y*-polarized excitation, even though the reflected light is linearly polarized with the DoLP of 1, the AoLP deviates from 0° in both the simulation and experiment [79]. Besides the intrinsic design limitations, we attribute this deviation to the unavoidable imperfections and errors in the fabrication process [79]. Therefore, we believe that with further refined optimization, the inclusion of additional parameters, and the potential integration of powerful artificial intelligence algorithms, we can achieve multifunctional optical metasurface waveplates more efficiently and accurately in the future.
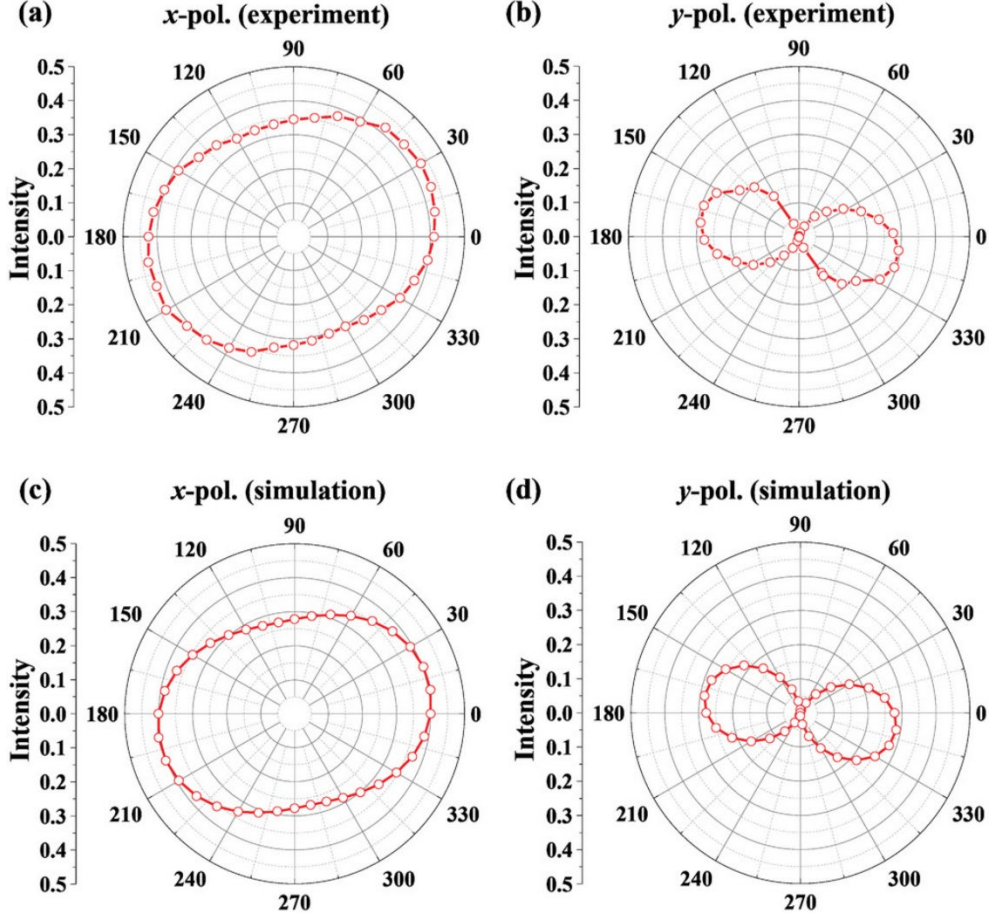
Figure 3.7 (a-b) Measured and (c-d) calculated polarization state diagrams of the reflected waves obtained under (a and c) *x*-polarized and (b and d) *y*-polarized incidence, respectively [79]. Reprinted from Ref. [79].

3.3   GSP metasurface QWPs for beam steering and metalenses

3.3.1   GSP nano-QWP library design and theoretical analysis

This section is based on my previous publication **Appendix C** [80] and incorporates pieces of text from that work. As illustrated in Figure 3.8(a), a typical MIM GSP meta-atom, comprising a top Au cross-shaped antenna, an intermediate SiO$_2$ spacer layer, and a bottom continuous Au mirror, was designed to function as a fundamental nano-QWP unit. Given the inherent anisotropic property of this birefringent meta-atom, with its major axes along *x*- and *y*- directions, $r_{xx} = |r_{xx}|e^{i\varphi_{xx}}$ and $r_{yy} = |r_{yy}|e^{i\varphi_{yy}}$ can be used to describe the complex reflection coefficients under *x*- and *y*-polarized excitations, respectively, which are predominantly determined by the dimensions of the meta-atom along its two principal axes [80]. At $\lambda = 850$ nm, all the values in the structure parameter space $\Omega =$ [w, t_m, t_s, d, Λ] = [50 nm, 40 nm, 100 nm, 100 nm, 400 nm] were preset to ensure high reflection efficiency and provide sufficient resonance phase coverage for constructing phase gradients [80]. Then we conducted 3D full-wave simulations, parametrically sweeping the dimensions (L_x and L_y) of the top gold antenna to obtain the complex reflection coefficients under *x*- and *y*-polarized excitations. Figure 3.8(b) shows the map of the simulated reflection coefficients of the meta-atom as a function of varying L_x and L_y at the wavelength of 850 nm for the incident *x*-polarized light [80]. Evidently, all meta-atom points situated along the two black solid lines ($\Delta\varphi = \varphi_{yy} - \varphi_{xx} = 90°$) function as nano-QWPs, each characterized by different amplitudes $|r_{xx}|$. To ensure a broad

34

operational bandwidth and high efficiency, four nano-QWPs marked with red circles (element #1 to #4, $\Delta\varphi$ of each matches to 90°) with a key resonance phase step of $\Delta\varphi_{xx} = 90°$ were selected to form a meta-atom library, as shown in Figure 3.8(c). This configuration covering a wide range up to 300° can facilitate simultaneous CP-to-LP polarization conversion and potential wavefront shaping. Notably, while this dissertation does not explore them, our design also provides a range of options for potential nano-HWPs, such as meta-atom points situated along the two black dotted lines ($\Delta\varphi = \varphi_{yy} - \varphi_{xx} = 180°$) in Figure 3.8(b).
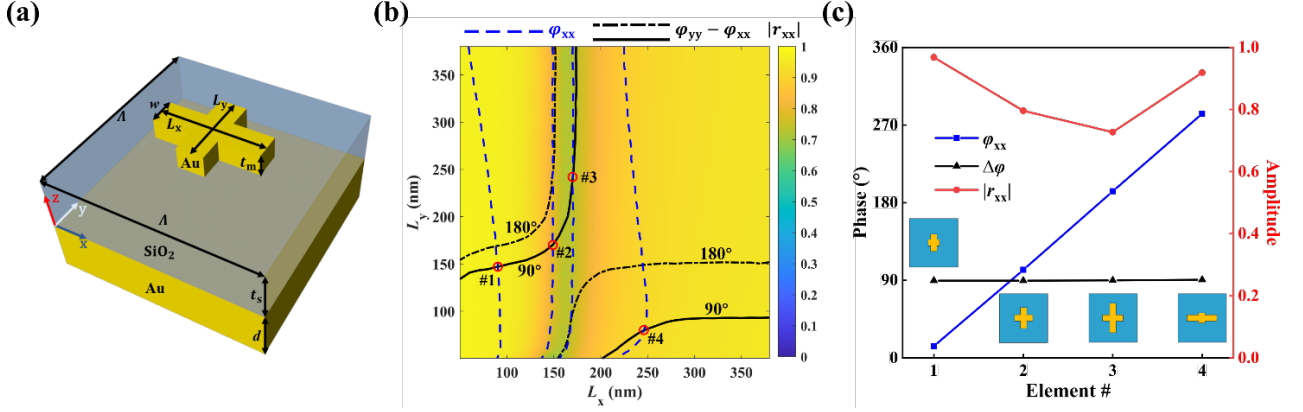
Figure 3.8 (a) Schematic of the anisotropic MIM meta-atom [80]. (b) Calculated reflection coefficients as a function of the dimensions at the wavelength of 850 nm for the *x*-polarized incident light. The map shows the reflection amplitude $|r_{xx}|$, while the blue dashed lines are contours of the reflection phase φ_{xx} with a step of 90°. Black solid and dotted lines indicate the meta-atoms with the phase difference of $\Delta\varphi = 90°$ and 180°, respectively [80]. (c) Calculated reflection phase φ_{xx}, relative phase difference ($\Delta\varphi = \varphi_{yy} - \varphi_{xx} = 90°$) and the reflection amplitude $|r_{xx}|$ of the four nano-QWPs with a resonance phase step of $\Delta\varphi_{xx} = 90°$ at the wavelength of 850 nm. The dimensions of element #1 to #4 are (1) $L_x = 91$ nm, $L_y = 147$ nm; (2) $L_x = 149$ nm, $L_y = 170$ nm; (3) $L_x = 170$ nm, $L_y = 242$ nm; (4) $L_x = 249$ nm, $L_y = 82$ nm. Reprinted from Ref. [80].

Holding on the nano-QWP library designed above, the Jones matrix $J(\theta)$ of the nano-QWP that is rotated by an angle θ relative to the *x*-axis can be described as follows:

$$J(\theta) = |r_{xx}|e^{i\varphi_{xx}} \begin{pmatrix} \cos(\theta) & -\sin(\theta) \\ \sin(\theta) & \cos(\theta) \end{pmatrix} \begin{pmatrix} 1 & 0 \\ 0 & i \end{pmatrix} \begin{pmatrix} \cos(\theta) & \sin(\theta) \\ -\sin(\theta) & \cos(\theta) \end{pmatrix}$$

$$= |r_{xx}|e^{i\varphi_{xx}} \begin{pmatrix} \cos(\theta)^2 + i\sin(\theta)^2 & \sin(\theta)\cos(\theta) - i\sin(\theta)\cos(\theta) \\ \sin(\theta)\cos(\theta) - i\sin(\theta)\cos(\theta) & \sin(\theta)^2 + i\cos(\theta)^2 \end{pmatrix}$$

$$\qquad 3.23$$

where $\begin{pmatrix} \cos(\theta) & \sin(\theta) \\ -\sin(\theta) & \cos(\theta) \end{pmatrix}$ represents the rotation matrix, and $\begin{pmatrix} 1 & 0 \\ 0 & i \end{pmatrix}$ is the Jones matrix of the designed nano-QWP with $\Delta\varphi = 90°$. Considering an LCP and RCP incident beam with $E_{in} = \frac{1}{\sqrt{2}}\begin{pmatrix} 1 \\ \pm i \end{pmatrix}$, the output light will be LP and AoLP is $\theta \mp \frac{\pi}{4}$, which can be described as:

$$E_{out} = |r_{xx}|e^{i\varphi_{xx}}e^{\pm i\theta} \begin{pmatrix} \cos\left(\theta \mp \frac{\pi}{4}\right) \\ \sin\left(\theta \mp \frac{\pi}{4}\right) \end{pmatrix} \qquad 3.24$$

For example, obviously, if the rotation angle θ of each nano-QWP is equal to −45°, the reflected beam will be *y*- / *x*- polarized for the LCP/RCP incident beam, respectively. Furthermore, the output LP

light can be decomposed into two CP components in the CP basis under respective LCP and RCP excitation, which can be written as:

$$E_{\text{out}} = \frac{1}{2}\,|r_{\text{xx}}|e^{i(\varphi_{\text{xx}}+\frac{\pi}{4})}\begin{pmatrix}1\\\pm i\end{pmatrix} + \frac{1}{2}\,|r_{\text{xx}}|e^{i(\varphi_{\text{xx}}-\frac{\pi}{4})}e^{\pm i2\theta}\begin{pmatrix}1\\\mp i\end{pmatrix} \qquad 3.25$$

where the first part represents the co-polarized reflective light, which retains the same helicity as the incident light. And the second part corresponds to the cross-polarized light exhibiting the reversed helicity with additional phase delay, which is known as the PB phase with a value of 2θ for LCP light and -2θ for RCP light.

3.3.2 GSP nano-QWPs for beam steering

This section is based on my previous publication **Appendix C** [80], and incorporates pieces of text from that work. In this section, we concisely present three types of GSP metasurfaces constructed from the aforementioned nano-QWP library, utilizing distinct phase control methods: resonance phase, geometric phase and a combination of both.

Firstly, we present the GSP gradient metasurface (MS1) only based on resonance phase, as shown in Figure 3.9. All the meta-atoms within MS1 supercell are uniformly rotated by an angle of θ_{LP0}. Therefore, the corresponding phase gradient along the x-direction is given as:

$$\frac{d\varphi_{\text{LP}}}{dx} = \frac{\partial(\varphi_{\text{xx}}(x,y)+\theta_{\text{LP0}})}{\partial x} = \frac{\Delta\varphi_{\text{xx}}}{N\cdot\Lambda} = m_{\text{LP}} \cdot \frac{2\pi}{\Lambda_{\text{sc}}} \qquad 3.26$$

where (x, y) indicates the coordinate of each meta-atom, N is the number of identical meta-atoms duplicated in a supercell, m_{LP} represents the diffraction order for the LP reflection field, and Λ_{sc} represents the total period of one supercell. Figure 3.9(a) schematically illustrates the working principle of MS1 which can convert RCP incident light into a LP wave with a spin-determined AoLP within the +1 diffraction order. The originally designed four nano-QWPs are duplicated to form an 8-element supercell, as shown in Figure 3.9(b), which increases the periodicity along the x-direction and reduces the diffraction angle of the steered light, ensuring it falls within the collection angle of the objective. In a supercell, each nano-QWP is rotated counterclockwise by 22.5° relative to the x-axis. As a result, each rotated nano-QWP can convert RCP incident light into a secondary LP light with an AoLP of 67.5°, or convert LCP incident light into a secondary LP light with an AoLP of −22.5°, according to formula derivation 3.24. Moreover, the secondary LP light develops a linear phase gradient along the x-axis, leading to the reflected LP light being directed into the +1 diffraction order. The same fabrication method was used to prepare the metasurface sample, and the SEM image can be seen in Figure 3.9(b). After fabrication, MS1 was characterized using the same custom-built, configured identically to the configuration described in *Section 3.2.3*. The optical image of the diffraction spots in the inset of Figure 3.9(c) reveals that nearly all the incident light is reflected into the +1 diffraction order, showcasing the excellent beam steering capability. The performance of our fabricated MS1 was further evaluated by measuring the corresponding diffraction efficiency in each order. As shown in Figure 3.9(c), the simulated and experimental diffraction efficiencies generally exhibit a strong agreement. In special, under RCP incident light at the wavelength of 850 nm, the experimental results indicate a total reflectivity nearing 50%, with the +1 order diffraction efficiency achieving approximately 40%. The measured reflectance (indicated by dark cyan star markers) as a function of the analyzer's orientation in front of the CCD camera for the +1 diffraction order under RCP excitation demonstrates excellent consistency with the simulation results at the design wavelength of 850 nm, as shown in Figure 3.9(d). Notably, the measured DoLP is 99.42%. Additionally, the fabricated MS1 facilitates efficient CP-to-LP conversion and beam steering over a

broad spectrum ranging from 800 to 900 nm. When the incident light is switched to LCP light, an LP beam with an AoLP of −22.5° is produced and directed into the +1 diffraction order (Figures S5-S6 of **Appendix C**). Beyond producing a single LP beam directed as desired under CP excitation, it is advantageous to simultaneously generate multiple LP beams with varying AoLPs in different spatial channels (MS2, Figure 3 and Figures S7-S8 of **Appendix C**). This approach enables enhanced control and flexibility in beam manipulation for various applications.
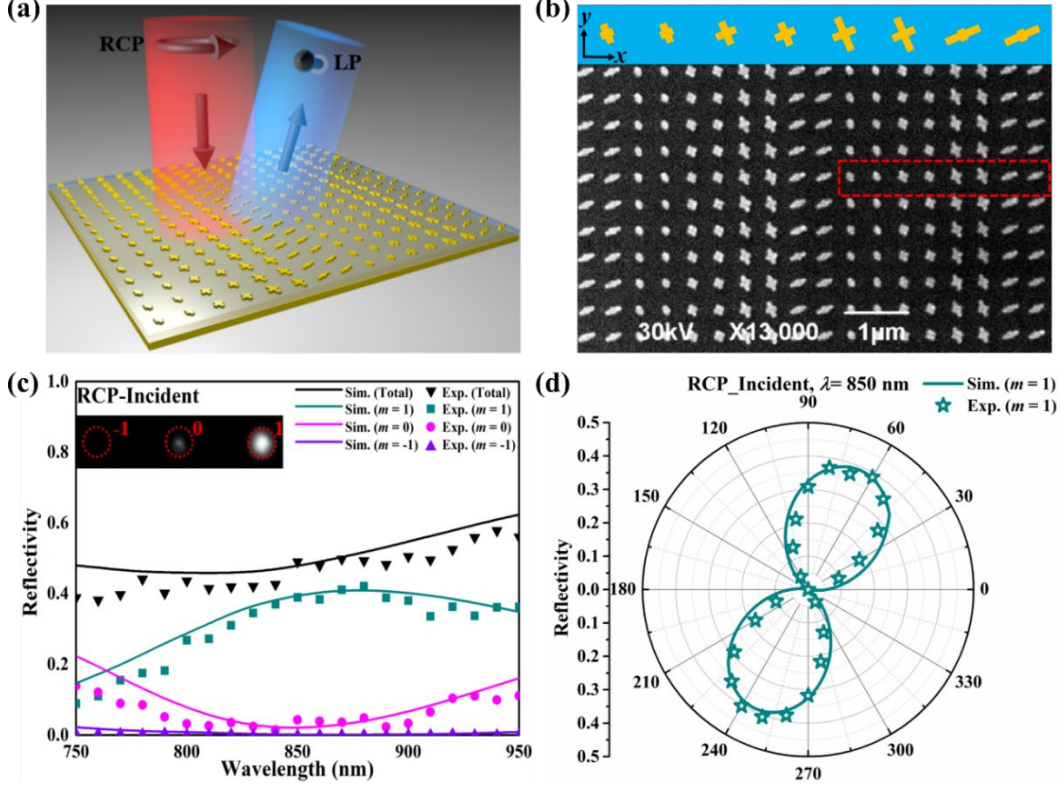
Figure 3.9 (a) Schematic of the GSP gradient MS1 for CP-to-LP conversion and beam steering under RCP excitation. (b) SEM image of the fabricated sample. The inset shows the layout of one supercell with each meta-atom rotated by an angle of 22.5° with respect to the *x*-axis along the counterclockwise direction. (c) Simulated (solid lines) and experimental (markers) diffraction efficiencies of different orders as a function of wavelength for RCP incident light. The inset shows the optical image of the diffraction spots at the wavelength of 850 nm. (d) Simulated (dark cyan solid line) and experimental (dark cyan star markers) polarization state diagrams of the steered beam within +1 diffraction order for RCP incident light at the wavelength of 850 nm [80]. Reprinted from Ref. [80].

Next, we present MS3 only based on the geometric phase under the CP basis, as shown in Figure 3.10. The corresponding phase gradients that allow to steer CP output channels are:

$$\frac{d\varphi_{co}}{dx} = \frac{\partial(\varphi_{xx}(x,y)+\frac{\pi}{4})}{\partial x} = \frac{\Delta\varphi_{xx}}{N\cdot\Lambda} = m_{co} \cdot \frac{2\pi}{\Lambda_{sc}} \qquad 3.27$$

$$\frac{d\varphi_{cr}}{dx} = \frac{\partial(\varphi_{xx}(x,y)-\frac{\pi}{4}-2\cdot\theta(x,y))}{\partial x} = \frac{\Delta\varphi_{xx}-2\cdot\Delta\theta}{N\cdot\Lambda} = m_{cross} \cdot \frac{2\pi}{\Lambda_{sc}} \qquad 3.28$$

where $\theta(x,y)$ is the rotated angle of each meta-atom, $\Delta\theta$ is the relative angle between two differently-sized meta-atoms, m_{co} and m_{cross} represent the respective diffraction orders for co- and cross-polarized reflection fields, respectively. Figure 3.10(a) schematically illustrates the working principle of MS3, which can reflect RCP incident light to co-polarized (RCP) and cross-polarized (LCP) channels towards the 0 and +1 diffraction orders, respectively. By substituting $m_{co} = 0$, $m_{cross} = 1$,

and $N = 2$ into the aforementioned equations, we derive the solutions of $\Delta\varphi_{xx} = 0$ and $\Delta\theta = -\frac{\pi}{4}$ for a metasurface supercell composed of 8 elements. Therefore, we only need to choose one nano-QWP from our meta-atom library and rotate each meta-atom accordingly to fulfil the geometric phase requirements. Considering the reflection efficiency, nano-QWP No.4 was selected and arranged to form a supercell. The meta-atoms are rotated by angles $\theta(x, y)$ of $-45°$, $-45°$, $-90°$, $-90°$, $-135°$, $-135°$, $-180°$, and $-180°$, respectively, as shown in Figure 3.10(b). As anticipated, nearly all the incident RCP light is reflected into the 0 and +1 diffraction orders, while the −1 diffraction order is significantly suppressed (approaching zero) over a broad spectral range from 750 to 950 nm, attributed to the broadband nature of the geometric phase (Figure 3.10(c)). Overall, the measured and calculated diffraction efficiencies show a strong correlation, validating the broadband beam steering capabilities for both co- and cross-polarized CP light. At the wavelength of 850 nm, the measured diffraction efficiencies for the 0 and +1 orders are approximately 37% and 32%, respectively. This is vividly demonstrated by the optical image in Figure 3.10(c), which shows two bright diffraction spots. To verify their polarization states, we plotted the simulated (dark cyan/magenta solid line) and experimental (dark cyan/magenta star markers) polarization state diagrams as a function of the analyzer's orientation for the 0 and +1 diffraction orders at the wavelength of 850 nm, as shown in Figure 3.10(d). The measured polarization diagrams generally form circular shapes, with DoCPs exceeding 93.70% and −92.40% for the 0 and +1 diffraction orders, respectively. These results are consistent with the simulated values of 99.60% and −99.30%. Additional simulated and experimental results for other wavelengths under RCP excitation are presented in Figure S9 of **Appendix C**.

Figure 3.10 (a) Schematic of the GSP gradient MS3 composed of identical meta-atoms with different rotation angles for steering of co- and cross-polarized CP waves to 0 and +1 diffraction orders. (b) SEM image of the fabricated sample. The inset shows the layout of one supercell composed of identical meta-atoms with different rotation angles. (c) Simulated (solid lines) and experimental (markers) diffraction efficiencies of different orders as a function of wavelength for RCP incident light. The inset shows the optical image of the diffraction spots at the wavelength of 850 nm. (d) Simulated (dark cyan/magenta solid line) and experimental (dark

cyan/magenta star markers) polarization state diagrams of the steered beams within 0 and +1 diffraction orders for RCP incident light at the wavelength of 850 nm [80]. Reprinted from Ref. [80].

Lastly, combing both resonance and geometric phases, we present MS4 which can steer the reflected co- and cross-polarized CP waves into −1 and +1 diffraction orders, respectively, as shown in Figure 3.11(a). By substituting $m_{co} = -1$, $m_{cross} = 1$ and $N = 2$ into equations 3.27−3.28, we selected all four nano-QWPs with varying dimensions and rotation angles to form an 8-element supercell, thereby providing both resonance and geometric phases simultaneously. As shown in the inset of Figure 3.11(b), the 8 elements are distributed in a certain order (i.e., meta-atoms No.1, No.1, No.4, No.4, No.3, No.3, No.2, and No.2) and the corresponding rotation angles $\theta(x, y)$ are −15°, −15°, 75°, 75°, 165°, 165°, 255°, and 255°, respectively. When the fabricated MS4 (SEM image in Figure 3.11(b)) was illuminated with an RCP wave at normal incidence, we measured the diffraction efficiencies for orders $|m| \leq 1$, as depicted in Figure 3.11(c). The results show a general agreement between the measured and calculated diffraction efficiencies, validating the intended steering capability. Nonetheless, there are some discrepancies, especially in the zero-order diffraction at shorter wavelengths. At the wavelength of 850 nm, the experimental diffraction efficiencies for the −1 and +1 orders are approximately 32.00% and 23.50%, respectively, as shown in Figure 3.11(c). The polarization state diagrams, both simulated (dark cyan/violet solid lines) and experimental (dark cyan/violet star markers), demonstrate strong agreement at the wavelength of 850 nm, as depicted in Figure 3.11(d). Quantitatively, the measured DoCPs are around 90.30% and −92.00%, indicating successful steering of co- and cross-polarized CP waves into the −1 and +1 diffraction orders, respectively. As expected, the reflected electric fields at two orthogonal CP states exhibit tilted planar wavefronts (Figures S10a and S10c of **Appendix C**). The simulated and experimental results at wavelengths of 800 nm and 900 nm under RCP incident light, shown in Figures S10b and S10d of **Appendix C**, further validate the broadband nature of the implemented sample.
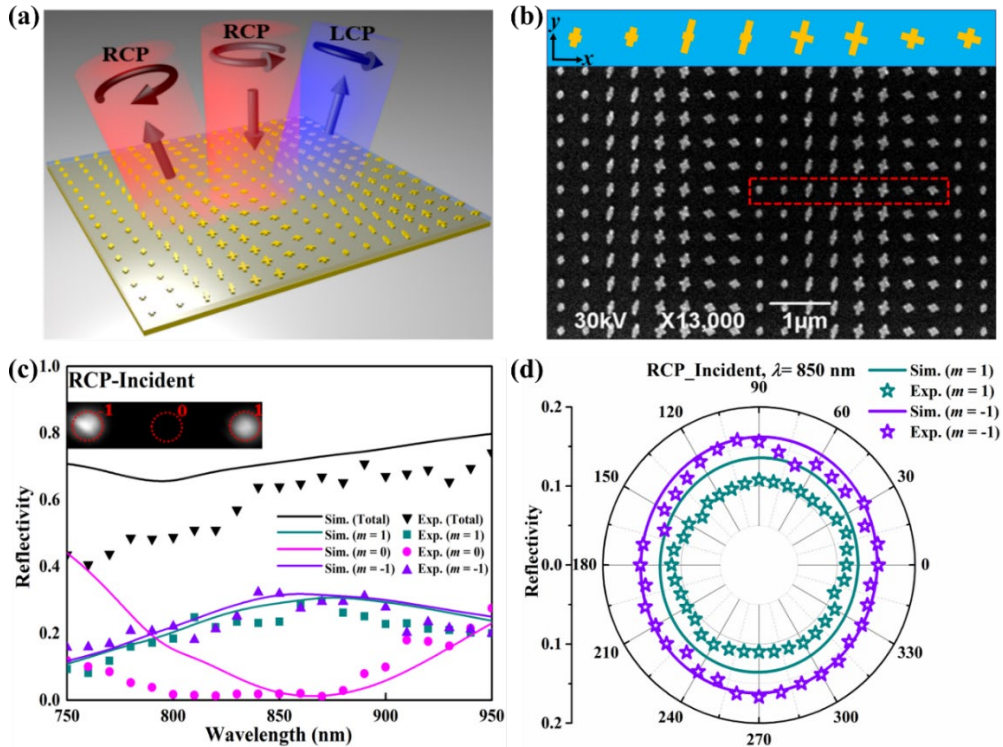

Figure 3.11 (a) Schematic of MS4 composed of meta-atoms with different dimensions and rotation angles for steering of co- and cross-polarized CP waves to −1 and +1 diffraction orders. (b) SEM image of the fabricated sample. The inset shows the layout of one supercell composed of meta-atoms with different dimensions and

rotation angles. (c) Simulated (solid lines) and experimental (markers) diffraction efficiencies of different orders as a function of wavelength for RCP incident light. The inset shows the optical image of the diffraction spots at the wavelength of 850 nm. (d) Simulated (dark cyan/violet solid line) and experimental (dark cyan/violet star markers) polarization state diagrams of the steered beam within −1 and +1 diffraction orders for RCP incident light at the wavelength of 850 nm [80]. Reprinted from Ref. [80].

3.3.3 GSP metalenses for focused scalar and vector beam generation

Scalar and vector beams, each demonstrating spatially homogeneous and variable polarization states respectively, are highly desired in photonics, especially when they are efficiently focused. Using the same nano-QWP library, we also designed and experimentally demonstrated spin-controlled GSP metalenses capable of generating focused scalar beams, like LP and CP beams, as well as vector beams, such as radially polarized (RP) and azimuthally polarized (AP) beams. The content of this section can be referenced in our forthcoming article (**Appendix D** [81]), and incorporates pieces of text from the published article (**Appendix C** [80]).

Similarly, in the first case, only the resonance phase was utilized. To produce a reflected focused beam while simultaneously converting an incident CP light to a LP light with required AoLP, the GSP QWP metasurface needs to be designed with an extra lens phase profile, which depends on the position of each nano-QWP and can be calculated using the following formula [97-100]:

$$\varphi(x,y) = \frac{2\pi}{\lambda_d}\left(\sqrt{x^2 + y^2 + f^2} - f\right) \qquad 3.29$$

where λ_d represents the designed center wavelength, f denotes the focal length, and (x, y) represents the independent position coordinate of each nano-QWP that forms the metalens. Figure 3.12(a) illustrates the schematic of our proposed metalens (MS1) with $D = f_1 = 50\ \mu m$, and the rotation angle of each nano-QWP $\theta = -45°$, which can enable simultaneous CP-to-LP polarization conversion, LCP ($|\ l >$) to y-polarized light ($|\ y >$) in (1) and RCP ($|\ r >$) to x-polarized light ($|\ x >$) in (2), and beam focusing at $\lambda_d = 850$ nm. The NA of MS1 is 0.4472. Figure 3.12(b) presents SEM images of our fabricated MS1 sample, referring to the phase distribution (Figure 3.12(c)) calculated by formula 3.29 and the designed geometry (Figure 3.12(d)). The fabricated sample MS1 effectively mirrors the intended shapes and dimensions of the designed meta-atoms, notwithstanding minor surface roughness and rounded corners.
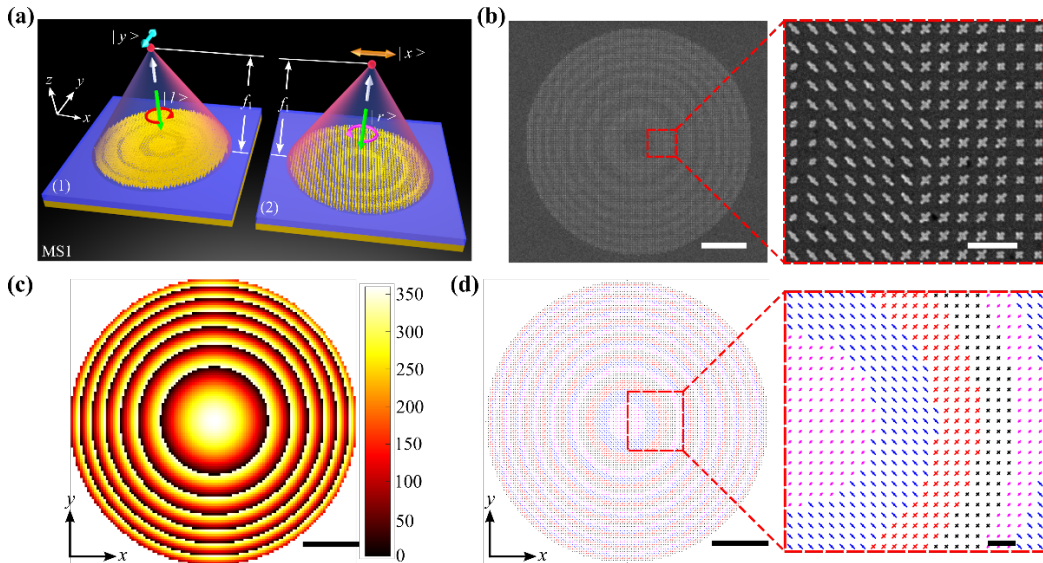
Figure 3.12 (a) Schematic of the optical GSP MS1 for single focused LP generation, LCP ($|l>$) to y-polarized light ($|y>$) in (1) and RCP ($|r>$) to x-polarized light ($|x>$) in (2), and beam focusing at $\lambda_d = 850$ nm. (b) SEM images of the fabricated MS1 (scale bars are 10 μm and 1 μm, respectively). (c-d) Calculated phase profile (c) and designed geometry (d) of MS1 with $D = f_1 = 50$ μm at $\lambda_d = 850$ nm. The scale bar in (c) and the left of (d) is 10 μm, scale bar in the right of (d) is 1 μm.

We subsequently measured the MS1 sample employing our custom-built setup, incorporating the principles of ray optics [77, 101], as illustrated in Figure 3.13(a). To validate the actual focusing effect, MS1 is moved away from plane A (the focal plane of the objective, $z = 0$), which can generate a reflected focal light spot under incident beam from the substrate plane without any structures, to plane B (twice the focal length of MS1 from the perspective of geometric optics, $z = \sim 2f$). As shown the measurement results for LCP incident light in Figure 3.13(b), using the 850 nm wavelength as a representative example, we first moved the reflected focused light spot from the substrate at plane A to MS1. Subsequently, the bright reflected focused light spot from MS1 can be observed once we shifted the sample from plane A to plane B. While for the same plane, the reflection from the substrate would be strong diverging. Other two wavelengths exhibit the similar performance. In addition, the measured normalized reflectivities, depending on the orientation of the analyzer positioned in front of the CCD camera for both LCP and RCP (Figure 3.13(c-d)) incident lights also demonstrate strong agreements with the theoretical results at $\lambda_d = 850$ nm [80]. (i) is labeled here to match the focused light spot with its polarization state for LCP incident light. In particular, both measured DoLPs for LCP and RCP incident lights are very close to 1. Results measured at $\lambda = 800$ and 900 nm can be seen in Figure S3 of **Appendix D**. We also measured the reflectivities across different wavelengths for both LCP and RCP incident lights, as shown in Figure 3.13(e). Specifically, the total reflectivities are close to 30% at $\lambda_d = 850$ nm for both CP incident lights.
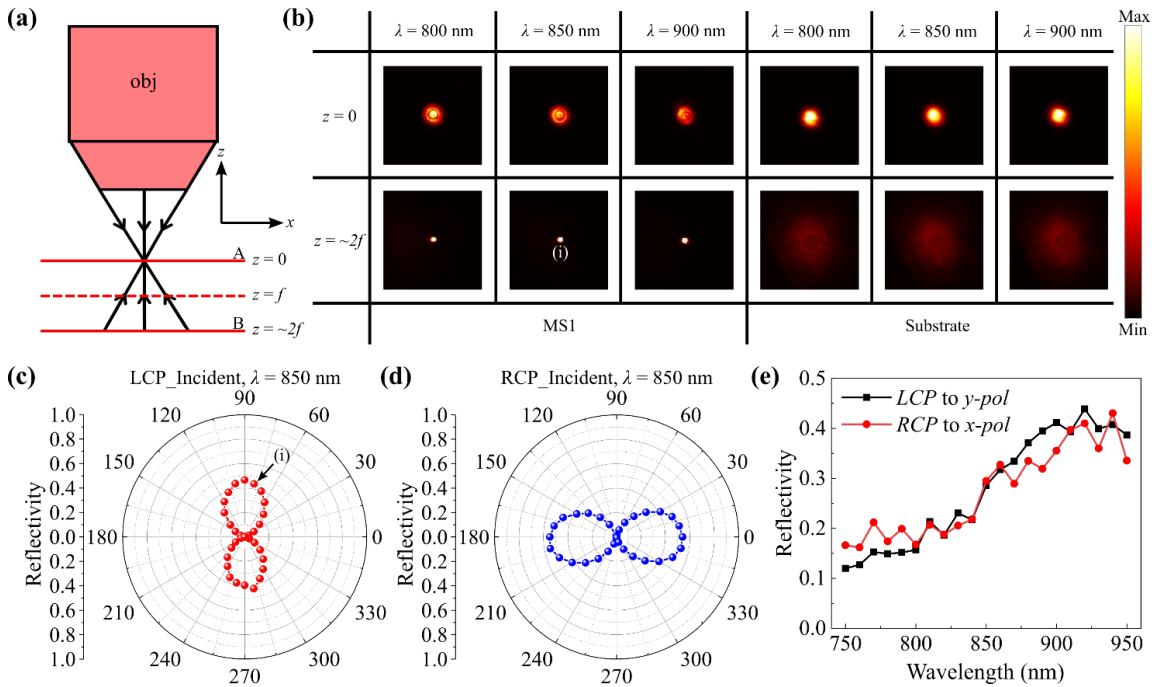
Figure 3.13 (a) Schematic of the characterization approach based on ray optics, in which the incident beam is focused at plane A (the focal plane of the objective, $z = 0$) and directed onto MS1 or the substrate without any structures at plane B (twice the focal length of MS1, $z = \sim 2f$). (b) Measured reflected optical images from MS1 and the substrate for incident LCP light with different wavelengths of 800, 850, and 900 nm, when the fabricated sample is moved from plane A to plane B. (c-d) Measured polarization state diagrams of the reflected

focused light spots from MS1 at plane B for LCP (c) and RCP (d) incident light, respectively, at λ_d = 850 nm. (e) The measured reflectivities across various wavelengths for both LCP and RCP incident lights.

In addition to the MS1 capable of generating single focal light spot along with CP-to-LP conversion, we advanced our method to create a dual-focal metalens (MS2) which can transform one incident CP light into two focused light spots featuring arbitrary AoLPs. Unlike MS1, the dual-focal MS2 is split into two distinct left and right sections, each featuring a unique phase profile:

$$\varphi(x, y) = \begin{cases} \frac{2\pi}{\lambda_d}\left(\sqrt{\left(x + \frac{D}{4}\right)^2 + y^2 + f^2} - \sqrt{\left(\frac{D}{4}\right)^2 + f^2} \right), (x \leq 0) \\ \frac{2\pi}{\lambda_d}\left(\sqrt{\left(x - \frac{D}{4}\right)^2 + y^2 + f^2} - \sqrt{\left(\frac{D}{4}\right)^2 + f^2} \right), (x > 0) \end{cases} \qquad 3.30$$

Figure 3.14(a) displays the schematic of MS2 with $D = f_2 = 50$ μm (NA$_{MS2}$ = 0.4472), according to the phase distribution (Figure 3.14(c)) calculated by formula 3.30. Once the rotation angle of each nano-QWP is set to θ_l = +45° in the left section and θ_r = −45° in the right section, respectively, MS2 can reflect an incident CP light to two focused orthogonal LP lights, e.g., $|l>$ to focused $|x>$ and $|y>$ in (1) and $|r>$ to focused $|y>$ and $|x>$ in (2), at λ_d = 850 nm. Figure 3.14(b) presents the SEM image of the MS2 sample we fabricated, corresponding to the geometry illustrated in Figure 3.14(d).
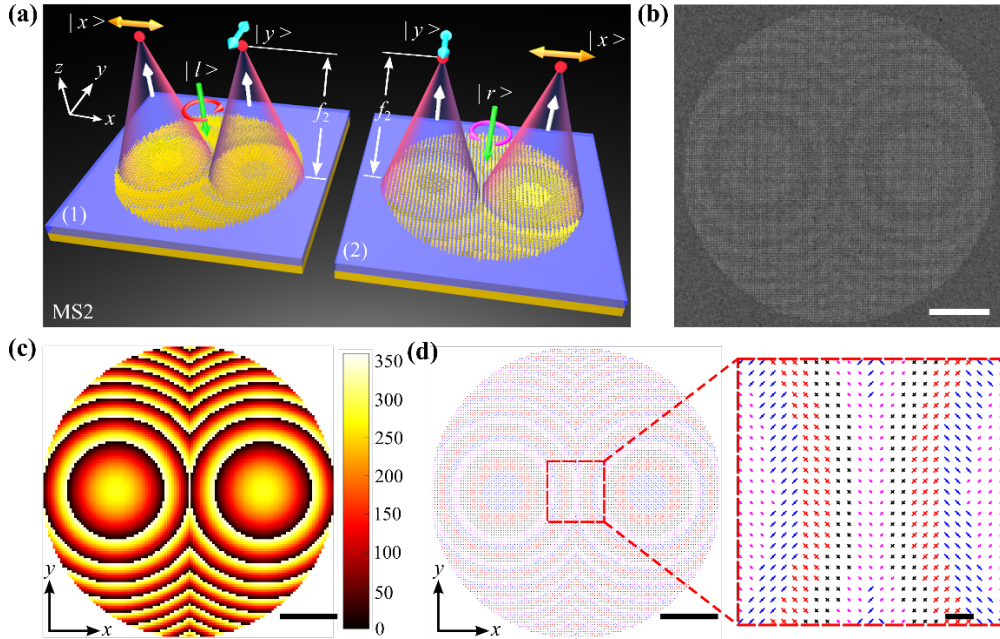
Figure 3.14 (a) Schematic of the optical GSP MS2 for dual-focal LP generation, $|l>$ to focused $|x>$ and $|y>$ in (1) and $|r>$ to focused $|y>$ and $|x>$ in (2), at λ_d = 850 nm. (b) The SEM image of the fabricated MS2 (scale bars is 10 μm). (c-d) Calculated phase profile (c) and designed geometry (d) of MS2 with $D = f_2 = 50$ μm at λ_d = 850 nm. The scale bar in (c) and the left of (d) is 10 μm, scale bar in the right of (d) is 1 μm.

Utilizing the same measured method as described above, Figure 3.15(a) shows the measured reflected optical images from MS2 for incident LCP light at λ = 800, 850, and 900 nm, two bright focused light spots can be observed when MS2 is moved from plane A to plane B for each wavelength. Figure 3.15(b) characterizes the measured polarization state diagrams of the two reflected focused light spots from MS2 at plane B for LCP incident light at λ_d = 850 nm, (i) and (ii) are labeled here to correspondingly match the two focused light spots with their respective polarization states. Moreover, the polarization states of the two light spots can be more clearly demonstrated using an analyzer, as

shown the optical images in Figure S4 of **Appendix D**. Measured DoLPs of (i) and (ii) in Figure 3.15(a) are both equal to ~ 1. Other measured results at λ = 800 and 900 nm for LCP incident light and the case for RCP incident light can be seen in Figure S5 of **Appendix D** [80]. In addition, measured reflectivities with respect to the wavelengths for LCP and RCP incident lights (Figure 3.15(c-d)), respectively. In particular, the reflectivities of focused $|x>$ and $|y>$ under LCP excitation are ~ 13% and ~ 10%, respectively; and the reflectivities of focused $|y>$ and $|x>$ under RCP excitation are ~ 14% and ~ 16%, respectively, at λ_d = 850 nm.
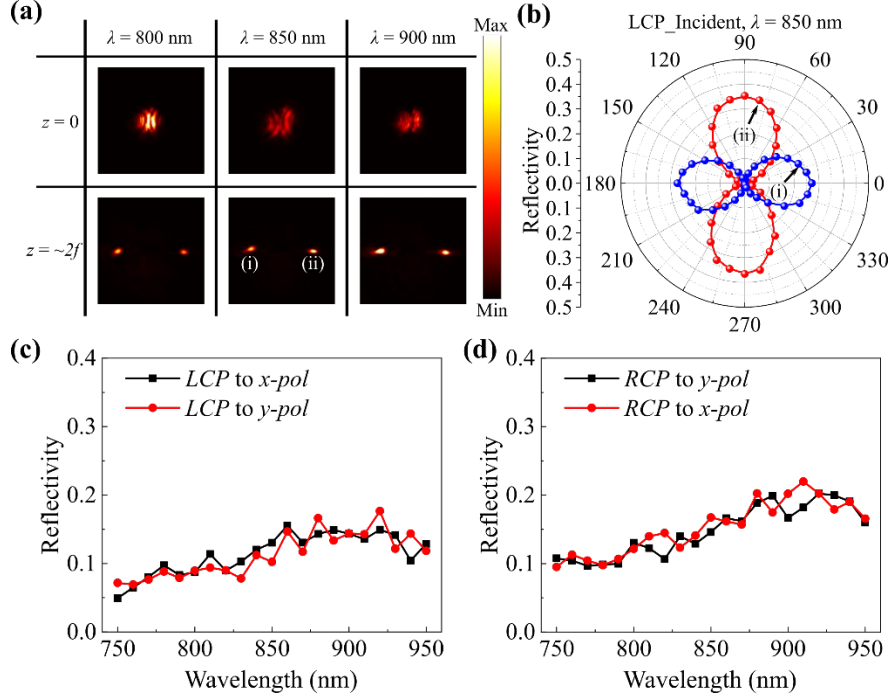
Figure 3.15 (a) Measured reflected optical images from MS2 for incident LCP light at λ = 800, 850, and 900 nm, when the fabricated sample is moved from plane A to plane B. (b) Measured polarization state diagrams of the reflected focused light spots from MS2 at plane B for LCP incident light at λ_d = 850 nm. (i) and (ii) are labelled here to correspondingly match the two focused light spots with their respective polarization states. (c-d) Measured reflectivities across different wavelengths for LCP (c) and RCP (d) incident lights, respectively.

By capitalizing on the remarkable properties of our designed four GSP nano-QWPs, we can achieve precise localization in tailoring the polarization state of the reflected light, which ultimately results in the creation of cylindrical vector beams with polarization vectors that vary spatially, paving the way for the realization of metalenses for focused vector vortex beam (VVB) generation. Both resonance and geometric phases were utilized here. For example, as shown in formula 3.31, if $\theta - \frac{\pi}{4}$ is set as φ, which is defined as the azimuthal angle $\varphi = tan^{-1}(\frac{y}{x})$, the reflected beam will be polarized locally with AoLP = φ under LCP excitation with $E_{in} = \frac{1}{\sqrt{2}}\begin{pmatrix}1\\i\end{pmatrix}$, and the Jones matrix can be described as:

$$E_{out} = |r_{xx}|e^{i\varphi_{xx}}e^{il\theta}\begin{pmatrix}\cos(\varphi)\\\sin(\varphi)\end{pmatrix} \qquad 3.31$$

where l here represents the topological charge of an orbital angular momentum (OAM). Obviously, by locally rotating each nano-QWP with an individual rotation angle $\theta = \varphi + \frac{\pi}{4} = tan^{-1}(\frac{y}{x}) + \frac{\pi}{4}$, and imposing the metasurface with a phase profile of a lens calculated by formula 3.29, a focused RP beam carrying a specific OAM with l = +1 can be achieved. In a similar manner, when the excitation

beam is changed to RCP with $E_{\text{in}} = \frac{1}{\sqrt{2}}\begin{pmatrix} 1 \\ -i \end{pmatrix}$ and set $\theta + \frac{\pi}{4} = \varphi + \frac{\pi}{2}$, the Jones matrix can be described as:

$$E_{\text{out}} = |r_{\text{xx}}|e^{i\varphi_{\text{xx}}}e^{-i(\varphi+\frac{\pi}{4})}\begin{pmatrix} \cos\left(\varphi + \frac{\pi}{2}\right) \\ \sin\left(\varphi + \frac{\pi}{2}\right) \end{pmatrix} \qquad 3.32$$

combining with formula 3.29, a focused AP beam carrying a specific OAM with $l = -1$ can also be achieved. According to formula 3.25, hence, the total reflected focused RP (AP) beam carrying a specific OAM with $l = \pm 1$ can be decomposed as one focused LCP (RCP) beam for the co-polarized CP channel and one focused vortex beam carrying a specific OAM with $l = \pm 2$ for the cross-polarized CP channel. The simulated far-field intensity profiles and phase distributions of co-polarized and cross-polarized channels at $\lambda_{\text{d}} = 850$ nm under LCP and RCP excitations can be seen in Figure S6 of **Appendix D**.

Considering the case under LCP excitation, Figure 3.16(a) displays the schematic of metalens MS3 with $D = f_3 = 50\ \mu$m (NA$_{\text{MS3}} = 0.4472$) according to the phase distribution (Figure 3.16(c)) calculated by formula 3.29, along with the location-related rotation angle of each nano-QWP $\theta = tan^{-1}\left(\frac{y}{x}\right) + \frac{\pi}{4}$. The total reflected focused RP beam carrying a specific OAM with $l = +1$ can be viewed as the superposition of one focused LCP beam for the co-polarized channel and one focused vortex beam carrying a specific OAM with $l = +2$ for the cross-polarized channel. Notably, due to the consideration of the change in propagation direction during the reflection process, the actual polarization state of the co-channel should be RCP. Figure 3.16(b) displays the SEM image of the MS3 sample we fabricated, corresponding to the geometry (Figure 3.16(d)). Figure 3.17(a) presents the measured reflected optical images from MS3 for incident LCP light at $\lambda = 800$, 850, and 900 nm at plane B, one reflected focused RCP light spot and one focused doughnut-shaped vortex beam carrying a specific OAM with $l = +2$ can be observed for each wavelength in the co- and cross-polarized channel, respectively. Meanwhile, as demonstrated in the rightmost column of Figure 3.17(a), +2$^{\text{nd}}$-order spherical shapes are clearly observed in the interference patterns for each wavelength, which possess the opposite topological charges compared to the case under RCP excitation with the same MS3 (Figure S7 of **Appendix D**). Figure 3.17(b) shows the total measured reflectivities across various wavelengths for LCP incident light focused into an RP beam. In addition, reflectivities in both channels for LCP incident light (Figure 3.17(c)). Specifically, the reflectivity of the focused RP beam under LCP excitation is $\sim 29\%$; and the reflectivities of the co- and cross-polarized channel are $\sim 12\%$ and $\sim 10\%$, respectively, at $\lambda_{\text{d}} = 850$ nm. Figure S7 in **Appendix D** shows other measured results for the case under RCP excitation.
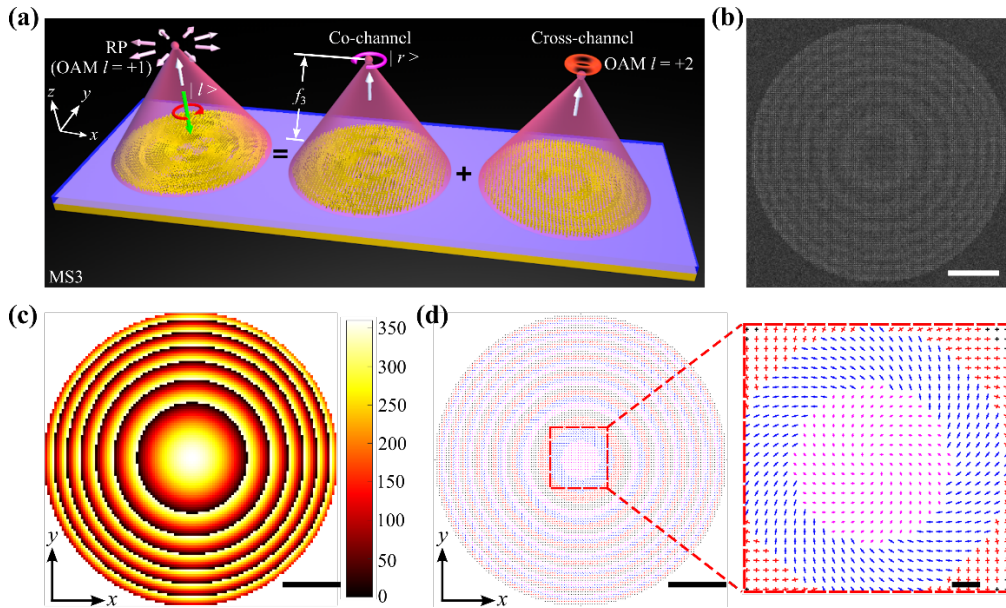
Figure 3.16 (a) Schematic of the optical GSP MS3 designed to generate a focused RP beam carrying a specific OAM with $l = +1$ under LCP excitation, which can be viewed as the superposition of one focused LCP beam for the co-polarized CP channel and one focused vortex beam carrying a specific OAM with $l = +2$ for the cross-polarized CP channel at $\lambda_d = 850$ nm. (b) The SEM image of the fabricated MS3 (scale bars is 10 μm). (c-d) Calculated phase profile (c) and designed geometry (d) of MS3 with $D = f_3 = 50$ μm at $\lambda_d = 850$ nm. The scale bar in (c) and the left of (d) is 10 μm, scale bar in the right of (d) is 1 μm.
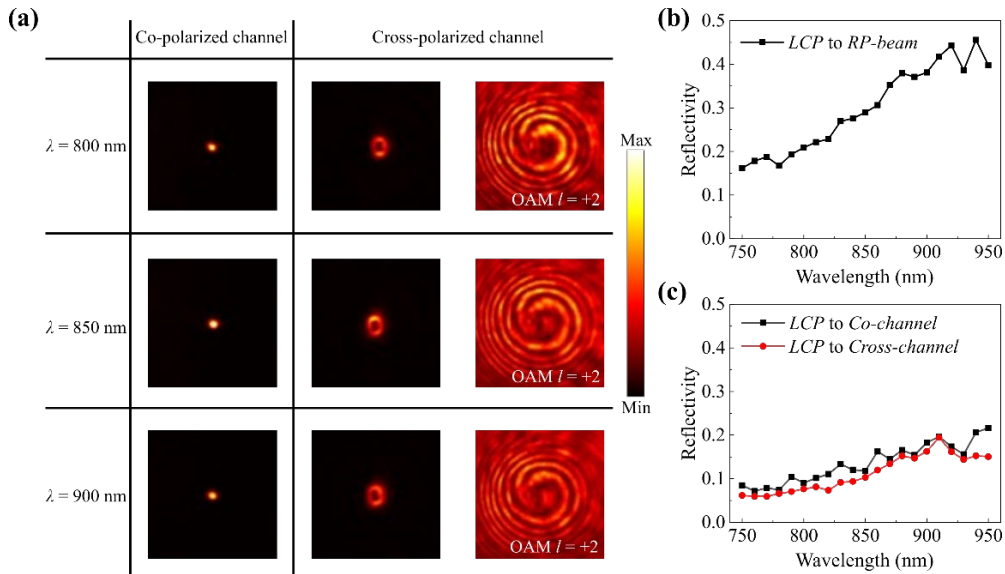
Figure 3.17 (a) Measured reflected optical images from MS3 for incident LCP light at $\lambda = 800$, 850, and 900 nm at plane B in the co- and cross-polarized channels. (b) Total reflectivities measured across different wavelengths for LCP incident light focused into an RP beam. (c) Reflectivities measured across various wavelengths for LCP incident light in both co-polarized and cross-polarized channels.

45

4 Piezoelectric MEMS-integrated metasurfaces for active wavefront shaping

In the previous chapter, we explored passive wavefront shaping employing MIM-based GSP metasurfaces. The inherent limitations of fixed optical responses have prompted us to explore avenues for active control. Therefore, in this chapter, we commence with a concise examination of the lead zirconate titanate (PZT) piezoelectric thin-film material, establishing a crucial foundation for the subsequent in-depth analysis of operational mechanisms of our newly developed MEMS-OMS dynamic control platform. Subsequently, we introduce the MEMS-OMS-based dynamic linear polarizer (DLP), providing a comprehensive account of its design, simulation, sample preparation, and characterization, followed by a discussion of two major applications derived from this technology. The related journal article that we have published is referenced in **Appendix E** [82]. Finally, we propose non-Hermitian MEMS-OMSs for tunable topological phase transitions, and present a detailed design along with experimental validation. The related journal article that we have published is referenced in **Appendix F** [83].

4.1 Piezoelectric MEMS metasurface overview

4.1.1 What is piezoelectricity?

The ability to flexibly and efficiently convert between electrical and mechanical energy is a fundamental feature of any microelectromechanical system [102]. Piezoelectric transduction, acting as one of the electromechanical transduction methods, is appealing for piezoelectric MEMS devices due to its robust, reliable, responsive, and scalable transduction capabilities [103]. Piezoelectricity refers to the property of certain materials to generate an electric charge in response to the applied mechanical stress. On the other hand, these substances can also undergo deformation when exposed to an electric field. This phenomenon arises from the non-centrosymmetric arrangement of the atoms in the crystal lattice of piezoelectric materials, which causes the generation of an electric dipole moment when stressed. The direct piezoelectric effect describes the polarization that arises within a material when mechanical stress is applied and is represented as:

$$P_i = d_{ijk}\sigma_{jk} \qquad 4.1$$

where i, j and k refer to directions or axes in the coordinate system, P_i is the induced polarization, d_{ijk} is the piezoelectric coefficient and σ_{jk} represents the stress. The converse piezoelectric effect involves the production of mechanical strain resulting from an applied electric field and can be expressed as:

$$x_{jk} = d_{ijk}E_i \qquad 4.2$$

where x_{jk} is the strain, representing the relative change in the deformation of a material, and E_i is the applied electric field. In addition, the efficiency of a piezoelectric material in converting input electrical energy into mechanical energy (or vice versa) can be described as:

$$k_{ij} = \frac{d_{ijk}}{\sqrt{s_{ijk}\varepsilon_{ij}}} \qquad 4.3$$

where k_{ij} is the electromechanical coupling factor, s_{ijk} is elastic compliance, and ε_{ij} is the permittivity. The value of k_{ij} is always less than 1, as electromechanical transduction is never perfect. Understanding and researching the relationship between d_{ijk}, s_{ijk} and ε_{ij}, can help improve the electromechanical transduction efficiency of piezoelectric materials. This is essential for the optimal design of piezoelectric materials used in fields like energy harvesting devices, sensors, and actuators.

Typical piezoelectric materials encompass barium titanate, Rochelle salt, quartz, and a variety of ceramics. Among these, PZT acting as a perovskite-structured ceramic material with the chemical formula $Pb(Zr, Ti)O_3$, is one of the most widely used and studied piezoelectric materials. In PZT, lead (Pb) occupies the A-site of the crystal structure, while zirconium (Zr) and titanium (Ti) are randomly distributed at the B-site. Oxygen (O) atoms occupy the vertices of the octahedra. The piezoelectric mechanism of PZT mainly relies on its polarization process [104]. During the polarization process, a strong electric field is exerted on the unpolarized PZT crystal, which forces the electric dipoles within the crystal to orient themselves along the electric field, leading to net polarization. This process is usually performed at a temperature above the Curie point, and then the crystal is cooled below it while maintaining the electric field, thereby locking in the polarization direction. When a polarized PZT crystal is subjected to an electric field, the reorientation of electric dipoles causes mechanical deformation (strain) within the crystal. Overall, PZT piezoelectric material is characterized by high sensitivity, durability, stability across a wide frequency and temperature range, and robust electromechanical coupling, making it an ideal choice for a broad spectrum of applications. Therefore, in this thesis, we utilize PZT as the piezoelectric material for the construction of MEMS mirrors.

4.1.2 Piezoelectric response in PZT thin-films

A piezoelectric MEMS is an intricate multilayer device, as illustrated in Figure 4.1(a), featuring a PZT thin-film situated between the top and bottom electrodes. Secured to the Si substrate, the PZT thin film and two electrodes facilitate electromechanical transduction by generating in-plane stress upon the imposition of an electric field, as shown in Figure 4.1(b). Because the Si substrate imposes a clamping effect, the PZT thin film's contraction within the plane is constrained, leading to tensile stress in both in-plane directions: $\sigma_1 = \sigma_2$. As a result, the substrate undergoes compressive stress in-plane. As the substrate constrains the thin film from any free in-plane expansion or contraction, the in-plane strains, x_1 and x_2, become equal and are effectively minimized to zero [104], which can be represented as follows:

$$x_1 = x_2 = (s_{11}^E + s_{12}^E)\sigma_{12} + s_{13}^E\sigma_3 = 0 \qquad\qquad 4.4$$

Conversely, the thin film is unrestricted in the out-of-plane direction since it is not clamped. Consequently, the out-of-plane strain x_3 becomes nonzero, and is represented as:

$$x_3 = 2s_{12}^E\sigma_{12} + s_{11}^E\sigma_3 \qquad\qquad 4.5$$

The piezoelectric coefficients of PZT thin films are invariably lower than those of their bulk equivalents due to substrate clamping, which limits in-plane deformation. This effect is represented by the effective piezoelectric coefficients, $e_{31,f}$ and $d_{33,f}$, and can be expressed as follows:

$$e_{31,f} = \frac{d_{31}}{s_{11}^E + s_{12}^E} \qquad\qquad 4.6$$

$$d_{33,f} = d_{33} - \frac{2s_{13}^E d_{31}}{s_{11}^E + s_{12}^E} \qquad\qquad 4.7$$

$e_{31,f}$ combines the piezoelectric characteristics and mechanical flexibility of the material, providing a comprehensive metric for evaluating the piezoelectric performance of thin films. $d_{33,f}$ reflects the actual piezoelectric response of the thin-film under an electric field, representing the true piezoelectric performance of the material. PZT piezoelectric thin-film MEMS devices rely on the in-plane contraction of clamped films to achieve the conversion between electrical and mechanical energy, which can achieve substantial mechanical displacements with comparatively low driving voltages due to the large active electrode area relative to its thickness. After sputtering a thick layer of gold on

the backside of the MEMS devices, ultra-thin reflective MEMS mirrors exhibiting nearly linear deformation with applied voltages will be constructed.

(a) E = 0   **(b)** E ≠ 0
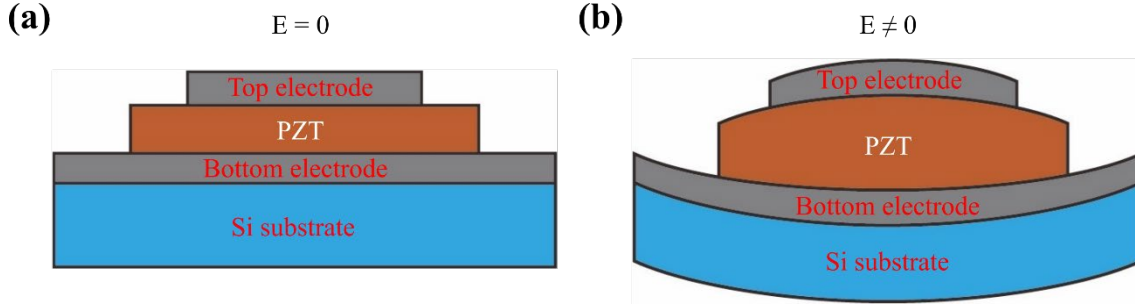
Figure 4.1 Schematic of a representative piezoelectric PZT thin-film stack configuration. (a) The piezoelectric PZT thin-film is generally placed between the top and bottom electrodes in the absence of applied voltages. (b) The PZT thin-film undergoes vertical deformation when a voltage is applied.

4.1.3 Piezoelectric MEMS-OMS design and working mechanism

This section is based on my previous publication **Appendix E** [82], and incorporates pieces of text from that work. In this thesis, we developed an electrically driven active MEMS-OMS platform, enabling dynamically reconfigurable wavefront shaping with stable switching process, high modulation efficiencies, and extremely short response time, by integrating PZT thin-film piezoelectric MEMS mirror with plasmonic OMSs. The core idea is to replace the middle SiO_2 dielectric layer of the GSP resonator described in *Section 3* with an electrically adjustable air gap, allowing the top OMS layer containing plasmonic meta-atoms and the bottom thick Au layer to be physically separated, featuring an ultra-flat MEMS mirror as a vertically movable back reflector. As shown the schematic in Figure 4.2(a), the OMS component, consisting of meticulously designed meta-atoms fabricated on top of a glass substrate, is positioned close to an electrically driven MEMS mirror with the separation (air gap T_a) precisely adjusted by tuning the actuation voltage V_m. Figure 4.2(b) illustrates the individual unit cell of the MEMS-OMS device.
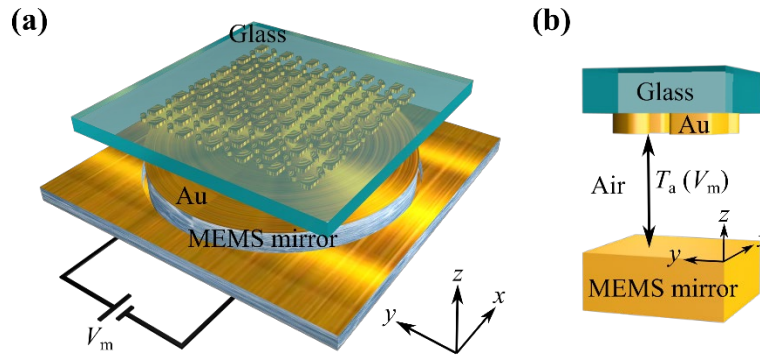
Figure 4.2 (a) Schematic of the electrically adjustable device based on MEMS-OMS technology, featuring an array of Au nanostructures fabricated on a glass substrate, with a pre-prepared gold MEMS mirror positioned underneath, separated by an air gap that is controlled by applied voltage. (b) Schematic of the unit cell that constitutes the MEMS-OMS-based device.

Next, we analyze the fundamental working mechanism from the perspective of the MEMS-OMS device configuration. When the device operates with a small air gap, e.g., $T_a < \sim \lambda/10$, the inevitable NFC between the OMS layer and the MEMS mirror induces GSP resonance. Similar as MIM-based GSP resonators, working in the GSP region can provide a slightly larger phase modulation range as

48

well as a broad working bandwidth (Figure 3.2). However, it is important to note that the minimum air gap obtained in the assembled MEMS-OMS sample is approximately 150 nm, making it suboptimal for GSP resonance [78]. Achieving closer separations is feasible but requires significantly more effort and time to select from a large batch of prepared samples, and it may be even more challenging to realize with larger MEMS mirror apertures. Fortunately, the MEMS-OMS platform is not confined to operating solely in the GSP region. When moving to the larger air gap, the MEMS-OMS configuration can be viewed as a tunable hybrid plasmonic FP cavity [82], which holds the secret to dynamic control as NFC diminishes. In a simple MEMS mirror reflection model without any metasurfaces (left panel of Figure 4.3), distinct alternating light and dark electric field distributions signal the formation of standard standing waves, resulting from the interference and superposition of the incident and reflected fields. When the metasurface is positioned at the interference minimum, such as at $T_{a1} = \sim \frac{\lambda}{2} + m\frac{\lambda}{2}$ (where $m = 0, 1, 2 \ldots\ldots$), it interacts with nodes of the standing wave and the entire system behaves as an Au mirror (mirror operation) with reflectance coefficients remaining independent of the size and shape of nanostructures composing the metasurface (middle panel of Figure 4.3). Once the metasurface is shifted a short distance Δt to the position of the interference maximum (right panel of Figure 4.3), interacting with anti-nodes of the standing wave at $T_{a2} = \sim (\frac{\lambda}{2} + \Delta t) + m\frac{\lambda}{2}$ (where $m = 0, 1, 2 \ldots\ldots$), the entire system will exhibit the functionalities of the designed metasurface (metasurface operation). Moreover, due to the properties of the FP cavity, both operations exhibit a periodic air-gap separation of $\frac{\lambda}{2}$ as they transition from the current FP mode to their respective subsequent FP modes. Therefore, our developed active MEMS-OMS platform allows stable switching between ON and OFF states, relating to respective metasurface operation and mirror operation, with extremely fast switching speed. Additionally, allowing for larger air gaps (e.g., $T_a > 1\ \mu$m) not only alleviates thin-film damping issues during the high-speed switching process, but also eases fabrication requirements, as achieving air gaps smaller than 50 nm necessitates exceptionally parallel and flat surfaces free of any particles or irregularities, which could otherwise hinder MEMS mirror movement [78].
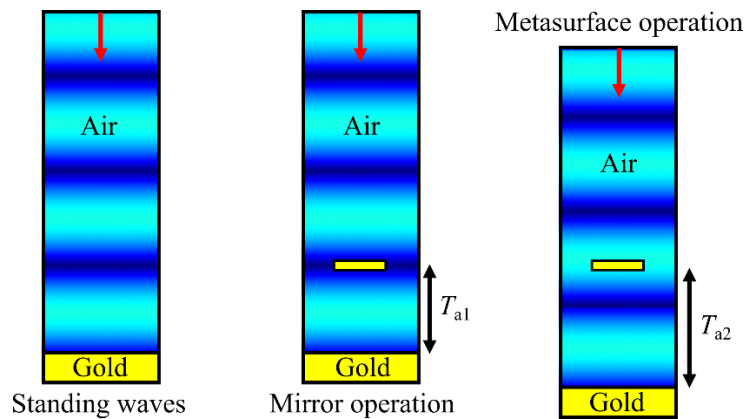
Figure 4.3 Schematic of the operating mechanism of MEMS-OMS devices utilizing an interference-based model. Left panel: schematic of the standard standing wave model without any metasurfaces. Middle panel: schematic of the mirror-operation model positioning metasurfaces at the interference minimum with air gap T_{a1}. Right panel: schematic of the metasurface-operation model positioning metasurfaces at the interference maximum with air gap T_{a2}.

The complex energy variations in the hybrid plasmonic FP cavity (Figure 4.4) can be further accurately described using the FP equation [51, 78]:

$$r_{\text{total}} = r_{12} + \frac{t_{12}t_{21}r_{23}e^{i2kn_2 T_a}}{1 - r_{21}r_{23}r_{23}e^{i2kn_2 T_a}} = r_{12} + r_0 \qquad 4.8$$

where r_{total} represents the complex reflection coefficient of the MEMS-OMS system, and r_{mn}/t_{mn} represents the complex reflection/transmission coefficients for the interface between media m and n with light incident from medium m [82]. The number 1, 2, and 3 represent glass, air and the MEMS mirror, respectively, with interface 12 representing a complex glass/OMS/air interface and interface 23 representing a bare air/gold interface [82]. k acting as the wavevector in a vacuum depends only on the wavelength λ, and n_2 is the refractive index of air. From formula 4.8, the dynamic total reflection r_{total} in the MEMS-OMS cavity can be viewed as the superposition of direct reflection r_{12}, which only depends on the OMS design, and all the other reflection r_0 that bounce back and forth between the OMS and MEMS mirror as the air gap changes. Therefore, the strength of the total reflection is determined by both the OMS and air gap T_a. To some extent, formula 4.8 has helped simplify the analysis of the hybrid plasmonic FP cavity and provided a quantitative method for numerical calculations. However, the term r_0 in formula 4.8 remains a broad mathematical expression for describing multiple reflections and transmissions in the hybrid FP cavity.
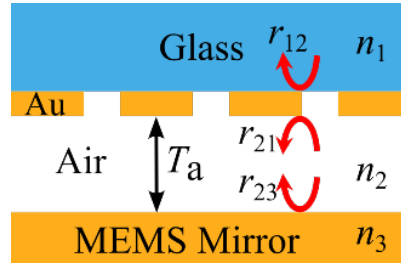
Figure 4.4 Schematic of the FP model consisting of media 1 (glass layer), an OMS layer located between glass/air interface, media 2 (air layer), and media 3 (MEMS mirror layer) [82]. Reprinted from Ref. [82].

Next, we provide further analysis and derivation by employing the transfer matrix method (TMM). When incident x- and y-polarized lights impinge on the FP cavity (**Figure 4.5**) at normal incidence, there are forward and back propagating waves in the FP cavity:

$$E_{2x}^f = t_{12xx}E_{1x}^f + r_{21xx}E_{2x}^b + t_{12xy}E_{1y}^f + r_{21xy}E_{2y}^b \qquad 4.9$$

$$E_{1x}^b = r_{12xx}E_{1x}^f + t_{21xx}E_{2x}^b + r_{12xy}E_{1y}^f + t_{21xy}E_{2y}^b \qquad 4.10$$

$$E_{2y}^f = t_{12yx}E_{1x}^f + r_{21yx}E_{2x}^b + t_{12yy}E_{1y}^f + r_{21yy}E_{2y}^b \qquad 4.11$$

$$E_{1y}^b = r_{12yx}E_{1x}^f + t_{21yx}E_{2x}^b + r_{12yy}E_{1y}^f + t_{21yy}E_{2y}^b \qquad 4.12$$
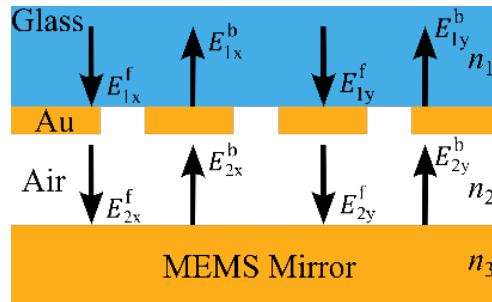
Figure 4.5 Schematic of the hybrid plasmonic FP cavity employing TMM.

where r_{mnij} (t_{mnij}) represents the complex reflection/transmission coefficients for the interface between media m and n with light incident from medium m [82], accompanied by the polarization conversion from j- to i-state. As an example, we consider the incident x-polarized light (E_{1x}^{f}), which means that the incident x-polarized light propagates forward in the media 1. Then the light passing though the interface12, marked as E_{2x}^{f}, will continue to propagate forward to the interface 23 in the media 2 with complex transmission coefficient t_{12xx} and then be reflected by the MEMS mirror with reflection coefficient r_{23xx}. The reflected light E_{2x}^{b} will propagate backward in the media 2 and undergo continuous reflection and transmission at their corresponding interfaces. Finally, E_{1x}^{b} serves as the total reflected light from the system. Then we change the equations 4.9-4.12 to the following matrix:

$$
\begin{pmatrix}
-t_{12xx} & -t_{12xy} & 0 & 0 \\
-r_{12xx} & -r_{12xy} & 1 & 0 \\
-t_{12yx} & -t_{12yy} & 0 & 0 \\
-r_{12yx} & -r_{12yy} & 0 & 1
\end{pmatrix}
\begin{pmatrix}
E_{1x}^{\mathrm{f}} \\
E_{1y}^{\mathrm{f}} \\
E_{1x}^{\mathrm{b}} \\
E_{1y}^{\mathrm{b}}
\end{pmatrix}
=
\begin{pmatrix}
-1 & 0 & r_{21xx} & r_{21xy} \\
0 & 0 & t_{21xx} & t_{21xy} \\
0 & -1 & r_{21yx} & r_{21yy} \\
0 & 0 & t_{21yx} & t_{21yy}
\end{pmatrix}
\begin{pmatrix}
E_{2x}^{\mathrm{f}} \\
E_{2y}^{\mathrm{f}} \\
E_{2x}^{\mathrm{b}} \\
E_{2y}^{\mathrm{b}}
\end{pmatrix}
\tag{4.13}
$$

We set:

$$
\begin{pmatrix}
-t_{12xx} & -t_{12xy} & 0 & 0 \\
-r_{12xx} & -r_{12xy} & 1 & 0 \\
-t_{12yx} & -t_{12yy} & 0 & 0 \\
-r_{12yx} & -r_{12yy} & 0 & 1
\end{pmatrix}
= A
\tag{4.14}
$$

$$
\begin{pmatrix}
-1 & 0 & r_{21xx} & r_{21xy} \\
0 & 0 & t_{21xx} & t_{21xy} \\
0 & -1 & r_{21yx} & r_{21yy} \\
0 & 0 & t_{21yx} & t_{21yy}
\end{pmatrix}
= B
\tag{4.15}
$$

then substitute equation 4.14 and 4.15 into equation 4.13, we could get:

$$
\begin{pmatrix}
E_{1x}^{\mathrm{f}} \\
E_{1y}^{\mathrm{f}} \\
E_{1x}^{\mathrm{b}} \\
E_{1y}^{\mathrm{b}}
\end{pmatrix}
= A^{-1} B
\begin{pmatrix}
E_{2x}^{\mathrm{f}} \\
E_{2y}^{\mathrm{f}} \\
E_{2x}^{\mathrm{b}} \\
E_{2y}^{\mathrm{b}}
\end{pmatrix}
\tag{4.16}
$$

Considering the complex reflection coefficient r_{23} of the MEMS mirror and the air gap T_{a} [82]:

$$
E_{2x}^{\mathrm{b}} = P_{\mathrm{m}} E_{2x}^{\mathrm{f}}
\tag{4.17}
$$

$$
E_{2y}^{\mathrm{b}} = P_{\mathrm{m}} E_{2y}^{\mathrm{f}}
\tag{4.18}
$$

$$
P_{\mathrm{m}} = r_{23} e^{i2n_2 k T_{\mathrm{a}}}
\tag{4.19}
$$

then we substitute equations 4.17-4.19 into equation 4.16, and set $A^{-1}B = M_{ij}$, we could get:

$$
\begin{pmatrix}
E_{1x}^{\mathrm{f}} \\
E_{1y}^{\mathrm{f}} \\
E_{1x}^{\mathrm{b}} \\
E_{1y}^{\mathrm{b}}
\end{pmatrix}
= M_{ij}
\begin{pmatrix}
E_{2x}^{\mathrm{f}} \\
E_{2y}^{\mathrm{f}} \\
P_{\mathrm{m}} E_{2x}^{\mathrm{f}} \\
P_{\mathrm{m}} E_{2y}^{\mathrm{f}}
\end{pmatrix}
\tag{4.20}
$$

We expand the equation 4.20 and get:

$$
E_{1x}^{\mathrm{f}} = M_{11} E_{2x}^{\mathrm{f}} + M_{12} E_{2y}^{\mathrm{f}} + M_{13} P_{\mathrm{m}} E_{2x}^{\mathrm{f}} + M_{14} P_{\mathrm{m}} E_{2y}^{\mathrm{f}}
\tag{4.21}
$$

$$E_{1y}^f = M_{21}E_{2x}^f + M_{22}E_{2y}^f + M_{23}P_mE_{2x}^f + M_{24}P_mE_{2y}^f \tag{4.22}$$

$$E_{1x}^b = M_{31}E_{2x}^f + M_{32}E_{2y}^f + M_{33}P_mE_{2x}^f + M_{34}P_mE_{2y}^f \tag{4.23}$$

$$E_{1y}^b = M_{41}E_{2x}^f + M_{42}E_{2y}^f + M_{43}P_mE_{2x}^f + M_{44}P_mE_{2y}^f \tag{4.24}$$

If we assume the incidence only containing x-polarized component ($E_{1x}^f = 1$, and $E_{1y}^f = 0$), we can obtain:

$$1 = (M_{11} + M_{13}P_m)E_{2x}^f + (M_{12} + M_{14}P_m)E_{2y}^f \tag{4.25}$$

$$0 = (M_{21} + M_{23}P_m)E_{2x}^f + (M_{22} + M_{24}P_m)E_{2y}^f \tag{4.26}$$

$$E_{1x}^b = (M_{31} + M_{33}P_m)E_{2x}^f + (M_{32} + M_{34}P_m)E_{2y}^f \tag{4.27}$$

$$E_{1y}^b = (M_{41} + M_{43}P_m)E_{2x}^f + (M_{42} + M_{44}P_m)E_{2y}^f \tag{4.28}$$

We set:

$$M_{11} + M_{13}P_m = a \tag{4.29}$$

$$M_{12} + M_{14}P_m = b \tag{4.30}$$

$$M_{21} + M_{23}P_m = c \tag{4.31}$$

$$M_{22} + M_{24}P_m = d \tag{4.32}$$

$$M_{31} + M_{33}P_m = e \tag{4.33}$$

$$M_{32} + M_{34}P_m = f \tag{4.34}$$

$$M_{41} + M_{43}P_m = g \tag{4.35}$$

$$M_{42} + M_{44}P_m = h \tag{4.36}$$

and can get:

$$E_{1x}^b = \frac{de-cf}{ad-bc} = r_{xx} \tag{4.37}$$

$$E_{1y}^b = \frac{dg-ch}{ad-bc} = r_{yx} \tag{4.38}$$

Similarly, if we assume a y-polarized incident beam ($E_{1y}^f = 1$, $E_{1x}^f = 0$), we could get:

$$E_{1x}^b = \frac{af-be}{ad-bc} = r_{xy} \tag{4.39}$$

$$E_{1y}^b = \frac{ah-bg}{ad-bc} = r_{yy} \tag{4.40}$$

Finally, the total complex reflection coefficient:

$$r_{\text{total-TMM}} = \begin{pmatrix} r_{\text{xx}} & r_{\text{yx}} \\ r_{\text{xy}} & r_{\text{yy}} \end{pmatrix} = \begin{pmatrix} \frac{de-cf}{ad-bc} & \frac{dg-ch}{ad-bc} \\ \frac{af-be}{ad-bc} & \frac{ah-bg}{ad-bc} \end{pmatrix} \qquad 4.41$$

can be obtained by using TMM. Generally, we can use full-wave simulations to calculate the entire MEMS-OMS structure and obtain values of r_{total}, but this requires significant computational effort as full-wave calculations must be performed for each air gap with a wide wavelength range. However, drawing from the TMM analysis, we can significantly reduce the computational load by performing simulations at different wavelengths for the structure without MEMS mirror and then using equation 4.41 to quickly calculate values of r_{total} for different air gaps, since complex reflection and transmission coefficients r_{12}, r_{21}, t_{12} and t_{21} are solely determined by the OMS structure. It's important to note that this method is ineffective for very small air gaps, e.g., $T_a < \lambda/10$ [78], where NFC and the resulting GSP excitation must also be considered.

4.2 MEMS-OMS-based DLPs and applications

This section is based on my previous publications **Appendix E-F** [82-83], and incorporates some texts from that two works. Leveraging the generally designed active MEMS-OMS platform and the comprehensive theoretical analysis, we designed a MEMS-OMS-based DLP, as shown in Figure 4.6(a), with a real-time electrically controlled extinction ratio (ER = $R_{\text{xx}} / R_{\text{yy}}$) for two orthogonal LP excitations in a rapid and reversible manner. By precisely tuning the polarization-sensitive coupling between an anisotropic plasmonic OMS made up of Au nano-bricks and a movable Au MEMS mirror, this device achieves distinct amplitude modulation, representing a significant departure from our previous work [51,77-78], which were exclusively centered on the phase modulation.

4.2.1 Design, simulation and analysis for DLPs

Upon electrical actuation, the DLP features a continuously varied reflectivity R_{yy} (V_m) under y-polarized ($|y\rangle$) excitation, while maintaining a high and nearly constant reflectivity R_{xx} (V_m) under x-polarized ($|x\rangle$) excitation. Particularly, the designed DLP transitions dramatically from nearly total reflection to nearly complete absorption under $|y\rangle$ excitation, exhibiting a polarizer-like operation with a large ER. After optimizations of the full-wave simulation on the dimensions of the unit cell shown in the right panel of Figure 4.6(a) as well as the air gap T_a and operating wavelength λ, a DLP is designed in the parameter space of $[l_x, l_y, t_m, P, T_a(V_m), \lambda] = [106$ nm, 196 nm, 50 nm, 500 nm, 325 nm, 831 nm] with $R_{\text{xx}} = 96.27\%$ and $R_{\text{yy}} = 1.41\%$, corresponding to an ER of ~ 68.28 (position I in Figure 4.6(b), and Figure 4.6(c)). For such a large air gap ($T_a = 325$ nm), the DLP response is determined by the hybrid plasmonic FP resonance (Supplement 1 Section 1 of **Appendix E**) [51,78, 105-106] instead of the GSP resonance [63, 79-80] owing to the negligible NFC between the gold meta-atom array and MEMS mirror, releasing the critical requirement of ultra-small air gaps for observing the polarizer-like performance. When we increase the air gap T_a slightly to 370 nm (position II), the corresponding mirror operation appears with an ER of ~ 1. Due to the inherent FP characteristics of the DLP, the overall response exhibits a natural periodicity of $\lambda/2$ in relation to the varying air gap T_a (Figure 4.6 (b)). For example, the position III ($T_a = 3649$ nm) and IV ($T_a = 3694$ nm) corresponding to the respective polarizer-like operation and mirror operation in the 8th-order FP regime, exhibiting reflectivities that are entirely identical to those of the 1st-order FP mode (Figure 4.6(b-d)). We also provide the TMM-FP-model based calculation results, which are not only perfectly consistent with the full-wave simulations but also quickly produce reflectivity maps depending on the wavelength λ and air gap T_a (Supplement Figs. S3 and S4 of **Appendix E**). In addition, the DLP exhibits robust performance for both air gaps of $T_a = 325$ nm and 3649 nm when the incident angle

is smaller than 30° (Supplement 1 Fig. S5 of **Appendix E**). However, if the periodicity of the metasurface is varied, the DLP performance deteriorates quite fast (Supplement 1 Fig. S6 of **Appendix E**).

Considering the wavelength-dependent response, it is immediately seen that, for larger air gaps, the MEMS-OMS DLP exhibits a pronounced mode splitting (Figure 4.6(d), and Supplement 1 Figs. S3 and S4 of **Appendix E**), which is ascribed to the strong coupling between the high-order FP and plasmonic resonances [105-106]. In order to explain the above results, we provide the corresponding electric field distributions at the wavelength of $\lambda = 831$ nm. Under $|x\rangle$ excitation, the OMS resonance does not couple with the FP resonance because the relevant plasmonic resonance is out of the investigated spectrum, leaving the interference pattern remaining unchanged (Supplement Fig. S2-S4 and Fig. S7 of **Appendix E**). But under $|y\rangle$ excitation, there is a strong coupling between the FP and plasmonic resonances (Figure 4.6(c-d)), leading to mode splitting of the plasmonic resonance at the wavelength of $\lambda = 861$ nm (Supplement Fig. S3 of **Appendix E**). Therefore, we can achieve nearly perfect absorption at one of the split modes with a shorter wavelength of $\lambda = 831$nm. At this wavelength, the electric field is intensely confined around the gold meta-atom, enhancing the interference pattern beneath it (Figure 4.6(c-d), I and III). While for the mirror operation, the plasmonic meta-atoms are ineffective regardless of their designed shaped and sizes, since they are positioned at the minimum of the interference pattern created by the MEMS mirror (Figure 4.6 (c-d), II and IV).
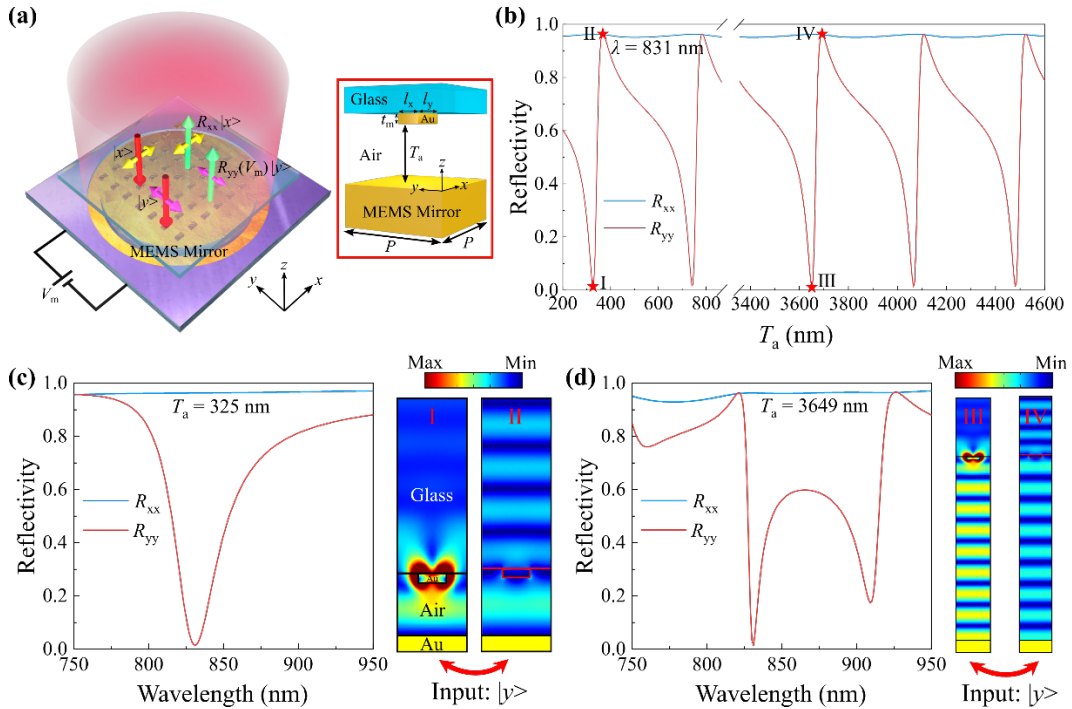
Figure 4.6 Design principle of the MEMS-OMS DLP. (a) Schematic of the electrically tunable MEMS-OMS-based DLP consisting of an array of 2D gold meta-atoms on a glass substrate, complemented by a thin-film movable piezoelectric MEMS mirror with a voltage-controlled air gap to realize the real-time rapid modulation of the reflected light under $|y\rangle$ incidence. The unit cell of the MEMS-OMS DLP is shown in the right panel, where all corners of the nanobricks are rounded with a radius of 5 nm. (b) Calculated reflectivities as a function of the air gap T_a at the design wavelength of $\lambda = 831$ nm for both $|x\rangle$ and $|y\rangle$ incidence. Red stars I and III mark the polarizer-operation states with the air gaps of $T_a = 325$ nm and 3649 nm, respectively, while red stars II and IV represent the mirror-operation states with the air gaps of $T_a = 370$ nm and 3694 nm, respectively. (c and d) Calculated reflectivities as a function of the wavelength at air gaps of $T_a = 325$ nm (c) and 3649 nm (d) for

both |x> and |y> incidence. The right panels in (c) and (d) show the electric field distributions under the |y> incidence at air gaps of T_a = 325 nm (I), 370 nm (II), 3649 nm (III), and 3694 nm (IV) [82]. Reprinted from Ref. [82].

4.2.2 MEMS mirror fabrication and DLP sample assembly

This section is summarized based on my previous publication **Appendix E-F** [82-83] and incorporates pieces of text from that two works. The MEMS-OMS-based DLP sample was fabricated and assembled from a separately prepared gold MEMS mirror in conjunction with an OMS on top of a glass substrate. The fabrication of the OMS followed the same procedure detailed in *Section 2.4*, with the exception of an additional step: a 40-nm-thick layer of conductive polymer (AR-PC 5090, Allresist) was spin-coated onto the PMMA layer. This conductive polymer layer can effectively dissipate the charges introduced by the electron beam, preventing charge accumulation that could interfere with its precise control, a crucial function given the insulating nature of the glass substrate.

The MEMS mirror was fabricated using standard semiconductor manufacturing processes [51, 77-78, 82-83], incorporating a thin-film PZT layer to enable electrical actuation with low voltage requirements and a long stroke. Initially, a bottom platinum (Pt) electrode, a 2-μm-thick PZT thin-film, and top electrodes made of TiW/Au were deposited onto a pre-prepared silicon-on-insulator (SOI) wafer (Figure 4.7(a)). Subsequently, a 3 mm central circular aperture was created employing deep reactive ion etching (DRIE) on the silicon, followed by etching the buried oxide layer. An annular trench was then etched on the backside of the wafer to release the circular plate (Figure 4.7(b)). The backside of the wafer was then deposited with a 100-nm-thick gold layer to function as a mirror, which was then inspected using white light interferometry (Zygo NewView 6000) to guarantee good flatness over the whole surface [83], a critical factor for the development of dynamic MEMS-OMS devices (Figure 4.7 (c)). After the fabrication of both OMS and MEMS mirror, the MEMS-OMS-based DLP sample was assembled by bonding the glass substrate with OMS to the MEMS mirror with a selected diameter of ~3 mm [82] (Figure 4.7(d)). Once the device was meticulously assembled, it was affixed to a PCB for stability [82]. The subsequent stage entailed intricate gold wire bonding, ensuring precise electrical connections for optimal actuation [82] (Figure 4.8(a)). Figure 4.8(b) presents SEM images of the OMS sample.
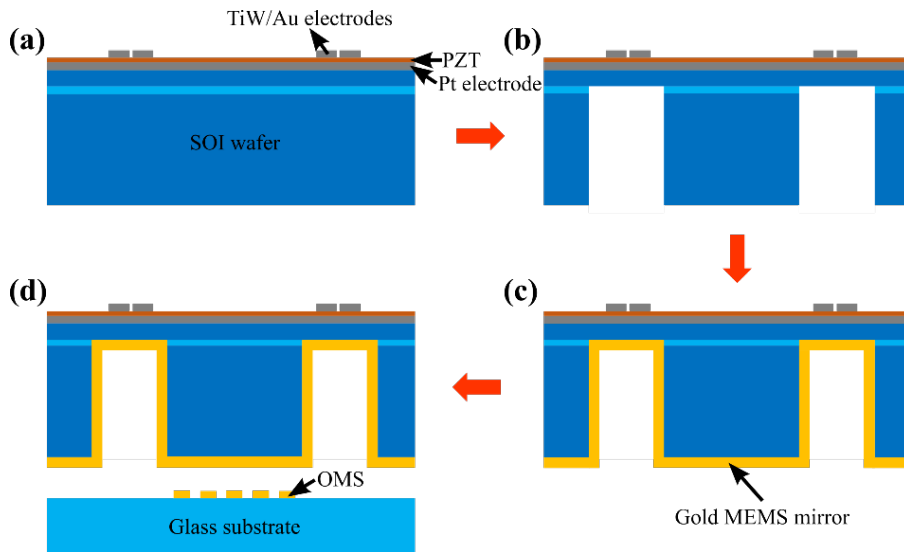

Figure 4.7 Simplified cross-sectional illustrations of the MEMS-OMS sample assembly process.
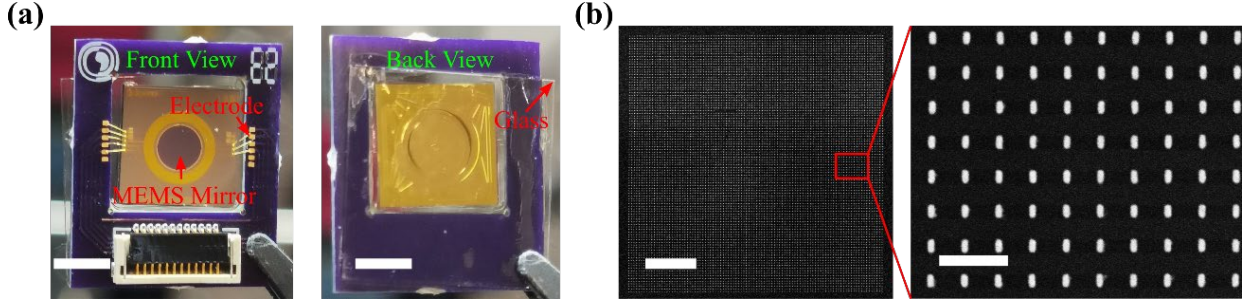
Figure 4.8 The fabricated MEMS-OMS-based DLP sample. (a) Typical photos of the fabricated MEMS-OMS-based DLP sample (scale bars are both 5 mm). (b) SEM images of the assembled OMS (scale bars are 10 μm and 1 μm, respectively) [82]. Reprinted from Ref. [82].

4.2.3 Optical characterizations of the DLP sample

Given the various uncertainties in the fabrication and assembly process, such as the force applied during glue dispensing, it is crucial to evaluate the performance of the MEMS-OMS sample by measuring its initial air gap and testing the parallelism between the MEMS mirror and OMS. This assessment helps determine whether the integrated MEMS mirror possesses a long stroke. The evaluation method involves comparing and fitting the measured spectra of reflected light from the glass/air/MEMS mirror substrate, excluding the nanostructures, normalized by the reflected light from a glass/Au structure illuminated by a halogen lamp, with the numerical calculations of a simple FP etalon model [78]. The initial air gap of the MEMS-OMS-based DLP sample in Figure 4.8 is approximately 4.8 μm. The relationship between different driving voltages and their corresponding air gaps is nearly linear, which preliminarily indicates good parallelism between the MEMS mirror and OMS. In the Supplement Fig. S9 of **Appendix E**, we present more detailed experimental data demonstrating the specific relationship between the applied voltage and the corresponding air gap.

Next, we performed the sample characterization using the same setup (*Section 2.5*) under x- ($|x>$) and y-polarized ($|y>$) excitations. The supercontinuum laser was directed through the coupling setup (Figure 4.9(a)) into the measurement setup, where a power meter was used to monitor and evaluate the final coupling efficiency. The photograph in Figure 4.9(b) shows our custom-designed sample holder, which is used to secure the MEMS-OMS sample and establish a stable connection to the control circuit board. In this measurement, the driving voltage was steadily increased from 0 to 20 V in a fixed interval of 0.2 V, which is fine enough for us to adjust the air gap and thus explore the dynamic transition between the polarizer-like operation and the mirror-operation, identifying specific positions where the incident y-polarized light is either absorbed or reflected. In the setup, supercontinuum laser and spectrometer were chosen to record the polarization-resolved reflection spectra. We correlated the *in-situ* air gap T_a with the actuated voltage V_m by extracting the wavelength points indicating mirror-operation states from the measured R_{yy} spectra (Supplement Fig. S9 of **Appendix E**) [51]. The measured spectra as a function of wavelengths under R_{xx} and R_{yy} has been presented in Figure 4.10(a) at each voltage V_m (air gap T_a), which is in good agreement with the TMM-based theoretical predictions (Supplement Fig. S3 of **Appendix E**). For $|x>$ incidence, the incident light is completely reflected for wavelengths larger than 825 nm irrespective of the actuated air gaps, which occurs because the OMS resonance falls within the short wavelength range. While for $|y>$ incidence, the reflectivity R_{yy} exhibits significant and periodic oscillations as the air gap T_a is controlled by the applied voltage V_m. To further illustrate the dynamic modulation capability of our DLP sample, we set the operating wavelength to 830.2 nm and analyzed the extracted reflectivities, R_{xx} and R_{yy}, as a function of V_m (T_a) (Figure 4.10(b)). The measurement results show that R_{xx} remains consistently high at around 98.36%, while R_{yy} exhibits periodic variations, alternating between

reflection and absorption. For instance, by driving the voltage from $V_m = 16.0$ V ($T_a \approx 3687$ nm) to $V_m = 16.8$ V ($T_a \approx 3640$ nm), the system achieves mirror-operation and polarizer-operation states with reflectivity R_{yy} reaching 95.05% and 7.46%, respectively, which allows for continuous tuning of the ER from 1.04 to 13.30, resulting in a measured modulation depth of approximately 92.15%. The measured ER values are significantly lower compared to the theoretical tuning range from 1 to 68.28. The reasons for this discrepancy, along with the proposed optimization solutions and some other discussions, are detailed in **Appendix E**. It is worth adding that, due to the presence of hysteresis and nonlinearity when actuating the MEMS mirror, it is essential to implement a feedback mechanism, such as optical, piezoresistive or capacitive feedback, for practical applications requiring more precise positioning (e.g., single nm-level). This implementation will also help improve the accuracy of the measurements to some extent. Despite these minor discrepancies, the experiments have successfully reproduced the characteristic resonances associated with coupled plasmonic modes and higher-order FP resonances, as well as their dynamic evolution (Supplement Fig. S10 of **Appendix E**).
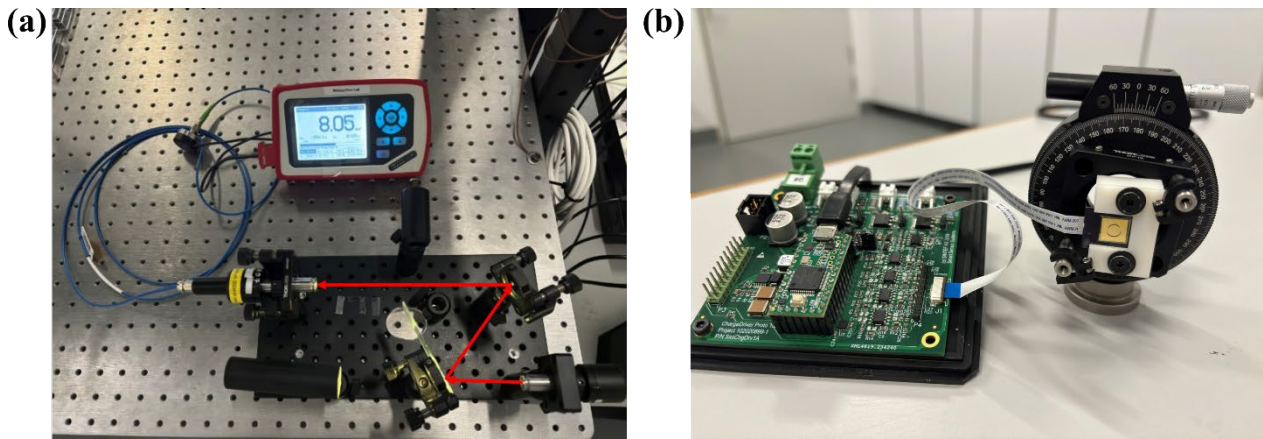
Figure 4.9 Photographs of the measurement setup for MEMS-OMS sample characterization. (a) Coupling setup for supercontinuum laser incident. (b) Photographs of a sample holder with MEMS-OMS sample, connecting to a circuit board for voltage controlling.

After replacing the supercontinuum laser and spectrometer with cw Ti:sapphire laser and CMOS camera [83], respectively, a pronounced contrast can be observed between the mirror and polarizer states for |y> incidence in both the direct and Fourier image planes when the MEMS mirror was actuated with a periodic rectangular signal (Figure 4.10(c-d)) at the wavelength of $\lambda = 830.2$ nm. In contrast to R_{yy}, the contrast for R_{xx} was consistently uniform. Similar modulation dynamics can be observed for the larger split wavelength at 891.73 nm (Supplement Fig. S11 of **Appendix E**). By replacing the CMOS camera with a photodetector (PD, PDA20CS-EC, Thorlabs) [82], we observed moderately fast switching using an oscilloscope (DSOX2024A, Keysight), with rise and fall times of approximately 2.27 ms and 1.68 ms, respectively (Figure 4.10(d)). Further optimization of the MEMS mirrors could reduce these times even more. This section is based on my previous publications **Appendix E-F** [82-83], and incorporates some texts from that two works.

Figure 4.10 Experimental results of the MEMS-OMS DLP sample. (a) Measured polarization-resolved reflectivities as a function of the applied voltage V_m (air gap T_a) and the wavelength λ. The black dashed lines mark the wavelengths of $\lambda = 830.2$ nm and 891.73 nm. (b)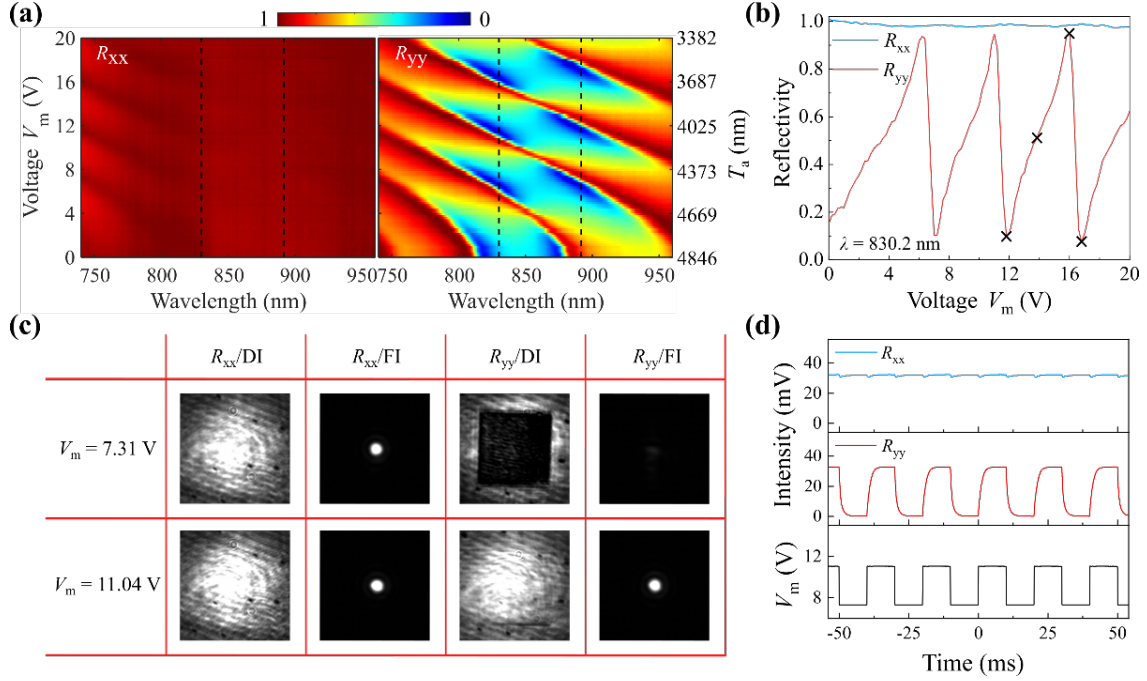 Measured reflectivities as a function of V_m at a fixed wavelength of $\lambda = 830.2$ nm for both $|x>$ and $|y>$ incidence. The black cross symbols mark the voltages of V_m = 11.8 V, 14.0V, 16.0 V, and 16.8 V, respectively. (c) Polarization-resolved direct and Fourier images (DI and FI) of the reflected light for the dynamic transition between polarizer-operation and mirror-operation states. (d) Temporal evolution of the reflected light for both $|x>$ and $|y>$ incidence by actuating the MEMS mirror with a periodic rectangular signal at the wavelength of $\lambda = 830.2$ nm [82]. Reprinted from Ref. [82].

4.2.4   Applications based on DLPs

This section is based on my previous publication **Appendix E** [82], and incorporates some texts from that work. Due to the polarization-selective reconfigurability, our DLP inherently provides the capability for encoding voltage-controlled grayscale imaging, making it a promising solution for anticounterfeiting applications [107-110]. As shown in Figure 4.11, we designed and experimentally demonstrated a dynamic voltage-controlled grayscale imaging based on the MEMS-OMS DLP, and more detailed description can be seen in **Appendix E**. Moreover, leveraging the DLP unit cell and Malus's law, dynamic grayscale imaging with continuous intensity modulation has also been implemented, which can be seen in Supplement 1 Fig. S12 of **Appendix E**.
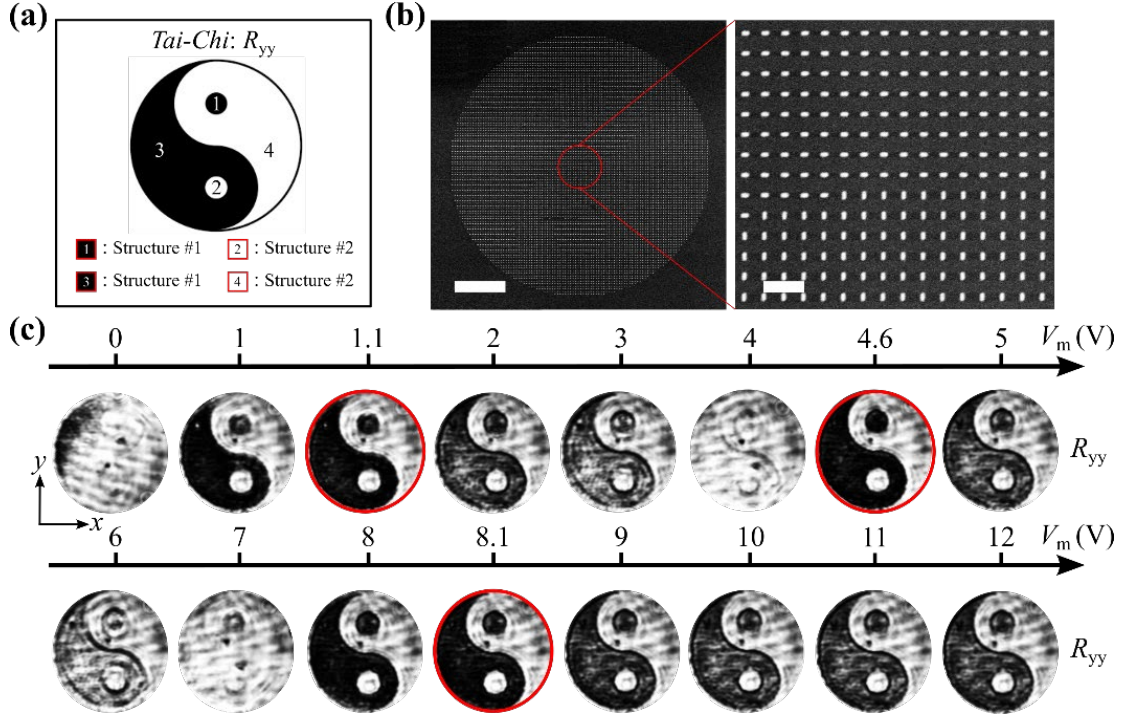
Figure 4.11 MEMS-OMS-based DLP for voltage-controlled grayscale imaging. (a) Design schematic of the voltage-controlled anticounterfeiting grayscale imaging with a *Tai-Chi* pattern. (b) SEM images of the fabricated OMS (scale bars are 10 μm and 1 μm, respectively). (c) Measured intensity profiles of the reflected beams as a function of the applied voltage in the co-polarized channel for $|y>$ incidence [82]. Reprinted from Ref. [82].

By employing spatially oriented DLP unit cells, we have also created a tunable VVB generator, which can transform an incident CP beam into either a reflective CP beam (mirror-operation state) or a cylindrical VVB (polarizer-operation state) that possesses spatially inhomogeneous polarization distributions and carries OAM [97, 111-114], depending on the applied voltage. For example, we can generate AP vortex beams with a topological charge of $l = 1$ by locally rotating each DLP nano-brick with an angle of $\theta_{AP} = \arctan(y/x) + \pi/2$, and actuating the MEMS mirror to the polarizer-operation state with a voltage of V_{AP} (e.g., $V_{AP} = 10.4$ and 16.9 V) at wavelength of $\lambda = 830.2$ nm, where the local coordinates of each element are represented by x and y (Figure 4.12(a-b)). When the MEMS mirror is set to its mirror-operation state (e.g., $V_{mirror} = 14$ and 20 V), it can reflect all incoming light to produce a CP beam, analogous to an information encryption process. As illustrated in Figure 4.12(c-d), the VVB intensity profile appears periodically when actuated voltages are applied at wavelength of $\lambda = 830.2$ nm for LCP incidence. Furthermore, the intensity profile transitions into an "s" shape and rotates in correspondence with the axis of the polarizer placed in front of the CMOS camera, thereby demonstrating the generation of an AP beam. By decomposing the total VVB into the CP basis and performing interference experiments, we confirmed the topological charges of $l = 0$ in the co-polarized CP channel and $l = 2$ in the cross-polarized CP channel. Detailed theoretical derivation and measurements can be seen in Supplement 1 Section 10 and 11 of **Appendix E**. As the applied voltage gradually deviates from V_{AP}, the generated AP vortex beam will progressively diminish and transition into a reflected CP beam. Similarly, RP vortex beams have been also experimentally demonstrated by rotating each DLP nano-brick with an angle of $\theta_{RP} = \arctan(y/x)$, as illustrated in Supplement 1 Section 12 of **Appendix E**. The experimental measurements indicate that the efficiencies of the generated AP and RP vortex beams are approximately 38.38% and 37.29%, respectively, which are slightly below the theoretical maximum of 50%.
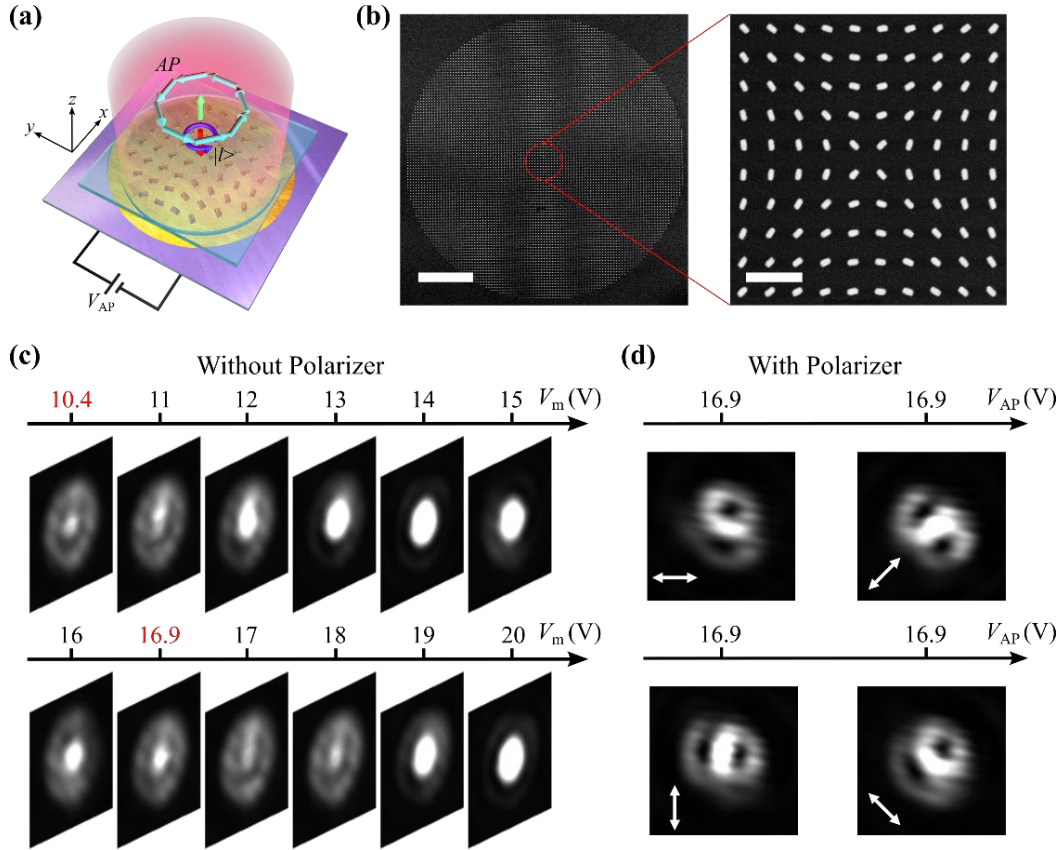
Figure 4.12 MEMS-OMS DLP for voltage-controlled AP vortex generation. (a) Schematic rendering of the AP vortex beam generation under LCP incidence with an actuation voltage of V_{AP}. (b) SEM images of the fabricated OMS (scale bars are 10 μm and 1 μm, respectively). (c) Measured intensity profiles of the reflected beams as a function of the applied voltage for LCP incidence. (d) Polarization-resolved intensity profiles of the reflected beams with an applied voltage of V_{AP} = 16.9 V for LCP incidence [82]. Reprinted from Ref. [82].

4.3　Non-Hermitian MEMS-OMSs for tunable topological phase transition

This section is based on my previous publication **Appendix F** [83], and incorporates some texts from that work.

4.3.1　Research background

In the realm of photonics, the exploration of exceptional points (EPs) has emerged as a fascinating avenue of research promising to reshape the landscape of light-matter interactions and optical manipulation [83, 115-119]. Rooted within the intricacies of non-Hermitian systems [120-121], EPs signify a unique configuration where distinct eigenvalues and eigenstates simultaneously coalesce, resulting in complex optical responses and enabling novel functionalities, including unidirectional transmission/reflection [122-123], exceptional sensing [124-125], asymmetric mode switching [126-128], and topological phase engineering [129]. Capitalizing on the potential of OMS platforms to achieve adaptive and precisely controlled optical functionalities, recent EP research has shifted its focus to non-Hermitian metasurfaces [83, 125, 129-134]. For example, Song's research group designed a MIM plasmonic chiral meta-atom (left panel of Figure 4.13(a)), by scanning the parameter space defined by L_1 and L_3 of the top structure to engineer non-Hermitian Jones matrices, they observed a distinct EP at the wavelength of 600 nm, characterized by the simultaneous degeneracy of eigenvalues and eigenvectors (middle panel of Figure 4.13(a)) [129]. Meanwhile, a topologically

protected full 2π-phase can be achieved in one of the polarization-dependent reflected channels by leveraging the topological characteristics of non-Hermitian Jones matrices near their EPs. Building on this foundation, the LCP and RCP channels can be decoupled due to the introduced extra PB phase, resulting in two distinct and independently controlled holographic projections (right panel of Figure 4.13(a)). In addition, Park et al. demonstrated a bilayer plasmonic symmetry-broken structure (Figure 4.13(b)), by scanning the parameters P_y and d_x of the structure to modulate the coupling between the resonator arrays, identifying a plasmonic EP where resonances and loss rates simultaneously become degenerate [125]. However, both of the aforementioned methods for exploring EPs rely on passive metasurfaces, which means that observing EPs requires fabricating a large number of samples with different geometrical parameters, inadvertently increasing fabrication errors. In addition, this method faces serious challenges in precisely attaining an EP, as unavoidable fabrication and measurement errors are amplified in the EP vicinity [83].
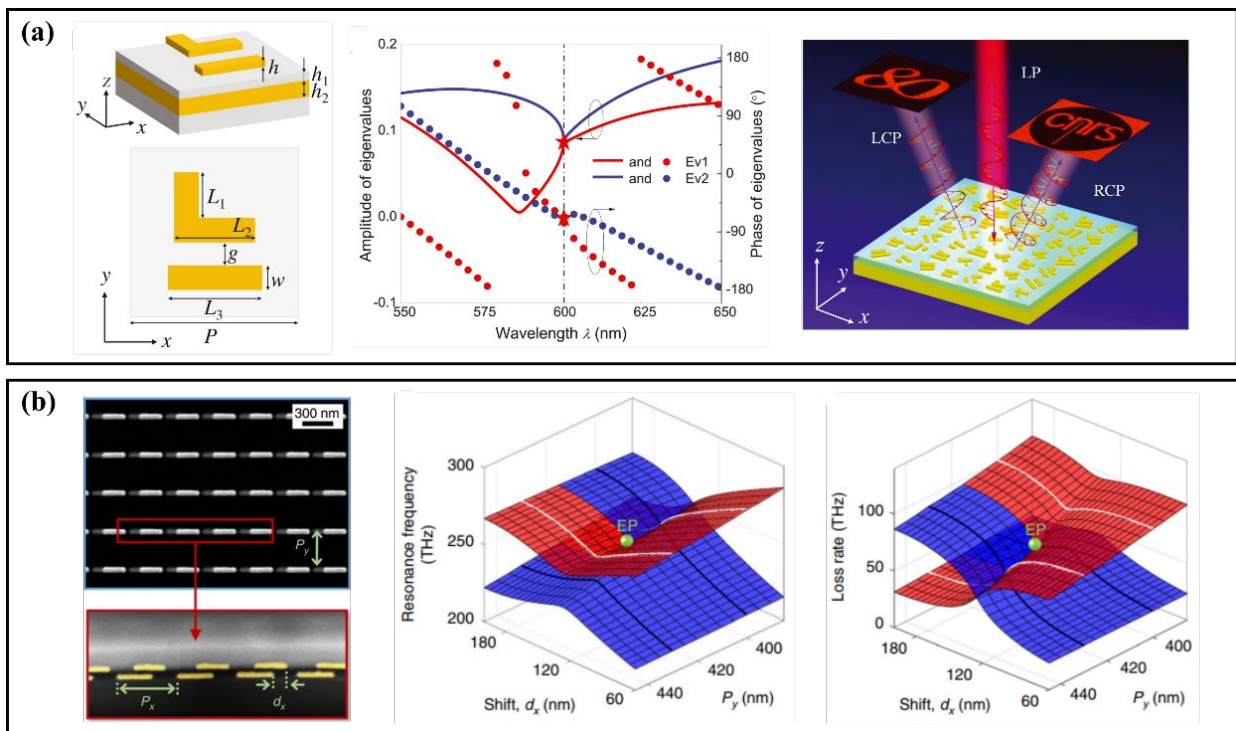
Figure 4.13 Passive Non-Hermitian metasurfaces for attaining an EP. (a) Left panel: schematic and top view of the 2D chiral unit cell forming a reflective Non-Hermitian metasurface. Middle panel: simulated amplitudes and phases of two eigenvalues as a function of wavelengths. Right panel: schematic illustrating the integrated design combining both exceptional topological (ET) phase and PB phase into a single metasurface, enabling independent manipulation of LCP and RCP channels under the incident LP light. Reprinted from Ref. [129]. (b) Left panel: the periodic plasmonic structure is shown from the top (*xy*-plane) and side (*xz*-plane) views, clearly revealing the distinct upper and lower metallic bars. Middle and right panels: the real and imaginary components of the eigenmodes (shown in red and blue) for hybridized plasmonic resonator arrays of uniform size, plotted as a function of d_x and P_y. Reprinted from Ref. [125].

In contrast, the emergence of dynamic, actively controlled metasurfaces indicates an alternative that would lead toward real-time control over the parameter space, facilitating the EP access and monitoring of the evolution of light-matter interactions near EPs within a single device [83]. For example, Ergoktas et al. experimentally demonstrated an active electrolyte-gated graphene device incorporating lactose microcrystals to dynamically explore EPs (Figure 4.14(a)) [135]. By simultaneously tuning the 2D parameter space governed by gate voltages V_1 and V_2, where V_1 adjusts

the loss imbalance by modifying the charge distribution within graphene, and V_2 tunes the detuning frequency by changing the cavity's geometry, an EP can appear once the coupling strengths completely compensate for the loss imbalance. In addition, Baek et al. proposed a non-Hermitian gated graphene metasurface to resolve chiral EPs by achieving degeneracy between the incident light frequency and the conductivity of a graphene microribbon array controlled by the gate voltage V_g (Figure 4.14(b)) [136]. While certain advances along this route have been demonstrated, the practical realization of actively controlled non-Hermitian metasurfaces remains confined to the terahertz domain [83]. The experimental observation of dynamically tuned EPs in the optical regime has thus far remained elusive, as the transition of EP metasurfaces from long-wavelength ranges (e.g., the terahertz range) to the optical range is nontrivial, involving not only scaling the dimensions down to a few hundred nanometers but also accounting for strongly dispersive optical constants, not to mention their dynamic tunability [83].
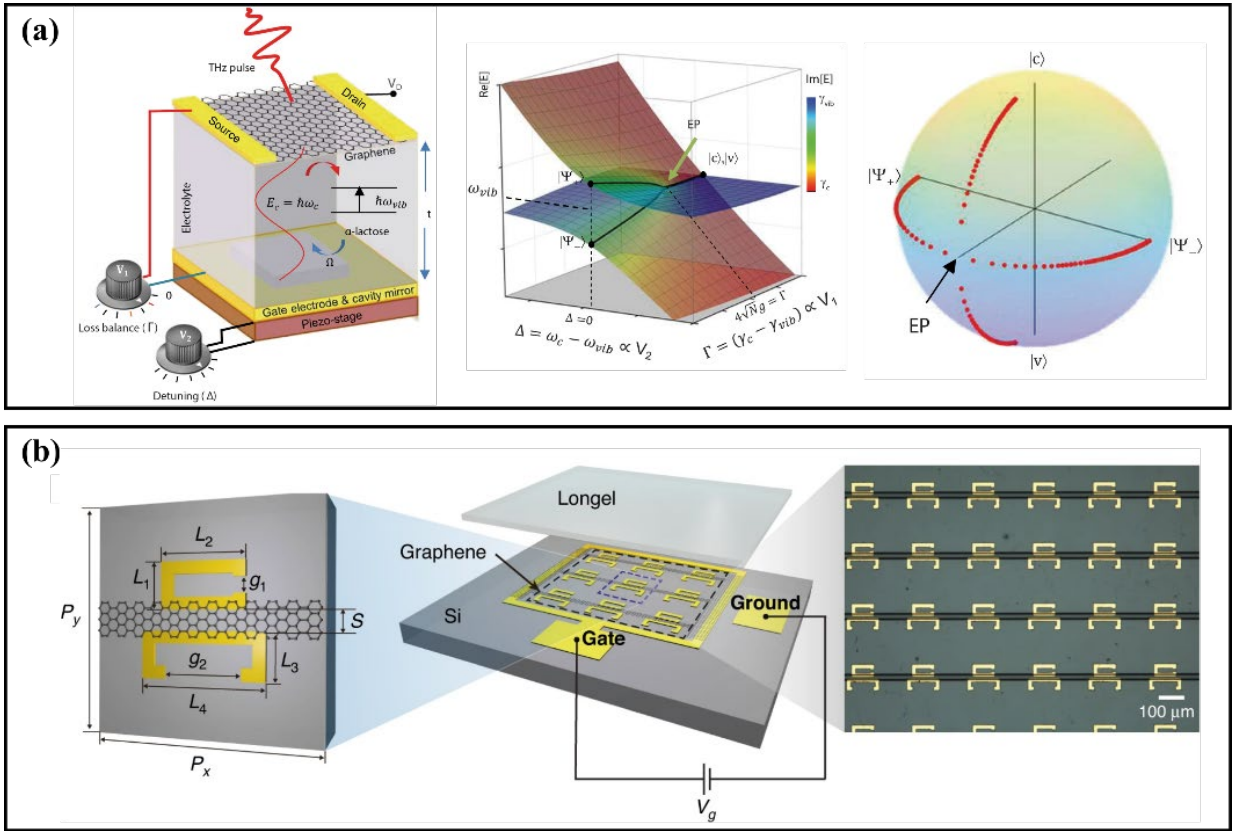
Figure 4.14 Active Non-Hermitian metasurfaces for attaining an EP. (a) Left panel: schematic of an active electrolyte-gated graphene device with a THz pulse to dynamically explore EPs. Middle panel: calculated Riemann surface to visualize the real and imaginary parts of eigenvalues influenced by V_1 and V_2. Right panel: depiction of the supermode evolution within the device, mapped onto a Bloch sphere, showing how it changes with adjustments to the gate voltage V_1 and the loss imbalance G. Reprinted from Ref. [135]. (b) Schematic and microscopic image of the non-Hermitian gated graphene metasurface. Reprinted from Ref. [136].

4.3.2 Design and simulation

This section is based on my previous publication **Appendix F** [83], and incorporates pieces of text from that work. Building on the detailed development of our piezoelectric MEMS-OMS platform, we present an in-depth dynamic investigation of optical EPs utilizing a fully electrically tunable non-Hermitian metasurface, as seen in Figure 4.15(a). By meticulously optimizing the dimensions of the

2D symmetry-broken gold chiral unit cell (Figure 4.15(b)) and concurrently adjusting the air gap, we can effectively engineer non-Hermitian Jones matrices within a 2D parameter space defined by the wavelength λ and air gap T_a, thereby allowing us to precisely locate the EP by determining whether the calculated eigenvalues and eigenvectors are simultaneously degenerate. The mirror-operation state here is represented by the diabolic point (DP), which is characterized by degenerate eigenvalues but orthogonal eigenstates. As a result, by precisely adjusting the cavity length of our optimized MEMS-based non-Hermitian metasurface using a movable MEMS mirror, we can achieve fine control over the resonant wavelength, thus enabling modulation of the coupling strength between the plasmonic and FP resonances. Simultaneously, this dynamic non-Hermitian metasurface facilitates precise control over the far-field radiation rate, effectively modulating radiation loss. Leveraging the synergistic interaction between the chiral metasurface and the MEMS mirror via a voltage-controlled air gap, we can induce a topological phase transition between EPs and DPs.
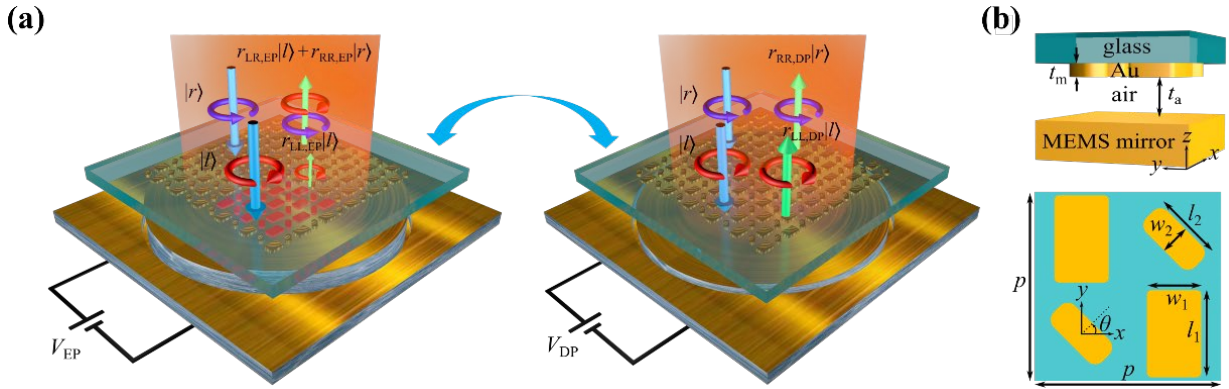

Figure 4.15 (a) Schematic illustration of the tunable non-Hermitian metasurface consisting of a chiral gold meta-atom array and a MEMS gold mirror with a voltage-controlled air gap, enabling the reconfiguration of the topological transition between a chiral EP and a DP. (b) Schematic illustration of a chiral unit cell [83]. Reprinted from Ref. [83].

The non-Hermitian Jones matrix used to describe the effective Hamiltonian of our designed dynamic metasurface can be expressed as follows:

$$\hat{r}(\Omega) = \begin{pmatrix} r_{LL}(\Omega) & r_{LR}(\Omega) \\ r_{RL}(\Omega) & r_{RR}(\Omega) \end{pmatrix} \qquad 4.42$$

where r_{ij} is the complex reflection coefficient from incident j-polarized light to reflected i-polarized light in the CP base with the subscript L and R representing the respective LCP and RCP light, and $\Omega = [l_1, w_1, l_2, w_2, t_a(V_m), \lambda]$ is the system parameter space shown in Figure 4.15(b). It is important to note that the alteration in propagation direction has not been accounted for in the assessment of the reflected light's chirality. Considering the inherent reciprocity and anisotropy of the chiral unit-cell, $r_{LL}(\Omega) = r_{RR}(\Omega)$ and $r_{LR}(\Omega) \neq r_{RL}(\Omega)$ will always be satisfied during the system modulation. Therefore, the two eigenvalues $\lambda_\pm$ of the non-Hermitian Jones matrix can be calculated as:

$$\sigma_{1,2} = r_{LL} \pm \sqrt{r_{LR} r_{RL}} \qquad 4.43$$

It is evident that the two eigenvalues will be identical only when either r_{LR} or r_{RL} is completely suppressed. By meticulously optimizing the dimensions of the chiral meta-atoms and adjusting the air gap with a proper actuation voltage V_{EP}, a EP can be observed in the parameter space of $\Omega_{EP} = $ [231.15 nm, 145.7 nm, 183.5 nm, 81.55 nm, 430.9 nm, 811.622 nm] (Figure 4.16(a)) with the simultaneous degeneracy of both eigenvalues and eigenstates (Figure 4.16(b)), signifying the

63

existence of a chiral EP, where an LCP state $|L\rangle$ emerges as the only eigenstate as a result of eigenvalue coalescence (Figure 4.16(c)). This degeneracy is further confirmed by the self-intersecting Riemann surfaces of the reflection matrix eigenvalues within the geometric parameter space (Fig. S2 and S3 of **Appendix F**). At the chiral EP, the reflection matrix is given by $\hat{r}(\Omega_{EP}) = \begin{pmatrix} r_{LL,EP} & r_{LR,EP} \\ 0 & r_{LL,EP} \end{pmatrix}$, where the two eigenvalues coalesce into $\sigma_{1,2} = r_{LL,EP}$, resulting in the singular behaviour from the non-Hermitian metasurfaces in the reflection of light. Specifically, under LCP excitation ($|E_i\rangle = |l\rangle$), the polarization conversion to orthogonal RCP is effectively suppressed and the incident LCP light is reflected into the co-polarized channel ($|E_o\rangle = r_{LL,EP}|l\rangle$) at the wavelength of 811.622 nm. Conversely, under RCP excitation ($|E_i\rangle = |r\rangle$), the reflected light contains both LCP and RCP components, expressed as $|E_o\rangle = r_{LR,EP}|l\rangle + r_{RR,EP}|r\rangle$. In a specific scenario where the incident polarization state is $|E_i\rangle = |l\rangle - \frac{r_{LL,EP}}{r_{LR,EP}}|r\rangle$, the reflected two LCP components interfere destructively, leading to the complete conversion of the incident light to the RCP state ($|E_o\rangle = -\frac{r_{LL,EP}^2}{r_{LR,EP}}|r\rangle$). The resulting RCP state is orthogonal to the degenerate polarization eigenstate $|l\rangle$, highlighting the reduced dimensionality of the polarization eigenspace at the chiral EP singularity. When the co-polarized components are forbidden, with $r_{LL,EP}$ approaching 0, the non-Hermitian metasurface effectively becomes a perfect absorber for LCP incident light. Simultaneously, it reflects RCP incident light into its cross-polarized state, resulting in pronounced CD.

Figure 4.16 (a-c) Simulated coefficients (a), eigenvalues (b) and eigenstates (c) of the reflection matrix as a function of wavelengths at the air gap of t_a = 430.9 nm. The eigenvalues and eigenstates degenerate simultaneously at λ = 811.622 nm, indicating the existence of a chiral EP, where $r_{RL} = 0$ and an LCP state $|l\rangle$ becomes the only eigenstate [83]. Reprinted from Ref. [83].

By varying the applied voltage V_m from V_{EP}, the FP cavity length and its resonance wavelength are precisely adjusted through the movement of the piezoelectric MEMS mirror relative to the chiral gold meta-atom array. This change shifts the non-Hermitian metasurface away from the chiral EP, thereby inducing a topological phase transition. Particularly, a DP (mirror-operation state) is achieved at the air gap of t_a = 357 nm, where the chiral meta-atoms are precisely positioned at the nodes of the standing wave within the non-Hermitian metasurface. At this point, cross-polarized reflections disappear (Figure 4.17(a)), eigenvalues coalesce (Figure 4.17(b)), and the associated eigenstates remain orthogonal (Figure 4.17(c)). Due to the imperfect conducting nature of the gold mirror, the DP exhibits complex eigenvalues, in contrast to the DP degeneracies in conservative Hermitian systems, which possess real eigenvalues. At the DP, the effective Hamiltonian changes to a diagonal reflection matrix $\hat{r}(\Omega_{DP}) = \begin{pmatrix} r_{LL,DP} & 0 \\ 0 & r_{LL,DP} \end{pmatrix}$ with eigenvalues coalescing into $\sigma_{1,2} = r_{LL,DP}$ and two polarization eigenstates being orthogonally aligned, thereby allowing simultaneous nulling of cross-polarized reflections under both LCP and RCP incidence (Figure 4.15(a) and Figure 4.17(a)).
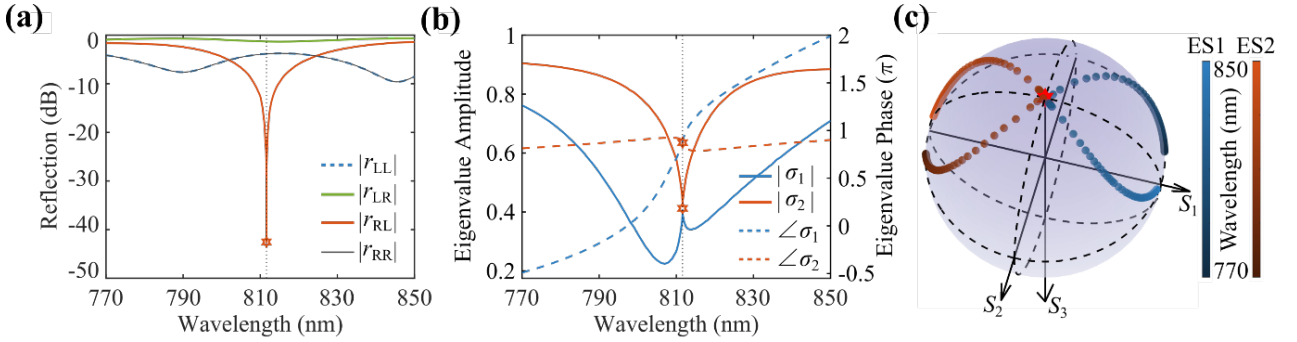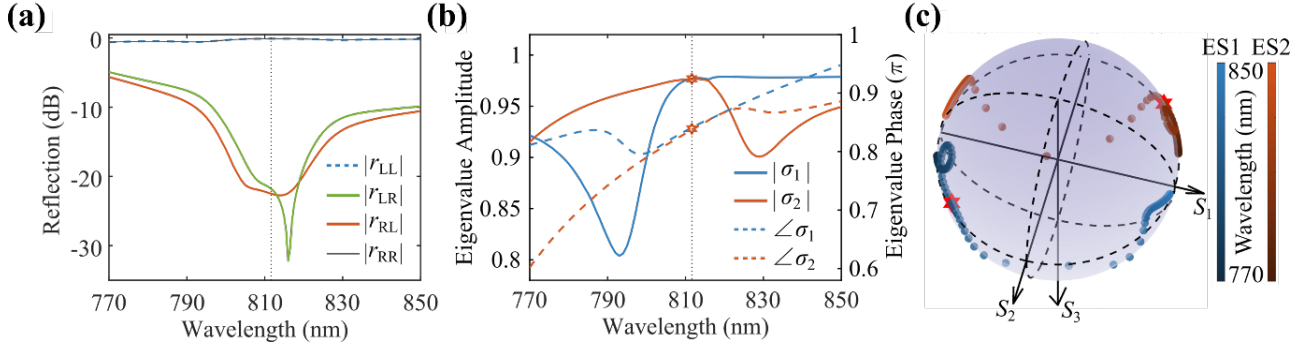
Figure 4.17 (a-c) Simulated coefficients (a), eigenvalues (b) and eigenstates (c) of the reflection matrix as a function of wavelengths at the air gap of $t_a = 357$ nm. The two eigenvalues degenerate, while the two eigenstates are nearly orthogonal at $\lambda = 811.622$ nm, confirming the presence of a DP [83]. Reprinted from Ref. [83].

4.3.3 Experimental results

This section is based on my previous publication **Appendix F** [83], and incorporates pieces of text from that work. The preparation of the non-Hermitian metasurface sample followed the same fabrication procedures and assembly techniques described above, with the only difference being the replacement of a MEMS mirror with a diameter of approximately 1 mm. The typical photo, optical microscopy images and the SEM image of the final assembled sample can be seen in Figure 4.18(a-c).

In this measurement, the MEMS mirror was driven with a smaller voltage step of 100 mV, corresponding to an average air gap adjustment of approximately 7.3 nm, allowing for finer construction of a 2D parameter space defined by wavelength λ (measurement precision is about 0.7 nm) and air gap t_a (V_m) to capture or approach the chiral EP. The movable range of the assembled sample was estimated to be approximately 868.6 nm when the MEMS mirror was moved far from the chiral meta-atom array by selectively actuating the four outer electrodes from 0 to 12 V. Conversely, when the mirror was moved closer to the array by actuating the four inner electrodes from 0 to 10 V, the range was approximately 730.1 nm (Figure S5 of **Appendix F**). This extensive range encompasses at least two adjacent FP resonances, providing sufficient scope for exploring the topological phase transition. By analysing the four measured polarization-dependent reflection maps as a function of λ and V_m (t_a) in the CP output channels (R_{LL}, R_{LR}, R_{RL} and R_{LR} in Figure S6-S7 of **Appendix F**), and combining them with eight polarization-dependent reflection maps in the LP output channels (R_{xL}, R_{yL}, R_{aL}, R_{bL}, R_{xR}, R_{yR}, R_{aR} and R_{bR}), the wavelength-resolved full Stokes parameters can be calculated, allowing for the determination of the non-Hermitian Jones matrix $\hat{r}$, which can be used to identify the EPs or DPs (Materials and Methods of **Appendix F**).

Take the outer electrodes as an example, when the voltage is driven to $V_m = 4.5$ V ($t_a \approx 2534.6$ nm), an anti-crossing of eigenvalue amplitudes and a crossing of eigenvalue phases are observed at the wavelength of 849.505 nm (Figure 4.18(d)). By varying the actuation voltage, the interaction between plasmonic and FP resonances is modulated, leading to a change in the crossing behavior of eigenvalue amplitudes and phases. Once the voltage is increased to 4.7 V ($t_a \approx 2546.8$ nm), a crossing of eigenvalue amplitudes and an anti-crossing of eigenvalue phases are observed at the same wavelength (Figure 4.18(e)). A chiral EP singularity unequivocally occurs at the wavelength of 849.505 nm when V_m is between 4.5 and 4.7 V (Figure 4.18(f)), where singularity points appear for R_{RL}. Despite deviations between the experimental and simulated results due to fabrication imperfections, these singularity points confirm the occurrence of the chiral EP. Due to the FP nature of the MEMS-based

non-Hermitian metasurface, the chiral EP singularity can be periodically observed at various air gaps (Figure S8 of **Appendix F**). As the voltage decreases from 4.7 V to 3.9 V, causing the air gap to reduce from 2546.8 nm to 2487.1 nm, the non-Hermitian metasurface transitions from an EP to a DP. This transition is marked by the crossing of eigenvalue amplitudes at the wavelength of 849.505 nm (Figure 4.18(g)). When the voltage is slightly increased to 4.0 V (($t_a \approx 2496.4$ nm)), the phases of the two eigenvalues approach a crossing state (Figure 4.18(h)). Unlike EPs which are extremely sensitive to small perturbations, non-Hermitian DPs are more robust, with their eigenvalues being only slightly affected by voltage changes. Meanwhile, simultaneous nulling of both cross-polarized reflections in the vicinity of the DP under RCP and LCP incidence is allowed (Figure 4.18(i)). It is worth noting that another pair of exceptional and diabolic points that enable the similar topological phase transition was observed in the $[t_a(V_m), \lambda]$ parameter space without repeated fabrication of several samples (Figs. S9 and S10 of **Appendix F**), which is ascribed to the tunability of our non-Hermitian MEMS metasurface.
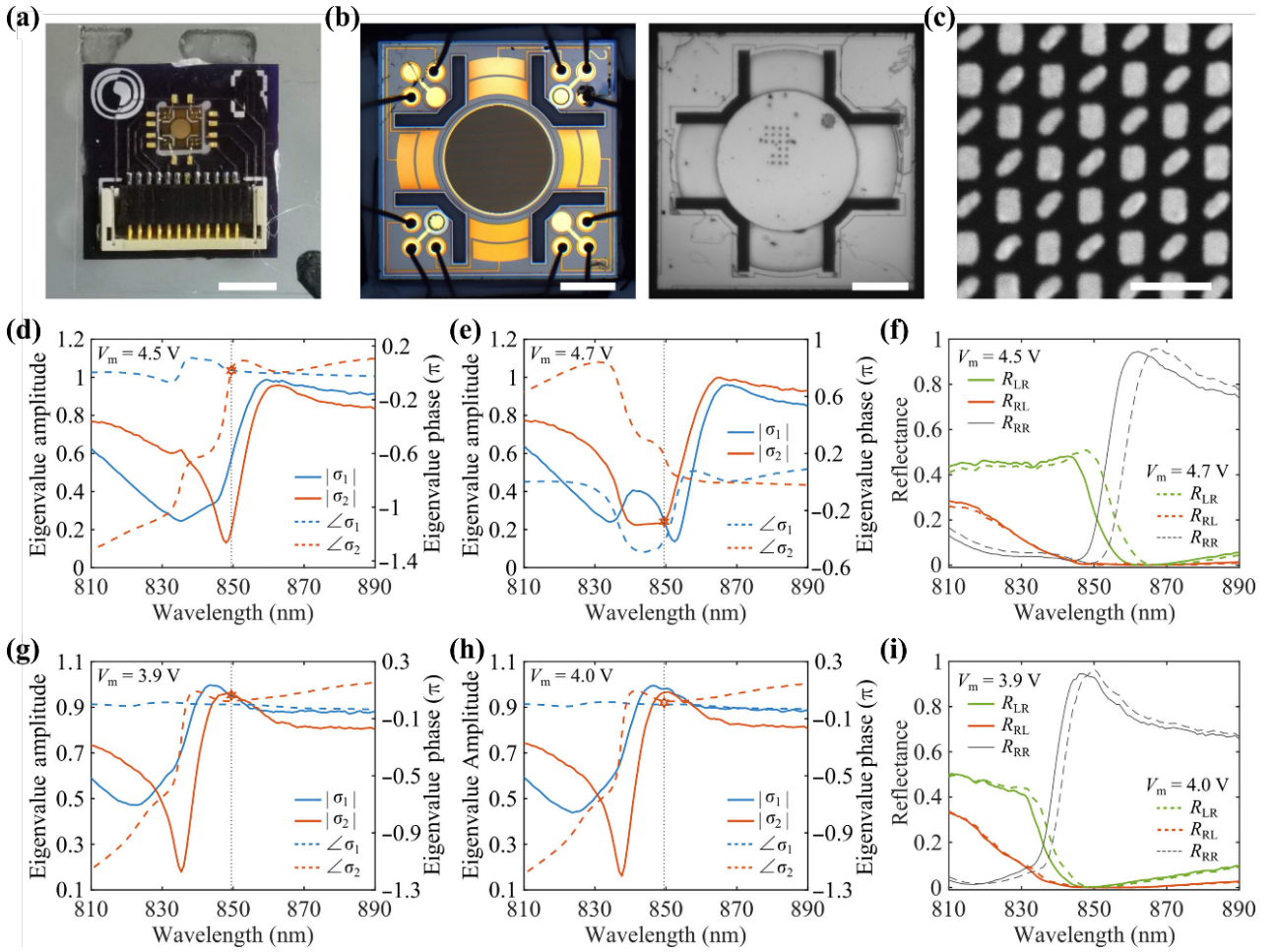
Figure 4.18 Experimental observation of the dynamic topological transition from an EP to a DP. (a to c) The typical photo (a), optical microscopy images (b), and scanning electron microscopy image (c) of the assembled non-Hermitian metasurface. Scale bars, 3 mm (a), 500 μm (b), and 500 nm (c). (d to f) Measured eigenvalues [(d) and (e)] and reflectance (f) as a function of wavelength at two different voltages of $V_m = 4.5$ and 4.7 V when driving four outer electrodes. Anti-crossing of eigenvalue amplitudes and crossing of eigenvalue phases are observed for $V_m = 4.5$ V, while crossing of eigenvalue amplitudes and anti-crossing of eigenvalue phases are observed for $V_m = 4.7$ V, revealing a chiral EP singularity at $\lambda = 849.505$ nm for V_m between 4.5 and 4.7 V. (g to i) Measured eigenvalues [(g) and (h)] and reflectance (i) as a function of wavelength at two different

voltages of V_m = 3.9 and 4.0 V when driving four outer electrodes. Crossing of eigenvalue amplitudes is observed for V_m = 3.9 V, indicating a DP at λ = 849.505 nm for V_m of ~3.9 V [83]. Reprinted from Ref. [83].

Beyond the dynamic non-Hermitian phase transition, we also examined the voltage-controlled polarization evolution as the air gap was continuously adjusted. For LCP incidence at λ = 849.505 nm, the cross-polarized reflection approaches zero regardless of the actuation voltage (Figure 4.19(a)). Upon switching the incident light to RCP, the output polarization state transforms into a superposition of co- and cross-polarized components, with their respective intensities being controlled by the applied voltage. Moreover, its corresponding polarization trajectory is one irregular closed curve on the Poincaré sphere, passing through two pivotal polarization states of $|l\rangle$ and $|r\rangle$ when the non-Hermitian metasurface hits the exceptional and diabolic points, and circulating repeatedly with the voltage (Figure 4.19(b)). In quantitative terms, DoCPs reach approximately −0.96 at EPs and 0.99 at DPs, as indicated by the red and blue stars in Figure 4.19(b). At chiral EPs, asymmetric polarization conversion was achieved, yielding a CD of approximately 0.49. This outcome is due to the reduced dimensionality of the polarization eigenspace. In addition to CP waves, linearly polarized reflections of high purity (DoCP < 0.02) were also achieved, as indicated by the black stars in Figure 4.19(b). The minimum voltage required to electrically switch the reflected light between the $|l\rangle$ and $|r\rangle$ states has decreased significantly to just 0.8 V, compared to the previously required 4.7 V. This reduction in voltage, which is approximately 34.5 times smaller, indicates a substantial decrease in switching power. Given that the MEMS arrangements used in both experiments are identical, this notable achievement is attributed to operating near the EP-DP transition. As anticipated, a comparable polarization evolution occurs when the four inner electrodes are activated to reduce the air gap (Figure S11 of **Appendix F**). To measure the non-Hermitian phase transition speed from an EP to a DP, we actuated the MEMS mirror with a periodic rectangular signal composed of alternating voltages marked in Figure 4.19(a) and detected polarization-resolved reflections with a fast PD. We observed high contrast between orthogonal polarization states (Figure 4.19(c)), good endurance (Figure 4.19(d), and movies S1 and S2 of **Appendix F**), and relatively fast switching with rise/fall times of ~0.30/0.25 ms (Figure 4.19(d)). Because response times are generally dependent on the properties of MEMS mirrors, one could expect faster switching even in the megahertz range via further optimization, which, however, is beyond the scope of our work.
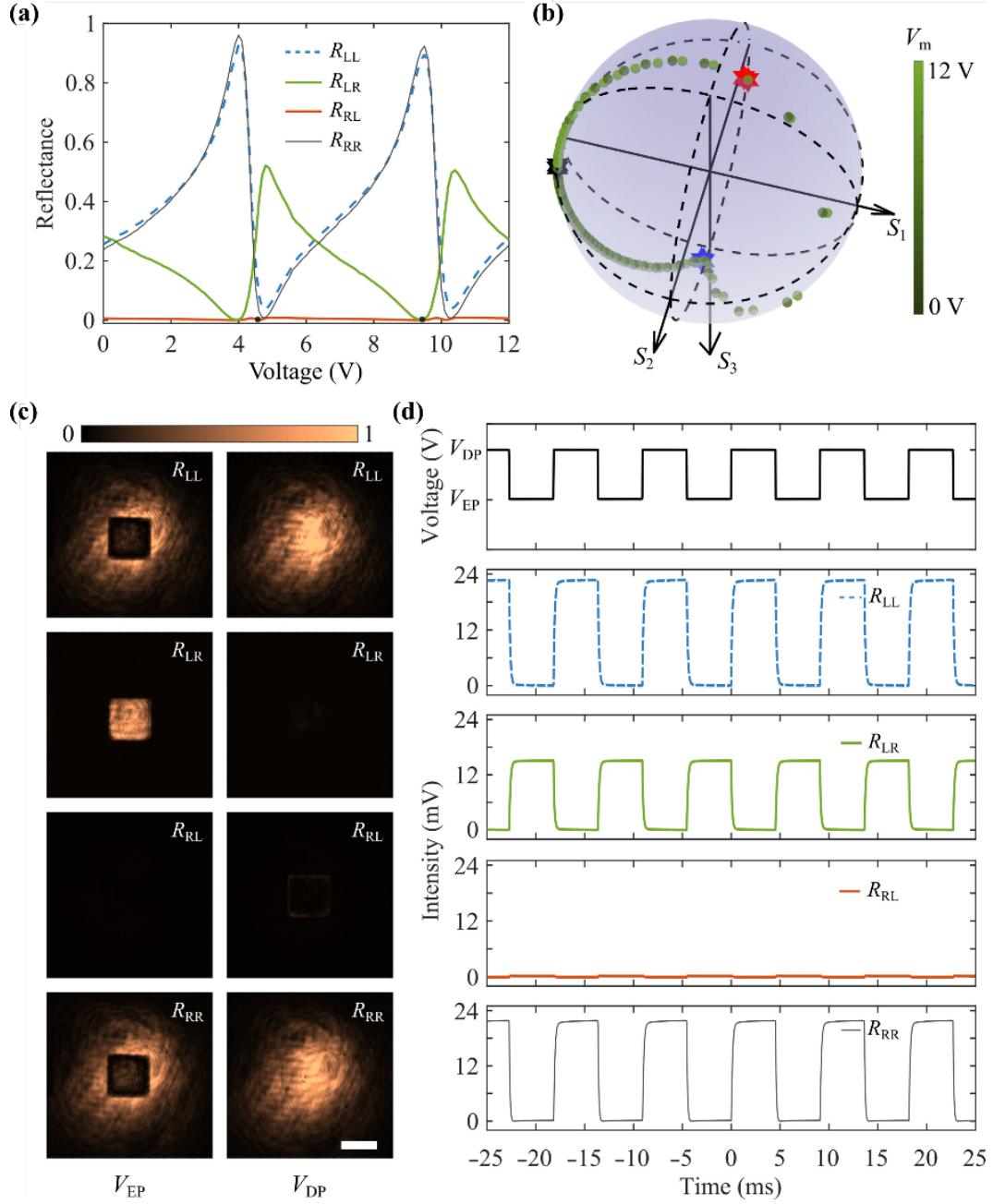
Figure 4.19 Voltage-controlled polarization evolution. (a) Measured reflectance as a function of the applied voltage. (b) Voltage-controlled polarization trajectory mapped on the Poincaré sphere for RCP incidence. (c) Polarization-resolved optical images of the reflected light for the EP and DP transition. The scale bar is 25 μm. (d) Temporal evolution of the reflected power for the topological EP-DP transition by actuating the non-Hermitian metasurface with a periodic rectangular voltage. The rise/fall times of the R_{LL}, R_{LR}, and R_{RR} channels are 260/250 μs, 290/220 μs, and 260/160 μs, respectively. The wavelength is fixed at λ = 849.505 nm and the four outer electrodes are actuated during the measurement [83]. Reprinted from Ref. [83].

5   Summary and Outlook

During my PhD research, I conducted an extensive investigation and achieved experimental validation of passive wavefront shaping using optical GSP metasurfaces, as well as active wavefront shaping utilizing piezoelectric MEMS-based optical metasurfaces. In *Chapter 1*, we present a concise review of current seminal examples of wavefront shaping using plasmonic optical metasurfaces, encompassing passive control methods in optical waveplates, beam steering, and metalenses, alongside several prevalent active control techniques, supplemented by **Appendix A**. *Chapters 2* provides the key theoretical concepts and primary analytical methods employed in this thesis, including the basic principles of polarization states and their common mathematical expressions, three common phase control methods (**Appendix A**), the numerical simulation method, the detailed sample fabrication process, along with the characterization setup and measurement methods. *Chapter 3* details the theoretical design and experimental validation of a GSP metasurface waveplate capable of dual-functional polarization conversion under orthogonal LP excitations at a wavelength of 850 nm (**Appendix B**). Utilizing our developed library of cross-shaped GSP nano-QWPs in the near-infrared range, we extend the spin-decoupled applications of GSP multifunctional metasurfaces to advanced beam steering (**Appendix C**) and metalens technologies (**Appendix D**). *Chapter 4* begins with an exploration of PZT piezoelectric thin-film material, laying the groundwork for an in-depth analysis of the operational mechanisms of our newly developed MEMS-OMS dynamic control platform. We then introduce the MEMS-OMS-based DLP, providing a comprehensive overview of its design, simulation, sample preparation, and characterization. And two significant applications derived from this technology (**Appendix E**) are then explored. Finally, we propose non-Hermitian MEMS-OMSs for tunable topological phase transitions and provide a detailed design and experimental validation (**Appendix F**). Following the summary, I will offer my insights on several promising future research directions:

(1) As we mentioned in the section '*Conclusions and perspectives*' of **Appendix A**, in the important subfield of controlling the polarization state of optical fields, three promising and innovative research directions will be given special consideration, including 'structured light beyond 2D', 'spatiotemporal meta-waveplates' and 'on-waveguide meta-waveplates'.

(2) Ultra-sensitive real-time nanoscale biomedical sensing based on active non-Hermitian systems. **Appendix F** details the rapid switching between EP and DP operating modes enabled by electrically tunable non-Hermitian optical MEMS metasurfaces. Inspired by Ref. [125], we propose utilizing electrically tunable non-Hermitian metasurface systems for ultra-sensitive real-time nanoscale biomedical sensing, irrespective of the sample solution concentration being dilute or dense. Furthermore, future dynamic control methods will not be confined to MEMS; materials such as LCs or graphene will also be explored to enhance the adsorption of sample solutions. We envision that this approach to real-time dynamic control using non-Hermitian metasurface systems will find practical application.

(3) Artificial intelligence (AI)-empowered advanced metasurface research. Each research project (**Appendices B-F**) in this thesis utilized complex COMSOL parameter scanning calculations to determine the dimensions of the nanostructure units. We need to develop more efficient metasurface design strategies that fully optimize computational resource utilization. Over the past few decades, AI has swiftly established itself as a transformative computational tool within the physical sciences, playing a crucial role in driving forward research in metasurfaces [137-142]. Looking ahead, a key research direction will involve harnessing the robust capabilities of AI in metasurface design, building upon the established wavefront control techniques to enhance design efficiency.

(4) <u>Integration of metasurface structures on fiber end faces.</u> The integration of metasurface structures on optical fiber end faces holds significant promise for various applications [143-144]. In the field of optical communication, these structures enhance signal transmission efficiency, reduce losses, and significantly minimize the physical dimensions of the system, resulting in lower power consumption and improved stability. In sensing applications, micro-nanostructures can improve sensitivity and specificity for detecting environmental changes, biological markers, and chemical substances. Furthermore, in medical diagnostics, they can enable more precise and minimally invasive procedures. Integrating these advanced structures has the potential to create compact, efficient, and high-performance optical devices, with applications spanning numerous industrial and scientific domains. Additionally, we plan to leverage mature focused ion beam (FIB) technology to further expand the design and application of microstructures on optical fiber end faces.

(5) <u>Metasurface waveplate-empowered metalens spectrometer.</u> By precisely engineering metasurfaces, light of different wavelengths can be focused onto distinct locations on the focal plane, facilitating wavelength demultiplexing and the development of compact micro-spectrometers [145-147]. The flexible design of metasurfaces also allows for the integration of polarization detection capabilities, facilitating the simultaneous demodulation of both wavelength and polarization characteristics. Traditionally, systems designed for spectral demodulation and polarization detection are large, complex in structure, consume high power, and lack sufficient stability. However, the inherent design flexibility and miniaturization potential of metasurfaces enable multiple functionalities to be achieved on a single metasurface. This makes our proposed solution highly attractive and promising for applications in various fields, including fundamental scientific research and materials science.

6   References

1. H.-T. Chen, A. J. Taylor, and N. Yu, "A review of metasurfaces: physics and applications," *Rep. Prog. Phys.* **79**(7), 076401 (2016).
2. Q. He, S. Sun, S. Xiao, *et al*., "High-Efficiency metasurfaces: principles, realizations, and applications," *Adv. Opt. Mater.* **6**(19), 1800415 (2018).
3. F. Ding, A. Pors, and S. I. Bozhevolnyi, "Gradient metasurfaces: a review of fundamentals and applications," *Rep. Prog. Phys.* **81**, 026401 (2018).
4. S. Yan, X. Zhu, J. Dong, *et al*., "2D materials integrated with metallic nanostructures: fundamentals and optoelectronic applications," *Nanophotonics* **9**, 1877-1900 (2020).
5. W. T. Chen, A. Y. Zhu, and F. Capasso, "Flat optics with dispersion-engineered metasurfaces," *Nat. Rev. Mater.* **5**(8), 604-620 (2020).
6. S. Chen, W. Liu, Z. Li, *et al*., "Metasurface-Empowered optical multiplexing and multifunction," *Adv. Mater.* **32**(3), 1805912 (2020).
7. Y. Guo, M. Pu, F. Zhang, *et al*., "Classical and generalized geometric phase in electromagnetic metasurfaces," *Photonics Insights* **1**(1), R03 (2022).
8. M. Pan, Y. Fu, M. Zheng, *et al*., "Dielectric metalens for miniaturized imaging systems: progress and challenges," *Light Sci Appl.* **11**, 195 (2022).
9. J. Yao, R. Lin, M. K. Chen, *et al*., "Integrated-resonant metadevices: a review," *Adv. Photon.* **5**(2), 024001 (2023).
10. S. A. Schulz, Rupert. F. Oulton, M. Kenney, *et al*., "Roadmap on photonic metasurfaces," *Appl. Phys. Lett.* **124**, 260701 (2024).
11. A. I. Kuznetsov, M. L. Brongersma, J. Yao, *et al*., "Roadmap for optical metasurfaces," *ACS Photonics* **11**, 816–865 (2024).
12. A. Pors, M. G. Nielsen, G. D. Valle, *et al*., "Plasmonic metamaterial wave retarders in reflection by orthogonally oriented detuned electrical dipoles," *Opt. Lett.* **36**, 1626 (2011).
13. Y. Zhao and A. Alù, "Manipulating light polarization with ultrathin plasmonic metasurfaces," *Phys. Rev. B* **84**, 205428 (2011).
14. S.-C. Jiang, X. Xiong, Y.-S. Hu, *et al*., "Controlling the polarization state of light with a dispersion-free metastructure," *Phys. Rev. X* **4**, 021026 (2014).
15. Z. Jiang, L. Lin, D. Ma, *et al*., "Broadband and wide field-of-view plasmonic metasurface-enabled waveplates," *Sci. Rep.* **4**, 7511 (2014).
16. N. Yu, F. Aieta, P. Genevet, *et al*., "A broadband, background-free quarter-wave plate based on plasmonic metasurfaces," *Nano Lett.* **12**, 6328–6333 (2012).
17. F. Ding, Z. Wang, S. He, *et al*., "Broadband high-efficiency half-wave plate: a supercell-based plasmonic metasurface approach," *ACS Nano* **9**, 4111–4119 (2015).
18. A. Pors, M. G. Nielsen, and S. I. Bozhevolnyi, "Plasmonic metagratings for simultaneous determination of Stokes parameters," *Optica* **2**, 716 (2015).
19. C. Meng, S. Tang, F. Ding, *et al*., "Optical gap-surface plasmon metasurfaces for spin-controlled surface plasmon excitation and anomalous beam steering," *ACS Photonics* **7**, 1849–1856 (2020).
20. A. Arbabi, Y. Horie, M. Bagheri, *et al*., "Dielectric metasurfaces for complete control of phase and polarization with subwavelength spatial resolution and high transmission," *Nature Nanotech.* **10**, 937–943 (2015).
21. M. Khorasaninejad, W. Chen, R. C. Devlin, *et al*., "Metalenses at visible wavelengths: Diffraction-limited focusing and subwavelength resolution imaging," *Science* **352**, 1190–1194 (2016).
22. S. Wang, P. C. Wu, V.-C. Su, *et al*., "Broadband achromatic optical metasurface devices," *Nat Commun.* **8**, 187 (2017).

23. E. Arbabi, S. M. Kamali, A. Arbabi, *et al.*, "Full-Stokes imaging polarimetry using dielectric metasurfaces," *ACS Photonics* **5**, 3132–3140 (2018).
24. F. Shi, J. Wen, and D. Lei, "High-efficiency, large-area lattice light-sheet generation by dielectric metasurfaces," *Nanophotonics* **9**, 4043–4051 (2020).
25. L. Li, Z. Liu, X. Ren, *et al.*, "Metalens-array–based high-dimensional and multiphoton quantum source," *Science* **368**, 1487–1490 (2020).
26. D. Sang, M. Xu, M. Pu, *et al.*, "Toward high-efficiency ultrahigh numerical aperture freeform metalens: from vector diffraction theory to topology optimization," *Laser Photonics Rev.* **16**, 2200265 (2022).
27. G. Zheng, H. Mühlenbernd, M. Kenney, *et al.*, "Metasurface holograms reaching 80% efficiency," *Nature Nanotech.* **10**, 308–312 (2015).
28. L. Huang, S. Zhang, and T. Zentgraf, "Metasurface holography: from fundamentals to applications," *Nanophotonics* **7**, 1169–1190 (2018)
29. R. Zhao, B. Sain, Q. Wei, *et al.*, "Multichannel vectorial holographic display and encryption," *Light Sci Appl.* **7**, 95 (2018).
30. C. Zhang, S. Divitt, Q. Fan, *et al.*, "Low-loss metasurface optics down to the deep ultraviolet region," *Light Sci. Appl.* **9**, 55 (2020).
31. Z. Li, C. Chen, Z. Guan, *et al.*, "Three-Channel metasurfaces for simultaneous meta-holography and meta-nanoprinting: a single-cell design approach," *Laser Photonics Rev.* **14**, 2000032 (2022).
32. F. Ding, Y. Chen, and S. Bozhevolnyi, "Metasurface-Based polarimeters," *Applied Sciences* **8**, 594 (2018).
33. M. Wuttig, H. Bhaskaran, and T. Taubner, "Phase-change materials for non-volatile photonic applications," *Nat. Photonics* **11**(8), 465-476 (2017).
34. Q. He, S. Sun, and L. Zhou, "Tunable/reconfigurable metasurfaces: physics and applications," *Research* **2019**, 1849272 (2019).
35. A. M. Shaltout, V. M. Shalaev, and M. L. Brongersma, "Spatiotemporal light control with active metasurfaces," *Science* **364**, eaat3100 (2019).
36. F. Ding, Y. Yang, and S. I. Bozhevolnyi, "Dynamic metasurfaces using phase-change chalcogenides," *Adv. Opt. Mater.* **7**(14), 1801709 (2021).
37. E. Mikheeva, C. Kyrou, F. Bentata, *et al.*, "Space and time modulations of light with metasurfaces: recent progress and future prospects," *ACS Photonics* **9**(5), 1458–1482 (2022).
38. O. A. M. Abdelraouf, Z. Wang, H. Liu, *et al.*, "Recent advances in tunable metasurfaces: materials, design, and applications," *ACS Nano* **16**(9), 13339-13369 (2022).
39. C. H. Chu, M. L. Tseng, J. Chen, *et al.*, "Active dielectric metasurface based on phase-change medium," *Laser Photonics Rev.* **10**(6), 986–994 (2016).
40. S.-Q. Li, X. Xu, R. Maruthiyodan Veetil, *et al.*, "Phase-only transmissive spatial light modulator based on tunable dielectric metasurface," *Science* **364**(6445), 1087-1090 (2019).
41. P. C. Wu, R. A. Pala, G. Kafaie Shirmanesh, *et al.*, "Dynamic beam steering with all-dielectric electro-optic III–V multiple-quantum-well metasurfaces," *Nat. Commun.* **10**(1), 3654 (2019).
42. P. Yu, J. Li, and N. Liu, "Electrically tunable optical metasurfaces for dynamic polarization conversion," *Nano Lett.* **21**(15), 6690-6695 (2021).
43. L. Lu, Z. Dong, F. Tijiptoharsono, *et al.*, "Reversible tuning of Mie resonances in the visible spectrum," *ACS Nano* **15**(12), 19722–19732 (2021).
44. C. Zeng, H. Lu, D. Mao, *et al.*, "Graphene-empowered dynamic metasurfaces and metadevices," *Opto-Electron. Adv.* **5**, 200098 (2022).
45. P. Moitra, Y. Wang, X. Liang, *et al.*, "Programmable wavefront control in the visible spectrum using low-loss chalcogenide phase-change metasurfaces," *Adv. Mater.* **35**(34), 2205367 (2023).
46. K. Z. Kamali, L. Xu, N. Gagrani, *et al.*, "Electrically programmable solid-state metasurface via

flash localised heating," *Light Sci. Appl.* **12**(1), 40 (2023).

47. A. Tittl, A. U. Michel, M. Schäferling, *et al.*, "A switchable mid-infrared plasmonic perfect absorber with multispectral thermal imaging capability," *Adv. Mater.* **27**, 4597-4603 (2015).

48. S. Zhang, J. Zhou, Y.-S. Park, *et al.*, "Photoinduced handedness switching in terahertz chiral metamolecules," *Nat Commun*. **3**, 942 (2012).

49. X. Duan, S. Kamin, F. Sterl, *et al.*, "Hydrogen-Regulated chiral nanoplasmonics," *Nano Lett.* **16**, 1462–1466 (2016).

50. P. Yu, J. Li, and N. Liu, "Electrically tunable optical metasurfaces for dynamic polarization conversion," *Nano Lett.* **21**, 6690–6695 (2021).

51. C. Meng, P. C. V. Thrane, F. Ding, *et al.*, "Full-range birefringence control with piezoelectric MEMS-based metasurfaces," *Nat Commun.* **13**, 2071 (2022).

52. Y. Deng, Z. Cai, Y. Ding, *et al.*, "Recent progress in metasurface-enabled optical waveplates," *Nanophotonics* **11**, 2219–2244 (2022).

53. D. H. Goldstein, "Polarized Light, 3rd ed." CRC Press (2016).

54. F. Wang, A. Chakrabarty, F. Minkowski, *et al.*, "Polarization conversion with elliptical patch nanoantennas," *Appl. Phys. Lett.* **101**, 023101 (2012).

55. A. Roberts and L. Lin, "Plasmonic quarter-wave plate," *Opt. Lett.* **37**, 1820–1822 (2012).

56. J. J. Cadusch, T. D. James, and A. Roberts, "Experimental demonstration of a wave plate utilizing localized plasmonic resonances in nanoapertures," *Opt. Express* **21**, 28450 (2013).

57. A. Pors, M. G. Nielsen, and S. I. Bozhevolnyi, "Broadband plasmonic half-wave plates in reflection," *Opt. Express* **38**, 513–515 (2013).

58. A. Pors and S. I. Bozhevolnyi, "Efficient and broadband quarter-wave plates by gap-plasmon resonators," *Opt. Express* **21**, 2942–2952 (2013).

59. Y. Dai, W. Ren, H. Cai, *et al.*, "Realizing full visible spectrum metamaterial half-wave plates with patterned metal nanoarray/insulator/metal film structure," *Opt. Express* **22**, 7465 (2014).

60. Z. Li, W. Liu, H. Cheng, *et al.*, "Realizing broadband and invertible linear-to-circular polarization converter with ultrathin single layer metasurface," *Sci. Rep.* **5**, 18106 (2015).

61. S. Kruk, B. Hopkins, L. L. Kravchenko, *et al.*, "Broadband highly efficient dielectric metadevices for polarization control," *APL Photonics* **1**, 030801 (2016).

62. Q. Qian, P. Liu, L. Fan, *et al.*, "None sharp corner localized surface plasmons resonance based ultrathin metasurface single layer quarter wave plate," *Sci. Rep.* **11**, 8956 (2021).

63. F. Ding, Y. Yang, R. A. Deshpande, *et al.*, "A review of gap-surface plasmon metasurfaces: fundamentals and applications," *Nanophotonics* **7**, 1129–1156 (2018).

64. Y. Yang, W. Wang, P. Moitra, *et al.*, "Dielectric meta-reflectarray for broadband linear polarization conversion and optical vortex generation," *Nano Lett.* **14**, 1394–1399 (2014).

65. W. Luo, S. Xiao, Q. He, *et al.*, "Photonic spin Hall effect with nearly 100% efficiency," *Adv. Opt. Mater.* **3**, 1102–1108 (2015).

66. S. Ma, X. Wang, W. Luo, *et al.*, "Ultra-wide band reflective metamaterial wave plates for terahertz waves," *Europhys. Lett.* **117**, 37007 (2017).

67. A. I. Kuznetsov, A. E. Miroshnichenko, M. L. Brongersma, *et al.*, "Optically resonant dielectric nanostructures," *Science* **354**, aag2472 (2016).

68. S. Gao, C. S. Park, S. S. Lee, *et al.*, "All-dielectric metasurfaces for simultaneously realizing polarization rotation and wavefront shaping of visible light," *Nanoscale* **11**, 4083–4090 (2019).

69. Q. Zhou, M. Liu, W. Zhu, *et al.*, "Generation of perfect vortex beams by dielectric geometric metasurface for visible light," *Laser Photon. Rev.* **15**, 2100390 (2021).

70. W. Liu and Y. S. Kivshar, "Generalized Kerker effects in nanophotonics and meta-optics," *Opt. Express* **26**, 13085 (2018).

71. X. Fu, F. Yang, C. Liu, *et al.*, "Terahertz Beam Steering Technologies: From Phased Arrays to

Field-Programmable Metasurfaces," *Adv. Opt. Mater.* **8**, 1900628 (2020).

72. S. Lin, Y. Chen, and Z. J. Wong, "High-performance optical beam steering with nanophotonics," *Nanophotonics* **11**, 2617–2638 (2022).

73. M. Pan, Y. Fu, M. Zheng, *et al.*, "Dielectric metalens for miniaturized imaging systems: progress and challenges," *Light Sci Appl.* **11**, 195 (2022).

74. X. Luo, F. Zhang, M. Pu, *et al.*, "Recent advances of wide-angle metalenses: principle, design, and applications," *Nanophotonics* **11**, 1 (2022).

75. A. Arbabi, A. Faraon, "Advances in optical metalenses," *Nat. Photon.* **17**, 16 (2022).

76. T. Li, C. Chen, X. Xiao, J. Chen, S. Hu, S. Zhu, "Revolutionary meta-imaging: from superlens to metalens," *Photonics Insights* **2**, R01 (2023).

77. C. Meng, P. C. V. Thrane, F. Ding, *et al.*, "Dynamic piezoelectric MEMS-based optical metasurfaces," *Sci. Adv.* **7**, eabg5639 (2021).

78. P. C. V. Thrane, C. Meng, F. Ding, *et al.*, "MEMS tunable metasurfaces based on gap plasmon or Fabry-Pérot resonances," *Nano Lett.* **22**, 6951–6957 (2022).

79. Z. Cai, Y. Deng, C. Wu, et al., "Dual-functional optical waveplates based on gap-surface plasmon metasurfaces," *Adv. Opt. Mater.* **9**, 2002253 (2021).

80. Y. Deng, C. Wu, C. Meng, et al., "Functional metasurface quarter-wave plates for simultaneous polarization conversion and beam steering," *ACS Nano* **15**, 18532–18540 (2021).

81. Y. Deng, C. Meng, S. I. Sande, *et al.*, "Spin-controlled gap-surface plasmon metalenses for focused scalar and vector beam generation," *To be submitted* (2024).

82. Y. Deng, C. Meng, P. C. V. Thrane, *et al.*, "MEMS-integrated metasurfaces for dynamic linear polarizers," *Optica* **11**, 326 (2024).

83. F. Ding, Y. Deng, C. Meng, *et al.*, "Electrically tunable topological phase transition in non-Hermitian optical MEMS metasurfaces," *Sci. Adv.* **10**, eadl4661 (2024).

84. S. D. Gupta, N. Ghosh, A. Banerjee. "Wave Optics - Basic Concepts and Contemporary Trends," CRC Press (2019).

85. Y. Yuan, S. Chen, B. Ratni, *et al.*, "Bi-functional meta-device with full energy utilization in co- and cross-polarization fields," *Appl. Phys. Lett.* **117**, 171602 (2020).

86. J. Li, Y. Wang, C. Chen *et al.*, " From lingering to rift: metasurface decoupling for near- and far-field functionalization," *Adv. Mater.* **33**, 2007507 (2021).

87. K. Zhang, Y. Yuan, X. Ding, *et al.*, "Polarization-Engineered noninterleaved metasurface for integer and fractional orbital angular momentum multiplexing," *Laser Photon. Rev.* **15**, 2000351 (2021).

88. N. Yu, P. Genevet, M. A. Kats, *et al.*, "Light propagation with phase discontinuities: generalized laws of reflection and refraction," *Science* **334**, 333–337 (2011).

89. D. Lin, P. Fan, E. Hasman, *et al.*, "Dielectric gradient metasurface optical elements," *Science* **345**, 298–302 (2014).

90. C. Chen, S. Gao, X. Xiao *et al.*, "Highly efficient metasurface quarter-wave plate with wave front engineering," *Adv. Photon. Res.* **2**, 2000154 (2021).

91. P. B. Johnson, R. W. Christy, "Optical constants of the noble metals," *Phys. Rev. B* **6**, 4370 (1972).

92. W. L. Barnes, A. Dereux, T. W. Ebbesen, "Surface plasmon subwavelength optics," *Nature* **424**, 824–830 (2003).

93. D. K. Gramotnev and S. I. Bozhevolnyi, "Plasmonics beyond the diffraction limit," *Nature Photon.* **4**, 83–91 (2010).

94. M. S. Tame, K. R. McEnery, Ş. K. Özdemir, *et al.*, "Quantum plasmonics," *Nature Phys.* **9**, 329–340 (2013).

95. H. A. Atwater and A. Polman, "Plasmonics for improved photovoltaic devices," *Nature Mater.* **9**, 205–213 (2010).

96. J. N. Anker, W. P. Hall, O. Lyandres, *et al.*, "Biosensing with plasmonic nanosensors," *Nat Mater.* **7**, 442–453 (2008).

97. F. Ding, Y. Chen, Y. Yang, *et al.*, "Multifunctional metamirrors for broadband focused vector-beam generation," *Adv. Opt. Mater.* **7**, 1900724 (2019).

98. F. Ding, Y. Chen, S. I. Bozhevolnyi, "Focused vortex-beam generation using gap-surface plasmon metasurfaces," *Nanophotonics* **9**, 371–378 (2020).

99. Y. Li, M. A. Ansari, H. Ahmed, *et al.*, "Longitudinally variable 3D optical polarization structures," *Sci. Adv.* **9**, eadj6675 (2023).

100. Y. Intaravanne, M. A. Ansari, H. Ahmed, *et al.*, "Creating wavelength-selective polarization digital numbers," *Adv. Opt. Mater.* **12**, 2203097 (2024).

101. A. Pors, M. G. Nielsen, R. L. Eriksen, "Broadband focusing flat mirrors based on plasmonic gradient metasurfaces," *Nano Lett.* **13**, 829 (2013).

102. M. K. Mishra, V. Dubey, P. M. Mishra, *et al.*, "MEMS Technology: A Review," *JERR* 1–24 (2019).

103. C.-B. Eom and S. Trolier-McKinstry, "Thin-film piezoelectric MEMS," *MRS Bull.* **37**, 1007–1017 (2012).

104. R. P. Dahl-Hansen, "Reliability of piezoelectric microelectromechanical systems in humid conditions," (n.d.). 125 (2020).

105. A. Berkhout and A. F. Koenderink, "Perfect absorption and phase singularities in plasmon antenna array etalons," *ACS Photonics* **6**, 2917–2925 (2019).

106. D. B. Haim, L. Michaeli, O. Avayu, *et al.*, "Tuning the phase and amplitude response of plasmonic metasurface etalons," *Opt. Express* **28**, 17923 (2020).

107. L. Deng, J. Deng, Z. Guan, *et al.*, "Malus-metasurface-assisted polarization multiplexing," *Light Sci. Appl.* **9**, 101 (2020).

108. J. Deng, L. Deng, Z. Guan, *et al.*, "Multiplexed anticounterfeiting metaimage displays with single-sized nanostructures," *Nano Lett.* **20**, 1830–1838 (2020).

109. J. Deng, Z. Li, J. Li, *et al.*, "Metasurface-assisted optical encryption carrying camouflaged information," *Adv. Opt. Mater.* **10**, 2200949 (2022).

110. X. Zhang, J. Cheng, W. Yue, *et al.*, "Twofold optical display and encryption of binary and grayscale images with a wavelength-multiplexed metasurface," *Nanophotonics* **12**, 3747–3756 (2023).

111. D. Wang, F. Liu, T. Liu, *et al.*, "Efficient generation of complex vectorial optical fields with metasurfaces," *Light Sci. Appl.* **10**, 67 (2021).

112. F. Yue, V. Aglieri, R. Piccoli, *et al.*, "Highly sensitive polarization rotation measurement through a high-order vector beam generated by a metasurface," *Adv. Mater. Technol.* **5**, 1901008 (2020).

113. U. Stella, T. Grosjean, N. De Leo, *et al.*, "Vortex beam generation by spin-orbit interaction with Bloch surface waves," *ACS Photonics* **7**, 774–783 (2020).

114. C. Wu, S. Kumar, Y. Kan, *et al.*, "Room-temperature on-chip orbital angular momentum single-photon sources," *Sci. Adv.* **8**, eabk3075 (2022).

115. L. Feng, R. El-Ganainy, and L. Ge, "Non-Hermitian photonics based on parity–time symmetry," *Nat. Photonics* **11**, 752–762 (2017).

116. R. El-Ganainy, K. G. Makris, M. Khajavikhan, *et al.*, "Non-Hermitian physics and PT symmetry," *Nat. Phys.* **14**, 11–19 (2018).

117. Ş. K. Özdemir, S. Rotter, F. Nori, and L. Yang, "Parity-time symmetry and exceptional points in photonics," *Nat. Mater.* **18**, 783–798 (2019).

118. M.-A. Miri and A. Alù, "Exceptional points in optics and photonics," *Science* **363** (6422), 7709 (2019).

119. A. Li, H. Wei, M. Cotrufo, *et al.*, "Exceptional points and non-Hermitian photonics at the

nanoscale," *Nat. Nanotech.* **18**, 706–720 (2023).

120. C. M. Bender and S. Boettcher, "Real spectra in non-Hermitian Hamiltonians having PT symmetry," *Phys. Rev. Lett.* **80**, 5243 (1998).

121. C. M. Bender, "Making sense of non-Hermitian Hamiltonians," *Rep. Prog. Phys.* **70**, 947 (2007).

122. Z. Lin, H. Ramezani, T. Eichelkraut, *et al.*, "Unidirectional invisibility induced by PT-symmetric periodic structures," *Phys. Rev. Lett.* **106**, 213901 (2011).

123. L . Feng, Y. L. Xu, W. S. Fegadolli, *et al.*, "Experimental demonstration of a unidirectional reflectionless parity-time metamaterial at optical frequencies," *Nat. Mater.* **12**, 108–113 (2013).

124. W. J. Chen, S. K. Ozdemir, G. M. Zhao, *et al.*, "Exceptional points enhance sensing in an optical microcavity," *Nature* **548**, 192–196 (2017).

125. J. H. Park, A. Ndao, W. Cai, *et al.*, "Symmetry-breaking-induced plasmonic exceptional points and nanoscale sensing," *Nat. Phys.* **16**, 462–468 (2020).

126. J. Doppler, A. A. Mailybaev, J. Böhm, *et al.*, "Dynamically encircling an exceptional point for asymmetric mode switching," *Nature* **537**, 76–79 (2016).

127. X. L. Zhang, T. Jiang, and C. T. Chan, "Dynamically encircling an exceptional point in anti-parity-time symmetric systems: asymmetric mode switching for symmetry-broken modes," *Light: Sci. Appl.* **8**, 88 (2019).

128. A. Schumer, Y. Liu, J. Leshin, *et al.*, "Topological modes in a laser cavity through exceptional state transfer," *Science* **375**, 884 (2022).

129. Q. Song, M. Odeh, J. Zúñiga-Pérez, *et al.*, "Plasmonic topological metasurface by encircling an exceptional point," *Science* **373**(6559), 1133–1137 (2021).

130. M. Lawrence, N. Xu, X. Zhang, *et al.*, "Manifestation of PT symmetry breaking in polarization space with terahertz metasurfaces," *Phys. Rev. Lett.* **113**, 093901 (2014).

131. S. H. Park, S. G. Lee, S. Baek, *et al.*, "Observation of an exceptional point in a non-Hermitian metasurface," *Nanophotonics* **9**, 1031–1039 (2020).

132. Z. Li, G. Cao, C. Li, *et al.*, "Non-Hermitian electromagnetic metasurfaces at exceptional points," *Prog. Electromagn. Res.* **171**, 1–20 (2021).

133. J. Yu, B. Ma, A. Ouyang, *et al.*, "Dielectric super-absorbing metasurfaces via PT symmetry breaking," *Optica* **8**, 1290–1295 (2021).

134. Y. Xu, L. Li, H. Jeong, *et al.*, "Subwavelength control of light transport at the exceptional point by non-Hermitian metagratings," *Sci. Adv.* **9**, eadf3510 (2023).

135. M. S. Ergoktas, S. Soleymani, N. Kakenov, *et al.*, "Topological engineering of terahertz light using electrically tunable exceptional point singularities," *Science* **376**, 184–188 (2022).

136. S. Baek, S. H. Park, D. Oh, *et al.*, "Non-Hermitian chiral degeneracy of gated graphene metasurfaces," *Light Sci Appl.* **12**, 87 (2023).

137. Z. Liu, D. Zhu, L. Raju, *et al.*, "Tackling photonic inverse design with machine learning," *Advanced Science* **8**, 2002923 (2021).

138. M. K. Chen, X. Liu, Y. Sun, and D. P. Tsai, "Artificial Intelligence in Meta-optics," *Chem. Rev.* **122**, 15356–15413 (2022).

139. W. Ji, J. Chang, H.-X. Xu, *et al.*, "Recent advances in metasurface design and quantum optics applications with machine learning, physics-informed neural networks, and topology optimization methods," *Light Sci Appl.* **12**, 169 (2023).

140. Y. Fu, X. Zhou, Y. Yu, *et al.*, "Unleashing the potential: AI empowered advanced metasurface research," *Nanophotonics* **13**, 1239–1278 (2024).

141. Z. Jakšić, "Synergy between AI and optical metasurfaces: a critical overview of recent advances," *Photonics* **11**, 442 (2024).

142. Z. Xue, T. Zhou, Z. Xu, *et al.*, "Fully forward mode training for optical neural networks," *Nature* **632**, 280–286 (2024).

143. M. Plidschun, H. Ren, J. Kim, *et al.*, "Ultrahigh numerical aperture meta-fibre for flexible optical trapping," *Light Sci Appl.* **10**, 57 (2021).
144. H. Ren, J. Jang, C. Li, *et al.*, "An achromatic metafiber for focusing and imaging across the entire telecommunication range," *Nat Commun.* **13**, 4183 (2022).
145. R. Wang, M. A. Ansari, H. Ahmed, *et al.*, "Compact multi-foci metalens spectrometer," *Light Sci Appl.* **12**, 103 (2023).
146. Y. Fan, W. Huang, F. Zhu, *et al.*, "Dispersion-assisted high-dimensional photodetector," *Nature* **630**, 77–83 (2024).
147. Z. Yue, T. Sipahi, H. Ahmed, *et al.*, "Multispectral Polarization States Generation with a Single Metasurface," *Laser Photonics Rev.* 2400176 (2024).

7 Declaration of Authorships

Appendix A

Authorship Agreement

This authorship agreement concerns the published review work conducted by PhD Student Yadong Deng, and co-authors Ziru Cai, Yingtao Ding, Sergey I. Bozhevolnyi and Fei Ding.

The review work includes following article:

Recent progress in metasurface-enabled optical waveplates

Nanophotonics, 11(10), 2219-2244 (2022)

Author contributions: Yadong Deng and Ziru Cai contributed equally.

In accordance with the criteria put forward at the Vancouver Convention for authorship (www.icmje.org), the undersigned Yadong Deng hereby confirms that he as first author is responsible for

- a substantial contribution of the intellectual content,
- all figures,
- the initial drafting of the article,
- the finalization of the published versions.

Similarly, the undersigned Ziru Cai, Yingtao Ding, Sergey I. Bozhevolnyi and Fei Ding confirm that they as co-authors have contributed quantitatively and qualitatively to the conception and design, the interpretation of the experimental evidence, the critical revision for important intellectual content, and the final approval of the published versions. As senior researcher Sergey I. Bozhevolnyi, stands as guarantor and takes public responsibility for the integrity of the review work as a whole, from inception to published articles.

Yadong Deng

First author, Yadong Deng

Ziru Cai

Co-author, Ziru Cai

Yingtao Ding

Co-author, Yingtao Ding

SergeyBozhevolnyi

Co-author, Sergey I. Bozhevolnyi

Fei Ding

Co-author, Fei Ding

Appendix B

Authorship Agreement

This authorship agreement concerns the published research work conducted by Ziru Cai, PhD Student Yadong Deng, Cuo Wu, Chao Meng, Yingtao Ding, Sergey I. Bozhevolnyi and Fei Ding.

The research work includes following article:

Dual-Functional optical waveplates based on gap-surface plasmon metasurfaces

Advanced Optical Materials, **9(11), 2002253 (2021)**

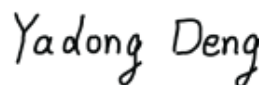**Author contributions: Ziru Cai and Yadong Deng contributed equally.**

In accordance with the criteria put forward at the Vancouver Convention for authorship (www.icmje.org), the undersigned Yadong Deng hereby confirms that he as co-author is responsible for

- a substantial contribution of the intellectual content,
- numerical simulations and theoretical analysis,
- metasurface fabrication and sample characterization,
- the acquisition and interpretation of experimental evidence,
- the finalization of the published versions.

Similarly, the undersigned Ziru Cai, Cuo Wu, Chao Meng, Yingtao Ding, Sergey I. Bozhevolnyi and Fei Ding confirm that they have contributed quantitatively and qualitatively to the conception and design, the interpretation of the experimental evidence, the critical revision for important intellectual content, and the final approval of the published versions. As senior researcher Sergey I. Bozhevolnyi, stands as guarantor and takes public responsibility for the integrity of the research work as a whole, from inception to published articles.
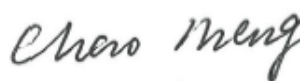
First author, Ziru Cai

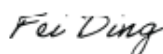Co-author, Yadong Deng

Co-author, Cuo Wu

Co-author, Chao Meng

Co-author, Yingtao Ding

Co-author, Sergey I. Bozhevolnyi

Co-author, Fei Ding

Appendix C

Authorship Agreement

This authorship agreement concerns the published research work conducted by PhD Student Yadong Deng, and co-authors Cuo Wu, Chao Meng, Sergey I. Bozhevolnyi and Fei Ding.

The research work includes following article:

Functional metasurface quarter-wave plates for simultaneous polarization conversion and beam steering

ACS Nano, 15(11), 18532-18540 (2021)

In accordance with the criteria put forward at the Vancouver Convention for authorship (www.icmje.org), the undersigned Yadong Deng hereby confirms that he as first author is responsible for

- a substantial contribution of the intellectual content,
- numerical simulations and theoretical analysis,
- metasurface fabrication and sample characterization,
- the acquisition and interpretation of experimental evidence,
- all figures,
- the initial drafting of the article,
- the finalization of the published versions.

Similarly, the undersigned Cuo Wu, Chao Meng, Sergey I. Bozhevolnyi and Fei Ding confirm that they as co-authors have contributed quantitatively and qualitatively to the conception and design, the interpretation of the experimental evidence, the critical revision for important intellectual content, and the final approval of the published versions. As senior researcher Sergey I. Bozhevolnyi, stands as guarantor and takes public responsibility for the integrity of the research work as a whole, from inception to published articles.

First author, Yadong Deng

Co-author, Cuo Wu

Co-author, Chao Meng

Co-author, Sergey I. Bozhevolnyi

Co-author, Fei Ding

81

Appendix D

Authorship Agreement

This authorship agreement concerns the research work to be submitted conducted by PhD Student Yadong Deng, and co-authors Chao Meng, Sören im Sande, Sergey I. Bozhevolnyi and Fei Ding.

The research work includes following article:

Spin-controlled gap-surface plasmon metalenses for focused scalar and vector beam generation

To be submitted (2024)

In accordance with the criteria put forward at the Vancouver Convention for authorship (www.icmje.org), the undersigned Yadong Deng hereby confirms that he as first author is responsible for

- a substantial contribution of the intellectual content,
- numerical simulations and theoretical analysis,
- metasurface fabrication and sample characterization,
- the acquisition and interpretation of experimental evidence,
- all figures,
- the initial drafting of the article,
- the finalization of the versions to be published.

Similarly, the undersigned Chao Meng, Sören im Sande, Sergey I. Bozhevolnyi and Fei Ding confirm that they as co-authors have contributed quantitatively and qualitatively to the conception and design, the interpretation of the experimental evidence, the critical revision for important intellectual content, and the final approval of the versions to be published. As senior researcher Sergey I. Bozhevolnyi, stands as guarantor and takes public responsibility for the integrity of the research work as a whole, from inception to published articles.

First author, Yadong Deng

Co-author, Chao Meng

Co-author, Sören im Sande

Co-author, Sergey I. Bozhevolnyi

Co-author, Fei Ding

Appendix E

Authorship Agreement

This authorship agreement concerns the published research work conducted by PhD Student Yadong Deng, and co-authors Chao Meng, Paul C. V. Thrane, Sören im Sande, Sergey I. Bozhevolnyi and Fei Ding.

The research work includes following article:

MEMS-Integrated metasurfaces for dynamic linear polarizers

Optica, 11(3), 326-332 (2024)

In accordance with the criteria put forward at the Vancouver Convention for authorship (www.icmje.org), the undersigned Yadong Deng hereby confirms that he as first author is responsible for

- a substantial contribution of the intellectual content,
- numerical simulations and theoretical analysis,
- metasurface fabrication and sample characterization,
- the acquisition and interpretation of experimental evidence,
- all figures and movies,
- the initial drafting of the article,
- the finalization of the published versions.

Similarly, the undersigned Chao Meng, Paul C. V. Thrane, Sören im Sande, Sergey I. Bozhevolnyi and Fei Ding confirm that they as co-authors have contributed quantitatively and qualitatively to the conception and design, the interpretation of the experimental evidence, the critical revision for important intellectual content, and the final approval of the published versions. As senior researcher Sergey I. Bozhevolnyi, stands as guarantor and takes public responsibility for the integrity of the research work as a whole, from inception to published articles.

First author, Yadong Deng

Co-author, Chao Meng

Co-author, Paul C. V. Thrane

Co-author, Sören im Sande

Co-author, Sergey I. Bozhevolnyi

Co-author, Fei Ding

Appendix F

8   Appendix A-F

Review

Yadong Deng, Ziru Cai, Yingtao Ding, Sergey I. Bozhevolnyi* and Fei Ding*

Recent progress in metasurface-enabled optical waveplates

Abstract: The polarization of light is crucial for numerous optical applications ranging from quantum information processing to biomedical sensing due to the fundamental role of polarization as another intrinsic characteristic of optical waves, which is uncorrelated with the amplitude, phase, and frequency. However, conventional optical waveplates that enable polarization control are based on the accumulated retardation between two orthogonally polarized electric fields when light propagates a distance much larger than its wavelength in birefringent materials, resulting in bulky configurations and limited functionalities. Optical metasurfaces, ultrathin arrays of engineered meta-atoms, have attracted increasing attention owing to their unprecedented capabilities of manipulating light with surface-confined configurations and subwavelength spatial resolutions, thereby opening up new possibilities for revolutionizing bulky optical waveplates with ultrathin planar elements that feature compactness, integration compatibility, broadband operation bandwidths, and multiple functionalities. Herein, we review the recent progress in metasurface-enabled optical waveplates, which covers both basic principles and emerging applications. We provide an overview of metasurface-based conventional half- and quarter-waveplates as well as their use in wavefront shaping applications, followed by a discussion of advanced waveplates, including multifunctional waveplates and all-polarization generators. We also discuss dynamic waveplates based on active metasurfaces. Finally, we conclude by providing our outlook in this emerging and fast-growing research field.

Keywords: dynamic; multifunctional; optical metasurface; waveplates.

1 Introduction

Polarization that describes the oscillation direction of electric fields is one of the fundamental and intrinsic properties of optical waves, which is uncorrelated with other properties, such as amplitude, phase, and frequency. Therefore, polarization can contain abundant valuable information and has been widely used in numerous applications, ranging from material property analysis, pharmaceutical ingredient identification, surface topography, remote sensing, to optical communication [1]. However, light emitted from many sources, such as incandescent lamps, consists of an equal mixture of different polarizations, which is referred to as unpolarized light. To produce polarized light with well-defined states of polarization (SoPs) and transform between different SoPs (e.g., linear, circular, or elliptical polarizations), bulky polarization optics have been employed. For instance, optical waveplates made up of birefringent materials (e.g., non-cubic crystals, plastics, and cotton fiber) are used to produce specific retardation between two orthogonally polarized electric fields when light propagates inside the medium. But due to the limited birefringence $\Delta n = n_e - n_o$ in natural materials (less than 10%), where n_e and n_o are the refractive indices along the extraordinary and ordinary axes, the waveplates should be thick enough to provide a sufficient propagation distance much larger than the wavelength [1], going against the growing requirement of miniaturization and dense integration in photonic devices. Besides bulky configurations,

Yadong Deng and Ziru Cai are equally contributed.

---

*Corresponding authors: Sergey I. Bozhevolnyi and Fei Ding, SDU Nano Optics, University of Southern Denmark, Campusvej 55, DK-5230 Odense, Denmark, E-mail: seib@mci.sdu.dk (S. I. Bozhevolnyi), feid@mci.sdu.dk (F. Ding). https://orcid.org/0000-0002-0393-4859 (S.I. Bozhevolnyi), https://orcid.org/0000-0001-7362-519X (F. Ding)
Yadong Deng, SDU Nano Optics, University of Southern Denmark, Campusvej 55, DK-5230 Odense, Denmark, E-mail: yd@mci.sdu.dk
Ziru Cai, SDU Nano Optics, University of Southern Denmark, Campusvej 55, DK-5230 Odense, Denmark; and School of Integrated Circuits and Electronics, Beijing Institute of Technology, Beijing, 100081, P. R. China, E-mail: zirucai.bit@gmail.com
Yingtao Ding, School of Integrated Circuits and Electronics, Beijing Institute of Technology, Beijing, 100081, P. R. China, E-mail: ytd@bit.edu.cn

conventional waveplates are suffering from limited functionalities and narrow bandwidths. Therefore, it is highly desired to realize miniaturized optical waveplates with excellent performance and diversified functionalities.

Optical metasurfaces, the two-dimensional (2D) analog of metamaterials in the optical range, have attracted increasing attention and rapidly emerged as a promising platform for versatile planar optics due to their unprecedented capabilities of manipulating light with surface-confined configurations and subwavelength spatial resolutions by judiciously engineering the shapes, dimensions, rotations, and locations of planar nanostructures (referred to as meta-atoms) [2–13]. In particular, among all the fascinating applications, optical metasurfaces open up new possibilities for revolutionizing bulky polarizers and waveplates with ultrathin planar elements that feature compactness, integration compatibility, broadband operation bandwidths, and multiple functionalities. For example, metasurface gratings have been widely implored to demonstrate compact and wideband polarizations [14–17]. In this paper, we aim to review the recent progress in metasurface-based waveplates (meta-waveplates) over the last few years. Due to the limited contents, hereby we mainly concentrate on the optical range although there are a lot of fancying meta-waveplates demonstrated in the low-frequency ranges [18–25]. Following the introduction part, we provide an overview of metasurface-based conventional half- and quarter-waveplates (HWPs and QWPs) as well as their use in wavefront shaping applications in Section 2. In Section 3, we discuss advanced meta-waveplates that include multifunctional waveplates and all-polarization generators. Then we summarize the state-of-the-art dynamic meta-waveplates based on active metasurfaces in Section 4. In the final section (Section 5), we provide a summary and outlook for future development in this fast-growing research field.

2 Metasurface-based optical HWPs and QWPs

Different from bulky optical waveplates that rely on limited birefringence from the natural materials with non-cubic structures, metasurfaces can provide a strong optical anisotropy at any interested wavelength range by designing nanostructured meta-atoms with distinct and polarization-dependent responses, thereby resulting in miniaturized planner meta-waveplates with excellent and fancy functionalities beyond conventional counterparts. In this section, we start our discussions on metasurface-based HWPs and QWPs.

2.1 Metasurface-based conventional HWPs and QWPs

We first consider a typical anisotropic meta-atom with global mirror symmetries, whose main axes are located along x- and y-directions. From a microscopic perspective, the optical characteristics of this anisotropic meta-atom can be described using the Jones matrix once excited by two linearly polarized (LP) electric fields (e.g., E_x and E_y):

$$J_{\text{LP}} = \begin{pmatrix} J_{xx} & 0 \\ 0 & J_{yy} \end{pmatrix} \tag{1}$$

where $J_{xx} = |J_{xx}|e^{i\varphi_{xx}}$ and $J_{yy} = |J_{yy}|e^{i\varphi_{yy}}$ are the transmission/reflection coefficients under x- and y-polarized excitations, which are mainly determined by the dimensions of the meta-atom along two principal axes. Specifically, $|J_{xx}|$ and $|J_{yy}|$ represent the amplitudes, φ_{xx} and φ_{yy} represent the corresponding phase delays, and $\Delta\varphi = \varphi_{xx} - \varphi_{yy}$ is defined as the relative phase difference. In general, once the amplitudes are equivalent (e.g., $|J_{xx}| = |J_{yy}|$) and $\Delta\varphi$ is equal to $\pm\pi/2$ or π, meta-QWPs [26–35] or meta-HWPs [36–39] could be realized in the optical range. By designing the anisotropic meta-atom supporting detuned resonances, the relative phase difference can be realized in a sub-micrometer thickness, superior to bulky waveplates. Here, it should be emphasized that the recent development of optical meta-waveplates has been largely following the pioneering work on anisotropic metamaterials in the microwave range by Zhou's group [40].

Capitalizing on the mechanism introduced above, we would like to discuss some typical examples. Early in 2011, a brick-shaped scatterer supporting perpendicular electrical dipoles was designed by Bozhevolnyi's group (left panel of Figure 1a), which could generate a phase difference of $\pi/2$ in the reflection mode at the center wavelength of 770 nm [26]. By optimizing the dimensions (e.g., L_1 and L_2) of the gold (Au) nano-brick atop of a substrate, the detuned electric dipole resonances could be supported to realize linear-to-circular polarization conversion under an LP incident beam with different polarization angles. For example, when $L_1 = 90$ nm and $L_2 = 140$ nm, the phase difference of $\pi/2$ could be satisfied under the LP incident light with a polarization angle of 45° in a narrow bandwidth between 748 and 796 nm (middle and right panels of Figure 1a). Although this work provided a conceptual method for designing subsequent wave retarders, the polarization conversion efficiency of such single-layered waveplates [26, 31, 34, 35] is restricted due to unwanted channels (transmission in this case), and the effective working bandwidth is obviously narrow. Similar to single-layered metallic meta-atoms, their

complementary counterparts can be employed to realize optical meta-waveplates [27, 29, 30]. Figure 1b shows a transmissive QWP designed by Zhao et al., where the unit cell is formed by two orthogonal rectangular nano-slits with optimized dimensions in an ultrathin silver (Ag) layer [27]. The phase difference of two LP transmission fields could be maintained to $\pi/2$ in a broadband wavelength range from 600 to 800 nm. Within the bandwidth from 616 to 746 nm, the simulated degree of linear polarization (DoLP) approaches 1, and the angle of linear polarization (AoLP) ranges from 28° to 55° with respect to the x-axis when the QWP is illuminated with right circularly polarized (RCP) and left circularly polarized (LCP) beams. Similar to single-layered waveplates, this complementary QWP is suffering from limited conversion efficiency due to the unavoidable reflection loss.

To increase efficiency and expand the working bandwidth, gap-surface plasmon (GSP) metasurfaces consisting of an array of metallic meta-atoms, a subwavelength dielectric spacer, and a thick metallic substrate, forming a typically metal–insulator–metal (MIM) resonator [41], have been employed to realize compact optical waveplates [28, 32, 33, 36–38, 42]. For GSP metasurfaces, the transmission channel is forbidden, and each building block is perfectly reflective. Meanwhile, the designed meta-atom possesses equally high reflection amplitudes and a proper phase difference (e.g., $\pm\pi/2$ or π) under linear excitations [43, 44]. For instance, Jiang et al. employed such an MIM configuration to realize the HWP and QWP for highly-efficient and angle-insensitive polarization transformation over more than an octave broad bandwidth that covers the visible and near-infrared ranges [33]. The ultrathin reflective broadband waveplates were designed by optimizing the anisotropic responses of a nanorod resonator array with strong coupling to tailor the interference of light between the top array and the ground plane at a subwavelength scale. As shown in the left and middle panels of Figure 1c, the nanostructure consisting of top Au nanorods, an intermediate silicon dioxide (SiO$_2$) layer, and a thick Au back reflector, could reflect a circularly polarized (CP) incident wave into an LP wave. The measured polarization conversion ratio (PCR) is higher than 91% within the expected broadband wavelength range from 640 to 1290 nm for an incident angle up to 40°, and the reflection magnitude could be larger than 92% (right panel of Figure 1c). Although the conversion efficiencies of MIM meta-waveplates could be increased to some degree, Ohmic losses in the metal do exist, especially at the short wavelength region. Therefore, a hybrid MIM metasurface composed of single-crystalline silicon (Si) bricks and an Ag

back-reflector separated by a dielectric spacer has been implemented as an efficient HWP in the telecom range [42].

Despite significant progress achieved with MIM meta-waveplates, they are constrained to work in the reflection mode, severely restricting the range of practical applications [45]. As such, all-dielectric anisotropic meta-atoms that consist of high-refractive-index and low-loss materials could also be employed to realize ultrathin optical waveplates [39, 46–50]. In such all-dielectric metasurfaces, electric and magnetic Mie resonances exploited by corresponding electric and magnetic hotspots with nanoscale volumes could be enhanced with similar strengths at a single frequency or a frequency range, thereby enabling complete and independent manipulations of amplitudes and phases for the transmitted fields [47]. Moreover, transmission efficiencies could be raised hugely since the reflection channel could be suppressed effectively by satisfying the Kerker condition [51]. In addition to the high efficiency, arbitrary and sufficiently large retardation could be generated by designing the optical anisotropy of the meta-atom, which could be much higher compared with the propagation phase accumulated in the birefringent crystals. Therefore, all-dielectric HWPs and QWPs with high conversion efficiencies in the transmission mode have been demonstrated [39, 46, 48]. For example, Kruk's group designed and experimentally demonstrated a type of transparent broadband all-dielectric metasurfaces composed of closely spaced Si nanopillars to realize high-efficiency polarization manipulation, as shown in the left panel of Figure 1d [39]. According to the generalized Huygens principle, the scattering profiles come from the spectrally overlapped electric and magnetic multipolar modes of the component Si particles, which results in destructive interference in the reflection channel over a broadband range. In terms of the designed meta-HWP (middle panel of Figure 1d), the transmission efficiency is close to 90% and the PCR is near to 99% in the telecom range. In particular, the equivalent birefringence Δn for a π phase difference was calculated to be as high as 0.9 at the wavelength of 1550 nm, almost one magnitude larger than those of natural birefringent materials.

At a final comment, it should be mentioned multi-layered transmissive metasurfaces that support both electric and magnetic responses and enable constructive interference in the transmission channel can be alternatively used to demonstrate high-efficiency transmissive meta-waveplates [52, 53], which are however mainly limited to the low-frequency ranges due to the intrinsic high loss and fabrication complexity in the optical range.
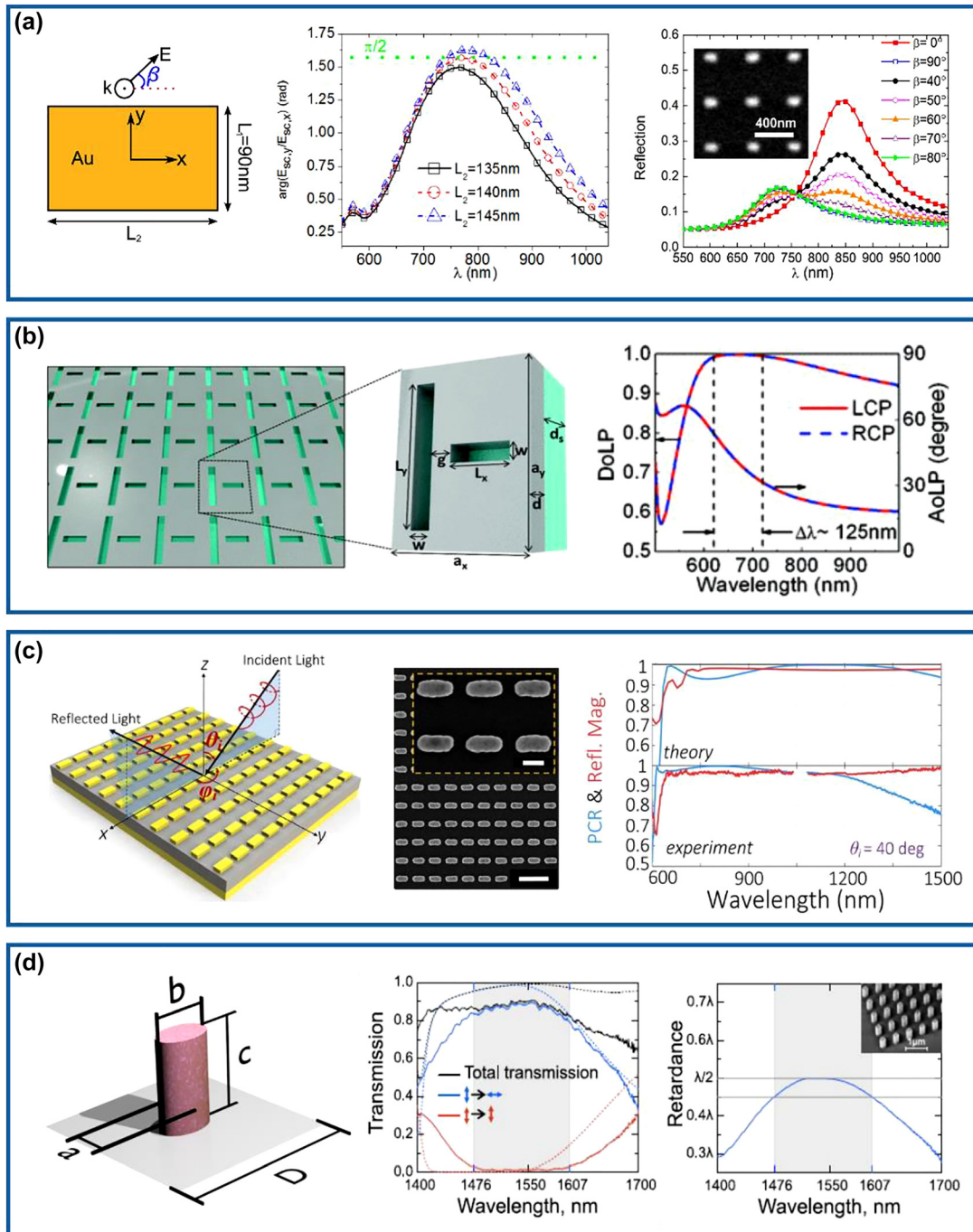
Figure 1: Metasurface-based conventional HWPs and QWPs. (a) Left panel: schematic of an Au brick-shaped meta-atom illuminated with a plane wave with the AoLP of β. Middle panel: simulated phase difference of the scattered electric fields for optimized nano-brick structures with different L_2. Right panel: normalized reflection spectra for different β as a function of the wavelength. The inset shows the scanning electron microscopy (SEM) image of the fabricated Au bricks. Reprinted from Ref. [26]. (b) Left panel: schematic of the complementary plasmonic metasurface with nano slits. Right panel: DoLP and AoLP of the designed nano-slit metasurface for LCP and RCP excited waves as a function of the wavelength. Reprinted from Ref. [27]. (c) Left panel: schematic of the MIM meta-QWP that converts a CP incident wave with an incident angle of $(\theta_i, \varphi_i = 0°)$ into an LP output wave. Middle panel: SEM image of the fabricated meta-QWP. Right panel: theoretical and experimental PCR and reflection magnitudes as a function of different wavelengths under one incident CP wave with $\theta_i = 40°$. Reprinted from Ref. [33]. (d) Left panel: schematic of the designed pillar-based Si meta-atom as a transmissive waveplate. Middle panel: experimental and theoretical transmission spectra of the designed meta-HWP. Right panel: measured retardance of the fabricated Si meta-HWP as a function of the wavelength. The gray region marks the spectral range with a deviation from $\lambda/2$ by less than 10%. The inset shows the SEM image of the fabricated sample. Reprinted from Ref. [39].

2.2 Metasurface-based multifunctional HWPs and QWPs

In addition to the basic functionality of polarization conversion, advanced wavefront shaping capabilities, such as vortex-beam generation [42, 50, 54–58], optical holograms [59–72], and beam steering [73–75], have realized by spatially integrating multiple HWP and QWP meta-atoms that supply versatile phase modulation.

2.2.1 Multifunctional meta-HWPs using resonance phase

The first method towards multifunctional meta-HWPs is to utilize the dimension-dependent resonance phase for the cross-polarized optical fields in a linear polarization basis, which can be realized by designing multiple HWPs enabling efficient linear-polarization conversion along with the complete phase control over cross-polarized fields [42, 54, 73, 76]. As shown in Figure 2a, Yang et al. proposed
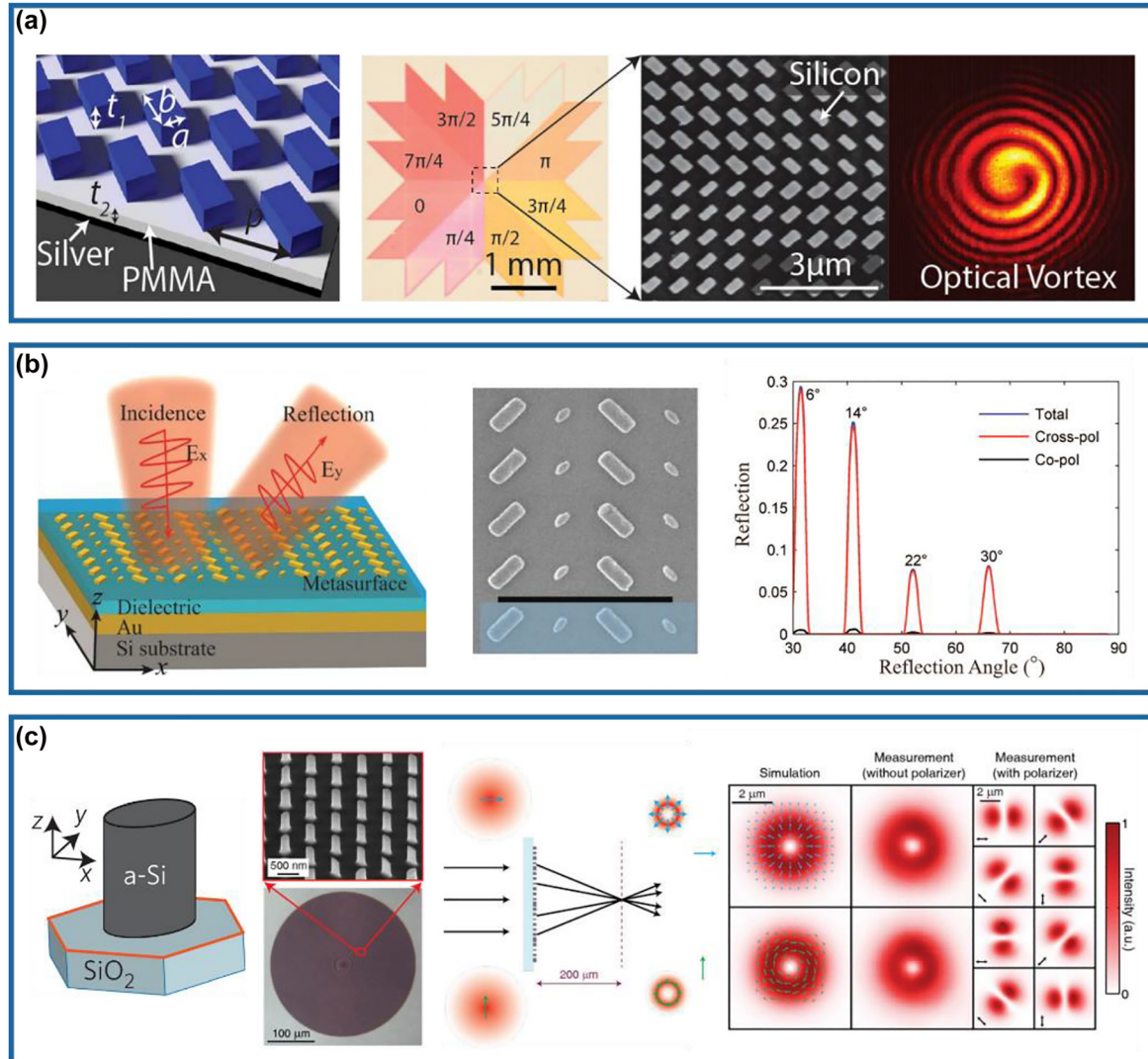

Figure 2: Multifunctional meta-HWPs using resonance phase. (a) Left panel: schematic of a reflective meta-HWP array consisting of Si bricks, a PMMA spacer, and an Ag reflector. Right panel: design and experimental demonstration of optical vortex beam generation in cross-polarization. Reprinted from Ref. [42]. (b) Left panel: schematic of the background-free plasmonic meta-HWP that enables polarization conversion and anomalous reflection in the cross-polarized channel. Middle panel: SEM image of the fabricated structure. Right panel: measured normalized reflection of the fabricated sample as a function of incident angle under x-polarized excitation at $\lambda = 1000$ nm. Reprinted from Ref. [73]. (c) Left panel: schematic, SEM, and optical microscope images of the elliptical Si posts on top of a SiO_2 substrate. Right panel: illustration and demonstration of focused radially (azimuthally) polarized Bessel–Gauss beam generation under the excitation of an x-polarized (y-polarized) Gaussian beam. Reprinted from Ref. [46].

and experimentally generated optical vortex beams possessing orthogonal linear polarization conversion by employing Si-PMMA-Ag hybrid MIM nano-HWPs to provide an azimuthally dependent spiral phase profile ranging from 0 to 2π [42]. By varying geometry dimensions of the topmost Si structures, four different meta-HWPs with relatively high cross-polarized reflectance and phase modulation are selected to provide a phase coverage of π for the cross-polarized reflected light with an incremental step of $\pi/4$. The additional π-phase range could be attained by simply rotating these antennas with an angle of 90°, thereby resulting in the full 2π coverage with near-unity efficiencies in cross-polarization. The vortex beam could be generated with high efficiency of ~94.5% in simulation over a wavelength range from 1500 to 1600 nm. In 2015, Ding and co-workers experimentally demonstrated a compact background-free GSP meta-HWP that integrates the functionalities of linear-to-linear polarization conversion and beam-steering in the near-infrared region [73]. As shown in the left and middle panels of Figure 2b, the designed meta-device is composed of four different nano-HWPs in one supercell, which creates a linear phase gradient along the x-direction for the cross-polarized reflected fields, leading to the anomalous reflection in the cross-polarized channel [77]. The right panel of Figure 2b shows that the co- and cross-polarized reflected waves could be separately manipulated with the co-polarized reflected wave completely suppressed and the cross-polarized reflected wave dominating in the designed direction, greatly boosting the polarization conversion efficiency. In particular, the cross-polarized reflection power is consistent with the total reflection power and the co-polarized reflection power is extremely low, which effectively proves the required functionality of linear-to-linear polarization conversion and beam steering. In addition, the power rate between the desired cross-polarized field and the orthogonal co-polarized field is above 20, and the integrated PCR is larger than 95%.

Except for plasmonic multifunctional meta-HWPs operating in reflection, all-dielectric meta-HWPs have also been employed to enable multiple functions beyond pure polarization conversion with high conversion efficiencies in the transmission mode [46, 47]. For example, Arbabi et al. designed a Si ellipse-shaped meta-atom with complete control of phase and polarization (the left panel of Figure 2c), through which advanced wavefront shaping could be achieved with high efficiency [46]. As shown in the right panel of Figure 2c, the implemented meta-HWP could convert an x-polarized (or y-polarized) Gaussian beam into a focused radially (or azimuthally) polarized Bessel–Gauss beam, thereby integrating functionalities of

a q-plate and a lens at the same time. Impressively, the measured conversion efficiencies for both x- and y-polarized waves are higher than 85%, due to the satisfied Kerker condition through spectrally overlapping the electric and magnetic resonances with identical strengths.

2.2.2 Multifunctional meta-HWPs using geometric phase

Whereas aforementioned multifunctional meta-HWPs rely on the resonance phase, with the consequent result that the operating bandwidth is usually limited to the dissimilar dispersion of the different meta-atoms, geometric or Pancharatnam–Berry (PB) phase is dispersionless in the sense that the phase on the cross-polarized CP light is solely determined by the orientation of a single meta-atom [78–82]. Here, it should be mentioned that the efficiency of the cross-polarized CP channel is still constrained by the dispersion of the meta-atom. But compared to the resonance phase contributed from several meta-atoms with different dimensions and spectral responses, the orientation-induced geometric phase from just one identical meta-atom is more broadband [50, 59–66, 83–87]. Here, we take the holograms [59, 64] and metalenses [83, 86] as examples to show the capabilities of multifunctional meta-HWPs.

In 2015, Zhang's group has realized phase-only geometric metasurface holograms by utilizing spatially-oriented meta-HWPs with diffraction efficiency up to 80% at the wavelength of 825 nm (Figure 3a) [59]. In this design, 16 phase levels have been introduced by precisely tailoring the rotation angle of the designed meta-atoms, which ensures a more robust fabrication quality (middle panel of Figure 3a). Remarkably, the working bandwidth is quite wide, ranging from 630 to 1050 nm with a high measured efficiency greater than 50%. To further increase the fidelity of reconstructed images, a complex-amplitude modulation method can be easily implemented by designing meta-atoms possessing different degrees of circular polarization conversion [64]. As shown in Figure 3b, Ren et al. experimentally demonstrated large-scale complex-amplitude metasurface-based orbital angular momentum (OAM) holography based on three-dimensionally laser-printed polymer nanopillars on the substrate SiO_2, which enables complete and independent amplitude and phase manipulation. Based on the design, useful information could be extracted by Fourier transform when the incident light carries different OAM modes, thereby reconstructing more than 200 orthogonal image channels encoded with different topological charges and holographic videos without any lenses.
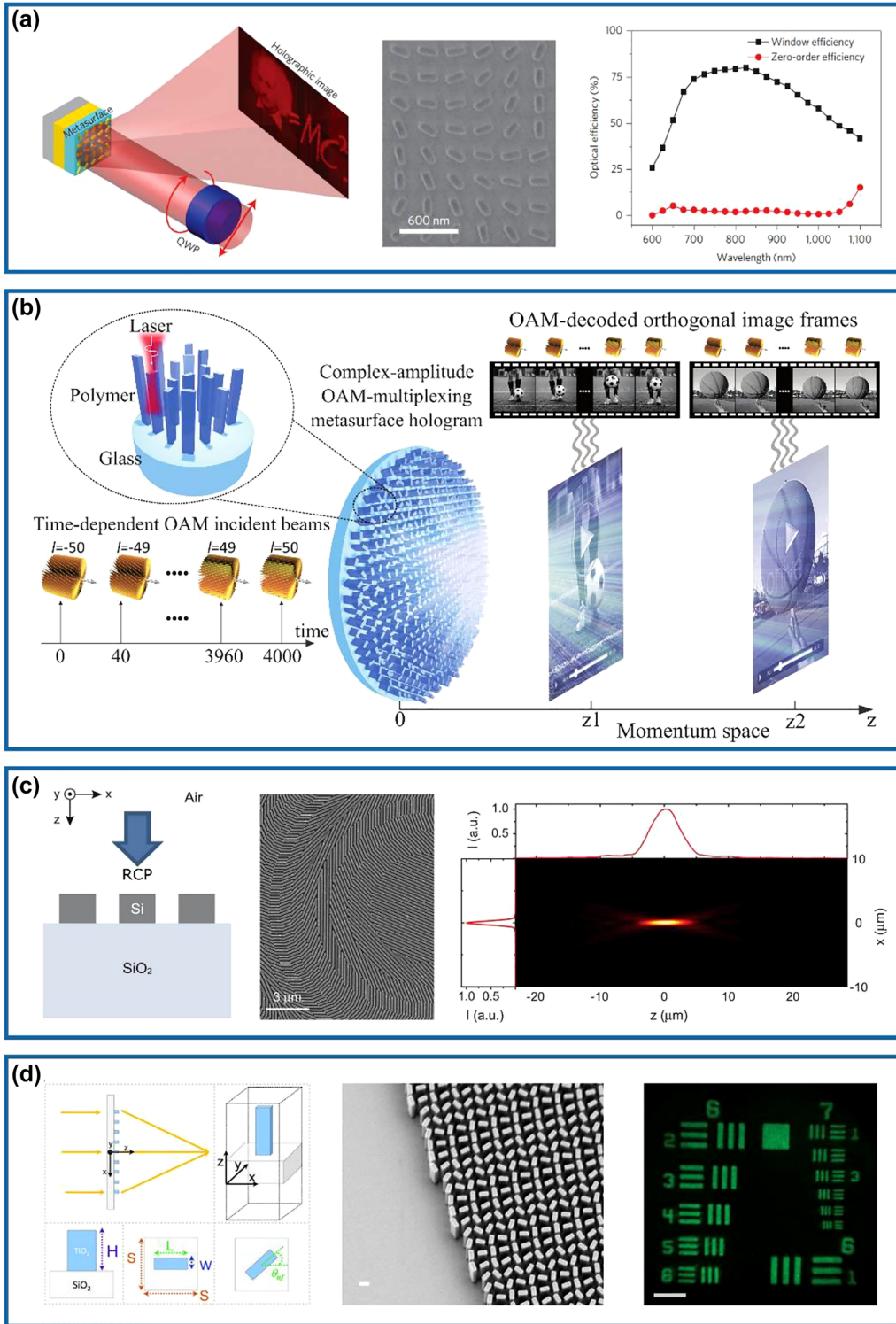
Figure 3: Multifunctional meta-HWPs using geometric phase. (a) Left panel: schematic of the reflective metasurface hologram under a CP incident light. Middle panel: SEM image of part of the fabricated sample. Right panel: measured holographic image and zero-order efficiencies as a function of the wavelength. Reprinted from Ref. [59]. (b) Schematic of the complex-amplitude OAM-multiplexing metasurface hologram that displays two separate holographic videos, both carrying a large amount of OAM-dependent orthogonal image frames, at two different image planes simultaneously in the momentum space. Reprinted from Ref. [64]. (c) Left panel: schematic view of the designed Si meta-HWP. Middle panel: SEM image of part of the fabricated metalens. Right panel: measured intensity distributions of the focusing light passing through the fabricated meta-lens along the vertical and horizontal axes in the *xz*-plane. Reprinted from Ref. [83]. (d) Left panel: illustration of the TiO$_2$ metalens and its unit cell. Middle panel: SEM image of the fabricated metalens. Right panel: resolution test image formed by the fabricated metalens at $\lambda = 530$ nm. Reprinted from Ref. [86].

Regarding metalenses based on the geometric phase, a typical example is shown in Figure 3c, where a 100-nm-thick Si gradient metasurface capable of efficiently focusing visible light has been realized from Brongersma's group [83]. As shown in the left panel of Figure 3c, the subwavelength-spaced Si nano-stripes act as nano-HWPs at the wavelength centered at 550 nm. By discretizing the geometric phase in eight steps, a hyperboloidal phase profile could be approximated to mimic a conventional focusing lens (middle panel of Figure 3c). The fabricated metalens can concentrate the RCP incident light into an LCP focal spot with the focal length and the numerical aperture (NA) of 100 μm and 0.43 at λ = 550 nm, respectively (right panel of Figure 3c). Due to the narrow bandgap of Si, the intrinsic loss does exist in the visible spectrum, thereby limiting the efficiency. To increase the efficiency, high-refractive-index, and low-loss dielectric materials with wider bandgaps, such as titanium dioxide (TiO_2) [86, 88], gallium nitride (GaN) [67, 89], and hafnium oxide (HfO_2) [90, 91], should be implemented. For example, Capasso's group has experimentally demonstrated a high-aspect-ratio TiO_2 metalens with an NA of 0.8, as shown in Figure 3d [86]. The diffraction-limited focusing has been achieved at wavelengths of 405, 532, and 660 nm with corresponding efficiencies of 86, 73, and 66%, respectively. The fabricated metalens could achieve a magnification up to 170× with extremely high image qualities comparable to a state-of-the-art commercial objective.

2.2.3 Multifunctional meta-HWPs using both resonance and geometric phases

Despite significant progress in geometric phase meta-HWPs, their functionalities are limited to the specific CP excitation due to the spin-locked nature of the geometric phase, where the RCP and LCP waves hold the conjugated phases. Currently, this spin-locked limitation has been released by combining the dimension-determined resonance phase and the orientation-dependent geometric phase from multiple meta-HWPs, providing a general scheme for the realization of spin-decoupled functionalities integrated into a single meta-device under orthogonal CP excitations [46, 68–71, 74, 92–100].

In 2015, the first spin-decoupled Si metasurface capable of producing focused OAM beams carrying different topological charges has been realized by Faraon's group at the near-infrared wavelength of 915 nm [46]. When the RCP and LCP incident beams pass through the designed meta-device possessing a spiral phase profile, the total OAM of the transmitted beams will become $m = 0$ and $m = 2$, respectively. In particular, the RCP incident light is focused into a nearly diffraction-limited spot, while the LCP counterpart is focused into a donut-shaped intensity pattern (Figure 4a). Therefore, the focal spot can be modified rapidly by changing the polarization of the incident light using a phase modulator with a fast response. Based on this concept, Huo et al. experimentally demonstrated a visible spin-multiplexed spatial filter composed of TiO_2 nano-HWPs, which could realize optical imaging switch between bright-field and spiral phase contrast imaging modes, as shown in Figure 4b [68]. In this design, a constant phase profile is imparted to LCP incident light while a spiral phase profile is imparted to RCP incident light, therefore dynamically realizing switchable ordinary diffraction imaging and isotropic edge detection, respectively. Besides phase modulation, the intensity can be simultaneously encoded within meta-HWPs for nanoprinting [70, 71, 101]. For example, Li and co-workers have proposed and experimentally demonstrated a three-channel metasurface composed of TiO_2 nano-HWPs, which could generate a near-field nano-printing image and two far-field holographic images simultaneously, as shown in Figure 4c [70]. In this work, the intensity modulation was governed by Malus's law and the phase modulation was supplied with both propagation (resonance) and geometric phases. Moreover, owing to the decoupled amplitude and phase algorithm introduced, the proposed multiplexing metasurface could guarantee independence and design freedom in different information channels to the utmost extent. To move the operating wavelength to the ultraviolet (UV) and even deep-UV regimes, Zhang et al. have utilized HfO_2 to demonstrate multiple high-performance meta-HWPs with resonance and geometric phases (the left and middle panels of Figure 4d) and implemented spin-controlled wavefront shaping functionalities [69]. As shown in the right panel of Figure 4d, a 330-μm-square meta-holographic has been designed to project a holographic "deep" image under LCP incident light and a "UV" image under RCP incident light at the wavelength of down to 266 nm, with the corresponding efficiencies of ~58.95 and ~61.23%, respectively.

In addition to the aforementioned spin-decoupled multifunctional meta-HWPs for transmitted optical fields, GSP-based meta-HWPs combining both resonance and geometric phases can be accordingly designed to control the reflected or surface-confined fields. In 2020, Ding's group has experimentally demonstrated an efficient spin-decoupled multifunctional GSP meta-device that enables unidirectional surface plasmon polariton (SPP) excitation and anomalous beam steering simultaneously under orthogonal CP incident beams in the near-infrared range (the left panel of Figure 4e) [74]. In this work, well-optimized meta-HWPs with different dimensions and
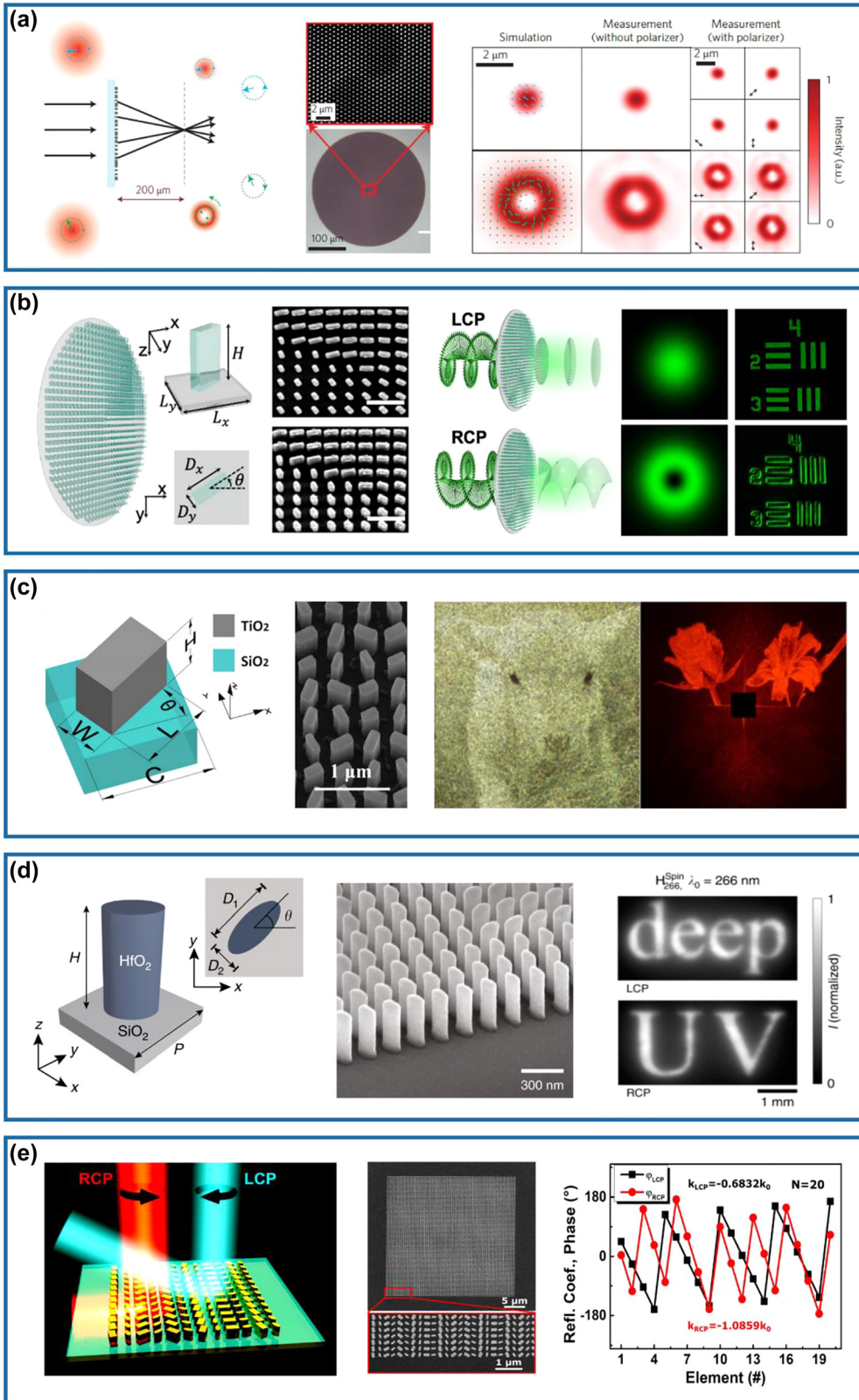
Figure 4: Multifunctional meta-HWPs using both resonance and geometric phases. (a) Left panel: schematic of the Si metasurface that can selectively focus the RCP and LCP light into a nearly diffraction-limited spot and a donut-shaped intensity pattern. Middle panel: SEM and optical microscope images of the fabricated sample. Right panel: simulated and measured intensity profiles. Reprinted from Ref. [46]. (b) Left

orientations that produce two distinct spin-sensitive linear-phase gradients along the x-direction are designed. For RCP light, the phase gradient is designed to match the wavevector of SPPs supported by the substrate at normal incidence. For LCP light, the phase gradient is designed smaller than the wavevector of free-space propagating light, which results in an anomalous deflection angle of the reflected light (the middle and right panels of Figure 4e). The fabricated multifunctional meta-device shows efficient unidirectional SPP excitation with a coupling efficiency above 22% in the wavelength range from 850 to 950 nm under the RCP incident light. Once the input is switched to LCP light, the anomalous beam steering with an averaged efficiency of 48% is achieved at the same spectrum.

2.2.4 Metasurface-based multifunctional QWPs

The left panel of Figure 5a shows the schematic of a multifunctional meta-QWP that enables simultaneous linear-to-circular polarization and beam steering in an ultra-broadband mid-infrared wavelength range [102]. The designed metasurface composed of two subunits of phased antennas with different dimensions and rotations could generate two transmission waves with consistent propagating directions, equal amplitudes, orthogonal polarization states, and a phase difference of $\pi/2$ under an LP excitation (middle panel of Figure 5a). Afterward, these two waves will interfere and generate an extraordinary CP wave which is directed in a particular direction away from the ordinary wave, producing a background-free QWP. Impressively, the calculated degree of circular polarization (DoCP) of the steered beam is larger than 0.95 from 6 to 10 μm (right panel of Figure 5a). In addition, the measured suppression ratio between the intensities of RCP and LCP is about 700 at 8 μm, which could prove the excellent performance of the linear-to-circular polarization conversion. However, this meta-QWP is suffering from low efficiency (~10%) due to the unwanted energy located to the ordinary reflection and refraction channels, which could be solved by using the MIM [32, 33, 36–38] or all-dielectric [39] QWP

designs. For example, relying on two different GSP-based meta-QWPs with high circular-to-linear polarization conversion efficiencies and phase difference of π between the reflected LP beams, simultaneous circular-to-linear polarization conversion and power splitting at the center wavelength of 850 nm has been demonstrated by Ding and co-workers [103]. In addition to power splitting, advanced functionalities can be, simultaneously and independently, achieved for co- and cross-polarized waves once more GSP-based meta-QWPs that enable efficient circular-to-linear polarization conversion along with the complete phase control over reflected fields are available [75], superior to multifunctional meta-HWPs that can only use the cross-polarized CP channel. In this design, four cross-shaped meta-atoms acting as nano-QWPs have been designed at the wavelength of 850 nm, with the romance phase covering a wide range up to 300°. By combining both resonance and geometric phases, polarization conversion and beam steering of both co- and cross-polarized fields under the RCP incident light could be realized, as shown in the left panel of Figure 5b. Specifically, upon the RCP excitation, the fabricated metasurface could steer the reflected co- and cross-polarized CP waves into −1 and +1 diffraction orders with the diffraction efficiencies of ~32 and ~23.5%, and the measured DoCPs of ~+90.30% and ~−92.00%, respectively (middle and right panel of Figure 5b).

Capitalizing on meta-QWPs, it is also possible to produce structured light under CP excitations [55–57]. The first example is shown in Figure 5c, where vector vortex beams (VVBs) possessing spatially distributed polarization vectors and carrying OAMs have been realized by employing meta-QWPs with azimuthally varied angles [56]. Under the RCP incident light, the AoLP of the reflected LP beam is identical to the azimuthal angle, producing a radially polarized (RP) beam. Meanwhile, this RP beam carries the spiral phase term corresponding to an OAM beam with a topological charge of $l = -1$. Once the incident light is changed to LCP, the output beam will be azimuthally polarized (AP) while the topological charge is reversed

panel: schematic of the TiO$_2$ metasurface and top view of the unit cell. Middle panel: SEM images of the fabricated sample. Right panel: illustration of the spin-selective focused Gaussian and OAM beam generation for bright-field and spiral phase imaging. Reprinted from Ref. [68]. (c) Left panel: schematic of the TiO$_2$ unit cell. Middle panel: SEM image of the fabricated sample. Right panel: measured nanoprinting image illuminated with a halogen lamp without filter (left) and measured holographic image with the sample illuminated by LP incident light at 600 nm (right). Reprinted from Ref. [70]. (d) Left panel: schematic of the HfO$_2$ unit cell. Middle panel: SEM image of the fabricated sample. Right panel: measured holographic image under LCP (top) and RCP (bottom) incident light at $\lambda = 266$ nm. Reprinted from Ref. [69]. (e) Left panel: schematic of the spin-decoupled GSP metasurface composed of nano-HWPs with different dimensions and orientations for unidirectional SPP excitation and beam-steering under RCP and LCP incidence, respectively. Middle panel: SEM images of the fabricated structure. Right panel: phase profiles of the reflected fields under RCP and LCP incident light at $\lambda = 850$ nm. Reprinted from Ref. [74].
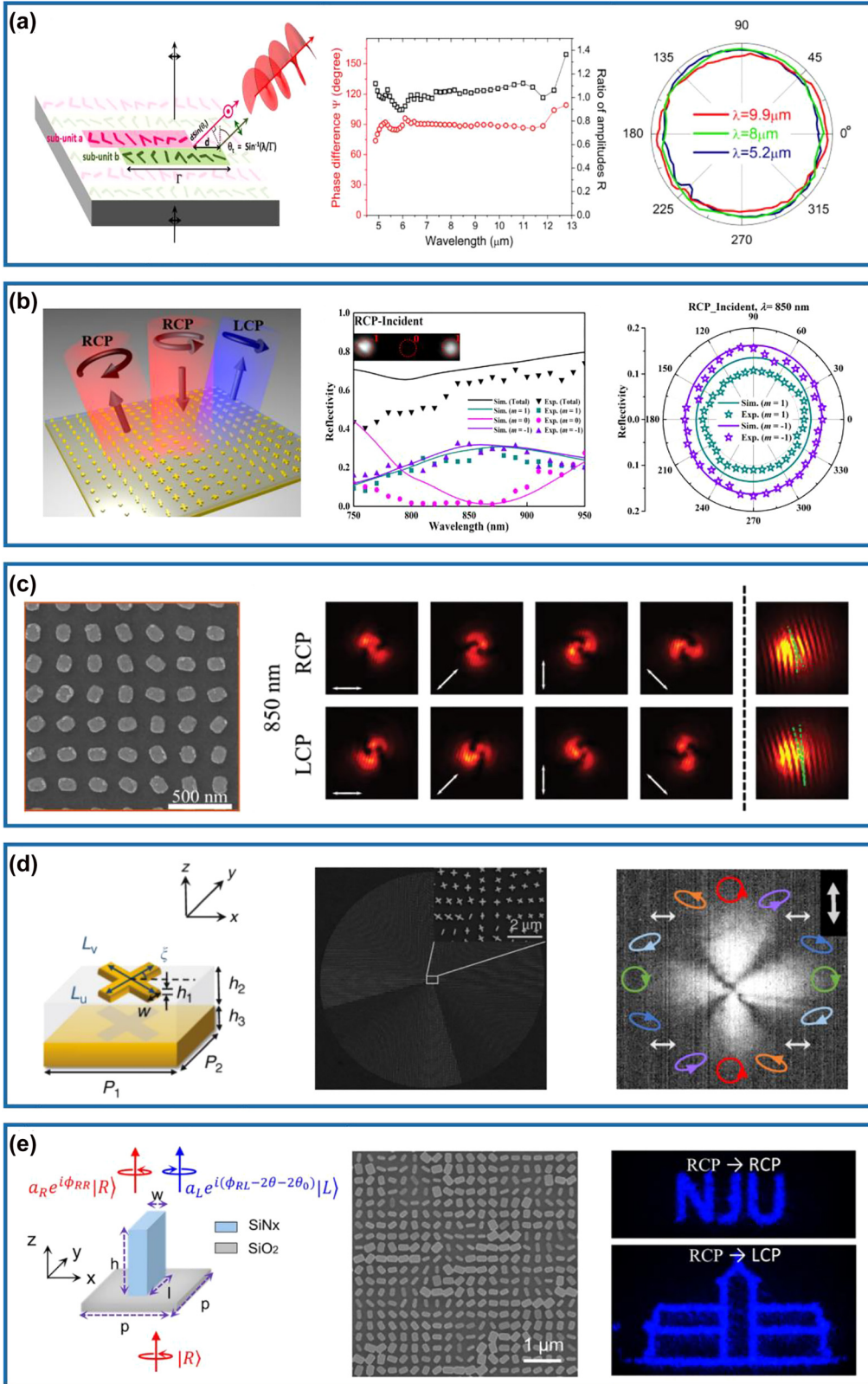
Figure 5: Multifunctional meta-QWPs. (a) Left panel: schematic of the background-free meta-QWP composed of two Au V-shaped antenna subunits. Middle panel: simulated phase difference and ratio of amplitudes between the two scattered waves from the subunits as a function of the wavelength. Right panel: measured SoPs of the extraordinary beam at wavelengths of 5.2, 8, and 9.9 μm. Reprinted from Ref. [102].

(e.g., $l = +1$). Since each QWP element enables broadband circular-to-linear polarization conversion with ~85% reflection efficiency, the demonstrated VVB generator produces RP and AP OAM beams with measured averaging efficiencies of about 72 and 68% in the wavelength spectrum ranging from 750 to 950 nm for the RCP and LCP incident light. Additionally, the generated VVBs can be considered as a superposition of two CP components: the co-polarized CP component carries no OAM (e.g., $l = 0$) and cross-polarized CP component carrying OAM with a topological charge of $l = \pm 2$ for the LCP and RCP incident waves, respectively [58, 104]. If more meta-QWPs with different resonances are involved, arbitrary vector optical fields can be implemented [57]. Zhou's group designed and experimentally demonstrated a vortex beam with varying ellipticity at the working wavelength of 1550 nm, as shown in Figure 5d. In their design, cross-shaped GSP-based QWPs with different resonance phases are properly rotated to supply the additional geometric phase (left and middle panels of Figure 5d). In the experiment shown in the right panel of Figure 5d, four intensity zeros appear when the polarizer is rotated to the vertical direction, manifesting the LP local states. While for the local elliptical or circular polarization states, the intensities with certain strengths are always regardless of the rotation of the polarizer.

Similar to multifunctional meta-HWPs, all-dielectric metasurfaces enable high-performance meta-QWPs with multiple diversified functionalities. Here, we would like to highlight a silicon nitride (SiNx) metasurface QWP with wavefront engineering capabilities for both cross- and co-polarized light simultaneously, as shown in Figure 5e [72]. Based on this platform, an independent spin-sensitive hologram metasurface has been implemented under the RCP incident light, in which the transmitted co-polarized RCP light could be manipulated with the resonance (i.e., propagation) phase to generate a far-field hologram image with "NJU", while the cross-polarized LCP light could be engineered with both resonance and geometric phases to produce a hologram building image of Nanjing University (right panel of Figure 5e).

3 Metasurface-based advanced waveplates

In addition to the aforementioned optical metasurface-based HWPs and QWPs that only perform a single polarization conversion functionality (e.g., linear-to-linear or linear-to-circular polarization conversion), advanced waveplates capable of generating multiple SoPs have been recently developed. In this section, we summarize the advances in this subfield.

3.1 Wavelength-multiplexed, direction-multiplexed, and input-polarization-multiplexed multifunctional meta-waveplates

Various advanced meta-waveplates possessing diverse polarization conversion functionalities beyond HWPs and QWPs have been accordingly demonstrated by multiplexing the wavelength, direction, or input polarization state [105–109]. For example, Cheng et al. have theoretically and experimentally demonstrated an ultrathin multifunctional MIM meta-waveplate that has distinct functionalities at different wavelengths [105]. By adjusting the structural parameters of the metal nanorods in the array, nearly perfect absorption, linear-to-circular conversion, and linear cross-polarization conversion have been integrated into one metasurface with high performance across a large range of incident angles (Figure 6a). Similarly, dielectric metasurfaces can be utilized to achieve wavelength-dependent multifunctional meta-waveplates by employing bilayer meta-atoms [106]. As shown in Figure 6b, by independently controlling the geometry and function of each layer composed of rectangular Si nanopillars, Zhou and co-workers have designed a bilayer metasurface that functions as an HWP at a wavelength of 1200 nm and a QWP at a wavelength of 1600 nm. The polarization conversion efficiency of HWP is larger than 80% over the wavelength range

(b) Left panel: schematic of the GSP gradient metasurface consisting of four cross-shaped QWP meta-atoms to steer co- and cross-polarized CP waves to −1 and +1 diffraction orders under the RCP incident light. Middle panel: simulated and measured diffraction efficiencies as a function of the wavelengths under the RCP incident light. The inset image shows the measured optical spots of diffraction orders at $\lambda = 850$ nm. Right panel: simulated and measured SoPs of the steered beams within −1 and +1 diffraction orders under the RCP incident light at $\lambda = 850$ nm. Reprinted from Ref. [75]. (c) Left panel: the SEM image of the fabricated sample for VVB generation. Right panel: measured intensity distributions of the fabricated sample in the far-field under the RCP and LCP incident light with a linear polarizer at $\lambda = 850$ nm. The rightmost part shows the interference images of the generated vector vortex beam and a copropagating tilted Gaussian beam. Reprinted from Ref. [56]. (d) Left panel: schematic of the cross-shaped MIM meta-QWP. Middle panel: SEM image of the fabricated structure. Right panel: measured optical image of the generated vectorial optical fields with a linear polarizer tilted by 90°. Reprinted from Ref. [57]. (e) Left panel: schematic of the SiNx nanopillar that acts as a meta-QWP. Middle panel: SEM image of the fabricated structure. Right panel: measured hologram images in the RCP and LCP channels under the RCP excitation. Reprinted from Ref. [72].

from 1180 to 1230 nm while the polarization conversion efficiency of QWP reaches 95% at the wavelength of 1616 nm. Except for multifunctional optical waveplates realized at different wavelengths, multifunctional meta-waveplates that work at a single wavelength also arouse great research enthusiasms. Based on plasmonic stepped slit-groove dimers, a novel direction-controlled bifunctional metasurface polarizer with the operating wavelength of 735 nm has been proposed and experimentally

demonstrated by Chen and co-workers, which can be explained by the spin-dependent mode coupling process inside the designed structure [107]. As it is given in Figure 6c, the metasurface behaves as a chiral linear polarizer in the forward direction, which only allows a certain incident spin to transmit and converts it to a specified linear polarization. As for the backward direction, the metasurface acts as an anisotropic circular polarizer, selectively converting a certain linear
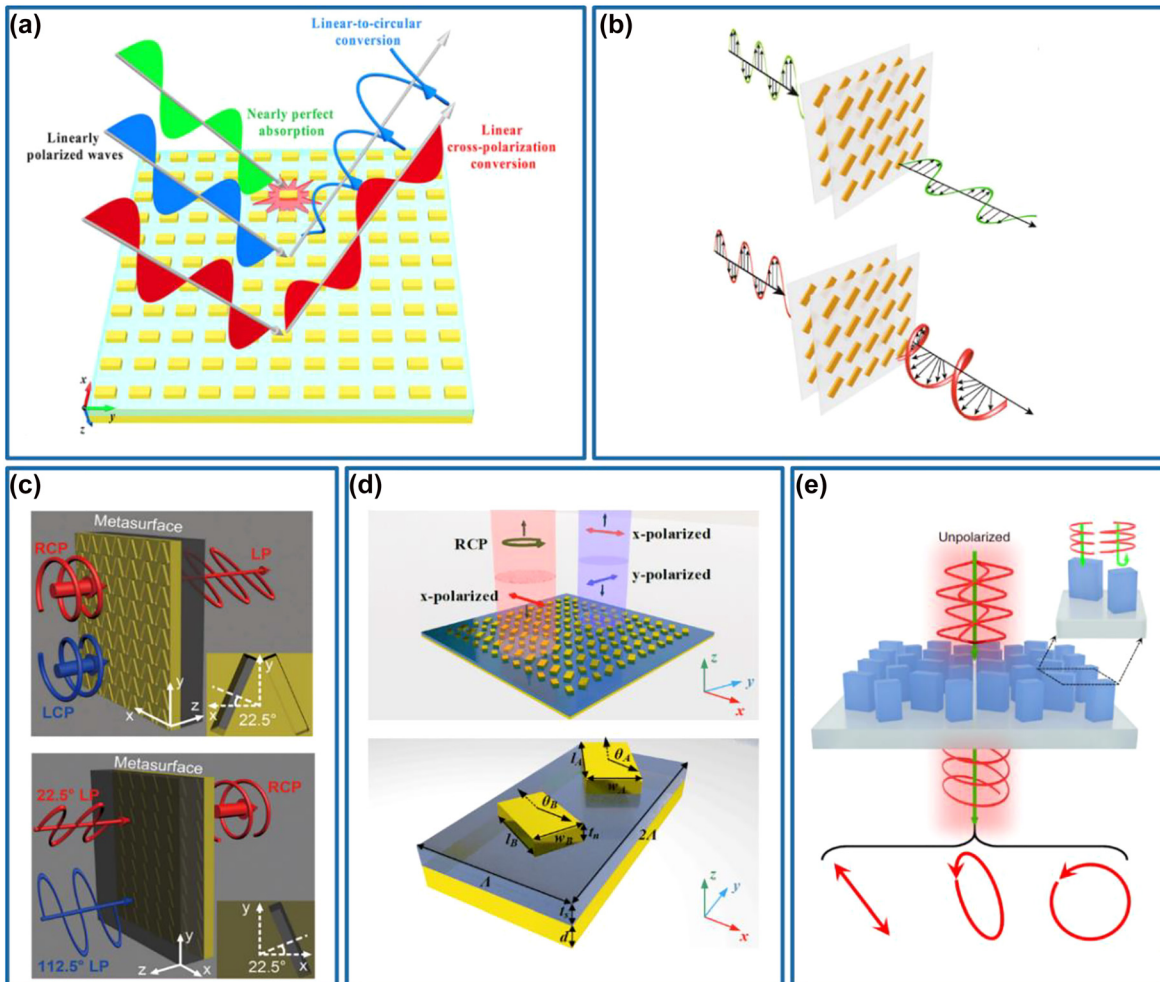

Figure 6: Wavelength-multiplexed, direction-multiplexed, and input-polarization-multiplexed multifunctional meta-waveplates. (a) Schematic of the proposed multifunctional metasurface with the functionalities of nearly perfect absorption, linear-to-circular conversion, and linear cross-polarization conversion at different wavelengths. Reprinted from Ref. [105]. (b) Schematic of the multiwavelength waveplate using a combination of two polarization-sensitive rectangular nanopillar geometries, which functions as an HWP and a QWP at two different and independent wavelengths. Reprinted from Ref. [106]. (c) Top panel: schematic of the metasurface used as a chiral linear polarizer when CP light is incident in the forward direction. Bottom panel: schematic of the metasurface acting as anisotropic circular polarizer when linear polarization light is illuminated in the backward direction. The corresponding unit-cell structures are depicted in the inset with the indicated normal direction of the slits, respectively. Reprinted from Ref. [107]. (d) Top panel: schematic of the dual-functional meta-waveplate that exhibits combined QWP and HWP functionalities for two orthogonal linear polarizations. Bottom panel: schematic of the meta-molecule unit cell. Reprinted from Ref. [108]. (e) Schematic of the all-in-one polarizer that can function at an arbitrary position on the Poincaré sphere, which can directly operate with unpolarized incident light and generate arbitrary polarization states, including linear, elliptical, and circular polarizations, regardless of the incident polarization state. Reprinted from Ref. [109].

polarization component into the desired circular polarization. Apart from the direction-controlled bifunctional meta-waveplate, Cai et al. have designed and experimentally demonstrated a reflective dual-functional meta-waveplate based on periodic GSP meta-molecules [108]. In the design, the theoretical derivation was carried out on the meta-molecule assembled of two GSP meta-atoms to obtain the desired reflection coefficients and rotation angles of the two meta-atoms, which meet the requirements of dual-polarization conversion with the x- and y-polarized incident waves being converted into the RCP and x-polarized reflected waves, respectively. Then, two meta-atoms with distinct dimensions and orientations were optimized and selected to comprise the meta-molecule, as shown in the bottom panel of Figure 6d. The fabricated GSP-based waveplate exhibits combined QWP and HWP functionalities with the measured efficiencies of around 73 and 30% at $\lambda = 850$ nm for orthogonal linear polarizations (top panel of Figure 6d). Furthermore, Wang et al. have presented an effective strategy for designing an all-in-one full Poincaré sphere polarizer with perfect and arbitrary polarization conversion dichroism based on a monolayer all-dielectric metasurface [109]. Based on the matrix transformation of a certain polarization state on the Poincaré sphere, the desired polarization conversion dichroism that allows preferential transmission and conversion of the arbitrary polarization state to its handedness-flipped state while completely blocking its orthogonal state can be physically realized by using two birefringent meta-atoms with distinct dimensions and orientations. The designed arbitrary polarization conversion dichroism metasurface composed of asymmetrically dimerized birefringent crystalline Si meta-atoms exhibits perfect dichroism close to 100% in the simulation and more than 90% in the experiment for arbitrary incident SoPs (Figure 6e).

3.2 Angle-multiplexed multifunctional meta-waveplates

Despite the impressive multiple functionalities achieved for meta-waveplates, most of those polarization-manipulation effects are only demonstrated under normal incidence. Recently, multifunctional meta-waveplates with angle-multiplexed functionalities have also been demonstrated [110–112]. Huang and co-workers have reported a bifunctional metasurface with the ability to produce 97% linear dichroism and 87% circular dichroism in the infrared region for the LP incident waves with different incident angles [110]. Due to the symmetry breaking of the patterned metal

structure, giant linear dichroism and circular dichroism can be realized simultaneously under incident light with orthogonal vertical azimuthal angles, as shown in Figure 7a. However, this design could only generate two different polarization states. To realize more SoPs in the output channel, Shi et al. have demonstrated a topology-optimized dielectric metasurface with continuously transformed birefringence by changing the angle of incidence [111]. In this way, such a single metasurface is able to operate in parallel as different waveplates to achieve different polarization transformations (top panel of Figure 7b). With a varied incident angle, the designed structure is continuously tuned from linear birefringence to elliptical birefringence, thereby enabling versatile polarization transformation. At normal incidence, the eigen-polarization states of the device are LP, which become elliptically polarized at oblique incidence (e.g., −60° and 60°). As a result, for the fixed horizontal linear polarization incidence, the output polarization state changes from the right circular polarization to the horizontal linear polarization and finally to the 45° linear polarization when the angle of incidence varies from −60° to 60° with a step of 60° (bottom panel of Figure 7b). Very recently, Zhou's group has established a general and systematic strategy to guide the design of optical metasurfaces with fully controlled angular dispersions and experimentally demonstrated an incident-angle-dependent multifunctional waveplate [112]. As shown in Figure 7c, the angular dispersions of the metasurface can be explained by the near-field couplings between meta-atoms and the radiation pattern of a single constituent meta-atom. Based on the derived strategies, they have successfully demonstrated an angle-multiplexed MIM meta-waveplate with a relative phase difference $\Delta\varphi$ between two orthogonal linear polarizations varying from 0 to 0.8π as the incident angle increases from 0° to 70° at the design wavelength of 1358 nm (right panel of Figure 7c), corresponding to different waveplates operating at off-normal incident angles.

3.3 Metasurface-based versatile waveplates for all-polarization generation

Except for the previously demonstrated conventional or multifunctional metasurface-based waveplates, a versatile meta-waveplate that is capable of generating arbitrary and well-defined polarization states and manipulating the corresponding output wavefronts simultaneously has become an emerging research topic. In recent years, some works of metasurfaces-based versatile optical waveplates have been reported with different methods [63, 81, 113–118]. Tsai's group has experimentally demonstrated a reflective
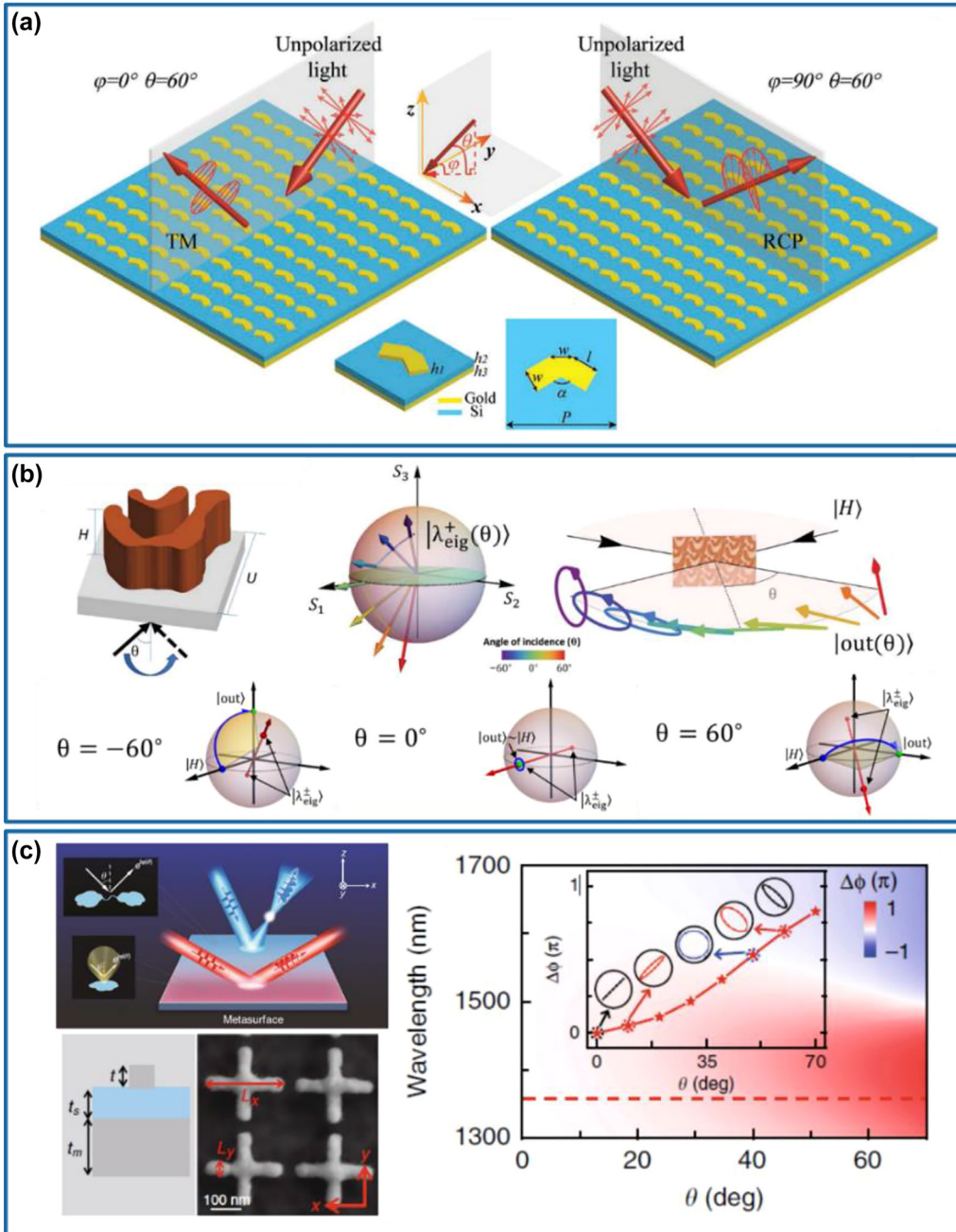
Figure 7: Angle-multiplexed multifunctional meta-waveplates. (a) Schematic of the dual-functional meta-waveplate: for an unpolarized incident wave with 0° azimuthal angle and 60° elevation angle, its TE-polarized component will be totally absorbed and an LP wave with TM polarization can be obtained, while the reflected wave becomes RCP, and the LCP component is absorbed for the incident light with 90° azimuthal angle and 60° elevation angle. The inset shows the 3D and top view of the unit cell. Reprinted from Ref. [110]. (b) Top panel: schematic of the optimized structure and angle-dependent polarization generation. Bottom panel: polarization space representation of the device functionality at different angles. Reprinted from Ref. [111]. (c) Left panel: physical origins of angular dispersions and schematics of the angle-dependent multifunctional meta-device. Right panel: simulated reflection-phase difference between orthogonal linear polarizations versus wavelength and incident angle. The inset shows the reflection phase difference and corresponding polarization states as a function of the incident angle at $\lambda = 1358$ nm. Reprinted from Ref. [112].

GSP-based aluminum meta-waveplate to produce six output beams with different SoPs (e.g., four linear polarization and two circular polarization states) in different diffraction channels under an LP incidence [81]. In the design, two supercells composed of spatially orientated HWP meta-atoms proving geometric phase are placed with different offset distances to induce an additional phase difference [80]. Therefore, the anomalously reflected LCP

and RCP waves are superposed with needed phase delay to produce the desired linear polarization states. However, the capability of wavefront engineering is limited to beam-steering. Wen and co-workers have used a similar method to realize a vectorial hologram image with a spatially continuous distribution of linear polarization states (Figure 8a) [113]. In this work, a phase-only hologram corresponding to the target image is generated with the Gerchberg–Saxton algorithm and achieved with the geometric phase from metal nanorods. Two types of symmetrically inverted nanorod are interleaved together to form the metasurface, in which two neighboring rows form a supercell. Under the x-polarized incidence that contains equal LCP and RCP components and zero phase difference, the obtained holographic image is a superposition of two orthogonal CP images. Based on the displacement of two rows composed of meta-atoms in the supercell of the design, a coordinate-related phase difference between two orthogonal CP images will be generated. As a result, with the determined displacement of two neighboring rows in the supercell, the polarization direction of the combined holographic image varies with the position in the observation plane (middle panel of Figure 8a). As shown in the right panel of Figure 8a, a target image consisting of 13 letters is designed and demonstrated, in which the polarization of the image varies gradually from horizontal polarization to vertical polarization. However, only arbitrary linear polarization states can be achieved with this strategy.

Recently, the geometric phase has been utilized for all-polarization generation and manipulation [63, 114]. For example, Kim and co-workers have proposed a bifunctional metasurface combining both structural color printing and vectorial holography with eight polarization channels simultaneously [114]. The desired bifunctionality is realized from the meta-atom that works as both a Mie-resonator and a waveguide, enabling independent reflection spectra and phase modulation at different locations of the metasurface. Two Si nanopillars are designed to behave as HWPs with the same polarization conversion efficiency but distinct spectral responses. Then, two meta-atom groups composed of meta-atoms rotated in the clockwise and counterclockwise directions with the same angle increment, which allows for the superposition of two orthogonal CP waves with a phase difference of 2δ (left panel of Figure 8b) under an LP incidence. Meanwhile, the amplitude ratio between two orthogonal CP components is controlled by the respective numbers of the two meta-atom groups. In this way, the phase and amplitude modulation of the two orthogonal CP output beams can be realized, thereby generating arbitrary polarization states. In order

to encode multiple holographic images with different polarization states, a pixelated metasurface is adopted, which consists of nine subpixels that are randomly placed with different meta-atom groups and elimination of unwanted grating effect. The right panel of Figure 8b shows nine holographic images with different SoPs. Due to the utilization of different meta-atoms, the conversion efficiency and propagation phase of the output wave are usually dispersive. As a result, the generation of arbitrary well-defined polarization states may only be implemented at a single wavelength. To address this problem, Song et al. have proposed a general strategy for the full-polarization state generation of diffracted signal over an unlimited wavelength range [115]. As shown in Figure 8c, in order to eliminate the dispersion of the conversion efficiency and propagation phase, only one nanopillar with the uniform size is utilized to compose three geometric phase supercells, where one is arranged in counterclockwise rotated line for the LCP output wave and two are arranged in clockwise rotated line for the RCP output wave. For an x-polarized incident wave, the output wave is the superposition of one LCP component and two RCP components, whose polarization state is only related to the starting rotation angle δ_{L1}, δ_{R1}, and δ_{R2} of the three supercells. Likewise, another configuration with one supercell for RCP output wave and two supercells for LCP output wave is also be obtained in the same way. In this way, arbitrary polarization generation with broadband property can be realized, which is experimentally demonstrated across the entire visible range from 475 to 675 nm. Although the above-mentioned versatile meta-waveplates for all-polarization generation have achieved good results, most of them suffer from the relatively large pixel size and the low efficiency due to two identical beams in two directions and unwanted ghost images generated by the periodicity of the supercells.

Different from the previous demonstrations based on the geometric phase, dielectric meta-atoms working as different types of waveplates with engineered phase responses have been used to efficiently produce arbitrary polarization states with controllable wavefronts and smaller pixel sizes [46, 116–118]. Faraon's group has designed a dielectric metasurface platform composed of high-contrast Si elliptical nanoposts to realize complete control of polarization and phase with a subwavelength spatial resolution [46]. Based on such a platform, they have designed a structurally birefringent dielectric metasurface for the realization of vectorial holograms with almost arbitrary polarization patterns for storage and projection of color image data, as shown in Figure 8d [116]. By
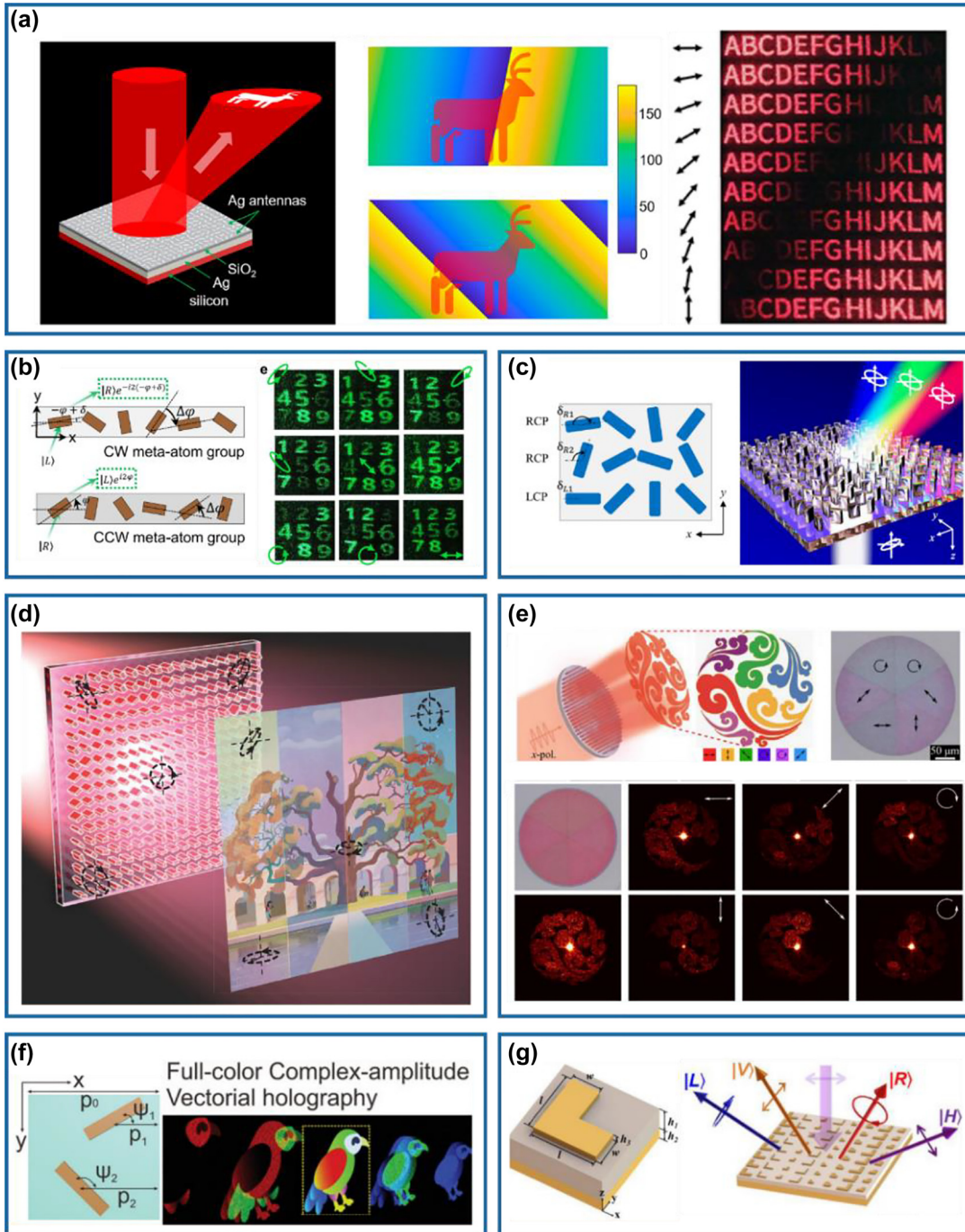
Figure 8: Optical meta-waveplate for all-polarization generation. (a) Left panel: schematic of the metasurface that generates the holographic pattern with continuous polarization distributions. Middle panel: holographic image (deer pattern) with different polarization maps by a slight adjustment of the supercell structure of the metasurface. Right panel: reconstructed holographic images for different polarization directions at $\lambda = 635$ nm. Reprinted from Ref. [113]. (b) Left panel: two types of meta-atom groups to generate outgoing RCP and LCP with arbitrary phase. Right panel: experimental demonstration of the hologram images carrying nine different polarization states. Reprinted from Ref. [114]. (c) Broadband polarization-maintaining design with a uniform size metasurface. Reprinted from Ref. [115]. (d) Schematic of a metasurface polarization hologram that encodes a polarization pattern into an RGB image. Reprinted from Ref. [116]. (e) Top left panel: schematic of the vectorial holographic display, where the holographic image with spatially-varying polarization states is generated with an x-polarized light. Top right panel: optical image of the fabricated meta-hologram. Bottom panel: measured holographic images by illuminating the whole meta-hologram with an x-polarized wave at $\lambda = 850$ nm. Reprinted from Ref. [118]. (f) Left panel: wavelength/angle-independent phase modulations with a diatomic meta-molecule that provides the geometric and detour phases with freely controllable orientations and displacements. Right panel: schematic of the full-color complex-amplitude vectorial meta-hologram. Reprinted from Ref. [120]. (g) Left panel: schematic of the L-shaped MIM meta-atom. Right panel: schematic of the metasurface generating two linear polarization and two circular polarization states. Reprinted from Ref. [122].

converting the red-green-blue (RGB) data in arbitrary color images to Stokes parameters, the required field distributions right after the metasurface are obtained. Based on amorphous Si nanoposts, simultaneous and independent control of the phase and polarization of the transmitted wave is achieved on a subwavelength lattice to generate a polarization hologram. Similarly, Ding et al. have adopted Si-based birefringent meta-atoms with engineered birefringence and phase responses for versatile polarization generation and manipulation. By tuning the dimensions and orientations of the meta-atom with rectangular or ellipse cross-sections, the polarization and phase of the transmitted light can be fully and independently controlled with high transmission efficiency at λ = 850 nm. Therefore, each meta-atom behaves locally as not only a meta-waveplate but a phase modulator, allowing for the conversion from an LP plane wave to any desired output wavefront with the well-defined polarization state. As shown in Figure 8e, six spatially separated transmitted beams with different polarization states as well as specific wavefronts (i.e., hologram) are simultaneously generated under LP incidence. The corresponding measured efficiency of the fabricated polarization-resolved vectorial hologram is ≈51%.

In addition to the great achievements mentioned above, versatile meta-waveplate for all-polarization generation have also been realized by utilizing diatomic meta-atoms [119, 120] and geometrical-scaling-induced (GSI) phase modulations [121, 122]. For instance, Deng and co-workers have proposed a novel diatomic metasurface consisting of meta-molecules formed by two orthogonally oriented meta-atoms for the reconstruction of holographic images with multiple polarization states [119]. Under oblique incidence, the phase and polarization of the reflected wave are modulated by adjusting the displacements and orientations of two identical meta-atoms. Based on the designed diatomic metasurfaces, they further extended the concept to multi-freedom metasurfaces for full-color complex amplitude vectorial holography (Figure 8f) [120]. By tailoring the displacements and orientations of two identical meta-atoms in each meta-molecule, the combination of the detour and geometric phases are used to simultaneously control the phase, amplitude, and polarization of the impinging wavefront element-by-element. Specifically, the detour and geometric phases are proportional to the displacement between adjacent meta-elements and the orientation angle of the meta-element, respectively, which are completely independent of the wavelength and incident angle. Gao et al. have designed metasurfaces made of L-shaped resonators with different geometrical features to generate different types of polarization states simultaneously, by introducing the GSI phase modulation that depends on the geometrical shape and size of each resonator [121, 122]. Upon illumination, the diffracted waves of each resonator with selected geometrical shape, size, and specific spatial sequence location in the unit cell interacted and led to the generation of multiple beams with different types of polarization states simultaneously. In addition, a matrix inversion approach was utilized to realize an easy, concise, and standard selection process for the unit cell. A specific number of diffracted beams with the desired polarization states are experimentally demonstrated, as shown in Figure 8g.

4 Dynamic meta-waveplates

Despite significant advances, the aforementioned optical meta-waveplates are passive and lack real-time tunability, which is not suitable for adaptive photonic integrated systems. In this case, it is crucial to realize dynamic waveplates for active polarization control. Very recently, dynamic optical metasurfaces [123, 124] have been explored to implement dynamic waveplates, where the optical anisotropy can be actively tuned in a wide range by applying external stimuli. In this section, we try to summarize some state-of-the-art dynamic waveplates explored with diverse metasurfaces.

4.1 Optically-triggered dynamic meta-waveplates

To achieve dynamic meta-waveplates, the first method is to optically modify the anisotropy of metasurfaces transiently, thereby resulting in ultrafast switching of light polarization [125–130]. In 2017, Nicholls and co-workers have demonstrated ultrafast all-optical modulation of visible light polarization in an anisotropic (hyperbolic) metamaterial, which is composed of periodic Au nanorods embedded in a dielectric host matrix using a self-assembly technique, as shown in the left panel of Figure 9a [125]. The assembled hyperbolic metamaterial exhibits a strongly enhanced nonlinear effect near its resonance and results in pronounced changes in the ordinary and extraordinary refractive indices upon the excitation of a femtosecond light pulse. Therefore, the retardation between the transmitted ordinary and extraordinary waves can be optically tuned, leading to a >60° rotation of the polarization state for a signal light pulse at the wavelength of 700 nm with a response time of ~10 ps, corresponding to a switch rate of

0.3 THz (right panel of Figure 9a). Specifically, this nonlinearity-induced effect has a working bandwidth of around 40 nm near the effective plasma frequency of the designed metamaterial, where different rotation angles can be observed. To decrease the response time to a sub-picosecond level, an ultrafast tunable high-quality factor perfect absorber based on low-loss and high-mobility indium-doped cadmium oxide (CdO) has been proposed and demonstrated at a wavelength of 2.08 μm, close to the epsilon-near-zero (ENZ) wavelength [126]. Upon sub-bandgap optical pumping (left panel of Figure 9b), the ENZ resonance (i.e., Berreman mode) has a pronounced redshift due to the transient increase of the ensembled-averaged effective electron mass of CdO. Therefore, the p-polarized reflectance increases from 1.0 to 86.3% while the s-polarized reflectance stays the same at the design wavelength, resulting in the polarization switching effect on a timescale of 800 fs for a 45° LP (half p- and s-polarized) input probe pulse (right panel of Figure 9b). For example, the elliptically polarized reflected wave rotates anticlockwise with the polarization angle rotated from −6° to 47° at a delay time of 250 fs after introducing the pump pulse. Despite the fast response and ease of fabrication, this device has a rather low efficiency since it is working in the perfect absorption regime. Additionally, the dynamic range of birefringence is quite limited. In 2021, Kuidong Wang et al. combined the advantages of the anisotropic nonlinear response of indium tin oxide (ITO) at its ENZ region and polarization-sensitive resonance from anisotropic meta-atoms to achieve a strong and ultrafast modulation of light polarization (left panel of Figure 9c) [130]. For a 45° LP incident signal, this ITO-antenna system functions as a transmissive polarizer without any pump due to the polarization selectivity of the plasmonic antennas and the ENZ material. Specifically, it is transparent for the s-polarized component and blocks the p-polarized component at the resonant wavelength of 1230 nm. When the femtosecond pump pulse is applied, an anisotropic nonlinear response is induced, leading to a much stronger amplitude modulation along the p-polarization direction than that for s-polarization one. The device becomes transparent for both s- and p-polarized light at the original resonant wavelength and the polarization ellipse shows a transient rotation. Compared to Ref. [126] where only the ENZ resonance is optically shifted to a longer wavelength, this coupled ITO-antenna system supplies an additional redshift due to the plasmonic resonance, thereby increasing the anisotropic nonlinearity. As a result, a 32.5° rotation of the light polarization together with a $\pi/7$ phase change within 600 fs has been demonstrated (right panel of

Figure 9c), proving the possibility of a high-speed modulation with a bandwidth of ~0.73 THz.

4.2 Electrically-triggered dynamic meta-waveplates

In contrast to optically-triggered dynamic meta-waveplates that necessitate ultrafast lasers, electrically tunable meta-waveplates can be stimulated by integrated electronics and thus are naturally appealing for miniaturized reconfigurable photonic networks and systems [131–135]. Very recently, Liu's group has experimentally demonstrated a liquid crystal (LC) integrated electrically-driven metasurfaces for polarization conversion at visible frequencies by combing both the geometric phase from Au nanorods and tunable propagation phase controlled by the LC layer of only 410 nm [132], which is different from conventional LC-based devices with μm-scale thickness. As shown in the left panel of Figure 10a, the metasurface supercell consists of two rows of Au nanorods with opposite rotation angles to produce reflected RCP and LCP beams in the same direction upon an LP excitation at normal incidence. By covering these two rows with PMMA and LC layers, the reflected RCP and LCP beams gain different and tunable propagation phases and finally superpose as an LP beam with the rotation angle controlled by the applied voltage. When the applied voltage is increased from 4 to 20 V, the polarization angle can be dynamically tuned from 90° to 0° with a measured switching speed of 100 ms (right panel of Figure 10a). To increase the tunable range of birefringence, tri-layer black phosphorus (TLBP) with electrically tunable optical dichroism has been integrated into a Fabry–Pérot (FP) cavity to realize broadband electro-optic polarization conversion in the telecom range [133]. The reflected beam can be azimuthally rotated or converted to circular polarization for an LP incident beam when voltage is applied between the back reflective mirror and TLBP, as shown in the left panel of Figure 10b. Impressively, the converted SoPs can span nearly half the Poincaré sphere. However, such electro-optic polarization conversion can only work in a narrow bandwidth and the performance is very sensitive to the wavelength. For example, the device acts as a QWP and an HWP at wavelengths of 1442 and 1444 nm, respectively (right panel of Figure 10b). In addition, the efficiency of the reflected beam with modulated polarization state is below 10%. Similar to BP, ITO with tunable carrier concentration has been used to design an MIM metasurface for active polarization manipulation with a smaller birefringence range [134].
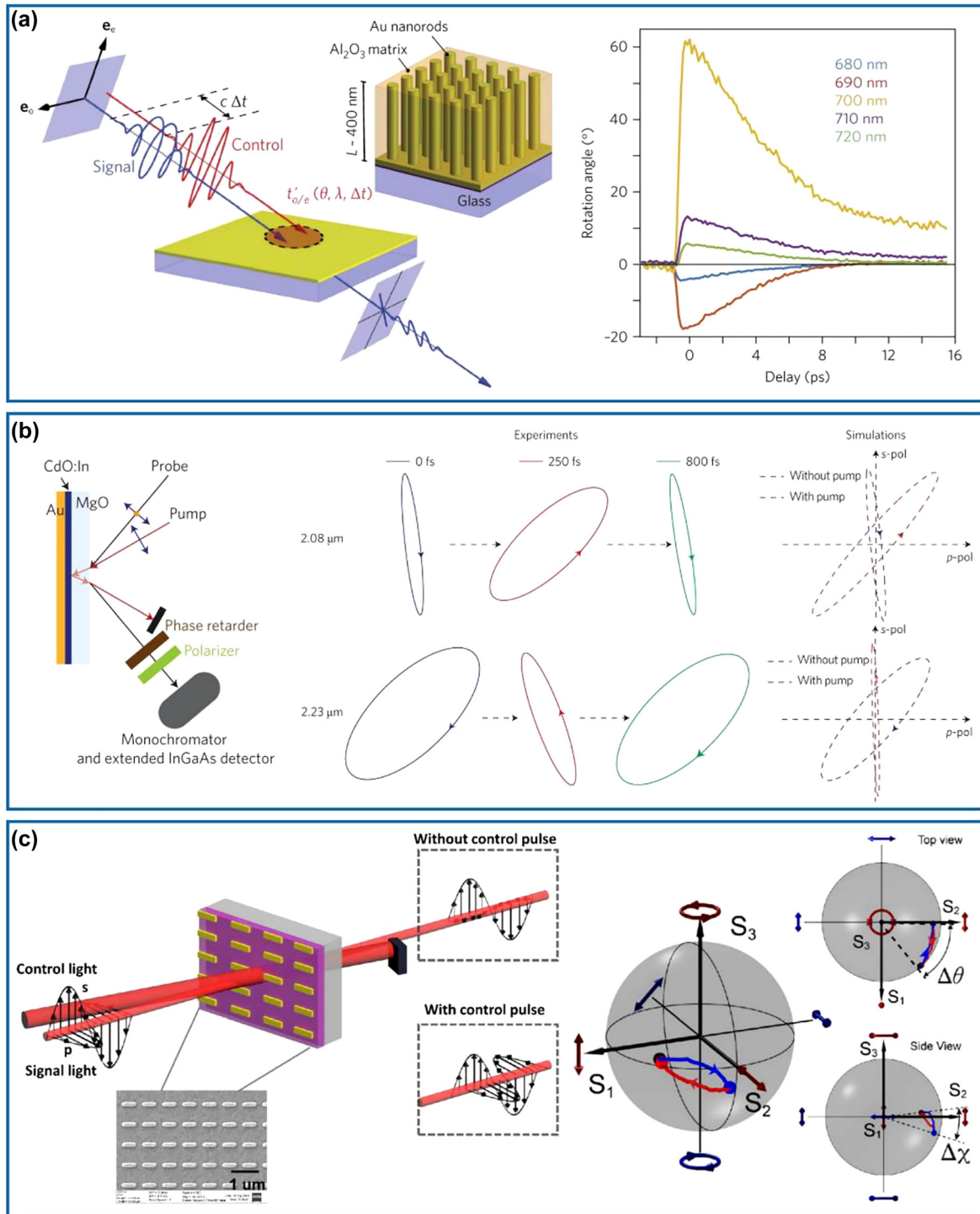
Figure 9: Optically-triggered dynamic meta-waveplates. (a) Left panel: schematic of all-optical switching of visible light polarization with a hyperbolic metamaterial composed of periodic plasmonic Au nanorods in a dielectric matrix, whose anisotropy is first modified by the pump and then probed by time-delayed signal light. Right panel: time-resolved rotation of the polarization ellipse at different wavelengths. Reprinted from Ref. [125]. (b) Left panel: schematic of ultrafast polarization switching with a CdO-based perfect absorber. Middle panel: measured polarization ellipses of the reflected beam at the wavelength of 2.08 and 2.23 μm at a delay time of 0, 250, and 800 fs. Right panel: simulated polarization ellipses of the reflected beam at the wavelength of 2.08 and 2.23 μm with and without a pump. Reprinted from Ref. [126]. (c) Left panel: schematic of the femtosecond light polarization manipulation in an ITO-integrated plasmonic nanoantenna array. Inset shows the SEM image of the fabricated Au nanoantennas. Right panel: dynamics of the polarization state of the transmitted signal light in the Poincaré sphere at the wavelength of 1230 nm. Reprinted from Ref. [130].
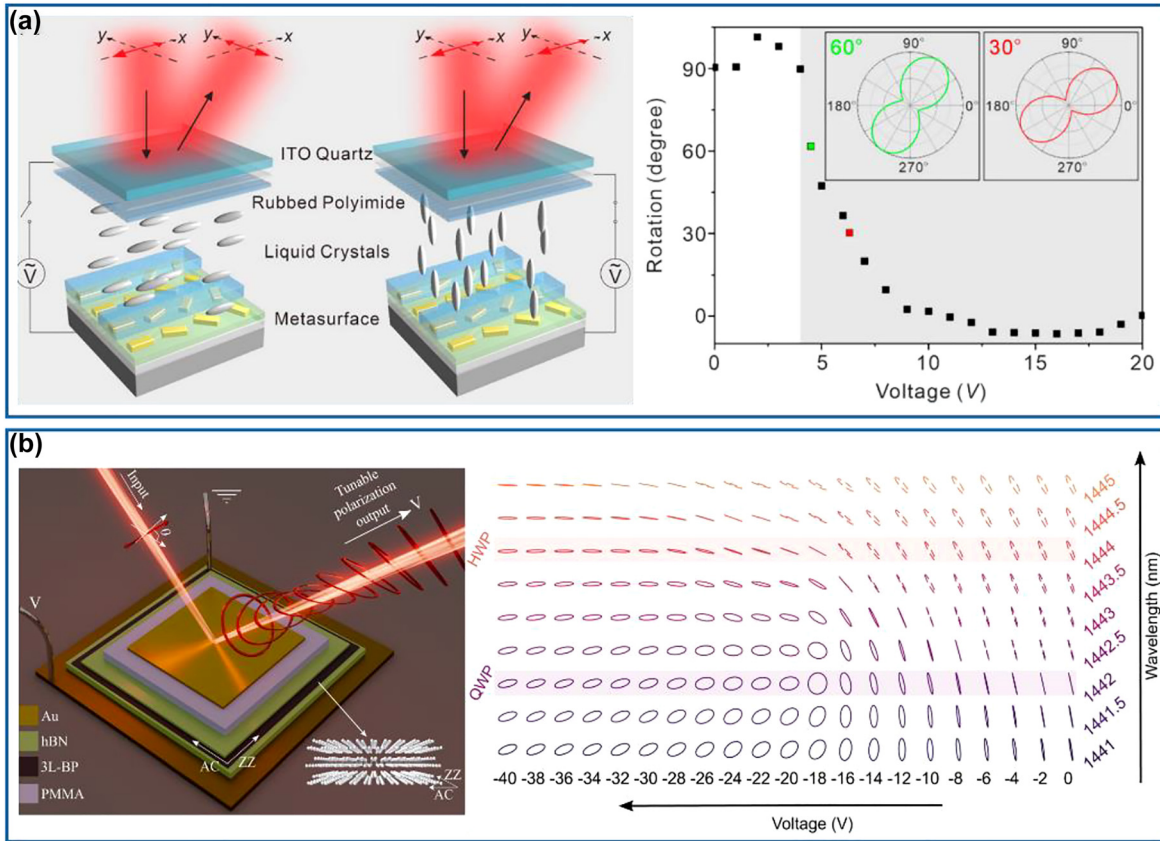
Figure 10: Electrically-triggered dynamic meta-waveplates. (a) Left panel: working principle of the electrically tunable metasurface for active polarization conversion by combining both the geometric from Au antennas and tunable propagation phase supplied by an LC layer. Right panel: measured rotation angle of the linear polarization as a function of the applied voltage. Reprinted from Ref. [132]. (b) Left panel: schematic of electrically tunable polarization conversion with an FP cavity incorporating TLBP with a larger tunability of birefringence. Right panel: measured reflected polarization ellipse for selected voltages and nine different wavelengths. Reprinted from Ref. [133].

5 Conclusions and perspectives

In this review, we have summarized the recent advances in metasurface-enabled optical waveplates, ranging from basic principles to emerging applications. Compared with conventional waveplates, meta-waveplates have not only proven to be a unique platform for polarization optics with compact footprints and largely boosted device performance, but also enabled multiple novel functionalities. With the rapid development in this research field, novel concepts and fancy applications have been witnessed almost every day. On the basis of this notion, here we would like to share our perspectives on three promising directions in the future:

(1) Structured light beyond two dimensions. Conventional structured light, such as complex vectorial optical field [57], is often restricted to the two dimensions of the transverse plane, which lacks the capability to control polarization along the propagation direction. As such,

the capability of generating 3D structured light beyond two dimensions has received intense interest [136]. Very recently, Capasso's group has demonstrated polarization transformation along the optical path by combining birefringent metasurfaces and matrix-based holography [137]. Owing to the versatility and feasibility of metasurfaces, 3D structured light with arbitrary spatial distributions of amplitude, phase, and polarization could be implemented in the near future.

(2) Spatiotemporal meta-waveplates. Spatiotemporal metasurfaces that incorporate both spatial- and time-varying modulation of optical fields have become an emerging research field due to the interesting physics and potential applications for ultrafast pulse shaping [11, 138]. Therefore, controlling the temporal polarization state within a single ultrashort pulse could be a fascinating development for truly arbitrary spatiotemporal pulse shaping. We expect high-performance spatiotemporal meta-atoms to appear in this subfield.

(3) On-waveguide meta-waveplates. So far, most of the meta-waveplates can only control the polarization states of free-space light. To meet the increased demand for bandwidth and speed in information processing, photonic integrated circuits (e.g., waveguides) should be able to utilize and manipulate SoPs of guided waves. However, traditional optical waveguides are hindered by limitations of restrained accessible functionalities and bulk footprint. Synergizing metasurfaces with various optical waveguides can largely empower conventional photonic devices [139–141]. For instance, on-waveguide meta-atoms with a linear phase gradient can bridge the wavevector mismatch between different modes to realize integrated mode converters [140]. However, lots of fundamental and technical issues should be solved before such devices can be really used to arbitrarily generate and manipulate the SoPs of guide modes.

References

[1] D. H. Goldstein, *Polarized Light*, 3rd ed., CRC Press, 2016.

[2] A. V. Kildishev, A. Boltasseva, and V. M. Shalaev, "Planar photonics with metasurfaces," *Science*, vol. 339, p. 1232009, 2013.

[3] N. F. Yu and F. Capasso, "Flat optics with designer metasurfaces," *Nat. Mater.*, vol. 13, pp. 139–150, 2014.

[4] H. T. Chen, A. J. Taylor, and N. F. Yu, "A review of metasurfaces: physics and applications," *Rep. Prog. Phys.*, vol. 79, p. 076401, 2016.

[5] P. Genevet, F. Capasso, F. Aieta, M. Khorasaninejad, and R. Devlin, "Recent advances in planar optics: from plasmonic to dielectric metasurfaces," *Optica*, vol. 4, pp. 139–152, 2017.

[6] H.-H. Hsiao, C. H. Chu, and D. P. Tsai, "Fundamentals and applications of metasurfaces," *Small Methods*, vol. 1, p. 1600064, 2017.

[7] F. Ding, A. Pors, and S. I. Bozhevolnyi, "Gradient metasurfaces: a review of fundamentals and applications," *Rep. Prog. Phys.*, vol. 81, p. 026401, 2018.

[8] S. M. Kamali, E. Arbabi, A. Arbabi, and A. Faraon, "A review of dielectric optical metasurfaces for wavefront control," *Nanophotonics*, vol. 7, pp. 1041–1068, 2018.

[9] X. G. Luo, "Subwavelength optical engineering with metasurface waves," *Adv. Opt. Mater.*, vol. 6, p. 1701201, 2018.

[10] S. L. Sun, Q. He, J. M. Hao, S. Y. Xiao, and L. Zhou, "Electromagnetic metasurfaces: physics and applications," *Adv. Opt. Photon*, vol. 11, pp. 380–479, 2019.

[11] A. M. Shaltout, V. M. Shalaev, and M. L. Brongersma, "Spatiotemporal light control with active metasurfaces," *Science*, vol. 364, p. eaat3100, 2019.

[12] Y. Q. Hu, X. D. Wang, X. H. Luo, et al., "All-dielectric metasurfaces for polarization manipulation: principles and emerging applications," *Nanophotonics*, vol. 9, pp. 3755–3780, 2020.

[13] N. A. Rubin, Z. J. Shi, and F. Capasso, "Polarization in diffractive optics and metasurfaces," *Adv. Opt Photon*, vol. 13, pp. 836–970, 2021.

[14] J. W. Yoon, K. J. Lee, and R. Magnusson, "Ultra-sparse dielectric nanowire grids as wideband reflectors and polarizers," *Opt. Express*, vol. 23, pp. 28849–28856, 2015.

[15] H. Hemmati, P. Bootpakdeetam, and R. Magnusson, "Metamaterial polarizer providing principally unlimited extinction," *Opt. Lett.*, vol. 44, pp. 5630–5633, 2019.

[16] P. Bootpakdeetam, H. Hemmati, and R. Magnusson, "Cascaded metamaterial polarizers for the visible region," *Opt. Lett.*, vol. 45, pp. 6831–6834, 2020.

[17] L. Y. M. Tobing, M. Wasiak, D. H. Zhang, W. J. Fan, and T. Czyszanowski, "Nearly total optical transmission of linearly polarized light through transparent electrode composed of GaSb monolithic high-contrast grating integrated with gold," *Nanophotonics*, vol. 10, pp. 3823–3830, 2021.

[18] T. Cai, S. W. Tang, G. M. Wang, et al., "High-performance bifunctional metasurfaces in transmission and reflection geometries," *Adv. Opt. Mater.*, vol. 5, p. 1600506, 2017.

[19] Z. H. Jiang, L. Kang, T. W. Yue, et al., "A single noninterleaved metasurface for high-capacity and flexible mode multiplexing of higher-order Poincaré sphere beams," *Adv. Mater.*, vol. 32, p. 1903983, 2020.

[20] Q. Hu, K. Chen, N. Zhang, et al., "Arbitrary and dynamic Poincaré sphere polarization converter with a time-varying metasurface," *Adv. Opt. Mater.*, vol. 10, p. 2101915, 2021.

[21] N. K. Grady, J. E. Heyes, D. R. Chowdhury, et al., "Terahertz metamaterials for linear polarization conversion and anomalous refraction," *Science*, vol. 340, pp. 1304–1307, 2013.

[22] L. Q. Cong, N. N. Xu, J. Q. Gu, R. J. Singh, J. G. Han, and W. L. Zhang, "Highly flexible broadband terahertz metamaterial quarter-wave plate," *Laser Photon. Rev.*, vol. 8, pp. 626–632, 2014.

[23] D. C. Wang, L. C. Zhang, Y. H. Gu, et al., "Switchable ultrathin quarter-wave plate in terahertz using active phase-change metasurface," *Sci. Rep.*, vol. 5, p. 15020, 2015.

[24] L. Q. Cong, Y. K. Srivastava, H. F. Zhang, X. Q. Zhang, J. G. Han, and R. Singh, "All-optical active THz metasurfaces for ultrafast polarization switching and dynamic beam splitting," *Light Sci. Appl.*, vol. 7, p. 28, 2018.

[25] F. Ding, S. M. Zhong, and S. I. Bozhevolnyi, "Vanadium dioxide integrated metasurfaces with switchable functionalities at terahertz frequencies," *Adv. Opt. Mater.*, vol. 6, p. 1701204, 2018.

[26] A. Pors, M. G. Nielsen, G. D. Valle, M. Willatzen, O. Albrektsen, and S. I. Bozhevolnyi, "Plasmonic metamaterial wave retarders in reflection by orthogonally oriented detuned electrical dipoles," *Opt. Lett.*, vol. 36, pp. 1626–1628, 2011.

[27] Y. Zhao and A. Alù, "Manipulating light polarization with ultrathin plasmonic metasurfaces," *Phys. Rev. B*, vol. 84, p. 205428, 2011.

[28] F. Wang, A. Chakrabarty, F. Minkowski, K. Sun, and Q. H. Wei, "Polarization conversion with elliptical patch nanoantennas," *Appl. Phys. Lett.*, vol. 101, p. 023101, 2012.

[29] A. Roberts and L. Lin, "Plasmonic quarter-wave plate," *Opt. Lett.*, vol. 37, pp. 1820–1822, 2012.

[30] J. J. Cadusch, T. D. James, and A. Roberts, "Experimental demonstration of a wave plate utilizing localized plasmonic resonances in nanoapertures," *Opt. Express*, vol. 21, p. 28450, 2013.

[31] Y. Zhao and A. Alù, "Tailoring the dispersion of plasmonic nanorods to realize broadband optical meta-waveplates," *Nano Lett.*, vol. 13, pp. 1086–1091, 2013.

[32] A. Pors and S. I. Bozhevolnyi, "Efficient and broadband quarter-wave plates by gap-plasmon resonators," *Opt. Express*, vol. 21, pp. 2942–2952, 2013.

[33] Z. H. Jiang, L. Lin, D. Ma, et al., "Broadband and wide field-of-view plasmonic metasurface-enabled waveplates," *Sci. Rep.*, vol. 4, p. 7511, 2014.

[34] Z. C. Li, W. W. Liu, H. Cheng, S. Q. Chen, and J. G. Tian, "Realizing broadband and invertible linear-to-circular polarization converter with ultrathin single layer metasurface," *Sci. Rep.*, vol. 5, p. 18106, 2015.

[35] Q. Y. Qian, P. F. Liu, L. Fan, L. Zhao, and C. H. Wang, "None sharp corner localized surface plasmons resonance based ultrathin metasurface single layer quarter wave plate," *Sci. Rep.*, vol. 11, p. 8956, 2021.

[36] A. Pors, M. G. Nielsen, and S. I. Bozhevolnyi, "Broadband plasmonic half-wave plates in reflection," *Opt. Express*, vol. 38, pp. 513–515, 2013.

[37] S. C. Jiang, X. Xiong, Y. S. Hu, et al., "Controlling the polarization state of light with a dispersion-free metastructure," *Phys. Rev. X*, vol. 4, p. 021026, 2014.

[38] Y. M. Dai, W. Z. Ren, H. B. Cai, H. Y. Ding, N. Pan, and X. P. Wang, "Realizing full visible spectrum metamaterial half-wave plates with patterned metal nanoarray/insulator/metal film structure," *Opt. Express*, vol. 22, p. 7465, 2014.

[39] S. Kruk, B. Hopkins, L. L. Kravchenko, et al., "Broadband highly efficient dielectric metadevices for polarization control," *APL Photonics*, vol. 1, p. 030801, 2016.

[40] J. M. Hao, Y. Yuan, L. X. Ran, et al., "Manipulating electromagnetic wave polarizations by anisotropic metamaterials," *Phys. Rev. Lett.*, vol. 99, p. 063908, 2007.

[41] F. Ding, Y. Q. Yang, R. A. Deshpande, and S. I. Bozhevolnyi, "A review of gap-surface plasmon metasurfaces: fundamentals and applications," *Nanophotonics*, vol. 7, pp. 1129–1156, 2018.

[42] Y. M. Yang, W. Y. Wang, P. Moitra, L. L. Kravchenko, D. P. Briggs, and J. Valentine, "Dielectric meta-reflectarray for broadband linear polarization conversion and optical vortex generation," *Nano Lett.*, vol. 14, pp. 1394–1399, 2014.

[43] W. J. Luo, S. Y. Xiao, Q. He, S. L. Sun, and L. Zhou, "Photonic spin Hall effect with nearly 100% efficiency," *Adv. Opt. Mater.*, vol. 3, pp. 1102–1108, 2015.

[44] S. J. Ma, X. K. Wang, W. J. Luo, et al., "Ultra-wide band reflective metamaterial wave plates for terahertz waves," *Europhys. Lett.*, vol. 117, p. 37007, 2017.

[45] F. Ding, S. W. Tang, and S. I. Bozhevolnyi, "Recent advances in polarization-encoded optical metasurfaces," *Adv. Photon. Res.*, vol. 2, p. 2000173, 2021.

[46] A. Arbabi, Y. Horie, M. Bagheri, and A. Faraon, "Dielectric metasurfaces for complete control of phase and polarization with subwavelength spatial resolution and high transmission," *Nat. Nanotechnol.*, vol. 10, pp. 937–943, 2015.

[47] A. I. Kuznetsov, A. E. Miroshnichenko, M. L. Brongersma, Y. S. Kivshar, and B. Lukyanchuk, "Optically resonant dielectric nanostructures," *Science*, vol. 354, p. aag2472, 2016.

[48] Q. Zhang, M. Z. Li, T. D. Liao, and X. D. Cui, "Design of beam deflector, splitters, wave plates and metalens using photonic elements with dielectric metasurface," *Opt. Commun.*, vol. 411, pp. 93–100, 2018.

[49] S. Gao, C. S. Park, S. S. Lee, and D. Y. Choi, "All-dielectric metasurfaces for simultaneously realizing polarization rotation and wavefront shaping of visible light," *Nanoscale*, vol. 11, pp. 4083–4090, 2019.

[50] Q. W. Zhou, M. Z. Liu, W. Q. Zhu, et al., "Generation of perfect vortex beams by dielectric geometric metasurface for visible light," *Laser Photon. Rev.*, vol. 15, p. 2100390, 2021.

[51] W. Liu and Y. S. Kivshar, "Generalized Kerker effects in nanophotonics and meta-optics," *Opt. Express*, vol. 26, p. 13085, 2018.

[52] W. J. Luo, S. L. Sun, H. X. Xu, Q. He, and L. Zhou, "Transmissive ultrathin Pancharatnam-Berry metasurfaces with nearly 100% efficiency," *Phys. Rev. Appl.*, vol. 7, p. 044033, 2017.

[53] M. Jia, Z. Wang, H. T. Li, et al., "Efficient manipulations of circularly polarized terahertz waves with transmissive metasurfaces," *Light Sci. Appl.*, vol. 8, p. 16, 2019.

[54] F. Ding, Y. T. Chen, and S. I. Bozhevolnyi, "Focused vortex-beam generation using gap-surface plasmon metasurfaces," *Nanophotonics*, vol. 9, pp. 371–378, 2020.

[55] F. Y. Yue, D. D. Wen, J. T. Xin, B. D. Gerardot, J. Li, and X. Z. Chen, "Vector vortex beam generation with a single plasmonic metasurface," *ACS Photonics*, vol. 3, pp. 1558–1563, 2016.

[56] J. T. Heiden, F. Ding, J. Linnet, Y. Q. Yang, J. Beermann, and S. I. Bozhevolnyi, "Gap-surface plasmon metasurfaces for broadband circular-to-linear polarization conversion and vector vortex beam generation," *Adv. Opt. Mater.*, vol. 7, p. 1801414, 2019.

[57] D. Y. Wang, F. F. Liu, T. Liu, S. L. Sun, Q. He, and L. Zhou, "Efficient generation of complex vectorial optical fields with metasurfaces," *Light Sci. Appl.*, vol. 10, p. 67, 2021.

[58] Z. R. Cai, C. Wu, J. Jiang, Y. T. Ding, Z. W. Zheng, and F. Ding, "Phase-change metasurface for switchable vector vortex beam generation," *Opt. Express*, vol. 29, p. 42762, 2021.

[59] G. X. Zheng, H. Mühlenbernd, M. Kenney, G. X. Li, T. Zentgraf, and S. Zhang, "Metasurface holograms reaching 80% efficiency," *Nat. Nanotechnol.*, vol. 10, pp. 308–312, 2015.

[60] L. L. Huang, H. Mühlenbernd, X. W. Li, et al., "Broadband hybrid holographic multiplexing with geometric metasurfaces," *Adv. Mater.*, vol. 27, pp. 6444–6449, 2015.

[61] D. D. Wen, F. Y. Yue, G. X. Li, et al., "Helicity multiplexed broadband metasurface holograms," *Nat. Commun.*, vol. 6, p. 8241, 2015.

[62] S. Choudhury, U. Guler, A. Shaltout, V. M. Shalaev, A. V. Kildishev, and A. Boltasseva, "Pancharatnam–Berry phase manipulating metasurface for visible color hologram based on low loss silver thin film," *Adv. Opt. Mater.*, vol. 5, p. 1700196, 2017.

[63] Q. H. Song, A. Baroni, R. Sawant, et al., "Ptychography retrieval of fully polarized holograms from geometric-phase metasurfaces," *Nat. Commun.*, vol. 11, p. 2651, 2020.

[64] H. R. Ren, X. Y. Fang, J. Jang, J. Bürger, J. Rho, and S. A. Maier, "Complex-amplitude metasurface-based orbital angular momentum holography in momentum space," *Nat. Nanotechnol.*, vol. 15, pp. 948–955, 2020.

[65] Y. J. Bao, J. H. Yan, X. G. Yang, C. W. Qiu, and B. J. Li, "Point-source geometric metasurface holography," *Nano Lett.*, vol. 21, pp. 2332–2338, 2021.

[66] X. Liang, L. G. Deng, X. Shan, et al., "Asymmetric hologram with a single-size nanostructured metasurface," *Opt. Express*, vol. 29, p. 19964, 2021.

[67] H. R. Ren, G. Briere, X. Y. Fang, et al., "Metasurface orbital angular momentum holography," *Nat. Commun.*, vol. 10, p. 2986, 2019.

[68] P. C. Huo, C. Zhang, W. Q. Zhu, et al., "Photonic spin-multiplexing metasurface for switchable spiral phase contrast imaging," *Nano Lett.*, vol. 20, pp. 2791–2798, 2020.

[69] C. Zhang, S. Divitt, Q. B. Fan, et al., "Low-loss metasurface optics down to the deep ultraviolet region," *Light Sci. Appl.*, vol. 9, p. 55, 2020.

[70] Z. L. Li, C. Chen, Z. Q. Guan, et al., "Three-channel metasurfaces for simultaneous meta-holography and meta-nanoprinting: a single-cell design approach," *Laser Photon. Rev.*, vol. 14, p. 2000032, 2020.

[71] J. X. Li, Y. Q. Wang, C. Chen, et al., "From lingering to rift: metasurface decoupling for near- and far-field functionalization," *Adv. Mater.*, vol. 33, p. 2007507, 2021.

[72] C. Chen, S. L. Gao, X. J. Xiao, et al., "Highly efficient metasurface quarter-wave plate with wave front engineering," *Adv. Photon. Res.*, vol. 2, p. 2000154, 2021.

[73] F. Ding, Z. X. Wang, S. L. He, V. M. Shalaev, and A. V. Kildishev, "Broadband High-Efficiency Half-Wave Plate: a supercell-based plasmonic metasurface approach," *ACS Nano*, vol. 9, pp. 4111–4119, 2015.

[74] C. Meng, S. W. Tang, F. Ding, and S. I. Bozhevolnyi, "Optical gap-surface plasmon metasurfaces for spin-controlled surface plasmon excitation and anomalous beam steering," *ACS Photonics*, vol. 7, pp. 1849–1856, 2020.

[75] Y. D. Deng, C. Wu, C. Meng, S. I. Bozhevolnyi, and F. Ding, "Functional metasurface quarter-wave plates for simultaneous polarization conversion and beam steering," *ACS Nano*, vol. 15, pp. 18532–18540, 2021.

[76] F. Ding, Y. T. Chen, and S. I. Bozhevolnyi, "Gap-surface plasmon metasurfaces for linear-polarization conversion, focusing, and beam splitting," *Photon. Res.*, vol. 8, pp. 707–714, 2020.

[77] N. F. Yu, P. Genevet, M. A. Kats, et al., "Light propagation with phase discontinuities: generalized laws of reflection and refraction," *Science*, vol. 334, pp. 333–337, 2011.

[78] Z. Bomzon, G. Biener, V. Kleiner, and E. Hasman, "Space-variant Pancharatnam–Berry phase optical elements with computer-generated subwavelength gratings," *Opt. Lett.*, vol. 27, pp. 1141–1143, 2002.

[79] Z. Bomzon, G. Biener, V. Kleiner, and E. Hasman, "Radially and azimuthally polarized beams generated by space-variant dielectric subwavelength gratings," *Opt. Lett.*, vol. 27, pp. 285–287, 2002.

[80] A. Shaltout, J. J. Liu, V. M. Shalaev, and A. V. Kildishev, "Optically active metasurface with non-chiral plasmonic nanoantennas," *Nano Lett.*, vol. 14, pp. 4426–4431, 2014.

[81] P. C. Wu, W. Y. Tsai, W. T. Chen, et al., "Versatile polarization generation with an aluminum plasmonic metasurface," *Nano Lett.*, vol. 17, pp. 445–452, 2017.

[82] Y. C. Qiu, S. W. Tang, T. Cai, H. X. Xu, and F. Ding, "Fundamentals and applications of spin-decoupled Pancharatnam–Berry metasurfaces," *Front. Optoelectron.*, vol. 14, pp. 134–147, 2021.

[83] D. M. Lin, P. Y. Fan, E. Hasman, and M. L. Brongersma, "Dielectric gradient metasurface optical elements," *Science*, vol. 345, pp. 298–302, 2014.

[84] M. Khorasaninejad and K. B. Crozier, "Silicon nanofin grating as a miniature chirality-distinguishing beam-splitter," *Nat. Commun.*, vol. 5, p. 5386, 2014.

[85] E. Maguid, I. Yulevich, D. Veksler, V. Kleiner, M. L. Brongersma, and E. Hasman, "Photonic spin-controlled multifunctional shared-aperture antenna array," *Science*, vol. 352, pp. 1202–1206, 2016.

[86] M. Khorasaninejad, W. T. Chen, R. C. Devlin, J. Oh, A. Y. Zhu, and F. Capassp, "Metalenses at visible wavelengths: diffraction-limited focusing and subwavelength resolution imaging," *Science*, vol. 352, pp. 1190–1194, 2016.

[87] Q. H. Song, A. Baroni, P. C. Wu, et al., "Broadband decoupling of intensity and polarization with vectorial Fourier metasurfaces," *Nat. Commun.*, vol. 12, p. 3631, 2021.

[88] W. T. Chen, A. Y. Zhu, V. Sanjeev, et al., "A broadband achromatic metalens for focusing and imaging in the visible," *Nat. Nanotechnol.*, vol. 13, pp. 220–226, 2018.

[89] S. M. Wang, P. C. Wu, V. C. Su, et al., "A broadband achromatic metalens in the visible," *Nat. Nanotechnol.*, vol. 13, pp. 227–232, 2018.

[90] G. D. Wilk, R. M. Wallace, and J. M. Anthony, "High-κ gate dielectrics: current status and materials properties considerations," *J. Appl. Phys.*, vol. 89, pp. 5243–5275, 2001.

[91] J. Robertson, "High dielectric constant oxides," *Eur. Phys. J. Appl. Phys.*, vol. 28, pp. 265–291, 2004.

[92] J. P. B. Mueller, N. A. Rubin, R. C. Devlin, B. Groever, and F. Capasso, "Metasurface polarization optics: independent phase control of arbitrary orthogonal states of polarization," *Phys. Rev. Lett.*, vol. 118, p. 113901, 2017.

[93] R. C. Devlin, A. Ambrosio, N. A. Rubin, J. P. B. Mueller, and F. Capasso, "Arbitrary spin-to–orbital angular momentum conversion of light," *Science*, vol. 358, pp. 896–901, 2017.

[94] A. C. Overvig, S. Shrestha, S. C. Malek, et al., "Dielectric metasurfaces for complete and independent control of the optical amplitude and phase," *Light Sci. Appl.*, vol. 8, p. 92, 2019.

[95] S. Q. Li, X. Y. Li, G. X. Wang, et al., "Multidimensional manipulation of photonic spin hall effect with a single-layer

dielectric metasurface," *Adv. Opt. Mater.*, vol. 7, p. 1801365, 2019.

[96] H. X. Xu, L. Han, Y. Li, et al., "Completely spin-decoupled dual-Phase hybrid metasurfaces for arbitrary wavefront control," *ACS Photonics*, vol. 6, pp. 211–220, 2019.

[97] Y. Xu, Q. Li, X. Zhang, et al., "Spin-decoupled multifunctional metasurface for asymmetric polarization generation," *ACS Photonics*, vol. 6, pp. 2933–2941, 2019.

[98] Q. B. Fan, W. Q. Zhu, Y. Z. Liang, et al., "Broadband generation of photonic spin-controlled arbitrary accelerating light beams in the visible," *Nano Lett.*, vol. 19, pp. 1158–1165, 2019.

[99] R. C. Jin, L. L. Tang, J. Q. Li, et al., "Experimental demonstration of multidimensional and multifunctional metalenses based on photonic spin hall effect," *ACS Photonics*, vol. 7, pp. 512–518, 2020.

[100] D. Y. Wang, T. Liu, Y. J. Zhou, et al., "High-efficiency metadevices for bifunctional generations of vectorial optical fields," *Nanophotonics*, vol. 10, pp. 685–695, 2021.

[101] F. Y. Yue, C. M. Zhang, X. F. Zang, et al., "High-resolution grayscale image hidden in a laser beam," *Light Sci. Appl.*, vol. 7, p. 17129, 2018.

[102] N. F. Yu, F. Aieta, P. Genevet, M. A. Kats, Z. Gaburro, and F. Capasso, "A broadband, background-free quarter-wave plate based on plasmonic metasurfaces," *Nano Lett.*, vol. 12, pp. 6328–6333, 2012.

[103] F. Ding, R. Deshpande, C. Meng, and S. I. Bozhevolnyi, "Metasurface-enabled broadband beam splitters integrated with quarter-wave plate functionality," *Nanoscale*, vol. 12, pp. 14106–14111, 2020.

[104] C. Wu, S. Kumar, Y. H. Kan, et al., "Room-temperature on-chip orbital angular momentum single-photon sources," *Sci. Adv.*, vol. 8, p. 3075, 2022.

[105] H. Cheng, X. Y. Wei, P. Yu, et al., "Integrating polarization conversion and nearly perfect absorption with multifunctional metasurfaces," *Appl. Phys. Lett.*, vol. 110, p. 171903, 2017.

[106] Y. Zhou, I. I. Kravchenko, H. Wang, H. Y. Zheng, G. Gu, and J. Valentine, "Multifunctional metaoptics based on bilayer metasurfaces," *Light. Sci. Appl.*, vol. 8, p. 80, 2019.

[107] Y. Chen, J. Gao, and X. D. Yang, "Direction-controlled bifunctional metasurface polarizers," *Laser. Photon. Rev.*, vol. 12, p. 1800198, 2018.

[108] Z. R. Cai, Y. D. Deng, C. Wu, et al., "Dual-functional optical waveplates based on gap-surface plasmon metasurfaces," *Adv. Opt. Mater.*, vol. 9, p. 2002253, 2021.

[109] S. Wang, Z.-L. Deng, Y. J. Wang, et al., "Arbitrary polarization conversion dichroism metasurfaces for all-in-one full Poincaré sphere polarizers," *Light. Sci. Appl.*, vol. 10, p. 24, 2021.

[110] Y. J. Huang, X. Xie, M. B. Pu, et al., "Dual-functional metasurface toward giant linear and circular dichroism," *Adv. Opt. Mater.*, vol. 8, p. 1902061, 2020.

[111] Z. J. Shi, A. Y. Zhu, Z. Y. Li, et al., "Continuous angle-tunable birefringence with freeform metasurfaces for arbitrary polarization conversion," *Sci. Adv.*, vol. 6, p. eaba3367, 2020.

[112] X. Y. Zhang, Q. Li, F. F. Liu, et al., "Controlling angular dispersions in optical metasurfaces," *Light. Sci. Appl.*, vol. 9, p. 76, 2020.

[113] D. D. Wen, J. J. Cadusch, J. J. Meng, and K. B. Crozier, "Vectorial holograms with spatially continuous polarization distributions," *Nano Lett.*, vol. 21, pp. 1735–1741, 2021.

[114] I. Kim, J. Jang, G. Kim, et al., "Pixelated bifunctional metasurface-driven dynamic vectorial holographic color prints for photonic security platform," *Nat. Commun.*, vol. 12, p. 3614, 2021.

[115] Q. Song, S. Khadir, S. Vézian, et al., "Bandwidth-unlimited polarization-maintaining metasurfaces," *Sci. Adv.*, vol. 7, p. eabe1112, 2021.

[116] R. Z. Zhao, B. Sain, Q. S. Wei, et al., "Multichannel vectorial holographic display and encryption," *Light. Sci. Appl.*, vol. 7, p. 95, 2018.

[117] E. Arbabi, S. M. Kamali, A. Arbabi, and A. Faraon, "Vectorial holograms with a dielectric metasurface: ultimate polarization pattern generation," *ACS Photonics*, vol. 6, pp. 2712–2718, 2019.

[118] F. Ding, B. D. Chang, Q. S. Wei, L. L. Huang, X. W. Guan, and S. I. Bozhevolnyi, "Versatile polarization generation and manipulation using dielectric metasurfaces," *Laser. Photon. Rev.*, vol. 14, p. 2000116, 2020.

[119] Z.-L. Deng, J. H. Deng, X. Zhuang, et al., "Diatomic metasurface for vectorial holography," *Nano Lett.*, vol. 18, pp. 2885–2892, 2018.

[120] Z.-L. Deng, M. K. Jin, X. Ye, et al., "Full-color complex-amplitude vectorial holograms based on multi-freedom metasurfaces," *Adv. Funct. Mater.*, vol. 30, p. 1910610, 2020.

[121] Y.-J. Gao, X. Xiong, Z. H. Wang, F. Chen, R.-W. Peng, and W. Wang, "Simultaneous generation of arbitrary assembly of polarization states with geometrical-scaling-induced phase modulation," *Phys. Rev. X*, vol. 10, p. 031035, 2020.

[122] Y.-J. Gao, Z. Y. Wang, W. J. Tang, et al., "Metasurface design for the generation of an arbitrary assembly of different polarization states," *Phys. Rev. B*, vol. 104, p. 125419, 2021.

[123] Q. He, S. L. Sun, and L. Zhou, "Tunable/reconfigurable metasurfaces: physics and applications," *Research*, vol. 2019, p. 1849272, 2019.

[124] F. Ding, Y. Q. Yang, and S. I. Bozhevolnyi, "Dynamic metasurfaces using phase-change chalcogenides," *Adv. Opt. Mater.*, vol. 7, p. 1801709, 2019.

[125] L. H. Nicholls, F. J. Rodríguez-Fortuño, M. E. Nasir, et al., "Ultrafast synthesis and switching of light polarization in nonlinear anisotropic metamaterials," *Nat. Photonics*, vol. 11, pp. 628–633, 2017.

[126] Y. M. Yang, K. Kelley, E. Sachet, et al., "Femtosecond optical polarization switching using a cadmium oxide-based perfect absorber," *Nat. Photonics*, vol. 11, pp. 390–395, 2017.

[127] M. Taghinejad, H. Taghinejad, Z. H. Xu, et al., "Ultrafast control of phase and polarization of light expedited by hot-electron transfer," *Nano Lett.*, vol. 18, pp. 5544–5551, 2018.

[128] A. Schirato, M. Maiuri, A. Toma, et al., "Transient optical symmetry breaking for ultrafast broadband dichroism in plasmonic metasurfaces," *Nat. Photonics*, vol. 14, pp. 723–727, 2020.

[129] L. Kang, C.-Y. Wang, X. X. Guo, X. J. Ni, Z. W. Liu, and D. H. Werner, "Nonlinear chiral meta-mirrors: enabling technology for ultrafast switching of light polarization," *Nano Lett.*, vol. 20, pp. 2047–2055, 2020.

[130] K. D. Wang, M. H. Li, H.-H. Hsiao, et al., "High contrast, femtosecond light polarization manipulation in epsilon-near-zero material coupled to a plasmonic nanoantenna array," *ACS Photonics*, vol. 8, pp. 2791–2799, 2021.

[131] J. Park, J.-H. Kang, S. J. Kim, X. G. Liu, and M. L. Brongersma, "Dynamic reflection phase and polarization control in metasurfaces," *Nano Lett.*, vol. 17, pp. 407–413, 2017.

[132] P. Yu, J. X. Li, and N. Liu, "Electrically tunable optical metasurfaces for dynamic polarization conversion," *Nano Lett.*, vol. 21, pp. 6690–6695, 2021.

[133] S. Biswas, M. Y. Grajower, K. Watanabe, T. Taniguchi, and H. A. Atwater, "Broadband electro-optic polarization conversion with atomically thin black phosphorus," *Science*, vol. 374, pp. 448–453, 2021.

[134] P. C. Wu, R. Sokhoyan, G. K. Shirmanesh, W.-H. Cheng, and H. A. Atwater, "Near-infrared active metasurface for dynamic polarization conversion," *Adv. Opt. Mater.*, vol. 9, p. 2100230, 2021.

[135] C. Meng, P. C. V. Thrane, F. Ding, and S. I. Bozhevolnyi, "Full-range birefringence control with piezoelectric MEMS-based metasurfaces," preprint, 2021. https://doi.org/10.21203/rs.3.rs-1137478/v1.

[136] A. Forbes, M. D. Oliveira, and M. R. Dennis, "Structured light," *Nat. Photonics*, vol. 15, pp. 253–262, 2021.

[137] A. H. Dorrah, N. A. Rubin, A. Zaidi, M. Tamagnone, and F. Capasso, "Metasurface optics for on-demand polarization transformations along the optical path," *Nat. Photonics*, vol. 15, pp. 287–296, 2021.

[138] S. Divitt, W. Zhu, C. Zhang, H. J. Lezec, and A. Agrawal, "Ultrafast optical pulse shaping using dielectric metasurfaces," *Science*, vol. 364, pp. 890–894, 2019.

[139] D. Ohana, B. Desiatov, N. Mazurski, and U. Levy, "Dielectric metasurface as a platform for spatial mode conversion in nanoscale waveguides," *Nano Lett.*, vol. 16, pp. 7956–7961, 2016.

[140] Z. Y. Li, M.-H. Kim, C. Wang, et al., "Controlling propagation and coupling of waveguide modes using phase-gradient metasurfaces," *Nat. Nanotechnol.*, vol. 12, pp. 675–683, 2017.

[141] Y. Meng, Y. Z. Chen, L. H. Lu, et al., "Optical meta-waveguides for integrated photonics and beyond," *Light Sci. Appl.*, vol. 10, p. 235, 2021.

Dual-Functional Optical Waveplates Based on Gap-Surface Plasmon Metasurfaces

Ziru Cai, Yadong Deng, Cuo Wu, Chao Meng, Yingtao Ding,* Sergey I. Bozhevolnyi, and Fei Ding*

Gap-surface plasmon (GSP) metasurfaces have attracted increasing attention and have become an emerging research area due to their planar configurations, high efficiencies, ease of fabrication, and unprecedented capabilities in manipulating reflected fields, thereby allowing one to reduce a set of bulky optical components to a single ultrathin element with multiplexed functionalities. Herein, a reflective dual-functional optical waveplate based on periodic GSP meta-molecules is designed and experimentally demonstrated, exhibiting combined quarter-waveplate and half-waveplate functionalities, i.e., providing linear-to-circular and linear-to-linear polarization conversion simultaneously, at the same operating wavelength for orthogonal linear polarizations. The proof-of-concept fabricated metasurface demonstrates excellent and distinct polarization conversion functionalities with the efficiencies of ≈73% and 30% at the design wavelength of 850 nm for the orthogonal incident polarizations, well in agreement with the simulations. Owing to the compactness and excellent performance, the demonstrated reflective dual-functional optical waveplate opens yet another avenue for further development of flat polarization optical components with multiplexed functionalities.

1. Introduction

Polarization is one of the most significant characteristics of light that plays an important role in devising and controlling light–matter interactions. Therefore, efficient and accurate manipulation of polarization is critical for numerous applications, such as polarization imaging,[1–3] nonlinear optics,[4,5] and information multiplexing.[6–8] One of the basic and widely used polarization converters, optical waveplates, is typically made

Z. Cai, Prof. Y. Ding
School of Information and Electronics
Beijing Institute of Technology
Beijing 100081, P. R. China
E-mail: ytd@bit.edu.cn

Y. Deng, C. Wu, Dr. C. Meng, Prof. S. I. Bozhevolnyi, Prof. F. Ding
Centre for Nano Optics
University of Southern Denmark
Odense M DK-5230, Denmark
E-mail: feid@mci.sdu.dk

C. Wu
Institute of Fundamental and Frontier Sciences
University of Electronic Science and Technology of China
Chengdu 610054, P. R. China

The ORCID identification number(s) for the author(s) of this article can be found under https://doi.org/10.1002/adom.202002253.

up of birefringent bulk materials, such as crystals and plastics, with the operation principle based on the accumulation of phase difference between two orthogonally polarized waves during their propagation. However, due to limited birefringence available with natural materials, conventional waveplates are inherently bulky and voluminous, characteristics that severely limit their miniaturization and integration prospects essential for modern photonic circuits and systems.

Recently, optical metasurfaces, 2D artificial nanostructure arrays with subwavelength thickness, have attracted progressively increasing attention due to their unprecedented control over optical fields and their significant advantages of featuring flat ultrathin profiles and exhibiting multiple functionalities, thereby providing prospective solutions for cost-effective and high-performance flat optics.[9–12] In contrast to traditional optical devices that shape optical waves with phase variations accumulated gradually as light propagates over distances much longer than its wavelength, metasurfaces are able to directly and locally tailor the amplitude, phase, and polarization of reflected and transmitted optical waves within subwavelength thickness. In recent years, numerous metasurface configurations have been developed demonstrating promising ultra-compact flat optical components and fascinating novel physics phenomena, including beam-steering,[13–18] focusing lenses,[19–26] optical holograms,[27–32] and waveplates.[33–41] For instance, metasurface-based quarter- and half-waveplates (QWPs and HWPs, respectively) that utilize anisotropic meta-atoms to impart different phase retardations on two orthogonally polarized optical components and thus result in high optical birefringence have been achieved.[34–41] However, the aforementioned optical metasurface waveplates can only yield one particular polarization conversion functionality (e.g., linear-to-linear[34,36–40] or linear-to-circular[35,37,39,41] polarization transformation) at the design wavelength, limiting thereby the design freedom and flexibility desirable for further development of ultra-compact integrated photonic devices. Although versatile polarization generators that produce multiple polarization states have been demonstrated by metasurfaces, they mainly rely on segmented or interleaved configurations with individual cells being responsible for specific polarization conversion.[42–45] Development of multifunctional waveplates capable of realizing distinct

ADVANCED
SCIENCE NEWS
www.advancedsciencenews.com

ADVANCED
OPTICAL
MATERIALS
www.advopticalmat.de

polarization conversions for different incident polarizations at the same wavelength would greatly enlarge design capabilities available within flat optics.

In this work, we design and experimentally demonstrate a reflective dual-functional optical waveplate composed of periodic gap-surface plasmon (GSP) meta-molecules with two meta-atoms possessing distinct dimensions and orientations, which operates either as a QWP or an HWP depending on the direction of incident linearly polarization in the near-infrared range. The fabricated multiplexed waveplate exhibits excellent capability of simultaneous linear-to-circular and linear-to-linear polarization conversion with measured efficiencies approaching 73% and 30% at the design wavelength of 850 nm for two orthogonal linear polarizations, respectively, well in agreement with the simulations. The implemented dual-functional GSP waveplate is a result of an innovative approach valuable for advanced research and applications in integrated polarization optics with compact footprints and multiple functionalities.

2. Design and Demonstration of the Dual-Functional Optical Waveplate

2.1. Design of the Dual-Functional Optical Waveplate

The targeted working principle of the reflective dual-functional optical waveplate requires an x-polarized plane wave normally incident on the GSP waveplate to be converted into a right-circular polarization (RCP) reflected wave, while a y-polarized wave should be reflected as the x-polarized one (**Figure 1a**). It is straightforward to show that a unit cell composed of a single subwavelength element is not able to achieve the dual-functional polarization conversion due to insufficient degrees of design freedom.[46] In our configuration, the rectangular GSP meta-molecule consists of two rectangular gold (Au) meta-atoms with different dimensions and orientations sitting on top of a silicon dioxide (SiO$_2$) spacer layer and a continuous bottom Au layer (Figure 1b). Each meta-atom supports two GSP resonances excited by orthogonal polarizations and associated with the resonant formation of standing-wave patterns (in two orthogonal directions) for two counterpropagating GSP modes.[47] The GSP meta-molecules considered in this work are periodically distributed in both the x- and y-directions with periodicities of Λ = 350 nm and 2Λ = 700 nm, respectively.
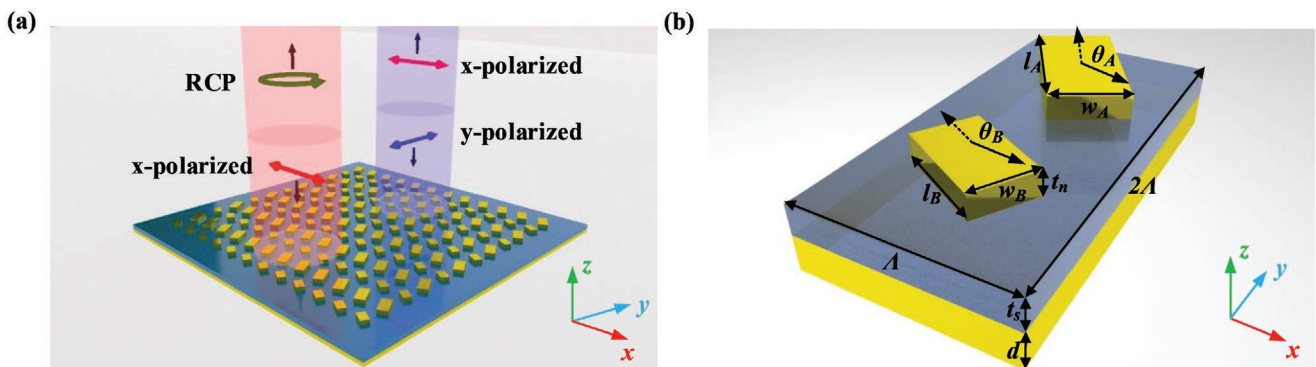
Other configuration parameters are as follows: the thickness of Au meta-atoms is t_n = 50 nm, the thickness of the SiO$_2$ spacer layer is t_s = 70 nm, the thickness of the bottom Au layer is d = 100 nm and thick enough to block light transmission, meta-atom A is tilted at an angle of θ_A with respect to the x-axis having the length and width l_A and w_A, respectively, and the corresponding parameters of meta-atom B are θ_B, l_B, and w_B (Figure 1b).

To realize the dual-polarization conversion with the x-polarization being converted into the RCP and the y-polarization into the x-polarization (at the design wavelength of λ = 850 nm), the reflection coefficient matrix $R = \begin{bmatrix} R_{xx} & R_{xy} \\ R_{yx} & R_{yy} \end{bmatrix}$ of the GSP unit cell should satisfy the following conditions

$$R_{yx} = iR_{xx} \neq 0 \tag{1}$$

$$R_{xy} \neq 0 \tag{2}$$

$$R_{yy} = 0 \tag{3}$$

where R_{xx} (R_{yy}) and R_{xy} (R_{yx}) are the complex reflection coefficients for the co-polarized and cross-polarized reflections, respectively. For example, R_{xy} represents the reflection coefficient for the x-polarized reflected wave when the incident light is y-polarized. According to the Jones matrix,[47] an anisotropic GSP meta-atom rotated with an angle of θ from the x-axis can be described as

$$M = \begin{bmatrix} \cos\theta & -\sin\theta \\ \sin\theta & \cos\theta \end{bmatrix} \begin{bmatrix} M_{xx} & 0 \\ 0 & M_{yy} \end{bmatrix} \begin{bmatrix} \cos\theta & \sin\theta \\ -\sin\theta & \cos\theta \end{bmatrix} \tag{4}$$

where M_{xx} and M_{yy} are the complex reflection coefficients for linearly polarized waves along the two primary axes of the anisotropic meta-atom, respectively. Therefore, the reflection matrices $R_A(R_B)$ of meta-atom A (B) can be expressed as

$$R_A = \begin{bmatrix} \cos\theta_A & -\sin\theta_A \\ \sin\theta_A & \cos\theta_A \end{bmatrix} \begin{bmatrix} r_{Axx}e^{i\delta_{Axx}} & 0 \\ 0 & r_{Ayy}e^{i\delta_{Ayy}} \end{bmatrix} \begin{bmatrix} \cos\theta_A & \sin\theta_A \\ -\sin\theta_A & \cos\theta_A \end{bmatrix} \tag{5}$$

Figure 1. a) Illustration of the working principle of the dual-functional optical waveplate. b) Schematic of the meta-molecule unit cell.

**ADVANCED
SCIENCE NEWS**

www.advancedsciencenews.com

**ADVANCED
OPTICAL
MATERIALS**

www.advopticalmat.de

$$R_B = \begin{bmatrix} \cos\theta_B & -\sin\theta_B \\ \sin\theta_B & \cos\theta_B \end{bmatrix} \begin{bmatrix} r_{Bxx}e^{i\delta_{Bxx}} & 0 \\ 0 & r_{Byy}e^{i\delta_{Byy}} \end{bmatrix} \begin{bmatrix} \cos\theta_B & \sin\theta_B \\ -\sin\theta_B & \cos\theta_B \end{bmatrix}$$

(6)

where r_{Nxx} (r_{Nyy}) and δ_{Nxx} (δ_{Nyy}), with N = A or B, are the reflection amplitudes and phases of the co-polarized components under x-polarized (y-polarized) incidence on meta-atom A or B, respectively. For simplicity, the reflection amplitudes of two meta-atoms are assumed to be equal (i.e., $r_{Axx} = r_{Ayy} = r_{Bxx} = r_{Byy} = r$) and the near-field coupling between meta-atoms is ignored. Provided that the GSP meta-molecule size is smaller than the wavelength and neglecting the near-field coupling between meta-atoms, the meta-molecule reflection matrix for normal incidence can be represented as the sum of individual contributions[46]

$$R = R_A + R_B$$

(7)

With four independent reflection phases and two meta-atoms' orientations, there is infinite multitude of solutions satisfying the requirements expressed by Equations (1)–(3). For this reason, we first set the rotation angles [θ_A, θ_B] as [120°, 150°] to decrease the number of unknown variables and simplify the problem. Then, a specific solution set of [δ_{Axx}, δ_{Ayy}, δ_{Bxx}, δ_{Byy}] = [−212°, −79°, −128°, 6°] is obtained, which gives the relative phase shifts of the reflected waves for both x- and y-polarized incidences.

In order to design the meta-atoms that would exhibit the desired reflection phases, 3D full-wave simulations were performed with COMSOL Multiphysics to map the phase-amplitude response of a GSP meta-atom with varying side lengths. In our simulations, a homogeneous 3D unit cell with a single Au meta-atom is analyzed using periodic boundary conditions applied in both the x- and y-directions, while a perfectly matching layer (PML) was introduced above the structure to truncate the simulation domain. The periodicities along the x- and y-directions were set to be Λ = 350 nm. An x-polarized plane wave was impinging on the structure along the $-z$-direction. The SiO$_2$ spacer layer is regarded as a lossless material with a constant relative permittivity of ε = 2.1 while the relative permittivity of Au is described with the Drude model fitted with

the experimental data, where the damping rate is increased by a factor of 3 to consider the surface scattering and grain boundary effects. The simulated reflection amplitude and phase distributions when the length and width of the Au antenna are both varied from 100 to 300 nm with a step of 10 nm at the design wavelength of 850 nm are shown in **Figure 2**. When l_A = 270 nm, w_A = 140 nm, l_B = 170 nm, and w_B = 110 nm, the phases [δ_{Axx}, δ_{Ayy}, δ_{Bxx}, δ_{Byy}] are equal to [−211.7°, −83.3°, −128.3°, −4.6°], approximating reasonably well the desirable phases. In addition, the corresponding reflection amplitudes r_{Axx}, r_{Ayy}, r_{Bxx}, and r_{Byy} are similar, all being larger than 0.8. As a final comment, it should be noted that the degree of freedom of rotation angles can be used to further improve the reflection amplitudes of the selected meta-atoms (Section S1, Supporting Information).

After selecting the two Au meta-atoms, we assembled the GSP meta-molecule shown in Figure 1b and validated its dual functionality with COMSOL simulations, where both the x- and y-polarized plane waves propagating along the $-z$-direction were alternatively used as the incident waves. The simulation results are shown in **Figure 3a**–c, displaying the reflection amplitudes r_{ji}, phase difference $\Delta\delta_i$, and ellipticity EP$_i$ to characterize the polarization properties of the reflected waves, which are defined as

$$\Delta\delta_i(\lambda) = \delta_{yi}(\lambda) - \delta_{xi}(\lambda)$$

(8)

$$EP_i(\lambda) = \frac{2r_{xi}r_{yi}\sin(\Delta\delta_i)}{r_{xi}^2 + r_{yi}^2}$$

(9)

where λ is the wavelength, and the subscript i stands for the direction of the incident linear polarization state. It is seen (Figure 3a) that the calculated r_{xx}, r_{yx}, and r_{xy} are found to be 0.709, 0.381, and 0.381, respectively, while a relatively large value of r_{yy} = 0.373 is observed at the design wavelength of λ = 850 nm, indicating that the designed metasurface does not satisfy the required conditions (Equations (1)–(3)) and thus is not suitable to function as a QWP and a HWP for the x- and y-polarized waves, respectively. Specifically, the x-polarized incident wave is not converted into the x- and y-polarized
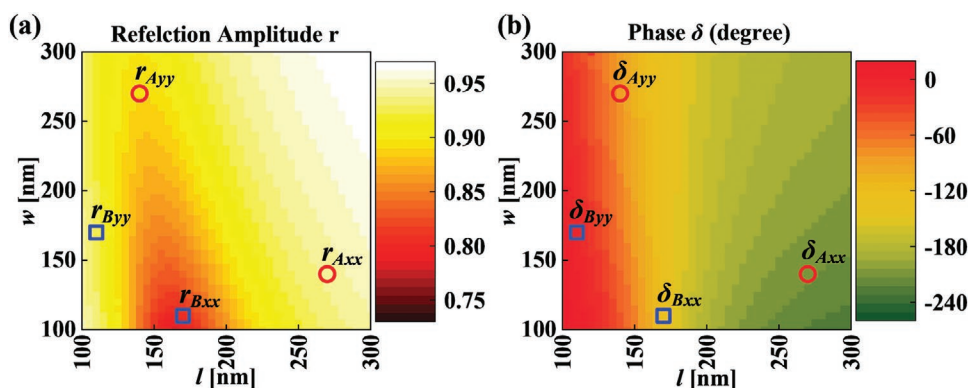

Figure 2. Simulated reflection a) amplitude and b) phase distributions of a single GSP meta-atom as functions of the meta-atom dimensions (i.e., l and w) for x-polarized incident light at the design wavelength λ = 850 nm.

**ADVANCED
SCIENCE NEWS**

www.advancedsciencenews.com

**ADVANCED
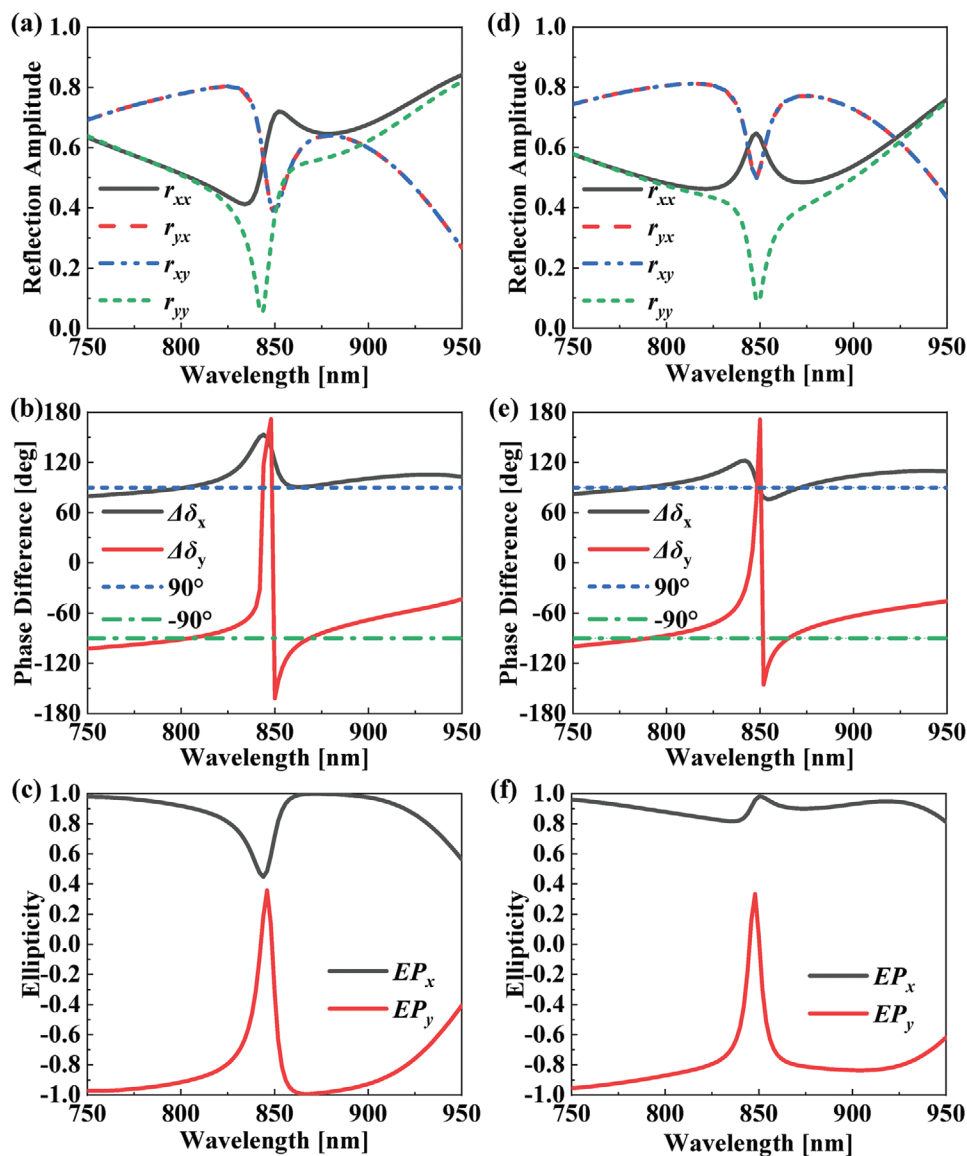OPTICAL
MATERIALS**

www.advopticalmat.de

Figure 3. Simulated a,d) reflection amplitudes, b,e) phase differences, and c,f) ellipticities for the a–c) as-designed and d–f) optimized GSP dual-functional waveplate.

components with similar amplitudes, and the co-polarized reflection (i.e., r_{yy}) is not sufficiently suppressed under the y-polarized excitation. Consequently, the calculated ellipticities are 0.71 and −0.31 for the x- and y-polarized excitations, respectively, deviating much from the theoretical values of 1 and 0. The fact that the two meta-atoms selected to satisfy the conditions stated in Equations (1)–(3) do not add up to make a suitable meta-molecule should be ascribed to the intrinsic near-field coupling between different meta-atoms[48] neglected in our simplified design procedure. Accounting for the near-field coupling would require discarding simple calculation of the meta-molecule reflection, i.e., Equation (5), a change that complicates enormously the design procedure.

Meanwhile, we notice that r_{yy} is greatly reduced to 0.059 while r_{xx} and r_{yx} and r_{xy} become close to each other at another, smaller wavelength of $\lambda = 844$ nm. Since a suitable wavelength

is found very close to the design one, the appropriate meta-molecule parameters at the design wavelength should be located close to those obtained with the simple approach. Conducting random-work optimization, the optimized structural parameters were found to be slightly changed to [θ_A, l_A, w_A, θ_B, l_B, w_B] = [121°, 271 nm, 135 nm, 152°, 175 nm, 110 nm]. The corresponding simulated results reveal a significantly improved performance (Figure 3d–f). Thus, it is seen that r_{xx}, r_{yx}, and r_{xy} have similar values and r_{yy} is significantly suppressed with a small amplitude of 0.096, manifesting that the optimized structure is able to convert the x-polarized incidence into x- and y-polarized components with equal intensities, and the y-polarized incident beam is converted into the x-polarized component at $\lambda = 850$ nm (Figure 3d). Moreover, the phase difference $\Delta\delta_x$ is approximately equal to 90° for the x-polarized incidence while the phase difference $\Delta\delta_y$ is close to 180° when it comes to

2002253 (4 of 8)

**ADVANCED
SCIENCE NEWS**

www.advancedsciencenews.com

**ADVANCED
OPTICAL
MATERIALS**

www.advopticalmat.de
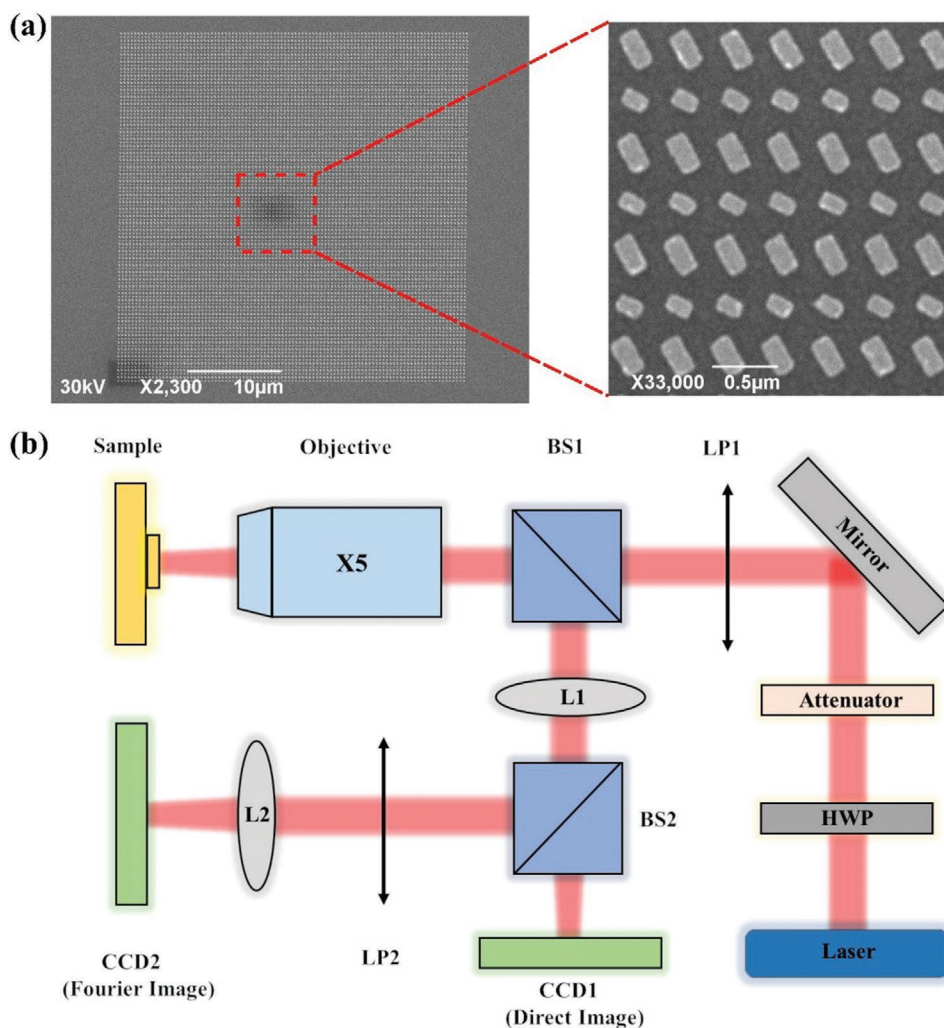
Figure 4. a) Top-view SEM images of the fabricated sample with different magnifications. b) Schematic of the experimental setup for characterizing the GSP dual-functional waveplate.

the y-polarized incidence (Figure 3e). Quantitatively, the calculated ellipticities EP_x and EP_y are approaching 1 and 0, respectively, manifesting the generation of the RCP and x-polarized reflected beams under the x- and y-excitations (Figure 3f).

2.2. Experimental Demonstration of the Dual-Functional Optical Waveplate

The designed reflective dual-functional optical waveplate was fabricated using the standard thin-film deposition, electron-beam lithography, and lift-off techniques (see the Experimental Section for details). The scanning electron microscopy (SEM) images of the sample with different magnifications are shown in **Figure 4**a. Following the fabrication, the prepared device is characterized using a custom-built optical setup, as shown in Figure 4b. The fiber-coupled optical beam from a Ti:Sapphire laser first passes through an HWP, an attenuator, and a linear polarizer (LP1) to adjust the intensity and input polarization (i.e., x- or y-polarization). Then the linearly polarized beam

passes through a beam splitter (BS1) and is slightly focused on the sample by an objective. After that, the reflected signal collected by the same objective is split into two different paths with a second beam splitter (BS2). The direct image on a charge-coupled device (CCD1) can help us to find the sample while the reflected signal is measured in the Fourier plane with CCD2, which ensures a high signal-to-noise ratio. The two focusing lenses (L1 and L2) have the focal lengths of 200 and 100 mm, respectively. To resolve the polarization state of the reflected light, a linear polarizer (LP2) is inserted in front of the CCD2 and rotated during the measurement.

Figure 5a,b displays the polarization measurements of the fabricated dual-functional waveplate for the x- and y-polarized incidences, respectively, where the reflected light was projected along the polarization axis of LP2 whose orientation is varied from 0° to 360° in a step of 10° with respect to the x-axis. From the polar plots, it can be clearly seen that the x-polarized incident beam is converted into an RCP reflected beam with the ellipticity approaching 0.98 while the y-polarized incident beam is rotated to a linearly polarized beam with the ellipticity of 0,
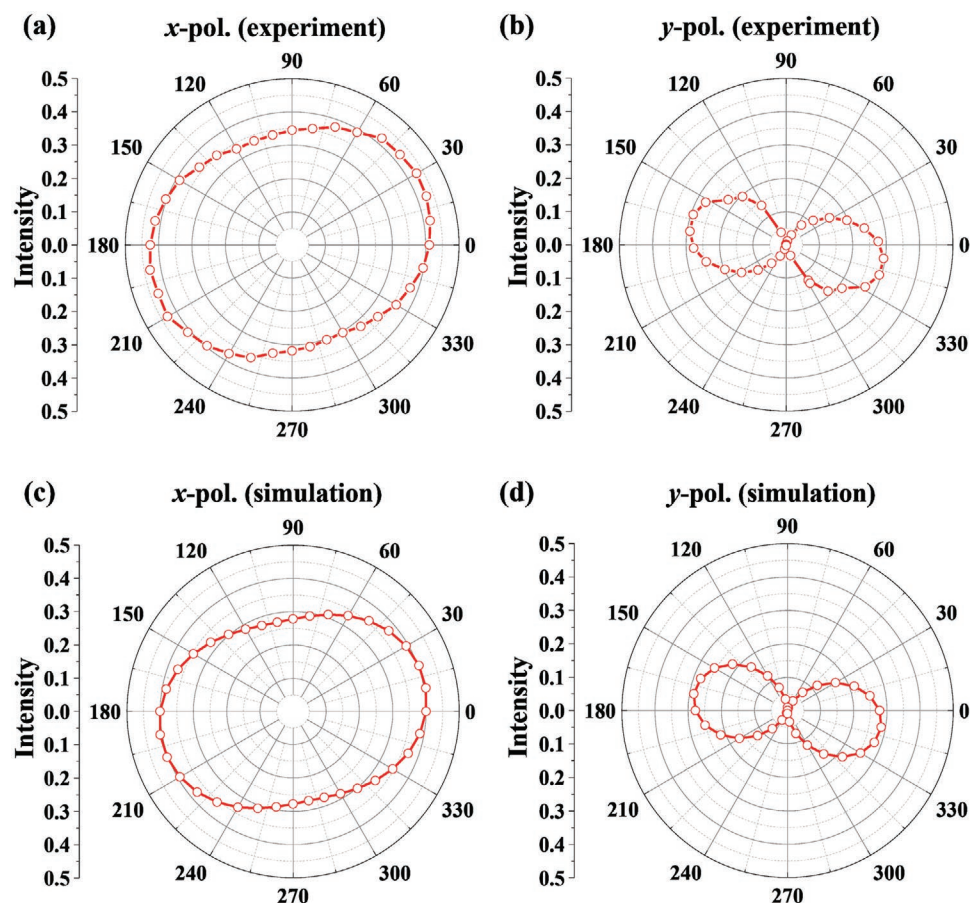
Figure 5. a,b) Measured and c,d) calculated polarization state diagrams of the reflected waves obtained under a,c) *x*-polarized and b,d) *y*-polarized incidence, respectively.

corresponding to the degree of linear polarization (DoLP) of 1. In addition, the measured efficiencies of the fabricated device reach ≈73% and 30% under *x*- and *y*-polarized linear excitations at the design wavelength of 850 nm, which is defined as the ratio of the power carried by the reflected wave to the power reflected from a bare substrate composed of SiO_2 and Au films. Compared to the simulated polar plots in Figure 5c,d, the measured results show excellent agreement in terms of the shapes and efficiencies. Impressively, the measured efficiencies are very close to the calculated efficiencies in simulation, which are around 68% and 29% for the orthogonal linear polarizations. Here it should be mentioned that due to the non-ideal amplitude and phase values, the dual-functional waveplate intrinsically (slightly) deviates in performance from a perfect QWP and an HWP under two linearly polarized excitations. For example, under the *y*-polarized excitation, even though the reflected light is linearly polarized with the DoLP of 1, the angle of linear polarization deviates from 0° in both the simulation and experiment. Specifically, in the measured polarization state diagram, the angle of linear polarization is increased from the simulated value of 10° to ≈12°, which is estimated by interpolating the experimental data. In addition to the intrinsic design limitation, we ascribe this deviation to the fabrication imperfections/errors (Section S2, Supporting Information). We believe that more elaborate optimizations with more parameters involved would enable the linearly polarized reflection along the angle close to or even perfectly along the *x*-axis under the *y*-polarized excitation (Section S3, Supporting Information).

3. Conclusion

In this work, we have utilized an array of periodic GSP meta-molecules to realize a reflective dual-functional optical wave-plate that exhibits combined QWP and HWP functionalities for two orthogonal linear polarizations. The fabricated GSP-based waveplate exhibits the excellent capability of linear-to-circular and linear-to-linear polarization conversions with efficiencies of around 73% and 30% at the wavelength of 850 nm under *x*- and *y*-polarized excitations, respectively, which are in good agreement with the simulation results. The efficiency of the demonstrated dual-functional waveplate can further be increased by exploiting a more elaborate design procedure as discussed above and making use of single-crystalline gold platelets for fabricating the meta-atoms with lower ohmic loss. The demonstrated functionality can be found useful in multifunctional polarization optics, for example by replacing conventional waveplates and implementing full-Stokes polarization cameras, and thereby open new perspectives in the development of ultra-compact and integrated photonic devices.

**ADVANCED
SCIENCE NEWS**

www.advancedsciencenews.com

**ADVANCED
OPTICAL
MATERIALS**

www.advopticalmat.de

4. Experimental Section

Fabrication: The samples were fabricated by using the standard thin-film deposition, electron-beam lithography, and lift-off techniques. First, a 3 nm Ti layer, a 100 nm Au layer, and a 1 nm Ti layer were deposited onto a silicon substrate through thermal evaporation successively. Then, a 70 nm SiO_2 spacer layer was deposited with RF-sputtering. Next, a 100 nm PMMA (2% in anisole, Micro Chem) layer was spin-coated on the SiO_2 layer, baked at 180 °C for 2 min, and exposed at an acceleration voltage of 30 keV to define the meta-molecule patterns. Then, the exposed wafer was developed in the solution of methyl isobutyl ketone (MIBK) and isopropyl alcohol (IPA) of MIBK/IPA = 1:3 for 45 s. After development, a 1 nm Ti adhesion layer and a 50 nm Au layer were deposited subsequently using thermal evaporation. Finally, the top Au nanoantennas were formed after a lift-off process.

Optical Characterization: The components used in the characterization setup (Figure 4b) include a Ti:Sapphire laser (Spectra-Physics, Model 3900S), an HWP (Thorlabs, AHWP05M-980), an attenuator (Thorlabs, FM1), two linear polarizers (LP1 and LP2, Thorlabs, LPN1R050-MP2), two beam splitters (BS1 and BS2, Thorlabs, CM1-BS014), an objective (Mitutoyo, M Plan Apo, 5× magnification), two charge-coupled devices (CCD1 and CCD2, Thorlabs, DCC1545M-GL), and two focusing lenses (L1, Thorlabs, TTL200-S8, f_1 = 200 mm and L2, Thorlabs, AC254-100-B-ML, f_2 = 100 mm).

Supporting Information

Supporting Information is available from the Wiley Online Library or from the author.

Acknowledgements

Conflict of Interest

The authors declare no conflict of interest.

Data Availability Statement

The data that support the findings of this study are available from the corresponding author upon reasonable request.

Keywords

[1] Z.-Y. Jia, F.-Z. Shu, Y.-J. Gao, F. Cheng, R.-W. Peng, R.-H. Fan, Y. Liu, M. Wang, *Phys. Rev. Appl.* **2018**, *9*, 034009.
[2] H. Hu, Q. Gan, Q. Zhan, *Phys. Rev. Lett.* **2019**, *122*, 223901.
[3] N. A. Rubin, D. Gabriele, C. Paul, Z. Shi, W. Chen, F. Capasso, *Science* **2020**, *365*, eaax1839.
[4] G. Li, S. Chen, N. Pholchai, B. Reineke, P. W. H. Wong, E. Y. B. Pun, K. W. Cheah, T. Zentgraf, S. Zhang, *Nat. Mater.* **2015**, *14*, 607.
[5] N. Segal, K. S. Keren-Zur, N. Hendler, T. Ellenbogen, *Nat. Photonics* **2015**, *9*, 180.
[6] J. Wang, J.-Y. Yang, I. M. Fazal, N. Ahmed, Y. Yan, H. Huang, Y. Ren, Y. Yue, S. Dolinar, M. Tur, A. E. Willner, *Nat. Photonics* **2012**, *6*, 488.
[7] Z.-Y. Chen, L.-S. Yan, Y. Pan, L. Jiang, A.-L. Yi, W. Pan, B. Luo, *Light: Sci. Appl.* **2017**, *6*, e16207.
[8] F. Zhang, M. Pu, X. Li, P. Gao, X. Ma, J. Luo, H. Yu, *Adv. Funct. Mater.* **2017**, *27*, 1704295.
[9] A. V. Kildishev, A. Boltasseva, V. M. Shalaev, *Science* **2013**, *339*, 1232009.
[10] N. Yu, F. Capasso, *Nat. Mater.* **2014**, *13*, 139.
[11] H.-T. Chen, A. J. Taylor, N. Yu, *Rep. Prog. Phys.* **2016**, *79*, 076401.
[12] F. Ding, A. Pors, S. I. Bozhevolnyi, *Rep. Prog. Phys.* **2018**, *81*, 026401.
[13] N. Yu, P. Genevet, M. A. Kats, F. Aieta, J.-P. Tetienne, F. Capasso, Z. Gaburro, *Science* **2011**, *334*, 333.
[14] X. Ni, N. K. Emani, A. V. Kildishev, A. Boltasseva, V. M. Shalaev, *Science* **2012**, *335*, 427.
[15] S. Sun, K. Y. Yang, C. M. Wang, T. K. Juan, W. T. Chen, C. Y. Liao, Q. He, S. Xiao, W. T. Kung, G. Y. Guo, L. Zhou, D. P. Tsai, *Nano Lett.* **2012**, *12*, 6223.
[16] A. Pors, O. Albrektsen, I. P. Radko, S. I. Bozhevolnyi, *Sci. Rep.* **2013**, *3*, 2155.
[17] Z. Li, E. Palacios, S. Butun, K. Aydin, *Nano Lett.* **2015**, *15*, 1615.
[18] F. Ding, R. A. Deshpande, S. I. Bozhevolnyi, *Light: Sci. Appl.* **2018**, *7*, 17178.
[19] A. Pors, M. G. Nielsen, R. L. Eriksen, S. I. Bozhevolnyi, *Nano Lett.* **2013**, *13*, 829.
[20] M. Khorasaninejad, W. T. Chen, R. C. Devlin, J. Oh, A. Y. Zhu, F. Capasso, *Science* **2016**, *352*, 1190.
[21] A. Arbabi, E. Arbabi, S. M. Kamali, Y. Horie, S. Han, A. Faraon, *Nat. Commun.* **2016**, *7*, 13682.
[22] S. Wang, J. Lai, T. Wu, C. Chen, J. Sun, *Opt. Express* **2017**, *25*, 7121.
[23] H. Yi, S.-W. Qu, B. J. Chen, X. Bai, K. B. Ng, C. H. Chen, *Sci. Rep.* **2017**, *7*, 3478.
[24] S. Wang, P. C. Wu, V.-C. Su, Y.-C. Lai, C. H. Chu, J.-W. Chen, S.-H. Lu, J. Chen, B. Xu, C.-H. Kuan, T. Li, S. Zhu, D. P. Tsai, *Nat. Commun.* **2017**, *8*, 187.
[25] W. T. Chen, A. Y. Zhu, V. Sanjeev, M. Khorasaninejad, Z. Shi, E. Lee, F. Capasso, *Nat. Nanotechnol.* **2018**, *13*, 220.
[26] L. Li, K. Yao, Z. Wang, Y. Liu, *Laser Photonics Rev.* **2020**, *14*, 1900244.
[27] W. T. Chen, K. Y. Yang, C. M. Wang, Y. W. Huang, G. Sun, I. D. Chiang, C. Y. L. Hsu, H. T. Lin, S. Sun, L. Zhou, A. Liu, D. Tsai, *Nano Lett.* **2014**, *14*, 225.
[28] G. Zheng, H. Mühlenbernd, M. Kenney, G. Li, T. Zentgraf, S. Zhang, *Nat. Nanotechnol.* **2015**, *10*, 308.
[29] Y.-W. Huang, W. T. Chen, W.-Y. Tsai, P. C. Wu, C.-M. Wang, G. Sun, D. P. Tsai, *Nano Lett.* **2015**, *15*, 3122.
[30] D. Wen, F. Yue, G. Li, G. Zheng, K. Chan, S. Chen, M. Chen, K. F. Li, P. W. H. Wong, K. W. Cheah, E. Y. B. Pun, S. Zhang, X. Chen, *Nat. Commun.* **2015**, *6*, 8241.
[31] X. Li, L. Chen, Y. Li, X. Zhang, M. Pu, Z. Zhao, X. Ma, Y. Wang, M. Hong, X. Luo, *Sci. Adv.* **2016**, *2*, e1601102.
[32] P. B. Mueller, N. A. Rubin, R. C. Devlin, B. Groever, F. Capasso, *Phys. Rev. Lett.* **2017**, *118*, 113901.
[33] N. Yu, F. Aieta, P. Genevet, M. A. Kats, Z. Gaburro, F. Capasso, *Nano Lett.* **2012**, *12*, 6328.
[34] A. Pors, M. G. Nielsen, S. I. Bozhevolnyi, *Opt. Lett.* **2013**, *38*, 513.
[35] A. Pors, S. I. Bozhevolnyi, *Opt. Express* **2013**, *21*, 2942.

**ADVANCED
SCIENCE NEWS**

www.advancedsciencenews.com

**ADVANCED
OPTICAL
MATERIALS**

www.advopticalmat.de

[36] N. K. Grady, J. E. Heyes, D. R. Chowdhury, Y. Zeng, M. T. Reiten, A. K. Azad, A. J. Taylor, D. A. Dalvit, H. T. Chen, *Science* **2013**, *340*, 1304.

[37] S. C. Jiang, X. Xiong, Y. S. Hu, Y. H. Hu, G. B. Ma, R. W. Peng, C. Sun, M. Wang, *Phys. Rev. X* **2014**, *4*, 021026.

[38] Y. Yang, W. Wang, P. Moitra, I. I. Kravchenko, D. P. Briggs, J. Valentine, *Nano Lett.* **2014**, *14*, 1394.

[39] Z. H. Jiang, L. Lin, D. Ma, S. Yun, D. H. Werner, Z. Liu, T. S. Mayer, *Sci. Rep.* **2014**, *4*, 7511.

[40] F. Ding, Z. Wang, S. He, V. M. Shalaev, A. V. Kildishev, *ACS Nano* **2015**, *9*, 4111.

[41] J. T. Heiden, F. Ding, J. Linnet, Y. Yang, J. Beermann, S. I. Bozhevolnyi, *Adv. Opt. Mater.* **2019**, *7*, 1801414.

[42] P. C. Wu, W.-T. Tsai, W. T. Chen, Y.-W. Huang, T.-Y. Chen, J.-W. Chen, C. Y. Liao, C. H. Chu, G. Sun, D. P. Tsai, *Nano Lett.* **2016**, *17*, 445.

[43] Z.-L. Deng, J. Deng, X. Zhuang, S. Wang, K. Li, Y. Wang, Y. Chi, X. Ye, J. Xu, G. P. Wang, R. Zhao, X. Wang, Y. Cao, X. Cheng, G. Li, X. Li, *Nano Lett.* **2018**, *18*, 2885.

[44] Y. Xu, Q. Li, X. Zhang, M. Wei, Q. Xu, Q. Wang, H. Zhang, W. Zhang, C. Hu, Z. Zhang, C. Zhang, X. Zhang, J. Han, W. Zhang, *ACS Photonics* **2019**, *6*, 2933.

[45] F. Ding, B. Chang, Q. Wei, L. Huang, X. Guan, S. I. Bozhevolnyi, *Laser Photonics Rev.* **2020**, *14*, 2000116.

[46] J. Zi, Y. Li, X. Feng, Q. Xu, H. Liu, X.-X. Zhang, J. Han, W. Zhang, *Phys. Rev. Appl.* **2020**, *13*, 034042.

[47] F. Ding, Y. Yang, R. A. Deshpande, S. I. Bozhevolnyi, *Nanophotonics* **2018**, *7*, 1129.

[48] R. A. Deshpande, V. A. Zenin, F. Ding, N. A. Mortensen, S. I. Bozhevolnyi, *Nano Lett.* **2018**, *18*, 6265.

ADVANCED OPTICAL MATERIALS

Supporting Information

Dual-Functional Optical Waveplates Based on Gap-Surface Plasmon Metasurfaces

Ziru Cai, Yadong Deng, Cuo Wu, Chao Meng, Yingtao Ding,* Sergey I. Bozhevolnyi, and Fei Ding*

Supporting Information

Dual-Functional Optical Waveplates Based on Gap-Surface Plasmon Metasurfaces

Ziru Cai, Yadong Deng, Cuo Wu, Chao Meng, Yingtao Ding,* Sergey I. Bozhevolnyi, and Fei Ding*

Section S1. Designing the dual-functional waveplate by using the degree of freedom of rotation angles

In contrast to the design process in the main text, it is also feasible to first select the structural parameters of meta-atom A and B and then determine their corresponding rotation angles by solving Equations (1-3). For example, as shown in Figure S1, we select the structural parameters $[l_A, w_A, l_B, w_B]$ as [255 nm, 135 nm, 190 nm, 115 nm] with the phases $[\delta_{Axx}, \delta_{Ayy}, \delta_{Bxx}, \delta_{Byy}]$ being [−208.4°, −68.8°, −166.2°, −16.5°] and reflection amplitudes $[r_{Axx}, r_{Ayy}, r_{Bxx}, r_{Byy}]$ being [0.935, 0.891, 0.915, 0.850]. The rotation angles of meta-atom A and B are calculated to be [110°, 160°]. In this new design, the reflection amplitudes are closer to each other, and in particular r_{Byy} experiences a noticeable increase, which can improve the performance of the combined meta-molecule for the expected function.
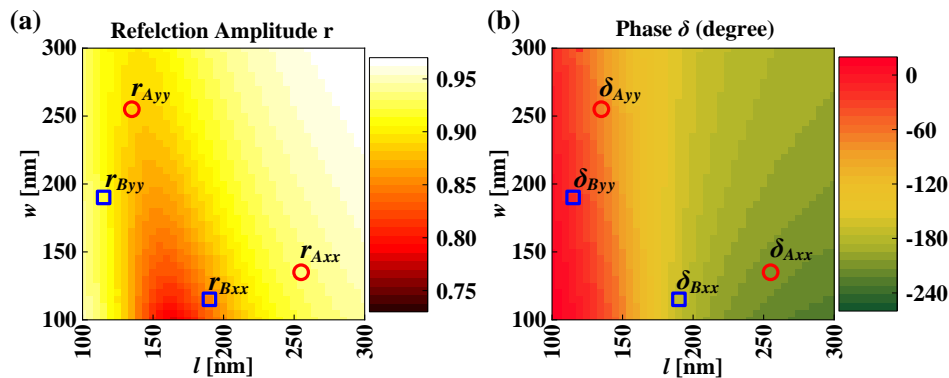
Figure S1. Simulated reflection a) amplitude and b) phase distributions of a single GSP meta-atom as functions of the meta-atom dimensions (i.e., l and w) for x-polarized incident light at the design wavelength $\lambda = 850$ nm.

Section S2. Simulated results of the design dual-functional waveplate with varied dimensional parameters under *y*-polarized incidence

Figure S2 gives the calculated polarization state diagrams of the reflected waves obtained under the *y*-polarized incidence with varied structural parameters. It can be easily seen that the calculated polarization state diagrams of the reflected waves obtained under the *y*-polarized incidence remain largely the same when l_A varies in steps of 5 nm. However, when it comes to other structural parameters, the angles of the calculated polarization state diagram change significantly. Since the metasurface has six-dimensional parameters, the collective effect from all, even small, uncertainties due to fabrication imperfection would influence the angle of linear polarization.

2
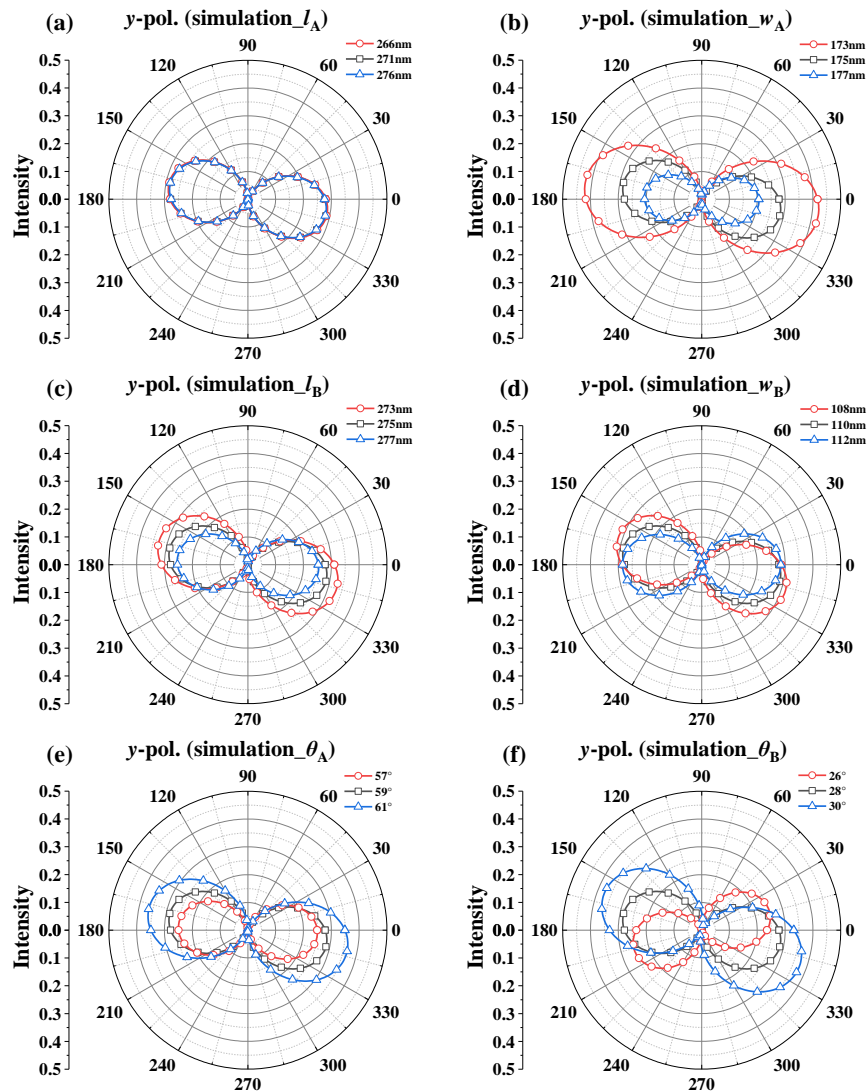
Figure S2. Calculated polarization state diagrams of the reflected waves obtained under y-polarized incidence with varied a) l_A, b) w_A, c) l_B, d) w_B, e) θ_A, and f) θ_B, respectively, while the other parameters are fixed. The original parameters are $[\theta_A, l_A, w_A, \theta_B, l_B, w_B] = [121°, 271$ nm, 135 nm, 152°, 175 nm, 110 nm].

Section S3. Dual-functional waveplate that achieves nearly x-polarized output under y-polarization

In order to realize a dual-functional waveplate that enables the (nearly) x-polarized output under the y-polarization, we conducted numerical simulations with a large range of the structure parameters based on the original structural parameters of $[\theta_A, l_A, w_A, \theta_B, l_B, w_B] =$ [121°, 271 nm, 135 nm, 152°, 175 nm, 110 nm]. The modified structural parameters are determined as $[\theta_A, l_A, w_A, \theta_B, l_B, w_B] = [121°, 304$ nm, 134 nm, 152°, 176 nm, 110 nm]. Figure S3 shows the calculated polarization state diagrams of the reflected waves obtained under x- and y-polarized incidences with original and modified structural parameters, respectively. It can be easily seen that the linear polarization is directed closer to the x-axis with a rotation angle as small as 4°. We believe that more elaborate optimizations with more parameters involved would enable the linearly polarized reflection along the x-axis. As a final comment, it is worth noting that the perfect x-polarized output under the y-polarized excitation can be realized with the metasurface being rotated with a small angle.
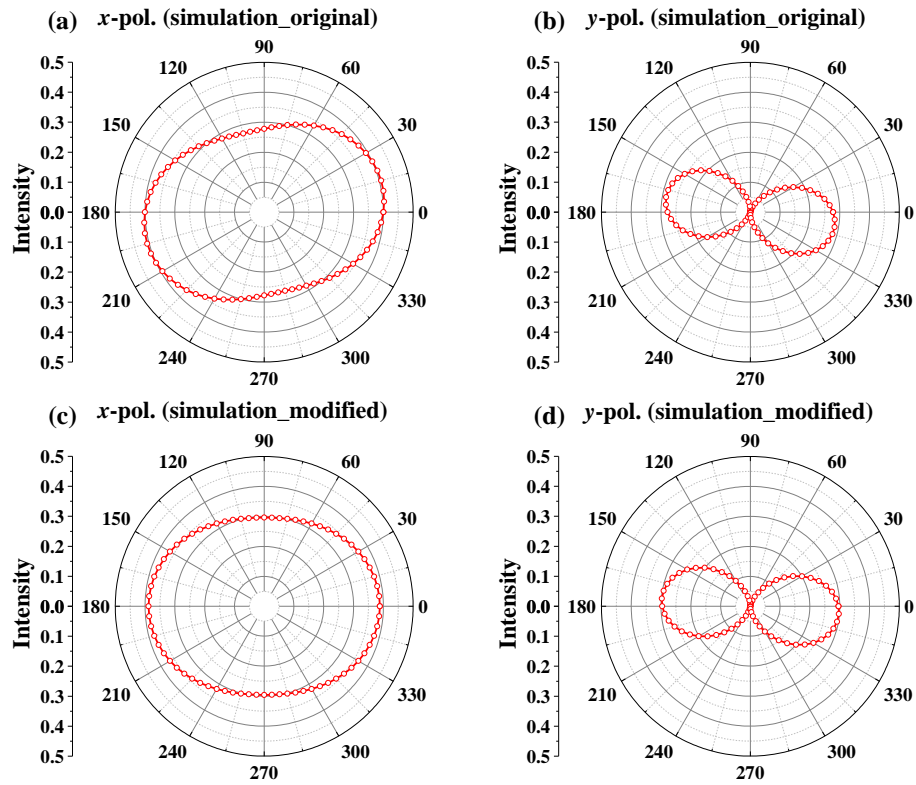
Figure S3. Calculated polarization state diagrams of the reflected waves obtained under a,c) *x*-polarized and b,d) *y*-polarized incidence with a,b) original and c,d) modified structural parameters, respectively.

ARTICLE

Functional Metasurface Quarter-Wave Plates for Simultaneous Polarization Conversion and Beam Steering

Yadong Deng, Cuo Wu, Chao Meng, Sergey I. Bozhevolnyi,* and Fei Ding*

Read Online

ACCESS | Metrics & More | Article Recommendations | SI Supporting Information

ABSTRACT: The capability to manipulate the polarization state of light at the nanoscale is of paramount importance in many emerging research areas ranging from optical communication to quantum information processing. Gap-surface plasmon (GSP) metasurfaces, which provide advantages and abilities of molding reflected fields, have been demonstrated excellently suited for integration of multifunctional polarization optics into a single device. Here, we establish a versatile GSP metasurface platform based on nanoscale quarter-wave plates (nano-QWPs) that enable efficient circular-to-linear polarization conversion along with the complete phase control over reflected fields. Capitalizing on the nano-QWP design, we demonstrate, both theoretically and experimentally, how resonance and geometric phases can be used in concert to achieve independent and simultaneous phase modulation of both co- and cross-polarized circularly polarized (CP) waves by realizing arbitrary beam steering of co- and cross-polarized CP channels in a broadband near-infrared range. The GSP metasurface platform established in our work provides versatile and flexible solutions to enrich multiple functionalities for diversified metasurface-based polarization optics exploited in modern integrated photonic devices and systems.

KEYWORDS: gap-surface plasmon metasurface, quarter-wave plates, resonance phase, geometric phase, polarization conversion, beam steering
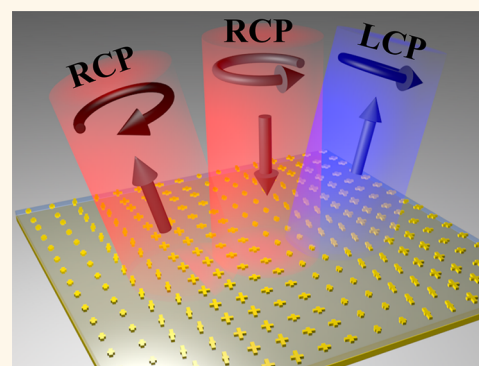
The capability to control and manipulate the polarization state of light, an inherent and important characteristic of optical radiation, is significantly important for contemporary optical instrumentation. Conventional polarization optical components are typically made up of birefringence materials (e.g., crystals and plastics) that introduce and accumulate the phase retardation between two orthogonally polarized electric fields when light propagates over long distances as compared to its wavelength.[1] As a result, these polarization components are inevitably bulky, intrinsically restricting the possibilities for their miniaturization and integration into photonic systems at the nanoscale.

Optical metasurfaces, two-dimensional artificial nanostructures consisting of dense arrays of meticulously designed meta-atoms, have earned a growing amount of attention owing to their unparalleled capabilities for controlling optical fields with subwavelength spatial resolutions.[2−8] In particular, by judiciously designing anisotropic meta-atoms with specific and distinct responses for light polarized along two orthogonal directions, the phase and polarization of reflected and transmitted (by metasurfaces) light can be efficiently manipulated, thereby substituting conventional bulky polar-

ization optics with planar, compact, and multifunctional metasurface-based polarization optics.[9−38] For example, nanoscale waveplates enabling simultaneous polarization transformation and wavefront shaping have been implemented.[19−35] However, most up-to-date functional metasurface waveplates have been focused on half-wave plates,[19,20,22−29,33−35] where only the cross-polarized light component could be manipulated by the orientation-dependent geometric phase or dimension-dependent resonance/propagation phase. Even though spin-decoupled metasurfaces[21,25,28,29,32−36] exhibit excellent performance, only one functionality can be achieved in the cross-polarized channel for a specific circularly polarized (CP) input. To increase the number of functional channels and thus the information capacity under the CP excitation, it would be
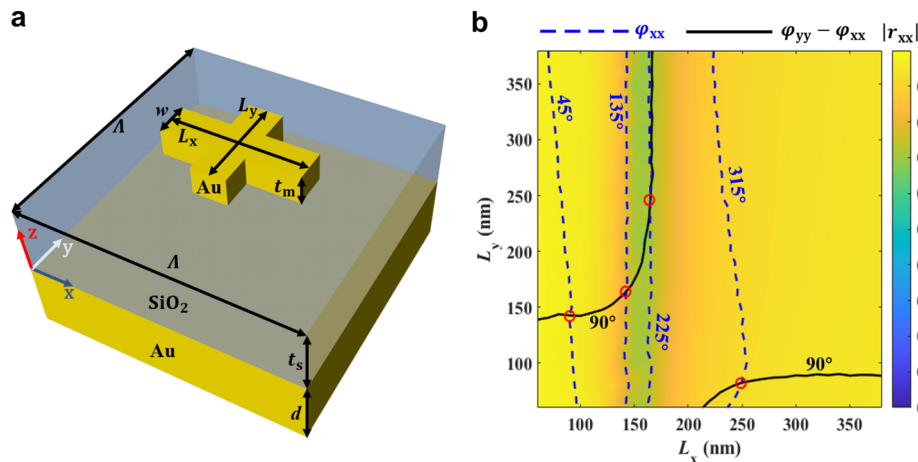
18532
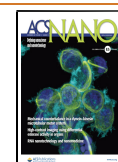
Figure 1. (a) Schematic of the anisotropic MIM meta-atom. (b) Calculated reflection coefficient as a function of the dimensions at the design wavelength of 850 nm for x-polarization. Note the reflection coefficient for y-polarization can be obtained by mirroring the map for x-polarization along the line of $L_x = L_y$. The color map shows the reflection amplitude $|r_{xx}|$, while the blue dashed lines are contours of the reflection phase φ_{xx} with a step of 90° and black solid lines indicate the meta-atoms with the phase difference $\Delta\varphi = \varphi_{yy} - \varphi_{xx}$ equal to 90°.

advantageous to realize similar or different functionalities for both CP waves. Therefore, it is highly desirable to demonstrate metasurface-based quarter-wave plates (QWPs) that utilize and manipulate both co- and cross-polarized output channels simultaneously.[39−42] It is important to note that the QWPs demonstrated thus far are typically operating in the microwave[39−41] or infrared[42] range. Functional nano-QWPs for effective polarization transformation and complete phase modulation are, however, rarely realized in the optical range.

In this paper, we design a set of nano-QWPs based on a gap-surface plasmon (GSP) metasurface configuration, which enable efficient circular-to-linear polarization conversion along with the complete phase control over reflected fields. Capitalizing on the nano-QWP design, we demonstrate how resonance and geometric phases can be complementary utilized to achieve independent and simultaneous phase modulation of both co- and cross-polarized CP waves under CP excitations by realizing arbitrary beam steering of co- and cross-polarized channels in a broadband near-infrared range. Our proposed GSP metasurface platform strengthens the practical applications of metasurfaces with simultaneous phase and polarization manipulation, providing versatile and flexible solutions to implement multifunctional meta-devices at the nanoscale.

RESULTS AND DISCUSSION

QWP Meta-Atom Design. Let us start with the basic principle of realizing metasurface QWPs by considering a birefringent meta-atom with its major axes along x- and y-directions. Generally, the response of such an anisotropic meta-atom could be described by the Jones matrix in the linear polarization basis:

$$J_{\text{linear}} = \begin{pmatrix} r_{xx} & 0 \\ 0 & r_{yy} \end{pmatrix} \tag{1}$$

where $r_{xx} = |r_{xx}|e^{i\varphi_{xx}}$ and $r_{yy} = |r_{yy}|e^{i\varphi_{yy}}$ are the reflection coefficients under x- and y-polarized excitations, which are mainly determined by the dimensions of the birefringent meta-atom along its two main axes. Once the reflection amplitudes are equal (i.e., $|r_{xx}| = |r_{yy}|$) and the relative phase difference $\Delta\varphi = \varphi_{yy} - \varphi_{xx}$ is ±90°, the birefringent meta-atom functions as a

nano-QWP. If the nano-QWP with $\Delta\varphi = 90°$ is rotated by an angle of θ with respect to the x-axis, the corresponding Jones matrix can be written as

$$J(\theta) = |r_{xx}|e^{i\varphi_{xx}}M^{-1}(\theta)\begin{pmatrix} 1 & 0 \\ 0 & i \end{pmatrix}M(\theta) \tag{2}$$

where $M(\theta) = \begin{pmatrix} \cos\theta & \sin\theta \\ -\sin\theta & \cos\theta \end{pmatrix}$ represents the rotation matrix. For the right-handed circularly polarized (RCP) incident light with $E_{\text{in}} = \frac{1}{\sqrt{2}}\begin{pmatrix} 1 \\ -i \end{pmatrix}$, the output field becomes linearly polarized (LP) and the angle of linear polarization (AoLP) is $\theta + \pi/4$

$$E_{\text{out}} = |r_{xx}|e^{i\varphi_{xx}}e^{-i\theta}\begin{pmatrix} \cos\left(\theta + \dfrac{\pi}{4}\right) \\ \sin\left(\theta + \dfrac{\pi}{4}\right) \end{pmatrix} \tag{3}$$

Additionally, the LP light gains an additional phase modulation of $\varphi_{xx} - \theta$. Meanwhile, the LP light can be decomposed into two CP components in the circular polarization basis, which is written as

$$E_{\text{out}} = \frac{1}{2}|r_{xx}|e^{i(\varphi_{xx}+\frac{\pi}{4})}\begin{pmatrix} 1 \\ -i \end{pmatrix} + \frac{1}{2}|r_{xx}|e^{i(\varphi_{xx}-\frac{\pi}{4})}e^{-i2\theta}\begin{pmatrix} 1 \\ i \end{pmatrix} \tag{4}$$

Equation 4 indicates that the reflected field contains two components; where the first part stands for the copolarized reflective wave that maintains the same helicity as the incident RCP wave, whereas the second part is the cross-polarized wave with the reversed helicity [i.e., left-handed circularly polarized (LCP)]. Here we define the copolarized and cross-polarized reflection coefficients as $r_{\text{co}} = \frac{\sqrt{2}}{2}|r_{xx}|e^{i(\varphi_{xx}+\frac{\pi}{4})}$ and $r_{\text{cr}} = \frac{\sqrt{2}}{2}|r_{xx}|e^{i(\varphi_{xx}-\frac{\pi}{4}-2\theta)}$ in the circular polarization basis, respectively. Thus, the phase of the copolarized CP beam $\varphi_{\text{co}} = \varphi_{xx} + \pi/4$ is only associated with the resonance phase, while cross-polarized CP phase distribution $\varphi_{\text{cr}} = \varphi_{xx} - \pi/4 - 2\theta$ is determined by both resonance and geometric phases, which depends on the meta-atom's dimensions and orienta-
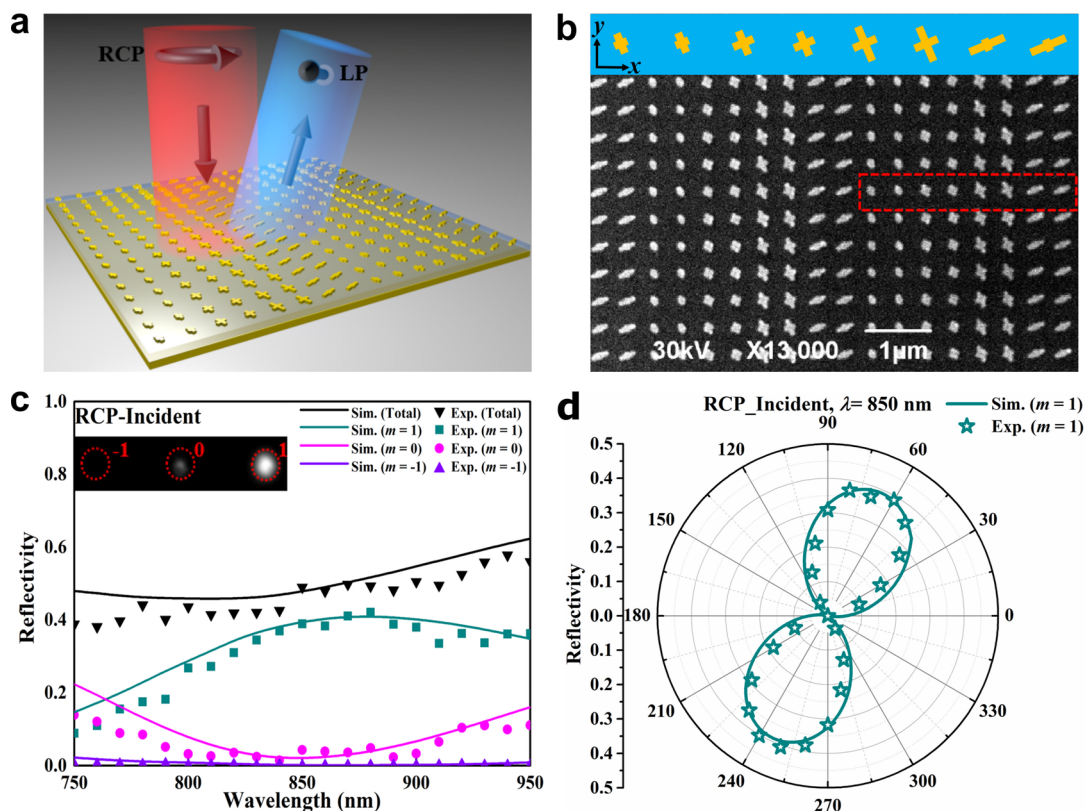
Figure 2. (a) Schematic of the GSP gradient MS1 for circular-to-linear polarization conversion and beam steering under RCP excitation. (b) SEM image of the fabricated MS1. The inset shows the layout of one MS1 supercell with each meta-atom rotated by an angle of 22.5° with respect to the x-axis along the counterclockwise direction. (c) Simulated (solid lines) and experimental (markers) diffraction efficiencies of different orders as a function of wavelength for RCP incident light. The inset shows the optical image of the diffraction spots at the wavelength of 850 nm. (d) Simulated (dark cyan solid line) and experimental (dark cyan star markers) polarization state diagrams of the steered beam within +1 diffraction order for RCP incident light at the wavelength of 850 nm.

tions, respectively. As a result, the co- and cross-polarized CP channels can be dependently or independently manipulated.

To design the anisotropic meta-atom that functions as a nano-QWP, we use a typical metal−insulator−metal (MIM) GSP resonator[43] as the fundamental building block. As shown in Figure 1a, the MIM unit cell consists of a gold (Au) cross-shaped nanoantenna, a silicon dioxide (SiO$_2$) spacer layer, and a continuous Au film. The periodicity of designed MIM unit cells is $\Lambda = 400$ nm, which is much smaller than the design wavelength of $\lambda = 850$ nm to eliminate the high-order diffraction. The thickness of the middle SiO$_2$ spacer layer is optimized to $t_s = 100$ nm, ensuring high reflection efficiency and sufficient resonance phase coverage. The thickness and width of topmost Au antennas are $t_m = 40$ nm and $w = 50$ nm, respectively, while the lengths (i.e., L_x and L_y) of the two rectangle constituent bars are varied. The thickness of the bottom Au layer is $d = 100$ nm, which is thick enough to block light transmission. We implemented three-dimensional (3D) full-wave simulations with the commercially available software Comsol Multiphysics (version 5.5) to calculate the complex reflection coefficients of the meta-atoms under x- or y-polarized incident light. In the simulation, L_x and L_y are varied while other geometrical parameters are kept constant. The relative permittivity of Au is described by the Drude model fitted with the experimental data,[44] and SiO$_2$ is taken as a lossless material with a constant refractive index of 1.45. An air domain is added above the meta-atom and truncated with a perfectly matched layer to minimize any reflection. An x- or y-

polarized plane wave is normally impinging on the MIM unit cell with periodic boundary conditions employed in both x- and y-directions. Figure 1b shows the calculated reflection coefficient of the meta-atom with varying L_x and L_y at the targeted wavelength of $\lambda = 850$ nm under x-polarized excitation, where nano-QWP candidates with $\Delta\varphi$ matched to 90° are marked with black solid lines. Meanwhile, the available resonance phase of nano-QWPs (i.e., φ_{xx}) can cover a wide range up to 300°. To maintain broad operation bandwidth and high efficiency, four nano-QWPs (red circles) with a phase step of $\Delta\varphi_{xx} = 90°$ are selected to comprise a meta-atom library, which enables simultaneous circular-to-linear polarization conversion and potential wavefront shaping. The geometric parameters and corresponding serial numbers of selected nano-QWPs are shown in Table S1. As a final comment, it is worth noting that the amplitudes of these four nano-QWPs are not perfectly equal, which may slightly affect the performance. To increase the reflection amplitudes of selected (poorly reflecting) meta-atoms, their widths can be propitiously designed (Figures S1 and S2, and Table S3 in the Supporting Information).

Gradient Metasurfaces for Broadband Circular-to-Linear Polarization Conversion and Beam Steering. After designing the four nano-QWPs, we first design gradient metasurfaces that enable simultaneous circular-to-linear polarization conversion and beam steering under LCP and RCP incident light. In this case, the co- and cross-polarized CP channels are molded only by the resonance phase and thus
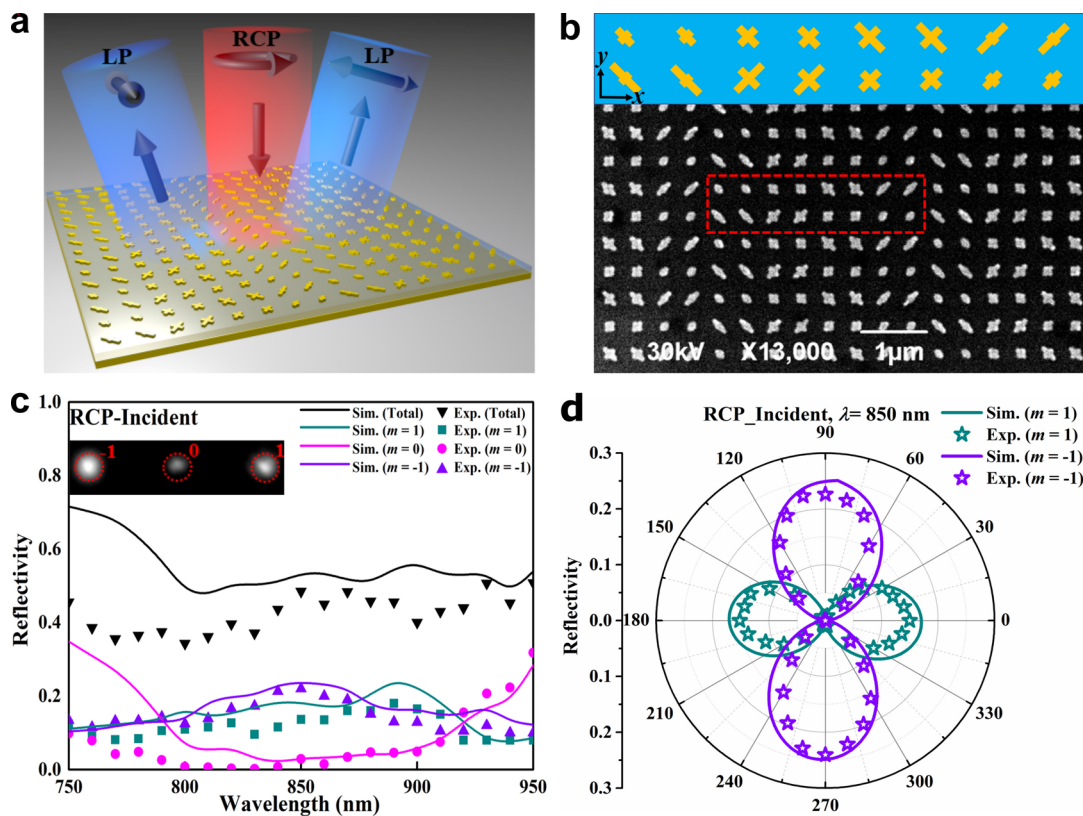
Figure 3. (a) Schematic of the GSP gradient MS2 for generating two spatially separated LP beams with different AoLPs under RCP excitation. (b) SEM image of the fabricated MS2. The inset shows the layout of one MS2 supercell with each nano-QWP rotated by 45° or 135° along the counterclockwise direction in the first and second rows, respectively. (c) Simulated (solid lines) and experimental (markers) diffraction efficiencies of different orders as a function of wavelength for RCP incident light. The inset shows the optical image of the diffraction spots at the wavelength of 850 nm. (d) Simulated (dark cyan/violet solid line) and experimental (dark cyan/violet star markers) polarization state diagrams of the steered beam within ±1 diffraction orders for RCP incident light at the wavelength of 850 nm.

steered to the same direction. Specifically, the meta-atoms comprising the metasurface supercell are all rotated with the same angle of θ_{LP0}. Therefore, the corresponding phase gradient along the x-direction is given as

$$\frac{d\varphi_{LP}}{dx} = \frac{\partial(\varphi_{xx}(x, y) + \theta_{LP0})}{\partial x} = \frac{\Delta\varphi_{xx}}{N \cdot \Lambda} = m_{LP} \cdot \frac{2\pi}{\Lambda_{sc}} \quad (5)$$

where (x, y) indicates the coordinate of each meta-atom, N is the number of identical meta-atoms duplicated in a supercell, m_{LP} represents the diffraction order for the LP reflection field, and Λ_{sc} represents the total period of one supercell. Figure 2a schematically illustrates the working principle of the first gradient metasurface (MS1) that converts and steers the CP (e.g., RCP) incident light into an LP wave with a spin-determined AoLP within +1 diffraction order. As shown in Figure 2b, MS1 is made up of four selected nano-QWPs that are all duplicated to make an 8-element supercell to enlarge the periodicity along the x-direction, thereby decreasing the diffraction angle of the steered light within the collection angle of the objective. Within the supercell, each meta-atom is rotated with an angle of $\theta_{LP0} = 22.5°$ with respect to the x-axis along the counterclockwise direction. As such, each meta-atom will convert the RCP (LCP) incident light to a secondary LP wave with a fixed AoLP of 67.5° (−22.5°). Additionally, the secondary LP wave gain a linear phase gradient along the x-axis, thereby forming the reflected LP light in +1 diffraction order.

To validate the performance, we first simulated the MS1 supercell and plotted the calculated diffraction efficiencies (solid lines in Figure 2c) of different orders from $m = -1$ to $+1$ as a function of wavelength for RCP incident light. It is worth noting that the damping rate of Au here is increased by a factor of 3 to account for additional losses in terms of surface scattering, grain boundary effects, and increased damping related to the 3 nm titanium (Ti) adhesion layer between Au and SiO$_2$ layers. As expected, the total reflectivity is restricted to 48% because of the increased ohmic loss, and the incident light is exclusively reflected into +1 diffraction order with a theoretical reflectivity of ~40% at the design wavelength of 850 nm under RCP incident light; however, the other diffraction orders are strongly suppressed. In addition, the simulated polarization state diagram (dark cyan solid line in Figure 2d) of the steered beam within +1 diffraction order indicates the excellent circular-to-linear polarization conversion at the wavelength of 850 nm, with the degree of linear polarization (DoLP) approaching 99.19%. After full-wave simulations, the designed MS1 was fabricated using the standard thin-film deposition, electron beam lithography, and lift-off techniques (see the Methods section for details). The scanning electron microscopy (SEM) image of MS1 is shown in Figure 2b, whose overall size is around 20 × 20 μm². Generally, the fabricated sample well replicates the designed meta-atoms in terms of shapes and dimensions despite the surface roughness and rounded corners. After fabrication, the sample was characterized using a custom-built optical setup shown in
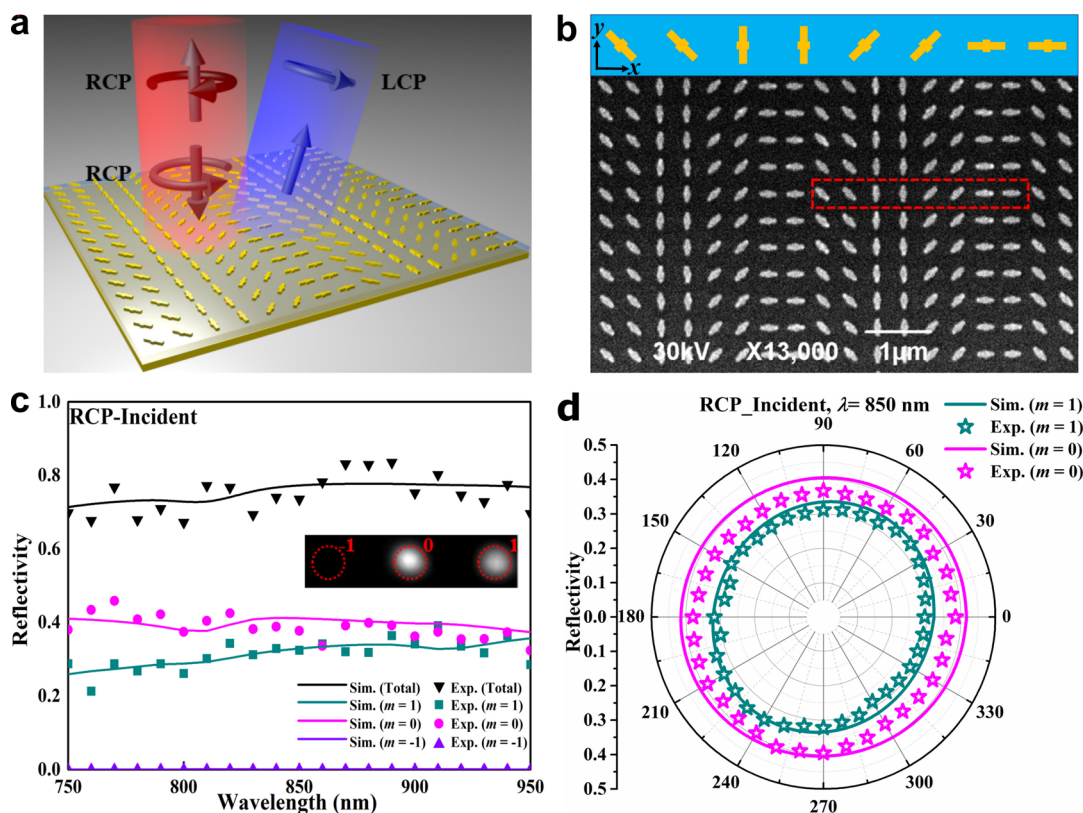
18535

Figure 4. (a) Schematic of the GSP gradient MS3 composed of identical meta-atoms with different rotation angles for steering of co- and cross-polarized CP waves to 0 and +1 diffraction orders. (b) SEM image of the fabricated MS3. The inset shows the layout of one MS3 supercell composed of identical meta-atoms with different rotation angles. (c) Simulated (solid lines) and experimental (markers) diffraction efficiencies of different orders as a function of wavelength for RCP incident light. The inset shows the optical image of the diffraction spots at the wavelength of 850 nm. (d) Simulated (dark cyan/magenta solid line) and experimental (dark cyan/magenta star markers) polarization state diagrams of the steered beams within 0 and +1 diffraction orders for RCP incident light at the wavelength of 850 nm.

Figure S4. From the optical image of the diffraction spots in the inset of Figure 2c, we could see that almost all the incident light has been reflected into +1 diffraction order, demonstrating the excellent capability of beam steering. The performance of our fabricated MS1 was further measured by determining the corresponding diffraction efficiency in each order. As displayed in Figure 2c, in general, the simulated and experimental diffraction efficiencies coincide fairly well. Specifically, the total reflectivity is close to 50% and the diffraction efficiency of +1 order is ∼40% at λ = 850 nm under RCP incident light in the experiment. The measured (dark cyan star markers) reflectance as a function of the orientation of the analyzer in front of the CCD camera for +1 diffraction order under RCP excitation also presents great consistency with the simulation result at the design wavelength of 850 nm, as shown in Figure 2d. In particular, the measured DoLP is 99.42%. Meanwhile, the MS1 enables efficient circular-to-linear polarization conversion and beam steering in a broadband spectrum ranging from 800 to 900 nm (Figure S5). Once the incident light is switched to LCP, an LP beam with the AoLP of −22.5° is generated and routed to +1 diffraction order (Figure S6).

In addition to producing a single LP beam in the desired direction under a CP excitation, it is interesting to simultaneously generate more LP beams with different AoLPs in spatially separated channels. Therefore, we design a second GSP metasurface (MS2) capable of converting the incident CP beam into two LP beams with orthogonal linear polarization states in the opposite directions (Figure 3a) by interweaving two metasurface subsupercells along the y-direction, where nano-QWPs are rotated by 45° or 135° along the counterclockwise direction in the first and second rows, respectively (Figure 3b). In particular, MS2 can convert the RCP incident beam into x- and y-polarized waves into respective ±1 diffraction orders. Once the incident light is switched to LCP, the reflected beams within ±1 diffraction orders become y- and x-polarized. The calculated diffraction efficiencies of MS2 as a function of wavelength for RCP incident light are shown in Figure 3c, which indicate a broadband response from 800 to 900 nm. Compared with MS1, the zero-order diffraction slightly increases, which may be ascribed to the enlarged periodicity of 2Λ = 800 nm between identical subsupercells along the y-direction, leaving away from the criterion of true subwavelength separation and thus degrading the performance of individual metasurfaces. Despite the disturbance, the desired reflectivities within ±1 diffraction orders are both ∼20% with the zero-order diffraction efficiency below 5% at the design wavelength of 850 nm. Analogously, we fabricated and characterized the sample MS2 using the same processes. Figure 3b shows the SEM image of the fabricated sample MS2 whose overall size is also about 20 × 20 μm^2. From the optical image of the diffraction spots in Figure 3c, we could observe that most of the energy has been reflected to ±1 diffraction orders, manifesting the desired beam steering capability at the design wavelength of 850 nm. Additionally, there is a reasonable
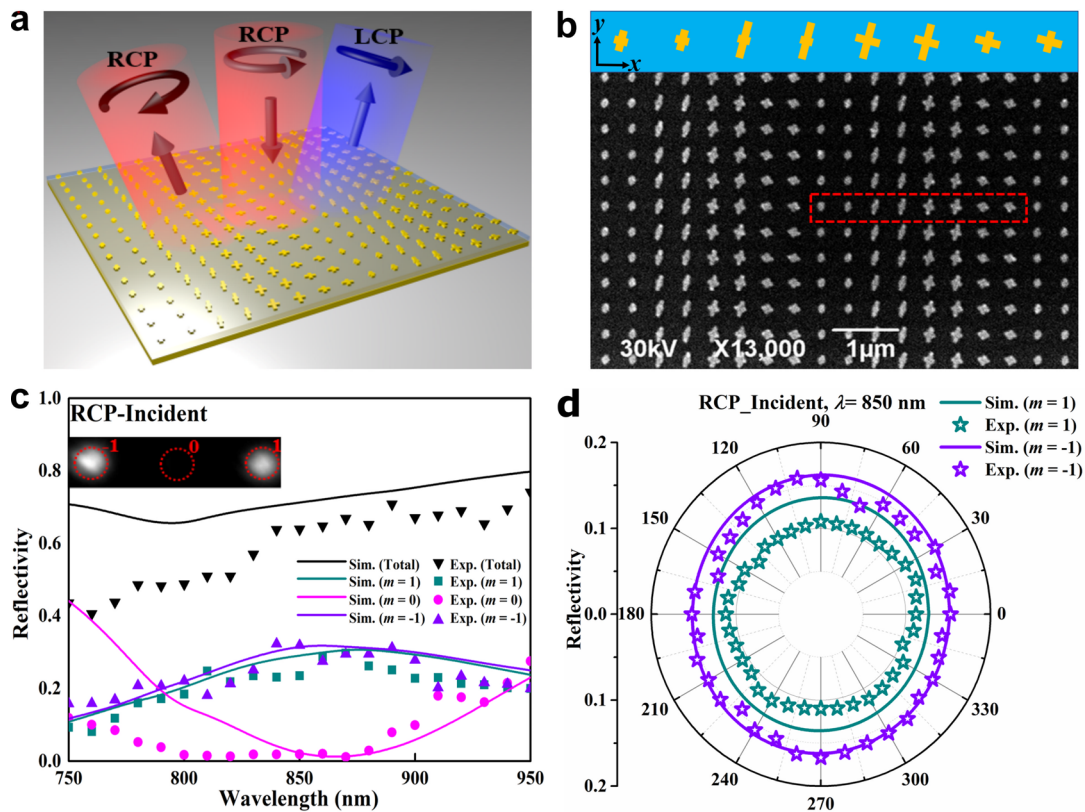
Figure 5. (a) Schematic of the GSP gradient MS4 composed of meta-atoms with different dimensions and rotation angles for steering of co- and cross-polarized CP waves to −1 and +1 diffraction orders. (b) SEM image of the fabricated MS4. The inset shows the layout of one MS4 supercell composed of meta-atoms with different dimensions and rotation angles. (c) Simulated (solid lines) and experimental (markers) diffraction efficiencies of different orders as a function of wavelength for RCP incident light. The inset shows the optical image of the diffraction spots at the wavelength of 850 nm. (d) Simulated (dark cyan/violet solid line) and experimental (dark cyan/violet star markers) polarization state diagrams of the steered beam within −1 and +1 diffraction orders for RCP incident light at the wavelength of 850 nm.

agreement between the simulated and experimental efficiencies of different orders at λ = 850 nm (simulation: ∼3.00%, ∼18.20% and ∼23.70% for the diffraction orders of m = 0 and ±1, respectively; experiment: ∼ 2.90%, ∼13.60% and ∼22.00% for the diffraction orders of m = 0 and ±1, respectively). Moreover, the similar simulated (dark cyan/violet solid line) and experimental (dark cyan/violet star markers) polarization state diagram as a function of the orientation of the analyzer under RCP excitation at the design wavelength of 850 nm could be observed in Figure 3d. Importantly, the measured DoLPs are as high as 99.54% and 99.36% for the diffraction orders of m = ± 1. The MS2 sample also exhibits reasonably good performance at other wavelengths and the measurements only show tiny inconsistency with simulations (Figure S7), a feature that we attribute to imperfections in the manufactured metasurface and some deviation during the measurement process. Similarly, the MS2 sample could operate equally well in the case of LCP incidence (Figure S8).

Gradient Metasurfaces for Independent Beam Steering of Co- and Cross-Polarized CP Waves. As shown in eq 4, the designed nano-QWPs enable simultaneous and independent phase modulation of co- and cross-polarized reflected waves in the circular polarization basis by employing the resonance and geometric phases at the same time. Specifically, the copolarized output channel gains a phase term of $\varphi_{co} = \varphi_{xx} + \pi/4$ imposed by the dimension-varied meta-atoms while the cross-polarized counterpart carries a phase shift of $\varphi_{cr} = \varphi_{xx} - \pi/4 - 2\theta$ determined by the

dimensions and orientations of meta-atoms for the RCP incident light. Since the selected meta-atoms function as nano-QWPs, the co- and cross-polarized channels share equal output energy. To validate the versatility and capability of independent beam steering in two orthogonal CP channels, we now design two gradient metasurfaces (MS3 and MS4) that can steer the reflected CP beams into spatially separated channels. As such, the corresponding phase gradients that allow to steer CP output channels are

$$\frac{d\varphi_{co}}{dx} = \frac{\partial\left(\varphi_{xx}(x,y) + \frac{\pi}{4}\right)}{\partial x} = \frac{\Delta\varphi_{xx}}{N\cdot\Lambda} = m_{co}\cdot\frac{2\pi}{\Lambda_{sc}} \quad (6)$$

$$\frac{d\varphi_{cr}}{dx} = \frac{\partial\left(\varphi_{xx}(x,y) - \frac{\pi}{4} - 2\cdot\theta(x,y)\right)}{\partial x} = \frac{\Delta\varphi_{xx} - 2\cdot\Delta\theta}{N\cdot\Lambda}$$

$$= m_{cross}\cdot\frac{2\pi}{\Lambda_{sc}} \quad (7)$$

where $\theta(x,y)$ is the rotated angle of each meta-atom, $\Delta\theta$ is the relative angle between two differently sized meta-atoms, m_{co} and m_{cross} represent the respective diffraction orders for co- and cross-polarized reflection fields, respectively. For MS3, it will reflect RCP incident light to copolarized (RCP) and cross-polarized (LCP) channels toward the 0 and +1 diffraction orders, respectively, as shown in Figure 4a. By substituting m_{co} = 0, m_{cross} = 1, and N = 2 into the above equations, we get the solutions of $\Delta\varphi_{xx}$ = 0 and $\Delta\theta$ = −$\pi/4$ with a metasurface

supercell composed of 8 elements. Therefore, we only need to choose one nano-QWP from our meta-atom library and rotate each meta-atom accordingly to fulfill the geometric phase requirements. Considering the reflection efficiency, meta-atom No.4 is selected and distributed to make a supercell, where meta-atoms are rotated with angles $\theta(x, y)$ of $-45°$, $-45°$, $-90°$, $-90°$, $-135°$, $-135°$, $-180°$, and $-180°$, respectively (Figure 4b). Such a design could be constructed by sequentially placing the 8 elements with a center-to-center distance of $\Lambda = 400$ nm and subsequently decrease the first-order diffraction angle to $15.4°$. As expected, almost all the incident RCP light is reflected into 0 and +1 diffraction orders and -1 diffraction order is strongly suppressed (approaching 0) in a wider spectrum range from 750 to 950 nm (Figure 4c), which is ascribed to the broadband nature of the geometric phase. Compared with MS1 and MS2, MS3 features a higher total reflectivity since only one highly efficient nano-QWP is involved. At the design wavelength of 850 nm, the reflected electric fields at two orthogonal CP states assemble well-defined wavefronts (Figure S9a,c). Based on the same setup, the diffraction efficiency of each order can be resolved in the investigated spectrum range. Overall, reasonable agreement is observed between the measured and calculated diffraction efficiencies, verifying the broadband beam steering for both co- and cross-polarized CP light. Specifically, the measured diffraction efficiencies of 0 and +1 orders are ∼37% and ∼32%, respectively, at the design wavelength of 850 nm, which is clearly seen from the optical image of two bright diffraction spots in Figure 4c. After validating the capability of steering CP waves in two spatially separated channels, it is important to verify their polarization states. As such, we plot the simulated (dark cyan/magenta solid line) and experimental (dark cyan/magenta star markers) polarization state diagram as a function of the orientation of the analyzer for 0 and +1 diffraction orders at $\lambda = 850$ nm in Figure 4d. In general, the measured polarization diagrams well assemble circular shapes with the degrees of circular polarization (DoCPs) above 93.70% and -92.40% for the diffraction orders of $m = 0$ and 1, respectively, which are consistent with the simulated values of 99.60% and -99.30%. More simulated and experimental results at other incident wavelengths under RCP excitation are shown in Figure S9b,d.

As a more general case, MS4 can steer the reflected co- and cross-polarized CP waves into -1 and +1 diffraction orders, respectively (Figure 5a). Thus, we substitute $m_{co} = -1$, $m_{cross} = 1$, and $N = 2$ into eqs 6 and (7) and select four nano-QWPs with different dimensions and rotation angles to form an 8-element supercell, which provides resonance and geometric phases simultaneously. As shown in the inset of Figure 5b, the 8 elements are distributed in a certain order (i.e., meta-atoms No.1, No.1, No.4, No.4, No.3, No.3, No.2, and No.2) and the corresponding rotation angles $\theta(x, y)$ are $-15°$, $-15°$, $75°$, $75°$, $165°$, $165°$, $255°$, and $255°$, respectively. Illuminating MS4 with an RCP wave at normal incidence, we measured diffraction efficiencies of orders $|m| \leq 1$, as shown in Figure 5c. In general, reasonable agreement is observed between the measured and calculated diffraction efficiencies, verifying the desired steering capability, albeit with some discrepancies regarding the zero-order diffraction, particularly at short wavelengths. Compared with MS3 composed of spatially oriented identical meta-atoms to supply geometric phase, MS4 can only work in a narrower bandwidth since more meta-atoms are involved and each meta-atom has its individual operating

bandwidth. At the design wavelength of 850 nm, the experimental diffraction efficiencies for -1 and +1 orders are found to be ∼32.00% and ∼23.50%, respectively (Figure 5c). In addition, the simulated (dark cyan/violet solid line) and experimental (dark cyan/violet star markers) polarization state diagrams are in good agreement with each other at $\lambda = 850$ nm, as shown in Figure 5d. Quantitatively, the measured DoCPs are around 90.30% and -92.00%, indicating that co- and cross-polarized CP waves have been successfully steered into -1 and +1 diffraction orders, respectively. As expected, the reflected electric fields at two orthogonal CP states exhibit tilted planar wavefronts (Figure S10a,c). The simulated and experimental results at wavelengths of 800 and 900 nm under RCP incident light could be seen in Figure S10b,d, validating the broadband nature of the implemented MS4.

CONCLUSIONS

In this paper, we have demonstrated a set of GSP nano-QWPs for efficient circular-to-linear polarization conversion along with the complete phase control over reflected fields. Based on the nano-QWP design, we have achieved independent and simultaneous phase modulation of both co- and cross-polarized CP waves under CP excitations by realizing arbitrary beam steering of co- and cross-polarized CP channels in the broadband near-infrared range. Specifically, we experimentally demonstrated two GSP gradient metasurfaces (MS1 and MS2) that employ only the resonance phase for efficient circular-to-linear polarization conversion and beam steering of two CP channels in the same direction. In addition, independent beam steering of co- and cross-polarized CP channels in separated channels has been further implemented with MS3 and MS4 that utilize the geometric phase modulation. As an additional comment, we want to emphasize that the efficiencies of considered metasurfaces could further be enhanced by employing differently wide nano-QWPs allowing for larger reflection amplitudes (Figure S2b) and/or using single-crystalline Au with lower absorption in the metasurface fabrication to reduce the metasurface damping (Figure S11). Finally, we would like to emphasize that the designed four GSP metasurfaces operate equally well in the case of the LP excitation (Table S4), which could further enrich the applications. The proposed versatile GSP nano-QWP platform established here strengthens the practical applications of multifunctional integrated metasurfaces with simultaneous phase and polarization manipulation, which can be combined with amplitude manipulation to further extend the information capacity.[45,46]

METHODS

Fabrication. All the samples were fabricated by employing the standard thin-film deposition, electron-beam lithography, and lift-off techniques. First, a 3 nm Ti layer, a 100 nm Au layer, and a 1 nm Ti layer were deposited onto a silicon substrate through thermal evaporation successively. Then, a 100 nm SiO$_2$ spacer layer was deposited with RF-sputtering. Next, a 100 nm PMMA (2% in anisole, Micro Chem) layer was spin-coated on the SiO$_2$ layer, baked at 180 °C for 2 min, and exposed at an acceleration voltage of 30 keV to define the patterns. After exposure, the wafer was developed in the solution of methyl isobutyl ketone (MIBK) and isopropyl alcohol (IPA) of MIBK: IPA = 1:3 for 35 s followed by 60 s in an IPA bath. After development, a 1 nm Ti adhesion layer and a 40 nm Au layer were deposited subsequently using thermal evaporation. Finally, top Au nanocross antennas were formed after a lift-off process.

ASSOCIATED CONTENT

Ⓢ Supporting Information

The Supporting Information is available free of charge at https://pubs.acs.org/doi/10.1021/acsnano.1c08597.

> Dimensions and reflection coefficients of the selected 4 meta-atoms; influence of the width of meta-atoms on the performance; the simulated performance of nano-QWPs with different orientations; the custom-built optical setup; supplementary simulation and experimental data for MS1, MS2, MS3, and MS4; calculated diffraction efficiencies for MS2 with the damping rate of bulk gold; and performance of designed metasurfaces under linearly polarized incidence (PDF)

AUTHOR INFORMATION

Corresponding Authors

Fei Ding − *Centre for Nano Optics, University of Southern Denmark, Odense M DK-5230, Denmark;* ⓞ orcid.org/0000-0001-7362-519X; Email: feid@mci.sdu.dk

Sergey I. Bozhevolnyi − *Centre for Nano Optics, University of Southern Denmark, Odense M DK-5230, Denmark;* ⓞ orcid.org/0000-0002-0393-4859; Email: seib@mci.sdu.dk

Authors

Yadong Deng − *Centre for Nano Optics, University of Southern Denmark, Odense M DK-5230, Denmark;* ⓞ orcid.org/0000-0002-2405-0251

Cuo Wu − *Centre for Nano Optics, University of Southern Denmark, Odense M DK-5230, Denmark; Institute of Fundamental and Frontier Sciences, University of Electronic Science and Technology of China, Chengdu 610054, People's Republic of China;* ⓞ orcid.org/0000-0001-9198-9173

Chao Meng − *Centre for Nano Optics, University of Southern Denmark, Odense M DK-5230, Denmark*

Complete contact information is available at:
https://pubs.acs.org/10.1021/acsnano.1c08597

Notes

The authors declare no competing financial interest.

ACKNOWLEDGMENTS

REFERENCES

(1) Pedrotti, F. L.; Pedrotti, L. S. *Introduction to Optics*; Prentice Hall: Upper Saddle River, NJ, 1993; pp 333−371.

(2) Chen, H. T.; Taylor, A. J.; Yu, N. A Review of Metasurfaces: Physics and Applications. *Rep. Prog. Phys.* **2016**, *79*, 076401.

(3) Hsiao, H. H.; Chu, C. H.; Tsai, D. P. Fundamentals and Applications of Metasurfaces. *Small Methods* **2017**, *1*, 1600064.

(4) Luo, X. G. Subwavelength Optical Engineering with Metasurface Waves. *Adv. Opt. Mater.* **2018**, *6*, 1701201.

(5) Ding, F.; Pors, A.; Bozhevolnyi, S. I. Gradient Metasurfaces: A Review of Fundamentals and Applications. *Rep. Prog. Phys.* **2018**, *81*, 026401−026445.

(6) Capasso, F. The Future and Promise of Flat Optics: A Personal Perspective. *Nanophotonics* **2018**, *7*, 953−957.

(7) Sun, S. L.; He, Q.; Hao, J. M.; Xiao, S. Y.; Zhou, L. Electromagnetic Metasurfaces: Physics and Applications. *Adv. Opt. Photonics* **2019**, *11*, 380−479.

(8) Shaltout, A. M.; Shalaev, V. M.; Brongersma, M. L. Spatiotemporal Light Control with Active Metasurfaces. *Science* **2019**, *364*, 6441.

(9) Hao, J. M.; Yuan, Y.; Ran, L. X.; Jiang, T.; Kong, J. A.; Chan, C. T.; Zhou, L. Manipulating Electromagnetic Wave Polarizations by Anisotropic Metamaterials. *Phys. Rev. Lett.* **2007**, *99*, 063908.

(10) Pors, A.; Nielsen, M. G.; Valle, G. D.; Willatzen, M.; Albrektsen, O.; Bozhevolnyi, S. I. Plasmonic Metamaterial Wave Retarders in Reflection by Orthogonally Oriented Detuned Electrical Dipoles. *Opt. Lett.* **2011**, *36*, 1626−1628.

(11) Yu, N. F.; Aieta, F.; Genevet, P.; Kats, M. A.; Gaburro, Z.; Capasso, F. A Broadband, Background-Free Quarter-Wave Plate Based on Plasmonic Metasurfaces. *Nano Lett.* **2012**, *12*, 6328−6333.

(12) Zhao, Y.; Alù, A. Tailoring the Dispersion of Plasmonic Nanorods to Realize Broadband Optical Meta-Waveplates. *Nano Lett.* **2013**, *13*, 1086−1091.

(13) Pors, A.; Nielsen, M. G.; Bozhevolnyi, S. I. Broadband Plasmonic Half-Wave Plates in Reflection. *Opt. Lett.* **2013**, *38*, 513.

(14) Pors, A.; Bozhevolnyi, S. I. Efficient and Broadband Quarter-Wave Plates by Gap-Plasmon Resonators. *Opt. Express* **2013**, *21*, 2942−2952.

(15) Jiang, Z. H.; Lin, L.; Ma, D.; Yun, S.; Werner, D. H.; Liu, Z. W.; Mayer, T. S. Broadband and Wide Field-of-View Plasmonic Metasurface-Enabled Waveplates. *Sci. Rep.* **2015**, *4*, 7511.

(16) Cong, L. Q.; Xu, N. N.; Gu, J. Q.; Singh, R. J.; Han, J. G.; Zhang, W. L. Highly Flexible Broadband Terahertz Metamaterial Quarter-Wave Plate. *Laser Photonics Rev.* **2014**, *8*, 626−632.

(17) Jiang, S. C.; Xiong, X.; Hu, Y. S.; Hu, Y. H.; Ma, G. B.; Peng, R. W.; Sun, C.; Wang, M. Controlling the Polarization State of Light with a Dispersion-Free Metastructure. *Phys. Rev. X* **2014**, *4*, 021026.

(18) Xiao, S. Y.; Mühlenbernd, H.; Li, G. X.; Kenney, M.; Liu, F.; Zentgraf, T.; Zhang, S.; Li, J. Helicity-Preserving Omnidirectional Plasmonic Mirror. *Adv. Opt. Mater.* **2016**, *4*, 654−658.

(19) Lin, D. M.; Fan, P. Y.; Hasman, E.; Brongersma, M. L. Dielectric Gradient Metasurface Optical Elements. *Science* **2014**, *345*, 298−302.

(20) Yang, Y. M.; Wang, W. Y.; Moitra, P.; Kravchenko, I. I.; Briggs, D. P.; Valentine, J. Dielectric Meta-Reflectarray for Broadband Linear Polarization Conversion and Optical Vortex Generation. *Nano Lett.* **2014**, *14*, 1394−1399.

(21) Arbabi, A.; Horie, Y.; Bagheri, M.; Faraon, A. Dielectric Metasurfaces for Complete Control of Phase and Polarization with Subwavelength Spatial Resolution and High Transmission. *Nat. Nanotechnol.* **2015**, *10*, 937−943.

(22) Zheng, G. X.; Mühlenbernd, H.; Kenney, M.; Li, G. X.; Zentgraf, T.; Zhang, S. Metasurface Holograms Reaching 80% Efficiency. *Nat. Nanotechnol.* **2015**, *10*, 308−312.

(23) Guo, Q. H.; Schlickriede, C.; Wang, D. Y.; Liu, H. C.; Xiang, Y. J.; Zentgraf, T.; Zhang, S. Manipulation of Vector Beam Polarization with Geometric Metasurfaces. *Opt. Express* **2017**, *25*, 14300−14307.

(24) Wu, P. C.; Tsai, W. Y.; Chen, W. T.; Huang, Y. W.; Chen, T. Y.; Chen, J. W.; Liao, C. Y.; Chu, C. H.; Sun, G.; Tsai, D. P. Versatile Polarization Generation with an Aluminum Plasmonic Metasurface. *Nano Lett.* **2017**, *17*, 445−452.

(25) Balthasar Mueller, J. P.; Rubin, N. A.; Devlin, R. C.; Groever, B.; Capasso, F. Metasurface Polarization Optics: Independent Phase Control of Arbitrary Orthogonal States of Polarization. *Phys. Rev. Lett.* **2017**, *118*, 113901.

(26) Yan, L. B.; Zhu, W. M.; Karim, M. F.; Cai, H.; Gu, A. Y.; Shen, Z. X.; Chong, P. H. J.; Tsai, D. P.; Kwong, D. L.; Qiu, C. W.; Liu, A. Q. Arbitrary and Independent Polarization Control *in Situ via* a Single Metasurface. *Adv. Opt. Mater.* **2018**, *6*, 1800728.

(27) Ding, F.; Chen, Y. T.; Bozhevolnyi, S. I. Gap-Surface Plasmon Metasurfaces for Linear-Polarization Conversion, Focusing, and Beam Splitting. *Photonics Res.* **2020**, *8*, 707.

(28) Meng, C.; Tang, S. W.; Ding, F.; Bozhevolnyi, S. I. Optical Gap-Surface Plasmon Metasurfaces for Spin-Controlled Surface Plasmon Excitation and Anomalous Beam Steering. *ACS Photonics* **2020**, *7*, 1849−1856.

(29) Zhang, C.; Divitt, S.; Fan, Q. B.; Zhu, W. Q.; Agrawal, A.; Lu, Y. Q.; Xu, T.; Lezec, H. J. Low-Loss Metasurface Optics Down to the Deep Ultraviolet Region. *Light: Sci. Appl.* **2020**, *9*, 55.

(30) Li, Z. C.; Liu, W. W.; Cheng, H.; Choi, D. Y.; Chen, S. Q.; Tian, J. G. Spin-Selective Full-Dimensional Manipulation of Optical Waves with Chiral Mirror. *Adv. Mater.* **2020**, *32*, 1907983.

(31) Ding, F.; Chang, B. D.; Wei, Q. S.; Huang, L. L.; Guan, X. W.; Bozhevolnyi, S. I. Versatile Polarization Generation and Manipulation Using Dielectric Metasurfaces. *Laser Photonics Rev.* **2020**, *14*, 2000116.

(32) Chen, C.; Gao, S. L.; Song, W. G.; Li, H. M.; Zhu, S. N.; Li, T. Metasurfaces with Planar Chiral Meta-Atoms for Spin Light Manipulation. *Nano Lett.* **2021**, *21*, 1815−1821.

(33) Wang, D. Y.; Liu, T.; Zhou, Y. J.; Zheng, X. Y.; Sun, S. L.; He, Q.; Zhou, L. High-Efficiency Metadevices for Bifunctional Generations of Vectorial Optical Fields. *Nanophotonics* **2020**, *10*, 685−695.

(34) Xu, H. X.; Wang, Y. Z.; Wang, C. H.; Wang, M. Z.; Wang, S. J.; Ding, F.; Huang, Y. J.; Zhang, X. K.; Liu, H. W.; Ling, X. H.; Huang, W. Deterministic Approach to Achieve Full-Polarization Cloak. *Research* **2021**, *2021*, 6382172.

(35) Liu, M. Z.; Huo, P. C.; Zhu, W. Q.; Zhang, C.; Zhang, Si.; Song, M. W.; Zhang, S.; Zhou, Q. W.; Chen, L.; Lezec, H. J.; Agrawal, A.; Lu, Y. Q.; Xu, T. Broadband Generation of Perfect Poincaré Beams *via* Dielectric Spin-Multiplexed Metasurface. *Nat. Commun.* **2021**, *12*, 2230.

(36) Qiu, Y. C.; Tang, S. W.; Cai, T.; Xu, H. X.; Ding, F. Fundamentals and Applications of Spin-Decoupled Pancharatnam−Berry Metasurfaces. *Front. Optoelectron.* **2021**, *14*, 134−147.

(37) Ding, F.; Tang, S. W.; Bozhevolnyi, S. I. Recent Advances in Polarization-Encoded Optical Metasurfaces. *Adv. Photonics Res.* **2021**, *2*, 2000173.

(38) Cai, Z. R.; Deng, Y. D.; Wu, C.; Meng, C.; Ding, Y. T.; Bozhevolnyi, S. I.; Ding, F. Dual-Functional Optical Waveplates Based on Gap-Surface Plasmon Metasurfaces. *Adv. Opt. Mater.* **2021**, *9*, 2002253.

(39) Yuan, Y. Y.; Sun, S.; Chen, Y.; Zhang, K.; Ding, X. M.; Ratni, B.; Wu, Q.; Burokur, S. N.; Qiu, C. W. A Fully Phase-Modulated Metasurface as an Energy-Controllable Circular Polarization Router. *Sci. Adv.* **2020**, *7*, 2001437.

(40) Zhang, K.; Yuan, Y. Y.; Ding, X. M.; Li, H. Y.; Ratni, B.; Wu, Q.; Liu, J.; Burokur, S. N.; Tan, J. B. Polarization-Engineered Noninterleaved Metasurface for Integer and Fractional Orbital Angular Momentum Multiplexing. *Laser Photonics Rev.* **2021**, *15*, 2000351.

(41) Yuan, Y. Y.; Zhang, K.; Ratni, B.; Song, Q. H.; Ding, X. M.; Wu, Q.; Burokur, S. N.; Genevet, P. Independent Phase Modulation for Quadruplex Polarization Channels Enabled by Chirality-Assisted Geometric-Phase Metasurfaces. *Nat. Commun.* **2020**, *11*, 4186.

(42) Wang, D. Y.; Liu, F. F.; Liu, T.; Sun, S. L.; He, Q.; Zhou, L. Efficient Generation of Complex Vectorial Optical Fields with Metasurfaces. *Light: Sci. Appl.* **2021**, *10*, 67.

(43) Ding, F.; Yang, Y. Q.; Deshpande, R. A.; Bozhevolnyi, S. I. A Review of Gap-Surface Plasmon Metasurfaces: Fundamentals and Applications. *Nanophotonics* **2018**, *7*, 1129−1156.

(44) Johnson, P. B.; Christy, R. W. Optical Constants of the Noble Metals. *Phys. Rev. B* **1972**, *6*, 4370−4379.

(45) Li, Z. L.; Chen, C.; Guan, Z. Q.; Tao, J.; Chang, S.; Dai, Q.; Xiao, Y.; Cui, Y.; Wang, Y. Q.; Yu, S. H.; Zheng, G. X.; Zhang, S. Three-Channel Metasurfaces for Simultaneous Meta-Holography and Meta-Nanoprinting: A Single-Cell Design Approach. *Laser Photonics Rev.* **2020**, *14*, 2000032.

(46) Li, J. X.; Wang, Y. Q.; Chen, C.; Fu, R.; Zhou, Z.; Li, Z. L.; Zheng, G. X.; Yu, S. H.; Qiu, C. W.; Zhang, S. From Lingering to Rift: Metasurface Decoupling for Near- and Far-Field Functionalization. *Adv. Mater.* **2021**, *33*, 2007507.

Supporting Information

Functional Metasurface Quarter-Wave Plates for Simultaneous Polarization Conversion and Beam Steering

Yadong Deng,[1] Cuo Wu,[1,2] Chao Meng,[1] Sergey I. Bozhevolnyi,[1,*] and Fei Ding[1,*]

[1]Centre for Nano Optics, University of Southern Denmark, Campusvej 55, Odense M DK-5230, Denmark

[2]Institute of Fundamental and Frontier Sciences, University of Electronic Science and Technology of China, Chengdu 610054, People's Republic of China

[*]Corresponding author: feid@mci.sdu.dk; seib@mci.sdu.dk

Dimensions and reflection coefficients of the selected 4 meta-atoms

The dimensions of the 4 meta-atoms that function as nanoscale quarter-wave plates (nano-QWPs) and provide effective phase modulation of the reflected fields are presented in Table S1. In addition, the calculated phases and amplitudes of these 4 meta-atoms are also shown in Table S1, respectively. Due to the uneven amplitudes, the performance of beam steering will be affected, resulting in decreased efficiency and increased unwanted diffraction orders.

Table S1. Dimensions and reflection coefficients of the selected 4 meta-atoms.

No. of the meta-atom	L_x/nm	L_y/nm	φ_{xx}/deg	$\Delta\varphi$/deg	$|r_{xx}|$
1	92	141	45.1	89.7	0.97
2	144	167	135.4	90.0	0.76
3	164	245	224.8	90.1	0.71
4	249	82	315.2	89.7	0.92

Influence of the width of meta-atoms on the performance

If the width w of the meta-atom is decreased from 50 to 30 nm, the reflection amplitude decreases while the available resonance phase of nano-QWPs (*i.e.*, φ_{xx}) becomes larger, covering a wide range of $> 315°$ (Figure S1a). Therefore, 8 meta-atoms that function as nano-QWPs providing the appropriate phase modulation of the reflected fields can be identified (Table S2). At the same time, elements No.4, No.5, and No.6 exhibit relatively low reflection amplitudes ($< 60\%$), thereby seriously decreasing the efficiency of the phase gradient metasurface (Figure S2a). Specifically, the total reflectivity is decreased from 48% to 36% at the designed wavelength of 850 nm, and the unwanted 0-order diffraction becomes significant. In addition, the dimensions of these nano-QWPs are too close to be realistically fabricated with an acceptable accuracy. When the width w is increased to 70 nm, the reflection amplitude is increased, although at the expense of a rather limited phase coverage of only $\sim 180°$, as shown in Figure S1b. Nevertheless, the selected 2 nano-QWPs with the width of 70 nm (Table S3) can be used to replace the low-amplitude elements shown in Table S1. For instance, if the original element No.2 providing the reflection phase of 135° is replaced with the new element No.2 ($w = 70$ nm, $L_x = 152$ nm, and $L_y = 183$ nm), the total reflectivity is increased by 5% (Figure S2b).
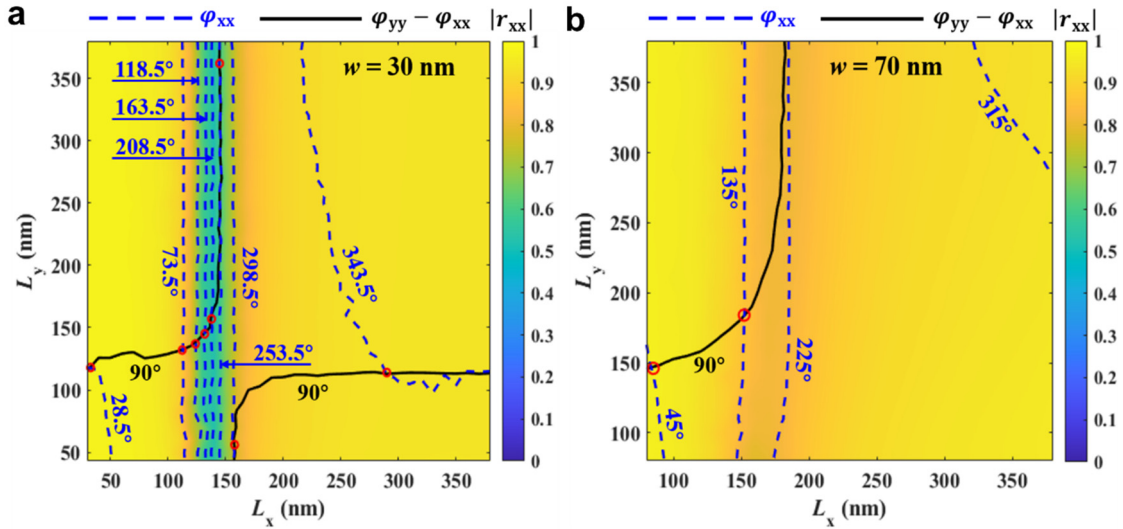
Figure S1. Calculated reflection coefficient as a function of the dimensions at the design wavelength of 850 nm for *x*-polarization with the width of **a)** 30 and **b)** 70 nm. The color map shows the reflection amplitude $|r_{xx}|$, while the blue dashed lines are contours of the reflection phase φ_{xx} with a step of 90° and black solid lines indicate the meta-atoms with the phase difference $\Delta\varphi = \varphi_{yy} - \varphi_{xx}$ equal to 90°. The other geometrical parameters are the same as those in Figure 1.

Table S2. Dimensions and reflection coefficients of the selected 8 meta-atoms with $w = 30$ nm.

No. of the meta-atom	L_x/nm	L_y/nm	φ_{xx}/deg	$\Delta\varphi$/deg	$\|r_{xx}\|$
1	33	116	28.47	89.50	0.98
2	115	132	73.52	90.68	0.86
3	126	137	118.52	89.20	0.69
4	133	145	163.57	90.58	0.54
5	139	157	208.46	90.10	0.52
6	145	362	253.43	89.83	0.57
7	154	52	298.41	90.17	0.76
8	284	114	343.52	89.97	0.94

Table S3. Dimensions and reflection coefficients of the selected 2 meta-atoms with $w = 70$ nm.

No. of the meta-atom	L_x/nm	L_y/nm	φ_{xx}/deg	$\Delta\varphi$/deg	$\|r_{xx}\|$
1	83	146	44.96	90.22	0.97
2	152	183	134.57	90.69	0.86
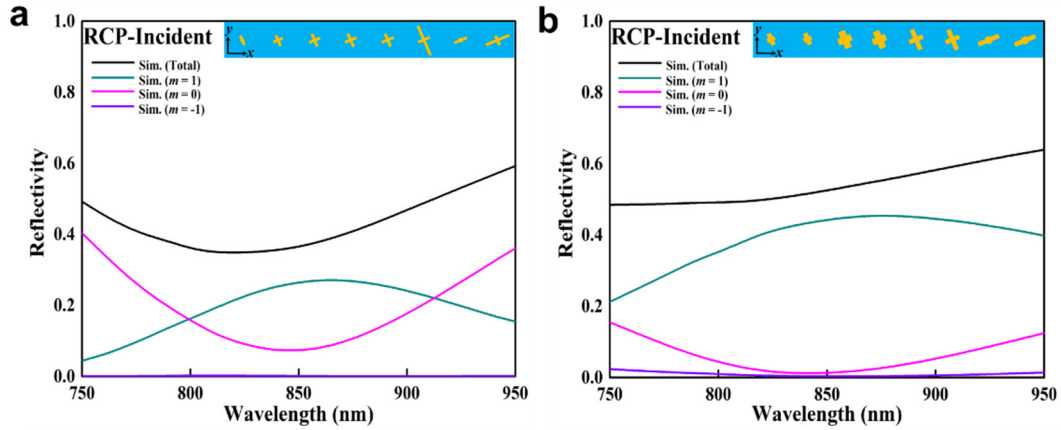
Figure S2. Simulated diffraction efficiencies of the GSP gradient MS1 for circular-to-linear polarization conversion and beam steering as a function of wavelength for RCP incident light. In **a)**, the MS1 supercell is composed of 8 elements with $w = 30$ nm selected from Table S2. In b), the original element No.2 ($w = 50$ nm, $L_x = 144$ nm, and $L_y = 167$ nm) that provides the phase of 135° is replaced with the new element No.2 ($w = 70$ nm, $L_x = 152$ nm, and $L_y = 183$ nm) while the other 3 elements are not changed.

The simulated performance of nano-QWPs with different orientations

Figure S3 shows the simulated degree of linear polarization (DoLP) and angle of linear polarization (AoLP) of the four designed nano-QWPs as a function of the rotation angle of θ with respect to the x-axis under RCP incident light at the wavelength of 850 nm. With the rotation angle θ changed from 0° to 90°, the DoLPs stay around 0.99 and AoLPs follow the linear distribution of $\theta + 45°$, which is consistent with the theoretical predictions in all cases. Therefore, our designed four meta-atoms are not affected by the near-field coupling between adjacent cells with respect to the nano-QWP rotation, continuing to function as excellent nano-QWPs.
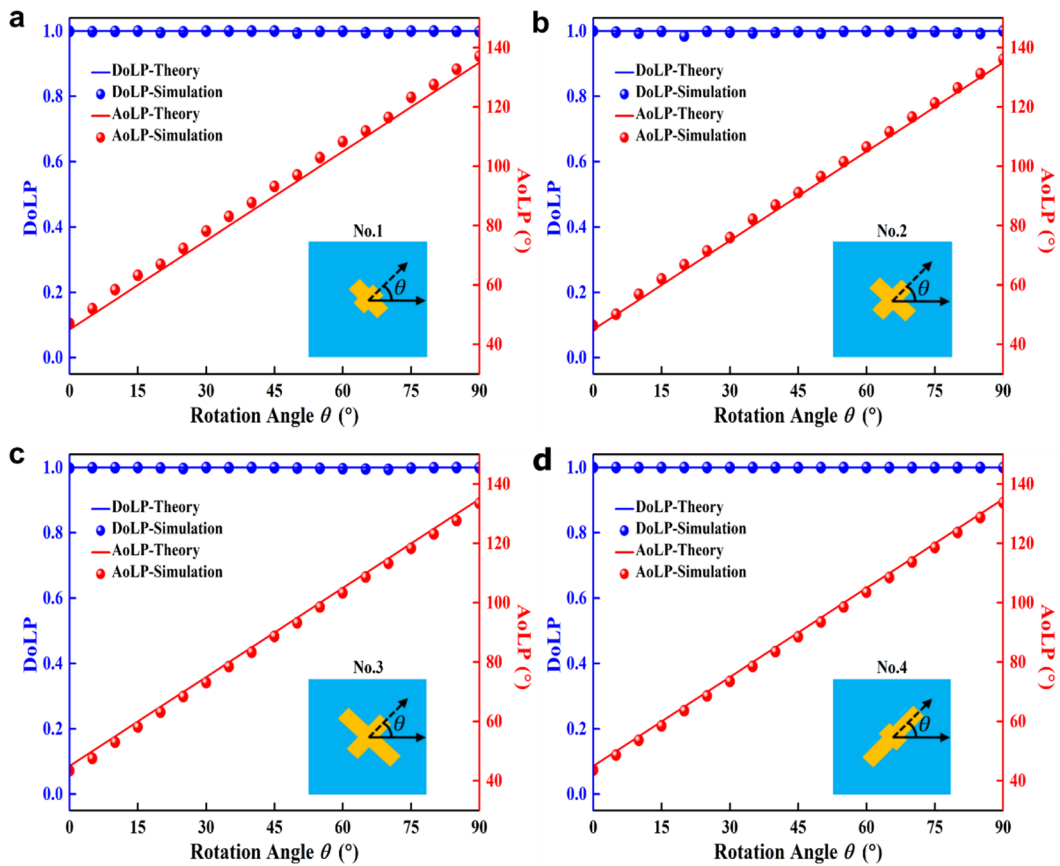
Figure S3. Calculated DoLPs and AoLPs the four designed nano-QWPs as a function of the rotation angle of θ with respect to the x-axis under RCP incident light at the wavelength of 850 nm.

The custom-built optical setup

In order to experimentally test and verify the performance of our fabricated metasurfaces, the prepared samples are characterized using a custom-built optical setup shown in Figure S4. The fiber-collimated near-infrared light from a tunable Ti: Sapphire laser (Laser, Spectra-Physics, Model 3900S) first passes through a half-wave plate (HWP, Thorlabs, AHWP05M-980) and an attenuator (Thorlabs, NE01B) to adjust the intensity of the output light. Then the output light passes through a linear polarizer (LP1, Thorlabs, LPN1R050-MP2) and a quarter-wave plate (QWP, Thorlabs, AQWP10M-980) to generate a left-handed circularly polarized (LCP) or right-handed circularly polarized (RCP) beam. Then the circularly polarized (CP) beam passes through one silver mirror (Mirror, Thorlabs, PF10-03-P01) and 2 beam splitters (BS1 and BS2, Thorlabs, CM1-BS014) which could adjust the direction of the beam propagation and compensate for the actual phase retardance caused by one single beam splitter. Then the CP beam is slightly focused on the sample with a spot size smaller than the sample area by a long working distance objective (Obj, Mitutoyo, M Plan Apo, 20×/0.42 NA). The reflected signal collected by the same objective passes through BS2, a tube lens (TL, Thorlabs, TTL200-S8, $f = 200$ mm) and then an iris (Thorlabs, ID12Z/M) that located at the first direct image plane to select a specific area of interest in the sample. The filtered first direct image is then imaged again by another relay lens (RL, Thorlabs, AC254-100-B-ML, $f = 100$ mm) onto one charge-coupled device (CCD1, Thorlabs, DCC1545M-GL). Note that another same CCD camera (CCD2) could be mounted at different positions to get Fourier images, and linear polarizer (LP2, Thorlabs, LPN1R050-MP2) is mounted between CCD2 and RL for polarization-resolved measurement. The efficiencies and polarization properties of the reflected light are measured on the Fourier plane, at which different diffraction orders are well separated in space.
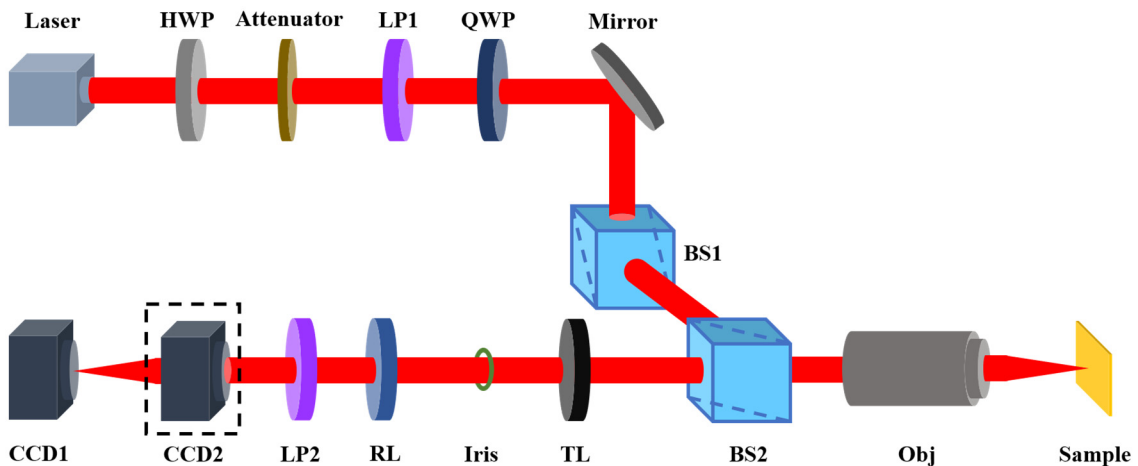
Figure S4. Schematic of the experimental setup for characterizing metasurfaces.

Supplementary simulation and experimental data for MS1

Under RCP incident light, the simulated (dark cyan solid line) and measured (dark cyan star markers) polarization state diagrams as a function of the orientation of the analyzer for +1 diffraction order at wavelengths of 800 and 900 nm are shown in Figure S5, which are in good agreement with each other. The measured degrees of linear polarization (DoLPs) are 99.56% and 99.16% at wavelengths of 800 and 900 nm, respectively, consistent with the DoLPs of 99.27% and 99.82% in the simulation.
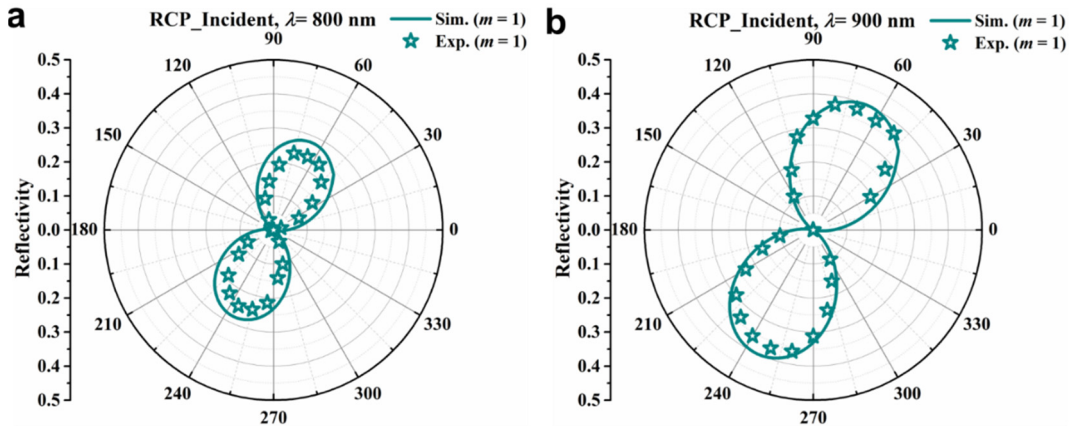
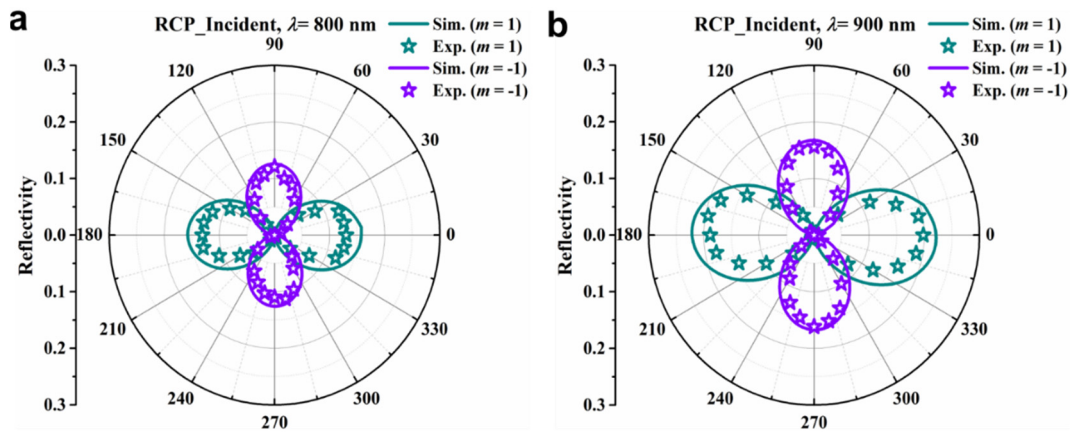**Figure S5.** Simulated (dark cyan solid line) and experimental (dark cyan star markers) polarization state diagrams of the steered beam within +1 diffraction order for RCP incident light at wavelengths of **a)** 800 nm and **b)** 900 nm.

Under LCP incident light, we include related simulations and measurements in Figure S6. Figure S6a compares the simulated (four colorful solid lines) and measured (colorful markers) diffraction efficiencies of different diffraction orders from $m = -1$ to $+1$ as a function of wavelength. In general, the simulated and measured diffraction efficiencies coincide fairly well. At the design wavelength of 850 nm, almost all the incident energy has been reflected to +1 diffraction order, demonstrate the excellent capability of steering. Quantitatively, the total measured reflected efficiency is 47.60% (simulated value is 50.20%) and the +1-order diffraction efficiency is 36.50% (simulated value is 40.00%) at $\lambda = 850$ nm. As shown in Figure S6b-S6d, there is a reasonable agreement between the measured and simulated efficiencies at different diffraction orders: the measured DoLPs (orange star markers) are 99.15%, 99.70%, and 99.71% at wavelengths of 800, 850, and 900 nm, respectively, and the simulated DoLPs (orange solid lines) are 99.82%, 99.13% and 99.36% at wavelengths of 800, 850, and 900 nm, respectively.
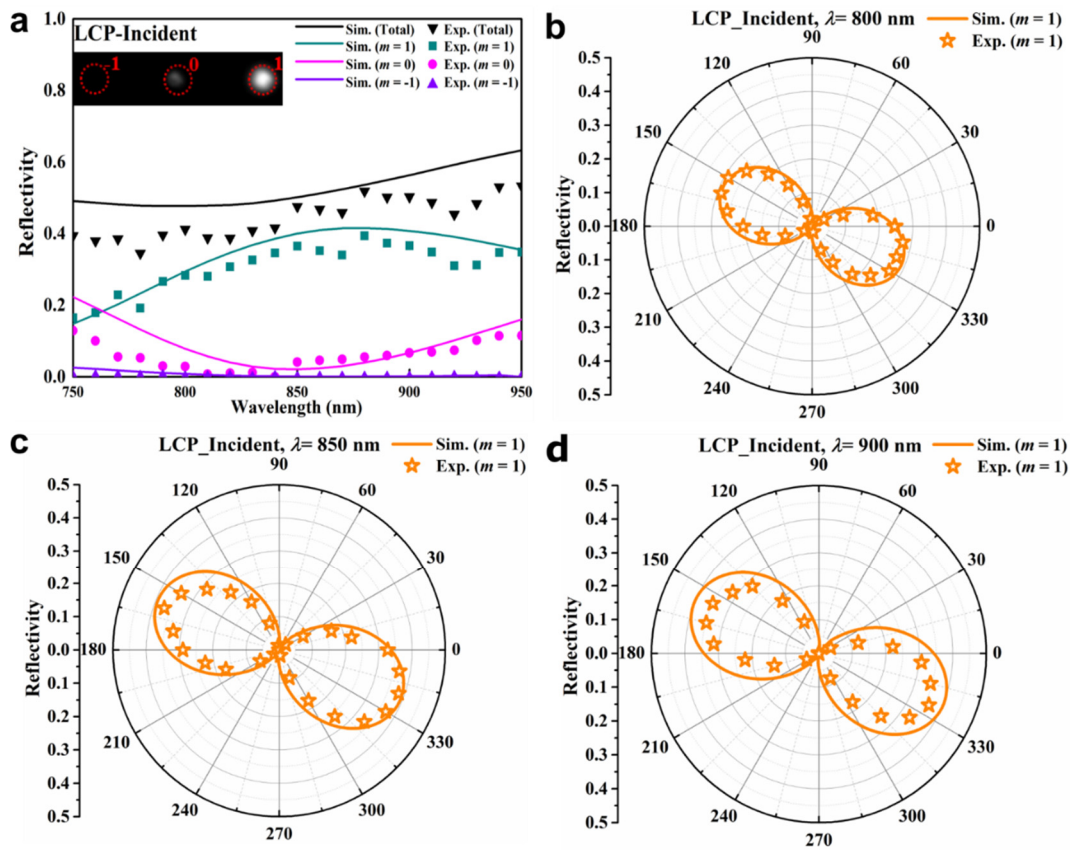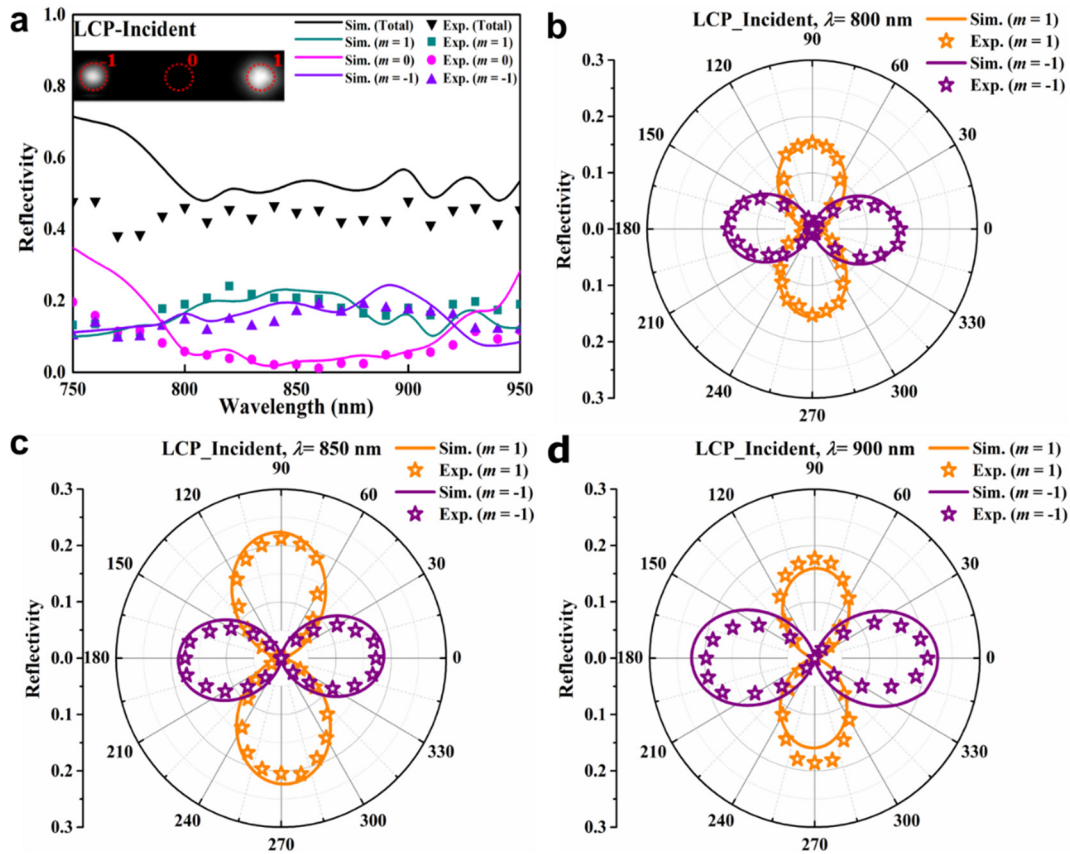
Figure S6. a) Simulated (solid lines) and experimental (markers) diffraction efficiencies of different orders as a function of wavelength for LCP incident light. The inset shows the optical image of the diffraction spots at the wavelength of 850 nm. Simulated (orange solid line) and measured (orange star markers) polarization state diagrams of the steered beam within +1 diffraction order for LCP incident light at wavelengths of **b)** 800 nm, **c)** 850 nm and **d)** 900 nm.

Supplementary simulation and experimental data for MS2

The simulated (dark cyan/violet solid line) and measured (dark cyan/violet star markers) polarization state diagrams as a function of the orientation of the analyzer for ±1 diffraction order at wavelengths of 800 and 900 nm under RCP excitation are shown in Figure S7. From Figure S7, it is clear that there is a good agreement between the simulated and measured DoLPs for different diffraction orders. At λ = 800 nm, the measured (simulated) DoLPs are 99.45% (99.19%) and 99.52% (99.32%) for diffraction orders of $m = \pm1$, respectively. At λ = 900 nm, the measured (simulated) DoLPs are 99.40% (99.50%) and 99.10% (99.52%) for diffraction orders of $m = \pm1$, respectively.

Figure S7. Simulated (dark cyan/violet solid line) and experimental (dark cyan/violet star markers) polarization state diagrams of the steered beams within ±1 diffraction orders for RCP incident light at wavelengths of **a)** 800 nm and **b)** 900 nm.

Under LCP incident light, the simulated (four colorful solid lines) and measured (colorful markers) diffraction efficiencies are well-matched with each other in Figure S8a. In particular, the diffraction efficiency of +1 order is 20.80% (simulated value is 23.00%) and the diffraction efficiency of −1 order is 17.00% (simulated value is 19.30%) at λ = 850 nm. As shown in Figure S8b-S8d, there is a reasonable agreement between the measured and simulated efficiencies at different diffraction orders: the measured DoLPs (orange/purple star markers) are 99.06%, 99.30%, and 99.26% for the +1 diffraction order and 99.10%, 99.61%, and 99.31% for the −1 diffraction order at wavelengths of 800, 850, and 900 nm, respectively; the simulated DoLPs (orange/purple solid line) are 99.73%, 99.65%, and 99.44% for the +1 diffraction order and 99.62%, 99.35%, and 99.41% for the −1 diffraction order at wavelengths of 800, 850, and 900 nm, respectively.

Figure S8. a) Simulated (solid lines) and experimental (markers) diffraction efficiencies of different orders as a function of wavelength for LCP incident light. The inset shows the optical image of the diffraction spots at the wavelength of 850 nm. Simulated (orange/purple solid line) and measured (orange/purple star markers) polarization state diagrams of the steered beams within ±1 diffraction orders for LCP incident light at wavelengths of **b)** 800, **c)** 850, and **d)** 900 nm.

Supplementary simulation and experimental data for MS3

To show the capability of steering co- and cross-polarized CP channels, we plot the electric field distributions of the reflection light for diffraction orders of $m = 0$ (Figure S9a) and 1 (Figure S9c) at the design wavelength of 850 nm for RCP incident light, which indicate the well-defined wavefronts. Figure S9b and S9d display the simulated (dark cyan/ magenta solid line) and experimental (dark cyan/ magenta star markers) polarization state diagrams as a function of the orientation of the analyzer at $\lambda = 800$ and 900 nm, manifesting reasonable agreements. Specifically, the measured degrees of circular polarization (DoCPs) (dark cyan/ magenta star markers) are 90.60% and 91.10% for 0 diffraction order and −93.40% and −90.70% for +1 diffraction order at wavelengths of 800 and 900 nm, respectively, which are a little lower than the simulated values (dark cyan/ magenta solid line) of 99.35% and 99.41% for 0 diffraction order and −99.44% and −99.65% for +1 diffraction order at $\lambda = 800$ and 900 nm, respectively.
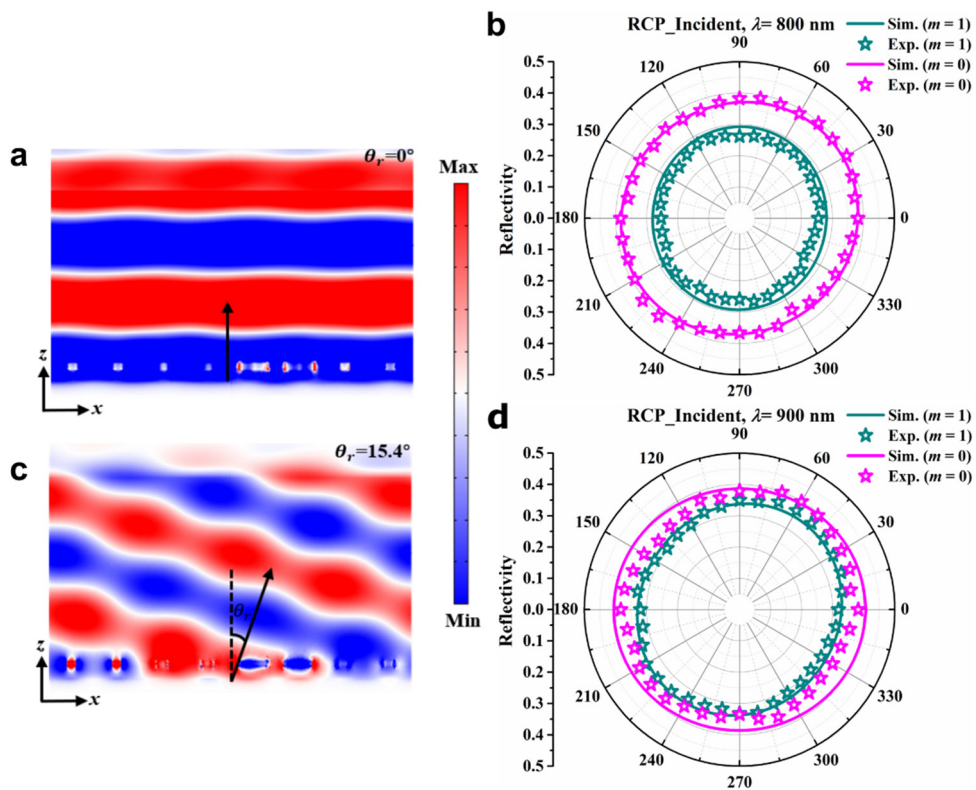
Figure S9. Electric field distributions of the reflection light for diffraction orders of **a)** $m = 0$ and **c)** $m = 1$ of MS3 at the design wavelength of 850 nm under RCP excitation. Simulated (dark cyan/magenta solid line) and experimental (dark cyan/magenta star markers) polarization state diagrams as a function of the orientation of the analyzer for RCP incident light at wavelengths of **b)** 800 and **d)** 900 nm.

Supplementary simulation and experimental data for MS4

For MS4, we also plot the electric field distributions of the reflection light for diffraction orders of m = −1 and 1 at λ = 850 nm under RCP excitation, where the well-defined tilted planar wavefronts can be clearly seen (Figure S10a and S10c). To verify the polarization state, the simulated (dark cyan/violet solid line) and experimental (dark cyan/violet star markers) polarization polar diagram as a function of the orientation of the analyzer at wavelengths of 800 and 900 nm are shown in Figure S10b and S10d, respectively. Generally, there is a reasonable agreement between the measured and simulated efficiencies at different diffraction orders, albeit with some discrepancies regarding the DoCPs. The measured DoCPs (dark cyan/ violet star markers) are 90.24% and 92.40% for −1 diffraction order and –90.10% and −89.30% for +1 diffraction order at λ = 800 and 900 nm, respectively, while the simulated DoCPs (dark cyan/ violet solid line) are 99.66% and 99.89% for −1 diffraction order and −99.60% and −99.65% for +1 diffraction order at wavelengths of 800 and 900 nm, respectively.
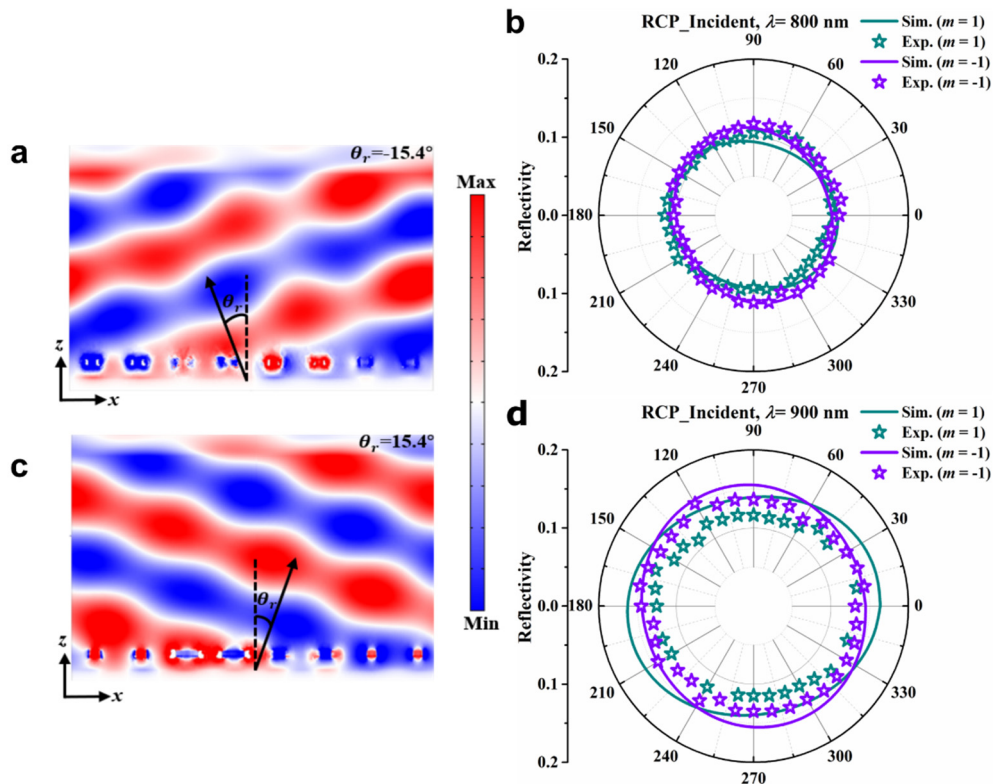
Figure S10. Electric field distributions of the reflection light for diffraction orders of **a)** m = 0 and **c)** m = 1 of MS4 at the design wavelength of 850 nm under RCP excitation. Simulated (dark cyan/magenta solid line) and experimental (dark cyan/magenta star markers) polarization state diagrams as a function of the orientation of the analyzer for RCP incident light at wavelengths of **b)** 800 and **d)** 900 nm.

Calculated diffraction efficiencies for MS2 with the damping rate of bulk gold
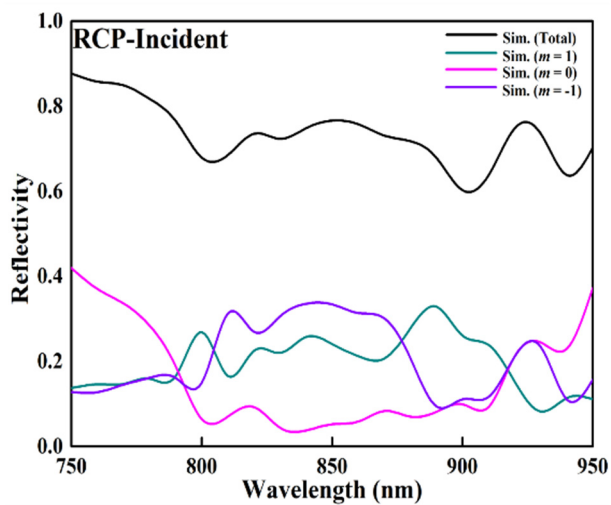
Figure S11. Simulated diffraction efficiencies of different orders as a function of wavelength for MS2 under the RCP excitation. The damping rate of Au meta-atoms is the same as that of bulk gold.

Performance of designed metasurfaces under linearly polarized incidence

Table S4 summaries the polarization states of reflected light within different diffraction orders for the designed four metasurfaces (MS1 to MS4) under a linearly polarized (LP) excitation at the designed wave length of 850 nm.

Table S4. Performance of designed metasurfaces under linearly polarized incidence

	Input (LP, AoLP)	Output ($m = -1$)	Output ($m = 0$)	Output ($m = 1$)
MS1	67.5°	×	×	RCP
	−22.5°			LCP
MS2	0°	LCP	×	RCP
	90°	RCP		LCP
MS3	0°	RCP	LP (0°)	LCP
	90°	RCP	LP (0°)	LCP
MS4	0°	LP (0°)	×	LP (30°)
	90°	LP (90°)		LP (120°)

Spin-Controlled Gap-Surface Plasmon Metalenses for Focused Scalar and Vector Beam Generation

Yadong Deng, Chao Meng, Sören im Sande, Sergey I. Bozhevolnyi* and Fei Ding*

Y. Deng, C. Meng, S. I. Sande, S. I. Bozhevolnyi, and F. Ding

Centre for Nano Optics, University of Southern Denmark, Campusvej 55, Odense DK-5230,

Denmark

E-mail: seib@mci.sdu.dk (S.I.B.) and feid@mci.sdu.dk (F.D.) of corresponding authors

Abstract

Scalar and vector beams, each demonstrating spatially homogeneous and variable polarization states respectively, are highly desired in photonics, especially when they are efficiently focused. Nevertheless, existing techniques for generating them either require bulky optical components or exhibit restricted functionalities, which impedes the advancements of integration-optics applications. Here, we propose a versatile gap-surface plasmon (GSP) metalens platform to generate focused scalar and vector beams based on nanoscale quarter-wave plates (nano-QWPs) with a certain spatial phase gradient. We exemplify our strategy through experimental demonstrations of a single-focal metalens to generate focused scalar beams, e.g., linearly polarized (LP) beams here, exclusively through resonance phase over reflected fields in a broadband near-infrared range. And this approach has been expanded to realize a dual-focal metalens with uniquely tailored wavefronts focused at various locations within the same focal plane. We next experimentally demonstrate how resonance and geometric phases can be used simultaneously to achieve focused vector beams, e.g., radially polarized (RP) and azimuthally polarized (AP) beams here, carrying a specific orbital angular momentum (OAM) with a topological charge of $l = \pm 1$ under a pair of orthogonal circularly polarized (CP) excitations, respectively. The generated focused RP (AP) vector beam can be further experimentally

decomposed into one focused Gaussian beam with the same helicity as excitation for the co-polarized CP channel and one focused vortex beam carrying OAM with twice the value of l for the cross-polarized CP channel. Our results establish an ultracompact platform for generating focused scalar and vector beams, broadening the utility of polarization in designing versatile metalenses. This also holds potential for applications in tunable structured light and diverse light-matter interactions.

1. Introduction

The polarization of light, an intrinsic and crucial characteristic of electromagnetic radiation, assumes a pivotal role in the realm of science [1]. Most researched beams, which have spatially homogeneous states of polarization (SOPs) such as linear, circular, and elliptical polarizations, are known as scalar beams serving for numerous applications like data storage [2], polarization imaging [3] and nonlinear optics [4], whose SOPs are independent of the spatial position within the beam's cross section. Unlike scalar beams, vector beams refer to light beams with spatially inhomogeneous SOPs at different points within the same beam cross-section on the same wavefront simultaneously [5]. Due to the additional degrees of freedom offered by vector beams for light manipulation, numerous unique functionalities and potential applications have been demonstrated [6-10]. However, conventional approaches to generating scalar and vector beams involve bulky optical waveplates and intricate optical configurations [11-12], significantly restricting the potential for miniaturizing and densely integrating photonic systems down to the nanoscale. Worse still, when these beams are effectively focused, particularly for vector beams which can be focused more sharply to enable high resolution imaging [13], high precision sensing [14] and high-quality lithography [15], more bulky components (e.g., lenses or parabolic reflectors) are additionally assembled, resulting in increasingly intricate optical systems.

In recent years, optical metasurfaces, consisting of two-dimensional artificial subwavelength meta-atoms with meticulously engineered phase and polarization responses, have emerged as a versatile platform revolutionizing optical technology, enabling unparalleled control over light properties and offering diverse functionalities within an ultra-thin and compact planar structure [16-24]. Metalenses, acting as a subset of metasurfaces, have garnered increasing research interest due to their ability to realize conventional optical components and systems while providing more innovative functionalities [25-28]. Metalenses exhibit several fundamental characteristics and provide numerous features, including the capacity to efficiently focus light into subwavelength spots, multifunctionality, an ultrathin planar form factor, and the potential for cost-effective manufacturing [29-33]. One standout advantage of metalenses compared to diffractive lenses is their multifunctional capability, arguably their most prominent feature. Due to its dependence on scattering phenomena, a metalens can exhibit varying functionalities based on different degrees of freedom of light, e.g., polarization [29], wavelength [34-35], and incident angle [36]. These attributes have paved the way for new applications and the implementation of high-performance miniature optical metasystems.

In this work, we design a set of GSP nano-QWPs with a certain spatial phase gradient for efficient circular-to-linear polarization conversion, offering comprehensive control over the phase of reflected fields. Based on the nano-QWP design, we propose a versatile GSP metalens platform to generate focused scalar and vector beams under CP excitations. In a broadband near-infrared range (750 – 950 nm), we designed and experimentally demonstrated two GSP metalenses that enable LP beam generation and beam focusing over reflected fields employing only the resonance phase [29, 37-38], with single focused light spot (MS1) and dual-focused light spots (MS2), respectively. We next experimentally demonstrated how resonance and geometric phases can be used simultaneously [39-41] by MS3 to achieve focused RP and AP beams carrying a specific OAM with a topological charge of $l = \pm 1$ for incident left circularly polarized (LCP) light and right circularly polarized (RCP) light, respectively. The generated focused RP (AP) vector beam can be further experimentally decomposed into one focused Gaussian beam with the same helicity as excitation for the co-polarized CP channel and one focused vortex beam carrying OAM with twice the value of l for the cross-polarized CP channel. Our proposed versatile GSP nano-QWPs platform enhances the practical applications of multifunctional integrated metalenses by enabling simultaneous manipulation of phase and polarization. We anticipate that the ultra-thin, uniquely designed metalens devices hold promise for lightweight optical polarization systems applicable to fields such as image steganography and virtual reality.

2. Results and Discussion

2.1 QWP Meta-Atom Design

To realize the aforementioned metalenses, a typical metal-insulator-metal (MIM) GSP meta-atom is initially designed to serve as the essential nano-QWP unit. As shown in Figure 1a, the birefringent MIM meta-atom comprises a top gold (Au) cross-shaped antenna, a middle silicon dioxide (SiO_2) spacer layer and a bottom continuous Au film. Given the inherent anisotropic property of this birefringent meta-atom, with its major axes along x- and y- directions, $r_{xx} = |r_{xx}|e^{i\varphi_{xx}}$ and $r_{yy} = |r_{yy}|e^{i\varphi_{yy}}$ can be used to describe the complex reflection coefficients under x- and y-polarized excitations, respectively, which are predominantly determined by the dimensions of the meta-atom along its two principal axes. Obviously, when the reflection amplitudes are equal (i.e., $|r_{xx}| = |r_{yy}|$) and the relative phase difference $\Delta\varphi = \varphi_{yy} - \varphi_{xx} = \pm 90°$, the meta-atom can operate as a dream nano-QWP.

At our design wavelength of 850 nm, all the values in the structure parameter space $\Omega = [w, t_m, t_s, d, p] = $ [50 nm, 40 nm, 100 nm, 100 nm, 400 nm] were preset according to the nano-QWP design principles [41-42], in particular, to ensure high reflection efficiency and provide sufficient resonance phase coverage for constructing phase gradients. Then we conducted three-dimensional (3D) full-wave simulations using the commercially available software Comsol Multiphysics (version 5.6), parametrically sweeping the dimensions (l_x and l_y) of the top gold antenna to obtain the complex reflection coefficients of the meta-atoms under x- and y-polarized excitations. An air domain is introduced above the meta-atom and truncated with a perfectly matched layer to minimize the external interference. The relative permittivity of Au is modeled using the Drude model, fitted with experimental data [43], while SiO_2 is considered as a lossless material with a constant refractive index of 1.45. The MIM unit cell is exposed to normally incident x- or y-polarized plane waves, while periodic boundary conditions are enforced in both the x- and y-directions. Figure 1b shows the calculated reflection amplitudes and phases of our carefully selected four nano-QWPs (element #1 to #4, $\Delta\varphi$ of each matches to 90°) with a key resonance phase step of $\Delta\varphi_{xx} = 90°$ at the design wavelength of 850 nm. To ensure a broad operational bandwidth and high efficiency, a meta-atom library is meticulously crafted by collecting all these four nano-QWPs. This configuration can facilitate simultaneous circular-to-linear polarization conversion and potential wavefront shaping.
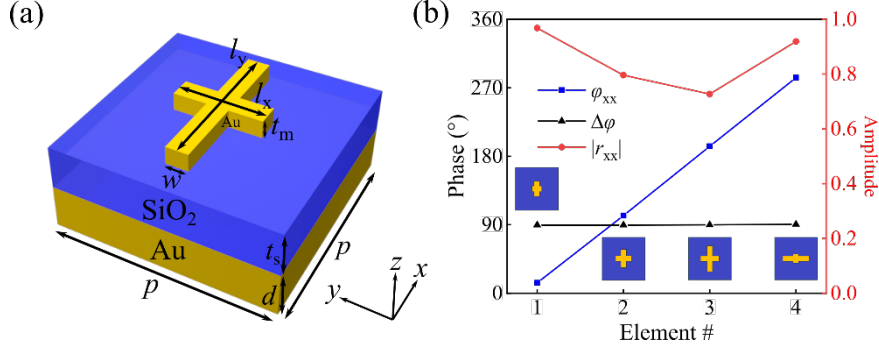
Figure 1. (a) Schematic of the anisotropic MIM meta-atom. (b) Calculated reflection amplitude $|r_{xx}|$, reflection phase φ_{xx} and the relative phase difference ($\Delta\varphi = \varphi_{yy} - \varphi_{xx} = 90°$) of the four QWP meta-atoms with a resonance phase step of $\Delta\varphi_{xx} = 90°$ at the design wavelength of 850 nm. The dimensions of element #1 to #4 are (1) $l_x = 91$ nm, $l_y = 147$ nm; (2) $l_x = 149$ nm, $l_y = 170$ nm; (3) $l_x = 170$ nm, $l_y = 242$ nm; (4) $l_x = 249$ nm, $l_y = 82$ nm.

2.2 GSP Metalenses for Focused Scalar Beam Generation

Holding the nano-QWP library designed above, we design optical GSP metalenses that realize focused scalar beam generation, capable of simultaneous circular-to-linear polarization conversion and beam focusing under LCP and RCP excitations. In this case, only the resonance phase related to the structural dimensions are utilized. The Jones matrix of the meta-atom rotated with an angle of θ from the x-axis can be written as:

$$J(\theta) = |r_{xx}|e^{i\varphi_{xx}}\begin{pmatrix} cos\theta & -sin\theta \\ sin\theta & cos\theta \end{pmatrix}\begin{pmatrix} 1 & 0 \\ 0 & i \end{pmatrix}\begin{pmatrix} cos\theta & sin\theta \\ -sin\theta & cos\theta \end{pmatrix} \tag{1}$$

where $M(\theta) = \begin{pmatrix} cos\theta & sin\theta \\ -sin\theta & cos\theta \end{pmatrix}$ represents the rotation matrix, and $\begin{pmatrix} 1 & 0 \\ 0 & i \end{pmatrix}$ is the Jones matrix of the designed nano-QWP with $\Delta\varphi = 90°$. Considering an LCP and RCP incident beam with $E_{in} = \frac{1}{\sqrt{2}}\begin{pmatrix} 1 \\ \pm i \end{pmatrix}$, the output light will be LP and the angle of linear polarization (AoLP) is $\theta \mp \frac{\pi}{4}$, which can be described as:

$$E_{out} = |r_{xx}|e^{i\varphi_{xx}}e^{\pm i\theta}\begin{pmatrix} cos\left(\theta \mp \frac{\pi}{4}\right) \\ sin\left(\theta \mp \frac{\pi}{4}\right) \end{pmatrix} \tag{2}$$

For example, obviously, if the rotation angle θ of each nano-QWP is equal to −45°, the reflected beam will be y- / x- polarized for the LCP/RCP incident beam, respectively. To generate a reflected focused beam with simultaneous circular-to-linear polarization conversion, the GSP metasurface should also be imposed with a phase profile of a lens, which can be calculated via the following formula [44-47]:

$$\varphi(x, y) = \frac{2\pi}{\lambda_d}\left(\sqrt{x^2 + y^2 + f^2} - f\right) \tag{3}$$

where λ_d is the design wavelength in free space, f is the focal length, and (x, y) represents the independent position coordinate of each nano-QWP in the metalens. Figure 2a displays the schematic of our designed metalens (MS1) with a diameter of $D = 50$ μm and a focal length of $f_1 = 50$ μm, and the rotation angle of each nano-QWP $\theta = -45°$, according to the phase distribution (Figure S1a) calculated by formula (3). The numerical aperture (NA) of MS1 is 0.4472. MS1 can enable simultaneous circular-to-linear polarization conversion, LCP ($| l \rangle$) to y - polarized light ($| y \rangle$) in (1) and RCP ($| r \rangle$) to x - polarized light ($| x \rangle$) in (2), and beam focusing at our design wavelength of λ_d = 850 nm. Figure 2b presents the scanning electron microscope (SEM) images of our fabricated MS1 sample using standard thin-film deposition, electron-beam lithography (EBL), and lift-off techniques (see the Methods section for details), referring to our designed geometry of MS1 (Figure S1b). The fabricated sample MS1 effectively mirrors the intended shapes and dimensions of the designed meta-atoms, notwithstanding minor surface roughness and rounded corners.

Following the fabrication, we characterized MS1 using the home-built optical setup shown in Figure S2. The characterization of MS1 is based on the principle of the ray optics [48-49], as illustrated in Figure 2c. To validate the actual focusing effect, MS1 is moved away from plane A (the focal plane of the objective, $z = 0$), which can result in a reflected focal light spot under incident beam from the substrate plane without any structures, to plane B (twice the focal length of MS1 from the perspective of geometric optics, $z = \sim 2f$). As shown the measurement results for LCP incident light in Figure 2d, taking the case at the wavelength of 850 nm as an example, we first moved the reflected focused light spot from the substrate at plane A to MS1. Subsequently, the bright reflected focused light spot from MS1 can be observed once we shifted the sample from plane A to plane B. While for the same plane, the reflection from the substrate would be strong diverging. Other two wavelengths exhibit similar performance. In addition, the measured normalized reflectivity as a function of the orientation of the analyzer in front of the CCD camera for LCP (Figure 2e) and RCP (Figure 2f) incident light also present great consistency with the theoretical results at the wavelength of 850 nm. (i) is labeled here to match the focused light spot with its polarization state for LCP incident light. In particular, both measured degree of linear polarization (DoLP) for LCP and RCP incident lights are very close to 1. Measurement results at the wavelengths of 800 and 900 nm can be seen in Figure S3. We also measured the reflectivities as a function of the wavelengths for both LCP and RCP incident lights, as shown in Figure 2g. Specifically, the total reflectivities are close to 30% at the wavelength of 850 nm for both CP incident lights.
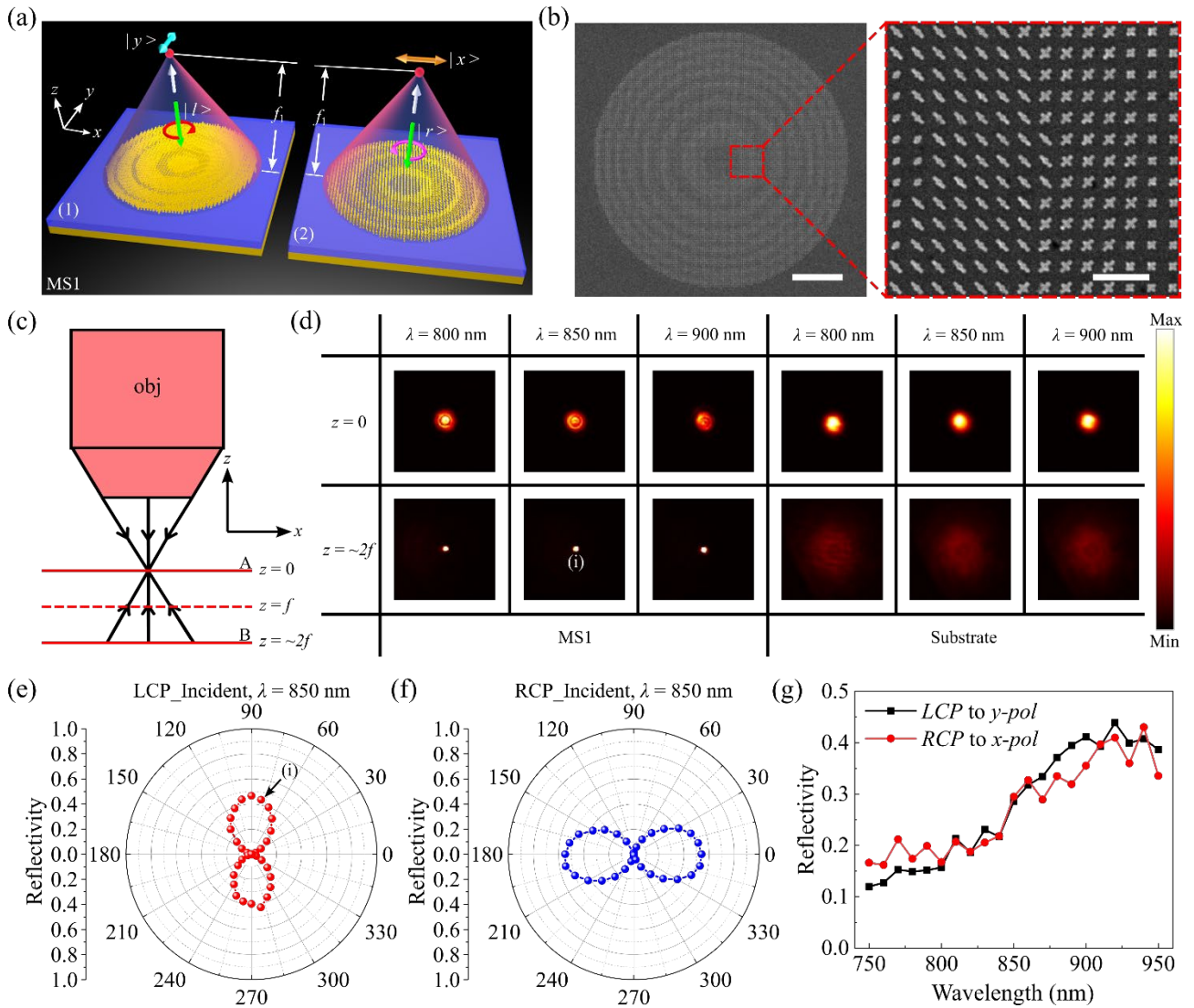
Figure 2. (a) Schematic of the optical GSP MS1 for single focused LP generation, LCP ($| l >$) to y - polarized light ($| y >$) in (1) and RCP ($| r >$) to x - polarized light ($| x >$) in (2), and beam focusing at the wavelength of 850 nm. (b) SEM images of the fabricated MS1 (scale bars are 10 µm and 1 µm, respectively). (c) Schematic of the measurement method in which the incident beam is focused at plane A (the focal plane of the objective, $z = 0$) and impinging on MS1 or the substrate without any structures at plane B (twice the focal length of MS1, $z = \sim 2f$). (d) Measured reflected optical images from MS1 and the substrate for incident LCP light with different wavelengths of 800, 850, and 900 nm, when the fabricated sample is moved from plane A to plane B. (e-f) Measured polarization state diagrams of the reflected focused light spots from MS1 at plane B for LCP (e) and RCP (f) incident light, respectively, at the wavelength of 850 nm. (g) The measured reflectivities as a function of the wavelengths for both LCP and RCP incident lights.

In addition to the aforementioned MS1 capable of generating single focal light spot along with circular-to-linear polarization conversion, we further developed our approach to realize a dual-focal metalens which can transform the incident CP light into two focused light spots with arbitrary AoLPs. Different from MS1, the dual-focal metalens (MS2) is split into two distinct left and right sections, each featuring a unique phase profile:

$$\varphi(x,y) = \begin{cases} \frac{2\pi}{\lambda_d}\left(\sqrt{\left(x+\frac{D}{4}\right)^2 + y^2 + f^2} - \sqrt{\left(\frac{D}{4}\right)^2 + f^2}\right), (x \leq 0) \\ \frac{2\pi}{\lambda_d}\left(\sqrt{\left(x-\frac{D}{4}\right)^2 + y^2 + f^2} - \sqrt{\left(\frac{D}{4}\right)^2 + f^2}\right), (x > 0) \end{cases} \tag{4}$$

Figure 3a displays the schematic of MS2 with $D = f_2 = 50$ μm (NA$_{MS2}$ = 0.4472), according to the phase distribution (Figure S1c) calculated by formula (4). Once the rotation angle of each nano-QWP is set to $\theta_l = +45°$ in the left section and $\theta_r = -45°$ in the right section, respectively, MS2 can reflect an incident CP light to two focused orthogonal LP lights, e.g., $|l>$ to focused $|x>$ and $|y>$ in (1) and $|r>$ to focused $|y>$ and $|x>$ in (2), at our design wavelength of $\lambda_d = 850$ nm. Figure 3b shows the SEM image of our fabricated MS2 sample referring to the geometry in Figure S1d. Utilizing the same measured method as described above, Figure 3c shows the measured reflected optical images from MS2 for incident LCP light with different wavelengths of 800, 850, and 900 nm, two bright focused light spots can be observed when MS2 is moved from plane A to plane B for each wavelength. Figure 3d characterizes the measured polarization state diagrams of the two reflected focused light spots from MS2 at plane B for LCP incident light at the wavelength of 850 nm, (i) and (ii) are labeled here to correspondingly match the two focused light spots with their respective polarization states. Moreover, by rotating the polarization analyzer in front of the CCD camera, the polarization states of the two light spots can be presented more intuitively, as shown the optical images in Figure S4. Measured DoLPs of (i) and (ii) in Figure 3d are both equal to ~ 1. Other measured results at the wavelengths of 800 and 900 nm for LCP incident light and the case for RCP incident light can be seen in Figure S5. In addition, measured reflectivities as a function of the wavelengths for LCP and RCP incident lights are shown in Figure 3e and 3f, respectively. In particular, the reflectivities of focused $|x>$ and $|y>$ under LCP excitation are ~ 13% and ~ 10%, respectively; and the reflectivities of focused $|y>$ and $|x>$ under RCP excitation are ~ 14% and ~ 16%, respectively, at the wavelength of 850 nm.
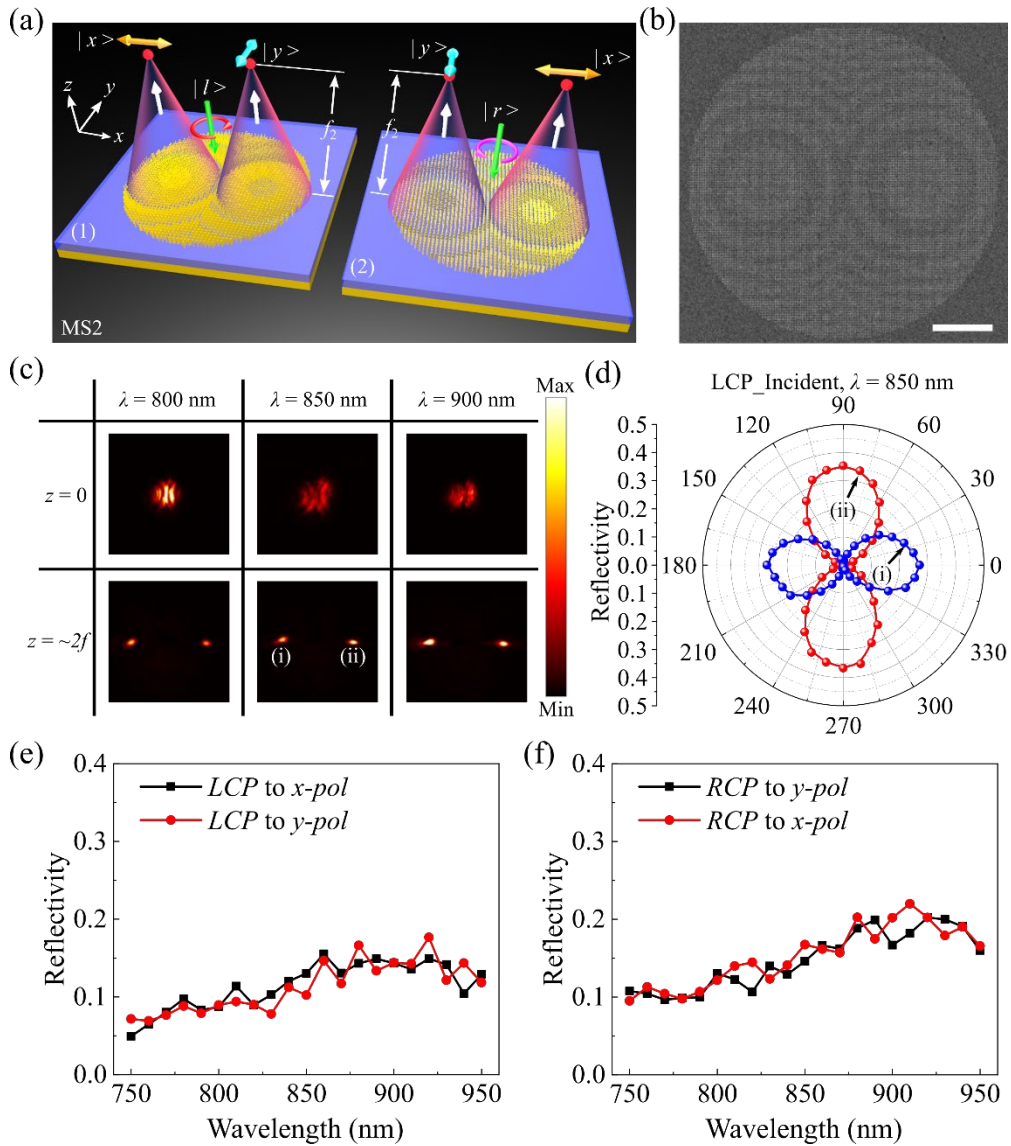
Figure 3. (a) Schematic of the optical GSP MS2 for dual-focal LP generation, $|l>$ to focused $|x>$ and $|y>$ in (1) and $|r>$ to focused $|y>$ and $|x>$ in (2), at the wavelength of 850 nm. (b) The SEM image of the fabricated MS2 (scale bars is 10 μm). (c) Measured reflected optical images from MS2 for incident LCP light with different wavelengths of 800, 850, and 900 nm, when the fabricated sample is moved from plane A to plane B. (d) Measured polarization state diagrams of the reflected focused light spots from MS2 at plane B for LCP incident light at the wavelength of 850 nm. (i) and (ii) are labeled here to correspondingly match the two focused light spots with their respective polarization states. (e-f) Measured reflectivities as a function of the wavelengths for LCP (e) and RCP (e) incident light, respectively.

2.3 GSP Metalenses for Focused Vector Vortex Beam (FVVB) Generation

By capitalizing on the remarkable properties of our designed four GSP nano-QWPs, we can achieve precise localization in tailoring the polarization state of the reflected wave, which ultimately results in the creation of cylindrical vector beams with polarization vectors that vary spatially, paving the way for the realization of metalenses for FVVB generation. For example, as shown in formula (2), if $\theta - \frac{\pi}{4}$ is set as φ, which is defined as the azimuthal angle $\varphi = tan^{-1}(\frac{y}{x})$, the reflected beam will be polarized locally with AoLP = φ under LCP excitation with $E_{in} = \frac{1}{\sqrt{2}}\begin{pmatrix}1\\i\end{pmatrix}$, and the Jones matrix can be described as:

$$E_{out} = |r_{xx}|e^{i\varphi_{xx}}e^{il\theta}\begin{pmatrix}\cos(\varphi)\\\sin(\varphi)\end{pmatrix} \tag{5}$$

where l here represents the topological charge of an OAM. Obviously, by locally rotating each nano-QWP with an individual rotation angle $\theta = \varphi + \frac{\pi}{4} = tan^{-1}(\frac{y}{x}) + \frac{\pi}{4}$, and imposing the metasurface with a phase profile of a lens calculated by formula (3), a focused RP beam carrying a specific OAM with $l = 1$ can be achieved. Similarly, if the excitation beam is switched to RCP with $E_{in} = \frac{1}{\sqrt{2}}\begin{pmatrix}1\\-i\end{pmatrix}$ and set $\theta + \frac{\pi}{4} = \varphi + \frac{\pi}{2}$, the Jones matrix can be described as:

$$E_{out} = |r_{xx}|e^{i\varphi_{xx}}e^{-i(\varphi+\frac{\pi}{4})}\begin{pmatrix}\cos(\varphi + \frac{\pi}{2})\\\sin(\varphi + \frac{\pi}{2})\end{pmatrix} \tag{6}$$

combining with formula (3), a focused AP beam carrying a specific OAM with $l = -1$ can also be achieved. Considering the simultaneous utilization of both resonance and geometric phases here, the reflected light by the metalens can be decomposed into two CP components in the CP basis under respective LCP and RCP excitation, which can be written as:

$$E_{out} = \frac{1}{2}|r_{xx}|e^{i(\varphi_{xx}+\frac{\pi}{4})}\begin{pmatrix}1\\\pm i\end{pmatrix} + \frac{1}{2}|r_{xx}|e^{i(\varphi_{xx}-\frac{\pi}{4})}e^{\pm i2\theta}\begin{pmatrix}1\\\mp i\end{pmatrix} \tag{7}$$

where the first part represents the co-polarized reflective light, which retains the same helicity as the incident light. Meanwhile, the second part corresponds to the cross-polarized light exhibiting the reversed helicity with additional phase delay, which is known as the Pancharatnam-Berry phase (geometric phase) with a value of 2θ for LCP light and -2θ for RCP light. Hence, the total reflected focused RP (AP) beam carrying a specific OAM with $l = \pm 1$ can be decomposed as one focused LCP (RCP) beam for the co-polarized CP channel and one focused vortex beam carrying a specific OAM with $l = \pm 2$ for the cross-polarized CP channel. In Figure S6, we depict the simulated far-field intensity profiles and phase distributions of co-polarized and cross-polarized channels at the design

wavelength of 850 nm under LCP and RCP excitations. The intensity profiles of the co-polarized channel follow Gaussian distributions, while the associated phase distributions remain constant within the intensity regions. The doughnut-shaped intensity distributions provide evidence of vortex beams, indicating the presence of cross-polarized CP components. The intensity regions display spiral phase distributions with a 2-fold 2π phase variation along the azimuthal direction, characterized by opposite signs in the cross-polarized channel. This pattern identifies the presence of OAM modes with topological charges of $l = \pm2$ under LCP and RCP excitations, respectively.

Considering the case under LCP excitation, Figure 4a displays the schematic of metalens MS3 with $D = f_3 = 50$ μm ($NA_{MS3} = 0.4472$) according to the phase distribution (Figure S1e) calculated by formula (3), along with the location-related rotation angle of each nano-QWP $\theta = tan^{-1}(\frac{y}{x}) + \frac{\pi}{4}$. The total reflected focused RP beam carrying a specific OAM with $l = +1$ can be viewed as the superposition of one focused LCP beam for the co-polarized channel and one focused vortex beam carrying a specific OAM with $l = +2$ for the cross-polarized channel. Notably, due to the consideration of the change in propagation direction during the reflection process, the actual polarization state of the co-channel should be RCP. Figure 4b presents the SEM image of our fabricated MS3 sample referring to the geometry in Figure S1f. Figure 4c shows the measured reflected optical images from MS3 for incident LCP light with different wavelengths of 800, 850, and 900 nm at plane B, one reflected focused RCP light spot and one focused doughnut-shaped vortex beam carrying a specific OAM with $l = +2$ can be observed for each wavelength in the co- and cross-polarized channel, respectively. Meanwhile, as demonstrated in the rightmost column of Figure 4c, $+2^{nd}$-order spherical shapes are clearly observed in the interference patterns for each wavelength, which possess the opposite topological charges compared to the case under RCP excitation with the same MS3 (Figure S7). Measured total reflectivities as a function of the wavelengths for LCP incident light to focused RP beam are shown in Figure 4d. In addition, reflectivities in both channels for LCP incident light are shown in Figure 4e. In particular, the reflectivity of the focused RP beam under LCP excitation is $\sim 29\%$; and the reflectivities of the co- and cross- polarized channel are $\sim 12\%$ and $\sim 10\%$, respectively, at the wavelength of 850 nm. Other measured results for the case under RCP excitation is shown in Figure S7.
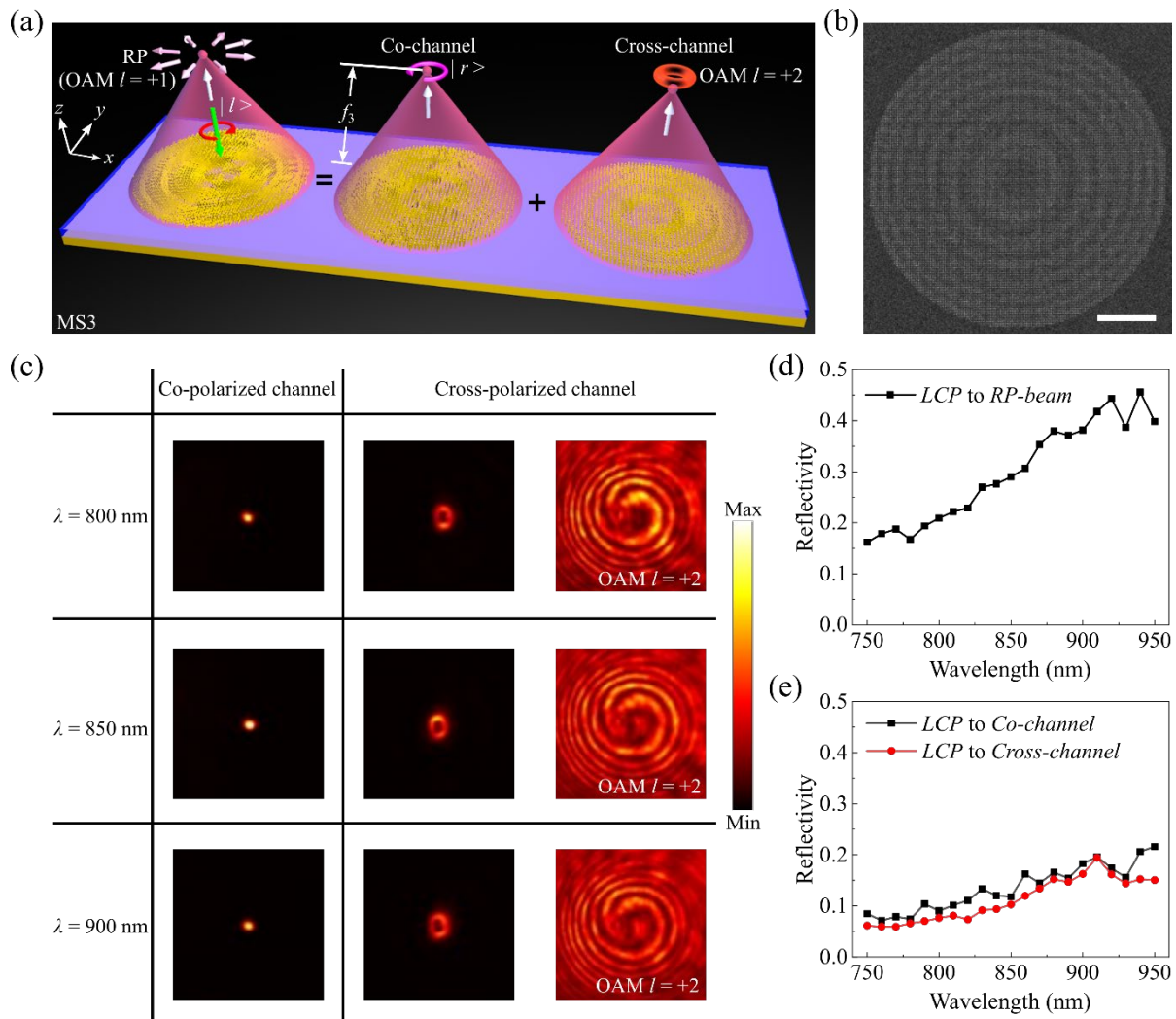
Figure 4. (a) Schematic of the optical GSP MS3 for generating focused RP beam carrying a specific OAM with $l = +1$ under LCP excitation, which can be viewed as the superposition of one focused LCP beam for the co-polarized CP channel and one focused vortex beam carrying a specific OAM with $l = +2$ for the cross-polarized CP channel at the wavelength of 850 nm. (b) The SEM image of the fabricated MS3 (scale bars is 10 µm). (c) Measured reflected optical images from MS3 for incident LCP light with different wavelengths of 800, 850, and 900 nm at plane B in the co- and cross-polarized channels. (d) Measured reflectivities as a function of the wavelengths for LCP incident light to focused RP beam. (e) Measured reflectivities as a function of the wavelengths for LCP incident light to both co- and cross-polarized channels.

3. Conclusion

In this work, we first constructed a library of four GSP nano-QWPs with a certain phase gradient for efficient circular-to-linear polarization conversion, offering comprehensive control over the phase of reflected fields. Based on the nano-QWP library, we propose a versatile GSP metalens platform to generate focused scalar and vector beams under CP excitations in a broadband near-infrared range (750 – 950 nm). We experimentally demonstrated two GSP metalenses (MS1 and MS2) that enable LP beam generation and beam focusing over reflected fields employing only the resonance phase, with single focused light spot (MS1) and dual-focused light spots (MS2), respectively. In addition, combining both resonance and geometric phases, focused RP and AP beams carrying OAM with a topological charge of $l = \pm 1$ have been implemented with MS3 under LCP and RCP excitations, respectively. Moreover, the total reflected focused RP (AP) beam has further been experimentally decomposed into one focused LCP (RCP) beam for the co-polarized channel and one focused vortex beam carrying a specific OAM with $l = \pm 2$ for the cross-polarized channel, respectively. Our proposed GSP metalens platform not only validates the multifunctional capabilities of the metalens in manipulating the light fields, providing flexible solutions for implementing versatile meta-devices at the nanoscale, but also establishes a foundation for the dynamic scalar and vector beam generation with extremely short response time [50-51].

4. Experimental Section/Methods

Sample fabrication. All samples in this work were fabricated utilizing standard thin-film deposition, EBL, and lift-off techniques. Initially, a sequence of deposition processes was performed on a silicon substrate using thermal evaporation. This included the successive deposition of a 3 nm Ti layer, a 100 nm Au layer, and a 2 nm Ti layer. Afterward, a 100 nm SiO$_2$ spacer layer was deposited using RF-sputtering. Subsequently, an approximately 100 nm PMMA layer (2% in anisole, Micro Chem) was spin-coated onto the SiO$_2$ layer. After baking at 180 °C for 2 minutes, the sample was exposed to define patterns using an acceleration voltage of 30 keV. After exposure, the wafer underwent development in a solution of methyl isobutyl ketone (MIBK) and isopropyl alcohol (IPA) with a ratio of MIBK to IPA of 1:3 for 35 seconds, followed by an additional 60 seconds in an IPA bath. Following that, a 1 nm Ti adhesion layer and a 40 nm Au layer were sequentially deposited using thermal evaporation. Lastly, top Au antennas were formed through a lift-off process.

Supporting Information

Supporting Information is available from the Wiley Online Library or from the author.

Author contributions

F.D. conceived the idea. Y.D., F.D. and S.I.S. performed the numerical simulations. Y.D. fabricated all the samples, conducted the optical measurements and analyzed the data. Y.D. made all the figures and drafted the manuscript. All authors contributed to the discussion of the results obtained and editing the manuscript. F.D. and S.I.B. supervised this project.

Conflict of Interest

The authors declare no conflicts of interest.

Data Availability Statement

The data that support the findings of this study are available from the corresponding author upon reasonable request.

Received: ((will be filled in by the editorial staff))
Revised: ((will be filled in by the editorial staff))
Published online: ((will be filled in by the editorial staff))

References

[1] F. L. Pedrotti, L. M. Pedrotti, L. S. Pedrotti, Prentice Hall, Upper Saddle River, NJ, **1993**; pp 333-371.

[2] Z.-Y. Chen, L.-S. Yan, Y. Pan, L. Jiang, A.-L. Yi, W. Pan, B. Luo, *Light Sci Appl.* **2017**, *6*, e16207.

[3] N. A. Rubin, G. D'Aversa, P. Chevalier, Z. Shi, W. T. Chen, F. Capasso, *Science* **2019**, *365*, eaax1839.

[4] H. Wang, Z. Hu, J. Deng, X. Zhang, J. Chen, K. Li, G. Li, *Sci. Adv.* **2024**, *10*, eadk3882.

[5] Q. Zhan, *Adv. Opt. Photon.* **2009**, *1*, 1.

[6] X. Li, T.-H. Lan, C.-H. Tien, M. Gu, *Nat Commun.* **2012**, *3*, 998.

[7] L. Hadžievski, A. Maluckov, A. M. Rubenchik, S. Turitsyn, *Light Sci Appl.* **2015**, *4*, e314.

[8] M. Neugebauer, P. Wozniak, A. Bag, G. Leuchs, P. Banzer, *Nat. Commun.* **2016**, *7*, 11286.

[9] B. Ndagano, B. Perez-Garcia, F. S. Roux, M. McLaren, C. Rosales-Guzman, Y. Zhang, O. Mouane, R. I. Hernandez-Aranda, T. Konrad, A. Forbes, *Nature Phys.* **2017**, *13*, 397.

[10] Y. Kozawa, D. Matsunaga, S. Sato, *Optica* **2018**, *5*, 86.

[11] W. Han, Y. Yang, W. Cheng, Q. Zhan, *Opt. Express* **2013**, *21*, 20692.

[12] J. Wang, A. Cao, H. Pang, M. Zhang, G. Wang, J. Chen, L. Shi, Q. Deng, S. Hu, *Opt. Express* **2017**, *25*, 12531.

[13] S. Segawa, Y. Kozawa, S. Sato, *Opt. Lett.* **2014**, *39*, 3118.

[14] M. Neugebauer, P. Woźniak, A. Bag, G. Leuchs, P. Banzer, *Nat. Commun.* **2016**, *7*, 11286.

[15] M. Meier, V. Romano, T. Feurer, *Appl. Phys. A* **2007**, *86*, 329.

[16] F. Ding, A. Pors, S. I. Bozhevolnyi, *Rep. Prog. Phys.* **2018**, *81*, 026401.

[17] S. L. Sun, Q. He, J. M. Hao, S. Y. Xiao, L. Zhou, *Adv. Opt. Photonics* **2019**, *11*, 380−479.

[18] A. M. Shaltout, V. M. Shalaev, M. L. Brongersma, *Science* **2019**, *364*, 6441.

[19] W. T. Chen, A. Y. Zhu, F. Capasso, *Nat. Rev. Mater.* **2020**, *5*, 604.

[20] Y. Guo, M. Pu, F. Zhang, M. Xu, X. Li, X. Ma, X. Luo, *Photonics Insights* **2022**, *1*, R03.

[21] Z. Liu, D. Wang, H. Gao, M. Li, H. Zhou, C. Zhang, *Adv. Photon.* **2023**, *5*, 034001.

[22] J. Yao, R. Lin, M. K. Chen, D. P. Tsai, *Adv. Photon.* **2023**, *5*, 024001.

[23] X. Hu, W. Xu, Q. Fan, T. Yue, F. Yan, Y. Lu, T. Xu, *Adv. Photon.* **2024**, *6*, 014002.

[24] A. I. Kuznetsov, M. L. Brongersma, J. Yao, M. K. Chen, U. Levy, D. P. Tsai, N. I. Zheludev, A. Faraon, A. Arbabi, N. Yu, D. Chanda, K. B. Crozier, A. V. Kildishev, H. Wang, J. K. W. Yang, J. G. Valentine, P. Genevet, J. A. Fan, O. D. Miller, A. Majumdar, J. E. Fröch, D. Brady, F. Heide, A. Veeraraghavan, N. Engheta, A. Alù, A. Polman, H. A. Atwater, P. Thureja, R. Paniagua-

Dominguez, S. T. Ha, A. I. Barreda, J. A. Schuller, I. Staude, G. Grinblat, Y. Kivshar, S. Peana, S. F. Yelin, A. Senichev, V. M. Shalaev, S. Saha, A. Boltasseva, J. Rho, D. K. Oh, J. Kim, J. Park, R. Devlin, R. A. Pala, *ACS Photonics* **2024**, *11*, 816.

[25] M. Pan, Y. Fu, M. Zheng, H. Chen, Y. Zang, H. Duan, Q. Li, M. Qiu, Y. Hu, *Light Sci Appl.* **2022**, *11*, 195.

[26] X. Luo, F. Zhang, M. Pu, Y. Guo, X. Li, X. Ma, *Nanophotonics* **2022**, *11*, 1.

[27] A. Arbabi, A. Faraon, *Nat. Photon.* **2023**, *17*, 16.

[28] T. Li, C. Chen, X. Xiao, J. Chen, S. Hu, S. Zhu, *Photonics Insights* **2023**, *2*, R01.

[29] A. Arbabi, Y. Horie, M. Bagheri, A. Faraon, *Nature Nanotech* **2015**, *10*, 937.

[30] M. Khorasaninejad, W. T. Chen, R. C. Devlin, J. Oh, A. Y. Zhu, F. Capasso, *Science* **2016**, *352*, 1190.

[31] F. Shi, J. Wen, D. Lei, *Nanophotonics* **2020**, *9*, 4043.

[32] L. Li, Z. Liu, X. Ren, S. Wang, V.-C. Su, M.-K. Chen, C. H. Chu, H. Y. Kuo, B. Liu, W. Zang, G. Guo, L. Zhang, Z. Wang, S. Zhu, D. P. Tsai, *Science* **2020**, *368*, 1487.

[33] Q. Fan, W. Xu, X. Hu, W. Zhu, T. Yue, C. Zhang, F. Yan, L. Chen, H. J. Lezec, Y. Lu, A. Agrawal, T. Xu, *Nat Commun* **2022**, *13*, 2130.

[34] E. Arbabi, A. Arbabi, S. M. Kamali, Y. Horie, A. Faraon, *Optica* **2016**, *3*, 628.

[35] D. Lin, A. L. Holsteen, E. Maguid, G. Wetzstein, P. G. Kik, E. Hasman, M. L. Brongersma, *Nano Lett.* **2016**, *16*, 7671.

[36] Y. Zhou, H. Zheng, I. I. Kravchenko, J. Valentine, *Nat. Photonics* **2020**, *14*, 316.

[37] Y. Yang, W. Wang, P. Moitra, I. I. Kravchenko, D. P. Briggs, J. Valentine, *Nano Lett.* **2014**, *14*, 1394.

[38] F. Ding, Z. Wang, S. He, V. M. Shalaev, A. V. Kildishev, *ACS Nano* **2015**, *9*, 4111.

[39] Y. Yuan, S. Chen, B. Ratni, Q. Wu, X. Ding, S. N. Burokur, K. Zhang, *Applied Physics Letters* **2020**, *117*, 171602.

[40] C. Zhang, S. Divitt, Q. Fan, W. Zhu, A. Agrawal, Y. Lu, T. Xu, H. J. Lezec, *Light Sci Appl* **2020**, *9*, 55.

[41] Y. Deng, C. Wu, C. Meng, S. I. Bozhevolnyi, F. Ding, *ACS Nano* **2021**, *15*, 18532.

[42] Z. Cai, Y. Deng, C. Wu, C. Meng, Y. Ding, S. I. Bozhevolnyi, F. Ding, *Adv. Opt. Mater.* **2021**, *9*, 2002253.

[43] P. B. Johnson, R. W. Christy, *Phys. Rev. B* **1972**, *6*, 4370.

[44] F. Ding, Y. Chen, Y. Yang, S. I. Bozhevolnyi, *Adv. Opt. Mater.* **2019**, *7*, 1900724.

[45] F. Ding, Y. Chen, S. I. Bozhevolnyi, *Nanophotonics* **2020**, *9*, 371–378.

[46] Y. Li, M. A. Ansari, H. Ahmed, R. Wang, G. Wang, X. Chen, *Sci. Adv.* **2023**, *9*, eadj6675.

[47] Y. Intaravanne, M. A. Ansari, H. Ahmed, X. Chen, *Adv. Opt. Mater.* **2024**, *12*, 2203097.

[48] A. Pors, M. G. Nielsen, R. L. Eriksen, S. I. Bozhevolnyi, *Nano Lett.* **2013**, *13*, 829.

[49] C. Meng, P. C. V. Thrane, F. Ding, J. Gjessing, M. Thomaschewski, C. Wu, C. Dirdal, S. I. Bozhevolnyi, *Sci. Adv.* **2021**, *7*, eabg5639.

[50] F. Ding, Y. Deng, C. Meng, P. C. V. Thrane, S. I. Bozhevolnyi, *Sci. Adv.* **2024**, *10*, eadl4661.

[51] Y. Deng, C. Meng, P. C. V. Thrane, S. I. Sande, S. I. Bozhevolnyi, F. Ding, *Optica* **2024**, *11*, 326.

Spin-Controlled Gap-Surface Plasmon Metalenses for Focused Scalar and Vector Beam Generation: Supplement

Yadong Deng, Chao Meng, Sören im Sande, Sergey I. Bozhevolnyi* and Fei Ding*

Y. Deng, C. Meng, S. I. Sande, S. I. Bozhevolnyi, and F. Ding

Centre for Nano Optics, University of Southern Denmark, Campusvej 55, Odense DK-5230,

Denmark

E-mail: seib@mci.sdu.dk (S.I.B.) and feid@mci.sdu.dk (F.D.) of corresponding authors
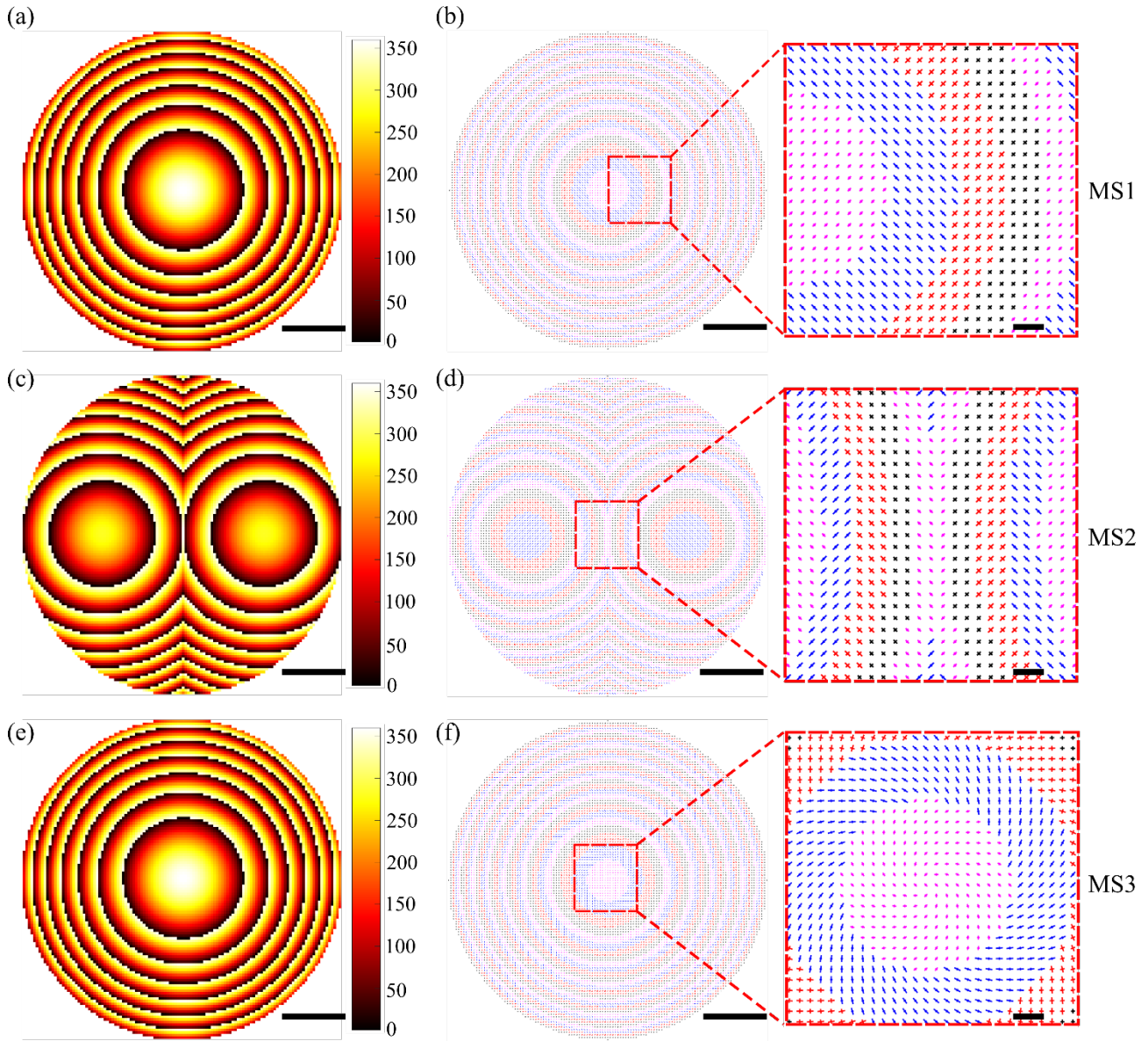
Figure S1. Calculated phase profile and designed geometry of MS1-MS3 with a same diameter of D = 50 µm and a same focal length of f = 50 µm at λ_d = 850 nm. (a-b) are for MS1, (c-d) are for MS2 and (e-f) are for MS3. The scale bar in (a), (c), (e) and the left of (b), (d) and (f) is 10 µm, scale bar in the right of (b), (d) and (f) is 1 µm.
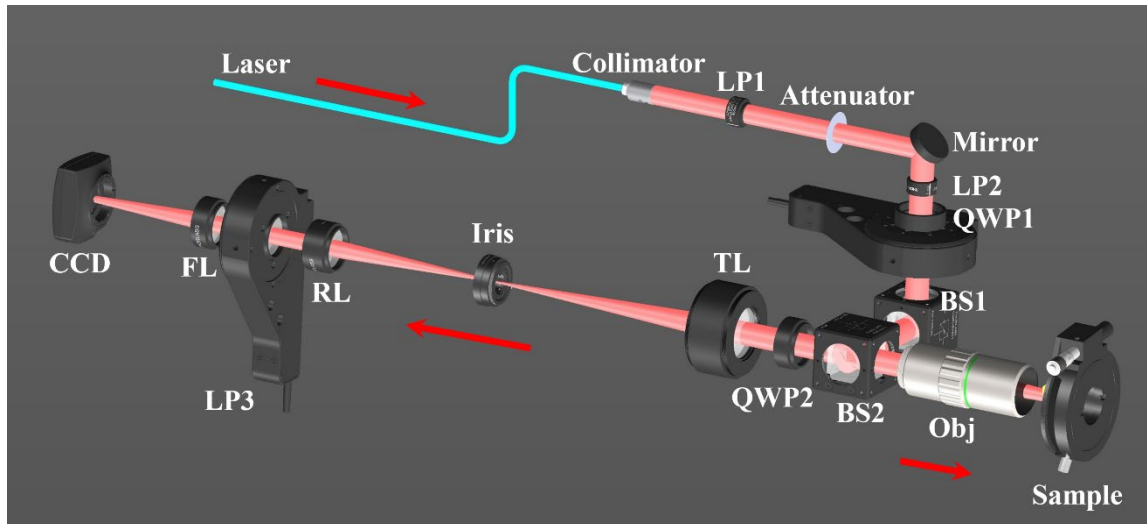
Figure S2. Schematic of the home-built experimental setup for characterizing fabricated sample MS1-MS3. A collimated fiber-coupled cw Ti:sapphire laser (Spectra-Physics 3900 S, wavelength from 700 to 1000 nm) first passes through a linear polarizer (LP1, LPNIR050-MP2, Thorlabs) and an attenuator (NE01B, Thorlabs) to adjust the light intensity. Then the light reflected by a silver mirror (PF10-03-P01, Thorlabs) is directed through a linear polarizer (LP2, LPNIR050-MP2, Thorlabs), a quarter-wave plate (QWP1, AQWP10M-980, Thorlabs) mounted on a motorized precision rotation stage (MPRS, PRM1Z8, Thorlabs), two beam splitters (BS1 and BS2, CCM1-BS014/M, Thorlabs) successively, and then slightly focused onto the sample by using a long working distance objective (Obj. M Plan Apo 20×/0.42NA, Mitutoyo). The combination of LP2 and QWP1 is utilized to generate left circularly polarized (LCP) and right circularly polarized (RCP) light in a controlled manner, while two beam splitters can change the direction of beam propagation and effectively compensates for the polarization-dependent phase shifts that would occur with one single beam splitter. The reflected signal light, collected by the same objective, passes through BS2 and a tube lens (TL, TTL200-S8, $f = 200$ mm, Thorlabs), creating the initial direct image plane where an iris (SM1D12SZ, Thorlabs) is positioned to filter out background signals outside the sample area. The filtered initial real image is further transformed by a relay lens (RL, AC254-200-B-ML, $f = 200$ mm, Thorlabs) to generate a Fourier image, which is then captured by a CMOS camera (CCD, DCC1545M, Thorlabs). For the co- and cross-polarized channel construction, a quarter-wave plate (QWP2, AQWP10M-980, Thorlabs) and a linear polarizer (LP3, LPNIR050-MP2, Thorlabs) are employed. To alternate between real and Fourier images, a flip lens (FL, AC254-100-B-ML, $f = 100$ mm, Thorlabs) is positioned between the relay lens and the CCD.
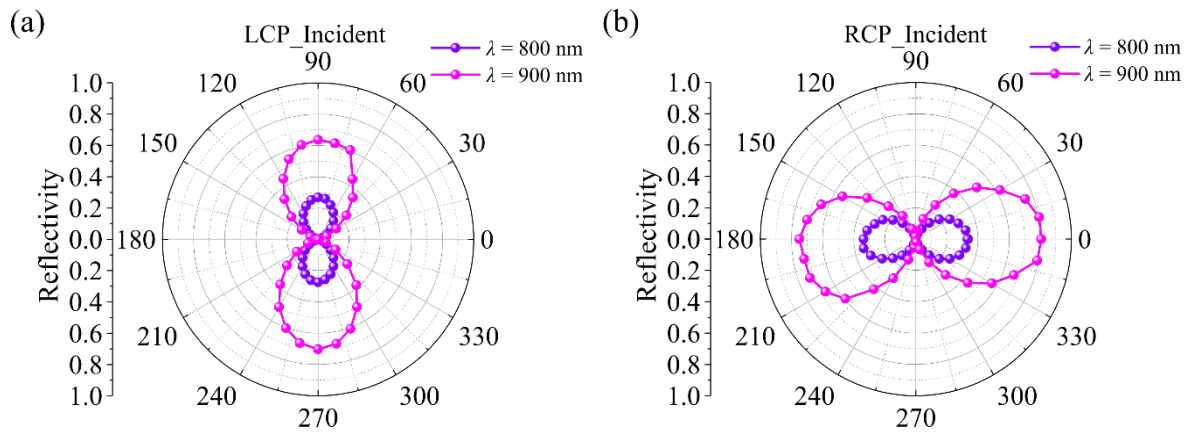
Figure S3. Measured polarization state diagrams of the reflected focused light spots from MS1 at plane B for LCP (a) and RCP (b) incident light, respectively, at the wavelength of 800 and 900 nm.
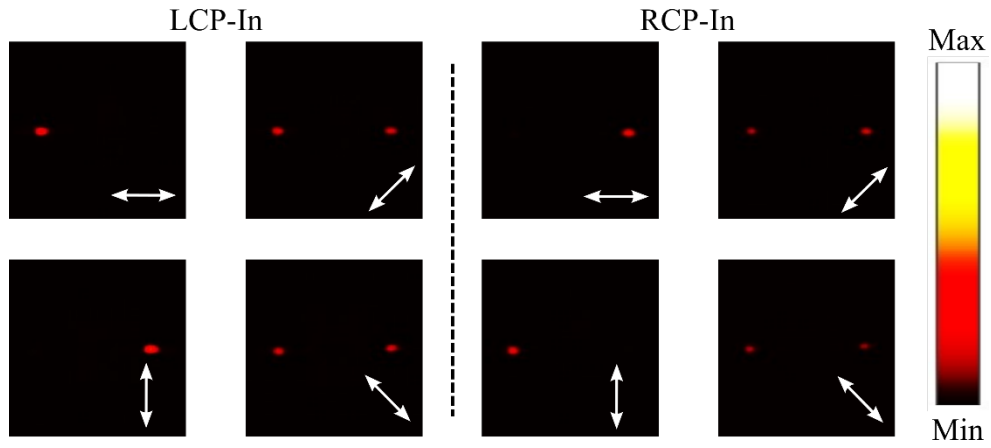
Figure S4. Measured intensity profiles of the focused light spots at plane B from MS2 with a linear polarizer in front of the CCD camera for LCP and RCP incident lights, respectively, at the wavelength of 850 nm.
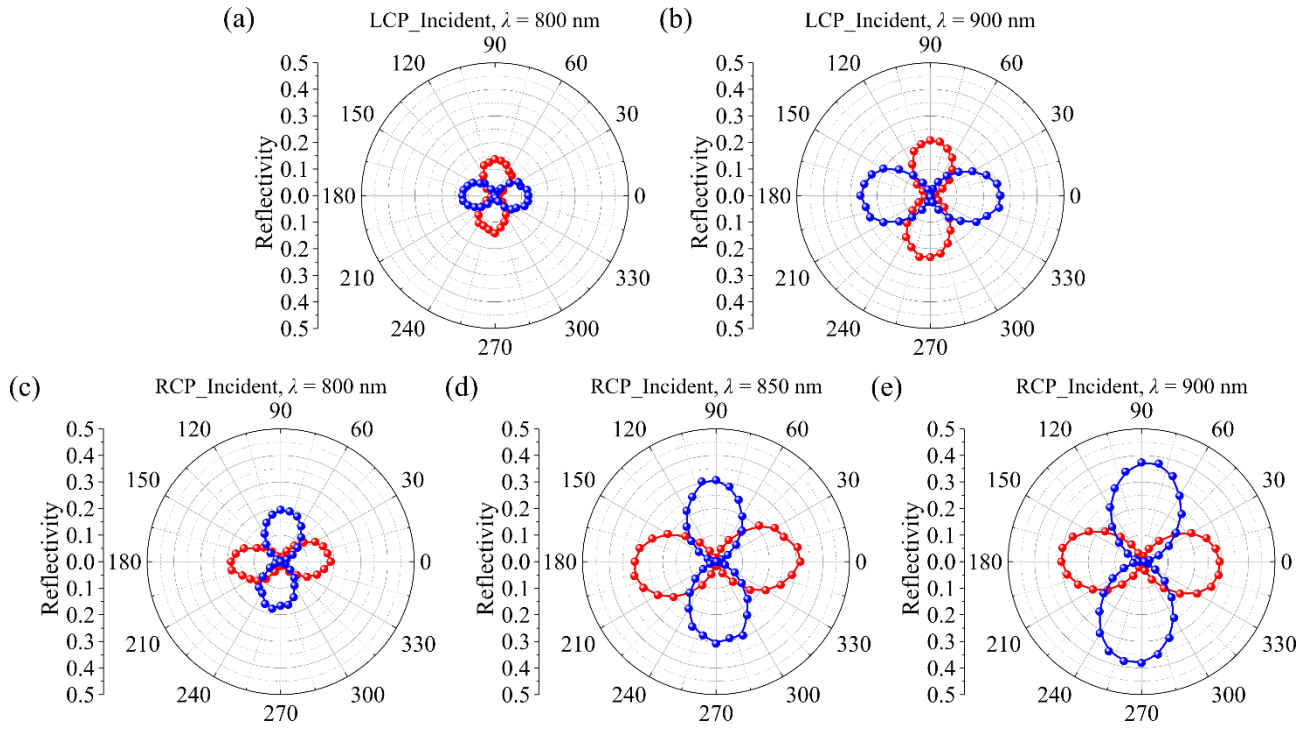
Figure S5. Measured polarization state diagrams of the two reflected focused light spots from MS2 at plane B for LCP incident light (a-b) at the wavelength of 800 and 900 nm, and RCP incident light (c-e) at the wavelength of 800, 850 and 900 nm.
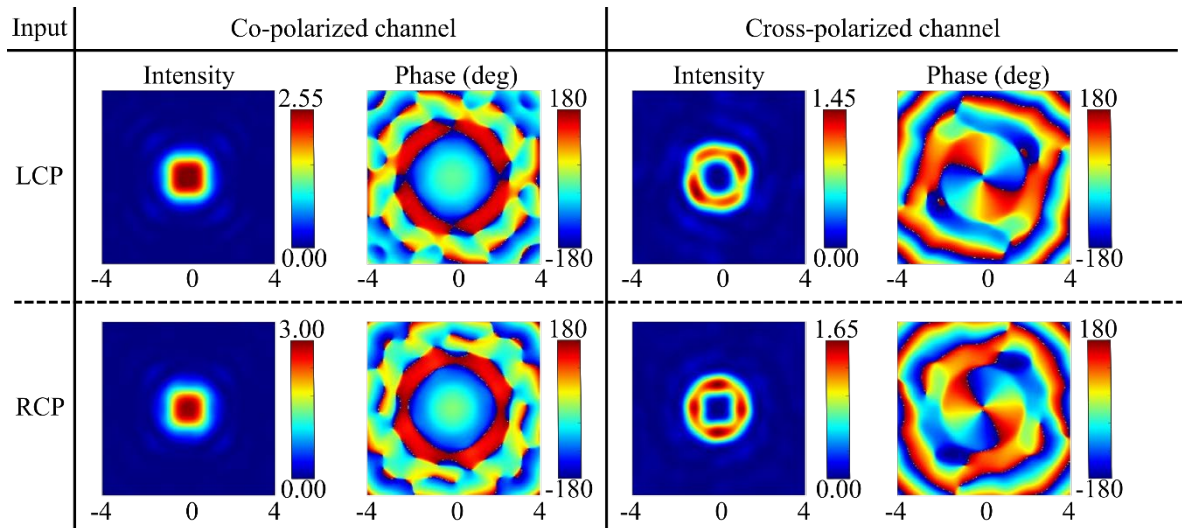
Figure S6. Numerical simulation results of the designed MS3. Far-field intensity profiles and phase distributions of the reflected co- and cross-polarized channels under both LCP and RCP excitations, at the wavelength of 850 nm.
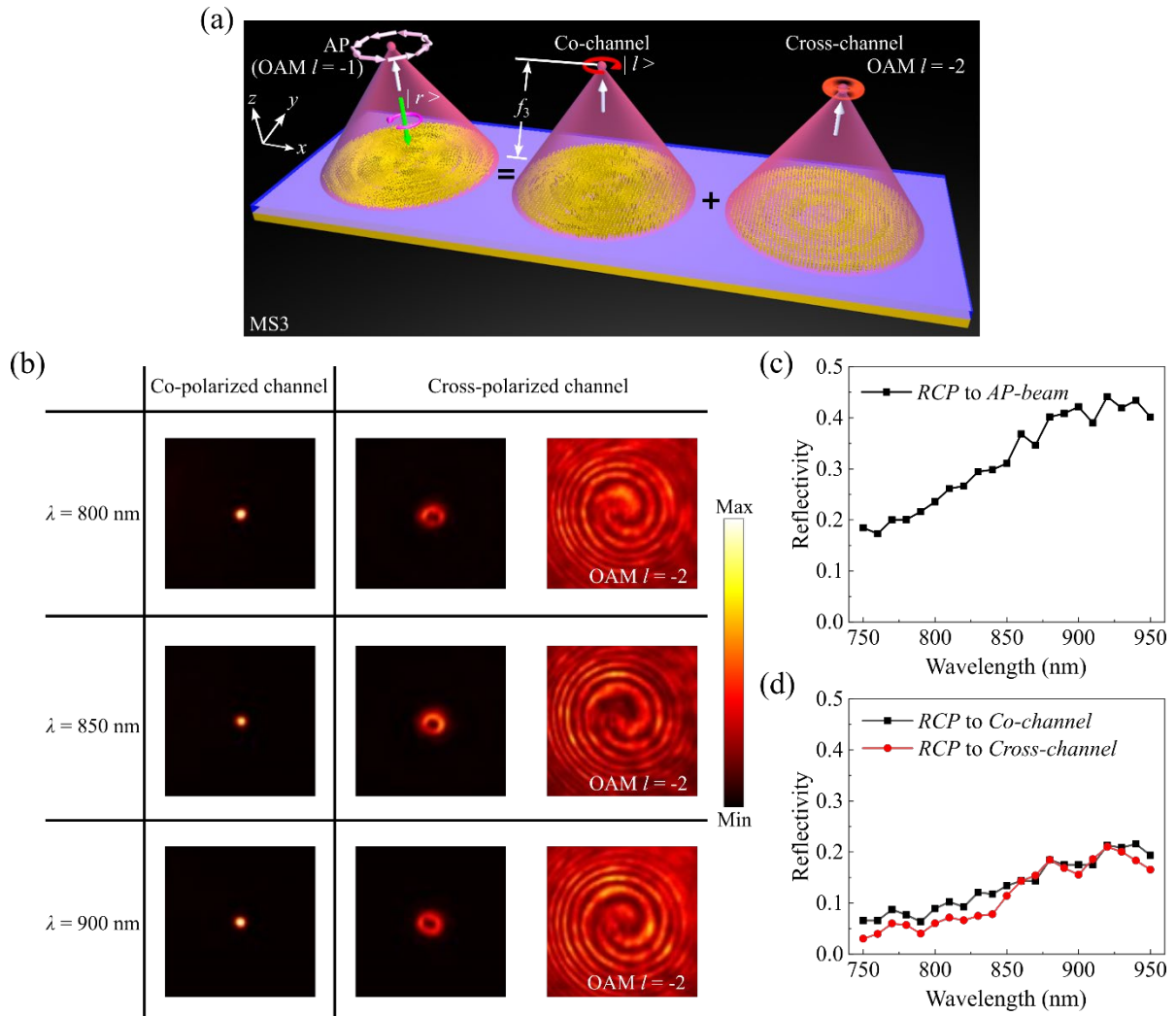
Figure S7. (a) Schematic of the optical GSP MS3 for generating focused AP beam carrying a specific OAM with $l = -1$ under RCP excitation, which can be viewed as the superposition of one focused RCP beam for the co-polarized CP channel and one focused vortex beam carrying a specific OAM with $l = -2$ for the cross-polarized CP channel at the wavelength of 850 nm. (b) Measured reflected optical images from MS3 for incident RCP light with different wavelengths of 800, 850, and 900 nm at plane B in the co- and cross-polarized channels. (c) Measured reflectivities as a function of the wavelengths for RCP incident light to focused AP beam. (d) Measured reflectivities as a function of the wavelengths for RCP incident light to both co- and cross-polarized channels.

OPTICA

MEMS-integrated metasurfaces for dynamic linear polarizers

Yadong Deng,[1] Chao Meng,[1] Paul C. V. Thrane,[1,2] Sören im Sande,[1]
Sergey I. Bozhevolnyi,[1,3] and Fei Ding[1,*]

[1]Centre for Nano Optics, University of Southern Denmark, Campusvej 55, Odense DK-5230, Denmark
[2]SINTEF Microsystems and Nanotechnology, Gaustadalleen 23C, 0737 Oslo, Norway
[3]seib@mci.sdu.dk
*feid@mci.sdu.dk

Optical metasurfaces (OMSs), planar arrays of meticulously designed meta-atoms, are renowned for remarkable capabilities in manipulating the polarization state of light at subwavelength scales. Nevertheless, most OMS-empowered polarization optics remain static, featuring well-defined optical responses determined by their configurations set during fabrication. Here, we demonstrate a MEMS-OMS-based dynamic linear polarizer (DLP) with an electrically controlled extinction ratio, which is tunable in a fast and reversible fashion, by combining an anisotropic plasmonic OMS with a thin-film piezoelectric MEMS mirror. Capitalizing on the MEMS-OMS DLP, we further implement voltage-controlled grayscale imaging and vector vortex beam generation under linearly and circularly polarized excitations, respectively. Our MEMS-OMS DLP design could enable adaptive photonic systems for advanced applications in optical image encryption, displays, and beyond. © 2024 Optica Publishing Group under the terms of the Optica Open Access Publishing Agreement

https://doi.org/10.1364/OPTICA.515524

1. INTRODUCTION

Optical metasurfaces (OMSs) have demonstrated exceptional proficiency in manipulating light at subwavelength spatial resolutions with ultrathin profiles, thereby facilitating the progress of compact and highly integrated photonic devices [1–7]. Among numerous fascinating applications, OMS-based polarization optics have gained significant attention [8–19], which stems from the recognition that polarization is an intrinsic and pivotal characteristic of optical radiation, holding paramount importance in developing contemporary optical instrumentation. Notably, various linear polarizers (LPs) enabling linear polarization manipulation with unprecedented properties and novel functionalities have been implemented with OMSs [20–24]. Despite these achievements, OMS-based LPs are predominantly static, thereby imposing considerable constraints, such as a lack of real-time tunability, on the continued evolution of promising OMS platforms towards highly integrated and sophisticated adaptive photonic systems. The realization of dynamic OMS-based LPs is a rather arduous issue due to the high density of elements that are arranged in ultra-thin planar configurations [25–30]. One of the common approaches relies on the direct integration of active media into the OMS structure, whose optical response can be actively controlled by external stimuli [25–38]. Although feasible, these approaches usually demand precise nanofabrication/assembly techniques and exhibit limited tunability ranges.

Capitalizing on our recent development of MEMS-based dynamic OMSs possessing the advantage of ease of fabrication and large tunability ranges [39–41], we demonstrate an electrically driven MEMS-OMS-based dynamic linear polarizer (DLP), benefiting from a tunable hybrid plasmonic Fabry–Perot (FP) cavity formed by an anisotropic plasmonic OMS and thin-film piezoelectric MEMS mirror and featuring a continuous and tunable, in a fast and reversible fashion, extinction ratio (ER) between two linearly polarized incident beams. Based on the designed DLP, we propose and experimentally implement dynamic grayscale imaging and vector vortex beam (VVB) generation under linearly and circularly polarized excitations, respectively, by varying the MEMS actuation voltage to finely tune the air gap between the MEMS mirror and OMS. We believe that the proposed MEMS-OMS DLP, featuring moderately fast and robust reconfigurability, can find many diverse applications in information encryption, image anticounterfeiting, and beyond.

2. DESIGN AND SIMULATION OF THE MEMS-OMS DLP

The designed MEMS-OMS-based DLP consists of a gold nanobrick array fabricated on top of a glass substrate and a thin-film piezoelectric MEMS mirror [39–41], separated by an air spacer whose thickness T_a could be finely adjusted by actuating the MEMS mirror with an electrical voltage V_m (Fig. 1A). Upon electrical actuation, the DLP features a continuously varied
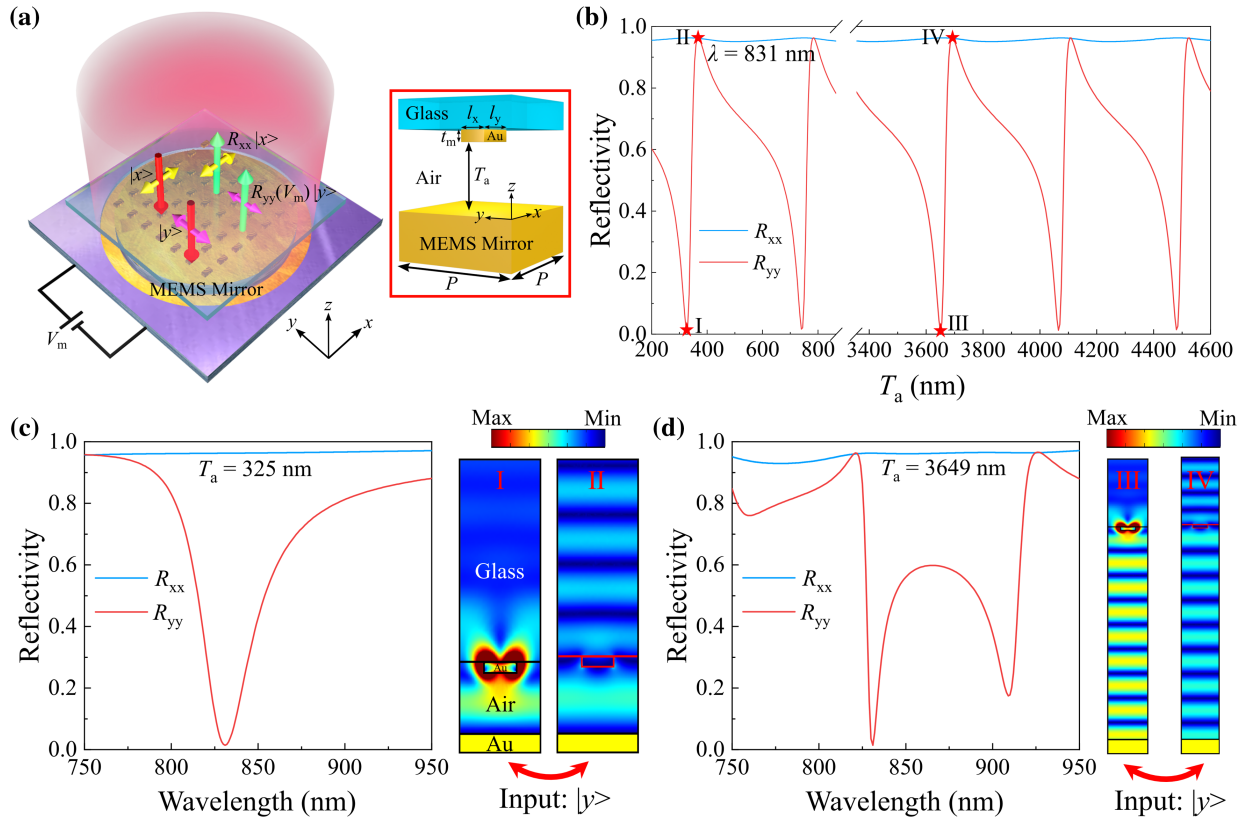
Fig. 1. Design principle of the MEMS-OMS DLP. (a) Schematic of the electrically tunable MEMS-OMS-based DLP consisting of an array of 2D gold meta-atoms on a glass substrate, complemented by a thin-film movable piezoelectric MEMS mirror with a voltage-controlled air gap to realize the real-time rapid modulation of the reflected light under $|y\rangle$ incidence. The unit cell of the MEMS-OMS DLP is shown in the right panel, where all corners of the nanobricks are rounded with a radius of 5 nm. (b) Calculated reflectivities as a function of the air gap T_a at the design wavelength of $\lambda = 831$ nm for both $|x\rangle$ and $|y\rangle$ incidence. Red stars I and III mark the polarizer-operation states with the air gaps of $T_a = 325$ nm and 3649 nm, respectively, while red stars II and IV represent the mirror-operation states with the air gaps of $T_a = 370$ nm and 3694 nm, respectively. (c) and (d) Calculated reflectivities as a function of the wavelength at air gaps of (c) $T_a = 325$ nm and (d) 3649 nm for both $|x\rangle$ and $|y\rangle$ incidence. The right panels in (c) and (d) show the electric field distributions under the $|y\rangle$ incidence at air gaps of $T_a = 325$ nm (I), 370 nm (II), 3649 nm (III), and 3694 nm (IV).

reflectivity $R_{yy}(V_m)$ under y-polarized ($|y\rangle$) excitation, while maintaining a high and practically constant reflectivity R_{xx} under x-polarized ($|x\rangle$) excitation. Specifically, the DLP undergoes a dramatic transition from total reflection to nearly complete absorption under $|y\rangle$ excitation, manifesting a polarizer-like functionality with a large ER, defined by the ratio between R_{xx} and R_{yy}. By optimizing the dimensions of gold meta-atoms along with the air gap T_a and operation wavelength λ, a DLP was designed in the parameter space of $[l_x, l_y, t_m, P, T_a(V_m), \lambda] = [106\ \text{nm}, 196\ \text{nm}, 50\ \text{nm}, 500\ \text{nm}, 325\ \text{nm}, 831\ \text{nm}]$ with reflectivities R_{xx} and R_{yy} reaching 96.27% and 1.41%, respectively, corresponding to an ER of ~ 68.28 [Figs. 1(b) and 1(c)]. For such a large air gap ($T_a = 325$ nm), the DLP response is determined by the hybrid plasmonic FP resonance (Supplement 1 Section 1) [40–43] instead of the gap-surface plasmon resonance [3,39] owing to the negligible near-field coupling between the gold meta-atom array and MEMS mirror, releasing the critical requirement of ultra-small air gaps for observing the polarizer-like performance. Given the inherent FP properties of our DLP, the overall response naturally follows a periodicity of $\lambda/2$ concerning the variable air gaps (Fig. 1B), a periodic gap-dependent response that is seen for all wavelengths (Supplement 1 Figs. S3 and S4). For example, at the design wavelength $\lambda = 831$ nm, the DLP with a relatively large air gap of $T_a = 3649$ nm, corresponding to the

eighth-order FP regime, exhibits entirely consistent reflectivities with the small air gap of $T_a = 325$ nm [Figs. 1(b) and 1(c), and Supplement 1 Fig. S4]. Moreover, the DLP exhibits robust performance at both air gaps of $T_a = 325$ nm and 3649 nm for incident angles smaller than 30° (Supplement 1 Fig. S5). However, if the periodicity of the metasurface is varied, the DLP performance deteriorates quite quickly (Supplement 1 Fig. S6).

Considering the wavelength-dependent response, it is immediately seen that, for larger air gaps, the MEMS-OMS DLP configuration exhibits a pronounced mode splitting [Fig. 1(d), and Supplement 1 Figs. S3 and S4], which is ascribed to the strong coupling between the high-order FP and plasmonic resonances [42,43]. To explain the significant difference between R_{xx} and R_{yy}, we plot the electric field distributions at $\lambda = 831$ nm. For $|x\rangle$ incidence, the OMS resonance is not coupled to the FP resonance because the corresponding plasmonic resonance is out of the investigated spectrum (Supplement 1 Figs. S2 and S4), leaving the interference pattern unchanged (Supplement 1 Fig. S7). On the contrary, there is a strong coupling between the plasmonic and FP resonances for $|y\rangle$ incidence [Figs. 1(c) and 1(d)], thereby resulting in mode splitting of the plasmonic resonance at $\lambda_{\text{OMS}} = 861$ nm (Supplement 1 Fig. S3). As a result, we achieved nearly perfect absorption at one of the split modes with a smaller wavelength of $\lambda = 831$ nm [Fig. 1(d) and Supplement 1 Fig. S3], where the

electric field is strongly confined in the vicinity of the gold meta-atom and the interference pattern beneath the meta-atom becomes more pronounced [Figs. 1(c) and 1(d)]. Once the MEMS mirror is slightly moved away from the critical point, the reflectivity R_{yy} is gradually increased while R_{xx} stays constant, decreasing the ER. In particular, an ER of ~1 is achieved for the DLP when the air gap T_a is actuated to 370 nm (or 3694 nm), where the plasmonic meta-atoms are located right at the minimum of the interference pattern formed by the MEMS mirror [Figs. 1(c) and 1(d)]. At precisely this point, the overall MEMS-OMS system is equivalent to a MEMS mirror with equally high reflectivities for both $|x\rangle$ and $|y\rangle$ incidence, which is considered as the mirror-operation state.

3. EXPERIMENTAL DEMONSTRATION OF THE MEMS-OMS DLP

The MEMS-OMS DLP sample was prepared by first assembling a separately fabricated gold meta-atom array (see Section 7 for

detailed information) and an exceptionally flat MEMS mirror and then connecting to a printed circuit board (PCB) through wire bonding, which eventually forms a finely tunable hybrid plasmonic FP cavity with a voltage-controlled air gap T_a [Figs. 2(a) and 2(b)]. To characterize the fabricated DLP, we employed a customized optical setup comprising a supercontinuum laser beam and a variety of optical components for polarization-resolved imaging and detection (see Section 7 and Supplement 1 Fig. S8). During the measurement, the driving voltage was steadily incremented from 0 to 20 V in a fixed step of 0.2 V, which is sufficiently fine to tune the air gap and thus explore the dynamic transition between polarizer-operation and mirror-operation states by locating certain typical positions where the y-polarized light is either absorbed or reflected. Meanwhile, we linked the *in situ* air gap T_a to the actuated voltage V_m by extracting wavelength points where mirror-operation states occur from the measured R_{yy} spectra (Supplement 1 Fig. S9). Figure 2C plots the polarization-resolved reflection spectra (R_{xx} and R_{yy}) at each V_m (T_a) in the experiment, in good agreement with
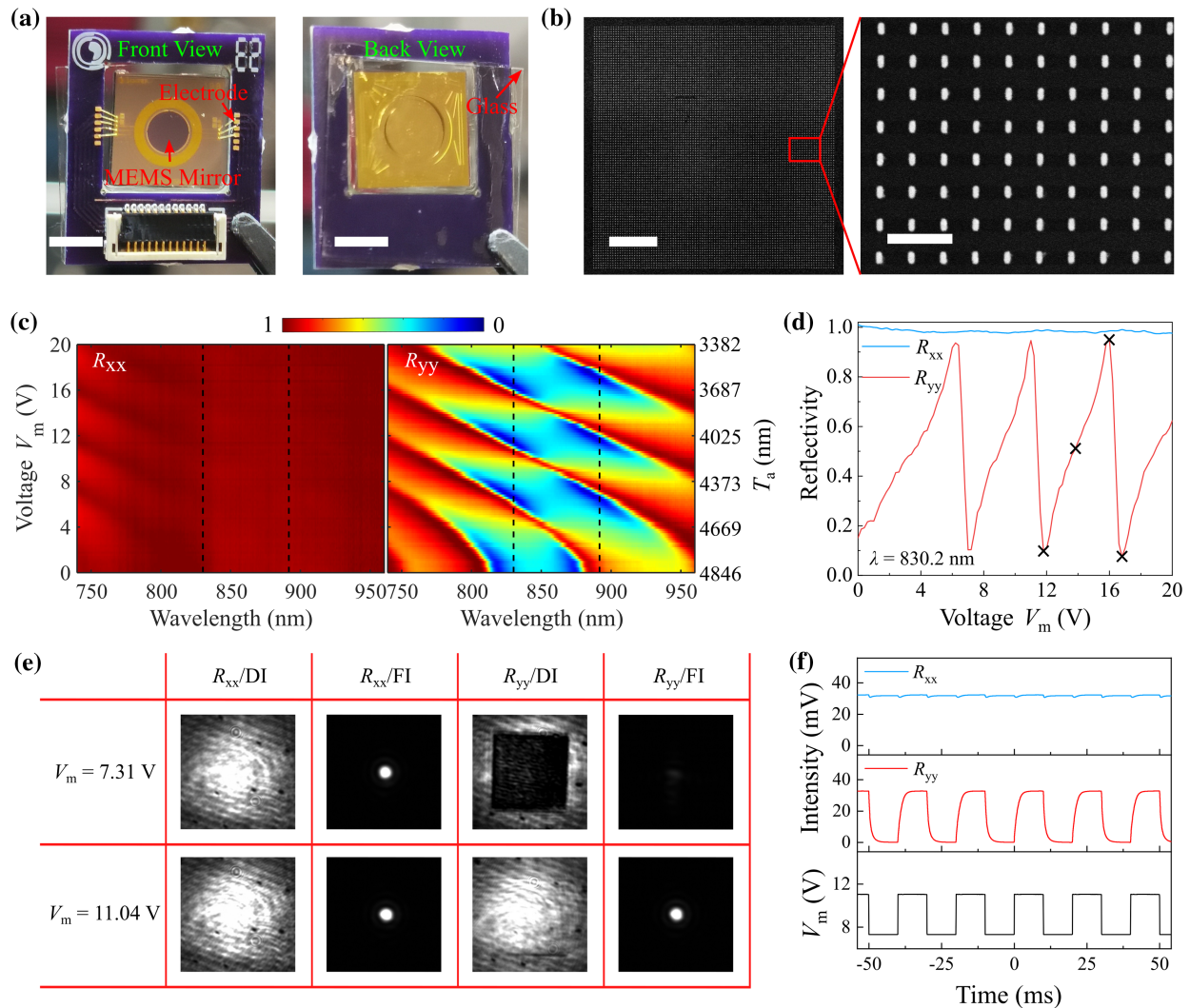
Fig. 2. Experimental demonstration of the MEMS-OMS DLP. (a) Typical photos of the fabricated MEMS-OMS-based DLP (scale bars are both 5 mm). (b) SEM images of the assembled OMS (scale bars are 10 μm and 1 μm, respectively). (c) Measured polarization-resolved reflectivities as a function of the applied voltage V_m (air gap T_a) and wavelength λ. The black dashed lines mark the wavelengths of $\lambda = 830.2$ nm and 891.73 nm. (d) Measured reflectivities as a function of V_m at a fixed wavelength of $\lambda = 830.2$ nm for both $|x\rangle$ and $|y\rangle$ incidence. The black cross symbols mark the voltages of $V_m = 11.8$ V, 14.0 V, 16.0 V, and 16.8 V, respectively. (e) Polarization-resolved direct and Fourier images (DI and FI) of the reflected light for the dynamic transition between polarizer-operation and mirror-operation states. (f) Temporal evolution of the reflected light for both $|x\rangle$ and $|y\rangle$ incidence by actuating the MEMS mirror with a periodic rectangular signal at the wavelength of $\lambda = 830.2$ nm.

the theoretical predictions (Supplement 1, Fig. S3). Generally, the fabricated DLP features distinct responses for the $|x\rangle$ and $|y\rangle$ incidence: for $|x\rangle$ incidence, the incident light is totally reflected for the wavelengths larger than 825 nm regardless of the actuated air gaps as the OMS resonance is in the short wavelength range; for $|y\rangle$ incidence, the reflectivity R_{yy} shows a dramatic and periodic oscillation once the air gap T_a is driven by the voltage V_m. To further show the dynamic modulation of our DLP, we fixed the operation wavelength at $\lambda = 830.2$ nm and extracted the reflectivities of R_{xx} and R_{yy} as a function of V_m (T_a) (Fig. 2D). It is evident that the $|x\rangle$ input consistently experiences a relatively high reflectance of $\sim 98.36\%$, while the $|y\rangle$ incident light is either reflected or absorbed with its reflectivity R_{yy} periodically varying. For example, the mirror-operation and polarizer-operation states are achieved at $V_m = 16.0$ V ($T_a \approx 3687$ nm) and $V_m = 16.8$ V ($T_a \approx 3640$ nm) with the R_{yy} reaching 95.05% and 7.46%, respectively. Therefore, the ER is continuously tuned from 1.04 to 13.30 once the DLP is triggered with a voltage from 16.0 to 16.8 V, resulting in a measured modulation depth of $\sim 92.15\%$. Compared to the theoretical ER tuning range, which spans from 1 to 68.28, the experimental values are considerably lower. This reduction is primarily attributed to the increase in R_{yy} due to fabrication imperfections, such as rounded corners and surface roughness. To enlarge the ER tuning range, it is crucial to consider these fabrication flaws during the design stage. Additionally, employing a finer voltage tuning step can aid in more precisely resolving all spectrum features. Despite these minor discrepancies, the typical resonances associated with coupled plasmonic and higher-order FP resonances, along with their evolution dynamics, have been successfully replicated in experiments (Supplement 1 Fig. S10). With respect to the theoretical ER tuning range, we remark that there is no limit on the maximum achievable ER once the configuration parameters (l_x, l_y, t_m, P, T_a, λ) are varying with sub-nanometer

accuracy. There is, however, little sense in doing that because of the currently achievable fabrication imperfections and fundamental physical limitations, such as roughness on the atomic scale. Additionally, we observed a significant contrast between the mirror and polarizer states for $|y\rangle$ incidence in both direct and Fourier image planes at $\lambda = 830.2$ nm by actuating the MEMS mirror with a periodic rectangular signal (Fig. 2E, Visualization 1 and Visualization 2). Different from R_{yy}, the contrast of R_{xx} is almost unanimous. Similar modulation dynamics can be obtained for the larger split wavelength at $\lambda = 819.73$ nm (Supplement 1 Fig. S11). By replacing the CMOS camera with a photodetector, we observed a moderately fast switching with the rise/fall times of ~ 2.27 ms/1.68 ms, respectively (Fig. 2F), which could further be shortened by optimizing the MEMS mirrors.

4. MEMS-OMS DLP FOR VOLTAGE-CONTROLLED GRAYSCALE IMAGING

Given the polarization-selective reconfigurability, our DLP naturally offers the possibility of encoding voltage-controlled grayscale imaging for anticounterfeiting [22–24,44]. For simplicity, we designed a binary *Tai-Chi* pattern, which is composed of two basic meta-atoms [Figs. 3(a) and 3(b)]. Meta-atom #2 is obtained by rotating meta-atom #1 (DLP unit cell) with an angle of 90°. Hence, it is evident that meta-atom #2 possesses an opposite optical response upon two linearly polarized excitations with respect to meta-atom #1: the $|x\rangle$ incident light is selectively absorbed or reflected depending on the applied voltage, while the $|y\rangle$ incidence is always reflected. Figure 3(c) and Visualization 3 display the measured intensity profiles of the reflected beam as a function of voltage V_m for the $|y\rangle$ incidence at the wavelength of $\lambda = 830.2$ nm, where the *Tai-Chi* pattern is clearly observed at voltages of $V_m = 1.1$ V,
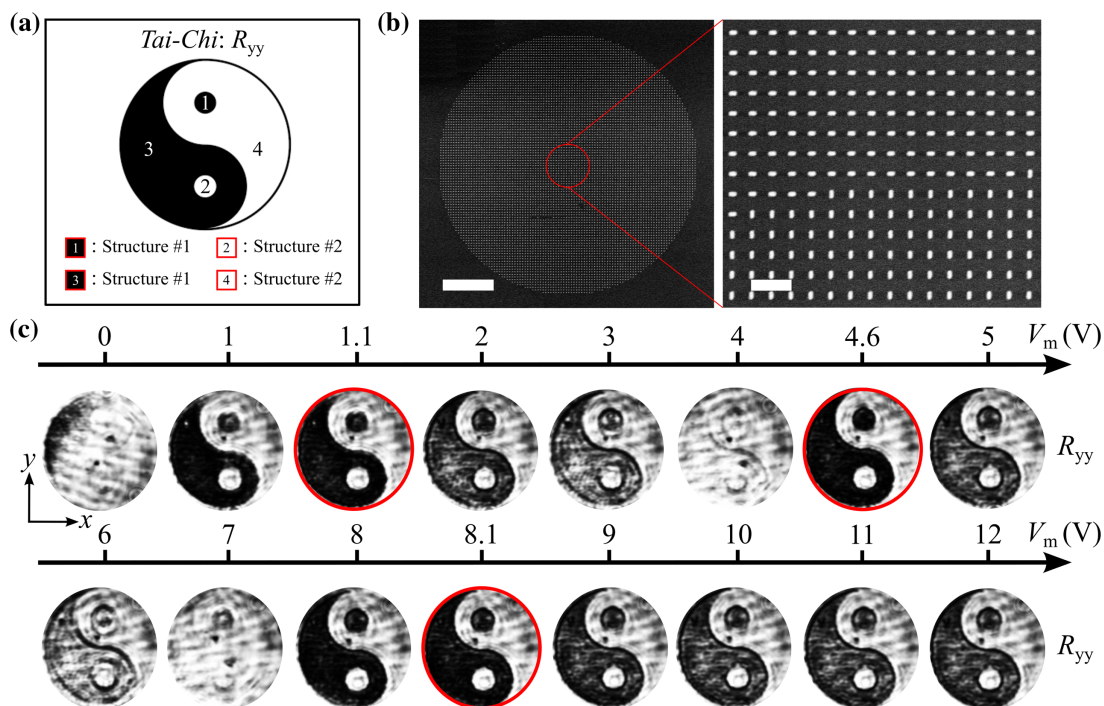

Fig. 3. MEMS-OMS DLP for voltage-controlled grayscale imaging. (a) Design schematic of the voltage-controlled anticounterfeiting grayscale imaging with a *Tai-Chi* pattern. (b) SEM images of the fabricated OMS (scale bars are 10 μm and 1 μm, respectively). (c) Measured intensity profiles of the reflected beams as a function of the applied voltage in the co-polarized channel for $|y\rangle$ incidence.

4.6 V, and 8.1 V. Meanwhile, for other voltages, the *Tai-Chi* pattern gradually fades away, especially at $V_m = 7$ V, which shows the great potential for the information encryption and anticounterfeiting. Capitalizing on the DLP unit cell and Malus's law, grayscale imaging with continuous intensity modulation has been implemented (Supplement 1 Fig. S12 and Visualization 4).

5. MEMS-OMS DLP FOR VOLTAGE-CONTROLLED VVB GENERATION

Utilizing spatially oriented DLP elements, we have implemented a tunable VVB generator that allows us to convert an incident circularly polarized (CP) beam into a reflective CP beam or a cylindrical VVB that possesses spatially inhomogeneous polarization distributions and carries orbital angular momentum (OAM) [12,45–48], depending on the actuated voltage. Specifically, azimuthally polarized (AP) vortex beams with topological charge of $l = 1$ can be generated by locally rotating each DLP nanobrick with an angle of $\theta_{AP} = \arctan(y/x) + \pi/2$ and actuating the MEMS mirror to the polarizer-operation state with a voltage of V_{AP} (T_{AP}) at wavelength of $\lambda = 830.2$ nm [Supplement 1 Section 10 and Figs. 4(a) and 4(b)], where x and y are the local coordinates of each element. Once the MEMS mirror is driven to the mirror-operation state, all the incoming light will be reflected to form a CP beam. As shown in Fig. 4(c) and Visualization 5, the VVB intensity profile appears periodically with actuated voltages

at the wavelength of $\lambda = 830.2$ nm for the left circularly polarized (LCP) incidence [47]. Moreover, the intensity profile changes into an "s" shape and rotates with the axis of the polarizer added in front of the CMOS camera, indicating the generation of an AP beam [Fig. 4(d)]. By decomposing the VVB in the circular polarization basis and conducting interference experiment, the topological charges of $l = 0$ and 2 were confirmed in the co- and cross-polarized channels (Supplement 1 Fig. S14). When the applied voltage is gradually deviated from V_{AP}, the generated AP vortex beam will slowly fade and transit towards a reflected CP beam. Similarly, radially polarized (RP) vortex beams have been demonstrated by rotating each DLP nanobrick with an angle of $\theta_{RP} = \arctan(y/x)$, as shown in Supplement 1 Fig. S15 and Visualization 6. The measured efficiencies of the generated AP and RP vortex beam are ~38.38% and ~37.29%, respectively, slightly lower than the theoretical limit of 50%.

6. CONCLUSION

To summarize, we have demonstrated an electrically driven MEMS-OMS-based DLP with a real-time tunable extinction ratio for two linearly polarized excitations between 13.30 and 1.04 in a fast (rise/fall times of ~2.3/1.7 ms) and reversible way by precisely controlling the polarization-dependent coupling between the plasmonic and FP resonances with a moveable MEMS mirror. Moreover, voltage-controlled grayscale image and VVB generation
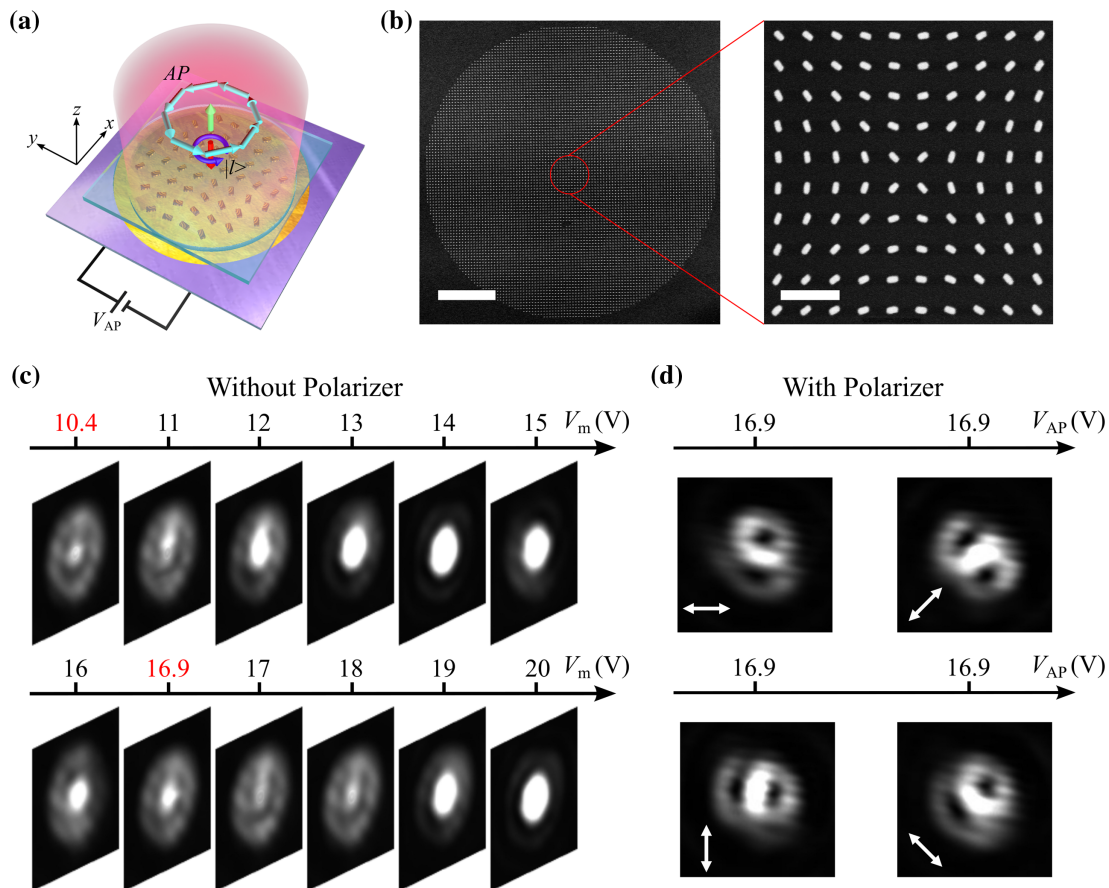
Fig. 4. MEMS-OMS DLP for voltage-controlled AP vortex generation. (a) Schematic rendering of the AP vortex beam generation under LCP incidence with an actuation voltage of V_{AP}. (b) SEM images of the fabricated OMS (scale bars are 10 µm and 1 µm, respectively). (c) Measured intensity profiles of the reflected beams as a function of the applied voltage for LCP incidence. (d) Polarization-resolved intensity profiles of the reflected beams with an applied voltage of $V_{AP} = 16.9$ V for LCP incidence.

have been further implemented based on our DLP platform under different excitations, both accompanied by the distinctive feature of rapid and stable modulation. Our results not only pave the way for the development of real-time tunable meta-devices but also unveil unexplored avenues within the fields of optical displays and anticounterfeiting, especially with more complicated meta-atoms being utilized. For example, our platform makes feasible designing dynamic chiral polarizers (Supplement 1 Fig. S16) with electrically controlled chirality. Combined with the large-scale MEMS technology [49], adaptive metasurface systems with modulation dynamics down to a single pixel level could be anticipated.

7. METHODS

A. Numerical Simulations

All numerical simulations were performed using the commercially available software COMSOL Multiphysics (version 5.6). In the simulation, one individual glass–gold–air–gold (or glass–gold–air) unit cell was modeled with periodic boundary conditions applied in both x and y directions and perfectly matched layers used in the z direction to truncate the simulation domain. The corners of the nanobricks are rounded with a radius of 5 nm to prevent singularities and reduce the deviation between the simulation and experiment. The permittivity of gold is derived from interpolated experimental data [50], while the glass layer is treated as an optically transparent dielectric with a constant refractive index of 1.46, devoid of any significant loss. To obtain complex reflection coefficients, x- and y-polarized light sources were incident onto the unit cell from the upper glass at normal incidence.

B. Device Fabrication

The gold OMS was fabricated employing electron beam lithography (EBL), thin-film deposition, and lift-off techniques. First, a 100-nm-thick resist (methyl methacrylate, PMMA A2, Micro Chem) and a 40-nm-thick conductive polymer (AR-PC 5090, Allresist) were successively spin-coated on a glass substrate (Borofloat 33 wafer, Wafer Universe). Then the metasurface patterns were exposed using EBL (JEOL JEM-6500F) with a voltage of 30 kV. After exposure, the sample was soaked in DI water for 1 min to remove the conductive polymer and subsequently developed in the solution of methyl isobutyl ketone (MIBK) and isopropyl alcohol (IPA) of MIBK: IPA = 1 : 3 for 35 s followed by 60 s in an IPA bath. After that, a 1 nm titanium adhesion layer and a 50 nm gold layer were deposited using thermal evaporation (Tornado 400, Cryofox). The gold nanobricks were eventually formed after a lift-off process in acetone. The MEMS-OMS-based DLP was assembled by gluing the glass substrate with pre-fabricated OMS and the selected clean MEMS mirror with a diameter of ∼3 mm [37–39]. Once the device was meticulously assembled, it was affixed to a PCB for stability. The subsequent stage entailed intricate gold wire bonding, ensuring precise electrical connections for optimal actuation.

and Y.D. fabricated samples, and P.C.V.T. assembled MEMS metasurfaces. Y.D. conducted the optical measurements and analyzed the data. Y.D. made all the figures and movies and drafted the manuscript. All authors contributed to the discussion of the results obtained and editing the manuscript. F.D. and S.I.B. supervised this project.

Disclosures. The authors declare no conflicts of interest. The paper authors C. Meng, P. C. V. Thrane, S. I. Bozhevolnyi, and F. Ding along with J. Gjessing and C. Dirdal from SINTEF are inventors on a related patent application led by the University of Southern Denmark and SINTEF under United States Patent Application No. 17/467542. The authors declare no other competing interests.

Data availability. All data are available in the manuscript or the supplementary materials.

Supplemental document. See Supplement 1 for supporting content.

REFERENCES

1. H.-T. Chen, A. J. Taylor, and N. Yu, "A review of metasurfaces: physics and applications," Rep. Prog. Phys. **79**, 076401 (2016).
2. Q. He, S. Sun, S. Xiao, *et al.*, "High-efficiency metasurfaces: principles, realizations, and applications," Adv. Opt. Mater. **6**, 1800415 (2018).
3. F. Ding, Y. Yang, R. A. Deshpande, *et al.*, "A review of gap-surface plasmon metasurfaces: fundamentals and applications," Nanophotonics **7**, 1129–1156 (2018).
4. W. T. Chen, A. Y. Zhu, and F. Capasso, "Flat optics with dispersion-engineered metasurfaces," Nat. Rev. Mater. **5**, 604–620 (2020).
5. S. Chen, W. Liu, Z. Li, *et al.*, "Metasurface-empowered optical multiplexing and multifunction," Adv. Mater. **32**, 1805912 (2020).
6. Y. Guo, M. Pu, F. Zhang, *et al.*, "Classical and generalized geometric phase in electromagnetic metasurfaces," Photon. Insights **1**, R03 (2022).
7. J. Yao, R. Lin, M. K. Chen, *et al.*, "Integrated-resonant metadevices: a review," Adv. Photonics **5**, 024001 (2023).
8. Y. Yang, W. Wang, P. Moitra, *et al.*, "Dielectric meta-reflectarray for broadband linear polarization conversion and optical vortex generation," Nano Lett. **14**, 1394–1399 (2014).
9. A. Arbabi, Y. Horie, M. Bagheri, *et al.*, "Dielectric metasurfaces for complete control of phase and polarization with subwavelength spatial resolution and high transmission," Nat. Nanotechnol. **10**, 937–943 (2015).
10. Y. Hu, X. Wang, X. Luo, *et al.*, "All-dielectric metasurfaces for polarization manipulation: principles and emerging applications," Nanophotonics **9**, 3755–3780 (2020).
11. Y. Deng, C. Wu, C. Meng, *et al.*, "Functional metasurface quarter-wave plates for simultaneous polarization conversion and beam steering," ACS Nano **15**, 18532–18540 (2021).
12. D. Wang, F. Liu, T. Liu, *et al.*, "Efficient generation of complex vectorial optical fields with metasurfaces," Light Sci. Appl. **10**, 67 (2021).
13. Z. Cai, Y. Deng, C. Wu, *et al.*, "Dual-functional optical waveplates based on gap-surface plasmon metasurfaces," Adv. Opt. Mater. **9**, 2002253 (2021).
14. G. Cao, H.-X. Xu, L.-M. Zhou, *et al.*, "Infrared metasurface-enabled compact polarization nanodevices," Mater. Today **50**, 499–515 (2021).
15. N. A. Rubin, Z. Shi, and F. Capasso, "Polarization in diffractive optics and metasurfaces," Adv. Opt. Photonics **13**, 836–970 (2021).
16. Y. Deng, Z. Cai, Y. Ding, *et al.*, "Recent progress in metasurface-enabled optical waveplates," Nanophotonics **11**, 2219–2244 (2022).
17. A. H. Dorrah and F. Capasso, "Tunable structured light with flat optics," Science **376**, eabi6860 (2022).
18. H. Hemmati, P. Bootpakdeetam, and R. Magnusson, "Metamaterial polarizer providing principally unlimited extinction," Opt. Lett. **44**, 5630–5633 (2019).
19. Y. Zhang, M. Pu, J. Jin, *et al.*, "Crosstalk-free achromatic full Stokes imaging polarimetry metasurface enabled by polarization-dependent phase optimization," Opto-Electron. Adv. **5**, 220058 (2022).
20. P. Bootpakdeetam, H. Hemmati, and R. Magnusson, "Cascaded metamaterial polarizers for the visible region," Opt. Lett. **45**, 6831–6834 (2020).
21. L. Y. M. Tobing, M. Wasiak, D. H. Zhang, *et al.*, "Nearly total optical transmission of linearly polarized light through transparent electrode composed of GaSb monolithic high-contrast grating integrated with gold," Nanophotonics **10**, 3823–3830 (2021).

22. L. Deng, J. Deng, Z. Guan, *et al.*, "Malus-metasurface-assisted polarization multiplexing," Light Sci. Appl. **9**, 101 (2020).

23. J. Deng, L. Deng, Z. Guan, *et al.*, "Multiplexed anticounterfeiting meta-image displays with single-sized nanostructures," Nano Lett. **20**, 1830–1838 (2020).

24. J. Deng, Z. Li, J. Li, *et al.*, "Metasurface-assisted optical encryption carrying camouflaged information," Adv. Opt. Mater. **10**, 2200949 (2022).

25. M. Wuttig, H. Bhaskaran, and T. Taubner, "Phase-change materials for non-volatile photonic applications," Nat. Photonics **11**, 465–476 (2017).

26. Q. He, S. Sun, and L. Zhou, "Tunable/reconfigurable metasurfaces: physics and applications," Research **2019**, 1849272 (2019).

27. A. M. Shaltout, V. M. Shalaev, and M. L. Brongersma, "Spatiotemporal light control with active metasurfaces," Science **364**, eaat3100 (2019).

28. F. Ding, Y. Yang, and S. I. Bozhevolnyi, "Dynamic metasurfaces using phase-change chalcogenides," Adv. Opt. Mater. **7**, 1801709 (2021).

29. E. Mikheeva, C. Kyrou, F. Bentata, *et al.*, "Space and time modulations of light with metasurfaces: recent progress and future prospects," .ACS Photonics **9**, 1458–1482 (2022).

30. O. A. M. Abdelraouf, Z. Wang, H. Liu, *et al.*, "Recent advances in tunable metasurfaces: materials, design, and applications," ACS Nano **16**, 13339–13369 (2022).

31. C. H. Chu, M. L. Tseng, J. Chen, *et al.*, "Active dielectric metasurface based on phase-change medium," Laser Photonics Rev. **10**, 986–994 (2016).

32. S.-Q. Li, X. Xu, R. Maruthiyodan Veetil, *et al.*, "Phase-only transmissive spatial light modulator based on tunable dielectric metasurface," Science **364**, 1087–1090 (2019).

33. P. C. Wu, R. A. Pala, G. Kafaie Shirmanesh, *et al.*, "Dynamic beam steering with all-dielectric electro-optic III–V multiple-quantum-well metasurfaces," Nat. Commun. **10**, 3654 (2019).

34. P. Yu, J. Li, and N. Liu, "Electrically tunable optical metasurfaces for dynamic polarization conversion," Nano Lett. **21**, 6690–6695 (2021).

35. L. Lu, Z. Dong, F. Tijiptoharsono, *et al.*, "Reversible tuning of Mie resonances in the visible spectrum," ACS Nano **15**, 19722–19732 (2021).

36. P. Moitra, Y. Wang, X. Liang, *et al.*, "Programmable wavefront control in the visible spectrum using low-loss chalcogenide phase-change metasurfaces," Adv. Mater. **35**, 2205367 (2023).

37. K. Z. Kamali, L. Xu, N. Gagrani, *et al.*, "Electrically programmable solid-state metasurface via flash localised heating," Light Sci. Appl. **12**, 40 (2023).

38. C. Zeng, H. Lu, D. Mao, *et al.*, "Graphene-empowered dynamic metasurfaces and metadevices," Opto-Electron. Adv. **5**, 200098 (2022).

39. C. Meng, P. C. V. Thrane, F. Ding, *et al.*, "Dynamic piezoelectric MEMS-based optical metasurfaces," Sci. Adv. **7**, eabg5639 (2021).

40. C. Meng, P. C. V. Thrane, F. Ding, *et al.*, "Full-range birefringence control with piezoelectric MEMS-based metasurfaces," Nat. Commun. **13**, 2071 (2022).

41. P. C. V. Thrane, C. Meng, F. Ding, *et al.*, "MEMS tunable metasurfaces based on gap plasmon or Fabry-Pérot resonances," Nano Lett. **22**, 6951–6957 (2022).

42. A. Berkhout and A. F. Koenderink, "Perfect absorption and phase singularities in plasmon antenna array etalons," .ACS Photonics **6**, 2917–2925 (2019).

43. D. B. Haim, L. Michaeli, O. Avayu, *et al.*, "Tuning the phase and amplitude response of plasmonic metasurface etalons," Opt. Express **28**, 17923 (2020).

44. X. Zhang, J. Cheng, W. Yue, *et al.*, "Twofold optical display and encryption of binary and grayscale images with a wavelength-multiplexed metasurface," Nanophotonics **12**, 3747–3756 (2023).

45. F. Ding, Y. Chen, Y. Yang, *et al.*, "Multifunctional metamirrors for broadband focused vector-beam generation," Adv. Opt. Mater. **7**, 1900724 (2019).

46. F. Yue, V. Aglieri, R. Piccoli, *et al.*, "Highly sensitive polarization rotation measurement through a high-order vector beam generated by a metasurface," Adv. Mater. Technol. **5**, 1901008 (2020).

47. U. Stella, T. Grosjean, N. De Leo, *et al.*, "Vortex beam generation by spin-orbit interaction with Bloch surface waves," .ACS Photonics **7**, 774–783 (2020).

48. C. Wu, S. Kumar, Y. Kan, *et al.*, "Room-temperature on-chip orbital angular momentum single-photon sources," Sci. Adv. **8**, eabk3075 (2022).

49. X. Zhang, K. Kwon, J. Henriksson, *et al.*, "A large-scale microelectromechanical-systems-based silicon photonics LiDAR," Nature **603**, 253–258 (2022).

50. P. B. Johnson and R. W. Christy, "Optical constants of the noble metals," Phys. Rev. B **6**, 4370–4379 (1972).

MEMS-integrated metasurfaces for dynamic linear polarizers: supplement

YADONG DENG,[1] CHAO MENG,[1] PAUL C. V. THRANE,[1,2] SÖREN IM SANDE,[1] SERGEY I. BOZHEVOLNYI,[1,3] AND FEI DING[1,*]

[1] *Centre for Nano Optics, University of Southern Denmark, Campusvej 55, Odense DK-5230, Denmark*
[2] *SINTEF Microsystems and Nanotechnology, Gaustadalleen 23C, 0737 Oslo, Norway*
[3] *seib@mci.sdu.dk*
[*] *feid@mci.sdu.dk*

MEMS-Integrated metasurfaces for dynamic linear polarizers: supplement

YADONG DENG,[1] CHAO MENG,[1] PAUL C. V. THRANE,[1,2] SÖREN IM SANDE,[1] SERGEY I. BOZHEVOLNYI,[1,3] AND FEI DING[1,*]

[1]*Centre for Nano Optics, University of Southern Denmark, Campusvej 55, Odense DK-5230, Denmark*
[2]*SINTEF Microsystems and Nanotechnology, Gaustadalleen 23C, 0737 Oslo, Norway*
[3]*seib@mci.sdu.dk*
feid@mci.sdu.dk

1. Hybrid plasmonic FP model for the MEMS-OMS DLP

We provide further insights into the designed DLP with a hybrid plasmonic FP model composed of two interfaces (Fig. S1A). The total reflection r_{FP} is the superposition of the direct reflection r_{12} from the interface containing the OMS layer (Fig. 2) and other reflection terms r_o that bounce back and forth between the OMS and MEMS mirror before escaping (Fig. S1B). Therefore, the strength of the total reflection is determined by both the OMS and air gap T_a. For $|x\rangle$ incidence, the total reflection coefficient r_{FP} (red solid circle) arising from the superposition of r_{12} (green dot) and r_o (blue solid circle) closely approximates the unit circle (black dotted circle) at $\lambda = 831$ nm, despite the increased air gap T_a (Fig. S1C). While for the $|y\rangle$ incident light, the total reflection coefficient r_{FP} significantly varies between the vicinity of the origin (polarizer-operation state) and the immediate vicinity of the unit circle (mirror-operation state) as a function of the air gap, which is also ascribed to the superposition of r_{12} and r_o, as shown in the complex plane of Fig. S1D.

A

B

$$r_{FP} = r_{12} + \frac{t_{12}t_{21}r_{23}e^{i2kn_2T_a}}{1 - r_{21}r_{23}e^{i2kn_2T_a}}$$
$$= r_{12} + r_o$$

C   **D**
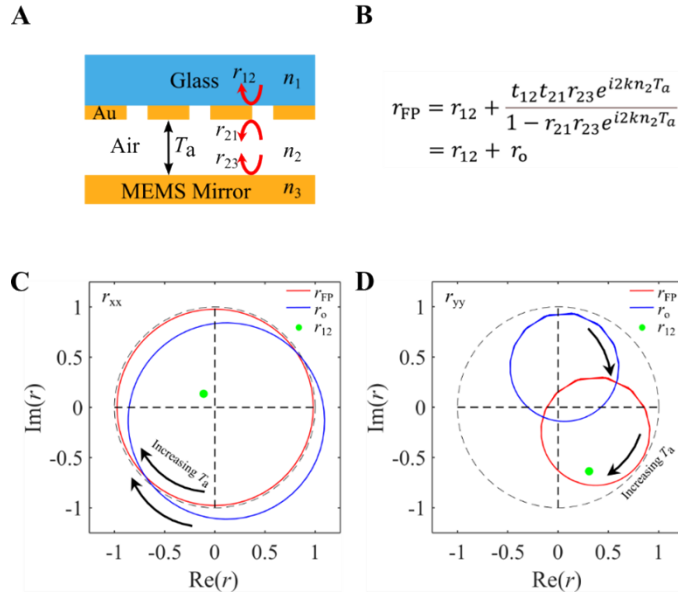
Fig. S1. Calculated complex reflection coefficients of the MEMS-OMS DLP with a FP model. (A) Schematic of the FP model consisting of media 1 (glass layer), an OMS layer located between glass/air interface, media 2 (air layer), and media 3 (MEMS mirror layer). Here r_{FP} represents the complex reflection coefficient of the MEMS-OMS system, and r_{mn}/t_{mn} represents the complex reflection/transmission coefficients for the interface between media m and n with light incident from medium m. Thus the interface 12 represents a complex glass/OMS/air interface and interface 23 represents a bare air/gold interface. (B) FP equation for the total reflection coefficient. (C and D) Calculated reflection coefficients of r_{12} (green dot), r_o (blue solid circle), and r_{FP} (red solid circle) in the complex planes for $|x\rangle$ (C) and $|y\rangle$ (D) incidence as a function of the increased air gap T_a.
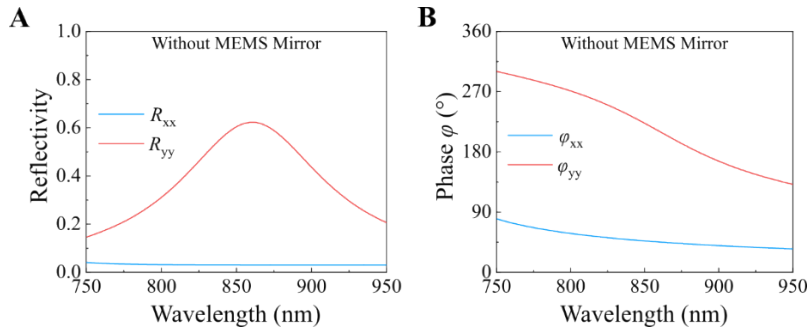
Fig. S2. Simulated reflectivity (A) and phase response (B) of the anisotropic metasurface on top of a glass substrate. The metasurface unit cell has the dimensions of $[l_x, l_y, t_m, P]$ = [106 nm, 196 nm, 50 nm, 500 nm].
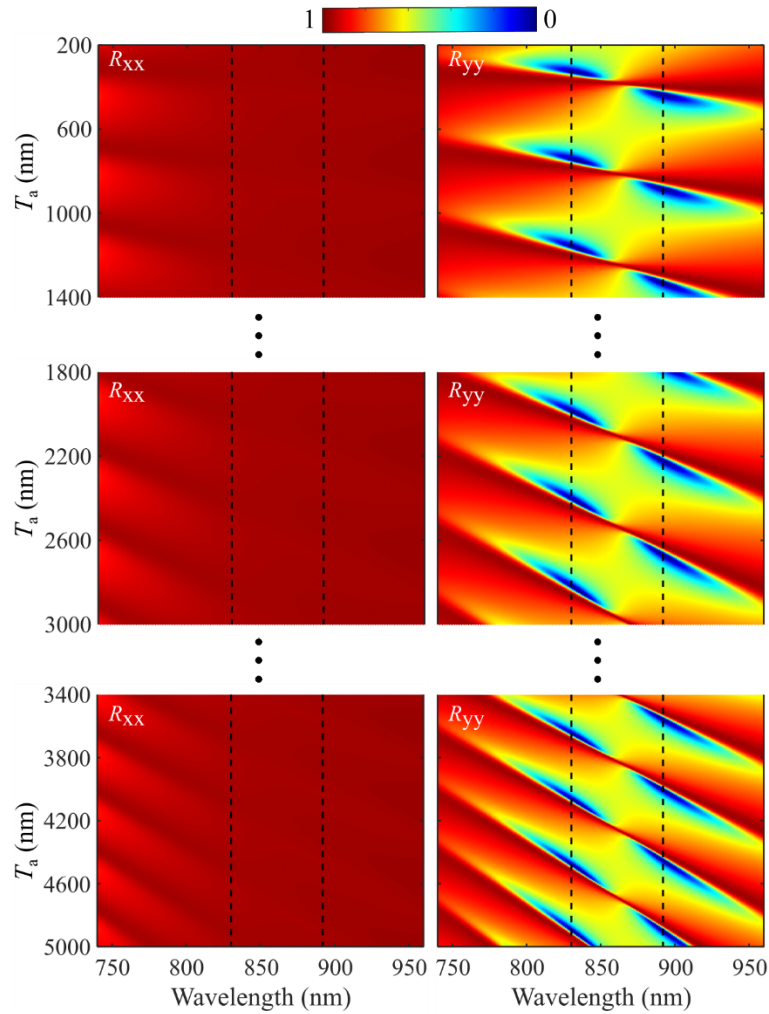
Fig. S3. Calculated reflectivities as a function of air gap T_a and wavelength using the FP model. The black dashed lines mark the wavelengths of λ = 831 nm and 892 nm.
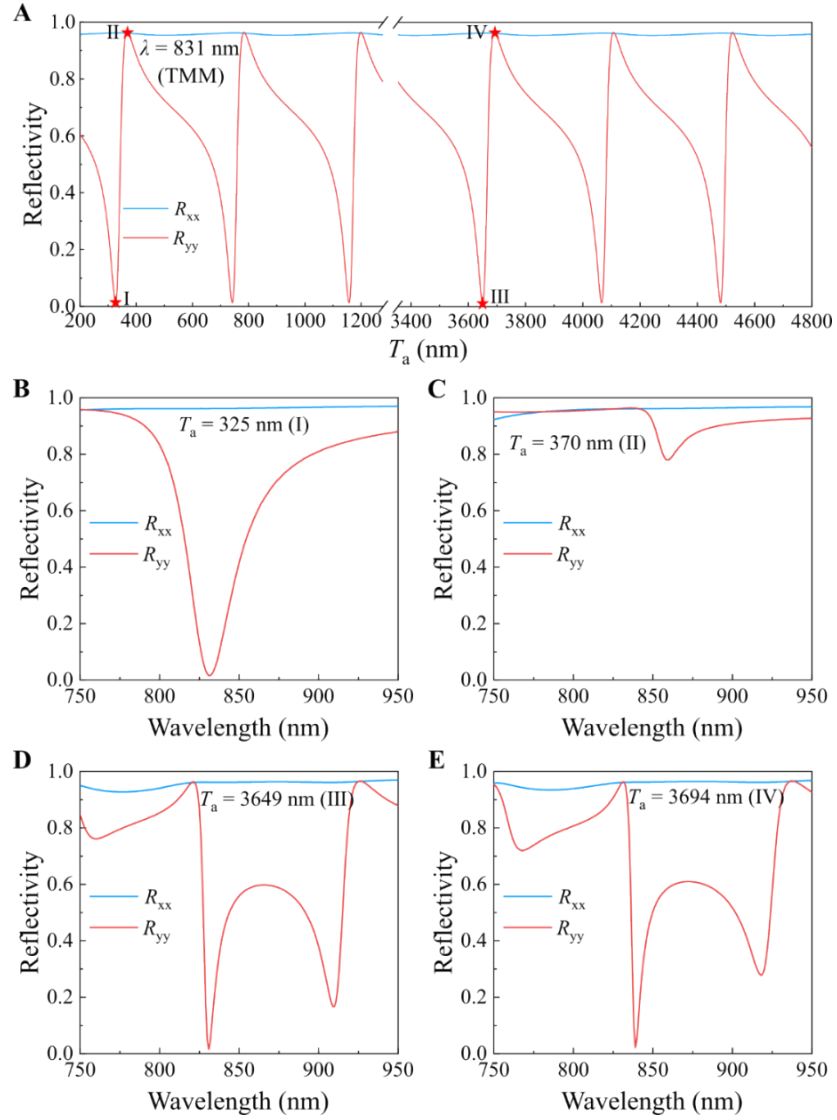
Fig. S4. Calculated reflectivities using the FP model. (A) Calculated reflectivities as a function of the air gap T_a at a fixed wavelength of $\lambda = 831$ nm for both $|x\rangle$ and $|y\rangle$ incidence. Red stars I and III mark the polarizer-operation states with the air gaps of $T_a = 325$ nm and 3649 nm, respectively, while red stars II and IV represent the mirror-operation states with the air gaps of $T_a = 370$ nm and 3694 nm, respectively. (B to E) Calculated reflectivities as a function of the wavelength at air gaps of $T_a = 325$ nm (B), 370 nm (C), 3649 nm (D), and 3694 nm (E) for both $|x\rangle$ and $|y\rangle$ incidence.

2. Angular sensitivity of the MEMS-OMS DLP
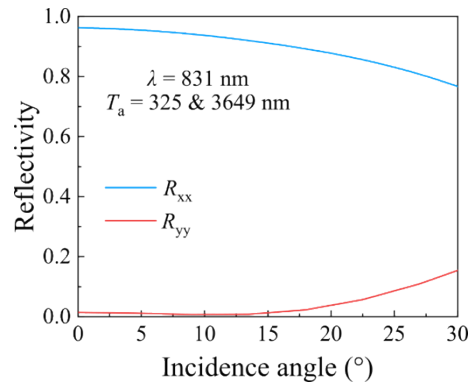
Fig. S5. Calculated reflectivities as a function of the incidence angle at $\lambda = 831$ nm with air gaps of $T_a = 325$ nm and 3649 nm. The DLP exhibits identical angular sensitivity at these two air gaps.

3. Effect of the periodicity on the performance of the MEMS-OMS DLP
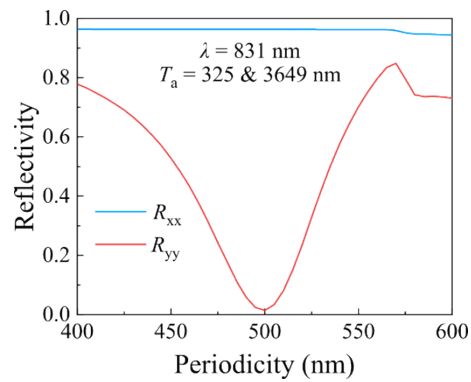
Fig. S6. Calculated reflectivities as a function of the periodicity at $\lambda = 831$ nm with air gaps of $T_a = 325$ nm and 3649 nm.

4. Electric field distributions for |x> incidence
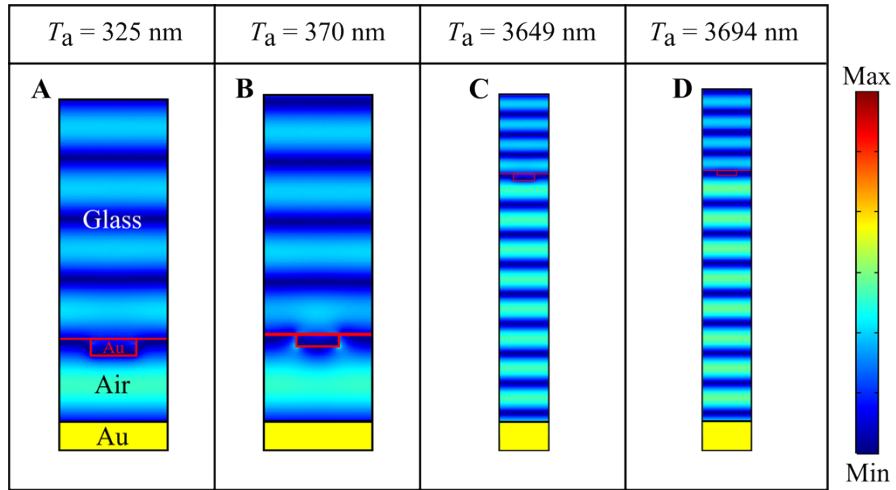
Fig. S7. Simulated electric field distributions at $\lambda = 831$ nm for $|x>$ incidence. (A and B) Electric field distributions of the 1st-order FP mode with an air gap of $T_a = 325$ nm (polarizer-operation state) and 370 nm (mirror-operation- state), respectively. (C and D) Electric field distributions of the 8th-order FP mode with an air gap of $T_a = 3649$ nm (polarizer-operation state) and 3694 nm (mirror-operation state), respectively.

5. Experimental setup
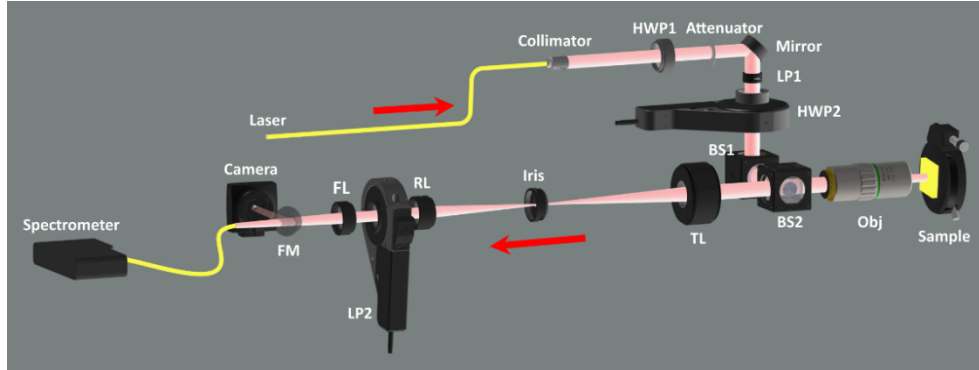
Fig. S8. Experimental setup for characterizing MEMS-OMS-based DLP device. A collimated fiber-coupled supercontinuum laser (SuperK Extreme, NKT Photonics) first passes through a half-wave plate (HWP1, AHWP10M-980, Thorlabs) and an attenuator (NE01B, Thorlabs) to modify the intensity of the light. Then the light reflected by a silver mirror (PF10-03-P01, Thorlabs) is directed through a linear polarizer (LP1, LPNIR050-MP2, Thorlabs), a half-wave plate (HWP2, ACHROMATIC, 690-1200 nm, Thorlabs) mounted on a motorized precision rotation stage (MPRS, PRM1Z8, Thorlabs), two beam splitters (BS1 and BS2, CCM1-BS014/M, Thorlabs) successively, and then slightly focused onto the samples by a long working distance objective (Obj. M Plan Apo 20×/0.42NA, Mitutoyo). The combination of LP1 and HWP2 is used for generating x- or y-polarized beams in a controlled manner, and two beam splitters could adjust the direction of the beam propagation. The reflected signal light collected by the same objective passes through BS2 and a tube lens (TL, TTL200-S8, f = 200 mm, Thorlabs), generating the first direct image plane where an iris (Iris, SM1D12SZ, Thorlabs) is positioned for filtering out the background outside the sample area. The filtered first real image is then transformed by a relay lens (RL, AC254-200-B-ML, f = 200 mm, Thorlabs) to create a Fourier image, which is captured by a CMOS camera (Camera, DCC1545M, Thorlabs) when the flip mirror (FM, PF10-03-P01, Thorlabs) is flipped up. A flip lens (FL, AC254-100-B-ML, f = 100 mm, Thorlabs) placed between the relay lens and the flip mirror is used for switching the real and Fourier images. A linear polarizer (LP2) and a spectrometer (QE Pro, Ocean Optics) are employed to collect polarization-resolved reflection spectra. To measure the switching speed between polarizer-operation and mirror-operation states, the input laser and spectrometer are replaced with a continuous wave Ti: Sapphire laser (Spectra-Physics 3900 S) and a photodetector (PD, PDA20CS-EC, Thorlabs), respectively. The signals from the PD are captured using an oscilloscope (DSOX2024A, Keysight). In the measurements, the MEMS-OMS-based DLP sample is actuated with periodically alternating voltages.
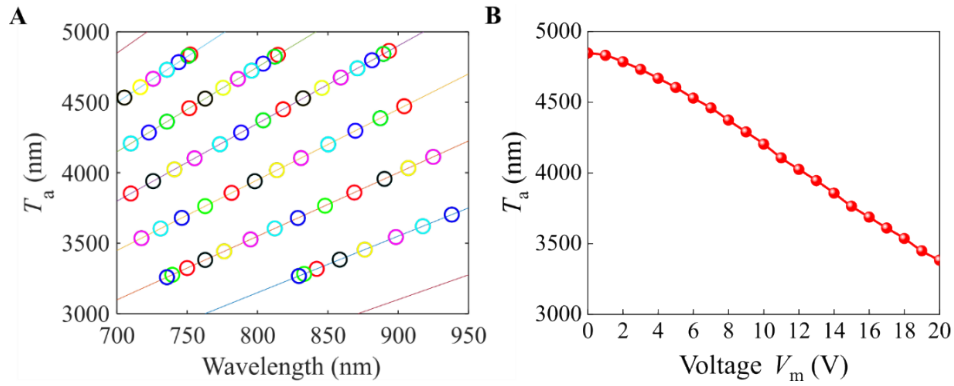
6. Air gap estimation

Fig. S9. Estimated air gap as a function of the voltage applied to the inner electrode. (A) Estimating practical air gaps T_a at different actuation voltages through mirror-operation states in our fabricated MEMS-OMS-based DLP. Colored lines depict the theoretical relationship between the air gap T_a and the wavelength for mirror-operation states, whereas colored circles represent the extracted wavelengths from the measured R_{yy} spectra with different voltages V_m. (B) Estimated air gap T_a as a function of the actuation voltage V_m.

7. Measured reflection spectra with different actuation voltages
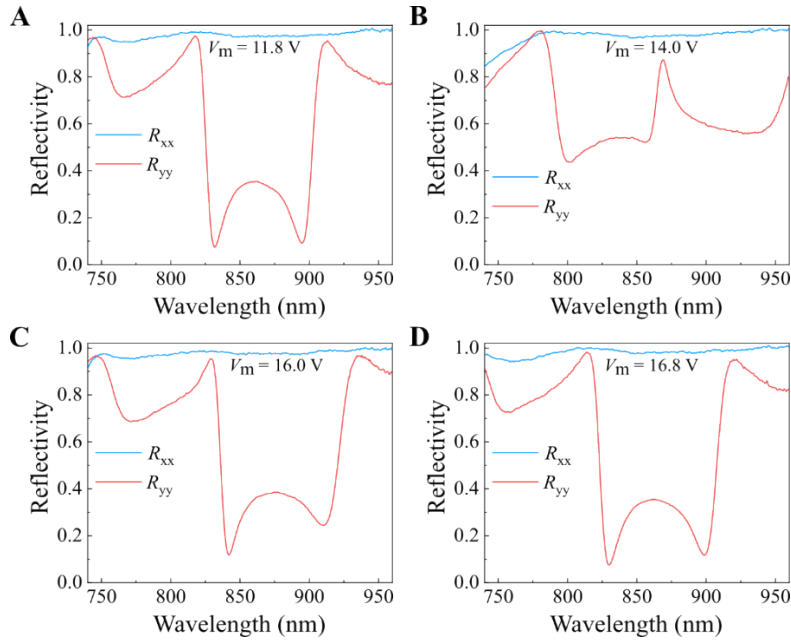
Fig. S10. Measured reflectivities as a function of wavelength with different actuation voltages.

8. Performance of the MEMS-OMS DLP at the larger split wavelength
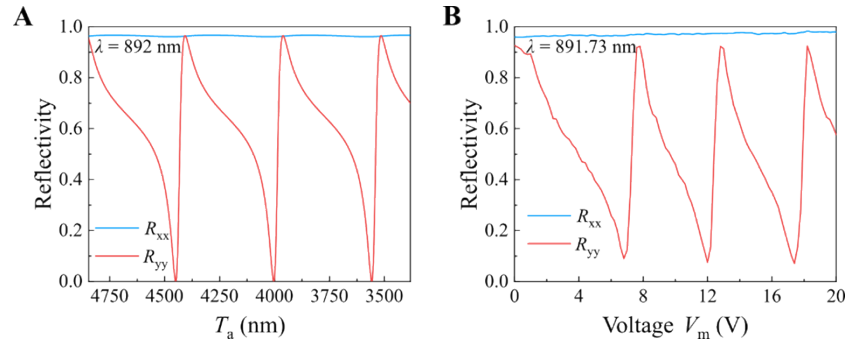
Fig. S11. Calculated (A) and measured (B) reflectivities as a function of T_a (A) and V_m (B).

9. MEMS-OMS DLP for voltage-controlled grayscale imaging with continuous intensity modulation
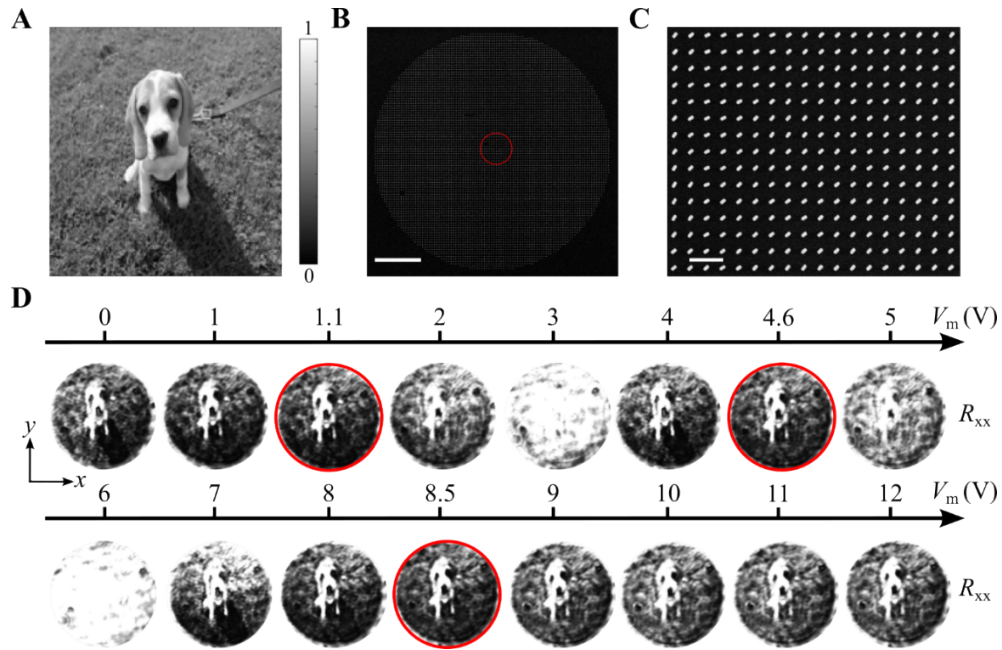
Fig. S12. MEMS-OMS DLP for voltage-controlled grayscale imaging with continuous intensity modulation. (A) The original grayscale picture of a dog. (B and C) SEM images of the fabricated metasurface. Scale bars in (B) and (C) are 10 μm and 1 μm, respectively. (D) Measured intensity profiles of the reflected beams as a function of the applied voltage in the co-polarized channel for $|x>$ incidence.

10. The performance of the MEMS-OMS DLP with different orientations

Figure S13 shows the simulated degree of linear polarization (DoLP) and angle of linear polarization (AoLP) of the designed DLP as a function of the rotation angle of θ with respect to the x-axis under the circularly polarized incident light at the wavelength of 831 nm. With the rotation angle θ varied from 0° to 90°, the DoLP stays above 0.97 and AoLP follows the linear distribution of θ, which is consistent with the theoretical prediction. Therefore, our designed polarizer works quite well regardless of the orientation, manifesting negligible near-field coupling between adjacent elements. The response of such a DLP with a rotation angle of θ could be described by the Jones matrix:

$$M(\theta) = \begin{pmatrix} \cos\theta & -\sin\theta \\ \sin\theta & \cos\theta \end{pmatrix} r_{xx} \begin{pmatrix} 1 & 0 \\ 0 & 0 \end{pmatrix} \begin{pmatrix} \cos\theta & \sin\theta \\ -\sin\theta & \cos\theta \end{pmatrix} = r_{xx} \begin{pmatrix} \cos^2\theta & \cos\theta\sin\theta \\ \cos\theta\sin\theta & \sin^2\theta \end{pmatrix} \#(1)$$

where r_{xx} is the reflection coefficient under the x-polarized excitation. For the left-handed circularly polarized (LCP) light with $E_{in} = \frac{1}{\sqrt{2}}\begin{pmatrix} 1 \\ i \end{pmatrix}$, the output field becomes $E_{out} = \frac{r_{xx}}{\sqrt{2}}e^{i\theta} \begin{pmatrix} \cos\theta \\ \sin\theta \end{pmatrix}$. If the orientation θ is equal to $\arctan(y/x) + \pi/2$, an azimuthally polarized (AP) beam can be generated with $E_{out} = \frac{r_{xx}}{\sqrt{2}}e^{i(\varphi + \frac{\pi}{2})}\begin{pmatrix} \cos(\varphi + \frac{\pi}{2}) \\ \sin(\varphi + \frac{\pi}{2}) \end{pmatrix}$, where x and y are the local coordinate of each element and $\varphi = \arctan(y/x)$ is the azimuthal angle. Meanwhile, the AP beam carries an orbital angular momentum (OAM) with the topological charge of $l = 1$, which can be further decomposed into two circularly polarized (CP) components:

$$E_{out} = \frac{r_{xx}}{2\sqrt{2}}\begin{pmatrix} 1 \\ i \end{pmatrix} - \frac{r_{xx}}{2\sqrt{2}}e^{i2\varphi}\begin{pmatrix} 1 \\ -i \end{pmatrix}\#(2)$$
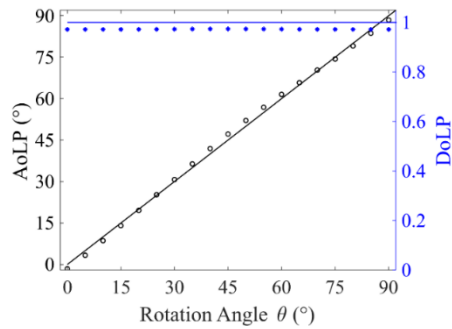
If the orientation θ is equal to φ, a radially polarized (RP) vortex beam can be generated with $E_{out} = \frac{r_{xx}}{\sqrt{2}}e^{i\varphi}\begin{pmatrix} \cos\varphi \\ \sin\varphi \end{pmatrix}$ under the LCP excitation, which possesses a spiral phase with the topological charge of $l = 1$. After decomposition, the CP components are written as

$$E_{out} = \frac{r_{xx}}{2\sqrt{2}}\begin{pmatrix} 1 \\ i \end{pmatrix} + \frac{r_{xx}}{2\sqrt{2}}e^{i2\varphi}\begin{pmatrix} 1 \\ -i \end{pmatrix}\#(3)$$

Fig. S13. Calculated DoLP and AoLP of our designed polarizer as a function of the rotation angle θ under the LCP excitation at $\lambda = 831$ nm with an air gap of $T_a = 3649$ nm.

11. Intensity distributions and interference pattern of the generated AP and RP vortex beams under LCP incidence in the circular polarization basis
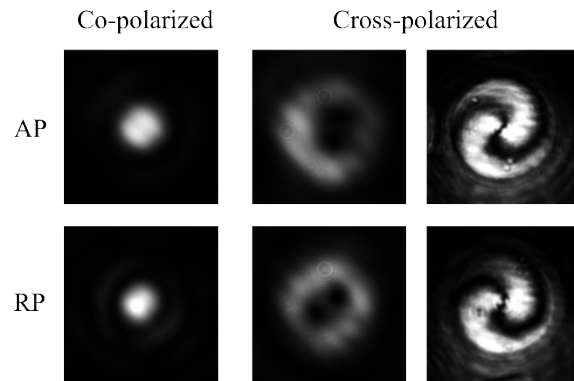
Co-polarized   Cross-polarized

Fig. S14. Intensity distributions (left and middle columns) and interference patterns (right column) of the generated AP and RP vortex beams under LCP incidence in the circular polarization basis. The interference patterns are produced by superposing the vector vortex beam with a reference Gaussian beam.

12. MEMS-OMS DLP for voltage-controlled RP vortex beam generation
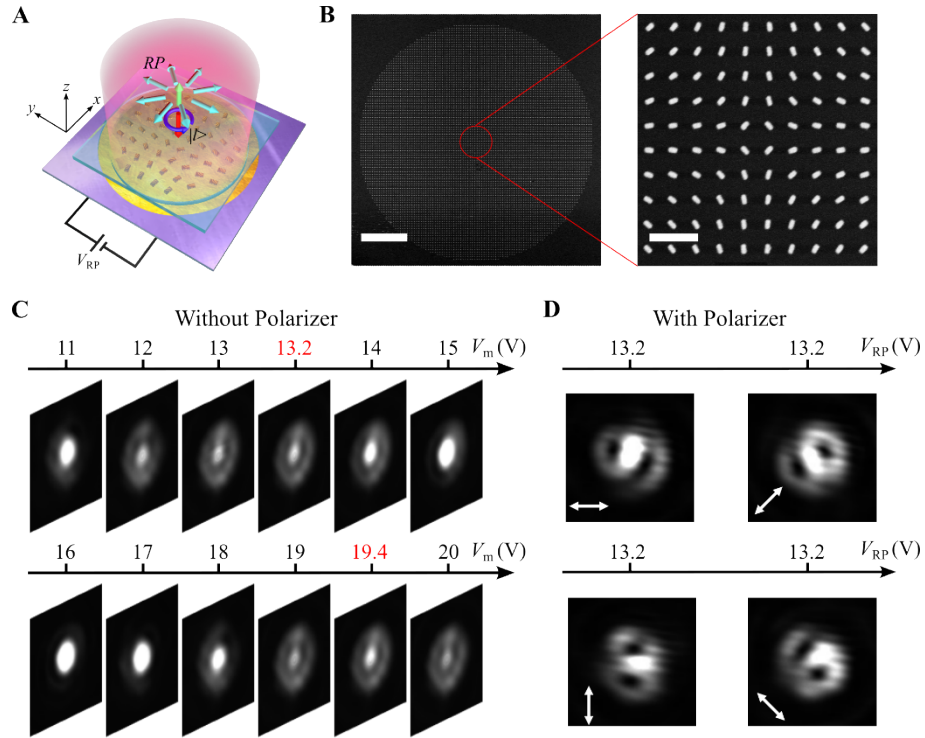
Fig. S15. MEMS-OMS DLP for voltage-controlled RP vortex beam generation. (A) Schematic rendering of the RP beam generation under LCP incidence with an actuation voltage of V_{RP}. (B) SEM images of the fabricated OMS (scale bars are 10 μm and 1 μm, respectively). (C) Measured intensity profiles of the reflected as a function of the applied voltage for LCP incidence. (D) Polarization-resolved intensity profiles of the reflected beams with an applied voltage of V_{RP} = 13.2 V for LCP incidence.

13. MEMS-OMS dynamic circular polarizer
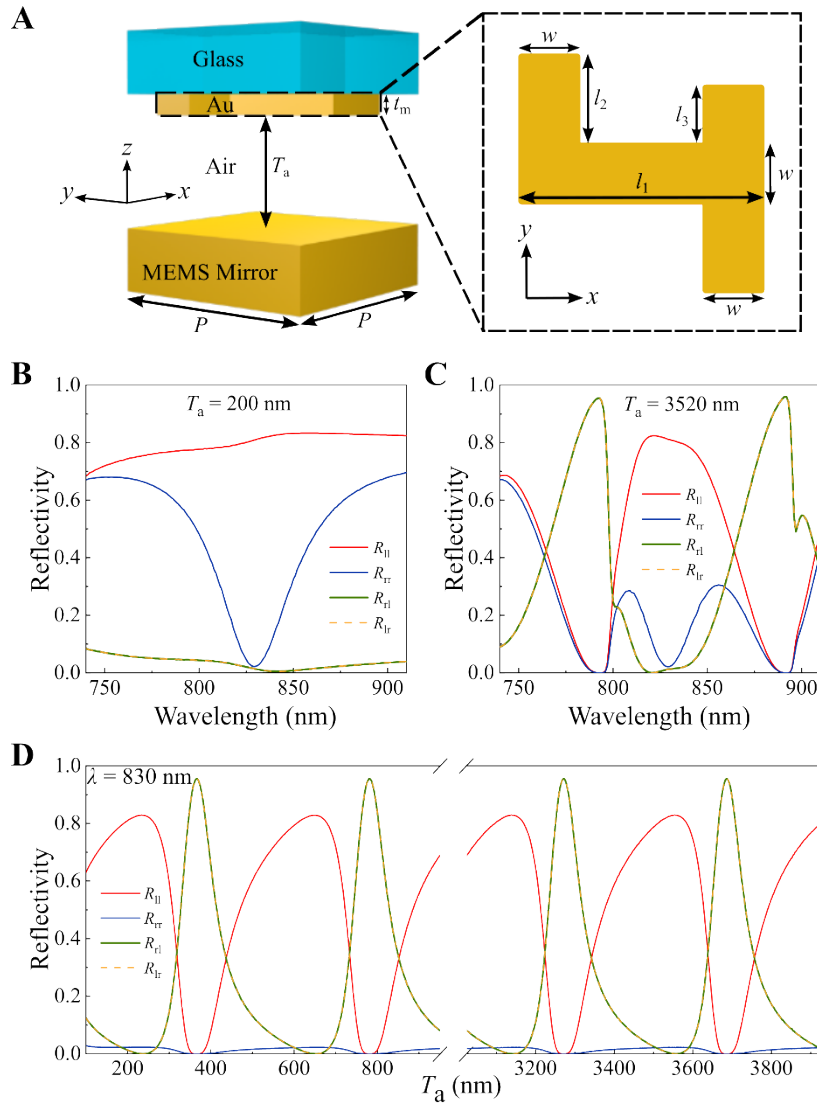
Fig. S16. Design principle of the MEMS-OMS dynamic circular polarizer. (A) Schematic of the MEMS-OMS unit cell including a chiral meta-atom and a MEMS mirror, separated by an air gap of T_a. The dimensions are set to be $l_1 = 408$ nm, $l_2 = 153$ nm, $l_3 = 102$ nm, $w = 102$ nm, $P = 500$ nm, and $t_m = 50$ nm. (B and C) Calculated reflectivities as a function of the wavelength at air gaps of $T_a = 200$ nm (B) and 3520 nm (C) in the circular polarization basis. The subscripts l and r represent left-handed and right-handed circularly polarized light, respectively. (D) Calculated reflectivities as a function of the air gap T_a at the design wavelength of $\lambda = 830$ nm in the circular polarization basis.

PHYSICS

Electrically tunable topological phase transition in non-Hermitian optical MEMS metasurfaces

Fei Ding[1]*†, Yadong Deng[1]†, Chao Meng[1]†, Paul C. V. Thrane[1,2], Sergey I. Bozhevolnyi[1]*

Exceptional points (EPs), unique junctures in non-Hermitian open systems where eigenvalues and eigenstates simultaneously coalesce, have gained notable attention in photonics because of their enthralling physical principles and unique properties. Nonetheless, the experimental observation of EPs, particularly within the optical domain, has proven rather challenging because of the grueling demand for precise and comprehensive control over the parameter space, further compounded by the necessity for dynamic tunability. Here, we demonstrate the occurrence of optical EPs when operating with an electrically tunable non-Hermitian metasurface platform that synergizes chiral metasurfaces with piezoelectric MEMS mirrors. Moreover, we show that, with a carefully constructed metasurface, a voltage-controlled spectral space can be finely tuned to access not only the chiral EP but also the diabolic point characterized by degenerate eigenvalues and orthogonal eigenstates, thereby allowing for dynamic topological phase transition. Our work paves the way for developing cutting-edge optical devices rooted in EP physics and opening uncharted vistas in dynamic topological photonics.

INTRODUCTION

In the realm of photonics, the exploration of exceptional points (EPs) has emerged as a fascinating avenue of research promising to reshape the landscape of light-matter interactions and optical manipulation (*1–5*). Rooted within the intricacies of non-Hermitian systems (*6, 7*), EPs signify a unique configuration where distinct eigenvalues and eigenstates simultaneously coalesce, resulting in complex optical responses and enabling novel functionalities, including unidirectional transmission/reflection (*8, 9*), exceptional sensing (*10, 11*), asymmetric mode switching (*12–14*), and topological phase engineering (*15*). Recent scholarly attention within EP research has been directed toward non-Hermitian metasurfaces (*11, 15–20*), a captivating platform that reveals the potential for implementing adaptive and precisely controlled optical functionalities through careful engineering of metasurface constituents' geometrical and material attributes (*21–24*).

Nonetheless, existing experimental endeavors have predominantly been centered on passive metasurfaces, where the EP observation necessitates the fabrication of numerous samples, each featuring varying geometrical parameters and thus inadvertently adding fabrication errors. In addition, this method faces serious challenges in precisely attaining an EP, as unavoidable fabrication and measurement errors are amplified in the EP vicinity. In contrast, the emergence of dynamic, actively controlled metasurfaces indicates an alternative that would lead toward real-time control over the parameter space, facilitating the EP access and monitoring of the evolution of light-matter interactions near EPs within a single device (*25, 26*). While certain advances along this route have been demonstrated, the practical realization of actively controlled non-Hermitian metasurfaces remains confined to the terahertz domain (*25, 26*). The experimental observation of dynamically tuned EPs in the optical regime has thus far remained elusive, as the transition of EP metasurfaces from long-wavelength ranges (e.g., the terahertz range) to the optical range is nontrivial,

involving not only scaling the dimensions down to a few hundred nanometers but also accounting for strongly dispersive optical constants, not to mention their dynamic tunability.

Here, we report on an in-depth exploration of optical EPs within a fully electrically tunable non-Hermitian metasurface platform that beneficially exploit the synergistic interplay between chiral metasurfaces and piezoelectric micro-electromechanical systems (MEMS) mirrors, thereby allowing for fine-tuning the system to construct a voltage-controlled spectral space containing not only the chiral EP but also the diabolic point (DP) characterized by degenerate eigenvalues and orthogonal eigenstates. By capitalizing on design flexibility and dynamic tunability, we demonstrate a voltage-controlled topological phase transition between EPs and DPs, representing a unique feature of the developed MEMS-based metasurface platform. Leveraging the dynamic attributes inherent to non-Hermitian optical metasurfaces, we endeavor initiating a new chapter characterized by fascinating prospects of enhanced light-matter interactions and advent of innovative EP-based optical devices.

RESULTS

Design of non-Hermitian metasurfaces for tunable topological phase transition

The electrically tunable non-Hermitian metasurface consists of a two-dimensional symmetry-broken chiral gold meta-atom array on a glass substrate and a thin-film piezoelectric MEMS mirror, where the air gap between the meta-atoms and MEMS mirror can be precisely controlled by applying an actuation voltage (Fig. 1A). For large air gaps, the near-field coupling between the gold meta-atoms and MEMS mirror disappears, switching the gap-surface plasmon resonance to a hybrid plasmonic Fabry-Pérot (FP) resonance that affords effective and dynamic control over reflected optical fields (*27–29*). The moveable MEMS mirror can vary the cavity length and, hence, tune the resonant wavelength, thereby modulating the coupling strength between the plasmonic and FP resonances. Meanwhile, a tunable far-field radiation rate (i.e., radiation loss) can be achieved with such a dynamic non-Hermitian metasurface (*30*). Capitalizing on the interplay between the plasmon and FP resonances via a

[1]Centre for Nano Optics, University of Southern Denmark, Campusvej 55, Odense DK-5230, Denmark. [2]SINTEF Microsystems and Nanotechnology, Gaustadalleen 23C, 0737 Oslo, Norway.
*Corresponding author. Email: feid@mci.sdu.dk (F.D.); seib@mci.sdu.dk (S.I.B.)
†These authors contributed equally to this work.

voltage-controlled air gap, one could realize an electrically controlled topology transition.

The effective Hamiltonian of our dynamic metasurface can be described by a non-Hermitian Jones matrix $\widehat{r}(\Omega) = \begin{bmatrix} r_{\text{LL}}(\Omega) & r_{\text{LR}}(\Omega) \\ r_{\text{RL}}(\Omega) & r_{\text{RR}}(\Omega) \end{bmatrix}$, where r_{ij} is the reflection coefficient from j-polarized incident light to i-polarized reflected light in the circular polarization base, the subscript L or R represents left-handed or right-handed circularly polarized (LCP or RCP) light, and $\Omega = [l_1, w_1, l_2, w_2, t_a(V_m), \lambda]$ is the system parameter space shown in Fig. 1B. Because of the reciprocity and anisotropy, we have $r_{\text{LL}}(\Omega) = r_{\text{RR}}(\Omega)$ and $r_{\text{LR}}(\Omega) \neq r_{\text{LR}}(\Omega)$. By adjusting the meta-atom properties and tuning the air gap with a proper actuation voltage V_{EP} (Supplementary Text and fig. S1), a singularity point has been observed in the parameter space of $\Omega_{\text{EP}} = [231.15, 145.7, 183.5, 81.55, 430.9, \text{and } 811.622 \text{ nm}]$ (Fig. 1C), with the degeneracy of both eigenvalues and eigenstates simultaneously (Fig. 1D), indicating

the existence of a chiral EP, where an LCP state $|L\rangle$ becomes the only eigenstate due to coalescence (Fig. 1E). This degeneracy was further proven by the self-interacting Riemann surfaces of the reflection matrix eigenvalues in the geometrical parameter space (figs. S2 and S3). At the chiral EP, the reflection matrix becomes $\widehat{r}(\Omega_{\text{EP}}) = \begin{pmatrix} r_{\text{LL,EP}} & r_{\text{LR,EP}} \\ 0 & r_{\text{LL,EP}} \end{pmatrix}$ with eigenvalues coalescing into $\sigma_{1,2} = r_{\text{LL,EP}}$, leading to the singular behavior in the reflection of light from the non-Hermitian metasurfaces. For LCP incidence ($|E_i\rangle = |l\rangle$), the reflected light is maintained co-polarized ($|E_o\rangle = r_{\text{LL,EP}}|l\rangle$), while the circular polarization conversion from LCP to RCP is prohibited. On the contrary, the reflected light superposes both LCP and RCP components ($|E_o\rangle = r_{\text{LR,EP}}|l\rangle + r_{\text{RR,EP}}|r\rangle$) under the RCP excitation ($|E_i\rangle = |r\rangle$). In a specific case where the incident polarization state equals to $|E_i\rangle = |l\rangle - \frac{r_{\text{LL,EP}}}{r_{\text{LR,EP}}}|r\rangle$, two reflected LCP components destructively
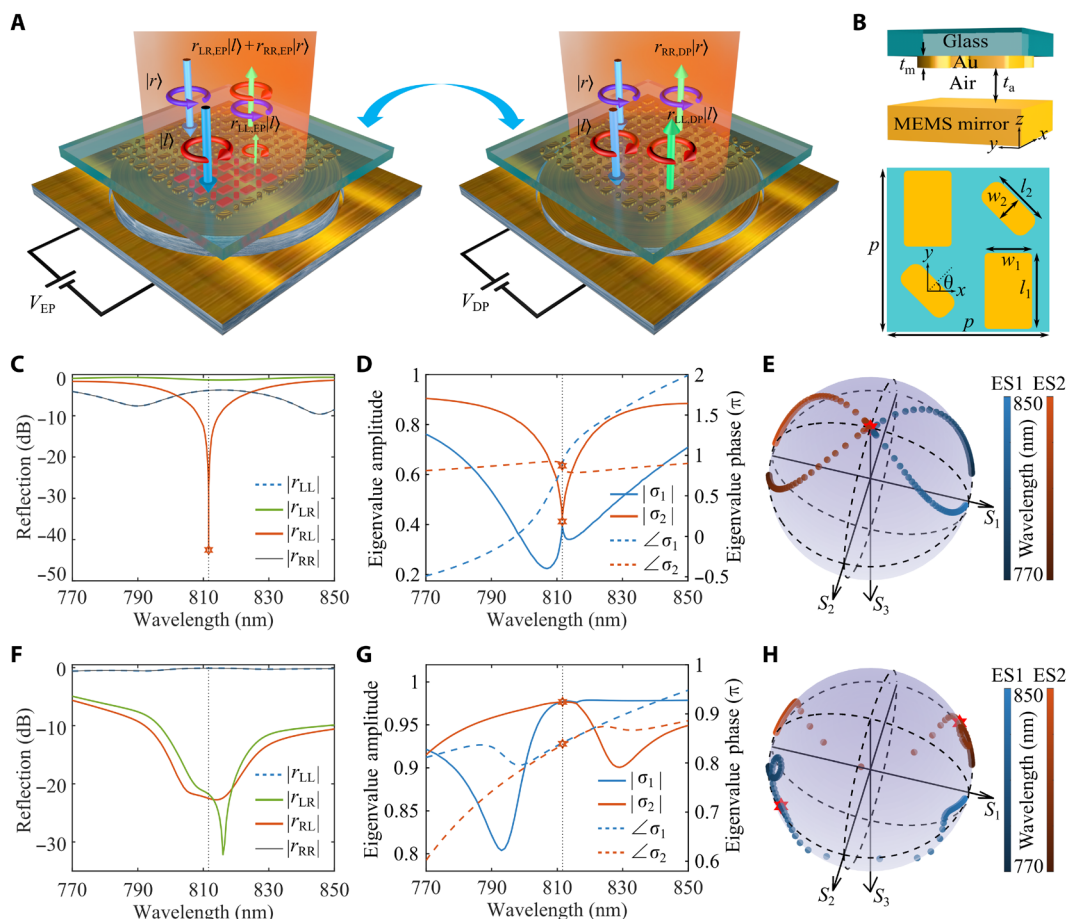

Fig. 1. Design principle of the electrically tunable topological phase transition in non-Hermitian metasurfaces. (**A**) Schematic rendering of the tunable non-Hermitian metasurface composed of a chiral gold meta-atom array separated by a MEMS gold mirror with a voltage-controlled air gap to reconfigure the topological transition between a chiral EP and a DP. Here, the change in the propagation direction has not been considered in determining the chirality of reflected light. (**B**) Schematic illustration of a chiral unit cell. The geometric dimensions of the unit cell are set to $l_1 = 231.15$ nm, $w_1 = 145.7$ nm, $l_2 = 183.5$ nm, $w_2 = 81.55$ nm, $\theta = 45°$, $p = 500$ nm, and $t_m = 50$ nm. The corners of small and large nanobricks are rounded with radii of 30 and 15 nm, respectively. (**C** to **E**) Simulated coefficients (C), eigenvalues (D), and eigenstates (E) of the reflection matrix as a function of wavelength at an air gap of $t_a = 430.9$ nm. The eigenvalues and eigenstates degenerate simultaneously at $\lambda = 811.622$ nm, indicating the existence of a chiral EP, where $r_{\text{RL}} = 0$ and an LCP state $|l\rangle$ becomes the only eigenstate. (**F** to **H**) Simulated coefficients (F), eigenvalues (G), and eigenstates (H) of the reflection matrix as a function of wavelength at $t_a = 357$ nm. The two eigenvalues degenerate, while the two eigenstates are nearly orthogonal at $\lambda = 811.622$ nm, indicating the existence of a DP.

interfere and leave all incident waves converted to the RCP state ($|E_o\rangle = -\frac{r_{LL,EP}^2}{r_{LR,EP}}|r\rangle$), which is orthogonal to the degenerated polarization eigenstate $|l\rangle$ and indicates the reduced polarization eigenspace dimensionality at the chiral EP singularity. If co-polarized components are suppressed with $r_{LL,EP}$ approaching 0, the non-Hermitian metasurface acts as a perfect LCP light absorber while reflecting the RCP light to its cross-polarized counterpart, enabling large circular dichroism (CD). Once the applied voltage V_m is varied from VEP, the length of the FP cavity and its resonance wavelength are finely tuned by moving the piezoelectric MEMS mirror with respect to the chiral gold meta-atom array, which switches the non-Hermitian metasurface away from the chiral EP and induces a topological phase transition. In particular, a DP was realized at an air gap of $t_a = 357$ nm (voltage V_{DP}) when the chiral meta-atoms are located right at the nodes of the standing wave inside the non-Hermitian metasurface, where cross-polarized reflections vanish (Fig. 1F) and eigenvalues coalesce (Fig. 1G), while their associated eigenstates are orthogonal (Fig. 1H). Because of the nonperfect conducting nature of the gold mirror, the DP has complex eigenvalues, which is different from DP degeneracies in conservative Hermitian systems that have real eigenvalues. At the DP, the effective Hamiltonian changes to a diagonal

reflection matrix $\hat{r}(\Omega_{DP}) = \begin{pmatrix} r_{LL,DP} & 0 \\ 0 & r_{LL,DP} \end{pmatrix}$ with eigenvalues coalescing into $\sigma_{1,2} = r_{LL,DP}$ and two polarization eigenstates being orthogonally aligned, thereby allowing simultaneous nulling of cross-polarized reflections under both LCP and RCP incidence (Fig. 1, A and F).

Experimental observation of the dynamic topological transition

To experimentally observe the topological phase transition between EPs and DPs, the dynamic non-Hermitian metasurface was fabricated by assembling a chiral gold meta-atom array, a ultraflat MEMS gold mirror, and a printed circuit board via wire bonding (see Materials and Methods and Fig. 2, A to C), forming a hybrid FP cavity with a variable air gap t_a, which is precisely controlled by electrically activating the MEMS mirror as a moveable back reflector (27–29). For the optical characterization of the fabricated non-Hermitian metasurface, we used a custom-built optical setup that consists of broadband laser sources and different optical components for polarization-resolved imaging and detection (see Materials and Methods and fig. S4). In the measurement, the MEMS metasurface was triggered with an
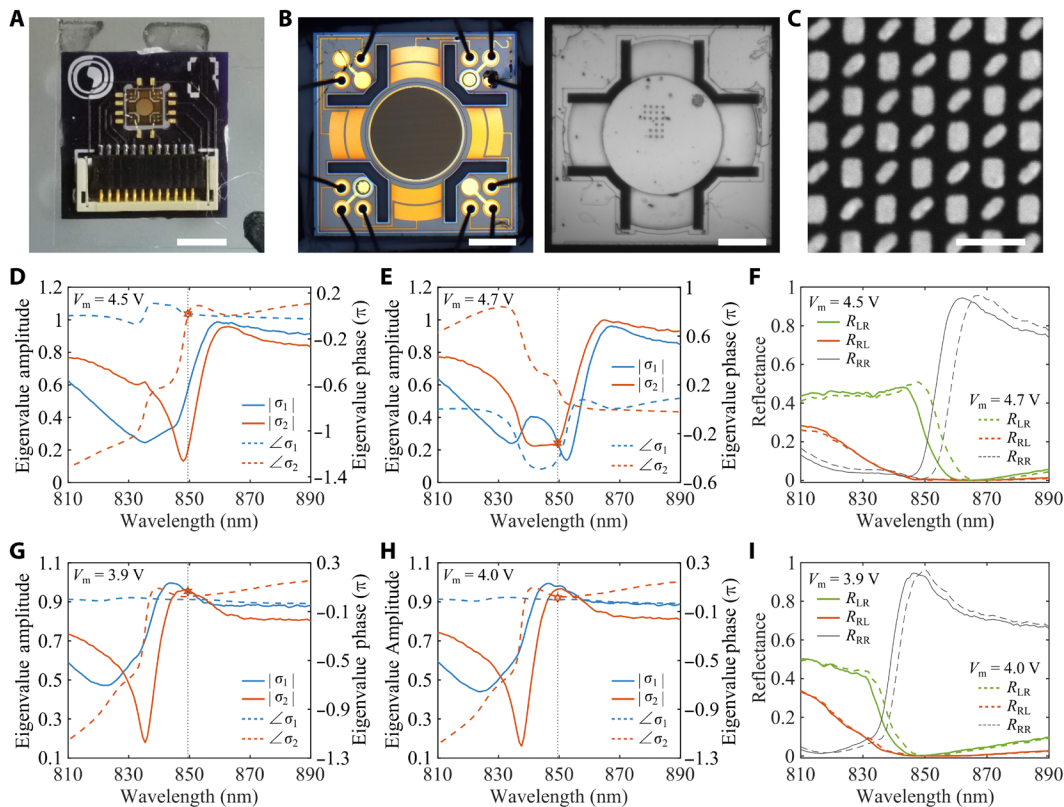

Fig. 2. Experimental observation of the dynamic topological transition from a chiral EP to a DP. (**A** to **C**) The typical photo (A), optical microscopy images (B), and scanning electron microscopy image (C) of the assembled non-Hermitian metasurface. Scale bars, 3 mm (A), 500 µm (B), and 500 nm (C). (**D** to **F**) Measured eigenvalues [(D) and (E)] and reflectance (F) as a function of wavelength at two different voltages of $V_m = 4.5$ and 4.7 V when driving four outer electrodes. Anti-crossing of eigenvalue amplitudes and crossing of eigenvalue phases are observed for $V_m = 4.5$ V, while crossing of eigenvalue amplitudes and anti-crossing of eigenvalue phases are observed for $V_m = 4.7$ V, revealing a chiral EP singularity at $\lambda = 849.505$ nm for V_m between 4.5 and 4.7 V. (**G** to **I**) Measured eigenvalues [(G) and (H)] and reflectance (I) as a function of wavelength at two different voltages of $V_m = 3.9$ and 4.0 V when driving four outer electrodes. Crossing of eigenvalue amplitudes is observed for $V_m = 3.9$ V, indicating a DP at $\lambda = 849.505$ nm for V_m of ~3.9 V.

actuation voltage V_m in a step of 0.1 V, corresponding to an averaged air gap moving step of ~7.3 nm, which allows us to finely detune the non-Hermitian metasurface to construct voltage-controlled parameter space. The moveable range of the assembled metasurface was estimated to be ~868.6 nm (~730.1 nm) when the MEMS mirror was moved far away from (close to) the chiral meta-atom array by selectively actuating four outer (inner) electrodes from 0 to 12 V (0 to 10 V) (fig. S5), which covers at least two adjacent FP resonances and is enough for investigating the topological phase transition. From the measured reflection spectra at each voltage (figs. S6 and S7), the wavelength-resolved Stokes parameters along with the non-Hermitian Jones matrix $\hat{r}$ can be obtained (see Materials and Methods). At a voltage of $V_m = 4.5$ V ($t_a \approx 2534.6$ nm), we observe an anti-crossing of eigenvalue phases and a crossing of eigenvalue amplitudes $\lambda = 849.505$ nm (Fig. 2D). As the actuation voltage varies, the coupling between plasmonic and FP resonances is tuned, leading to the interchange in the crossing behavior of amplitudes and phases. When V_m is decreased to 4.7 V ($t_a = 2546.8$ nm), we see crossing in amplitudes and anti-crossing in phases (Fig. 2E). Therefore, a chiral EP singularity unambiguously occurs at $\lambda = 849.505$ nm for V_m between 4.5 and 4.7 V (11, 17) where singularity points are observed for R_{RL} (Fig. 2F), although the experimental wavelength and air gap are deviated from simulated results due to the imperfections in fabrication. Owing to the FP nature of the non-Hermitian metasurface, the chiral EP singularity can be periodically observed at other air gaps (fig. S8). Given the high sensitivity of non-Hermitian systems near EPs, we detuned the MEMS metasurface to demonstrate a non-Hermitian phase transition of a chiral EP singularity to a DP by carefully altering the air gap with an actuation voltage. When the voltage is continuously varied from 4.7 to 3.9 V, corresponding to the air gap decrease from 2546.8 to 2487.1 nm, the non-Hermitian metasurface gradually transits from an EP to a DP with a crossing of eigenvalue amplitudes at the wavelength of $\lambda = 849.505$ nm (Fig. 2G). For a slightly increased voltage of $V_m = 4.0$ V ($t_a = 2496.4$ nm), the phases of two eigenvalues approach a crossing state (Fig. 2H). Different from the EPs that are extremely sensitive to small perturbations (10, 11), non-Hermitian DPs are more robust with eigenvalues slightly affected by the voltage. Meanwhile, simultaneous nulling of both cross-polarized reflections in the vicinity of the DP under RCP and LCP incidence is allowed (Fig. 2I). It is worth noting that another pair of exceptional and diabolic points that enable the similar topological phase transition was observed in the $[t_a(V_m), \lambda]$ parameter space without repeated fabrication of several samples (figs. S9 and S10), which is ascribed to the tunability of our non-Hermitian MEMS metasurface.

Voltage-controlled polarization evolution

In addition to the dynamic non-Hermitian phase transition, we also explored voltage-controlled polarization evolution when the air gap is continuously varied. For LCP incidence at $\lambda = 849.505$ nm, the cross-polarized reflection approaches zero regardless of the actuation voltage (Fig. 3A). Once the incident light is switched to RCP, the output polarization state becomes a superposition of co- and cross-polarized components, whose intensities are electrically modulated (Fig. 3A). Moreover, its corresponding polarization trajectory is one irregular closed curve on the Poincaré sphere, passing through two pivotal polarization states of $|l\rangle$ and $|r\rangle$ when the non-Hermitian metasurface hits the exceptional and diabolic points, and circulating repeatedly with the voltage (Fig. 3B). Quantitatively, the degrees of circular

polarization (DoCPs) reach ~−0.96 and ~0.99 at EPs and DPs, respectively (red and blue stars in Fig. 3B). At chiral EPs, asymmetric polarization conversion with a measured CD of ~0.49 was obtained, resulting from the reduced polarization eigenspace. Besides circularly polarized (CP) waves, linearly polarized reflections of high purity (DoCP < 0.02) were realized (black stars in Fig. 3B). Note that the minimum voltage range to electrically switch the reflected light between $|l\rangle$ and $|r\rangle$ states is only 0.8 V, which is smaller than the previously required value of 4.7 V (28). Because the MEMS arrangements used in both experiments are identical, such a strong decrease in the switching voltage signifies a marked decrease (by ~34.5 times) in the switching power, thereby manifesting a very substantial achievement resulting from the operation near the EP-DP transition. As expected, a similar polarization evolution is seen when the four inner electrodes are actuated to decrease the air gap (fig. S11). To measure the non-Hermitian phase transition speed from an EP to a DP, we actuated the MEMS mirror with a periodic rectangular signal composed of alternating voltages marked in Fig. 3A and detected polarization-resolved reflections with a fast photodetector (see Materials and Methods). We observe high contrast between orthogonal polarization states (Fig. 3C), good endurance (Fig. 3D and movies S1 and S2), and relatively fast switching with rise/fall times of ~0.30/0.25 ms (Fig. 3D). Because response times are generally dependent on the properties of MEMS mirrors, one could expect faster switching even in the megahertz range via further optimization, which, however, is beyond the scope of our work.

DISCUSSION

In this work, we have demonstrated an electrically tunable non-Hermitian MEMS metasurface to investigate optical chiral EPs in a voltage-controlled spectral domain through meticulous system detuning. By carefully actuating the air gap between the chiral metasurface and MEMS mirror, we have realized a fast (<0.30 ms) voltage-driven topological phase transition between EPs and DPs. Notably, our implementation of the non-Hermitian MEMS metasurface facilitates the robust and dynamic polarization conversion between two circular polarization states (i.e., $|l\rangle$ and $|r\rangle$) with an extremely small voltage step of 0.8 V. Furthermore, compared to other tunable optical metasurfaces that use active materials with reconfigurable properties to directly build meta-atoms (31–34), our non-Hermitian MEMS metasurface vertically integrates the functional metasurface with moveable MEMS mirror and is thus not limited by the submicrometer-thin planar configuration, thereby exhibiting considerably large tunability ranges for achieving the EP-DP phase transition in a fast and reversible fashion. Our results not only pave the way for the development of cutting-edge EP-empowered optical devices at small scales [e.g., adaptive polarization optics for biomedical applications (35) and advanced sensors by combining the EP and DP operation modes (fig. S12)] but also unveil unexplored avenues within the dynamic landscape of topological photonics.

MATERIALS AND METHODS
Numerical simulations

All numerical simulations were performed using the wave optics module in COMSOL Multiphysics version 5.6, where we modeled one glass-gold-air-gold unit cell. The corners of small and
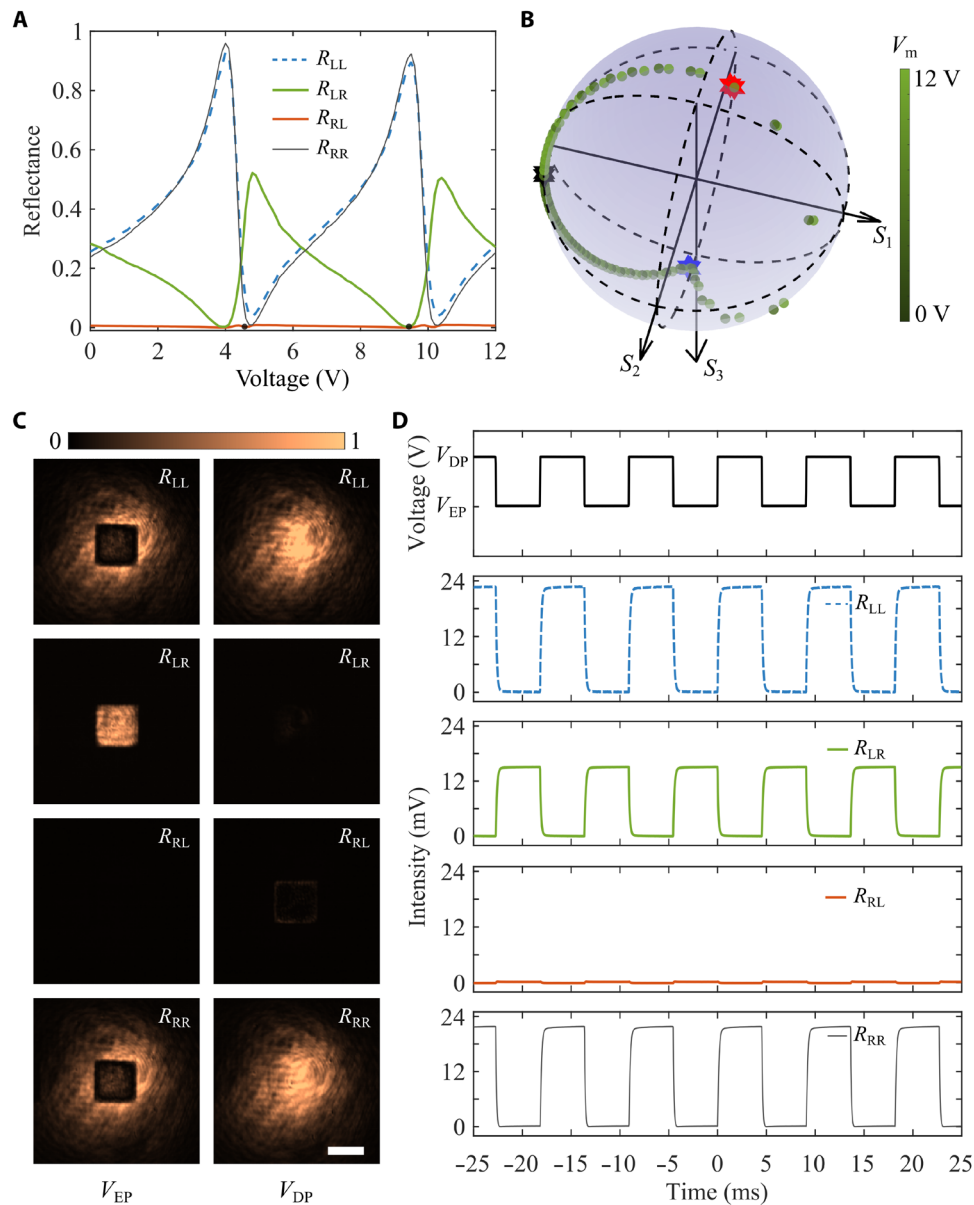
Fig. 3. Voltage-controlled polarization evolution. (**A**) Measured reflectance as a function of the applied voltage. (**B**) Voltage-controlled polarization trajectory mapped on the Poincaré sphere for RCP incidence. (**C**) Polarization-resolved optical images of the reflected light for the topological EP-DP transition. Scale bar, 25 μm. (**D**) Temporal evolution of the reflected power for the topological EP-DP transition by actuating the non-Hermitian metasurface with a periodic rectangular voltage. The rise/fall times of the R_{LL}, R_{LR}, and R_{RR} channels are 260/250 μs, 290/220 μs, and 260/160 μs, respectively. The wavelength is fixed at λ = 849.505 nm, and the four outer electrodes are actuated during the measurement.

large nanobricks are rounded with radii of 30 and 15 nm, respectively. Periodic boundary conditions were applied in both the x and y directions, and perfectly matched layers were used in the z direction to truncate the simulation domain. To obtain complex reflection coefficients in both linear and circular polarization bases, x- and y-polarized light sources were incident onto the chiral gold meta-atom from the upper glass at normal incidence. The glass layer was regarded as a lossless dielectric with a constant refractive index of 1.46, and the permittivity of gold was interpolated from experimental values (*36*).

Device fabrication

The chiral gold meta-atoms were fabricated using electron beam lithography (EBL), thin-film deposition, and lift-off techniques. First, a 100-nm-thick poly(methyl methacrylate) (2% in anisole, Micro Chem) layer and a 40-nm-thick conductive polymer layer (AR-PC 5090, Allresist) were successively spin-coated on a glass substrate (Borofloat 33 wafer, Wafer Universe). Then, the metasurface patterns were defined in the center area of the glass substrate using EBL (JEOL JEM-6500F) at an acceleration voltage of 30 kV. After exposure, the sample was soaked in deionized water for 1 min to

remove the conductive polymer and subsequently developed in the solution of methyl isobutyl ketone (MIBK) and isopropyl alcohol (IPA) of MIBK:IPA = 1:3 for 35 s followed by 60 s in an IPA bath. After that, a 1-nm titanium adhesion layer and a 50-nm gold layer were deposited using thermal evaporation (Tornado 400, Cryofox). Last, the gold structures were formed atop the glass substrate after a liftoff process in acetone. The MEMS mirror is fabricated using standard semiconductor manufacturing processes, where thin-film lead zirconate titanate is incorporated to achieve enduring and low-voltage electrical actuation (*27*–*29*). After depositing a 100-nm-thick gold layer to function as a back reflector, the MEMS mirror surface is inspected using white light interferometry (Zygo NewView 6000) to guarantee good flatness over the whole MEMS mirror with a diameter of ~1 mm. The non-Hermitian MEMS metasurface was assembled by gluing the glass substrates with prefabricated chiral meta-atoms and the selected clean MEMS mirror. Last, the assembled metasurface was glued to a printed circuit board, followed by gold wire bonding for electrical connection and actuation.

Optical characterization

Figure S4 shows the optical setup for characterizing non-Hermitian MEMS metasurfaces. A fiber-coupled supercontinuum laser (SuperK Extreme, NKT Photonics) passes through a collimator (TC06APC-780, Thorlabs), a half-wave plate (AHWP10M-980, Thorlabs), an attenuator (NE01B, Thorlabs), a sliver mirror (PF10-03-P01, Thorlabs), a linear polarizer (LP1, LPNIR050-MP2, Thorlabs), a quarter-wave plate (QWP1; AQWP10M-980, Thorlabs) mounted on a motorized precision rotation stage (PRM1Z8, Thorlabs), and two beam splitters (BS1 and BS2, CCM1-BS014/M, Thorlabs) successively to create CP light with controlled intensity. The two beam splitters could compensate for the polarization-dependent phase shifts caused by one single beam splitter. The CP light is then slightly focused onto the sample by using a long working distance objective (Objective M Plan Apo 20×/0.42 numeric aperture, Mitutoyo). The reflected light is collected by the same objective and passes through BS2, a flip quarter-wave plate (QWP2; AQWP10M-980, Thorlabs), and a tube lens ($f = 200$ mm; TTL200-S8, Thorlabs), generating the first real image plane where an iris (SM1D12SZ, Thorlabs) is positioned for filtering out the background outside the sample area (scale bar is 10 μm). The filtered first real image is transformed by a relay lens ($f = 200$ mm; AC254-200-B-ML, Thorlabs) to create a Fourier image, which is captured by a complementary metal oxide semiconductor camera (DCC1545M, Thorlabs) when a flip mirror (PF10-03-P01, Thorlabs) is flipped up. To switch between real and Fourier images, a flip lens ($f = 100$ mm; AC254-100-B-ML, Thorlabs) is placed between the relay lens and the flip mirror. For full Stokes polarimetry, a Stokes analyzer composed of QWP2, a linear polarizer (LP2; LPNIR050-MP2, Thorlabs), and a spectrometer (QE Pro, Ocean Optics) is used.

In the measurement, we used a fiber-coupled spectrometer to record polarization-resolved spectra of $I_x(\lambda)$, $I_y(\lambda)$, $I_a(\lambda)$, $I_b(\lambda)$, $I_r(\lambda)$, and $I_l(\lambda)$ under the RCP and LCP incident light. We also recorded the reflection spectrum from the MEMS gold mirror $I_{sub}(\lambda)$. The Stokes parameters (s_1, s_2, and s_3) without any normalization can be calculated as

$$s_1(\lambda) = [I_x(\lambda) - I_y(\lambda)]/I_{sub}(\lambda) \times T_{QWP}(\lambda) \qquad (1)$$

$$s_2(\lambda) = [I_a(\lambda) - I_b(\lambda)]/I_{sub}(\lambda) \times T_{QWP}(\lambda) \qquad (2)$$

$$s_3(\lambda) = [I_r(\lambda) - I_l(\lambda)]/I_{sub}(\lambda) \qquad (3)$$

where $T_{QWP}(\lambda)$ is the measured transmittance of the QWP. The reflected light $\begin{bmatrix} E_x(\lambda) \\ E_y(\lambda) \end{bmatrix}$ in the linear polarization base can be retrieved as

$$E_x(\lambda) = \sqrt{\frac{s_1(\lambda) + \sqrt{s_1(\lambda)^2 + s_2(\lambda)^2 + s_3(\lambda)^2}}{2}} \qquad (4)$$

$$E_y(\lambda) = \sqrt{\frac{-s_1(\lambda) + \sqrt{s_1(\lambda)^2 + s_2(\lambda)^2 + s_3(\lambda)^2}}{2}} e^{i \cdot \text{atan} \frac{s_3(\lambda)}{s_2(\lambda)}} \qquad (5)$$

Then, the reflected light in the circular polarization base can be written as

$$\begin{bmatrix} E_l(\lambda) \\ E_r(\lambda) \end{bmatrix} = \frac{\sqrt{2}}{2} \begin{pmatrix} 1 & -i \\ 1 & i \end{pmatrix} \begin{bmatrix} E_x(\lambda) \\ E_y(\lambda) \end{bmatrix} \qquad (6)$$

Last, the measured non-Hermitian Jones matrix $\hat{r}(\lambda) = \begin{bmatrix} r_{LL}(\lambda) & r_{LR}(\lambda) \\ r_{RL}(\lambda) & r_{RR}(\lambda) \end{bmatrix}$ can be obtained.

To measure the response time of the phase transition between exceptional and diabolic points, the experimental setup in fig. S4 is modified by replacing the input laser and spectrometer with a continuous wave Ti:sapphire laser (Spectra-Physics 3900 S) and a photodetector (PDA20CS-EC, Thorlabs), respectively. The signals from the photodetector are captured using an oscilloscope (DSOX2024A, Keysight). In the measurements, the non-Hermitian MEMS metasurface sample is actuated with periodically alternating voltages.

Supplementary Materials

This PDF file includes:
Supplementary Text
Figs. S1 to S12
Legends for movies S1 and S2

Other Supplementary Material for this manuscript includes the following:
Movies S1 and S2

REFERENCES AND NOTES

1. L. Feng, R. El-Ganainy, L. Ge, Non-Hermitian photonics based on parity-time symmetry. *Nat. Photonics* **11**, 752–762 (2017).
2. R. El-Ganainy, K. G. Makris, M. Khajavikhan, Z. H. Musslimani, S. Rotter, D. N. Christodoulides, Non-Hermitian physics and PT symmetry. *Nat. Phys.* **14**, 11–19 (2018).
3. Ş. K. Özdemir, S. Rotter, F. Nori, L. Yang, Parity-time symmetry and exceptional points in photonics. *Nat. Mater.* **18**, 783–798 (2019).
4. M.-A. Miri, A. Alù, Exceptional points in optics and photonics. *Science* **363**, eaar7709 (2019).
5. A. Li, H. Wei, M. Cotrufo, W. Chen, S. Mann, X. Ni, B. Xu, J. Chen, J. Wang, S. Fan, C.-W. Qiu, A. Alù, L. Chen, Exceptional points and non-Hermitian photonics at the nanoscale. *Nat. Nanotechnol.* **18**, 706–720 (2023).
6. C. M. Bender, S. Boettcher, Real spectra in non-hermitian hamiltonians having *PT* symmetry. *Phys. Rev. Lett.* **80**, 5243–5246 (1998).
7. C. M. Bender, Making sense of non-Hermitian Hamiltonians. *Rep. Prog. Phys.* **70**, 947–1018 (2007).
8. Z. Lin, H. Ramezani, T. Eichelkraut, T. Kottos, H. Cao, D. N. Christodoulides, Unidirectional invisibility induced by *PT*-symmetric periodic structures. *Phys. Rev. Lett.* **106**, 213901 (2011).
9. L. Feng, Y. L. Xu, W. S. Fegadolli, M. H. Lu, J. E. B. Oliveira, V. R. Almeida, Y. F. Chen, A. Scherer, Experimental demonstration of a unidirectional reflectionless parity-time metamaterial at optical frequencies. *Nat. Mater.* **12**, 108–113 (2013).

10. W. J. Chen, S. K. Ozdemir, G. M. Zhao, J. Wiersig, L. Yang, Exceptional points enhance sensing in an optical microcavity. *Nature* **548**, 192–196 (2017).

11. J. H. Park, A. Ndao, W. Cai, L. Hsu, A. Kodigala, T. Lepetit, Y.-H. Lo, B. Kanté, Symmetry-breaking-induced plasmonic exceptional points and nanoscale sensing. *Nat. Phys.* **16**, 462–468 (2020).

12. J. Doppler, A. A. Mailybaev, J. Böhm, U. Kuhl, A. Girschik, F. Libisch, T. J. Milburn, P. Rabl, N. Moiseyev, S. Rotter, Dynamically encircling an exceptional point for asymmetric mode switching. *Nature* **537**, 76–79 (2016).

13. X. L. Zhang, T. Jiang, C. T. Chan, Dynamically encircling an exceptional point in anti-parity-time symmetric systems: Asymmetric mode switching for symmetry-broken modes. *Light Sci. Appl.* **8**, 88 (2019).

14. A. Schumer, Y. Liu, J. Leshin, L. Ding, Y. Alahmadi, A. Hassan, H. Nasari, S. Rotter, D. Christodoulides, P. LiKamWa, M. Khajavikhan, Topological modes in a laser cavity through exceptional state transfer. *Science* **375**, 884–888 (2022).

15. Q. Song, M. Odeh, J. Zúñiga-Pérez, B. Kanté, P. Genevet, Plasmonic topological metasurface by encircling an exceptional point. *Science* **373**, 1133–1137 (2021).

16. M. Lawrence, N. Xu, X. Zhang, L. Cong, J. Han, W. Zhang, S. Zhang, Manifestation of *PT* symmetry breaking in polarization space with terahertz metasurfaces. *Phys. Rev. Lett.* **113**, 093901 (2014).

17. S. H. Park, S.-G. Lee, S. Baek, T. Ha, S. Lee, B. Min, S. Zhang, M. Lawrence, T.-T. Kim, Observation of an exceptional point in a non-Hermitian metasurface. *Nanophotonics* **9**, 1031–1039 (2020).

18. Z. Li, G. Cao, C. Li, S. Dong, Y. Deng, X. Liu, J. S. Ho, C.-W. Qiu, Non-Hermitian electromagnetic metasurfaces at exceptional points (Invited Review). *Prog. Electromagn. Res.* **171**, 1–20 (2021).

19. J. Yu, B. Ma, A. Ouyang, P. Ghosh, H. Luo, A. Pattanayak, Q. Li, Dielectric super-absorbing metasurfaces via PT symmetry breaking. *Optica* **8**, 1290–1295 (2021).

20. Y. Xu, L. Li, H. Jeong, S. Kim, I. Kim, J. Rho, Y. Liu, Subwavelength control of light transport at the exceptional point by non-Hermitian metagratings. *Sci. Adv.* **9**, eadf3510 (2023).

21. H. H. Hsiao, C. H. Chu, D. P. Tsai, Fundamentals and applications of metasurfaces. *Small Methods* **1**, 1600064 (2017).

22. F. Ding, A. Pors, S. I. Bozhevolnyi, Gradient metasurfaces: A review of fundamentals and applications. *Rep. Prog. Phys.* **81**, 026401 (2018).

23. S. Sun, Q. He, J. Hao, S. Xiao, L. Zhou, Electromagnetic metasurfaces: Physics and applications. *Adv. Opt. Photonics* **11**, 380–479 (2019).

24. A. M. Shaltout, V. M. Shalaev, M. L. Brongersma, Spatiotemporal light control with active metasurfaces. *Science* **364**, eaat3100 (2019).

25. M. S. Ergoktas, S. Soleymani, N. Kakenov, K. Wang, T. B. Smith, G. Bakan, S. Balci, A. Principi, K. S. Novoselov, S. K. Ozdemir, C. Kocabas, Topological engineering of terahertz light using electrically tunable exceptional point singularities. *Science* **376**, 184–188 (2022).

26. S. Baek, S. H. Park, D. Oh, K. Lee, S. Lee, H. Lim, T. Ha, H. S. Park, S. Zhang, L. Yang, B. Min, T. T. Kim, Non-Hermitian chiral degeneracy of gated graphene metasurfaces. *Light Sci. Appl.* **12**, 87 (2023).

27. C. Meng, P. C. Thrane, F. Ding, J. Gjessing, M. Thomaschewski, C. Wu, C. Dirdal, S. I. Bozhevolnyi, Dynamic piezoelectric MEMS-based optical metasurfaces. *Sci. Adv.* **7**, eabg5639 (2021).

28. C. Meng, P. C. Thrane, F. Ding, S. I. Bozhevolnyi, Full-range birefringence control with piezoelectric MEMS-based metasurfaces. *Nat. Commun.* **13**, 2071 (2022).

29. P. C. V. Thrane, C. Meng, F. Ding, S. I. Bozhevolnyi, MEMS tunable metasurfaces based on gap plasmon or Fabry-Pérot resonances. *Nano Lett.* **22**, 6951–6957 (2022).

30. R. Ameling, H. Giessen, Microcavity plasmonics: Strong coupling of photonic cavities and plasmons. *Laser Photon. Rev.* **7**, 141–169 (2013).

31. C. H. Chu, M. L. Tseng, J. Chen, P. C. Wu, Y. H. Chen, H. C. Wang, T. Y. Chen, W. T. Hsieh, H. J. Wu, G. Sun, D. P. Tsai, Active dielectric metasurface based on phase-change medium. *Laser Photon. Rev.* **10**, 986–994 (2016).

32. P. C. Wu, R. A. Pala, G. Kafaie Shirmanesh, W. H. Cheng, R. Sokhoyan, M. Grajower, M. Z. Alam, D. Lee, H. A. Atwater, Dynamic beam steering with all-dielectric electro-optic III–V multiple-quantum-well metasurfaces. *Nat. Commun.* **10**, 3654 (2019).

33. G. Qu, W. Yang, Q. Song, Y. Liu, C.-W. Qiu, J. Han, D.-P. Tsai, S. Xiao, Reprogrammable meta-hologram for optical encryption. *Nat. Commun.* **11**, 5484 (2020).

34. P. C. Wu, R. Sokhoyan, G. K. Shirmanesh, W. H. Cheng, H. A. Atwater, Near-infrared active metasurface for dynamic polarization conversion. *Adv. Opt. Mater.* **9**, 2100230 (2021).

35. C. He, H. He, J. Chang, B. Chen, H. Ma, M. J. Booth, Polarisation optics for biomedical and clinical applications: A review. *Light Sci. Appl.* **10**, 194 (2021).

36. P. B. Johnson, R. W. Christy, Optical constants of the noble metals. *Phys. Rev. B* **6**, 4370–4379 (1972).

Science Advances

The PDF file includes:

Supplementary Text
Figs. S1 to S12
Legends for movies S1 and S2

Other Supplementary Material for this manuscript includes the following:

Movies S1 and S2

Supplementary Text

<u>Design of the non-Hermitian optical MEMS metasurface</u>

To design the non-Hermitian metasurface possessing a chiral exceptional point (EP), we first consider a glass-gold-air-gold building block with only one gold nanobrick that is not rotated (e.g., the period is 250 nm). After sweeping the lateral dimensions of L_x and L_y, we select two elements that function as half-wave plates (HWPs) with equal reflection amplitudes but an intrinsic phase difference of $\pi/2$ at the design wavelength of $\lambda = 810$ nm with an air gap of $t_a = 430$ nm (fig. S1, A and B). The Jones matrices of these two HWPs in the circular polarization base are given by $\hat{r}_1 = r_{xx1} \begin{pmatrix} 0 & 1 \\ 1 & 0 \end{pmatrix}$ and $\hat{r}_2 = r_{xx2} \begin{pmatrix} 0 & 1 \\ 1 & 0 \end{pmatrix} = r_{xx1} e^{-i\frac{\pi}{2}} \begin{pmatrix} 0 & 1 \\ 1 & 0 \end{pmatrix}$ respectively, where r_{xx1} and r_{xx2} are the co-polarized reflection coefficients in the linear polarization base under x-polarized excitation. The reflection matrix of HWP2 with a rotation angle of $\theta_0 = 45°$ is expressed as $\hat{r}_2(\theta_0) = r_{xx1} \begin{pmatrix} 0 & 1 \\ -1 & 0 \end{pmatrix}$. By arranging these two HWPs in a unit cell with a period of $p = 500$ nm, the averaged Jones matrix can be approximately derived as $\hat{r} \approx \frac{1}{2}[\hat{r}_1 + \hat{r}_2(\theta_0)] = r_{xx1} \begin{pmatrix} 0 & 1 \\ 0 & 0 \end{pmatrix}$, which shows the potential to design the chiral non-Hermitian metasurface. However, due to the near-field coupling between nanobricks within the designed unit cell, the metasurface does not show the expected performance at $\lambda = 810$ nm (fig. S1C). Therefore, the meta-atom dimensions, air gap, and wavelength should be iteratively optimized to realize chiral EP singularity. On the contrary, the diabolic point can still be observed near the wavelength of ~ 812 nm with the air gap of $t_a = 357$ nm (fig. S1D), where the metasurface is located right at the nodes of the standing wave with zero illumination intensity.
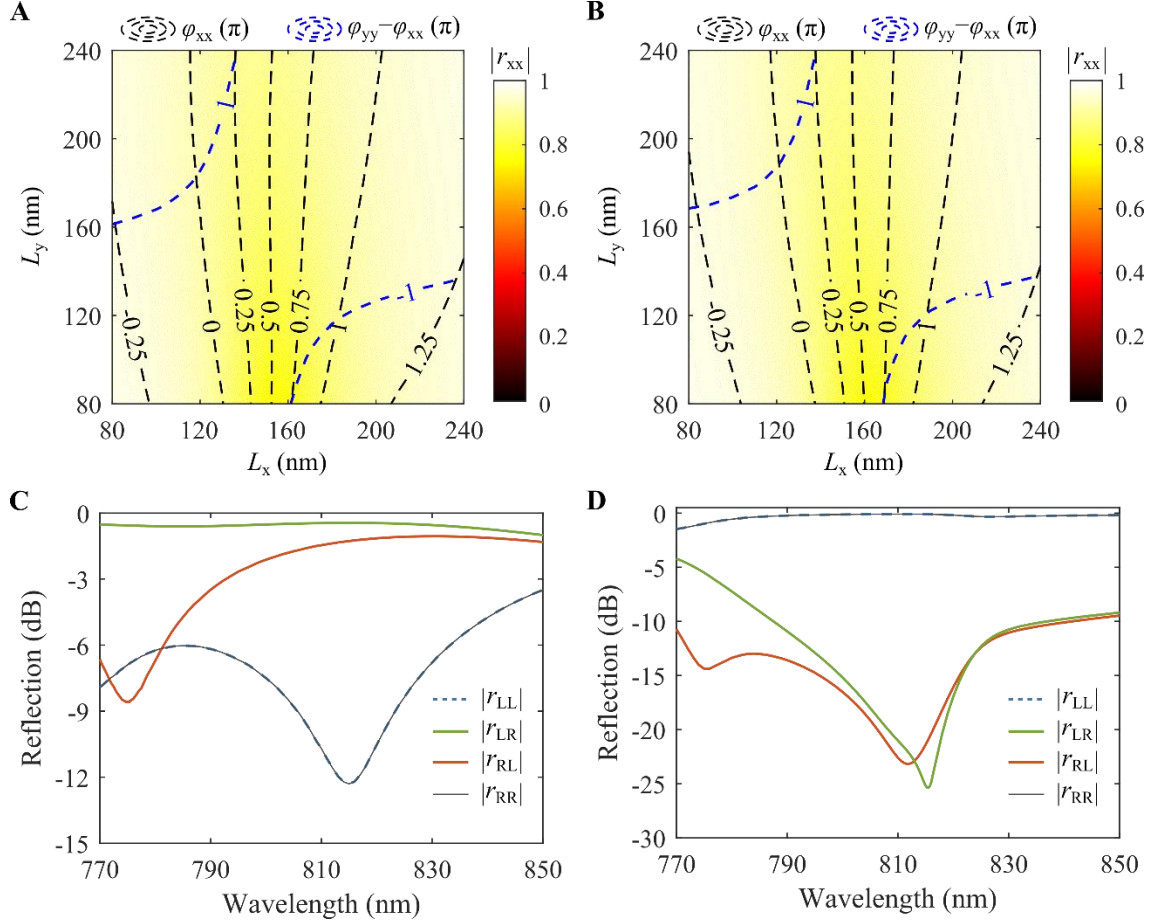
Fig. S1. Simulation of the as-designed non-Hermitian optical metasurfaces. (A and B) Simulated complex reflection coefficients of the glass-gold-air-gold building block with only one nanobrick (period is 250 nm) as a function of nanobrick dimensions of L_x and L_y in the linear polarization base. The other parameters are as follows: $\lambda = 810$ nm, $t_m = 50$ nm, and $t_a = 430$ nm. The nanobricks are rounded with radii of 15 nm (A) and 30 nm (B), respectively. $|r_{xx}|$ is the reflection amplitude under x-polarized excitation, and φ_{xx} and φ_{yy} represent the corresponding phase shifts under x- and y-polarized excitations. (C and D) Simulated coefficients of the reflection matrix as a function of wavelength at air gaps of $t_a = 430$ nm (C) and 357 nm (D). The geometric dimensions of the unit cell (same configuration as that in Fig. 1B) are set to $l_1 = 232$ nm, $w_1 = 135$ nm, $l_2 = 168$ nm, $w_2 = 79$ nm, $\theta = 45°$, $p = 500$ nm, and $t_m = 50$ nm. The corners of small and large nanobricks are rounded with radii of 30 nm and 15 nm, respectively.
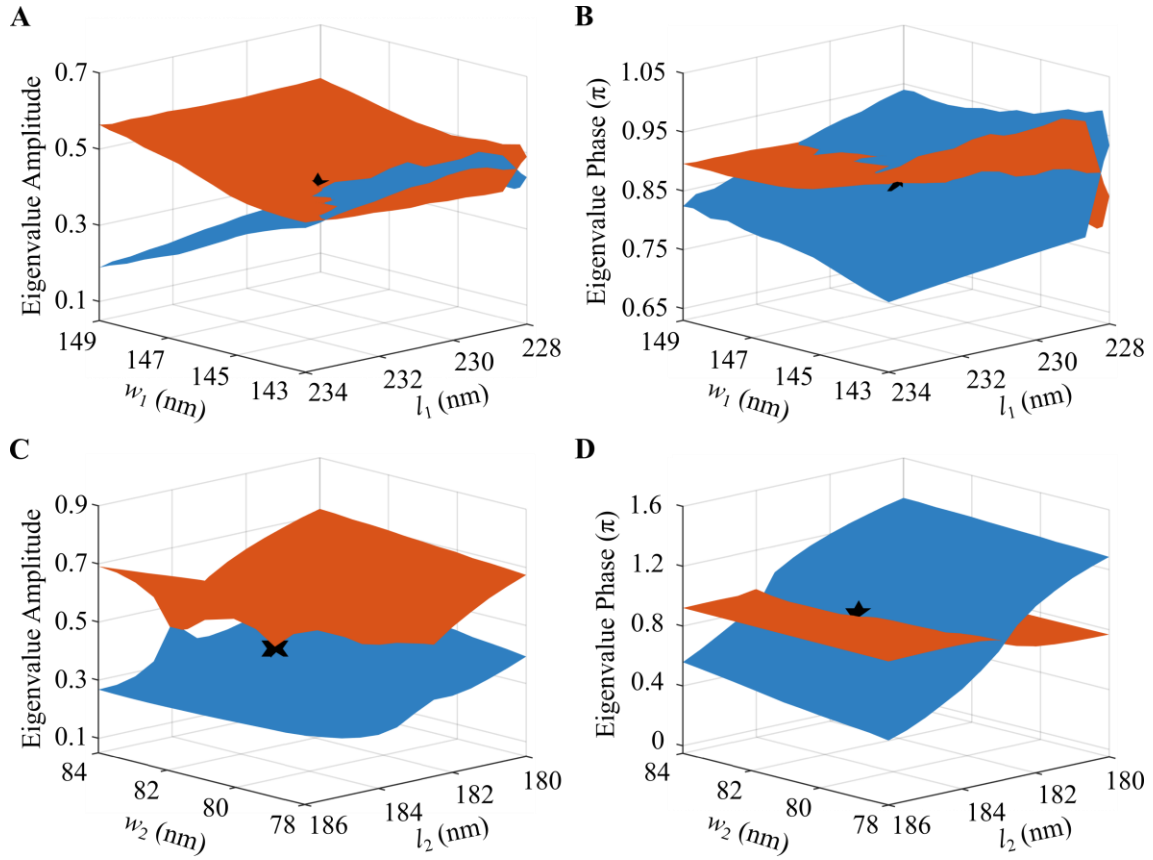
Fig. S2. Simulated amplitudes (A and C) and phase (B and D) of the reflection matrix eigenvalues in the geometrical parameter space $\Omega = [l_1, w_1]$ (A and B) and $[l_2, w_2]$ (C and D). Self-intersecting Riemann surfaces are observed. The wavelength and air gap are set as 811.622 nm and 430.9 nm, respectively.
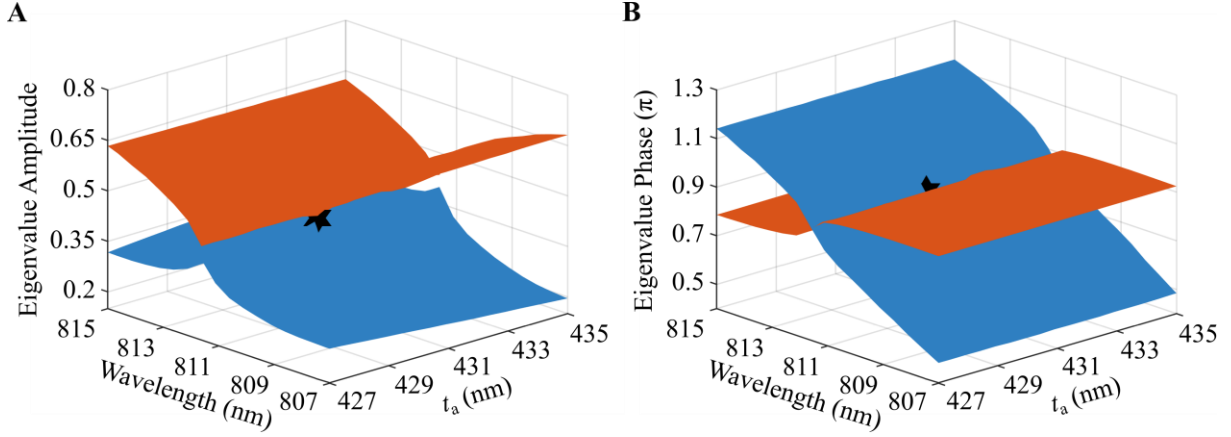
Fig. S3. Simulated amplitudes (A) and phase (B) of the reflection matrix eigenvalues in the geometrical parameter space $\Omega = [t_a, \lambda]$. A self-intersecting Riemann surface is observed. The dimensions of the chiral meta-atom are the same as those in the main text.
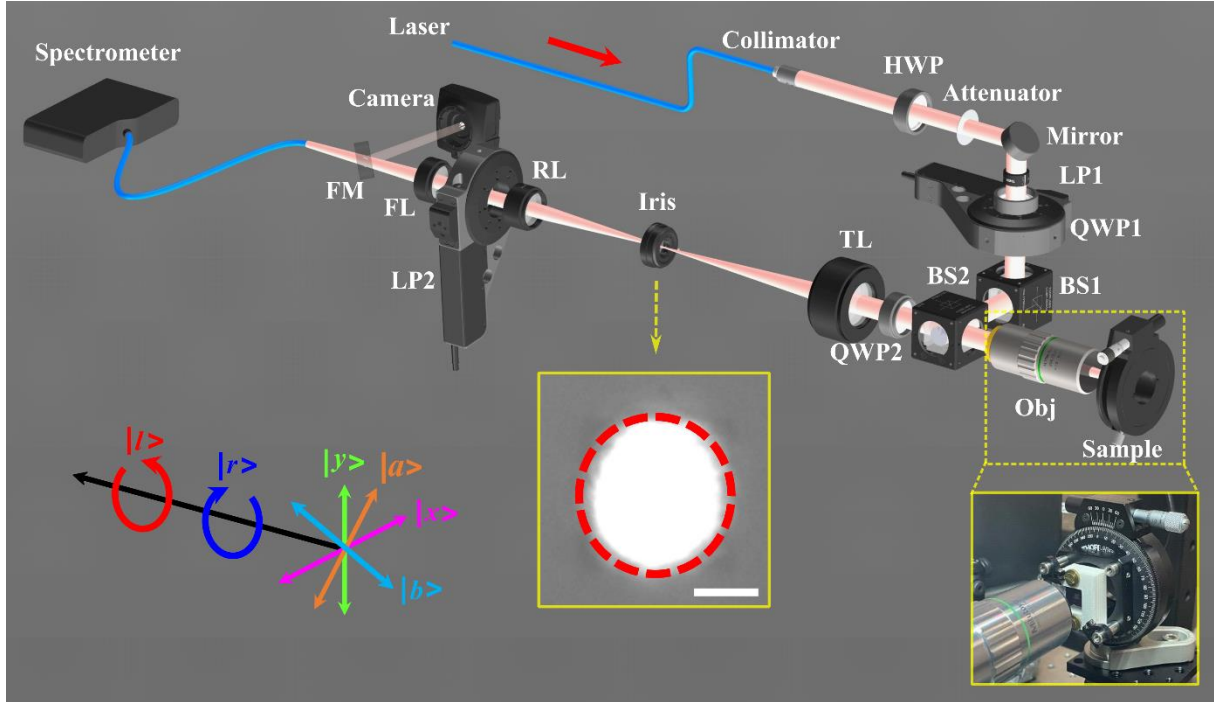
Fig. S4. Experimental setup for characterizing non-Hermitian MEMS metasurfaces. Laser: fiber-coupled supercontinuum laser (SuperK Extreme, NKT Photonics); Collimator: fiber collimator (TC06APC-780, Thorlabs); HWP: half-wave plate (AHWP10M-980, Thorlabs); Attenuator: absorptive neutral density filter (NE01B, Thorlabs); Mirror: protected sliver mirror (PF10-03-P01, Thorlabs); LP1 and LP2: linear polarizer (LPNIR050-MP2, Thorlabs); QWP1 and QWP2: quarter-wave plate (AQWP10M-980, Thorlabs); BS1 and BS2: beam splitters (CCM1-BS014/M, Thorlabs); Obj: long working distance objective (M Plan Apo 20×/0.42NA, Mitutoyo); TL: tube lens (TTL200-S8, $f = 200$ mm, Thorlabs); Iris: spatial filter (SM1D12SZ, Thorlabs); RL: relay lens (AC254-200-B-ML, $f = 200$ mm, Thorlabs); Camera: CMOS camera (DCC1545M, Thorlabs); FM: flip mirror (PF10-03-P01, Thorlabs); FL: flip lens (AC254-100-B-ML, $f = 100$ mm, Thorlabs); Spectrometer (QE Pro, Ocean Optics).
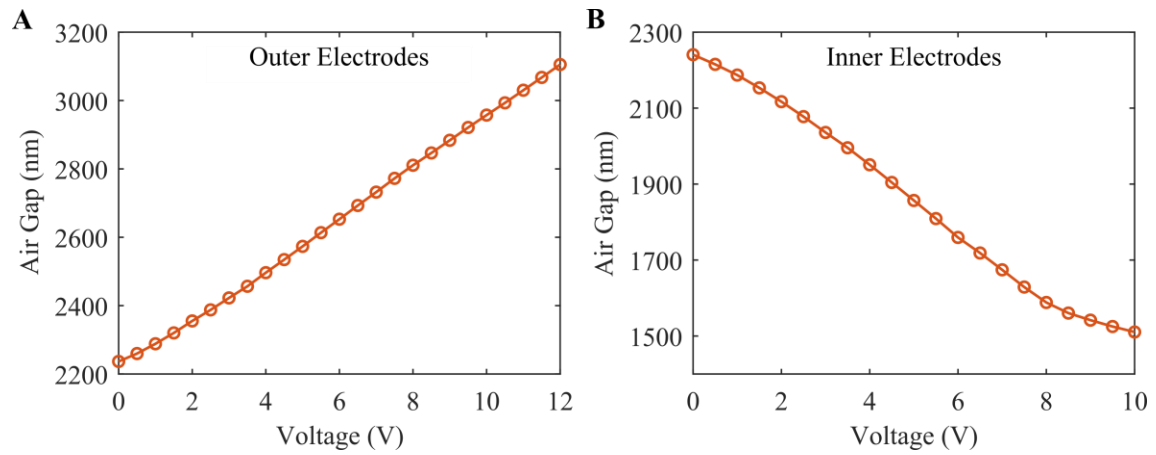
Fig. S5. Estimated air gap as a function of the voltage applied to the outer (A) and inner (B) electrodes. The outer electrodes enable quasi-linear movement for all voltages ranging from 0 V to 12 V, while the inner electrodes exhibit a nonlinear response for large voltages above 8 V.
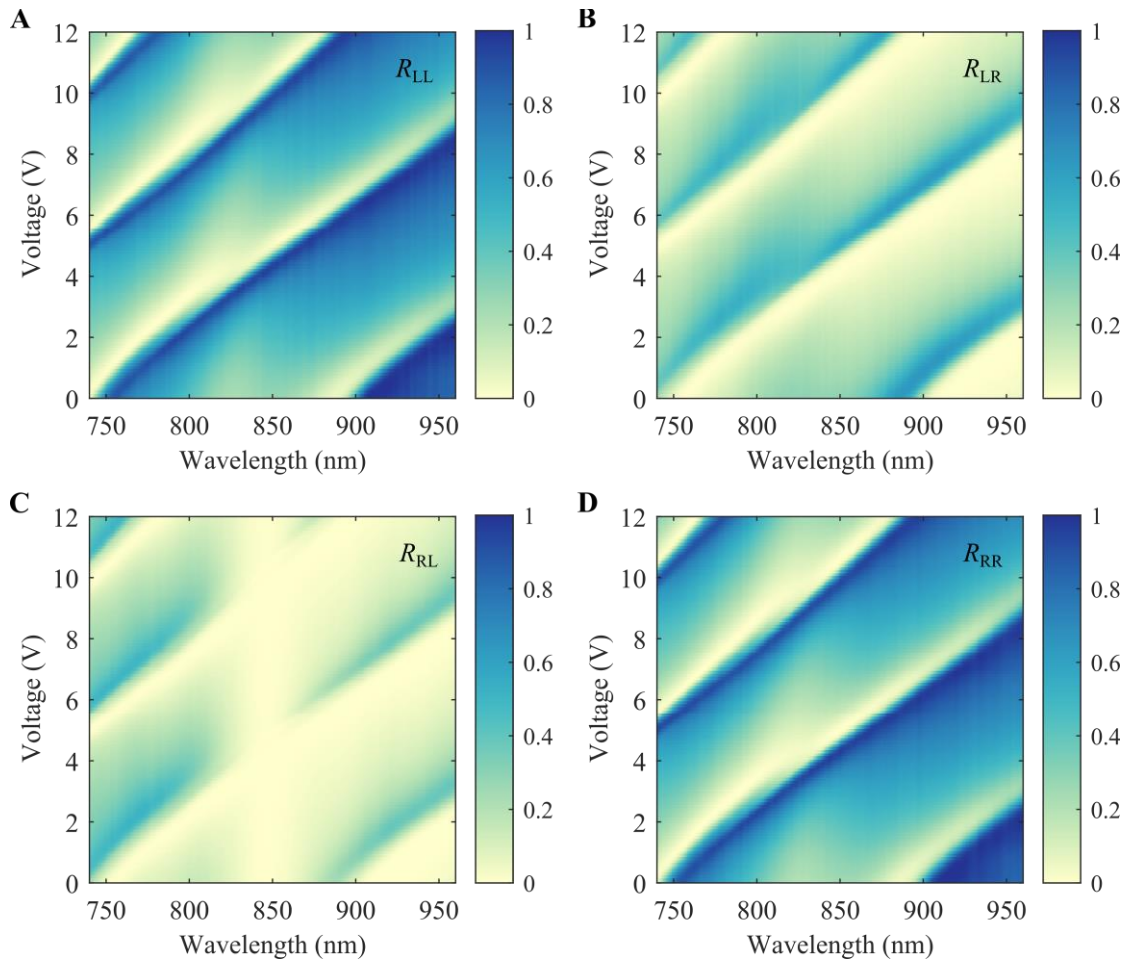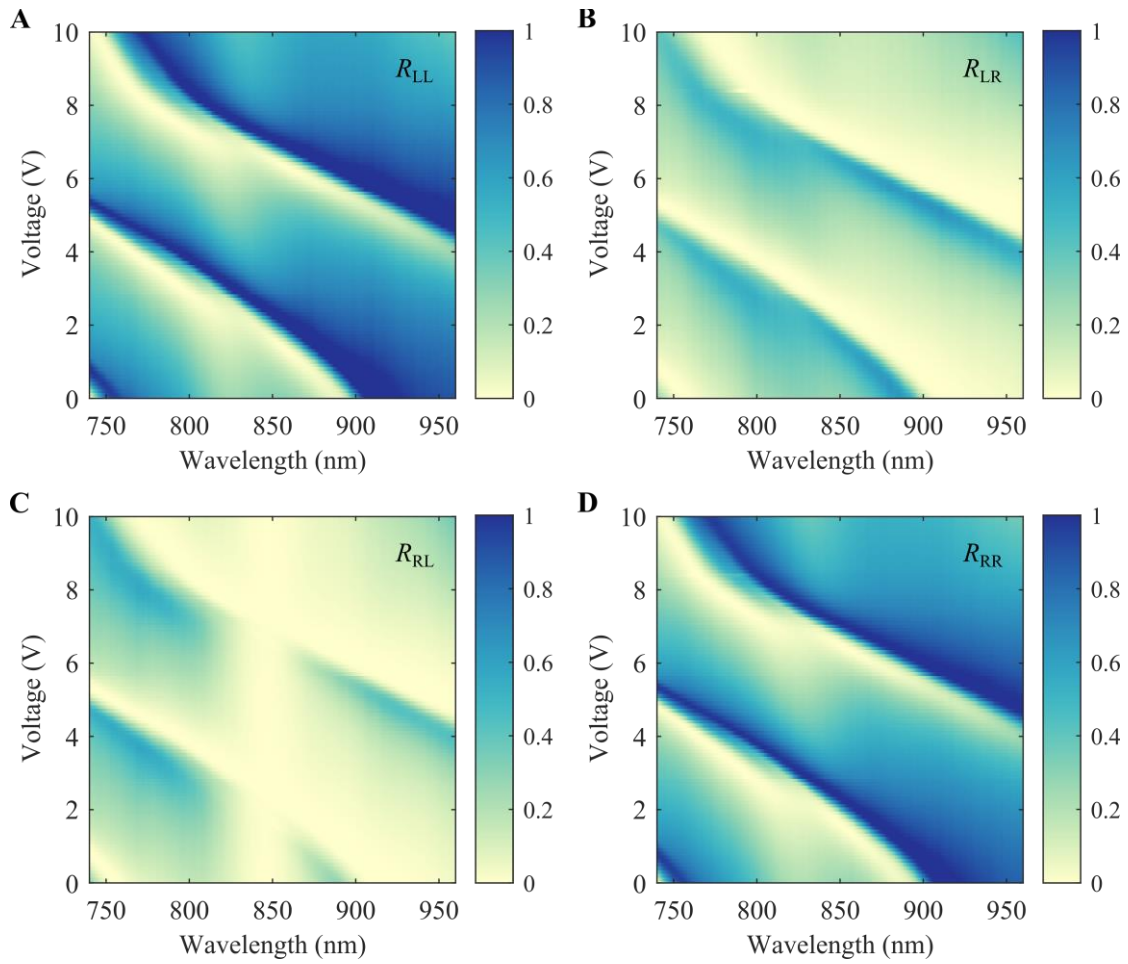
Fig. S6. Measured polarization-resolved reflectance R_{LL} (A), R_{LR} (B), R_{RL} (C), and R_{RR} (D) under LCP and RCP incidence when four outer electrodes are actuated from 0 V to 12 V in a step of 0.1 V.
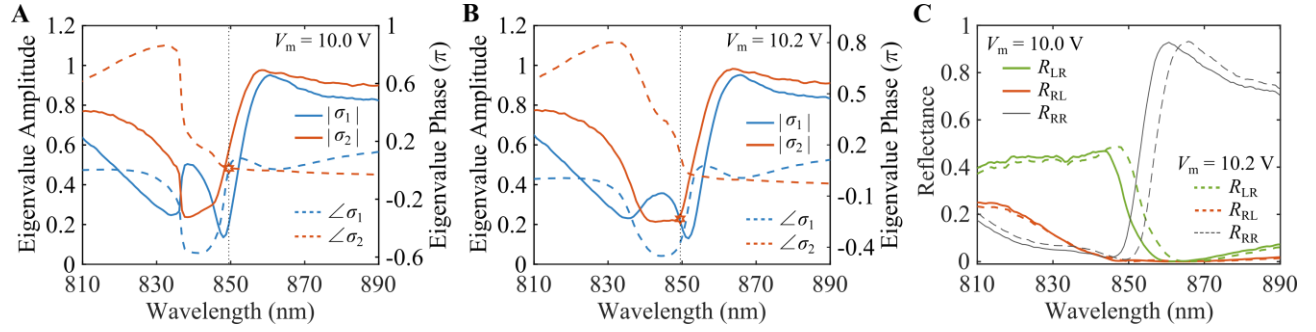
Fig. S7. Measured polarization-resolved reflectance R_{LL} (A), R_{LR} (B), R_{RL} (C), and R_{RR} (D) under LCP and RCP incidence when four inner electrodes are actuated from 0 V to 10 V in a step of 0.1 V.

Fig. S8. Experimental observation of another chiral EP at $\lambda = 849.505$ nm when four outer electrodes are actuated. Measured eigenvalues (A and B) and reflectance (C) as a function of wavelength at two different voltages of $V_m = 10.0$ V and 10.2 V when driving four outer electrodes. Anti-crossing of eigenvalue amplitudes and crossing of eigenvalue phases are observed for $V_m = 10.0$ V, while crossing of eigenvalue amplitudes and anti-crossing of eigenvalue phases are observed for $V_m = 10.2$ V, revealing a chiral EP singularity at $\lambda = 849.505$ nm for V_m between 10.0 V and 10.2 V. The estimated air gaps t_a at the voltages of $V_m = 10.0$ V and 10.2 V are ~ 2957.2 nm and ~ 2975.1 nm, respectively.
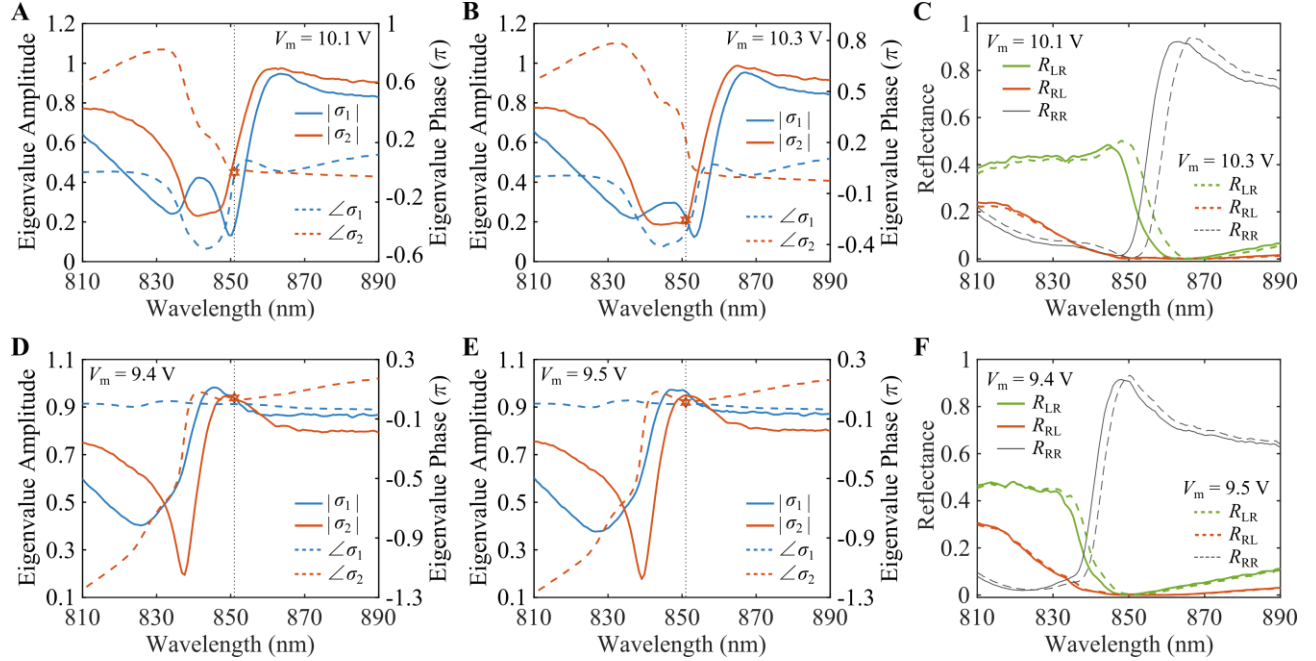
Fig. S9. Experimental observation of the dynamic topological transition from a chiral EP to a DP at λ = 850.991 nm when four outer electrodes are actuated. (**A** to **C**) Measured eigenvalues (A and B) and reflectance (C) as a function of wavelength at two different voltages of V_m = 10.1 V and 10.3 V when driving four outer electrodes. Anti-crossing of eigenvalue amplitudes and crossing of eigenvalue phases are observed for V_m = 10.1 V, while crossing of eigenvalue amplitudes and anti-crossing of eigenvalue phases are observed for V_m = 10.3 V, revealing a chiral EP singularity at λ = 850.991 nm for V_m between 10.1 V and 10.3 V. (**D** to **F**) Measured eigenvalues (D and E) and reflectance (F) as a function of wavelength at two different voltages of V_m = 9.4 V and 9.5 V. Crossing of eigenvalue amplitudes is observed for V_m = 9.4 V, indicating a DP at λ = 850.991 nm for V_m of ~ 9.4 V. The estimated air gaps t_a at the voltages of V_m = 9.4 V, 9.5 V, 10.1 V, and 10.3 V are ~ 2913.4 nm, ~ 2920.3 nm, ~ 2966.0 nm, and ~ 2981.1 nm, respectively.
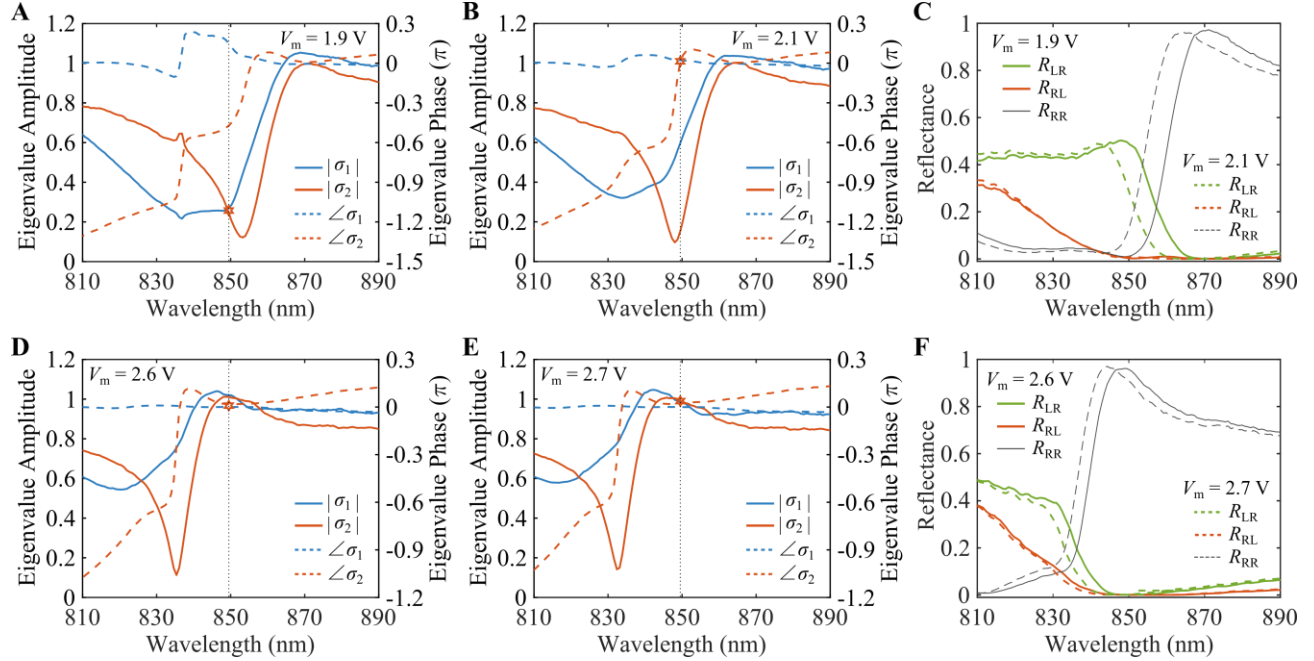
Fig. S10. Experimental observation of the dynamic topological transition from a chiral EP to a DP at λ = 849.505 nm when four inner electrodes are actuated. (**A** to **C**) Measured eigenvalues (A and B) and reflectance (C) as a function of wavelength at two different voltages of V_m = 1.9 V and 2.1 V. Crossing of eigenvalue amplitudes and anti-crossing of eigenvalue phases are observed for V_m = 1.9 V, while anti-crossing of eigenvalue amplitudes and crossing of eigenvalue phases are observed for V_m = 2.1 V, revealing a chiral EP singularity at λ = 849.505 nm for V_m between 1.9 V and 2.1 V. (**D** to **F**) Measured eigenvalues (D and E) and reflectance (F) as a function of wavelength at two different voltages of V_m = 2.6 V and 2.7 V. Crossing of eigenvalue amplitudes is observed for V_m = 2.7 V, indicating a DP at λ = 849.505 nm for V_m of ~ 2.7 V. The estimated air gaps t_a at the voltages of V_m = 1.9 V, 2.1 V, 2.6 V, and 2.7 V are ~ 2124.9 nm, ~ 2109.6 nm, ~ 2071.5 nm, and ~ 2063.9 nm, respectively.
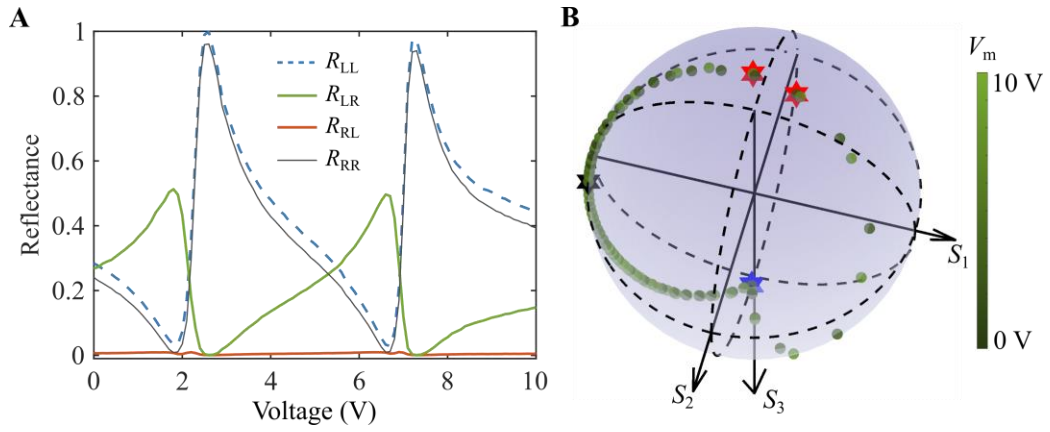
Fig. S11. Voltage-controlled polarization evolution at λ = 849.505 nm when four inner electrodes are actuated. (**A**) Measured reflectance as a function of the applied voltage. (**B**) Voltage-controlled polarization trajectory mapped on the Poincaré sphere for RCP incidence.
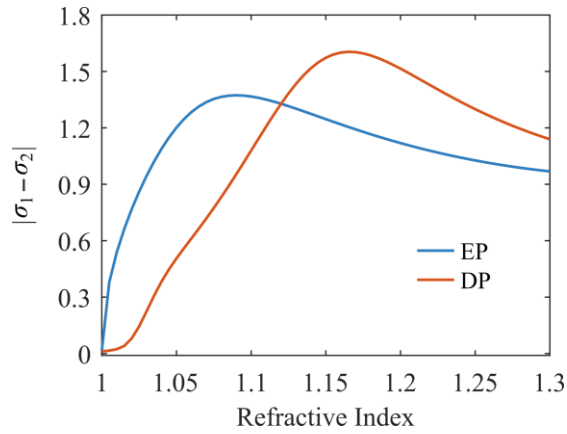
Fig. S12. Sensing with the non-Hermitian MEMS metasurface. The simulated absolute value of the difference of two eigenvalues as a function of the refractive index of the chemical that fills the gap between the chiral gold array and MEMS mirror. The EP mode shows higher sensitivity for ultra-small refractive index changes, while the DP mode is more sensitive to large changes. We could selectively drive the non-Hermitian MEMS sensor to work in the EP or DP mode to detect chemicals at any concentration with high sensitivity. The wavelength, air gap, and dimensions of the chiral meta-atom are the same as those in the main text.

Movie S1. Polarization-resolved optical images for dynamic topological EP-DP transition at λ **= 849.505 nm when four outer electrodes are actuated with alternating voltages at 1 Hz.**

Movie S2. Polarization-resolved Fourier images for dynamic topological EP-DP transition at λ **= 849.505 nm when four outer electrodes are actuated with alternating voltages at 1 Hz.**